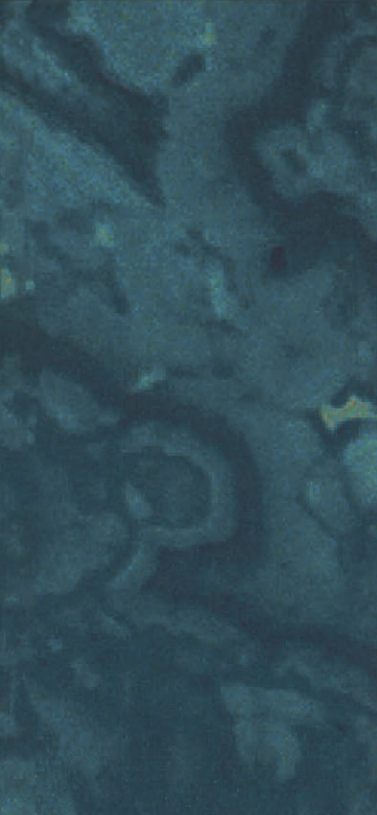
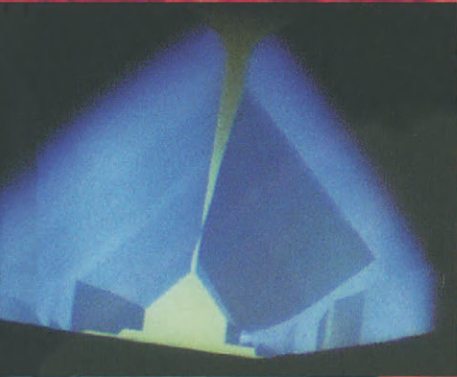


M. Pagel
V. Barbin
P. Blanc
D. Ohnenstetter
(Eds.)

Cathodoluminescence in Geosciences



Springer

M. PAGEL V. BARBIN P. BLANC D. OHNENSTETTER (Eds.)

Cathodoluminescence in Geosciences

Springer-Verlag Berlin Heidelberg GmbH

M. Pagel V. Barbin P. Blanc
D. Ohnenstetter (Eds.)

Cathodoluminescence in Geosciences

With 205 Figures and 37 Tables



Springer

Professor Dr. MAURICE PAGEL
Université de Paris XI
Centre Scientifique d'Orsay
Département des Sciences de la Terre
UMR 8616 Orsayterre Bat 504
91405 Orsay Cedex, France
E-mail: pagel@geol.u-psud.fr

Dr. PHILIPPE BLANC
Université Pierre et Marie Curie
4, place Jussieu
75252 Paris Cedex 05, France
E-mail: Blancmeh@ccr.jussieu.fr

Dr. VINCENT BARBIN
Université de Reims Champagne-Ardenne
Centre de Recherches Agronomiques
2, esplanade Roland Garros
51100 Reims, France
E-mail: vincent.barbin@univ.reims.fr

Dr. DANIEL OHNENSTETTER
Centre de Recherches Pétrographiques
et Géochimiques
15, rue Notre Dame des Pauvres
BP 20
54501 Vandoeuvre-les Nancy Cedex
France
E-mail: dohnen@crpg.cnrs-nancy.fr

ISBN 978-3-642-08526-0

Library of Congress Cataloging-in-Publication Data
Cathodoluminescence in geosciences / Maurice Pagel ... [et al.] (eds.). p. cm.
Includes bibliographical references.
ISBN 978-3-642-08526-0 ISBN 978-3-662-04086-7 (eBook)
DOI 10.1007/978-3-662-04086-7

1. Luminescence spectroscopy. 2. Cathodoluminescence. 3. Geology. I. Pagel, Maurice.
QE33.2.S6 C38 2000 552'.06 21-dc21

This work is subject to copyright. All rights are reserved, whether the whole or part of the material is concerned, specifically the rights of translation, reprinting, reuse of illustrations, recitation, broadcasting, reproduction on microfilm or in any other way, and storage in data banks. Duplication of this publication or parts thereof is permitted only under the provisions of the German copyright Law of September 9, 1965, in its current version, and permission for use must always be obtained from Springer-Verlag Berlin Heidelberg GmbH. Violations are liable for prosecution under the German Copyright Law.

© Springer-Verlag Berlin Heidelberg 2000
Originally published by Springer-Verlag Berlin Heidelberg New York in 2000
Softcover reprint of the hardcover 1st edition 2000

The use of general descriptive names, registered names, trademarks, etc. in this publication does not imply, even in the absence of a specific statement, that such names are exempt from the relevant protective laws and regulations and therefore free for general use.

Cover Design: design & production, 69121 Heidelberg, Germany
Production: ProEdit GmbH, 69126 Heidelberg, Germany
Printed on acid free paper SPIN 10573241 32/3136 Re 5 4 3 2 1 0

Preface

The introduction of the electron microprobe in the 1960s led to cathodoluminescence (CL) becoming a very useful method for mineral studies. From the late 1980s up to now, the development of in situ analytical techniques, such as SIMS and PIXE, promoted the use of CL. The benefit is mutual. On the one hand, growth, structural and alteration patterns revealed by CL are necessary to obtain representative in situ analyses. The section in this volume on geochronology is a good illustration of the importance of CL in U-Pb dating of zircon. On the other hand, a better understanding of CL images requires the use of in situ analyses. The availability of new CL apparatuses which permit the study of minerals that are only slightly luminescent opens up new avenues of research. Several fields are emerging: CL in structural geology and fluid circulation, CL in ceramics, CL in petrology.

Noting this formidable growth of CL in geosciences and geomaterials, a group of French mineralogists (Vincent Barbin, Philippe Blanc, Fabien Cesbron, Daniel Ohnenstetter and Maurice Pagel) decided, at the beginning of 1995, to organize a CL meeting. The International Conference on Cathodoluminescence and Related Techniques in Geosciences and Geomaterials (Nancy, France, September 2–4, 1996) was supported by three scientific societies: Society for Geology Applied to Mineral Deposits (SGA), Society for Luminescence Microscopy and Spectroscopy (SLMS) and Société Française de Minéralogie et de Cristallographie (SFMC) in cooperation with the Institut Lorrain des Géosciences. There were 110 participants from 18 countries; the meeting was held in the “Palais des Congrès”. Some 82 oral and poster communications were presented and the abstracts were printed in a volume of 175 pages.

This Conference was successful in many aspects. The scientific exchanges between geologists and physicists were very constructive and informative. Participants compared their instrumentation and results and expressed their commitment to promote this rapidly developing science.

We gratefully acknowledge the support received from BRGM, CREGU, Elf Aquitaine Production, Jeol, OPEA, Oxford and Total. All the members of the Scientific Committee are thanked for their support, for agreeing to give a lecture and for advertisement of the Conference.

We have selected most of the invited lectures as well as communications of general interest or describing a new approach in CL to be published in this book. For the reviews, we thank Yves Bernabe, Jean Michel Bertrand, Anne Marie Boul-

lier, William L. Brown, Georges Calas, Marc Chaussidon, Stefan Claesson, Michèle Clarke, Lluís Fontboté, Emmanuel Fritsch, Michael Gaft, Jens Götze, John M. Hanchar, Otto Kopp, David Leach, Guy Libourel, Rolf D. Neuser, Gérard Panczer, Matthew R. Phillips, Karl Ramseyer, Guy Remond, Detlev K. Richter, Rolf Romer, Martine M. Savard, Peter D. Townsend and Graham Walker.

Orsay, Reims, Nancy and Paris,
Winter 1999

MAURICE PAGEL, VINCENT BARBIN,
PHILIPPE BLANC
and DANIEL OHNENSTETTER

Table of Contents

Chapter 1

Cathodoluminescence in Geosciences: An Introduction

M. PAGEL, V. BARBIN, P. BLANC, D. OHNENSTETTER 1

Chapter 2

Physical Parameters for the Identification
of Luminescence Centres in Minerals

G. WALKER 23

Chapter 3

Information Encoded in Cathodoluminescence Emission Spectra

P. D. TOWNSEND, A. P. ROWLANDS 41

Chapter 4

Importance of Instrumental and Experimental Factors
on the Interpretation of Cathodoluminescence Data
from Wide Band Gap Materials

G. RÉMOND, M. R. PHILLIPS, C. ROQUES-CARMES 59

Chapter 5

Systematic Cathodoluminescence Spectral Analysis
of Synthetic Doped Minerals:

Anhydrite, Apatite, Calcite, Fluorite, Scheelite and Zircon

P. BLANC, A. BAUMER, F. CESBRON, D. OHNENSTETTER,

G. PANCZER, G. RÉMOND 127

Chapter 6

The Status of the Standards Program of the Society
for Luminescence Microscopy and Spectroscopy

D. J. MARSHALL, O. C. KOPP 161

Chapter 7

Geologic Application of Cathodoluminescence of Silicates

KARL RAMSEYER, JOSEF MULLIS 177

<i>Chapter 8</i> Cathodoluminescence Microcharacterisation of Silicon Dioxide Polymorphs M. A. STEVENS KALCEFF, M. R. PHILLIPS, A. R. MOON, W. KALCEFF	193
<i>Chapter 9</i> Brittle Deformation in Sandstone Diagenesis as Revealed by Scanned Cathodoluminescence Imaging with Application to Characterization of Fractured Reservoirs K. L. MILLIKEN, S. E. LAUBACH	225
<i>Chapter 10</i> High-Resolution Cathodoluminescence Studies of Feldspar Minerals J. GÖTZE, M. R. KRBETSCHKEK, D. HABERMANN, D. WOLF	245
<i>Chapter 11</i> Application of Cathodoluminescence to Carbonate Diagenesis H. G. MACHEL	271
<i>Chapter 12</i> Cathodoluminescence of Carbonate Shells: Biochemical vs Diagenetic Process V. BARBIN	303
<i>Chapter 13</i> Quantitative High Resolution Spectral Analysis of Mn ²⁺ in Sedimentary Calcite D. HABERMANN, R. D. NEUSER, D. K. RICHTER	331
<i>Chapter 14</i> Systems of Interacting Luminescence Centers in Natural Diamonds: Laser-Induced Time-Resolved and Cathodoluminescence Spectroscopy G. PANCZER, M. GAFT, A. MARFUNIN	359
<i>Chapter 15</i> Use of Cathodoluminescence for U-Pb Zircon Dating by Ion Microprobe: Some Examples from the Western Alps D. RUBATTO, D. GEBAUER	373
<i>Chapter 16</i> A Combination of Single Zircon Dating by TIMS and Cathodoluminescence Investigations on the Same Grain: The CLC-Method – U-Pb Geochronology For Metamorphic Rocks ULRIKE POLLER	401

Chapter 17

Relevance of Cathodoluminescence for the Interpretation
of U-Pb Zircon Ages, with an Example of an Application to a Study
of Zircons from the Saxonian Granulite Complex, Germany

U. KEMPE, T. GRUNER, L. NASDALA, D. WOLF 425

Chapter 18

Cathodoluminescence in Applied Geosciences

J. GÖTZE 457

Chapter 19

Cathodoluminescence as a Tool in Gemstone Identification

J. PONAHLÖ 479

Subject Index 501

List of Contributors

BARBIN, VINCENT

Université Reims Champagne-Ardenne, Centre de Recherches Agronomiques,
Laboratoire des Sciences de la Terre, EA 2062,
2 esplanade Roland Garros, 51100 Reims, France
(E-mail: vincent.barbin@univ-reims.fr)

BAUMER, ALAIN

Université de Nice, Unité Mixte de Recherches n 6526, parc Valrose,
06108 Nice Cedex, France

BLANC, PHILLIPE

Université Pierre et Marie Curie, Unité de Recherche Associée,
Centre National de la Recherche Scientifique n°7073,
Boîte 104, place Jussieu, 75252 Paris Cedex 05, France
(E-mail: Blancmeb@ccr.jussieu.fr)

CESBRON, FABIEN

Université d'Orléans, Unité de Recherche Associée,
Centre National de la Recherche Scientifique n1366, EREM-ESEM,
8 rue Léonard de Vinci, 45072 Orléans Cedex 2, France
(E-mail: fabien.Cesbron@wanadoo.fr)

GAFT, MICHAEL

The Open University of Israel, Department of Life and Earth Sciences,
16 Klausner St., 61392 Tel Aviv, Israel
(E-mail: michael@shaked.cc.openu.ac.il)

GEBAUER, DIETER

Swiss Federal Institute of Technology (ETH), Department of Earth Sciences,
Zürich, Switzerland
(E-mail: Gebauer@erdw.ethz.ch)

GÖTZE, JENS

Freiberg University of Mining and Technology, Institute of Mineralogy,
Brennhausgasse 14, 09596 Freiberg, Germany
(E-mail: goetze@mineral.tu-freiberg.de)

GRUNER, TORSTEN

Freiberg University of Mining and Technology, Institute of Mineralogy,
Brennhausgasse 09596 Freiberg, Germany
(E-mail: tgruner@mineral.tu-freiberg.de)

HABERMANN, DIRK

Ruhr-University Bochum, Department of Geology,
44780 Bochum, Germany
Present address: University of Mining and Technology,
Department of Experimental Physics, 09596 Freiberg, Germany

KALCEFF, WALTER

University of Technology, Microstructural Analysis Unit,
Faculty of Science, P.O. Box 123, Broadway, NSW 2007, Sydney, Australia

KEMPE, ULF

Freiberg University of Mining and Technology,
Institute of Mineralogy,
Brennhausgasse 14, 09596 Freiberg, Germany
(E-mail: kempe@mineral.tu-freiberg.de, Fax +49-3731-39-3129)

KOPP, OTTO C.

University of Tennessee, Department of Geological Sciences,
Knoxville, TN 37996, USA
(E-mail: okopp@utk.edu)

KRBETSCHKE, MATTHIAS R.

Saxon Academy of Sciences, Research Group Freiberg,
B.-v.-Cotta Straße 4, 09596 Freiberg, Germany

LAUBACH, STEPHEN E.

The University of Texas at Austin, Bureau of Economic Geology,
Austin, TX 78713, USA
(E-mail: laubachs@begv.beg.utexas.edu)

MACHEL, HANS G.

University of Alberta, Department of Earth and Atmospheric Sciences,
Edmonton, AB T6G 2E3, Canada
(E-mail: hans.machel@ualberta.ca)

MARFUNIN, ARNOLD

3 University of Moscow, Department of Mineralogy,
Leninscic Gory, 119899 Moscow, Russia
(E-mail: marfunin@enigma.geol.msu.ru)

MARSHALL, DONALD J.

Relion Industries, P.O. Box 12, Bedford, MA 01730, USA
(E-mail: dmrelion@world.std.com)

MILLIKEN, KITTY L.

The University of Texas at Austin, Department of Geological Sciences,
Austin, TX 78712, USA
(E-mail: kitty@maestro.geo.utexas.edu)

MOON, ANTHONY R.

University of Technology, Microstructural Analysis Unit,
Faculty of Science, P.O. Box 123, Broadway, NSW 2007, Sydney, Australia
(E-mail: tonym@phys.uts.edu.au)

MULLIS, JOSEF

University of Basel, Institute of Mineralogy and Petrography,
Bernoullistrasse 30, 4056 Basel, Switzerland

NASDALA, LUTZ

Freiberg University of Mining and Technology,
Institute of Theoretical Physics, 09596 Freiberg, Germany

NEUSER, ROLF D.

Ruhr-University Bochum, Department of Geology,
Universitätsstraße 150, 44780 Bochum, Germany
(E-mail: Rolf.D.Neuser@ruhr-uni-bochum.de)

OHNNSTETTER, DANIEL

Centre de Recherches Pétrographiques et Géochimiques,
Centre National de la Recherche Scientifique,
BP 20, 15, rue Notre Dame des Pauvres,
54501 Vandoeuvre-lès-Nancy Cedex, France
(E-mail: dohnen@crpg.cnrs-nancy.fr)

PAGEL, MAURICE

Université de Paris XI
Centre Scientifique d'Orsay
Département des Sciences de la Terre
UMR 8616 Orsayterre Bat 504
91405 Orsay Cedex, France
(E-mail: pagel@geol.u-psud.fr)

PANCZER, GÉRARD

Université Claude Bernard Lyon 1, Laboratoire de Physico-Chimie
des Matériaux Luminescents, Unité Mixte de Recherche,
Centre National de la Recherche Scientifique n5620, 43,
Boulevard du 11 novembre 1918,
69622 Villeurbanne Cedex, France
(E-mail: panczer@univ-lyon1.fr)

PHILLIPS, MATTHEW R.

University of Technology, Microstructural Analysis Unit,
Faculty of Science, P.O. Box 123, Broadway, NSW 2007, Sydney, Australia
(E-mail: matthew.phillips@uts.edu.au)

POLLER, ULRIKE

Max Planck Institute for Chemistry, Department of Geochemistry,
P.O. Box 3060, 55020 Mainz, Germany
(E-mail: ulrike@geobar.mpch-mainz.mpg.de)

PONAHLO, JOHANN

Department for Mineralogy and Petrography,
Museum for Natural History, Burgring 7, 1014 Vienna, Austria
(Fax: 004318764904)

RAMSEYER, KARL

University of Bern, Institute of Geology,
Baltzerstrasse 1, 3012 Bern, Switzerland
(E-mail: karl.ramseyer@geo.unibe.ch)

RÉMOND, GUY

32 Avenue de la Mouillère, 45100 Orléans, France
Present address: University of Sydney, The Australian Key Centre for Microscopy
and Microanalysis, Australia
(E-mail: guy@valcofim.fr)

RICHTER, DETLEV K.

Ruhr-University Bochum, Department of Geology, 44780 Bochum, Germany

ROQUES-CARMES, CLAUDE

Laboratoire de Microanalyse des Surfaces, ENSMM, Besançon, France
(E-mail: lms-sec@ens2m.fr)

ROWLANDS, ALEC P.

University of Sussex, Chemistry, Physics and Environmental Science,
Brighton BN1 9QJ, United Kingdom

RUBATTO, DANIELA

Department of Earth Sciences,
Swiss Federal Institute of Technology (ETH),
Zürich, Switzerland

Present address: The Australian National University, Research School of Earth
Sciences, Mills Road, 0200 ACT Canberra, Australia,
(E-mail: Daniela.Rubatto@anu.edu.au)

STEVENS KALCEFF, MARION A.

University of Technology, Microstructural Analysis Unit,
Faculty of Science, P.O. Box 123, Broadway, NSW 2007, Sydney, Australia
(E-mail: marion@phys.uts.edu.au)

TOWNSEND, PETER D.

University of Sussex, Chemistry, Physics and Environmental Science,
Brighton BN1 9QJ, United Kingdom
(E-mail: P.D.Townsend@sussex.ac.uk)

WALKER, GRAHAME

Physics Department, UMIST, P.O.Box 88, Manchester, M60 1QD, United Kingdom
(E-mail: Grahame.Walker@UMIST.ac.uk)

WOLF, DIETER

Freiberg University of Mining and Technology, Institute of Mineralogy,
Brennhausgasse 14, 09596 Freiberg, Germany
(E-mail: wolf@mineral.tu-freiberg.de)

Cathodoluminescence in Geosciences: An Introduction

MAURICE PAGEL, VINCENT BARBIN, PHILIPPE BLANC,
DANIEL OHNSTETTER

1

Introduction

A wide variety of processes induces different kinds of luminescence, which is an emission of photons mainly in the visible domain (Marfunin 1979; Machel et al. 1991):

- *Radioluminescence* is excited by X-ray photons, γ -rays, and α and β nuclear particles bombardment.
- *Chemiluminescence* is the result of chemical reactions (chemical radicals, oxidation of phosphorus, etc.).
- *Electroluminescence* is generated by application of an electric field.
- *Triboluminescence* is due to mechanical deformation (breaking of crystals bonds).
- *Ionoluminescence* is generated under energetic ion beam, for example in an ion microprobe.
- *Bioluminescence* is generated by biological processes.
- *Thermoluminescence* is light emission due to an activator in a mineral when the mineral is heated and is also referred to as thermally stimulated relaxations (McKeever 1985).
- *Photoluminescence* involves the selective energy of photons to excite electronic levels of luminescent centers.
- *Cathodoluminescence* is produced by energetic electrons.

Thermoluminescence (TL), photoluminescence (PL) and cathodoluminescence (CL) are the most common luminescence phenomena used for studying minerals. Two types of light emissions occur: fluorescence, in which light is emitted during less than 10^{-8} s, and phosphorescence, when the luminescence effect persists longer than 10^{-8} s (Garlick 1949; Leverenz 1950; Curie 1960). As pointed out by Tarashchan and Waychunas (1995), these terms give no information about the kinetics of the emission and of the energy transfer processes and the distinction between what is slow or fast is arbitrary.

2 History

As stated by Leverenz (1950), the term “phosphor” was introduced in 1603 by Casciarolo of Bologna, Italy, and named after the Greek “phosphoros=light bearer” for natural solids that have glowing properties in the dark after daylight exposure. The term luminescence, from Latin “lumen=light +escence”, was introduced in 1888 by Wiedemann (quoted in Nichols et al. 1928). Hittorf (1869) observed the green emission of a glass under cathodic excitation (quoted in Urbain 1909). In 1879 Crookes examined the first samples under cathodoluminescence: synthetic calcium sulfides shine blue-violet, yellow, orange; diamonds are the most luminescent with bright blue, pale blue, apricot, red yellowish-green orange and bright green hues; natural and synthetic rubies glow red; emeralds give a crimson-red color; sapphires appear bluish gray; cassiterite, called “tinstone” gives a pale yellow light. In the same paper, Crookes (1879) also described the cathode-luminescence of zircon as follows: “ In an optically positive crystal the ordinary ray (ω) was of a pale pink hue, the extraordinary ray (ϵ) of a very beautiful lavender-blue color. In another crystal, like the former from Expailly (Espally, Haute-Loire, France; see Lacroix 1893), the ordinary ray (ω) was pale blue, the extraordinary ray (ϵ) of a deep violet. A large crystal from Ceylon (Sri Lanka) gave the ordinary ray (ω) of a yellow color, the extraordinary ray (ϵ) of a deep violet-blue.” Crookes (1879) has thus emphasized that zircon can have different hues under electron bombardment, corresponding to the two main zircon populations defined by CL (Ohnenstetter et al. 1991), and that the color varies according to the different refractive indices. This could correspond to the polarization effect which was later reported by Görz et al. (1970) and Cesbron et al. (1993, 1995). Lecoq de Boibaudran observed, in 1885, the different fluorescences of rare earths and that, while Y and La give no fluorescence, Yb, Tm and Er give narrow peaks (Lecoq de Boibaudran 1887). In the same year, Demarçay (1887) recorded the spectra for Pr, Nd (called “didyme” at that time) and Sm. Crookes (1880a,b) shows, in the study of yttrium and samarium spectra, also the importance of a chemical control of the different spectra. “... c’est que les conclusions tirées de l’analyse spectrale per se sont sujettes à de graves causes de doute, à moins qu’à chaque pas le spectroscopiste ne donne la main au chimiste. La spectroscopie peut nous fournir de précieux renseignements, mais la Chimie doit après tout rester la cour suprême d’appel” (Crookes 1880b). Servigne and Vassy (1937) and Servigne (1937) showed that 10^{-6} g Sm could be detected by spectroscopy in solution and that the Sm band is proportional to its concentration. Servigne (1938) showed that Sm, Eu, Dy have small peaks and that some rare earth elements (REE) could exhibit emission in the near infrared. All the spectroscopic properties of rare earths have been summarized by Wybourne (1965). In 1885, Becquerel observed that calcite (“spath d’Islande”) is orange, quartz is yellow, and aragonite is green under electric discharge in a vacuum tube. The Mn activator in calcite was discovered in 1859 by Becquerel (quoted in Nichols et al. 1928). Schulman et al. (1947) showed that auxiliary impurities such as lead, thallium and cerium play a role as sensitizers. Medlin (1959, 1961, 1963, 1964, 1967) extensively studied calcite by TL and found that beside Mn^{2+} , Pb^{2+} is also an activator whereas Fe^{2+} , Co^{2+} and Ni^{2+} are

quenchers. The limestones and dolomites from Belgium were studied by CL in 1969 by Martin and Zeegers and the quenching effect of iron in dolomite was also demonstrated by CL (Pierson 1981; Walker 1983). The incorporation of REE oxides into some minerals and their luminescence properties were pointed out by Blase (1970), Blase and Bril (1967) and Calderon et al. (1983, 1984). The energy levels for Mn^{2+} in calcite were given by Aguilar and Osendi (1982). In fluorite and apatite, luminescence due to REE was studied by Wick (1924), Haberlandt (1934, 1938) and Haberlandt et al. (1934). Luminescence was abandoned in the 1920s (White 1975). However, the study of luminescence reached a peak during the late 1940s and mid-1950s, with extensive literature on phosphors (Kröger 1948; Garlick 1949; Pringsheim 1949; Leverenz 1950). This was followed by a new decline in the mid-1960s. Apatites from different environments were studied by PL (Portnov and Gorobets 1969). CL petrography under the microscope with a cold cathode was developed (Weiblen 1964; Mariano 1978; Marshall 1988). The development of the electron probe by Castaing (1951) and the wide use of this instrument in geosciences brought new interest in the in situ CL observations under the electron beam.

Emission of CL, observed using an electron probe micro-analyzer (EPMA) or a scanning electron microscope (SEM), has been used as a petrologic tool since the studies of Long and Agrell (1965), Smith and Stenstrom (1965), Coy-Yll (1969), Rémond (1977) and Nickel (1978). CL images of minerals can be compared with secondary (SE) or backscattered electron images (BSE) and X-ray mapping (Rémond 1977; Rémond et al. 1970, 1992, 1995). Such image comparisons have recently been made for zircon crystals (Henry and Toney 1987; Hanchar and Miller 1993; Hanchar and Rudnik 1995; Rémond et al. 1992, 1995). Since the pioneer work of Mariano and Ring (1975) and Mariano (1978), only a few CL images and/or CL spectra have been made in the field of igneous petrology (Mariano 1988, Roeder et al. 1987; Mariano 1989; Rae and Chambers 1988; Hayward and Jones 1991; Wenzel and Ramseyer 1992; Blanc et al. 1994; Koberski and Keller 1995; Coulson and Chambers 1996) compared to those reported in the sedimentary petrology literature (Sippel and Glover 1965; Sommer 1972 a, 1972 b; Meyers 1974; Gies 1976; Ebers and Kopp 1979; Amieux 1982, 1987; Frank et al. 1982; Fairchild 1983; Machel 1985; Banner et al. 1988; Barbin et al. 1989; Hemming et al. 1989; Meunier et al. 1990; Machel et al. 1991; Machel and Burton 1991; Major and Wilber 1991; Walker and Burley 1991; also see references in Baker and Kopp 1991; Demars et al. 1996; Seyedolali et al. 1997). Lunar rocks have also been studied by CL (Sippel 1971). CL microscopy is an efficient method for revealing growth zoning in minerals (Have and Heijnen 1985; Reeder and Prosky 1986; Marshall 1988; Raven and Dickson 1989; Vavra 1990, 1993, 1994; Reeder 1991; Ohnenstetter et al. 1991; Widom et al. 1993; Hanchar and Rudnik 1995) or for recognizing those minerals which are often difficult to identify such as wöhlerite (Mariano and Roeder 1989). Doped minerals have been synthesized to assign the different peaks observed in natural samples to the different activators (Morozov et al. 1970; Mariano and Ring 1975; Have and Heijnen 1985; Mason and Mariano 1990; Machel et al. 1991; Cesbron et al. 1993, 1995; Fillippelli and Delaney 1993; El Ali et al. 1993; Blanc et al. 1995, 2000; Baumer et al. 1997; Mitchell et al. 1997). Laser induced microluminescence (LIL) allows spectral and kinetic studies of luminescence

through a time range of a few nanoseconds to milliseconds, as shown by Blanc et al. (2000, this Vol.), Panczer et al. (2000, this Vol.) and Rémond et al. (2000, this Vol.). The distribution of Mn^{2+} in the different sites in carbonates has been determined (El Ali et al. 1993) by coupling of CL and electron paramagnetic resonance (EPR). Thus CL coupled with other analytical techniques such as EPMA, EPR, SEM, particle induced X-ray emission (PIXE), transmission electron microscopy (TEM) and secondary ion mass spectrometry (SIMS) is a powerful tool in geosciences.

3 Luminescence Phenomena

Interaction between electrons and solids under TEM are of three types: (1) unscattered electrons which pass through the sample, (2) elastically scattered electrons due to interaction with nuclei of the atoms, and (3) complex inelastically scattered electrons (Morgan 1985; Eberhardt 1989). Under SEM and EPMA only the two latter phenomena occur. Inelastically scattered electrons interact with electrons of the atoms and their nuclei and are characterized by a loss of energy transferred to the sample. Electron-matter interactions (Morgan 1985, Eberhardt 1989, Reed 1975, Heinrich 1981) produce ionization of the atoms from the sample with: (1) emission of characteristic X-rays from the inner shell of an atom (shells K, L, M) which can be analyzed by a wavelength dispersive spectrometer (WDS) or by an energy dispersive spectrometer (EDS), (2) a continuum radiation or bremsstrahlung, (3) low energy (<50 eV) SE used in topographical imaging, (4) high energy (close to incident energy) back scattered electrons (BSE) which provide a compositional image, (5) Auger electrons which consist of electrons ejected from the outer shell and (6) CL, characterized by long wavelength (in the domain ranging from UV to visible to IR) photons.

Different types of interaction between photons and crystals occur: some are reflected from the mineral surface, some are refracted, some are absorbed and some pass through the mineral with no real interaction.

The CL activators are trace elements that are present in a mineral at equivalent valence states within specific sites in the crystal lattice. The valence electron is captured by the conduction band and when it returns to its equilibrium state yields a photon with a determined wavelength corresponding to the gap of energy, or to the sub-levels of the radiative transitions. The activators are transition elements, REE and actinide ions. The CL emission spectra are associated with two types of transitions, i.e., *f-f* and *f-d* transitions (Tarashchan 1978; Marfunin 1979; Remond et al. 1992; Barbin and Schvoerer 1997). The *f-d* transitions are broad (Imbusch 1978) and the *f-f* transitions are responsible for the narrow lines (Marfunin 1979; Gorobets and Walker 1995). According to Monod-Herzen (1966) only Sm, Eu, Gd, Tb, and Dy exhibit narrow emission lines, Pr, Nd, Ho, Er and Tm show narrow emission peaks and La, Ce Yb and Lu give broad emission bands.

The literature contains numerous values for the transitions of these trace elements, nevertheless collecting the spectra of synthetic doped crystals is the simplest way to constitute a reference data bank (Blanc et al. 2000, this Vol.).

It is necessary to know the symmetry of the site and the valence of the trace element in each crystal. Dy^{3+} in the Ca I site of a chlorapatite emits at 480 and 574 nm. This example is similar to emissions with narrow peaks, but there are also broad bands like those of Mn^{2+} . The REE narrow peaks allow recognition, without possibility of error, of the excitor; however, broad bands are often more ambiguous. For this reason, it is possible to misidentify the correct assignments of Mn and Th in apatite. Qualitative recognition of CL excitators is possible by comparison with synthetic mineral spectra from a data bank. It is possible to index the different observed REE peaks and to assign the peaks to transition energy levels (Dieke 1968).

There are other ways to recognize the nature of the emission center (Walker 2000, this Vol.), although these are rarely used in geosciences. In the future, variation of recording temperatures and luminescence decay time will probably be used more frequently.

In this volume, the nature of activators are further discussed in silicates by Ramseyer and Mullis (2000), in feldspars by Götze et al. (2000), in silicon dioxide polymorphs by Stevens Kalceff et al. (2000) and in carbonates by Machel (2000) and Barbin (2000). A special mention must be made of the work of Stevens Kalceff et al. (2000, this Vol.), who show that the intrinsic defects are significant contributors to the CL emission of SiO_2 .

4 Cathodoluminescence Techniques

The CL analytical system could be subdivided in two types: (1) CL attachment to electron microprobe, scanning electron microscope and transmission electron microscope and (2) CL generated by an electron gun coupled to an optical microscope. Other combinations are possible such as the attachment of a hot cathode to an optical microscope (Ramseyer et al. 1989).

4.1 Cold Cathode Optical Microscope Cathodoluminescence System

In cold cathode microscopic equipment, the electrons are generated by an electric discharge between two electrodes under a low gas pressure (Marshall 1988; Rémond et al. 1992). The commercially available CL stages consist of an electron gun, a vacuum chamber with windows and an X-Y stage movement. The conditions are usually 17 keV (15 ± 5 keV) and 450 mA. The advantages of using this type of equipment are:

- The low price of the stage, which is adaptable to an optical microscope.
- Easy to use due to the simple low vacuum system.
- A large field of observation, up to 2 cm.
- No coating is necessary, the positive ions generated in the gas phase are sufficient to neutralize the charge effects.
- Easy check of the chemical composition of minerals when coupled to an EDS.

This apparatus is useful in petrologic studies, but there are several inconveniences:

- Low spatial resolution.
- Instability due to variation of the gas pressure in many apparatuses.
- Damaging of the surface from the electron bombardment.
- Integral luminescence in the visible domain.
- The recording system generally gives qualitative results only, although some devices are now equipped with a CL spectrometer.

Recently, new cold CL equipment was introduced by the OPEA (Laboratoire d'Optique Electronique Appliquée). This apparatus allows both better observations and spectral analysis because the stability is very good. The beam current may be more than 20 keV with a 320 mA or less beam current density. The use of argon as residual gas improves the stability (Barbin and Hoan, pers. observ.).

4.2

Hot Cathode Cathodoluminescence

The electron gun can be associated with a SEM (Rémond et al. 1970) (Fig. 1) or an EPMA or with an optical microscope (Ramseyer et al. 1989). The electrons are generated by heating a filament (2000–3000 °C) and are focused on the sample by magnetic optics. Compared to the cold CL system, the advantages are:

- Good spatial resolution due to the low size of the electron beam.
- High magnification.
- Possibility of imaging at a given wavelength.
- Coupling with BSE and X-ray mapping.
- Local higher current density.

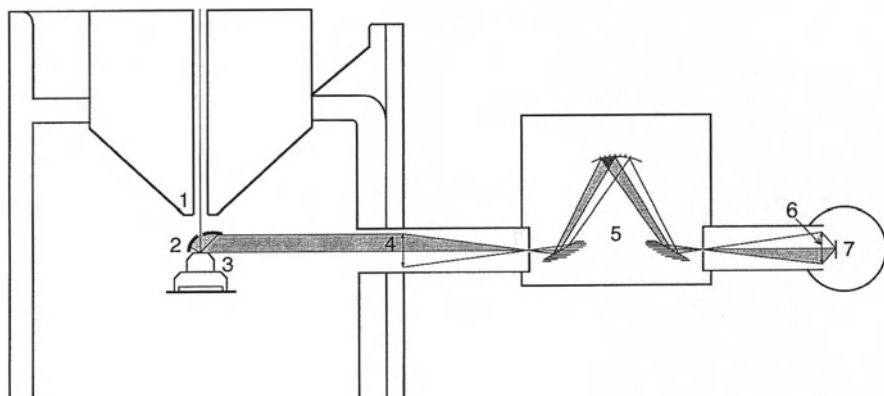


Fig. 1. The Blanc-Perray CL apparatus. 1 Electron gun; 2 parabolic mirror; 3 sample; 4 silica lens; 5 monochromator; 6 condenser; 7 photomultiplier

Some disadvantages are:

- Coating is absolutely recommended (carbon, aluminum, nickel, palladium or gold).
- A high vacuum is necessary.
- For SEM-CL, phosphorescence phenomena induce difficulties in obtaining images in some material (e.g., calcite).
- For SEM-CL, images are always in black and white (a recording in false color is also possible).

In hot CL, the conditions depend on the response of the different samples. It should be noted that the luminescence of Nd doped YAG is observed from 5 kV.

The spectrum could be divided into different wavelengths, corresponding to various energies, the farthest in the UV being the more energetic. In accordance with these conditions, the bombardment may excite the spectrum more or less completely. For shorter wavelengths, more energy is necessary to excite these emissions.

The value of the high voltage between the filament and the anode determines the energy of the electrons. It has been shown that the maximum of excitation for a given crystal is not always the highest acceleration voltage. To obtain CL images, it is typical to work with 10^{-7} A. SE images are obtained with very low beam currents, in the region of 10^{-10} A, and the BSE images at 10^{-9} A. The resolution of the image will be affected by the beam current. Increasing magnification decreases the scanning surface, consequently the value of the electric intensity increases. It is necessary to take into consideration the current intensity and the surface area to reduce excessively destructive conditions. The mirror collector has been calculated for a precise working distance of the sample, therefore the focusing distance from the sample must be always adjusted.

The acquisition of a spectrum is made under two chosen slits to obtain a given resolution of the spectrum. The acquisition of a panchromatic or monochromatic image requires working, respectively, through the spectrometer at the zero position, or at a precise wavelength (e.g. 575–579 nm for Dy^{3+}), with slits corresponding to the width of the peak. If the sample shows a strong emission, it is possible to use finer slits, thus increasing the resolution (Fig. 2). However, it is preferable to analyze with given slits under conditions that give higher quality spectra. For example, slits of 1 mm correspond to 8 nm of dispersion and slits of 0.1 mm to 1 nm of resolution with the equipment described in Fig. 1. It is recommended to work in the zone in which the photomultiplier gives a linear response. This value should not be exceeded, otherwise distortion and noisy spectra will appear.

5

Quantification of Mineral Phases by Cathodoluminescence

There are several methods available for quantification of mineral phases under optical microscopy or SEM. However, it is very difficult to recognize several generations of the same mineral, For example, with optical microscopy it is very dif-

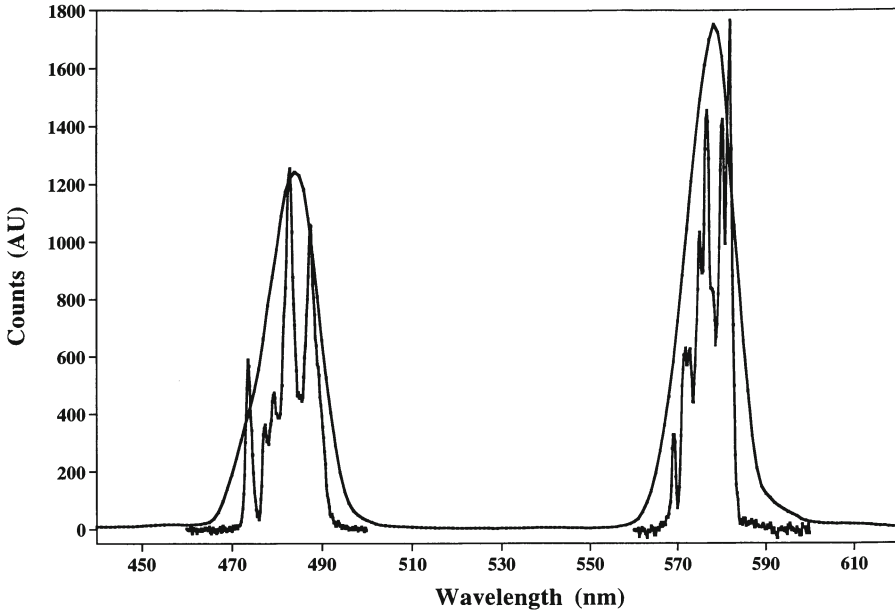


Fig. 2. Spectra of a zircon doped with Dy^{3+} . Comparison between 1 and 8 nm resolution spectra showing the fine structure of the emission peaks. Analytical conditions: carbon coating, accelerating voltage 25 keV, beam current 10^{-7} A, room temperature

difficult to recognize all the quartz overgrowth areas in one thin section of sandstone (Evans et al. 1994; Demars et al. 1996).

Quantification of mineral phases is important especially in diagenetic processes because the percentage of one mineral cement may be the main factor controlling the porosity in a sedimentary formation. Automatic analysis of both BSE and CL images has been successfully applied to determine the volume of detrital quartz and authigenic quartz in sandstones. On a SEM about eight images per standard thin section should be collected to get representative results, depending on the amount of quartz cement and the magnification (Evans et al. 1994). This allows rapid quantification of a large number of samples with an excellent reliability and reproducibility. Other techniques such as chemical analyses could be used but they require longer times for image acquisition.

6

Cathodoluminescence Spectral Analysis

The spectral field of CL is limited by the capabilities of the detector. It covers the UV, visible and IR domains. Each apparatus possesses its own spectral field defined by the necessities of a given study. For semi-conductors the infra-red domain is studied with a germanium detector. In earth sciences, CL studies have begun in the visible domain. However, present studies also are in the UV and IR

domains. The spectral field 200–900 nm is accessible by a detector alone, if every optical part is UV transparent, e.g., for a high UV quality silica glass. The spectrometers and spectrographs with low resolution (1 nm at 500 nm, with a dispersion of 8 nm by a slit of 1 mm) permit obtaining spectra of weak luminescent materials with enough definition to recognize the different REE contribution.

According to the report of the standards program of the Society for Luminescence Microscopy and Spectroscopy (Marshall and Kopp 2000, this Vol.), there are large variations among laboratories either in spectral acquisition capability or photographic recording. It is therefore necessary to report all experimental data in publications and to be very cautious when comparing data obtained from different laboratories. Standardization of CL is urgently needed to increase the recognition of CL in geosciences.

Each CL system must be calibrated for the detector system response characteristics including the monochromator and photomultiplier. The correction curve is obtained by standardization of the ratio of the experimental and theoretical spectrum of a standard lamp covering the same spectral field (Fig. 3). The main difficulty of this method of calibration is that it is impossible to obtain a standard lamp that covers the entire spectrum. In the UV range, a deuterium lamp is used up to 350 nm, whereas from 350–400 nm to near IR region, a xenon lamp or a quartz-iodine lamp is recommended to obtain the normalization curve. The wavelength is calibrated with a standard Hg lamp.

The best method should use a well-known activator in a known spectral domain with continuous emission covering the entire spectrum. For this reason,

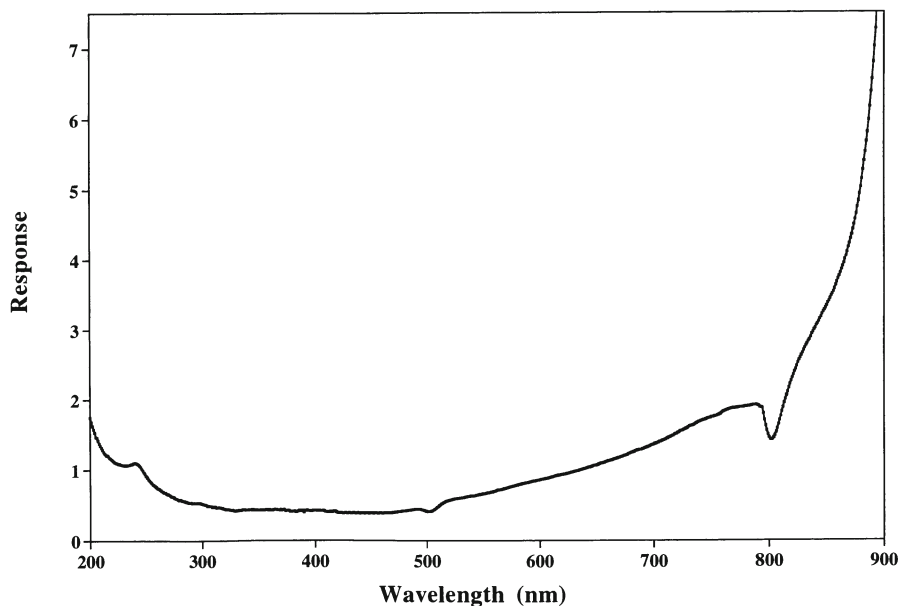


Fig. 3. An example of a correction curve for total CL apparatus response: the Blanc-Perray apparatus at the Pierre and Marie Curie University in Paris

it is proposed to use a well known standard, such as the Nd-doped YAG, with emissions covering the 250–900 nm range. At the same time, this standard permits measuring both the spectral resolution and the spatial homogeneity of the image collected by the mirror.

7

Analytical Conditions

The spectrum of a doped crystal is not the same when it is presented with its *c* axis parallel to the mirror axis, or perpendicular to it (Remond et al. 1995). Thus, the CL emission is polarized. This effect is very strong in the self-activated peaks and is also observed in the narrow REE peaks because the multiplets are modified.

In the preparation of CL study, thinning by emery powder creates a dead or destructured layer that is removed by polishing to observe the maximum luminescence. A well-polished slab or thin section is necessary to obtain a good CL image.

The CL emission is linked to the temperature for both the position and the width of the peaks. Close to 0 K, the transitions are phonon-free, pure and noiseless. Therefore, the peaks appear as narrow lines and with a much higher intensity. For example, quartz has an intensity multiplied by 100 or 1000, when changing from room temperature to $-100\text{ }^{\circ}\text{C}$ (Hanusiak 1975; Hanusiak et al. 1975). The electronic beam increases strongly the temperature of the sample. This emphasizes the problem for the beam conditions in the scanning mode: focused or not focused spot, slow scan or TV scan.

The observed colors are not stable over time with an optical microscope. In the first seconds there is a fugacious emission and therefore the sample is difficult to photograph. Afterwards, there is a new color set-up which is often stable. Instead of optical observation of the colors, it is possible to record these changes in spectra. With CCD detectors, the entire spectrum is recorded in a very short time and can be recorded repeatedly. Instead of using the mean or the sum of the spectra, it is more efficient to observe the variation at a given wavelength with time. The CL spectrum from 200–900 nm requires 4 min with a simple detector, i.e. a photomultiplier behind a spectrometer. The decreases or increases are diverse, sometimes intricate variations with changes in the rate of decrease (Figs. 4, 5).

The intensity could increase with time when new centers are created under the electron beam. In this case, self-activated peaks corresponding to bound defects or oxygen vacancy, the number of defects increases under the beam with time.

One of the new and very interesting approaches is valence changing during electron bombardment. For example, Eu^{3+} ions can capture electrons and be reduced to Eu^{2+} ions (Barbin et al. 1996; d'Almeida 1997). Spectrum of the CL emission of Eu-doped CaF_2 crystals have been made at 77 K and peaks at 424 nm and 588 nm are observed corresponding to the emission of Eu^{2+} and Eu^{3+} , respectively. Under continuous electronic bombardment at regular time intervals, increased Eu^{2+} and decreased Eu^{3+} emissions are observed, which means that the charge conversion mechanism is not totally reversible (d'Almeida 1997).

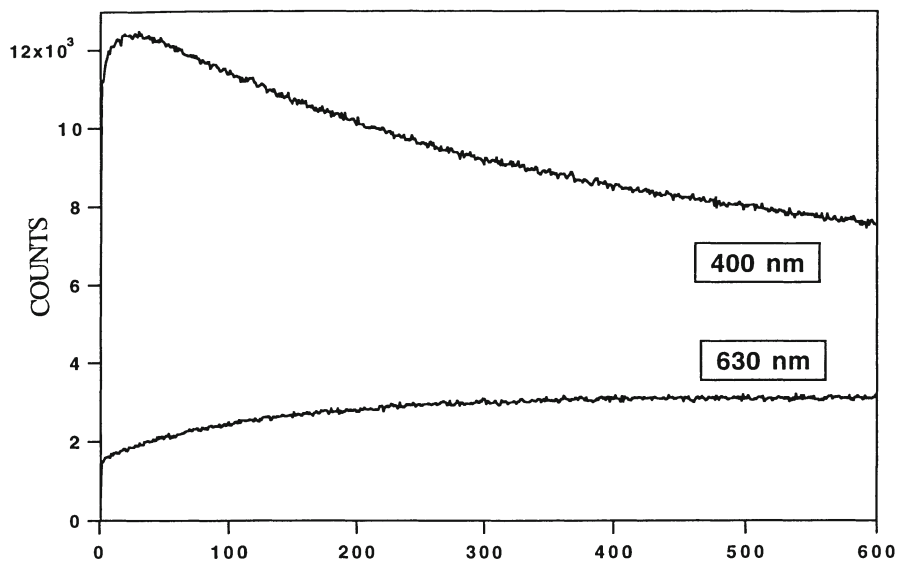


Fig. 4. Variation of the CL intensity with time in quartz at 400 and 630 nm. Analytical conditions: carbon coating, accelerating voltage 25 keV, beam current 10^{-7} A, room temperature

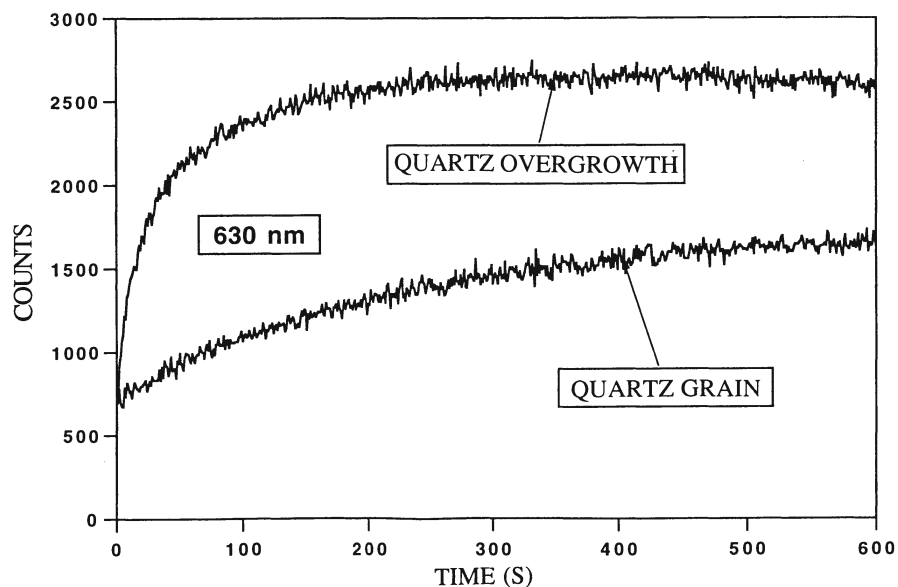


Fig. 5. Variation of the CL intensity with time in a detrital quartz grain and its quartz overgrowth at 630 nm. Analytical conditions: carbon coating, accelerating voltage 25 keV, beam current 10^{-7} A, room temperature

8 Cathodoluminescence Applications

Cathodoluminescence is a very informative method for trace element identification in minerals. In some cases, no additional data can be obtained relative to BSE images, or to observations with an optical microscope. For other cases, CL studies give unique information that cannot be easily obtained with other methods. For example, CL studies can provide the distribution of trace elements in certain minerals, the existence of different mineral species with low trace amounts, the healed microfractured or the recrystallized area of crystals, etc. The recent development of in situ analytical methods (PIXE, SIMS, ICPMS with laser ablation) requires excellent knowledge of the analyzed minerals in order to reduce the number of analyses necessary to obtain representative compositions (the meaning of an analysis on different zones could be misleading). When using CL, it is necessary to make observations at different scales and for different purposes. However, as Machel (2000) points out, many factors govern the CL color, intensity and zonation pattern of carbonates and there are numerous pitfalls in correlation and back-calculation of fluid composition.

Some of the main applications of CL in the field of geosciences are presented below. However, the number of applications is presently restricted and many more applications should appear in the future.

8.1 Quantitative Separation of Different Mineral Species

The general CL characteristics of minerals could be used to improve and facilitate petrographic studies. It is easier to recognize the mineral species from a quick look by CL and easy to estimate the percentage of the mineral present in a given sample. To illustrate the usefulness of CL in petrography, three cases are cited. The presence of kaolinite in a clay cement can easily be detected by its bright blue luminescence. If there is a close association of calcite and aragonite, CL is well adapted because the Mn CL band is located at 615 nm for calcite and 540 nm for aragonite (Sommer 1972a; Barbin 2000). The blue CL luminescence of K-feldspar is easily differentiated from the green color of plagioclase (Götze et al 2000, this Vol.). In gemology, CL is an interesting tool because it is a non-destructive, quick and accurate method to differentiate a natural gemstone from a synthetic one (Ponahlo 2000). However, no general rules could be given and CL alone is not a method for mineral determination.

8.2 Evidence of Different Mineral Generations from Cathodoluminescence Observations

For certain minerals, it is often difficult to recognize the different generations if present in a thin section. Quartz is the best example because it contains very low trace element amounts. CL is well adapted to classify the different detrital quartz

grains in a siliciclastic rock. The recognition of different generations of carbonates is also an easy task with CL. Some recent observations of ash material show the importance of CL for the differentiation of glass (Götze 2000). The application to minerals of carbonatites, with new luminescent minerals such as götzenite and ramsayite, is useful in understanding the paragenetic evolution of carbonatitic melts (Verhulst et al. 1997). The use of CL for U-Pb dating is illustrated by three examples in this volume. Rubatto and Gebauer (2000) and Kempe et al. (2000) selected zones in zircon, based on CL studies, for U-Pb dating by SHRIMP (sensitive high resolution ion microprobe). Even if such an apparatus is not available, an investigation of a zircon population by CL permits selection of a few grains which are representative of the different geological events (Poller 2000, this Vol.).

8.3

Zonation of Crystals

One of the most interesting CL observations is the identification of zoning in crystals. This is absolutely crucial for application of the new chemical and isotopic in-situ methods. Reeder (1991) has convincingly demonstrated that in carbonate four types of zoning could be observed: growth zoning, oscillatory zoning, sectorial zoning and intrasectorial zoning. The existence of these two latter types of zoning has also been observed in quartz.

This zoning results from disequilibrium partitioning on crystallographically non-equivalent faces or parts of faces. CL is also used to reveal the growth lines in carbonate shells (Barbin et al. 1991; Barbin 2000).

8.4

Microfracturing, Brecciation, Crushing

The existence of a microfractured healed plane is easily detected in many minerals by CL observations. The primary and secondary fluid inclusions are easily differentiated from their location on growth zones or on healed microfractures.

It should be remembered that an isolated inclusion can be located on a healed microfracture. In certain cases of recrystallization, CL is a powerful approach to detect brecciation events (Milliken and Laubach 2000, this Vol.). In other cases, it is also important to show that no fracturing has occurred. The importance of CL in fractured siliciclastic hydrocarbon reservoirs is illustrated by Milliken and Laubach (2000, this Vol.).

8.5

Textural Relationships Between Minerals

Cathodoluminescence observations can help to establish the succession of paragenetic associations in rocks, especially when considering growth zones, microfracturing, dissolution and recrystallization grain-boundary alteration features. For example, the ghost of a fossil could appear in a carbonate area. The observation of tiny mineral inclusions in glass will be easier using CL.

8.6

Location of Trace Elements

In some cases, it is important to know if trace elements are located in a crystal lattice or sorbed on its surface. For example, REE can be located by CL analysis of carbonate at levels down to 0.1 ppm (Habermann et al. 2000).

8.7

Zone of Past α -Irradiation

Radiation-damage due to α particles in quartz is not visible under transmitted light by optical microscopy but could easily be revealed by CL (Owen 1988; Meunier et al. 1990). The width of the rim agrees well with the Bragg-Kleeman rule and corresponds to the most energetic particles in the ^{238}U -series. CL is useful to recognize ancient zones or episodes of accumulation and leaching of α -emitting particles from the U-series.

A more detailed discussion and further applications to silicate (Ramseyer and Mullis 2000), feldspars (Götze et al. 2000) and carbonate (Machel 2000 and Barbin 2000) can be found in this volume. Two chapters in particular deal with the applications of CL in applied geosciences (Götze 2000, this Vol.) and gemology (Ponahlo 2000, this Vol.). Götze emphasizes the role of CL in industrial raw materials, products of coal and waste combustion, metallurgical slags and dust, ceramics, glasses, refractory materials and archaeological materials.

9

Conclusion and Perspectives

During the last few decades, CL has often been used to provide beautiful color images which were sometimes overinterpreted (see Machel 2000, this Vol.). CL is now becoming much more quantitative, but fundamental research is still needed as CL is the least understood method in luminescence phenomena (Townsend and Rowlands 2000, this Vol.). Furthermore, there are large variations among laboratories, either in spectral acquisition capability or photographic recording (Marshall and Kopp 2000, this Vol.). It seems necessary to bring together physicists and geologists in order to properly interpret CL information. As discussed above, and suggested in all the chapters published in this book, much more could be done with CL.

Before discussing trace elements distribution from color pictures, it is necessary to determine the CL bands that explains the total luminescence. It is necessary to correct the spectra and to accomplish spectral deconvolution. Variation of the intensities of the different trace elements must be understood. After completion of these normalizing processes, a data bank should be established and published (Blanc et al. 2000, this Vol.).

As shown by Habermann et al. (2000, this Vol.), CL spectrometry can be used to obtain semi-quantitative analyses of certain trace elements. Due to the complexity of spectra, sensitization and annealing, CL spectrometric analyses of trace

elements would certainly remain semi-quantitative but they present the advantages of being rapid and of high sensitivity.

The use of CL can assist in the dating field, as already shown for the U-Pb method (Rubatto and Gebauer 2000; Kempe et al. 2000; Poller 2000, this Vol.), and can also be useful for other applications such as ^{40}Ar - ^{39}Ar dating of feldspar or fission track chronothermometry. In addition, the development of in situ stable isotope geochemistry would greatly benefit from CL studies.

The microfissuration of rocks would increase the knowledge of paleopermeability, but the nature of the CL bands in quartz should be clearly understood.

CL is potentially an interesting tool for studying redox conditions using Mn, Fe and Eu but some fundamental research is necessary because some valence changes are observed under the electron beam.

CL is now an efficient tool for studying fluctuation in manganese content in biogenic carbonates. This tool can be used to determine if the CL emission is due to diagenetic or biogeochemical processes. For example, it has been demonstrated that recent biogenic carbonates generally exhibit a luminescence which may be correlated with growth rate and probably with environmental factors (Barbin et al. 1991; Barbin 2000, this Vol.).

New subjects could be investigated with CL techniques including allochthonous versus autochthonous soil, alterations during transportation, paleopermeability and paleoporosity reconstruction, automatic quantification of minerals, paleoenvironmental studies, etc.

References

- Aguilar GM, Osendi MI (1982) Fluorescence of Mn^{2+} in CaCO_3 . *J Luminescence* 27: 365–375
- Amieux P (1982) La cathodoluminescence: Méthode d'étude sédimentologique des carbonates. *Bull Centre Explor Prod Elf Aquitaine* 6: 437–483
- Amieux P (1987) Description pétrographique de foraminifères par combinaison d'images en lumière naturelle et en cathodoluminescence. *C R Acad Sci Paris II*, 304: 741–744
- Banner JL, Hanson GN, Meyers WJ (1988) Determination of initial Sr isotopic compositions of dolostones from the Burlington-Keokuk formation (Mississippian): constraints from cathodoluminescence, glauconite paragenesis and analytical methods. *J Sed Petrol* 58: 673–687.
- Barbin V (2000) Cathodoluminescence of carbonate shells: biochemical vs diagenetic process (this Vol.)
- Barbin V, Jouart JP, D'Almeida T (1996) Cathodoluminescence and laser-excited luminescence spectroscopy of Eu^{3+} and Eu^{2+} in synthetic CaF_2 : a comparative study. *Chem Geol* 130: 77–86
- Barbin V, Ramseyer K, Debenay JP, Schein E, Roux M, Decrouez D (1991) Cathodoluminescence of recent biogenic carbonates: an environmental and ontogenic fingerprint. *Geol Mag*, 128, 1: 19–26
- Barbin V, Ramseyer K, Decrouez D, Herb R (1989) Mise en évidence par la cathodoluminescence d'indices de remaniements synsédimentaires. *Geobios* 22: 253–259
- Barbin V, Ramseyer K, Decrouez D, Burns SJ, Chamay J, Maier JL (1992) Cathodoluminescence of white marbles: an overview. *Archaeometry*, 34, 2: 175–183
- Barbin V, Schvoerer M (1997) Cathodoluminescence et géosciences. *C R Acad Sci Paris* 325: 157–169
- Baumer A, Blanc P, Cesbron F, Ohnenstetter D (1997) Cathodoluminescence of synthetic (doped with rare-earth elements) and natural anhydrites. *Chem Geol*, 138: 73–80.

- Becquerel E (1885) Etude spectrale des corps rendus phosphorescents par l'action de la lumière ou par des décharges électriques. *C R Acad Sci Paris* 101: 205–210
- Baker CE, Kopp OC (1991) Luminescence microscopy and spectroscopy: qualitative and quantitative applications. *Soc. Sedim. Geol., Short course, Dallas*, 25: 195
- Blanc Ph, Baumer A, Cesbron F, Ohnenstetter D (1995) Les activateurs de cathodoluminescence dans des chlorapatites préparées par synthèse hydrothermale. *C R Acad Sci Paris, sér II* 321: 1119–1126
- Blanc Ph, Baumer A, Cesbron F, Ohnenstetter D, Panczer G, Rémond G (2000) Systematic cathodoluminescence spectral analysis of synthetic doped minerals: anhydrite, apatite, calcite, fluorite, scheelite and zircon. (this Vol.)
- Blanc Ph, Roger G, Couto H (1994) Recherche de signatures magmatique et hydrothermale dans des apatites du Nord du Portugal: étude par cathodoluminescence, microscopie électronique à balayage et microsonde électronique. *Bull Soc géol Fr* 165: 329–339
- Blase G (1973) Crystal chemistry and rare-earth luminescence of mixed metal oxides. *Rev Chimie Minér* 10: 39–46
- Blase G, Bril A (1967) Investigation of some Ce^{3+} - activated phosphors. *J Chem Phys* 47: 5139–5145
- Blase G, Bril A (1970) Luminescences caractéristiques. *Philips Techn Review*, 31: 13–47
- Calderon T, Aguilar M, Coy-Yill R (1983) Relationship between blue color and radiation damage in calcite. *Radiation Effects Lett* 76: 187–191
- Calderon T, Aguilar M, Jaque F, Coy-Yill R (1984) Thermoluminescence from natural calcites. *J Phys C/ Solid State Phys* 17: 2027–2038
- Castaing R (1951) Application des sondes électroniques à une méthode d'analyse ponctuelle chimique et cristallographique. Thèse Doctorat Univ Paris
- Cesbron F, Blanc Ph, Ohnenstetter D, Rémond G (1995) Cathodoluminescence of rare earth doped zircons. Part I: their possible use as reference materials. *Scanning Microscopy, suppl.* 9: 35–56
- Cesbron F, Ohnenstetter D, Blanc Ph, Rouer O, Sichere MC (1993) Incorporation des terres rares dans des zircons de synthèse: étude par cathodoluminescence. *C R Acad Sci Paris, sér II* 316: 1231–1238
- Coulson IM, Chambers AD (1996) Patterns of zonation in rare-earth-bearing minerals in nepheline syenites of the North Qôroq center, South Greenland. *Can Min*, 34: 1163–1178.
- Coy-Yill R (1969) Quelques aspects de la cathodoluminescence des matériaux. *Chem Geol*, 5: 243–245
- Crookes W (1879) Contributions to molecular physics in high vacua. Magnetic deflection of molecular trajectory.-Laws of magnetic rotation in high and low vacua.-Phosphorogenic properties of molecular discharge. *Phil Trans Royal Soc London* 170: 641–662
- Crookes W (1880a) Sur la spectroscopie par la matière radiante. *C R Acad Sci Paris*, 100: 1380–1382
- Crookes W (1880b) Sur la spectroscopie par la matière radiante. Excitation mutuelle des spectres d'yttrium et de samarium. *C R Acad Sci Paris*, 100: 1495–1497
- Curie D (1960) Luminescence cristalline. Dunod, Paris
- D'Almeida T (1997) Cathodoluminescence des ions de terres rares dans les fluorures alcalino-terreux: utilisation comme sonde locale de température et applications. Thèse de doctorat de l'Université de Reims Champagne-Ardenne, unpublished, 210 p.
- Demarçay E (1887) Sur les spectres du didyme et du samarium. *C R Acad Sci Paris* 105: 276–277
- Demars C, Pagel M, Deloule E, Blanc Ph (1996) Cathodoluminescence of quartz from sandstones: interpretation of the UV range by determination of the trace element distribution and of fluid inclusion P,T,X properties in authigenic quartz. *Am Mineral*, 81: 891–901
- Dieke GH (1968) Spectra and energy levels of rare earth ions in crystals. John Wiley, New York
- Eberhardt JP (1989) Analyse structurale et chimique des matériaux. Dunod, Paris
- Ebers ML, Kopp OC (1979) Cathodoluminescence microstratigraphy in gangue dolomite, the Mascot-Jefferson city district, Tennessee. *Econ Geol* 74: 908–918

- El Ali A, Barbin V, Calas G, Cerville B, Ramseyer K, Bouroulec J (1993) Mn²⁺-activated luminescence in dolomite, calcite and magnesite: quantitative determination of manganese and site distribution by EPR and CL spectroscopy. *Chem Geol* 104, 189–202
- Evans J, Hogg AJC, Hopkins MS, Howarth RJ (1994) Quantification of quartz cements using combined SEM, CL and image analysis. *Jour. sed. Pet.*, A64: 334–338
- Fairchild IJ (1983) Chemical controls of cathodoluminescence of natural dolomites and calcites: new data and review. *Sedimentology*, 30: 579–583
- Fillippilli GM, Delaney ML (1993) The effects on manganese (II) and iron (II) on the cathodoluminescence signal in synthetic apatite. *J Sed Petrol* 63: 167–173
- Frank JR, Carpenter AB, Ogelsby TW (1982) Cathodoluminescence and composition of calcite cement in the Taum Sauk Limestone (Upper Cambrian), Southeast Missouri. *J Sed Petrol* 52: 631–638
- Garlick GFJ (1949) *Luminescent materials*. Oxford University Press, London
- Gies H (1976) Zur Beziehung zwischen photolumineszenz und chemismus natürlicher karbonate. *Neues Jahrbuch Mineral. Abh.*, 127: 1–46
- Gorobets BS, Walker G (1995) Origins of luminescence in minerals: a summary of fundamental studies and applications. In: Marfunin AS (ed.) *Advanced Mineralogy*. Springer Verlag, Berlin, 2, pp 124–135
- Görz HN, Bhalla RJR, White E (1970) Detailed cathodoluminescence characterization of common silicates. *Penn State Univ Spec Pub* 70–101: 62–70
- Götze J (2000) *Cathodoluminescence in applied geosciences (this Vol.)*
- Götze J, Krebschek MR, Habermann D, Wolf D (2000) High-resolution cathodoluminescence studies of feldspar minerals (this Vol.)
- Haberlandt H (1934) Lumineszenzuntersuchungen an fluoriten und andere mineralen. *Sitzungsberichte akademie Wissenschaft Math naturwissenschaft Wien, ser IIA* 143: 591–596
- Haberlandt H (1938) Spektralanalytische untersuchungen und lumineszenzbeobachtungen an fluoriten und apatiten. *Sitzungsberichte Akademie Wissenschaft Math naturwissenschaft Wien, ser IIA* 147: 137–150
- Haberlandt H, Karlik B, Przibram K (1934) Zur fluoreszenz des fluoriten II. *Sitzungsberichte Akademie Wissenschaft Math naturwissenschaft Wien, ser IIA* 143: 151–161
- Habermann D, Neuser RD, Richter DK (2000) Quantitative high resolution spectral analysis of Mn²⁺ activated CL in sedimentary calcite (this Vol.)
- Hanchar JM, Miller CF (1993) Zircon zonation patterns as revealed by cathodoluminescence and backscattered electron images: implications for interpretation of complexes crustal histories. *Chem Geol* 110: 1–13
- Hanchar JM, Rudnik RL (1995) Revealing hidden structures: The application of cathodoluminescence and backscattered electron imaging to dating zircons from lower crustal xenoliths. *Lithos* 36: 289–303
- Hanusiak WM (1975) Low temperature cathodoluminescence of crystalline silica for use in the characterisation of respirable dusts, MSc Thesis, State College, Penn State University
- Hanusiak WM, White EW (1975) SEM cathodoluminescence for characterization of damaged and undamaged alpha-quartz in respirable dusts. In: Johari O, Corvin I (eds) *Proceedings of the 8th annual Scanning Electron Microscope Symposium*, pp 125–132
- Have T ten, Heijnen W (1985) Cathodoluminescence activation and zonation in carbonate rocks: an experimental approach. *Geol Mijnbouw* 64: 297–310
- Hayward CL, Jones AP (1991) Cathodoluminescence petrography of middle Proterozoic extrusive carbonatite from Qasiarsuk, South Greenland. *Mineral Mag* 55: 591–603
- Heinrich KFJ (1981) *Electron beam X-ray micranalysis*. Van Nostrand Reinhold Cie, New York
- Heinrich KFJ, Newbury DE (1991) *Electron Probe Quantitation*. Plenum Press, New York
- Hemming NG, Meyers WJ, Grams JC (1989) Cathodoluminescence in diagenetic calcites: the roles of Fe and Mn as deduced from electron probe and spectrophotometric measurements. *J Sed Petrol* 59: 404–411

- Henry DJ, Toney JB (1987) Combined cathodoluminescence/backscattered electron imaging and trace element analysis with the electron microprobe: applications to geological materials. In: Geiss, R.H. (ed.) *Microbeam Analysis*, pp. 339–342.
- Imbusch MD (1978) Inorganic luminescence. In: Lumb MD (ed.) *Luminescence Spectroscopy*. Academic Press, London, pp 1–92
- Kempe U, Gruner T, Naslada L, Wolf D (2000) Relevance of cathodoluminescence for the interpretation of U-Pb zircon ages (with an example of application to a study of zircons from the Saxonian Granulite Complex, Germany) (this Vol.)
- Koberski U, Keller J (1995) Cathodoluminescence observations of natrocarbonatites and related peralkaline nephelinites at Oldoinyo Lengai. In: Bell K, Keller J (eds.) *Carbonatite Volcanism. Oldoinyo Lengai and the petrogenesis of natrocarbonatites*. Springer Verlag, Berlin, pp. 87–99
- Kröger FA (1948) Some aspects of the luminescence of solids. Elsevier, Amsterdam
- Lacroix A (1893) *Minéralogie de la France et de ses colonies*
- Lecoq de Boisbaudran (1885) Sur la fluorescence des terres rares. *C R Acad Sci Paris* 101, 552–555 and 588–592
- Lecoq de Boisbaudran (1887) Nouvelles fluorescences à raies spectrales bien définies. *C R Acad Sci Paris* 105, 301–304 and 343–348
- Leverenz HW (1950) *An introduction to luminescence of solids*. John Willey, New York
- Long JVO, Agrell O (1965) The cathodo-luminescence of minerals in thin section. *Mineral Mag* 34: 318–326
- Machel HG (1985) Cathodoluminescence in calcite and dolomite and its chemical interpretation. *Geosc Canada* 12: 139–147
- Machel HG (2000) Application of cathodoluminescence to carbonate diagenesis (this Vol.)
- Machel HG, Burton EA (1991) Factors governing cathodoluminescence in calcite and dolomite, and their implications for studies of carbonates diagenesis. In: Baker CE, Kopp OC (eds.) *Luminescence microscopy and spectroscopy: qualitative and quantitative applications*. Soc. Sedim. Geol., Short course, Dallas, 25, pp 37–57
- Machel HG, Mason RA, Mariano AN, Mucci A (1991) Causes and emission of luminescence in calcite and dolomite. In: Baker CE, Kopp OC (eds.) *Luminescence microscopy and spectroscopy: qualitative and quantitative applications*. Soc. Sedim. Geol., Short course, Dallas, 25, pp 9–25
- Major RP, Wilber RJ (1991) Crystal habit, geochemistry, and cathodoluminescence of magnesian calcite marine cements from the lower slope of Little Bahama bank. *Geol Soc Amer Bull* 103: 461–471
- Mariano AN (1978) The application of cathodoluminescence for carbonatite exploration and characterization. IN braga (ed.) *Proc 1st Inter Symp Carbonatites Juhno 1976, Poços de Caldas, Brasil*, pp 39–57
- Mariano AN (1988) Some further geological applications of cathodoluminescence. In: Marshall DJ (ed.) *Cathodoluminescence of geological Materials*. Unwin Hyman, Boston, pp 94–123
- Mariano AN (1989) Cathodoluminescence emission spectra of rare earth element activators in minerals. In: Lipin BR, McKay GA (eds.) *Geochemistry and Mineralogy of rare earth elements*. *Min Soc Amer, Rev Mineral* 21, pp 339–348
- Mariano AN, Ring PJ (1975) Europium activated cathodoluminescence in minerals. *Geoch Cosmochim Acta* 39: 649–660
- Mariano AN, Roeder PL (1989) Wöhlerite: chemical composition, cathodoluminescence and environment of crystallization. *Can Min*, 27: 709–720
- Marfunin AS (1979) *Spectroscopy, luminescence and radiation centers in minerals*. Springer-Verlag, Berlin
- Marshall DJ (1988) *Cathodoluminescence of geological Materials*. Unwin Hyman, Boston
- Marshall DJ, Kopp OC (2000) The status of the standards program of the Society for Luminescence Microscopy and Spectroscopy (this Vol.)
- Martin H, Zeegers H (1969) Cathodo-luminescence et distribution du manganèse dans les calcaires et dolomies du Tournaisien supérieur au Sud de Dinant (Belgique). *C R Acad Sci Paris* 269,:1922–1924

- Mason RA, Mariano AN (1990) Cathodoluminescence activation in manganese bearing and rare earth bearing synthetic calcites. *Chem Geol* 88: 191–208
- McKeever SWS (1985) *Thermoluminescence of solids*. Cambridge University Press, Cambridge
- Medlin WL (1959) Thermoluminescent properties of calcite. *J Chem Phys* 30: 451–458
- Medlin WL (1961) Anisotropy of color centers in calcite. *Phys Rev* 124: 1754–1757
- Medlin WL (1963) Emission centers in thermoluminescent calcite, dolomite, magnesite, and anhydrite. *J Optical Soc Amer* 53: 1276–1285
- Medlin WL (1964) Trapping centers in thermoluminescent calcite. *Phys Rev* 135: 1770–1779
- Medlin WL (1967) Color center growth curves in calcite. *J Phys Chem Solids* 28: 1725–1733
- Meunier JD, Sellier E, Pagel M (1990) Radiation-damage rims in quartz from uranium-bearing sandstones. *J Sed Geol* 60: 53–58
- Meyers WJ (1974) Carbonate cements stratigraphy of the Lake Valley formation (Mississippian), Sacramento Mountains, New Mexico. *J Sed Petrol* 44: 837–861
- Milliken KL, Laubach SE (2000) Brittle deformation in sandstone diagenesis as revealed by scanned cathodoluminescence imaging with application to characterization of fractured reservoirs (this Vol.)
- Mitchell RH, Xiong J, Mariano AN, Fleet MA (1997) Rare-earth-element-activated cathodoluminescence in apatite. *Can Min*, 35: 979–998
- Monod-Herzen G (1966) *Luminescence*. Dunod, Paris
- Morgan AJ (1985) X-ray microanalysis in electron microscopy for biologists. *Royal Micro Soc Micros Handbook*, 5: 79
- Morozov AM, Morozova LG, Trefimov AK, Feofilov PP (1970) Spectral and luminescent characteristics of fluoroapatite single crystals activated by rare earth ions. *Optika i spektroskopia* 29: 590–596
- Nickel E (1978) The present status of cathode luminescence as a tool in sedimentology. *Minerals Sci Engng* 10: 73–100
- Nichols EL, Howes HL, Wilber DT (1928) *Cathodo-Luminescence and the luminescence of incandescent solids*. Carnegie Institute of Washington, 384, Washington: 350
- Ohnenstetter D, Cesbron F, Rémond G, Caruba R, Claude JM (1991) Emissions de cathodoluminescence de deux populations de zircons naturels: tentative d'interprétation. *C R Acad Sci Paris* 313: 641–647
- Owen MR (1988) Radiation-damage halos in quartz. *Geology*, 16: 529–532
- Panczer G, Gaft M, Marfunin AS (2000) Systems of interacting centers in natural diamonds: laser-induced time-resolved and CL spectroscopy (this Vol.)
- Pierson BJ (1981) The control of cathodoluminescence in dolomite by iron and manganese. *Sed* 28: 601–610
- Poller U (2000) A combination of single zircon dating by TIMS and cathodoluminescence investigations on the same grain: the CLC-method geochronology for metamorphic rocks (this Vol.)
- Ponahlo J (2000) Cathodoluminescence as a tool in gemstone identification (this Vol.)
- Portnov AM, Gorobets BS (1969) Luminescence of apatite from different rock types. *Doklad Akad Nauk SSSR* 184: 110–113
- Pringsheim P (1949) *Fluorescence and phosphorescence*. Wiley, New York
- Rae DA, Chambers AD (1988) Metasomatism in the North Qôroq centre, South Greenland: cathodoluminescence and mineral chemistry of alkali feldspars. *Trans Royal Soc Edinburgh, Earth Sciences* 79: 1–12
- Ramsayer K, Baumann J, Matter A, Eberhardt P, Geiss J (1989) A cathodoluminescence microscope for low luminescence. *J Sed Petrol*, 59: 619–622
- Ramsayer K, Mullis J (2000) Geologic application of cathodoluminescence of silicates (this Vol.)
- Raven MJ, Dickson JAD (1989) Fire-tree zoning: an indicator of pulsed crystallization in calcite cement crystals. *Sed Geol* 65: 249–259
- Reed SJB (1975) *Electron microprobe analysis*. Cambridge University Press, Cambridge
- Reeder RJ (1991) An overview of zoning in carbonate minerals. In: Baker CE, Kopp OC (eds.) *Luminescence microscopy and spectroscopy: qualitative and quantitative applications*. Soc. Sedim. Geol., Short course, Dallas, 25: 77–83

- Reeder RJ, Prosky JL (1986) Compositional sector zoning in dolomite. *J Sed Petrol.*, 56: 237–247
- Rémond G (1977) Applications of cathodoluminescence in mineralogy. *J Lumin* 15: 121–155
- Rémond G, Blanc Ph, Cesbron F, Ohnenstetter D, Rouer O (1995) Cathodoluminescence of rare earth doped zircons. Part II: relationship between the distribution of the doping elements and the contrasts of CL images. *Scanning Microscopy*, suppl. 9, pp. 57–76
- Rémond G, Cesbron F, Chapoulie R, Ohnenstetter D, Roques-Carmes C, Schvoerer M (1992) Cathodoluminescence applied to the microcharacterization of mineral materials: a present status in experimentation and interpretation. *Scanning Microscopy* 6, pp. 23–68
- Rémond G, Kimoto S, Okuzumi H (1970) Use of the SEM in cathodoluminescence observations in natural specimens. *Scanning Electron Microsc.* 33–40
- Rémond G, Phillips M, Roques-Carmes RC (2000) Importance of instrumental and experimental factors on the interpretation of CL data from wide band gap materials (this Vol.).
- Roeder PL, Mac Arthur D, Ma XP, Palmer GL, Mariano AN (1987) Cathodoluminescence and microprobe study of rare-earth elements in apatite. *Am Min.* 72: 801–811
- Rubatto D, Gebauer D (2000) Use of cathodoluminescence for U-Pb zircon dating by ion microprobe: some examples from the Western Alps (this Vol.)
- Seyedolali A, Krinsley DH, Boggs S Jr, O'Hara PF, Dypvik H, Goles GG (1997) Provenance interpretation of quartz by scanning electron microscope-cathodoluminescence fabric analysis. *Geology* 25: 787–790
- Servigne M (1937) Sur une méthode sensible pour la recherche de traces d'éléments de terres rares. *C R Acad Sci Paris* 204: 863–865
- Servigne M (1938) Sur une application de la luminescence à l'analyse quantitative: micro-dosage de l'élément samarium. *C R Acad Sci Paris* 207: 1566–1568
- Servigne M, Vassy E (1937) Sur l'émission infrarouge de luminescence de quelques éléments rares. *C R Acad Sci Paris* 204: 905–907
- Schulman JH, Evans LW, Ginther RJ, Murata KJ (1947) The sensitized luminescence of manganese-activated calcite. *J Applied Phys* 18: 732–739
- Sippel RF (1971) Luminescence petrography of the Apollo 12 rocks and comparative features in terrestrial rocks and meteorites. *Proc Second Lunar Sci Conf* 1: 247–263
- Sippel RF, Glover ED (1965) Structures in carbonate rocks made visible by luminescence petrography. *Science* 167: 677–679
- Smith JV, Stenstrom RC (1965) Electron-excited luminescence as a petrologic tool. *J Geol* 73: 627–655
- Sommer SE (1972a) Cathodoluminescence of carbonates, 1. Characterization of cathodoluminescence from carbonate solid solutions. *Chem Geol* 9: 257–273
- Sommer SE (1972b) Cathodoluminescence of carbonates, 2. Geological applications. *Chem Geol* 9: 275–284
- Stevens Kalceff MA, Phillips MR, Moon AR (2000) Cathodoluminescence microcharacterization of silicon dioxide polymorphs (this Vol.)
- Tarashchan AN (1978) Luminescence of minerals. *Nauk Dumka, Kiev* (in Russian)
- Tarashchan A, Waychunas G (1995) Interpretation of luminescence spectra in terms of band theory and crystal field theory. In: Marfunin AS (ed.) *Advanced Mineralogy*. Springer Verlag, Berlin, 2, pp 124–135
- Townsend P, Rowlands AP (2000) Information encoded in cathodoluminescence emission spectra (this Vol.)
- Urbain G (1909) La phosphorescence cathodique des terres rares. *Ann Chim Phys*, 8, XVIII: 222–375
- Vavra G (1990) On the kinematics of zircon growth and its petrogenetic significance: a cathodoluminescence study. *Contrib Mineral Petrol* 106: 90–99
- Vavra G (1993) A guide to quantitative morphology of accessory zircon. *Chem Geol* 110: 15–28
- Vavra G (1994) Systematics of internal zircon morphology in major variscan granitoid types. *Contrib Mineral Petrol* 117: 331–344
- Verhulst A, Demaiffe D, Ohnenstetter D, Blanc Ph, Balaganskaya E, Kirmarsky Y (1997) Cathodoluminescence petrography of carbonates and associated alkaline silicate rocks from the Kola peninsula (Russia). *GAC-MAC, Ottawa*, 19–21 may 1997

- Walker G (1983) Luminescence centres in minerals. *Chemistry in Britain* 19: 823–824
- Walker G (2000) Physical parameters for the identification of luminescence centres in minerals (this Vol.)
- Walker G, Abumere OE, Kamaluddin B (1989) Luminescence spectroscopy of Mn^{2+} centres in rock-forming carbonates. *Min Mag*, 53: 201–211
- Walker G, Burley S (1991) Luminescence petrography and spectroscopic studies of diagenetic minerals. In: Baker CE, Kopp OC (eds.) *Luminescence microscopy and spectroscopy: qualitative and quantitative applications*. Soc. Sedim. Geol., Short course, Dallas, 25, pp 83–96
- Weiblen P (1964) Investigation of cathodo-luminescence with the petrographic microscope. *Dev Applied Spectroscopy* 4: 245–251
- Wenzel T, Ramseyer K (1992) Mineralogical and mineral-chemical changes in a fractionation-dominated diorite-monzodiorite-monzonite sequence: evidence from cathodoluminescence. *Eur J Mineral* 4: 1391–1399
- Wick FG (1924) A spectroscopic study of the cathodoluminescence of fluorite. *Phys Rev*, 2, 24: 272–282.
- White WB (1975) Luminescent materials. *Trans Am Crystallogr Assoc* 11: 31–49
- Widom E, Gill JB, Schmincke HU (1993) Syenite nodules as a long-term record magmatic activity in Agua de Pao volcano, Sao Miguel, Azores. *J Petrol* 34: 920–953
- Wybourne BG (1965) *Spectroscopic properties of rare earths*. Wiley, New York
- Yacobi BG, Holt DB (1990) *Cathodoluminescence microscopy of inorganic solids*. Plenum Press, New York

Physical Parameters for the Identification of Luminescence Centres in Minerals

GRAHAME WALKER

1 Introduction

Cathodoluminescence (CL) has proved to be an invaluable technique in petrology, particularly for determining the diagenesis of sediments and for ascertaining provenance (Barker and Kopp 1991), but a knowledge of the causes of CL in minerals is essential if CL is to be more than a fingerprinting or fabric-revealing technique. The determination of the nature of the luminescence centres responsible is not, however, in general a trivial task. Correlation of the observation of specific luminescence bands with particular impurity concentrations may give an indication of the source of the emission but it is not proof of origin, and can sometimes be misleading. Furthermore, it does not give any details about the precise nature of the centre.

Spectroscopic studies are often much more diagnostic, particularly in the case of transition-metal ion or rare-earth centres, and a number of important parameters which aid identification can be determined from the measurement of luminescence spectra. In some cases it is difficult to really know precisely how many different luminescence centres are present in a particular mineral specimen let alone what they are! In order to provide a clear idea of what the luminescence spectra of known luminescence impurity centres might look like in particular minerals, synthetic samples doped with specific impurities have often been used. The evidence provided by such samples, however, depends crucially on the purity of the starting materials and the preparation techniques used.

The purpose of this chapter is to examine how such problems may be resolved and, in particular, what information concerning the nature of the luminescence centres can be revealed. A number of specific examples will be discussed in order to illustrate what can be achieved using various spectroscopic techniques, and the advantages of using a pulsed rather than continuous electron beam for CL excitation will be demonstrated.

The theory of luminescence as applied to minerals has been expounded elsewhere (Henderson and Imbusch 1989; Marfunin 1979; Walker 1985) and will not be repeated in detail here. Some theoretical concepts will, however, be discussed in the context of understanding the importance of certain experimentally determined parameters. We shall discuss the various types of luminescence measurements that can be performed on mineral samples and analyse what information each of these yield.

2 Cathodoluminescence Emission Spectra

Firstly we shall consider the various forms of conventionally determined spectra, as distinct from time-resolved spectra (see later), which can be obtained using either continuous or pulsed electron or laser excitation. Pulsed or chopped excitation, however, allows lock-in amplification techniques (or gated photon counting) to be employed which eliminate any background light and improve the signal-to-noise ratio.

The measurement of emission spectra enables parameters such as the spectral position, spectral width, and spectral intensity to be determined; moreover, the variation of these parameters with temperature is also important in deciding the origin of spectral bands. Quite often the luminescence from single crystals is polarised and this can also give information as to the nature of the centre; care must be exercised, however, when using spectrometers to ensure that the light entering the spectrometer is unpolarised otherwise erroneous spectral intensities may be recorded.

If sharp lines are apparent at room temperature, these can be indicative of the presence of trivalent rare-earth ions such as Eu^{3+} , Dy^{3+} or Sm^{3+} , etc., even at the level of a few ppm; these ions almost invariably substitute for Ca (or sometimes Ba, Sr or Zr) in natural minerals and usually give rise to well-spaced multiple lines. Sharp line emission in the region of 680–700 nm, however, may be due to Cr^{3+} commonly substituting in octahedral Al-sites. Because of strong crystal-field effects, Cr^{3+} is not found in tetrahedral sites. Nevertheless, in general, most CL emission is broad-band rather than line spectra and frequently the spectrum consists of overlapping bands although band separation can often be achieved using time-resolved techniques (see below). Figures 1–3 show various types of spectra and the way in which these vary with temperature.

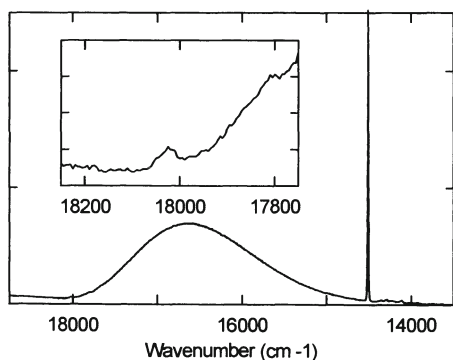


Fig. 1. Luminescence emission spectrum of spodumene (Brazil; BM1967,14) at very low temperature (12 K) showing a broad-band emission due to Mn^{2+} in Li-sites and sharp-line emission with a weak single-phonon side-band due to Cr^{3+} in Al-sites. Note the hint of structure on the high energy edge of the Mn^{2+} band (see inset) showing what is probably the zero-phonon line and a first phonon “replica” which is due to one phonon being created of energy equal to its separation from the zero-phonon line (i.e. about 220 cm^{-1}). (Walker et al. 1997; see Acknowledgements)

Fig. 2. Luminescence emission spectrum of a chromium-rich spodumene (hiddenite, N. Carolina; BM53913) at room temperature and at 55 K. Cr^{3+} in Al-sites is again responsible. For a detailed discussion of this spectrum see Sect. 4.1. (Adapted from Walker et al. 1997; see Acknowledgements)

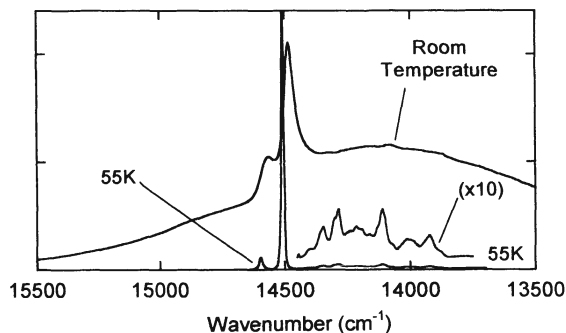
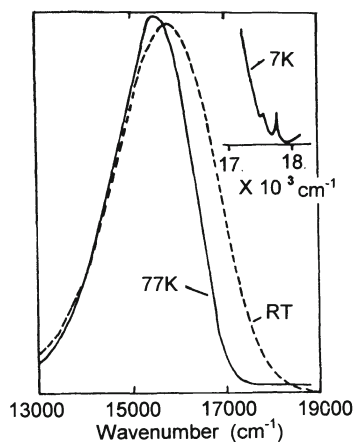


Fig. 3. Cathodoluminescence (CL) emission spectrum of Mn^{2+} in a calcite (Derbyshire) again showing very weak phonon structure at 77 K. Note also the narrowing of the band on cooling and slight shift of the peak position. Calculation of the Huang-Rhys factor from the low temperature band-width indicates a value of between 7 and 8!



At low temperatures some emission bands, which are broad and featureless at room temperature, begin to narrow and to show sharp lines or broader secondary peaks on the short wavelength (higher energy) edge. Sometimes such features may be very weak and perhaps only one or two peaks are discernible. These features are due to the resolution at low temperatures of transitions in which one, two, or more, phonons of a particular vibrational mode are created. The strongest and sharpest line, however, at the shortest wavelength in emission is usually the transition in which no phonons are created at all. This zero-phonon line (ZPL) is therefore a purely electronic transition and its spectral position gives us the precise separation of the emitting state and the final state (usually the ground state). Sometimes the zero-phonon line is the dominant feature in the spectrum and can even be seen at room temperature in certain cases, e.g. the Cr^{3+} R-lines or trivalent rare-earth emission lines. There is in fact a parameter which describes the degree to which a centre exhibits a zero-phonon line which is called the Huang-Rhys factor S . This parameter can be defined as the number of phonons of a particular mode which are created in emission (or absorption) (Walker 1985) and is a measure of the differing interaction of the emitting electronic state and the final state of the luminescence centre with the vibrating lattice in which it finds itself.

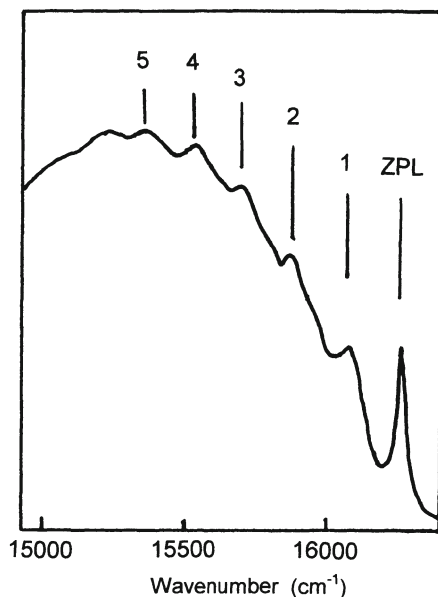
If $S > 6$ or 7, then the interaction with the lattice is so strong that a zero-phonon line cannot usually be detected even at 4 K. If on the other hand $S < 1$, then the spectrum is dominated by the zero-phonon line although a weak single-phonon sideband may be also be present at longer wavelengths, as often occurs in Cr^{3+} spectra. This sideband is merely a spectrum of the various vibrational or phonon modes associated with the luminescent ion and its immediate environment.

Spectra of Mn^{2+} emission at very low temperature often, but not always, show a zero-phonon line with up to five or six phonon “replicas” (that is transitions in which up to six identical phonons may be created) superimposed on a broad multi-phonon sideband and therefore have $S=5$ or 6 (see Fig. 4).

Many CL emission bands do not show any structure at all even at low temperatures and we may therefore conclude that in such emission centres there is a strong interaction with the vibrating lattice, e.g. in quartz. In some cases, however, the absence of a zero-phonon line (ZPL) may be due to what is known as inhomogeneous broadening; in other words the centres are not all identical but have a statistical size distribution which smears out the ZPL. Clearly any disorder in the crystal structure may result in such broadening and will be particularly critical in cases in which the Huang-Rhys factor is around the limiting value for a ZPL to be seen ($S \sim 7$). For example, the ZPL is often difficult to detect for Mn^{2+} centres in carbonates such as calcite (see Fig. 3).

To the author’s knowledge, a ZPL has never been detected for the common Fe^{3+} emission band in feldspars although a ZPL has been observed in Fe^{3+} emission bands in other materials (Walker and Glynn 1992; O’Connor et al. 1991).

Fig. 4. CL emission spectrum of Mn^{2+} in synthetic forsterite at 5 K showing very clear phonon structure with a ZPL and about five phonon replicas. Counting the number of replicas, which are equally spaced in energy (about 180 cm^{-1} in this case), up to the peak of the band gives us an estimate of the Huang-Rhys factor if only one dominant mode is evident. Its value is clearly between 5 and 6 in this case



Whether a ZPL is observed or not, broad-band emission usually narrows appreciably when the specimen is cooled; the band width W is in fact proportional to the square root of the Huang-Rhys factor S or

$$W^2 = 5.6 (\hbar\omega)^2 S$$

where $\hbar\omega$ is the energy of the dominant phonon mode.

If a ZPL and sideband are observed, then the proportion of the integrated intensity in the ZPL is given by

$$I_{\text{ZPL}} = I_{\text{TOTAL}} \exp(-S)$$

This relation, however, has to be applied with care and not when the ZPL is of magnetic dipole character and the sideband is due to phonon-assisted electric-dipole transitions, a situation which can occur when a centre of inversion symmetry is present, e.g. emission from Mn^{2+} in calcite (Walker et al. 1989) or Ni^{2+} in M1 sites in synthetic forsterite (Walker et al. 1994; see Fig. 5).

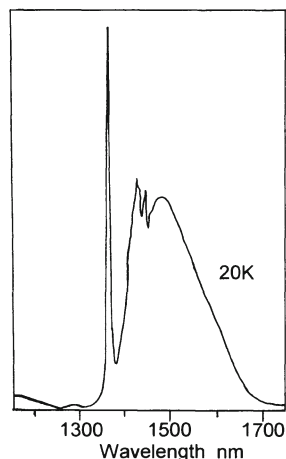
3

Luminescence Lifetime and Time-Resolved Spectra

A very important parameter which gives further evidence of the nature of the centre is the luminescence lifetime or decay time which is a measure of the transition probability from the emitting state; it is therefore a characteristic and unique property of the centre and no two luminescence emissions will have exactly the same decay time.

If the excitation source (electron-beam or laser-beam) is pulsed or chopped then the luminescence lifetime can be measured relatively easily. In the simplest case the intensity of the emission decays exponentially with time after the

Fig. 5. Luminescence emission spectrum of Ni^{2+} in the infrared in synthetic forsterite at 20 K. Here there are at least two dominant phonon modes; in fact up to 6 first phonon replicas have been distinguished. The Huang-Rhys factor in this case is less than two whichever phonon mode is chosen



removal of excitation; i.e. $I=I_0\exp(-t/\tau)$ where τ is the decay time and is the time for the intensity I to fall to 37% of its initial value I_0 .

The decay time depends on the probability of two processes – radiative decay which gives rise to luminescence and non-radiative decay in which the excitation energy is dissipated solely into lattice vibrations (i.e. the production of phonons). Clearly, if the latter process dominates then the luminescence will be weak or absent.

The probability of radiative decay is determined by the oscillator strength of the transition which in turn depends on the transition dipole moment. (For a definition and discussion of the transition electric dipole moment, see Walker 1985). Suffice it to say that this latter parameter should be non-zero for a transition to be allowed and the “allowedness” of the transition is reflected in the radiative part of the decay time. A short decay time is therefore more allowed than a longer one. Curiously, many of the most common types of luminescence centres have very long decay times and therefore low radiative transition probabilities. The fact that these centres are strongly luminescent indicates that the non-radiative probabilities must be even smaller.

A very long luminescence lifetime of several tens of milliseconds is indicative of a strongly “forbidden” transition as occurs in, for example, Mn^{2+} centres (see Walker 1985 for a discussion of “forbidden” and “allowed” transitions). On the other hand, a relatively short lifetime, in the microsecond regime, would indicate that the emission is not likely to be due to d^5 ions (Mn^{2+} , Fe^{3+}), line emission from d^3 ions (Cr^{3+}) nor most trivalent rare-earth ions (excepting Ce^{3+}), all of which involve what are known as “spin-forbidden” transitions, but rather to “spin-allowed” transitions in other ion-impurity or intrinsic defect centres.

Even Mn^{2+} emission centres, although always “spin-forbidden”, have different decay times in different minerals and indeed in different substitutional cation sites in the same mineral – e.g. in Mg and Ca sites in dolomite or diopside. This is because the radiative transition probability is sensitive to the symmetry of the centre (Walker 1985). Moreover, the lifetime may even be different for the same centre in different specimens of the same mineral if, for example, one specimen contained more quenching centres such as Fe^{2+} than the other, but this would be accompanied by a reduction in luminescence intensity. Perhaps a brief explanation of the role of such quenching centres may be useful at this point. If such centres are present in sufficient concentrations then the transfer of excitation energy from an excited state of a luminescence centre to an excited state of the quencher may occur by resonance transfer provided that the states are of similar energy and the distance between the two centres is not too large. The quenching centre then rapidly de-activates usually by non-radiative transitions down a ladder of closely-spaced energy states (although it is also possible for emission to occur at a lower energy, for example in the infra-red). Such processes deplete the population of excited states of the emitting centres and hence reduce the lifetime of these states. For example, strong Mn^{2+} emission in synthetic forsterite can be drastically reduced in intensity if the forsterite contains 2% Ni. In this case the decay time of the Mn^{2+} emission is reduced from 30 ms (in samples with minimal Ni) to 4 ms.

A combination of the spectral and temporal nature of the emission can be determined by time-resolved spectra. Such techniques can often separate over-

lapping features which have different origins and therefore different luminescence lifetimes. There are several ways of achieving time resolution: the “standard” method involves recording the intensity in a specific time “window” at a given delay after the excitation pulse for which both the delay and the gate width (or “window”) have to be carefully chosen. A cruder but simpler method of varying the modulation frequency of the excitation relies on the reduction and eventual disappearance of spectral features which have longer decay times as the modulation frequency is increased. The more sensitive method of phase-tuning, however, can be used to null out bands with a particular decay time and has proved to be very useful in separating overlapping bands in mineral CL. This method will therefore be discussed in more detail with some examples from recent CL work.

3.1 Phase-Tuned Spectra

In all time-resolved luminescence techniques it is necessary to use pulsed or chopped excitation and, for this particular technique, also a phase-sensitive detector or lock-in amplifier. Usually, for conventional measurements using lock-in techniques, the phase of the reference voltage which is derived from the excitation beam modulation is adjusted for maximum output signal, i.e. for zero phase difference between the reference and the detected luminescence signal. In phase-tuned spectra, however, the phase is adjusted so that a particular luminescence emission intensity is nulled out at a particular wavelength, i.e. the phase difference between the reference and the luminescence signal is 90° . Any residual signal then present at any other wavelength has a different phase and therefore has a different decay time. Depending on the phase difference, residual bands may appear as positive or negative signals. If, for example, after tuning out one particular band there are two residual bands it is possible that the intensity of these bands may have opposite signs (see Fig. 6). With a modern dual-phase lock-in amplifier, it is not necessary to carry out phase-nulling during the experimental measurement since such instruments can record both the magnitude and phase of the luminescence signal during a spectral scan. The data can then be placed on a spreadsheet and any phase angle added or subtracted to give a 90° phase difference between reference and signal at any chosen wavelength. Any number of different phase-tuned spectra can therefore be obtained from one set of experimental data. As in all forms of time-resolved spectra the choice of modulation frequency is critical for good results. It is clearly not sensible to use a low modulation frequency to separate two bands with fast decay times.

Figure 6 shows how phase-tuned spectra have been used to separate luminescence bands in a jadeite sample. In particular, it was possible to show that there were two bands of different but similarly long decay times and two of much shorter decay times. Combined with luminescence excitation spectra (see later) it was possible to demonstrate that Mn^{2+} was present in both Na and Al sites giving two emission bands and to show that the Mn^{2+} emission in the red was overlapping with another emission band with a much shorter decay time which has been ascribed to broad-band Cr^{3+} emission.

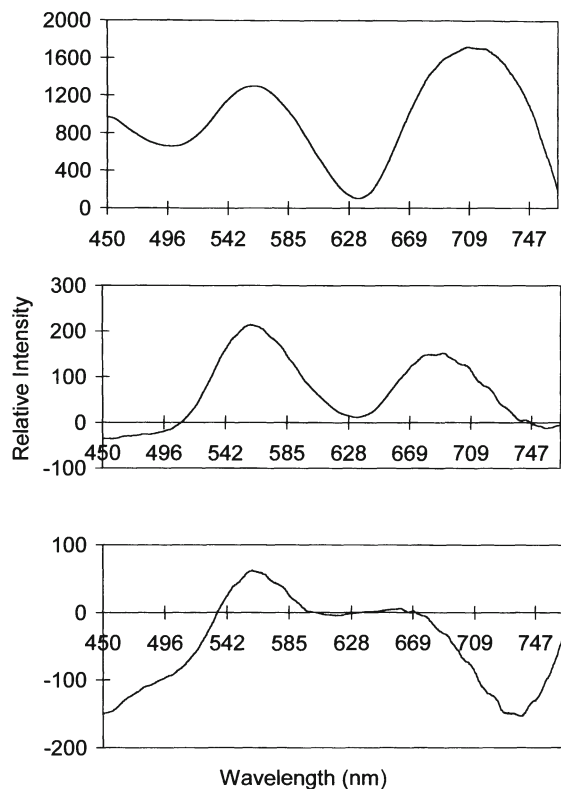


Fig. 6. Cathodoluminescence (CL) emission spectra of jadeite (BM1912, 525). The *top* spectrum is a conventional emission spectrum measured at 100 K which apparently shows two main bands although the band on the edge of the infra-red does appear as though it might be a composite one. The *middle* spectrum is a phase-tuned spectrum where the emission intensity has been nulled at 750 nm. It reveals that there are two emission bands of similar decay times (which are later shown to be due to Mn^{2+} in two different sites) and shows that the long wavelength band in the conventional spectrum is indeed composite. The lower spectrum is again a phase-tuned one but this time nulled at 660 nm. One of the two bands in the spectrum nulled at 750 nm disappears completely and another is drastically reduced in intensity. However, two other bands appear with negative intensity at opposite ends of the spectrum; (we could invert this spectrum by introducing a 180° phase shift). There are therefore four emission bands present in total and the components of the composite long-wavelength band have been separated. The wavelengths at which the spectra were nulled are not arbitrary but chosen so that one component of the composite band was unlikely to contribute much to the intensity at that wavelength

Dolomites usually exhibit a strong red luminescence due to Mn^{2+} in Mg sites. However, there is both visual and spectral evidence that the emission band broadens and shifts to shorter wavelengths in some dolomites (Walker et al. 1989). Indeed spectral studies have shown that Mn^{2+} can also populate the Ca-site in certain conditions and the broad emission band, particularly at low temperature, shows evidence of being two overlapping bands. Using phase-tuned spectra an

almost complete separation of these components (again due to Mn^{2+} in two different cation sites) can be achieved.

One of the most difficult problems in the CL of minerals is the elucidation of the luminescence properties of quartz, particularly authigenic quartz. The literature abounds with conflicting reports and a plethora of suggestions of the origins of CL emission bands (see, for example, Stevens-Kalceff and Phillips 1995 and this book for a review).

It was suggested sometime ago (Alonso et al. 1983) that, on the basis of the intensity variations with temperature, the “blue” emission in quartz actually consisted of three overlapping bands and, although they were not able to resolve them spectrally, Gaussian de-convolution techniques were used to show that the band could be a summation of three bands which had different quenching temperatures. Recently phase-tuning techniques have been used on the CL emission of orientated synthetic high-purity hydrothermal quartz crystals, where it has been possible to obtain direct experimental evidence that the “blue” CL emission band consists of at least four overlapping bands which have different but very similar decay times (Gorton et al. 1997). The band at the shortest wavelength in the near ultra-violet is the one which has been associated with alkali-compensated aluminium centres but the others are probably due to intrinsic defect centres which may be transient in nature. One, centred around 450-470 nm, is most com-

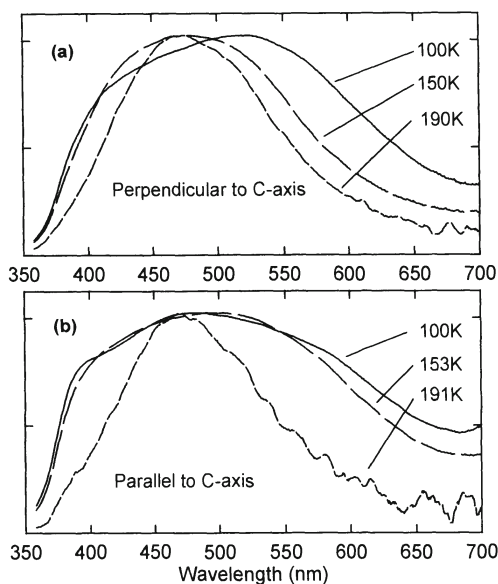


Fig. 7a,b. Polarised cathodoluminescence (CL) emission spectra of an ultra high-purity (i.e. <0.1 ppm Al) synthetic quartz crystal, **a** polarised perpendicular to the c-axis and **b** polarised parallel to the c-axis. There is evidence from the shape of the broad emission that it is a composite band and the fact that the band narrows with increasing temperature rather than the usual broadening suggests that some of the component bands are quenching faster than others as the temperature is raised. (Gorton et al. 1997; see Acknowledgements)

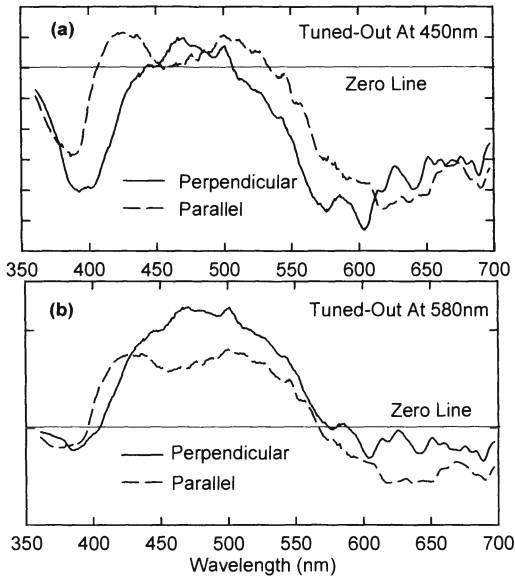


Fig. 8. Phase-tuned spectra cathodoluminescence (CL) spectra of the same quartz crystal as in Fig. 7 measured at 100 K with the intensity nulled-out at two different wavelengths as indicated. The polarisation with respect to the *c*-axis is also indicated. If the band was a single one then the spectrum would reduce to the zero intensity line but its variations above and below this line show that there are several component bands present. An obvious one, which has been linked with compensated Al centres, shows up at around 390 nm in both polarisations while others at about 420 and 500 nm appear to be particularly noticeable in the spectra polarised parallel to the *c*-axis. The spectra are rather noisy since the phase differences involved are no more than 2 or 3 degrees because of the small differences in decay times of the component bands. (Gorton et al. 1997; see Acknowledgements)

monly ascribed to the recombination of a self-trapped exciton (STE) (Trukhin 1992, 1994). Although there is still much debate about the origins of these component bands, there is for the first time unequivocal experimental evidence of their existence (see Figs. 7, 8). Clearly, the relative intensities of these component bands will decide the visual colour or shade of the CL observed. These are, of course, in addition to the red CL band which is actually created by electron irradiation and is particularly noticeable at room temperature.

Such intrinsic defect luminescence centres are much more difficult to characterise and identify than transition-metal-ion centres and will almost certainly require additional evidence and information from other experimental techniques for their elucidation. They are characterised in general by having a large Huang-Rhys factor and consequentially having broad and structureless emission bands even at very low temperatures. Decay times at room temperature are invariably short ($\sim 1 \mu\text{s}$) but can be very much longer at low temperatures, where the intensity may also be considerably enhanced (10–1000 \times).

4 Luminescence Excitation Spectra

The problem in general with emission spectra is that only information about the electronic states involved in the luminescence transition is revealed. Luminescence excitation spectra of a particular emission (which is a photo-luminescence technique) can reveal the absorption profile of the centre and therefore the position of all excited states which are directly or indirectly connected with the emitting state, not just those responsible for the emission (Walker 1985). In practice, the wavelength of the excitation is scanned and the integrated intensity of a particular luminescence emission band is monitored by a suitable detector. In general, the more light that is absorbed by the luminescence centre, the more light is emitted as luminescence. (Absorption by non-luminescent species can of course also take place but in practice is not usually important unless it is either very strong or very structured in the region of interest.) Experimental details can be found elsewhere (Walker 1985). It is a technique which, in the weak absorption limit, yields the absorption spectrum of the luminescent species under investigation in circumstances where measurement of conventional absorption spectra may be practically impossible; for example, the sample may be in microcrystalline powder form or the impurity or defect may only be present in extremely low concentrations. The technique also enables absorption bands due to different centres to be spectrally separated in a way that would not be possible using conventional absorption measurements. For transition-metal ion centres in particular, the absorption profile is very characteristic and enables the ligand-field parameters $10Dq$, B and C , to be determined (Marfunin 1979; Walker 1985). These parameters give information about the environment of the ion, i.e. the site in which it resides. For example, as we have already seen, Mn^{2+} emission can arise due to the ion substituting in more than one type of metal-cation site.

If single crystals are available then polarised excitation spectra can be determined in many cases and the band intensities in differing polarisations can be analysed in terms of the selection rules governing the transitions by considering an appropriate pseudosymmetry for the suspected centre and its orientation with respect to the crystallographic or indicatrix axes (see, for example, Green and Walker 1985).

The separation in energy between the maximum of the emission band and that of the corresponding absorption band (due to a transition between the same electronic states) is known as the Stokes shift, which can be shown to be equal to $2S\hbar\omega$, where $\hbar\omega$ is the energy of the dominant phonons created during the transition (Walker 1985). This quantity can clearly be determined from measurements of emission and excitation spectra and gives an immediate indication of the strength of the interaction between luminescence centre and the vibrating lattice.

4.1 Ligand-Field Parameters

It is perhaps instructive to look briefly at the application of ligand-field theory to two very common types of luminescence centre, namely $3d^5$ ions such as Mn^{2+} and Fe^{3+} , and $3d^3$ ions such as Cr^{3+} . Ligand-field diagrams can be constructed from measurements taken from luminescence excitation spectra and a “best fit” of the ligand-field strength $10Dq$ made. This parameter gives a very strong indication of the size of the site which the ion is occupying and enables us to distinguish between different sites. The measurement of the electron repulsion parameter B (Racah parameter) also gives some indication of how cramped the site is

Fig. 9. Excitation spectra of Mn^{2+} in the M1 and M2 sites in jadeite. Note the clear difference between the spectra for a low-field (i.e. large) M2 site (*upper* spectrum) and a high-field (i.e. small) M1 site (*lower* spectrum). The Racah parameters B and C are determined from the position of the ${}^4E(G)$ and ${}^4E(D)$ states. The energy difference between the ${}^4T_1(G)$ state and the ${}^4E(G)$ state gives an indication of the ligand-field strength

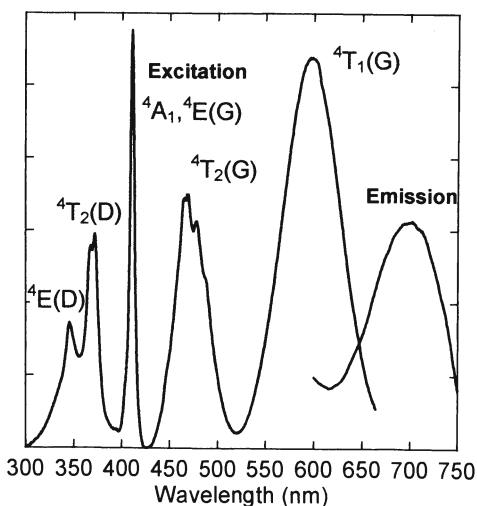
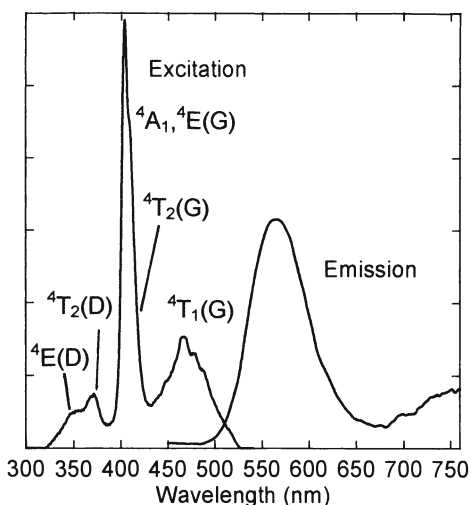
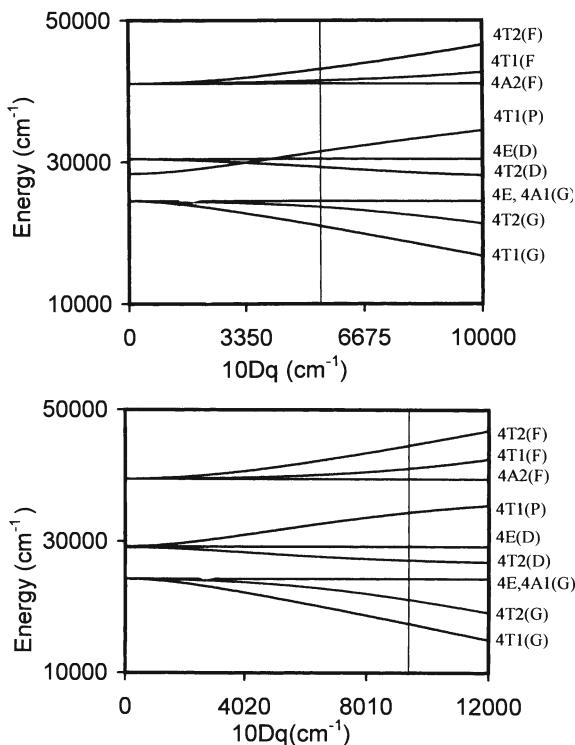


Fig. 10. Ligand-field diagrams for Mn^{2+} in the M1 and M2 sites in jadeite. The upper diagram is drawn for the M2 site with Racah parameters $B=850\text{ cm}^{-1}$ and $C=3200\text{ cm}^{-1}$. A best fit value to the band positions gives $10Dq=5500\text{ cm}^{-1}$. The lower diagram is drawn for the M1 site with $B=670\text{ cm}^{-1}$ and $C=3465\text{ cm}^{-1}$. Here the best fit value for $10Dq$ is 9500 cm^{-1} . Note the large difference in the size of the ligand-field parameter for the two sites. The luminescence transition is from the ${}^4T_1(G)$ state to the 6A_1 ground state (not shown but which is parallel to the horizontal axis)



for a particular ion; a large reduction from the free-ion value indicates considerable orbital overlap between the ion and the coordinating ligands which would result from a smaller than optimum site size.

As an example, we will look at Mn^{2+} in two different sites in jadeite where the M1 metal-cation site (usually occupied by Al but occasionally also by Mg or Fe) is much smaller than optimum and the M2 site (usually occupied by Na but occasionally also by Ca) much larger than optimum. (The optimum size of site for a Mn^{2+} ion is around 2.21 \AA for the average cation-ligand distance such as exists in Mn minerals such as rhodochrosite or rhodonite.) For the M1 site we would expect the ligand-field parameter $10Dq$ to be large and the Racah parameter B to be noticeably smaller than the free-ion value B_0 . For the M2 site, on the other hand, we expect a much lower $10Dq$ value but a higher B -value closer to that of the free-ion. We find that this is indeed the case (see Figs. 9, 10). The same argument applies to the two different metal-cation sites (Mg and Ca) in dolomite or diopside. In dolomite the partitioning of Mn between the two metal-cation sites varies from sample to sample and is probably indicative of differing conditions of formation or subsequent history. For example, high pressure should favour increased population of the Ca site by Mn in dolomites (Walker et al. 1989).

Chromium emission occurs in many minerals where Cr^{3+} in octahedral coordination usually but not always substitutes for aluminium, for example in grossu-

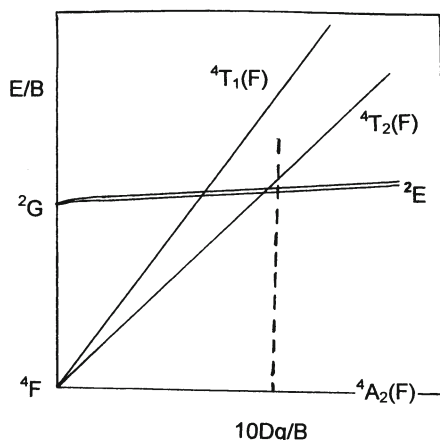


Fig. 11. A partial ligand-field diagram for Cr^{3+} in octahedral co-ordination. The *dashed* line represents the energy-level spacings for spodumene (see text for discussion). Note that unlike Mn^{2+} , in which the quartet excited states are all derived from different states of the free ion to that of the sextet ground state, spin-allowed transitions are possible between quartet states derived from the same free-ion state as the ground state. The transition responsible for the R-line emission, however, is the spin-forbidden ${}^2\text{E}-{}^4\text{A}_2$ transition

lar garnets (Mazurak 1994), emerald, and, as we have already seen, in spodumene. A simplified strong-field ligand-field diagram for $3d^3$ ions is shown in Fig. 11. The crucial region of the diagram is where the ${}^2\text{E}$ and ${}^4\text{T}_2(\text{F})$ levels cross. If the value of $10\text{Dq}/\text{B}$ (i.e. the ligand-field strength divided by the Racah parameter B) is to the right of the cross-over point then the emission will be R_1 -line emission at least at low temperature. When the value of $10\text{Dq}/\text{B}$ is smaller and lies to the left of the cross-over point the emission will be broad-band and due to the ${}^4\text{T}_2-{}^4\text{A}_2$ transition. Quite often, however, for Cr^{3+} octahedrally coordinated by oxygen ions, $10\text{Dq}/\text{B}$ is such that it is very close to the cross-over point but slightly to the right of it. In this case, at low temperature we see the R_1 -line (from the ${}^2\text{E}$ state) in emission but at higher temperatures the ${}^4\text{T}_2$ state becomes thermally populated resulting in the appearance of broad-band emission from this state in addition to the R-lines. At higher temperatures there are usually two R-lines since the ${}^2\text{E}$ state is often split because of non-cubic components of the ligand field (i.e. the site may not be a perfect octahedron) and the R_2 -line at higher energy is the result of thermal population of the upper split component of the doublet E state. The emission spectrum of a chromium-rich spodumene (hiddenite) in Fig. 2 demonstrates this behaviour, and the excitation spectrum of the chromium emission (Fig. 12) shows all the states of this ion up to $25,000\text{ cm}^{-1}$. In the case of Cr^{3+} , the position of the peak of the ${}^4\text{T}_2(\text{F})$ band in absorption or excitation gives the ligand-field parameter 10Dq directly (usually measured in cm^{-1}).

Another interesting point is the fact that emission from the ${}^2\text{E}$ state (i.e. the R-lines) is spin-forbidden and therefore has a long luminescence decay time (usually ms) whereas emission from the ${}^4\text{T}_2$ state to the ${}^4\text{A}_2$ ground state is spin-allowed

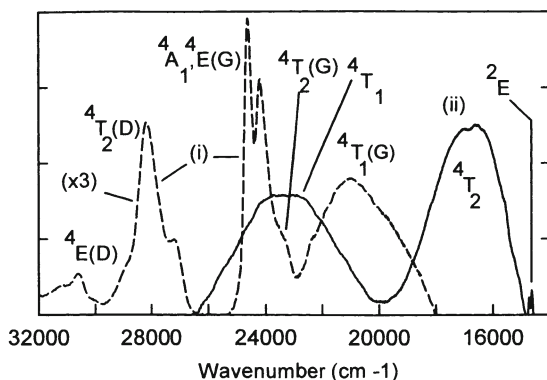


Fig. 12. Luminescence excitation spectra of Mn^{2+} and Cr^{3+} in spodumene. Note that the Mn^{2+} spectrum is that of a low-field site (i.e. the Li site rather than the Al site). With Racah parameters of $B=857\text{ cm}^{-1}$ and $C=3210\text{ cm}^{-1}$, the ligand-field strength $10Dq=6000\pm 300\text{ cm}^{-1}$ (see the values for the M2 site in jadeite; see Fig. 10). The Cr^{3+} spectrum is very characteristic with sharp R-lines due to transitions to the 2E state, which being ZPLs are in the same spectral position as in the emission spectrum. The broad bands due to absorption transitions to the 4T_2 and 4T_1 states from the 4A_2 ground state are spin-allowed and therefore much stronger than the spin-forbidden R-line transitions. The position of the 4T_2 band gives the value of $10Dq$ directly and is $16,600\pm 200\text{ cm}^{-1}$. (Walker et al. 1997; see Acknowledgements)

and therefore has a very much shorter decay time. When the two states are populated in thermal equilibrium, however, the decay time will necessarily be the same for both states and at higher temperatures will approach that of the spin-allowed transition, for example, Cr^{3+} in synthetic forsterite (Glynn et al. 1991) and in kyanite (Czaja et al. 1995).

In this case it would not be possible to separate the R-line emission from the broad-band by time-resolved techniques.

5 Summary and Conclusions

The luminescence emission spectrum and the way it varies with temperature can give useful clues as to its origin. The luminescence decay time is a very important parameter in the determination of the nature of the centre and the fact that luminescence from different centres have different decay times enables us to separate spectrally overlapping bands using time-resolved spectral techniques and indeed to determine exactly how many different bands are actually present. Such measurements are, however, only possible if the excitation is pulsed or modulated.

Luminescence excitation spectra can be very diagnostic for transition-metal ions and allow ligand-field parameters to be determined which can give a strong indication of the site occupation. Polarised excitation spectra of single crystals can also give information concerning the site symmetry.

If both emission and excitation spectra are measured then the Stokes shift and the Huang-Rhys factor can be determined although the latter can also be estimated from the emission spectrum alone and is a crucial indicator of the nature of the centre.

Acknowledgements. Thanks are due to the Mineralogy Department of the British Museum, and to the many individuals, too numerous to mention by name, who have kindly provided many of the samples upon which we have been able to carry out measurements. The author would like to acknowledge the contributions made to this work over many years by his former research students. Financial support from British Petroleum and British Gas at various stages of the work is also acknowledged. The author would also like to express his gratitude to colleagues at UCG, Galway, Ireland, for their continued support and cooperation, and for the facilities put at his disposal during many visits there, and also to the British Council for providing grants to make such visits possible. Figures 1, 2 and 12 are reprinted from *J. Luminescence*, 72–74, Walker et al., “Luminescence spectroscopy of Cr^{3+} and Mn^{2+} in spodumene ($\text{LiAlSi}_2\text{O}_6$)”, pp 287–280 (1997) and Figs. 7 and 8 from *J. Luminescence*, 72–74, Gorton et al., “Experimental analysis of the composite blue cathodoluminescence emission in quartz”, pp. 669–671 (1997) with the kind permission of Elsevier Science, NL, Sara Burgerhartstraat 25, 1055 KV Amsterdam, The Netherlands.

References

- Alonso PJ, Halliburton LE, Kohnke EE, Bossoli RB (1983) X-ray induced luminescence in crystalline SiO_2 . *J Appl Phys* 54: 5369–5375
- Barker CE, Kopp OC (1991) Papers in luminescence microscopy and spectroscopy: qualitative and quantitative applications. SEPM
- Czaja M, Mazurak Z, Lukowiak E (1995) Spectroscopic properties and crystal-field analysis of Cr^{3+} in kyanite. *J Appl Spectroscopy* 62: 44–52
- Glynn TJ, Imbusch GF, Walker G (1991) Luminescence from Cr^{3+} centres in forsterite. *J Luminescence* 48/49: 541–544
- Gorton NT, Walker G, Burley SD (1997) Experimental analysis of the composite blue cathodoluminescence in quartz. *J Luminescence* 72–74: 669–671
- Green GR, Walker G (1985) Luminescence excitation spectra of Mn^{2+} in synthetic forsterite. *Phys Chem Minerals* 12: 271–278
- Henderson B, Imbusch GF (1989) Optical spectroscopy of inorganic solids. Oxford University Press, Oxford
- Marfunin AS (1979) Spectroscopy, luminescence and radiation centres in minerals. Springer, Berlin.
- Mazurak Z (1994) Luminescence and excited state 2E_g decay kinetics of Cr^{3+} in Grossular $\text{Ca}_3\text{Al}_2(\text{SiO}_4)_3$. *Optical Materials* 3: 89–93
- O'Connor G, McDonagh C, Glynn TJ (1991) Luminescence from Fe^{3+} in octahedral sites in LiGa_5O_8 . *J Luminescence* 48/49: 545–548
- Stevens Kalceff MA, Phillips MR (1995) Cathodoluminescence microcharacterization of the defect structure of quartz. *Phys Rev B* 52: 3122–3134
- Trukhin AN (1992) Excitons in SiO_2 : a review. *J Non-Crystal Solids* 149: 32–45
- Trukhin AN (1994) Self-trapped exciton luminescence in α -quartz. *Nuclear Instr and Methods in Phys Research B* 91: 334–337

- Walker G (1985) Mineralogical Applications of Luminescence Techniques. In Berry FJ, Vaughan DJ (eds) Chemical bonding and spectroscopy in mineral chemistry. Chapman and Hall, London, pp103–140
- Walker G and Glynn TJ (1992) Infra-red luminescence of iron-doped synthetic forsterite. *J Luminescence* 54: 131–137
- Walker G, Abumere OE, Kamaluddin B (1989) Luminescence spectroscopy of Mn^{2+} centres in rock-forming carbonates. *Mineral Mag* 53: 201–211
- Walker G, Kamaluddin B, Glynn TJ, Sherlock R (1994) Luminescence of Ni^{2+} centres in forsterite (Mg_2SiO_4). *J Luminescence* 60/61: 123–126
- Walker G, El Jaer A, Sherlock R, Glynn TJ, Czaja M, Mazurak Z (1997) Luminescence spectroscopy of Cr^{3+} and Mn^{2+} in spodumene ($LiAlSi_2O_6$). *J Luminescence* 72–74: 278–280

Information Encoded in Cathodoluminescence Emission Spectra

P.D. TOWNSEND, A.P. ROWLANDS

1 Introduction

The development of cathodoluminescence (CL) phosphors for television and computer screens has been extremely successful in terms of colour quality and long-term stability of the screens but these achievements have been made in a semi-empirical fashion and do not imply the same degree of maturity for analytical uses of CL. This is unfortunately the case even though CL has more than a century of history, with numerous routine applications in geological and mineral studies. Indeed the first cited example was excitation of a natural crystal, diamond (Crookes 1879). Current mineralogical usage is often qualitative, with visual, or photographic, inspection of the luminescence. Information is provided by variations in intensity and colour which can be helpful in separating mineral composites, and certainly will clearly indicate the presence of zoning and the diversity of component minerals in a particular sample. One bonus of the CL equipment is that the electron beams generate characteristic X-rays from the target elements and thus from the complementary X-ray analyses it is possible to map some of the compositional variations within a sample and relate these to the emission patterns. CL is also compatible with electron microscopy imaging and can in principle be followed down to the micron grain size level. Thus for mineralogical studies the combination of techniques is clearly valuable (Yacobi and Holt 1986, 1990; Marshall 1988; Ozawa 1990; Walker and Burley 1991; Remond et al. 1992).

Despite the photogenic appearance of many CL images it is essential to decide what quantitative information is desirable, if it is actually possible to gain such data, and to assess if the problems associated with sample preparation influence the signal. In addition, there are changes introduced by the electron beam bombardment and it is essential to apply signal corrections associated with the recording equipment. Some of the problems are immediately obvious as for example even the photographic colour images vary greatly as a result of different electron beam intensities, exposure and developing conditions. Finally, one would like to know if the luminescence signals can be directly correlated with specific and detailed models of the lattice distortions or the impurity structures which provide the luminescence sites. Whilst this is a fundamental objective, the historical precedents are not totally encouraging, in that whilst there is often a broad understanding of the mechanisms and lattice imperfections which control the

Table 1. Examples of current understanding for optical technologies

Example	Year	Basic concept	Details of process (%)
Thermoluminescence	1663	Yes	60
Photographic process	1830	Yes	70
Cathodoluminescence	1879	Yes	40
Fluorescent lamps	1910	Yes	50
Photocathodes	1930	Yes	40
Solid state lasers	1960	Yes	80
Optical fibres	1965	Yes	80

luminescence emission, progress to detailed lattice site structures is extremely rare, and examples of reliable prediction of the effects of change, are negligible. This is not specifically a problem of CL but of all imperfection controlled processes (i.e. all modern materials technology!). Even for the few textbook classic examples of successful structural identification of colour centres in alkali halides the process has taken 60 years and perhaps as much as 5,000 research years per detailed defect model. It is thus abundantly clear that, for most studies, progress and interpretation are based on a compromise situation between a broad overview and a working model of the processes for a specific example. Rather than appear critical of progress with CL analyses one can place this approach in context by considering the historical developments and the degree of confidence available at present from a range of industrially important optical processes or analytical technologies and techniques. Table 1 indicates a personal estimate of the situation. The table gives approximate dates when the examples were first reported or used, and it underlines that even though some techniques have been mentioned in the literature for a considerable period of time, and are widely used, there is rarely a profound understanding of the detailed mechanisms, despite having some confidence in the broad concepts.

2

Essential Experimental Considerations

Before discussing any specific examples of the benefits to be gained from knowledge of the CL emission spectra it is worth first noting some inherent problems associated with the collection of the signals. These considerations are particularly relevant for the mineralogical and geological applications since for historical reasons CL in these areas often involves unfortunate practices which, whilst not serious for earlier simplistic intercomparisons of signals, will be severely limiting and/or misleading on attempting to extract quantitative and more detailed information. These difficulties will become increasingly apparent as the full power of the technique using spectrally resolved CL is exploited. A list of factors which need consideration is first given, and subsequently some more detailed examples will be provided.

1. The preparation of the CL geological slices involves sectioning and polishing methods which change the surface CL emission relative to the bulk material.
2. The electron beam is not a passive probe of the surface and it can generate colour centres, cause ionic diffusion, compositional changes, or even decomposition (e.g. Agullo Lopez et al. 1988).
3. As the result of electron beam driven damage and charge redistribution within the trapping and luminescence centres in insulating materials, the CL intensities, spectra and excited state lifetimes will be a function of the current density, electron beam energy, sample temperature and, where used, the modulation frequency (Yacobi and Holt 1986, 1990; Marshall 1988; Ozawa 1990; Walker and Burley 1991; Remond et al. 1992). Since these variations are strongly dependent on the impurity content of the samples, they will differ between specimens of the same material, and between different zones of the same sample (Krbetschek et al. 1998).
4. Rather than merely record panchromatic signals via broadly filtered spectral zones, as for colour photographs, the use of wavelength dispersive systems invariably requires longer signal collection times, or higher beam currents, hence damage and changes are exacerbated. In scanning monochromator equipment spectral resolution into 100 channels implies an increase in irradiation time by at least 100-fold. Wavelength multiplexed systems, which avoid this problem, can be used for CL, but they are much more expensive than scanning systems.
5. A serious experimental problem is that diffraction gratings and photomultipliers vary considerably in efficiency as a function of wavelength. Diffraction gratings typically fall to about 10% of their maximum efficiency by about 50% and 200% of their optimum wavelength, which is controlled by the “blaze” or “apodisation” applied during manufacture of the grating. This wavelength performance is polarisation sensitive which can cause further spectral distortions when examining single crystals. Similarly, photomultiplier tubes are strongly wavelength dependent, and are always relatively inefficient in the red end of the spectrum. Consequently, the recorded wavelength dependence of the signal differs greatly from that of the original emission at the sample. For example in one Sussex scanning monochromator system, (with a grating blazed near 350 nm and an S20 red sensitive PM tube) the overall sensitivity falls by 200 times from the maximum near 400 nm to detection at 800 nm. All too often the first attempts at spectrally resolved CL fail to correct for such changes and hence the data are valueless except for trivial purposes. The only excusable exception could be for detection of rare earth impurities where the identification is made by the position of the characteristic narrow line features, as in this case corrected intensity data will only be needed for quantitative estimates.
6. Even when data are processed to correct for the system response, there has been a historic tendency to plot luminescence spectra as a function of wavelength, rather than on a physically more meaningful energy axis. Two facts should be noted, firstly the conversion of the wavelength to energy scale is simply by using $E=1239.6/\lambda$ (in eV and nm), secondly with a grating monochro-

mator the intensity axis is $I(\lambda)d\lambda$, but on conversion this must be transposed to $I(E)dE$ by scaling by λ^2/hc , (e.g. signals of equal intensity at 400 and 800 nm on the wavelength presentation differ in intensity by a factor of 4 on the energy plot, with the red signal being the stronger one).

7. Having applied systematic corrections and produced energy related spectra, it is possible to attempt deconvolution of broad band emission spectra into component bands. This process can be greatly assisted if the electron beam can be spatially modulated and the signals recorded in a time resolved mode or via a lock-in amplifier. Since in general different emission bands will have different lifetimes the intercomparison of spectra taken at various times after excitation, or at different modulation frequencies, will aid deconvolution and allow separation of component features (Townsend et al. 1999).
8. Deconvolution of the spectra will require assumptions about the shapes of the emission bands and Gaussian or Lorentzian band shapes are normally the first guesses to try for the features which involve multi-phonon processes, and hence have full widths at half maximum of at least 0.5 eV. Such bands will normally become narrower at low temperature and cooling may change the pattern from broad bands to reveal the presence of zero-phonon lines (Agullo Lopez et al. 1988). The presence of narrow line features can be valuable for identifying the presence of rare earth ions or for observing localised transitions between energy states of specific impurities, as will be described below.
9. Although it may seem obvious, it is essential to correct for filament light which is scattered into the spectral analyser. Unfortunately one can readily cite examples where an error has been made, and the mistake is not limited to detection of weak signals, but can equally occur when part of the spectrum contains a strong emission band but detection extends over a wide range. The problem can effectively be avoided when using lock-in detection.

3

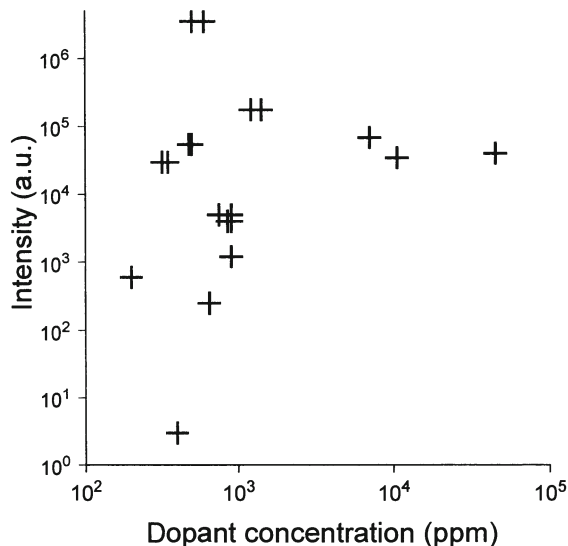
Spectral Information

3.1

Manganese in Carbonates

Clues as to composition or distribution of impurities are fairly clear since variations in intensity or colour may correlate with changes in impurity distributions. A frequently cited classic example of an impurity signature colouration is the orange emission recorded from manganese impurities in the carbonates, such as calcite (Walker et al. 1989; Calderon et al. 1996). It should be immediately recognised that the luminescence intensity of phosphors are rarely, if ever, a simple linear function of the concentration of the impurity ions. Mn in CaCO_3 is no exception and Fig. 1 describes a typical pattern of Mn luminescence intensity as a function of impurity concentration (Calderon et al. 1996). This figure, although based on thermoluminescence data, is particularly instructive as it shows that the maximum in the output intensity is a function of the total impurity content, not just the Mn which provides the signal. However, the pattern of luminescence

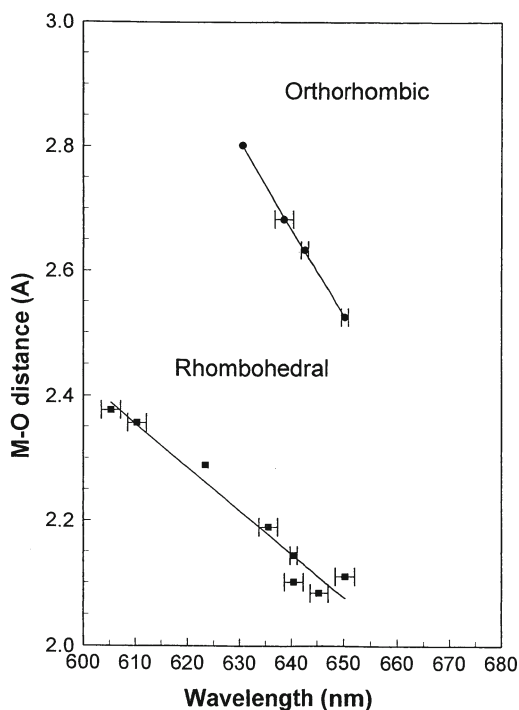
Fig. 1. The thermoluminescence emission intensity for the glow peak recorded near 120°C for Mn doped calcite as a function of total impurity content (Mn, Fe, etc.). Note the orange emission is primarily the result of the Mn impurities



quenching at high dopant concentrations, greater than $\sim 0.1\%$, is typical. Most interpretations of such data propose that at higher impurity concentrations the added ions are statistically so close that they interact and provide non-radiative energy transfer between the ions. This may be the result of the distortions the impurities impose on the lattice structure or, in order for the lattice to reach a minimum free energy, the growth process involved the formation of closely associated pairs, or clusters, of impurities. This model is consistent with many examples of impurity inclusion during crystal growth, and at higher concentrations not only pairs and clusters, but also phase precipitates develop, rather than a uniform dispersion of dopants throughout the lattice. Such variants in the way the impurities are incorporated will be reflected by changes in the luminescence properties. Typically there will be shifts in the transitions energies, and so the emission bands or lines of the defect sites will differ in wavelength, width, lifetime, quantum efficiency and temperature dependence (Hallensleben et al. 1999).

In addition to the visual information, more detailed spectral analysis of the peak wavelength of the impurity emission can indicate the type of lattice sites, host composition and the crystal phase. Examples for Mn in carbonates are well documented and show that the main Mn signals move to shorter wavelengths for carbonate lattices with larger metal-oxygen bond lengths. In cases such as dolomite where there are two alternative sites for the Mn, emission at both wavelengths has been observed in intensity ratios appropriate to the site occupancy. The spectral information from recording broad band emission is often difficult to interpret, not least because the impurities themselves may not provide a clear signature, rather, they change the relative intensities of emission sites intrinsic to the lattice, or merely modify the position of the bands. Figure 2 plots the wavelengths of thermo- and radio-luminescence (TL and RL) maxima for a set of carbonate minerals from which it is apparent that not only are the changes in metal-oxygen

Fig. 2. The wavelength dependence of the Mn emission bands in different carbonates as a function of the metal-oxygen bond spacing. Note the effect of different lattice structures. These data are for RL and TL, and careful analysis of the CL reveals a similar pattern



bond length shifting the spectra, but also the changes depend on the crystal structure. The pattern of movement for the rhombohedral and orthorhombic crystals are clearly different (Calderon et al. 1996).

It is not immediately obvious if the same patterns of wavelength shift with lattice dimensions exist in CL of these minerals as the trends do not emerge with the same clarity. The basic problem is that in the CL examples the relative intensities of competing emission processes make it difficult to immediately recognise which peaks relate to the same transitions. The CL excitation favours a wider range of allowed luminescence transitions than are recorded from TL or RL and it is sensitive to distortions and defects within the near surface layers. This problem is shown rather clearly in Fig. 3 which presents the CL spectra from two samples of aragonite. Even for one mineral, the highest peak intensities do not always occur at the same wavelengths as the spectrally resolved signals comprise a mixture of narrow line features and broader emission bands corresponding to transitions between discrete Mn levels, relaxed states and lattice defects. In attempting just a simple visual intercomparison, for construction of a plot of the types shown in Fig. 2, the use of values from just the most intense bands, leads to scattered data and poorly defined patterns. Indeed an early CL attempt had suggested an inverse sense to the wavelength shifts from that shown in Fig. 2. In hindsight this can be seen to be the result of a confusion between different components and/or sample heating. More importantly one must separate out the component features, as is done for the examples of Fig. 3. The precise fit may depend on the starting

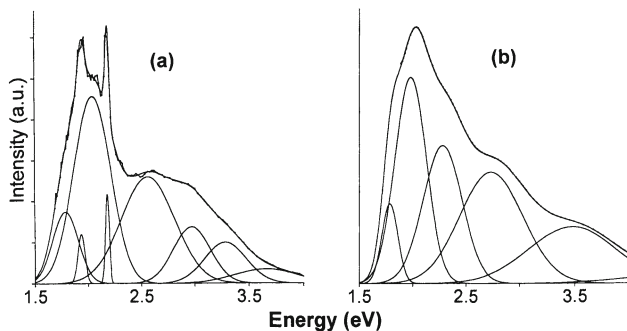


Fig. 3. Cathodoluminescence (CL) of two aragonite samples which show a combination of narrow line and broader band emission features. These have been computer resolved as Gaussian shaped emission bands. The *upper lines* of both figures display the original data and the sum of the component bands

assumptions, and in the examples shown the free running computer fits arrive at different solutions in terms of the component peaks. Nevertheless, it is clear that the analysis of such spectra involves a mixture of narrow line and broad band emissions and, after deconvolution, the visually obvious line features may in fact be among the smaller luminescence signals.

As a final example of the complexity involved in the apparently simple CL of Mn doped carbonates, Fig. 4 shows a set of spectra obtained using a lock-in amplifier detector. These data were obtained with a logarithmically increasing sequence of modulation frequencies from 9 Hz to 90 kHz. At low frequencies all the orange (Mn related) signals appear to respond to the modulated excitation but at progressively higher frequencies the signals from transitions with long excited state lifetimes are rejected by the lock-in detection. The spectra therefore change with increasing modulation frequency. A long wavelength signal has frequently been attributed to the presence of iron. In wavelength uncorrected data values are cited from 700 to 780 nm in various minerals for Fe^{3+} CL emission (Marshall 1988). In a recent example of CL studies of glass, where iron is included to make green glass, the spectral corrections place the peak near 780 nm (1.59 eV) (Townsend et al. 1997).

This brief selection of carbonate examples underlines the facts that not only do various ways of recording luminescence offer different facets of the information, but in addition the CL technique can benefit by reference to other types of luminescence data. Even having separated the number of component processes, there still remains the much more difficult stage of identifying the specific processes, and providing a detailed model of the lattice structures. This step requires input from as many other different techniques as possible. Unfortunately very few methods are available which can uniquely provide detailed defect structures, virtually the only common exceptions are electron paramagnetic resonance (EPR) and electron nuclear double resonance (ENDOR), and these have a weakness that they do not separate spatially separated changes in the samples, which are a characteristic feature of the zoning seen by CL of minerals.

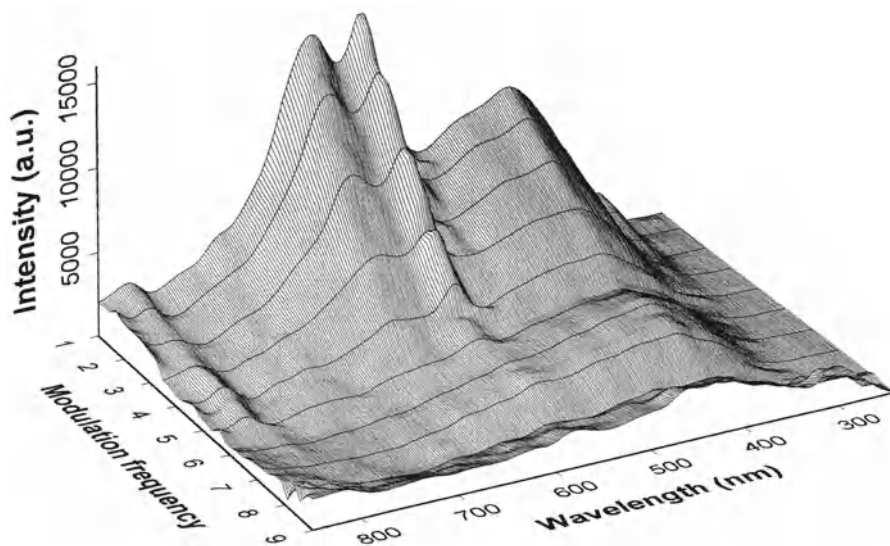


Fig. 4. Lock-in amplifier recorded CL spectra from Mn and Fe doped aragonite as a function of modulation frequency. The modulation frequencies are in logarithmic steps from (9 Hz to 90 kHz

3.2 Rare Earth Impurity Ions

In the case of rare earth ion emission sites, where there are transitions between inner electron shell energy levels, the levels are often relatively well shielded from the host lattice, hence the spectra display “free ion like” very narrow line luminescence (Cesbron et al. 1993; Yang et al. 1992). Because the lines are narrow and well defined, small changes in the local crystal fields can be sensed by high resolution spectroscopic detection of the line movements. In principle CL should be an efficient method of detecting and identifying the presence of rare earth ions since the signals have unique wavelength signatures, and so separation of different rare earths is possible. A common feature of rare earth doped insulators is that the rare earth sites provide a large capture cross section for emission and so may suppress emission from other types of luminescence site. Detection of the presence of rare earth ions via their CL spectra is frequently cited, but quantitative determinations of their relative concentrations is extremely difficult. Not least because the various rare earth ions in the same host lattice can differ greatly in luminescence efficiency, and further, where the total polychromatic light intensity is recorded via a photomultiplier tube the variations in spectral distribution distort the apparent luminescence efficiencies in favour of those emitting in the blue region, where the PM tubes are most efficient. It must be recognised that, except for the lowest impurity concentrations of a few ppm, the rare earth ions preferentially form in pairs or clusters, and these more complex defect sites frequently inhibit radiative decay. Hence, whilst

detection of a rare earth line emission signature is evidence for the presence of a dopant, failure to detect a signals is not proof that it is absent. There are numerous photoluminescence (PL) and TL articles which show that the radiative efficiency changes between equal quantities of rare earth ions results in signals differing by factors of up to 10^6 . For example in a recent study of TL in bismuth germanate (Raymond et al. 1994) the rare earth dopants: (a) totally suppress the intrinsic emission bands above about 100 K, (b) the TL peak temperatures move with the size of the rare earth ion and (c) in multiply doped material there were no signals from the heavily doped constituents (0.4% Nd and Er), but clear signals from Eu which was only present at the level of ~ 3 ppm. This pattern of behaviour must be recognised in the interpretation of CL spectra. An intuitive feeling is that it is perhaps less of a problem with CL than other luminescence methods, since the electron beam provides a very high excitation density which stimulates normally forbidden decay routes. CL signals thus contain components not only from "normal" luminescence processes, but also from those which may be selection rule forbidden. Less helpfully, there is a greater wealth of CL signals compared with many other luminescence methods, since CL responds to transient defects, and structures formed during the radiation damage created by the electron beam itself (as mentioned later).

3.3

CL from Surface Relaxations and Electron Damage

Cathodoluminescence is both a probe and a source of surface damage (Heiderhoff et al. 1994; Peto et al. 1997). This poses problems since the electron beam can both redistribute electrons between existing trapping and luminescence sites, and generate new transient defects. In this dynamic situation the transient defects may interact with the more stable entities to modify the emission spectra. As an example of the power of the CL as a surface probe of defects in relatively stable materials CL has recently been used to probe the damage and dislocation density in the surface of Nd:YAG crystals used for the fabrication of waveguide lasers (Peto et al. 1997). Preparation of laser crystals requires careful cutting and polishing, with the inherent problems of generation of surface dislocations and polishing stresses in the outer few microns of the surface layer. Such defects are not always visible, and the laser crystal surface may optically appear excellent. However the presence of dislocations can quench luminescence and, for sensitive lattice probes such as the internal transitions of rare earth ions, be reflected by movement of the emission wavelengths. The polishing problems do not always attract much attention for bulk laser crystals, but for waveguide lasers, these problems are disastrous. The polishing damage often extends several microns in depth below the surface, which is precisely the depth scale used for the laser waveguides. In order to probe the surface damage, CL spectra have been recorded as a function of energy in conventionally polished Nd:YAG, and material free from the polishing induced dislocations has been generated by use of an amorphisation and enhanced chemical etching technique. Figure 5 indicates the scale of the spectral shifts which develop. Some depth dependent information was revealed by varying the electron energy to excite only near surface material or a greater spread in

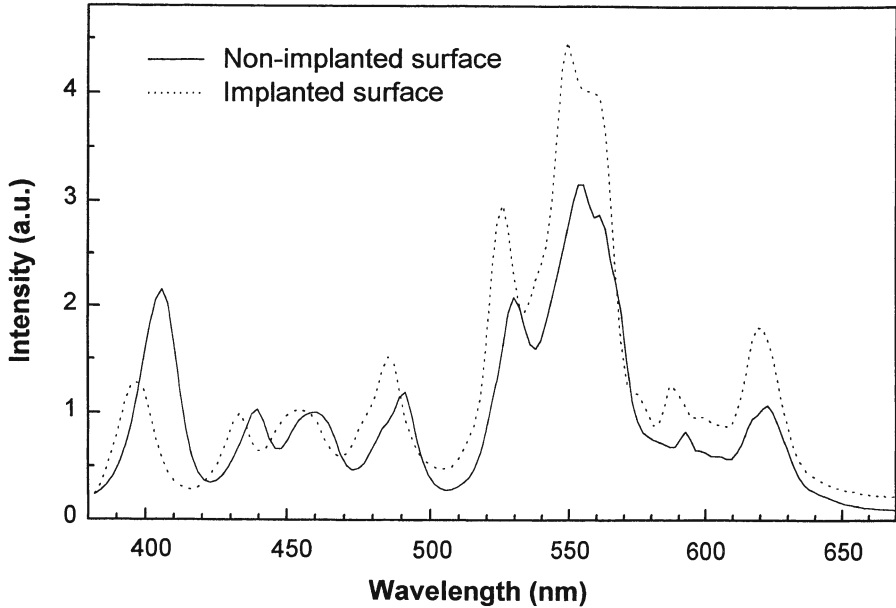


Fig. 5. A comparison of cathodoluminescence (CL) spectra from Nd:YAG obtained from a heavily damaged and an undamaged surface

depth. Confirmation that the CL was giving signals typical of the bulk material was made by noting an agreement in the emission wavelengths between radioluminescence and the dislocation free surfaces.

In the Nd:YAG example the luminescence intensity is reduced by the presence of damage, which offers non-radiative decay of the excitation energy. Such luminescence quenching is relatively common and the CL beam can be used to reveal grain boundaries and dislocation lines. Intrinsic defects, such as dislocation lines, frequently appear as dark lines on a brighter CL background. However, as is typical of defect processes, this is not a universal rule, and in some materials impurity ions are displaced from the lattice and accumulate as a decoration of the dislocation lines. Where such impurities offer a characteristic CL emission they may offer the inverse situation of strongest emission along the lines. In either case the CL will reveal details of the surface quality and, with the benefit of spectral analysis, may indicate how impurities migrate throughout the crystallites.

Whilst many oxides and silicates, such as garnets, quartz or sapphire, are assumed to be relatively stable to electron beam bombardment, virtually all oxides dissociate to some extent and lose oxygen ions from the outermost layers (Agullo Lopez et al. 1988). Thus the outer tens of atomic layers may be oxygen deficient or relaxed into new structures, but these depth scales are normally small compared with the depths excited during CL. The situation is however very different for most of the halide materials, such as the alkali halides, where the electron energy powers mechanisms which allow halogen ions to relax, restructure,

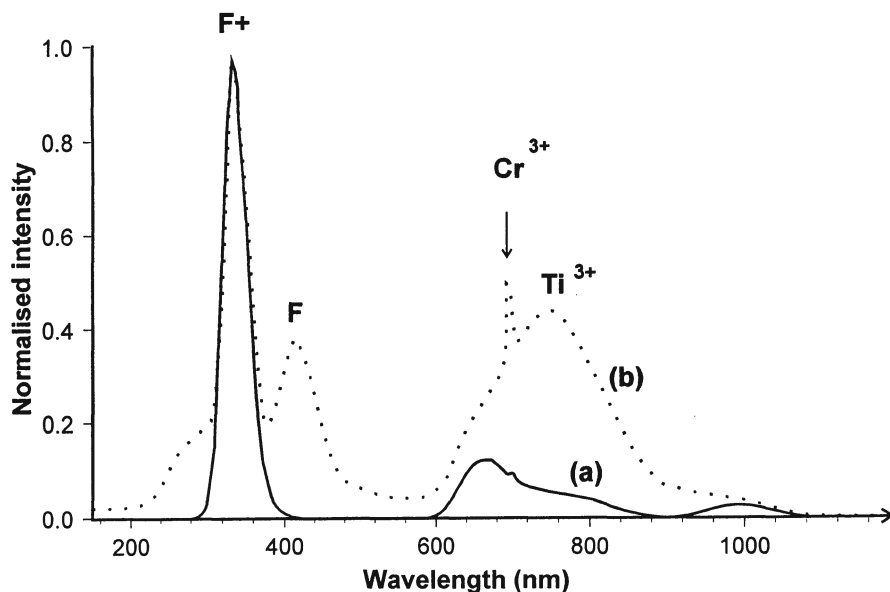


Fig. 6. The intensity normalised CL spectra of a sapphire sample obtained at two different electron beam currents. Note curve (a) was 40 times more intense but the current density was only increased by ~ 20 times

and move from their lattice sites and so form intrinsic defects in the lattice structure. Intrinsic defects can be relatively stable, as in alkali halides, or have a transient lifetime before restructuring into the original lattice geometry. Some oxides, such as amorphous silica, are similarly permanently damaged by the ionisation from the electron beam and not only form oxygen defects but also alter the density (i.e. a compaction of several % in this case). In the dynamic situation of CL production both types of process contribute to the complexity of the emission. This adds considerably to the list of processes which can generate the light, even if the atomic displacements and transient defects are thermally unstable. In all cases the signals result from a competition between radiative and non-radiative processes as the electrons and holes are stimulated from their stable locations. Unfortunately these same excitations generate electronic conversions between different charge states of the imperfections and modification of existing defects, coupled with production of new defects and interactions between the new (albeit transient) defects and those pre-existing in the material. Cathodoluminescence is therefore a very powerful probe of the multitude of ensuing defect sites, but it is not a passive tool, and the signals can change considerably as a result of electron beam conditions. This will be demonstrated by reference to Figs. 6–8. The CL data of Fig. 6 were obtained for a stable oxide, sapphire (Al_2O_3), which shows two strong blue/UV emission bands from the presence of intrinsic oxygen vacancy centres. These are the F and F^+ centres which represent oxygen vacancies containing either two or one electrons respectively. Natural sapphire contains many

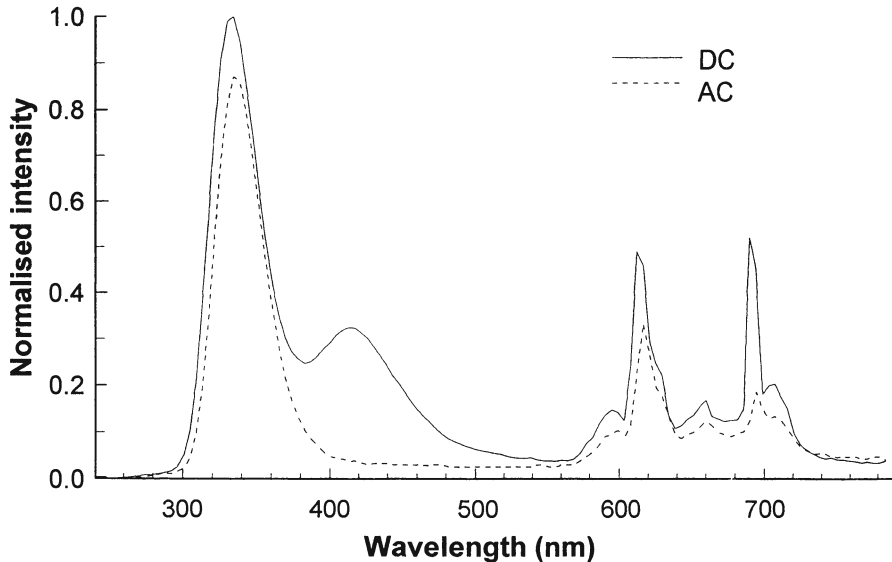


Fig. 7. Cathodoluminescence (CL) spectra obtained from a sapphire sample with a constant beam current but recorded at very low frequency (DC) and with phase detection for a modulated beam

trace impurities and in this example the spectra also show some red line emission from Cr^{3+} impurities (i.e. as in ruby) and broader red bands from Ti^{3+} ions in the lattice (i.e. as in blue sapphire). Whilst the CL spectra clearly detect all four types of defect sites it is extremely difficult to make any quantitative judgement as to the defect concentrations. The relative intensities of the component bands differ as a function of electron current density and Fig. 6 records spectra from the same sample but for two different electron beam currents. This clearly shows changes in the dynamic balance of the signals from the F and F^+ sites. There is also a difference between the relative intensity of signals from the Ti and Cr dopants. The two sites also differ in their excited state lifetimes, hence the use of phase sensitive signal detection (with a lock-in amplifier) can be used to suppress signals from the longer lived site. The CL spectra of a sapphire samples are shown in Fig. 7 for identical beam currents but contrasted between DC and modulated detection.

For the more complex situation of CL obtained from a material such as NaCl, which readily damages and forms transient halogen vacancy type defects during bombardment, great care must be made in specifying the irradiation conditions. In one such study (Aguilar et al. 1979) the variants included changing the electron beam energy, sample temperature, beam current, square wave modulating of the beam for lock-in amplifier detection, and using variations in the duration of the on to off times to alter the density of transient defects. The spectra obtained from the NaCl in all these cases had a similarity in that there are two main emission regions broadly centred around 2.4 and 3 to 3.5 eV. Photoluminescence studies

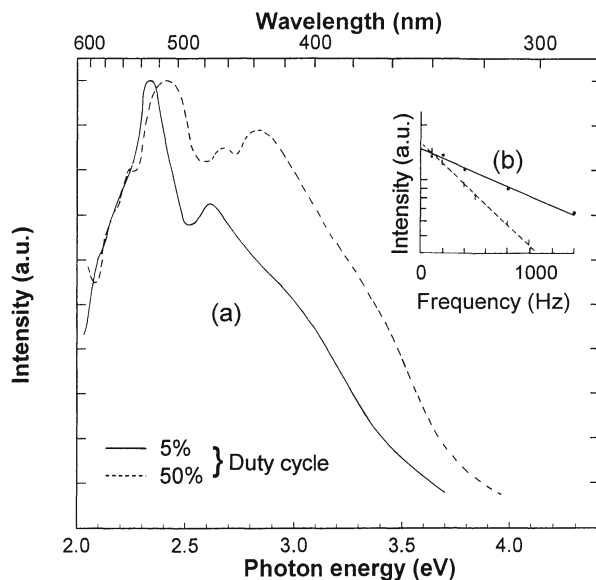


Fig. 8. Cathodoluminescence (CL) spectra of NaCl obtained at room temperature using 2.5 keV electrons. The main figure records data from 100 Hz modulation with duty cycles of 50 and 5%. The inset shows intensity dependence on modulation frequency for these two duty cycles for the signal at 425 nm (2.92 eV)

indicate emission from the decay of the σ and π states of the intrinsic excitons is near 3.4 and 5.4 eV respectively. Emission nearer the low energy 2.4 eV region had been ascribed to variants of transitions between (V^k+e^-) levels (Aguilar et al. 1979; Song and Williams 1993). However, these exciton-like emissions are extremely sensitive monitors of the lattice perfection and therefore the spectra show a multitude of perturbed emission bands corresponding to the presence, and decay, of other defects. Consequently the detailed spectra changed for each of the CL variations mentioned above. Figure 8 gives some examples which include the movement of the emission peaks near 2.5 eV, and major changes in the relative intensities of the lower and higher photon energy peaks. The inset in Fig. 8 also indicates how the lock-in amplifier signal varies with modulation frequency. This is indirectly related to excited state lifetimes and clearly shows a shift defined by the duration of the excitation duty cycle. This was interpreted as evidence for transient defect effects which modify the CL spectra.

As exemplified by the sapphire and NaCl examples, the emission from electron-hole recombination can occur by the formation of an exciton (an electron-hole bound pair), or as a variant with one of the charges localised at a defect site. These tend to have relatively long lifetimes, and so can respond to small relaxations in the local environment. Despite this site sensitivity the primary energy of the emission of the relaxed energy is not strongly dependent on the lattice and therefore most commonly studied materials, including quartz, feldspars, zircon, fluorides and oxides etc, always emit near 400 nm in the blue region. The more

detailed spectral analyses can reveal, as for NaCl, the smaller shifts associated with changes in impurity sites, or inbuilt stresses from different growth processes. The presence of impurities will also influence the stability and transition probability of intrinsic defect sites. Hence additions of impurities may enhance an emission band, but this does not automatically imply that the band is generated at the dopant site, only that the dopant has enhanced the process of emission. For example in float glass the presence of tin, which diffuses into the surface during production, strongly raises the CL intensity of the emission peaks near 575 nm. These bands also occur in “pure” glass, quartz and silica, and probably relate to an oxygen vacancy site with modified Si-O bonds (Stevens-Kalceff and Phillips 1995). The Sn²⁺ dopants perturb the normal bonding and so enhance the number of broken Si-O bonds. This gives an indirect correlation of Sn concentration with the emission intensity (Townsend et al. 1998).

4

The Scale of Cathodoluminescence Radiation Dosage

Materials which are sensitive to radiation damage pose particular problems for CL studies. The list of materials is not limited to organics or alkali halides, but is considerably greater since the electron beam of a few tens of keV energy is often tightly focused in order to give detailed spatial imaging. However, in order to generate sufficient light intensity for easy recording, the tendency is to maintain a high beam current. Within the focused beam spot this means there is an extremely high rate of ionisation and power delivered to the target. The scale of the radiation doses and local heating which occurs within the beam area are easily overlooked, since the total beam current may be only measured in tens of nanoamps and, if the beam is rastered across the sample as in a TV screen or CL imaging mode, the average power delivered per unit area will be thousands of times less than the peak power density. Estimates of the radiation dose rate are precise since this is merely a definition of power density per unit mass of material, however estimates of the heating excursions as the beam spot is focused or rastered over the sample are complicated since they involve many poorly known parameters. The thermal conductivity of the surface layer may be altered by the electron beam and the generation of free carriers, and the conductivity will be temperature dependent. In principle the heat flow problems have been considered for some considerable time (Marshall 1988; Ozawa 1990; Carslaw and Jaeger 1959) and one expression used to estimate the heating excursion caused by the beam (in units of watts, cm, K) is

$$\text{Temperature rise} = \text{Power} \times (4.27 \times \text{radius} \times \text{thermal conductivity})^{-1}$$

The effects of this simple estimate for steady state continuous beam conditions for the temperature increases expected, together with the radiation dose rates, are given in the following Table 2, for a variety of typical electron beam conditions. The table clearly demonstrates that imaging and focus to a small area, gives

Table 2. Examples of ionisation and heating effects for a 30 keV beam into quartz or silica

Spot size (μm)	Current (A)	Current density (A/cm ²)	Power density (W/cm ²)	Temperature rise (°C)		Radiation dose (Gy/s)
				Quartz	Silica	
3×10^{-2}	10^{-11}	140	4.2×10^6	3.6	14.4	$\sim 10^{10}$
3	10^{-6}	14	4.2×10^5	360	1,440	$\sim 10^9$
10^4	10^{-5}	$\sim 10^{-5}$	~ 0.13	1	4.3	~ 300

local heating and intense ionisation levels. Rapid passage of a scanned beam does not reduce the transient radiation levels even though the integrated dosage will be reduced for larger scan sizes. The influence of the thermal conductivity is demonstrated in the table by comparing values for crystalline quartz with those for the lower conductivity amorphous silica. The scale of these beam effects is frequently overlooked since many CL systems use a scanning spot at microamp current levels and the average power over the scanned area is extremely small. Nevertheless, at each point in the scan the beam will reside on a microsecond, or longer, timescale and so a key question is to estimate the temperature rise within this first microsecond, rather than calculate the average beam heating. Since the beam induced temperature pulsing effects in CL scanning are somewhat contentious and the values cited are difficult to measure, it may be helpful to consider the data from the rather similar, but better documented, situation of pulse laser annealing and pulse laser ablation. In this field there is considerable unequivocal evidence of heat pulse induced changes (Miller 1994; Can et al. 1995; Townsend and Olivares 1997). The laser pulses are normally shorter, at around 10 ns, than the power pulses from a scanning electron beam but nevertheless at pulse energies of say 100 mJ/cm² they can clearly result in localised heating equivalent to temperature rises of $\sim 1,000^\circ\text{C}$ in silica (Can et al. 1995). This power density is comparable to that for the middle example in the Table 2, where the steady state estimate for silica yields a similar temperature rise. The key feature to note from the laser examples is that the thin surface layers reach the predicted temperatures on time scales measured in tens of nanoseconds, which supports the relevance of the heat conductivity calculations for CL. Cooling may be equally rapid, hence long range thermal diffusion may not appear too significant. Nevertheless, many features, notably changes in the CL luminescence efficiency with temperature, are altered dramatically by the heating caused by the passage of the electron beam.

5 Conclusion

The preceding examples have been selected to emphasise that cathodoluminescence is an extremely powerful tool for analysis of impurity and mineral composition, but it is a technique which requires considerable appreciation of not only the potential strengths of the method, but also the very real difficulties in terms of CL generated artefacts. It is equally evident that CL analysis made in isolation from other techniques would provide little information, except to note differences or non-uniformity in the minerals under study. However, when combined with other methods of analysis, it provides an extremely simple, effective and highly sensitive method of investigating composition, dopants and the state of perfection of surface layers. This chapter has assumed throughout that the objectives are to gain maximum information on the targets and thus it is essential to collect quantitative information on the emission spectra and to benefit from the possibilities of electron beam modulation to obtain lifetime and temperature resolved data. Many of these options have not yet been incorporated into routine CL imaging, but undoubtedly they will become standard features of future CL systems. Cathodoluminescence has already a history of more than a century and plays a major role in daily life via TV and computer screens. One can therefore confidently predict a very intense and continuing development in exploiting the analytical roles which it can provide.

References

- Aguilar M, Chandler PJ, Townsend PD (1979) Luminescence in NaCl I: Electron and ion beam excited spectra. *Radiation Effects* 40:1-7
- Agullo Lopez F, Catlow CRA, Townsend PD (1988) *Point Defects in Materials*. Cambridge University Press, London
- Calderon T, Townsend PD, Beneitez P, Garcia-Guinea J, Millan A, Rendell HM, Tookey A, Urbina M, Wood RA (1996) Crystal field effects on the thermoluminescence of manganese in carbonate lattices. *Rad Measurements* 26:719-731
- Can N, Townsend PD, Hole DE, Snelling HV, Ballesteros JM, Afonso CN (1995) Enhancement of luminescence by pulse laser annealing of ion-implanted europium in sapphire and silica. *J Appl Phys* 78:6737-6744
- Carslaw HS, Jaeger JC (1959) *Conduction of heat in solids*. Oxford University Press, Oxford
- Cesbron F, Ohnenstetter D, Blanc P, Rouer O, Sichere MC (1993) Interpretation de terres rares dans des zircons de synthese: etude par cathodoluminescence. *C R Acad Sci Paris* 316:1231-1238
- Crookes W (1879) Contributions to molecular physics in high vacua. *Philos Trans R Soc* 170: 641-642
- Hallensleben S, Rowlands AP, Karali T, Townsend PD (1999) Photon imaging of Thermoluminescence. *Rad Protect Dosim*, 84:115-118
- Heiderhoff R, Spitzl R, Maywald M, Raiko V, Balk LJ, Engemann J (1994) Characterization of MPCVD diamond films grown on porous silicon. In: *Diamond film semiconductors*. Proc SPIE 2151:59-70
- Krbetschek MR, Gotze J, Dietrich A, Trautmann T (1998) Spectral information from minerals relevant for luminescence dating. *Rad Measurements* 27: 695-748

- Marshall DJ (1988) Cathodoluminescence of geological materials. Unwin Hyman, London
- Miller JC (ed) (1994) Laser ablation. Series in Materials Science 28, Springer, Berlin Heidelberg New York
- Ozawa L (1990) Cathodoluminescence, theory and applications. Kodansha, Tokyo
- Peto A, Townsend PD, Hole DE, Harmer S (1997) Luminescence characterisation of lattice site modifications of Nd in Nd:YAG surface layers. *J Modern Optics* 44:1217–1230
- Raymond SG, Luff BJ, Townsend PD, Xiqi Feng, Quanqing Hu (1994) Thermoluminescence spectra of doped $\text{Bi}_4\text{Ge}_3\text{O}_{12}$. *Rad Measurements* 23:195–202
- Remond G, Cesbron F, Chapoulie R, Ohnenstetter D, Roques-Carmes C, Schvoerer M (1992) Cathodoluminescence applied to the microcharacterization of mineral materials: a present status in experimentation and interpretation. *Scanning Microscopy* 6:23–68
- Stevens-Kalceff MA, Phillips MR (1995) Cathodoluminescence microcharacterization of the defect structure of quartz. *Phys Rev B* 52:3122–3134
- Song KS, Williams RT (1993) Self-trapped excitons. Springer Verlag, Berlin
- Townsend PD, Can N, Chandler PJ, Farmery BW, Lopez-Heredero R, Peto A, Salvin L, Underdown D, Yang B (1998) Comparisons of tin depth profile analyses in float glass *J Non-Cryst Solids* 223:73–85
- Townsend PD, Karali T, Rowlands AP, Smith VA, Vazquez G (1999) Recent examples of cathodoluminescence as a probe of surface structure and composition. *Mineralogical Magazine*, 63:221–226
- Townsend PD, Olivares (1997) Laser processing of insulator surfaces. *Appl Surf Sci* 109/110: 275–282
- Walker G, Abumere OE, Kamaluddin B (1989) Luminescence spectroscopy of Mn^{2+} centres in rock-forming carbonates. *Min Mag* 53:201–211
- Walker, G Burley S (1991) Luminescence petrography and spectroscopic studies of diamagnetic minerals. In: *Luminescence Microscopy*, Barker CE, Kopp OC (eds)
- Yacobi BG, Holt DB (1986) Cathodoluminescence scanning electron microscopy of semiconductors. *J Appl Phys* 59:R1–R24
- Yacobi BG, Holt DB (1990) *Cathodoluminescence Microscopy of Inorganic Solids*. Plenum Press, New York
- Yang B, Luff BJ, Townsend PD (1992) Cathodoluminescence of natural zircons. *J Phys Condensed Matter* 4:5617–5624

Importance of Instrumental and Experimental Factors on the Interpretation of Cathodoluminescence Data from Wide Band Gap Materials

GUY REMOND, MATTHEW R. PHILLIPS,
CLAUDE ROQUES-CARMES

1 Introduction

Electron beam excited optical photons ($E_{hv}=6-0.7$ eV) can be detected and used for cathodoluminescence (CL) microscopy and spatially resolved CL spectroscopy by attaching a light collector and monochromator to an electron probe-micro-analyser (EPMA) or a scanning electron microscope (SEM). Colour CL images measured using an EPMA were first reported by Long and Agrell (1965) when the EMPA technique was originally applied to mineralogy. In this initial approach the CL emission was excited with a stationary beam and recorded on a colour photographic plate through the eyepiece of the optical microscope attached to the EPMA. Over the past 30 years, there have been significant improvements in CL measurement instrumentation and analysis techniques. High resolution CL spectra as well as CL digital images with submicron spatial resolution are now measured using high sensitivity UV-VIS-NIR photon detectors and a scanned electron probe with a well defined energy, diameter and current. As a result of these developments CL microscopy and microanalysis are now routinely used for the analysis of structural defects and impurities in a wide range of materials.

Geoscientists regularly use a crude electron source, a flood gun, attached to an optical microscope to reveal contrast not normally visible with conventional light optics. This CL contrast is often related to the concentration and spatial distribution of luminescent impurities. Throughout the evolution of the CL microanalysis technique in mineralogical studies, there have been many comparative studies between CL image contrast and trace element distribution obtained via X-ray or ion mass spectrometry (Rémond et al. 1970, 1992 and references therein; Rémond 1977). From these investigations, it was apparent that CL could complement EPMA for studying the localisation and the distribution of trace elements in minerals. However, the interpretation of CL data from wide band gap minerals is complex and requires a deeper understanding of the CL generation and emission mechanisms.

CL microscopy provides a rapid method for revealing the spatial distribution of structural defects and impurities. Unfortunately, in many cases CL spectral analysis does not provide a direct identification of the luminescence (recombination) centres. No unique relationship exists between the energy of the emitted CL

photons and the chemical state of a luminescent impurity as exists for X-ray emission (Moseley's Law where the $E_{X\text{-ray}} \propto Z^2$). Electronic transitions involving core (or inner) shell electronic states of an element leads to the generation of a characteristic set of mono-energetic X-ray lines which are generally independent of the element's chemical environment. CL emission on the other hand results from electronic transitions involving valence (or bonding) electrons and so this signal provides information about the chemical state of the emitter. It is important to note that CL generation via a recombination process is a competitive process. The generated CL intensity is dependent on both the recombination efficiency and concentration of all radiative and non-radiative recombination centres. Therefore the intensity of the CL emission band may not be proportional to the concentration of the emitter as in X-ray emission.

As the CL emission is dependent on the electronic band structure of the solid, assignment of CL peaks to particular defect centres or impurities is often difficult. In many cases synthetic crystals doped with one or several impurities must be prepared as standards so that their CL properties can be compared with those of the unknown specimen. To illustrate this procedure a set of synthetic zircons doped with a single REE was prepared by Cesbron et al. (1995) in an attempt to generate a data bank of reference spectra. This study clearly demonstrated that the shape and intensity of the CL bands critically depend on both collection/measurement system and experimental factors such as slit width and electron beam excitation conditions. The CL intensity, the band shape and the band position in a CL spectrum are determined by the wavelength response function of each component in the CL measurement system; the optical mirror collector, the monochromator (grating or prism), the photosensitive detector and all optical components such as focusing lenses, mirrors and fibre bundles. Each of these components has a non-linear response as a function of wavelength (energy). Therefore it is not possible to directly compare CL spectra acquired with different CL spectrometer systems as shown by a round-robin CL measurement reliability test between fourteen laboratories (Marshall and Kopp 1999, this Vol.).

The electron beam dose (beam current \times time/interaction volume) used to generate the CL signal is another important parameter in CL microscopy and micro-analysis. In some specimens prolonged, high dose, electron beam irradiation may cause significant changes in the CL spectra due to saturation effects, radiolytic processes and/or electron beam induced phenomena such as electromigration or electron stimulated desorption of some species. The magnitude of each of these processes also depends on the specimen (physical properties, crystal structure and defect structure) and the specimen preparation method.

Reliable interpretation of CL data can only be achieved when CL spectra are corrected for system response, and when detailed information on the experimental (excitation and measurement settings) as well as specimen preparation conditions is readily available. To date most CL studies have not provided the excitation/measurement conditions and the data presented have not been corrected for the detection response of the CL measurement system. Therefore extreme care must be exercised when referring to the current CL "data base" available in the CL literature to interpret CL spectra and images.

In this chapter the importance of the instrumental and experimental factors on the reliability of CL data measurement is discussed in terms of qualitative interpretation of CL microanalysis data. The role of the CL excitation conditions and the effect of each component in the CL measurement process are described in detail and illustrated using CL data collected from natural and synthetic specimens. An experimental procedure is provided to: (1) generate a system response curve for the CL detection and measurement system, and (2) carry out routine wavelength calibration of the spectrometer. In addition a comprehensive section on CL generation mechanisms in insulators is provided to assist in the CL qualitative analysis of geomaterials. A fundamental understanding of the physical processes which produce CL in specimens with low electrical conductivity is essential to confidently interpret CL images and spectra measured from this type of material. It is hoped that this chapter will inspire other workers in CL microscopy and microanalysis to publish CL data with details of the excitation conditions used in the analysis and corrected for system response. In this way a reliable CL spectral data base can be established in the scientific literature.

2

Electron-Solid Interactions

2.1

Elastic Scattering and Inelastic Scattering

When an energetic electron impinges on a specimen its energy is dissipated by a variety of electron solid interactions. The emission signals that result from these processes are used by electron microscopists and microanalysts to image and analyse a specimen at high spatial resolution. The interaction between monoenergetic electrons and a solid results in elastic and inelastic scattering phenomena. During an elastic scattering event, the trajectory of the electron is changed without significant loss of energy causing the beam to: (1) diverge as it penetrates into the specimen or (2) backscatter out of the specimen producing backscattered electrons (BSE). Therefore when a stationary electron beam with energy E_0 is incident on the surface of a specimen, an interaction volume exists as each electron straggles in the specimen due to elastic scattering processes. The electron range, R_{KO} , is the depth below the surface of the specimen at which an incident electron has lost all of its kinetic energy (Fig. 1).

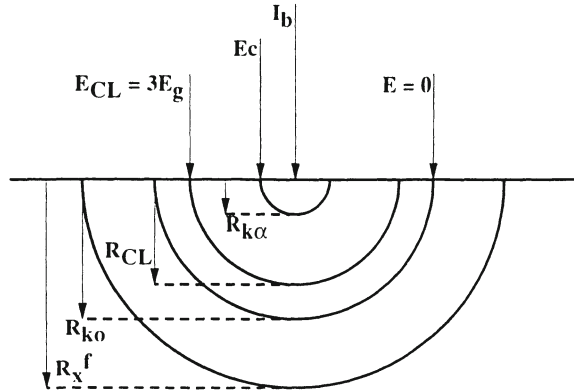
As reported by Kanaya and Okyama (1972), the electron range R_{KO} can be expressed according to

$$R_{KO} = 0.0276 A E_0^{1.76} / (0.889 \rho Z) \mu\text{m} \quad (1)$$

where E_0 is the primary electron beam energy in keV, A is the atomic weight of the specimen in g mol^{-1} , ρ is the density in g cm^{-3} and Z is the mean atomic number.

During an inelastic scattering event the energy of the incident electron is transferred to the solid. A number of inelastic scattering processes are possible

Fig. 1. The spatial distribution of the CL and X-ray photon signal intensity as a function of depth where E_c is the X-ray critical edge, E_g the bandgap, E_{cl} the formation energy, $R_{K\alpha}$ X-ray production range, R_{CL} CL generation range, R_{KO} electron range and R_{X^f} secondary photon generation range



each with its own cross section (probability of occurrence) producing emission signals such as: (1) fast ($E_{FSE} > 50$ eV, following core shell excitation) and slow secondary electrons ($E_{SSE} 50$ eV, following outer shell excitation), (2) X-rays (characteristic and continuum), (3) phonons, i.e., quantised lattice vibrations (heat), (4) CL (in semiconductors and insulators) and (5) plasmons (delocalised oscillations of specimen electrons). For a comprehensive review of electron solid interactions, see Goldstein et al. (1992).

2.2 Analytical Electron Microscopy

The emission signals which result from the inelastic scattering processes can be used to image and analyse the specimen. Variation in the emission signal intensity as an electron beam with a constant probe current is scanned over the specimen produces image contrast. Magnification is simply achieved by reducing the scan area and displaying the image on a viewing screen of fixed dimensions. The relative intensity of each emission signal depends on the specimen (Z , A and ρ), signal generation/escape depth and the surface topography. Each of the emission signals, produced via energy loss, carries different information about the specimen. The variation of signal intensity as a function of depth up to R_{KO} (see Fig. 1) results from: (1) the dependence of each inelastic scattering event cross section on the energy of the primary electron, i.e. excitation depth, (2) signal loss via matrix absorption and (3) signal gain by secondary processes.

2.2.1 Secondary and BSE Emission

The short mean free path (< 5 nm) and low energy of slow secondary electrons (SEs) makes this emission signal ideal for high spatial resolution imaging of surface topography as only SE produced within 10 nm of the surface can escape for detection.

BSE are primary beam electrons that leave the specimen as a result of a single large angle scattering or multiple small angle scattering processes. The fraction of

the primary beam electrons which leave the specimen, $\eta = I_{\text{BSE}}/I_{\text{B}}$, increases with the mean atomic number of the specimen, where I_{B} is the beam current entering the sample and I_{BSE} is the BSE current leaving the specimen. This dependence of backscatter yield on mean atomic number allows for compositional imaging of flat surfaces with submicron resolution.

2.2.2

X-ray Emission

X-ray emission signals can be used to provide high spatial resolution, quantitative information about the elemental composition of the specimen. Core shell electrons can be removed (ionised) from an atom when the primary electron beam energy is above the critical edge energy, E_{c} , the core shell electron's binding energy to the nucleus. In this process, the energy is absorbed by the atom producing a fast secondary electron and a hole ("missing electron") state at the core shell energy level. The atom relaxes from this excited state either radiatively by emitting a unique set of X-ray photon emission bands or non-radiatively via a rearrangement of the atomic levels producing characteristic Auger electrons.

2.3

Cathodoluminescence Emission Primary Processes

Chemical information about impurities and structural defects in semiconductor and insulator specimens can be obtained from the CL emission signal. Specimen electrons involved in the chemical bonding, (i.e. valence band electrons), can be excited to higher energy non-bonding states (i.e. the conduction band electrons). The energy difference between the conduction and valence band is known as the band gap, E_{g} . The generation of a slow secondary electron and a valence band hole occurs when a loosely bound electron at the top of the valence band is promoted to the conduction band during an inelastic electron scattering event. In some materials (generally at low temperature in semiconductors), the electron and hole pair can bind via coulomb interaction to form an exciton, a charge neutral crystal excitation. In semiconductors, excitons generally form at low temperature (5 K) but in some wide band gap materials excitons can be observed at room temperature (especially in materials in which significant lattice dilatation accompanies the excitation). The spatial dimensions of excitons are determined by the dielectric constant, ϵ , of the material which also determines the binding energy of the exciton, $E_{\text{B}} \propto \epsilon^{-2}$. For materials with a small dielectric constant, the exciton will be strongly bound and highly localised. Alternatively, the electron and hole can move independently (diffuse) in the conduction and valence band, respectively, until captured by a charge trap centre. Recombination of the electron and hole states can then occur either: (1) radiatively with the emission of optical photons (CL) or (2) non-radiatively with the emission of phonons (heat) or Auger electrons via a cascade process.

The CL photon emission can be either intrinsic, characteristic of the specimen with $E_{\text{hv}} \leq E_{\text{g}}$, or extrinsic, in which the CL emission band parameters (energy and half-width) are characteristic of the radiative recombination centre (e.g., a structural defect or an impurity). Impurities and structural defects can either be

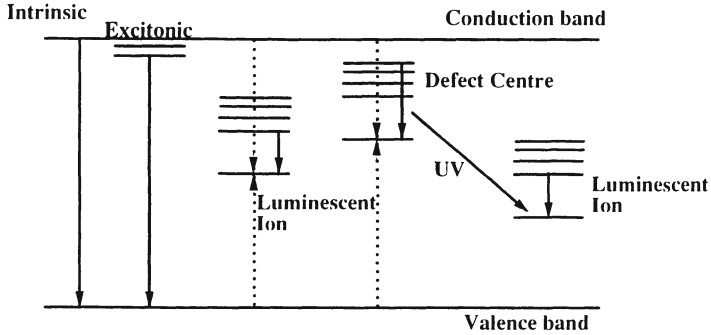


Fig. 2. Radiative recombination mechanisms in wide band gap materials

super-, sub- or iso-valent with their host. Supervalent impurities are called donors as they contribute electrons to the conduction band while subvalent impurities, which supply holes to the valence band, are known as acceptors. Extrinsic CL emission can either relate to the energy position of the charge trap in the band gap or the electronic structure of the recombination centre, e.g. first and second order transition metals with incomplete *d* and *f* shells, respectively. In the later process the energy released during recombination is transferred to the centre, exciting the 3d (or 4f) electrons from ground to excited states with deexcitation producing characteristic luminescence. The degeneracy of the 3d and 4f levels is removed through the influence of the ligand field produced by the coordination symmetry and interatomic distance of surrounding atoms. The radiative recombination mechanisms are summarised in Fig. 2. A primary beam electron normally has an energy three orders of magnitude above E_g and so can excite all possible CL processes. Therefore, in wide band gap materials the energy of the CL emission can range from the ultraviolet for intrinsic emission to the infrared for recombination at near band edge states.

3 Cathodoluminescence Generation and Emission Mechanisms

3.1 Electron-Hole Pair Generation Rate

As there are a number of possible inelastic scattering energy loss mechanisms, the average energy required to produce an electron/hole pair is

$$E_{eh} = 2.8 E_g + M \text{ eV} \quad (2)$$

where M is a constant $0 < M < 1$ eV (Yacobi and Holt 1990). The generation factor, G , the number of electron/hole pairs generated per incident beam electron is defined by

$$G = E_o(1-R)/E_{eh} \quad (3)$$

where R is the fractional energy loss due to the electron backscattering,

$$1 - R = \frac{\text{actual } E \text{ deposited in sample}}{\text{total } E \text{ deposited in sample if no backscattering}} \quad (4)$$

In the first approximation, the energy loss is proportional to the number of BSE, therefore it can be assumed that $R = (1 - \eta)$, where η is the backscattered electron coefficient, and the generation factor becomes $G = E_o(1 - \eta)/E_{eh}$. Therefore a single energetic (keV) electron is capable of producing thousands of electron/hole pairs within the interaction volume. For example, a single electron with $E_o = 30$ keV will produce approximately 1,300 electron/hole pairs in zircon where $E_g = 5.4$ eV (Fielding 1970) and $\bar{\eta} = 0.27$.

The number of electron/hole pairs varies as a function of depth as the primary beam losses energy as it travels in the specimen. The depth distribution of electron/hole pairs can then be expressed as

$$N_{eh}(z) = g(z)Gn_e = g(z)n_e(1-R)E_o(I_b/e)/E_{eh} \propto E_o I_b (\text{Beam Power}) \quad (5)$$

where $g(z)$ is the normalised depth dose function, G is the generation factor and n_e is the number of incident electrons, $n_e = I_b/e$, I_b is the electron beam current and e is the electron charge, $e = 1.6 \times 10^{-19}$ coulomb.

The shape and dimensions of the interaction volume in which the electron energy is dissipated has been investigated by Everhart and Hoff (1971) and Everhart et al. (1972). According to Koyama (1980), the normalised depth dose function, $g(z)$, can be approximated by the Gaussian form of the normalised Everhart-Hoff universal depth-dose function,

$$g(z) = \exp \left[-\frac{1}{2} \left(\frac{(z/R_{KO}) - 0.318}{0.322} \right)^2 \right] \quad (6)$$

where the maximum energy loss occurs at a $0.318R_{KO}$ (Koyama 1980).

3.2 Recombination Mechanisms

Recombination of electron and hole pairs is a competitive process. Each radiative and non-radiative recombination centre has a characteristic capture cross section, σ , for electron or holes. The magnitude of σ depends on the charge state of the recombination centre (RC), i.e. whether the RC attracts or repels the electron or hole. The lifetime, τ , for the electron or hole before capture is given by

$$\tau = (N_{RC} \sigma V_{th})^{-1} \quad (7)$$

where N_{RC} is the RC concentration, σ the capture cross section and V_{th} the thermal velocity of the electron (or hole). The recombination rate RR is

$$RR \propto \tau^{-1}(N_{RC}\sigma V_{th}) \quad (8)$$

The maximum distance that an electron (or hole) can diffuse before recombination is known as the recombination length, L , with $L^2 = \tau D$, where D is the diffusion coefficient of the electron or hole.

When a number of competitive recombination centres are present the recombination rate is given by

$$RR = 1/\tau = 1/\tau_{RR} + 1/\tau_{NR} = 1/\tau_1 + 1/\tau_2 + \dots + 1/\tau_{NR} \quad (9)$$

where τ_1, τ_2, \dots are the lifetimes for radiative RC 1, 2, ..., N and τ_{NR} is the lifetime for a non-radiative centre. The radiative recombination efficiency, γ , is given by

$$\gamma = \frac{\tau}{\tau_{RR}} = \frac{1}{1 + \tau_{RR}/\tau_{NR}} = \frac{P_{RR}}{P_{RR} + P_{NR}} \quad (10)$$

where P_{NR} and P_{RR} are the non-radiative and radiative transition probabilities, respectively. The dependence of P_{NR} (and so γ) on temperature

$$P_{NR} \propto \exp\left(\frac{-E_a}{k_b T}\right) \quad (11)$$

accounts for quenching of CL with increasing temperature where E_a is the activation energy required to cause a non-radiative transition between excited and ground vibronic states, k_b is Boltzmann's constant and T is temperature.

This competitive nature of the recombination process has a number of important consequences relating to both the qualitative interpretation of CL images and spectra as well the optimisation of CL excitation conditions:

1. The CL intensity may not be proportional to the concentration of the luminescence centre but may depend on the concentration of other more efficient radiative or non-radiative RCs.
2. Non-radiative centres (pre-existing or created by the electron beam and/or specimen preparation) can significantly reduce the CL emission efficiency.
3. Minimum detection limit for each radiative RC can be dependent on the relative concentration of other radiative and non-radiative centres.
4. At low accelerating voltages (small R_{KO}) surface states (disruption of the three-dimensional bulk electronic band structure due to the presence of a two-dimensional surface and surface defects induced by specimen preparation) may have a significant impact on the observed CL spectra. The incident beam must have sufficient energy, ($E_o > eV_o$) to penetrate the *deadlayer* produce by the surface states to generate CL emission

$$I_{CL} = f(I_b, d_p, t) (V - V_o)^m \quad (12)$$

where V is the accelerating voltage, V_0 is the “dead voltage”, t is time, d_p is the beam diameter and $1 \leq m \leq 2$. For insulators, internal electric fields may change the V_0 value as a function of the density of charge trapping centres.

The position, intensity and shape of CL emission peaks are strongly dependent on the temperature of the specimen during electron irradiation. At low temperature, the intrinsic CL peak: (1) shifts to higher energy as the crystal contracts which increases E_g and (2) increases in intensity (with an associated decrease in extrinsic CL) due to a reduction in the electron (or hole) diffusivity and an increase in γ (see Eq. 10). In addition, the CL emission peaks become sharper as the temperature is lowered due to the decrease in the number of phonons involved in the electronic transition.

3.3

Cathodoluminescence Emission at the Specimen Surface – Generation and Matrix Effects

An expression for the measured CL intensity can be derived by assuming:

1. The total number of CL photons produced in the specimen is the sum of photons induced by electrons (primary, backscattered and fast secondary) and photons excited by all other forms of energy released in the solid (CL exciting photoluminescence, X-rays exciting radioluminescence, phonons causing thermoluminescence or quenching)

$$I_{gen} = \int_V \gamma^{elect} N_{eh}^{elect}(z) dV_z + \int_V \gamma^{X-ray} N_{eh}^{X-ray}(z) dV_z + \int_V G_{PL} dV_z \quad (13)$$

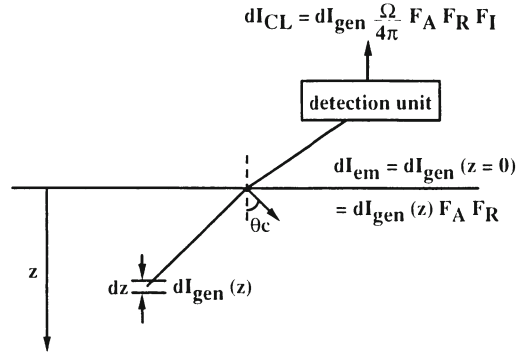
where γ is the radiative recombination efficiency, $N_{eh}(z) = g(z)Gn_e$, G is the generation factor, n_e is the number of incident electrons, $g(z)$ is the normalised depth dose function, and G_{PL} is the photoluminescence excited by cathodoluminescence.

2. All CL photons generated at different depths below the specimen surface interact with the matrix before they escape into the vacuum for analysis (Fig. 3). The measured CL intensity, I_{CL} , the number of photons emitted at the specimen surface per unit time, can be expressed by the following equation

$$I_{CL} = \sum_i (\Omega / 4\pi) F_A^i F_R^i F_I^i I_{gen}^i \quad (14)$$

where i refers to each separate CL generation process (electron, X-ray and optical photon), $\Omega/4\pi$ is solid angle of collection in which the fraction of emitted photons actually entering the detector, F_I , is a factor accounting for instrumental parameters (collection and transmission efficiency of the detection system), F_A is a factor to account for optical absorption along the escape path length and F_R is a factor which corrects for internal reflection and refraction at the specimen surface.

Fig. 3. Relationship between the CL intensity (dI_{gen}) generated within a layer of thickness dz at depth z below the specimen surface, the intensity lost due to internal total reflection (dI_{+}), the intensity emitted (dI_{em}) at the specimen surface and the intensity measured (dI_{CL}) at the output of the detection unit



The F_A Term. The term F_A^i is the absorption correction factor accounting for the decrease in CL intensity due to optical absorption along the photon escape path length. Optical absorption obeys Beer's law and so

$$F_A^i \propto \exp(-\alpha^i z^i) \quad (15)$$

where α is the effective absorption coefficient of the matrix at each λ and z^i is the path length of the photon generated at depth z , with $z_{max} \cong R_{KO}$ for CL. In wide band gap materials, CL absorption by the matrix is generally negligible as α is small and the average exit path length is on a micron scale. However, CL absorption by optical centres within a large bandgap matrix can be significant in cases in which the CL overlaps with the centre's characteristic optical absorption bands. In semiconductors, α is large due to the small band gap and optical absorption can have a pronounced effect on the CL spectra especially when excited using high E_o (i.e. large R_{KO}).

The F_R Term. The F_R factor accounts for refraction and reflection losses at the specimen surface. Although the CL is generated isotropically, only a small fraction (a few percent!) inside a cone of semi-angle, θ_c , escapes into the vacuum. The angle, θ_c , is known as the critical angle, and is defined by

$$\sin\theta_c = 1/n \quad (16)$$

where n is the refractive index of the material. According to Reimer (1985), the F_R factor can be approximated by:

$$F_R = \left[1 - \left(\frac{n-1}{n+1} \right)^2 \right] \frac{1}{4\pi} \int_0^{\theta_c} 2\pi \sin\theta d\theta = \left[1 - \left(\frac{n-1}{n+1} \right)^2 \right] \frac{n - \sqrt{n^2 - 1}}{2n} \quad (17)$$

See Table 1 for θ_c and F_R values for quartz, sapphire, zircon and GaAs.

The F_I Term. The F_I term takes into account the CL intensity losses due to the collection, transmission and detection properties of the CL measurement system.

Table 1. Refractive index, critical angle and the reflectance factor (see Sect. 3.3.1) for a variety of materials

Crystal	n	θ_c (degrees)	$F_R\%$
Quartz	1.55	40.2	10.0
Sapphire	1.76	34.6	8.2
Zircon	1.96	30.1	6.3
GaAs	3.40	17.0	1.6

The two main components of the F_1 term are the collection solid angle of the light collector and the wavelength detection efficiency of all components (collector, diffraction grating, mirrors and photon detectors) in the CL measurement system. The F_1 term can be determined using a system response curve using a calibrated light source (see instrumentation section).

3.4 Cathodoluminescence Emission Peak Shape

A number of parameters determine the natural peak shape of the CL emission band; the nature of the RC, the degree of electron-phonon coupling with the lattice (a measure of the number of phonons emitted during the electronic transition), the specimen temperature and electron beam excitation conditions. Knowledge of the influence of each of these parameters on the peak shape greatly assists in the assignment of the CL emission peaks to particular luminescent centres. In addition, simple experiments can be undertaken to confirm or refute the identification of the RC. In practice, CL identification requires spectra to be measured over a wide range of temperature and electron probe excitation conditions.

3.4.1 Sharp Lines

3.4.1.1 *Rare Earth Element Impurities and R-line Emission*

Trivalent, rare earth element (REE) radiative recombination centres are characterised by sharp visible and NIR luminescence. The luminescence results from electronic transitions between the partially filled 4f shells which are well shielded (screened) from the lattice by outer shell electrons. The CL emission spectrum from each trivalent REE has a characteristic set of CL peaks (Dicke 1968; Marfunin 1979) which can be used to identify the REE. CL emission spectra from divalent REE have fewer peaks with broader half-widths.

First order transition metals, in particular Cr^{3+} in octahedral coordination, can give rise to sharp emission peaks (R-line emission) in the red end of the optical spectrum. For example, for Cr^{3+} in Al_2O_3 , the sharp R-line doublet emission occurs at 694 nm. These peaks are often surrounded by satellite lines due to electron-phonon coupling (see Sect. 3.4.1.2) or concentration pairing effects.

3.4.1.2

Zero Phonon Lines

Zero phonon lines (ZPL) result from radiative electronic transitions without the participation of phonons. The observation of this type of emission depends on the temperature and degree of electron-phonon coupling between the vibrating lattice and the electronic states of the luminescence centre. ZPL emission is observed at low temperature for moderate and weak electron phonon coupling and not at all with strong coupling. The ZPL is often superimposed on the high energy side of a broad emission band. The ZPL peak can be surrounded by sharp peaks where phonons are absorbed/emitted during the electronic transition. These satellite peaks are known as phonon replicas. The spacing between these peaks is equal to $n\hbar\omega$ where $n=0,1,2,\dots,n$ and ω is generally the longitudinal optical phonon frequency. A well defined relationship exists between the relative intensity of the emission and the peak width of phonon replicas. The phonon replica peaks are less intense and broader with increasing n (Henderson and Imbush 1989). Another characteristic of this type of emission is that the intensity of high energy side phonon replicas decrease at low temperature.

3.4.1.3

Donor-Acceptor Pairs

Donor-acceptor pair (DAP) emission is observed when an electron captured by a donor recombines with a hole captured by an acceptor. The DAP emission energy $h\nu(r)$, is given by

$$h\nu(r)=E_g-(E_A+E_D)+e^2/\epsilon r \quad (18)$$

where E_g is the band gap, E_A and E_D are the acceptor and donor gap energies, respectively, r is the distance between donor and acceptor and ϵ is the refractive index for small r or the static dielectric constant for large r . As r can only take specific values related to the crystal structure, the emission is often characterised by a series of sharp emission peaks. The DAP emission peaks are sharpest when r is small with discrete values. The peaks become broader when r is larger with a more diffuse value. A simple way to establish that the emission is due to a DAP centre is to vary the beam power. At high beam power the DAP emission shifts to higher energy as large r DAP centres saturate and small r DAP emission dominates. Saturation occurs because DAP transition probability decreases as r increases.

3.4.1.4

Exciton Lines

At low temperature an electron in the conduction band can bind with a hole in the valence band (see Sect. 2.3). The correlation between the electron and hole can produce a series of sharp lines with $E_{em} < E_g$. The spacing between lines can be simply calculated, $E_n = E_g - E_b/n^2$, where E_g is the band gap, E_b is the exciton binding energy and $n=1,2,3,\dots,n$. The sharp line exciton emission spectra can be complicated due to coupling of phonons with the electronic states. Generally, excitonic emission is observed at low temperatures and results from excitons bound to

neutral donors/acceptors. Free exciton emission is rarely observed as crystal momentum must be conserved during the electronic transition.

3.4.1.5

Molecular Species

Recombination on a molecular ion, e.g. O_2^- , S_2^- can produce quasi-linear sharp vibrational structure superimposed on a broad luminescent band. The spacing between peaks results from intramolecular vibrations, $n\hbar\omega$, coupling with the electronic states of the molecule. The intramolecular vibrations are generally smaller than free molecule vibration due to perturbation by the host crystal. The emission can look similar to DAP emission, but relative intensities and peak widths of the molecular species emission do not obey the expected DAP relationships. There is no general rule to describe the thermal behaviour of this type of emission as it depends on host material, type of molecule and the location of the molecule within the crystal structure.

3.4.2

Broad Peaks

A broad natural peak width of the CL emission indicates that the excited and ground states of the electronic radiative transitions are strongly coupled with the vibrating lattice. Stronger coupling indicates that more phonons are emitted in the electronic transition. Broad featureless CL peaks can be difficult to interpret. The system response of the CL detection system can significantly affect the intensity, position and shape of broad peaks. Spectra must be corrected for system response and curve fitted so that accurate peak parameters, intensity, half-width and position are known for each measurement condition (see Sect. 5.3). Edge filters can be used to eliminate second order peaks that occur at $2\times\lambda_{em}$ (nm) (see Sect. 4.2.3).

3.4.2.1

Broad Intrinsic Emission – Self Trapped Exciton

Broad intrinsic emission generally results from self trapped exciton (STE) which are highly localised excitons trapped by their own self induced lattice distortion. STEs are generally produced in crystals with a deformable lattice (e.g. SiO_2) which are characterised by strong electron-phonon coupling. The emission energy of the STE is generally much lower than the band gap of the material due to the energy lost by phonon emission during the electronic transition. At room temperature the characteristic STE emission peak shape is asymmetric being Gaussian at the peak with exponential tails. At low temperature the peak intensity increases (as the STE diffusivity decreases) and peak shape becomes Lorentzian. STE emission is also characterised by long relaxation times which produce horizontal streaking at rapid scan speeds in a scanning CL system.

3.4.2.2

First Order Transition Metals

Broad CL peaks can result from excitation of cations with partially filled 3d orbital (Ti to Cu) which are only weakly screened from the lattice by the outer shell 4s electrons. The peak position, half-width and intensity of the CL depends

on the element, oxidation state and coordination. The position can be calculated using ligand field theory applied to the atomic 3d levels of the cation perturbed by the symmetry and proximity of the surrounding atoms. The intensity of the emission relates to the standard spectroscopy parity and spin selection rules (Marfunin 1979). Complementary techniques such as photoluminescence excitation spectroscopy can be used to determine which energies excite emission peak. These values can be compared with theoretical absorption energies to confirm the CL assignment (Marfunin 1979).

3.4.2.3

Defect Centres

Excitation of electrons or holes trapped (dangling bonds in covalent crystals) at point defects such as vacancies, interstitial and point defect clusters usually produce broad structureless CL peaks at all temperatures. This type of emission is often difficult to identify and characterise as: (1) the featureless broad nature of the peak and (2) the peak position often shifts due to the presence of impurities which provide charge compensation. In general, other spectroscopic techniques must be used to assist in the assignment.

3.5

Electron Beam-Induced Effects

3.5.1

Radiolysis

Structural defects such as vacancy–interstitial pairs can be created in wide band gap materials when irradiated by an electron beam with an energy well below the “knock on” energy (>1000 keV). In this process, known as radiolysis, the potential energy of the charge neutral excitation created by the low energy beam is dissipated via atomic displacement. Radiolysis is generally observed in wide band gap materials as the stored energy in the excitation is large and the excitation can be highly localised. These defects created by the beam can act as charge traps and rapidly induce large electric fields about the irradiated region (Stevens Kalceff and Phillips 1995a,b; Stevens Kalceff et al. 1996, 1999).

3.5.2

Charge Trapping and Subsurface

Electric Fields Generation

When an electron beam is incident on the surface of a conductor in a vacuum, a flow of electrons, I_{ABS} , occurs either from or to ground potential to maintain charge balance. Therefore, for charge balance

$$I_{in} = I_B = I_{out} = I_{ABS} + I_{SE} + I_{BSE} \quad (19)$$

However, if an insulator is bombarded with an incident beam current, I_B , charge conservation leads to the following relationship

$$I_{in} = I_B = I_{out} = I_{SE} + IBS + dQ/dt + I_{ABS} \quad (20)$$

where dQ/dt is the charge trapped per unit time and I_{ABS} is the absorbed current. Using the secondary electron emission coefficient, $\delta=I_{SE}/I_B$ and the backscattered electron emission coefficient $\eta=I_{BSE}/I_B$ Eq. (20) can be rewritten as:

$$I_B = \delta I_B + \eta I_B + dQ/dt + I_{ABS} \quad (21)$$

In a SEM or EPMA, the dQ/dt component produces an electric field within the specimen that induces charging phenomena such as image drift, image flicker and flashover. In addition the induced electric field can de-accelerate the primary beam reducing R_{KO} and distorting the interaction volume. A conductive coating can prevent the electric field penetrating into the vacuum and therefore eliminate the above surface charging phenomena (Cazaux 1986, 1996). However, it is important to note that conductive coating *does not* cancel the trapped charge induced subsurface electric field which can bring about migration of charged species and in severe charging cases mass loss (Jbara et al. 1996; Rémond et al. 1979).

Surface charging effects are minimal in an optical CL systems as surface charge is dissipated via charge leakage through the gas phase in the specimen area. In a conventional SEM, after coating the specimen with a conductive coating, Eq. (21) becomes

$$I_B = \delta^* I_B + \eta^* I_B + dQ/dt + I_{ABS}^* \quad (22)$$

where δ^* , η^* are the secondary and backscattered electron emission coefficients under electron irradiation conditions, respectively, and I_{ABS}^* is the specimen current accounting for the contribution of the electron released by traps via the induced electric field (Cazaux 1996). Although trapping and detrapping are competitive processes, a steady state is attained after a certain irradiation time ($Q \neq 0$ but $dQ/dt = 0$). However, it is important to point out that the trapped charge density is not equal to zero when this steady state condition is attained and subsurface electric fields are still present. These internal electrical fields may be strong enough to ionise shallow donor levels located immediately below the conduction band. The electron released from the donor level can be accelerated in the conduction band and depending on its diffusion length may recombine with a luminescence centre with the production of a photon, a process similar to light generation by electroluminescence. The internal electrical field may be strong enough to release a trapped electron well away ($>100 \mu\text{m}$) from the beam spot impinging the specimen surface. This effect leads to the secondary electron cascade in insulating materials as illustrated by Vigouroux et al. (1985). Similar effects have been reported by Rémond et al. (1992), who observed bright luminescent streaks $100 \mu\text{m}$ in length spreading out from the stationary electron beam at the surface of a ZnS surface.

4 Instrumentation

4.1 Cathodoluminescence Optical Microscopy with a Stationary Unfocused Beam

Cathodoluminescence microscopy using an EPMA was first performed by Long and Agrell (1965) as well as Goni and Rémond (1969) and Rémond (1977). These EPMA CL images were measured by irradiating the specimen with a stationary defocused electron beam and photographed through the EPMA optical microscope. However, the maximum diameter, 300–400 μm , of the unfocused beam in the EPMA placed severe limitations on the maximum dimensions of the CL image size. To overcome this field of view restriction, optical CL microscopes were constructed to allow simultaneous large area (up to 3 mm) observation of geological thin sections using CL reflected and transmitted light. Commercial optical CL microscopes are now readily available for a wide range of mineralogical and petrological applications. The fundamental design of all the optical CL microscopes is based on the system initially designed by Sippel (1965). The optical CL microscope consists of a cold cathode electron gun (flood electron gun) attached to the specimen stage of an optical microscope. The CL image is observed and recorded on a photographic plate through the ocular of the microscope. Marshall (1988) provides a detailed description of the optical CL microscope instrumentation as well as information on operation techniques and applications.

Brighter electron sources such as thermoionic electron gun similar to those used in EPMA have been developed by Le Poole et al. (1968) and later by Ramseyer et al. (1989). With these systems a stationary electron probe is focused onto the specimen increasing the CL signal.

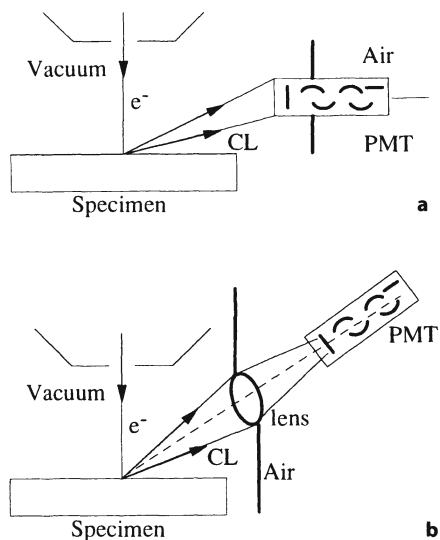
4.2 Scanning Cathodoluminescence Microscopy and Microanalysis

Scanned CL microscopy can be simply performed by attaching a light detector to an EPMA or SEM. The output from the photon sensor can be then used to modulate the brightness on a cathode ray tube (CRT) viewing screen to produce a high spatial resolution CL image.

With scanning CL microscopy, CL excitation conditions can be well defined as the electron probe diameter (nm to μm), energy (5–40 keV), and beam dwell time per picture point (seconds to microseconds) can be precisely controlled. Furthermore, complementary analytical information using secondary and backscattered electrons as well as characteristic X-rays can be obtained concurrently greatly assisting with interpretation of CL images.

Panchromatic CL images (unresolved wavelength CL emission) were first obtained using a photomultiplier tube (PMT) as a detector attached to the electron column of the SEM. The PMT can be mounted on the electron column of the SEM so that the entrance window of the detector is placed directly inside the vac-

Fig. 4a,b. Simple CL collections systems for panchromatic CL imaging with the SEM. Note that the front window of the PMT placed in vacuum (a) or the intermediate glass lens (b) may emit spurious CL emission induced by BSE as discussed by Rémond et al. (1972)



uum. This can be simply done by removing the scintillator positioned in front of the PMT in the Everhart-Thornley SE detector. Alternatively, the PMT can be placed outside the electron column with an intermediate silica or glass lens for improving the collection efficiency and isolate the PMT from the vacuum (Fig. 4). The PMT output signal modulates the SEM CRT brightness providing a panchromatic CL image. It should be noted that contrast in these panchromatic images reflects variations in the intensity of the CL emission over all wavelengths convoluted with response function of the collector-detector assembly.

In either of the above PMT arrangements, CL image resolution is compromised as a large component of the measured CL signal is generated by X-ray and BSE far from the electron beam irradiation point. These spurious luminescence signals arise from excitation by BSE of luminescent components within the specimen chamber such as the front window of the PMT, glass focusing lenses and optical wave guide (Rémond et al. 1972). With a homogenous polished specimen, the BSE emission is uniform and the BSE induced CL provides a constant DC offset to the total CL signal. However, for high atomic number multiphase specimens variation in the total CL signal will reflect changes in the BSE emission coefficient as the beam scans over the specimen. Consequently, non-luminescent materials of high mean atomic number may appear more luminescent than luminescent materials of lower atomic numbers. Therefore it is essential for qualitative interpretation of CL images to ensure that the front surface of the PMT does not emit CL when exposed to BSE.

Solid state (SS) photodiode detectors have been used for panchromatic CL imaging in a SEM. The type of SS sensor (Si, Ge, PbS or InAs) used is determined by desired CL emission wavelength detection range. The SS detector is mounted below the pole piece of the objective lens to improve the solid angle of collection. In order to prevent BSE induced artefacts the SS detector is embedded in a glass

mounting and the surface is coated with an optically transparent metallic film to remove surface charge generated by BSE. It is important to note that when a SS detector is used for BSE imaging of luminescent materials, image contrast can also be produced by the CL signal leading to false BSE contrast (Bresse et al. 1996).

4.2.1

Cathodoluminescence Collectors Used in Scanning Cathodoluminescence Microscopy

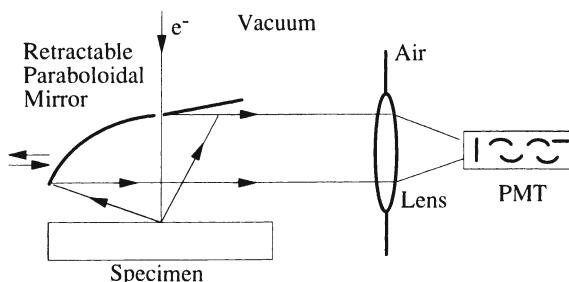
An EPMA has a built-in optical device. Usually the optical microscope is equipped with a Cassegrain objective type consisting of two spherical mirrors. No such device has been designed for a SEM, and in order to improve the collection efficiency of the emitted CL several types light collectors have been installed in the SEM chamber.

An optical lens collector was developed by Semo (1974). However, the most frequently used optical collectors are ellipsoidal or parabolic metallic mirrors placed immediately above the specimen surface as discussed by Steyn et al. (1976), Hörl and Roschger (1980), Trigg (1985) and Yaccobi and Holt (1990). A hole in the mirror permits the incident electron beam to reach the specimen surface. A set of external manipulators allows the adjustment of the mirror position (x , y and z) which allows optimum alignment of the mirror for signal detection and full retraction to enable concurrent detection of BSE and SE.

When using an ellipsoidal mirror, the beam spot (the point CL source) is placed at one of the focusing points of the mirror. The CL light is collected at the second focusing point and directed towards the detector through the exit window by means of either a light pipe or a second inverted ellipsoidal mirror.

When using a parabolic mirror, the CL source is placed at the focal point of the mirror and the parallel reflected light is directed towards the exit window for measurement (Bond et al. 1974). The most common arrangements of optical collectors within the SEM chamber for panchromatic (spectrally unresolved) CL microscopy are shown in Fig. 5. The light output from the parabolic mirror is highly dependent on the specimen being exactly positioned at the mirror focal plane. There is a rapid decrease in the measured light intensity as the CL point source is moved away (x , y or z) from the mirror focal position. This is similar to the X-ray signal intensity decrease observed when specimen moves off the focusing circle of a wavelength dispersive spectrometer.

Fig. 5. Common arrangement of optical collectors using a paraboloidal mirror in the SEM chamber



4.2.2

Polarisation Resulting from Reflections on Metallic Surfaces

Both the parabolic mirror attached to a SEM and the two spherical mirrors assembly in the EPMA collect the CL via an optical reflection process. Therefore the optical properties, absorption and reflectance, of the metallic coating determines the wavelength transmission efficiency of the CL collector.

For a metal, the refractive index n is a complex number which can be expressed using Cauchy's notations as:

$$n = v - j\chi \quad (23)$$

where v is the real part of the refractive index, n , and χ is the extinction coefficient.

For a p polarised incident wave (electrical vector parallel to the incident plane, $E_{//}$), the reflectance coefficient for the amplitude $r_{//}$ is:

$$r_{//} = -[\tan(\theta_i - \theta_r) / \tan(\theta_i + \theta_r)] \quad (24)$$

where θ_i and θ_r are the incident and the refractive angle, respectively.

For a s polarised incident wave (electrical vector perpendicular to the incident plane, E_{\perp}), the reflectance coefficient for the amplitude is:

$$r_{\perp} = -[\sin(\theta_i - \theta_r) / \sin(\theta_i + \theta_r)] \quad (25)$$

As the refractive index of a metal is complex, the reflectance coefficient, r , for the amplitude of a wave incident onto a metallic surface is also a complex number with $r = \rho e^{j\varphi}$ and results in a phase change of φ between the incident and the reflected waves.

The reflectance coefficients for the intensity of a s and p polarised incident waves $R_{//}$ and R_{\perp} , respectively, are thus given by $R_{//} = r_{//} \cdot r_{//}^*$ and $R_{\perp} = r_{\perp} \cdot r_{\perp}^*$ where $r_{//}^*$ and r_{\perp}^* are the complex conjugates of the reflectance coefficients for the amplitudes of the incident wave.

For an unpolarised incident light the reflection coefficient for the intensity is given by

$$R = 1/2(R_{\perp} + R_{//}) \quad (26)$$

$$R = \frac{1}{2} \left[\frac{\cos(\theta_i) - \sqrt{n^2 - \sin^2(\theta_i)}}{\cos(\theta_i) + \sqrt{n^2 - \sin^2(\theta_i)}} \right]^2 + \frac{1}{2} \left[\frac{n^2 \cos(\theta_i) - \sqrt{n^2 - \sin^2(\theta_i)}}{n^2 \cos(\theta_i) + \sqrt{n^2 - \sin^2(\theta_i)}} \right]^2 \quad (27)$$

where the first term corresponds to the reflection of the incident wave with the electrical vector being perpendicular (R_{\perp}) to the incident plane, the second term corresponding to the reflection for the electrical vector parallel ($R_{//}$) to that plane.

Let us first consider that the incident wave has a constant angle of incidence, $\theta_i = 45^\circ$ with respect to the normal to the metallic plane surface. The intensity of the

specularly reflected light is a function of the incident wavelength. The reflectance curves for both silver and aluminium, for a fully p polarised wave, $R_{//}(\lambda)$, for a fully s polarised incident wave, $R_{\perp}(\lambda)$, and an unpolarised light, $R(\lambda)$ are shown in Fig. 6. Due to the variations of the optical constants, the ν and χ indices, as a function of the incident wavelength, discontinuities are present in the Ag and Al reflectance curves. A sharp drop is observed around 400 nm in Ag and a broad dip around 800 nm is characteristic of Al. Note that the relative difference in reflectance between the s and p polarised waves is higher for the aluminium than for the silver.

The reflectance coefficient for the intensity of a monochromatic incident wavelength is also a function of the incident angle on the reflecting surface (see Eq. 27). The reflection coefficients $R_{\perp}(\theta)$, $R_{//}(\theta)$ and $R(\theta)$ where $R(\theta) = 1/2 (R_{\perp}(\theta) + R_{//}(\theta))$ as a function of the incident angle for a plane aluminium mirror are shown in Fig. 7 for incident wavelengths at 300 and 700 nm.

Fig. 6. Reflectance curves for aluminium and silver with s , p and unpolarised light

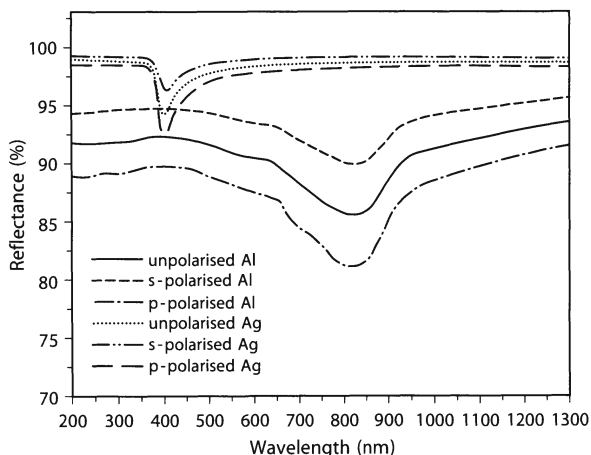


Fig. 7. Reflectance from aluminium as a function of angle of incidence for s , p and unpolarised light with 300 and 700 nm light

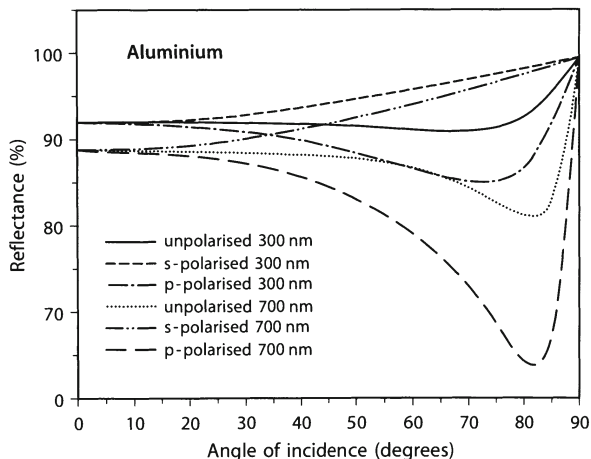
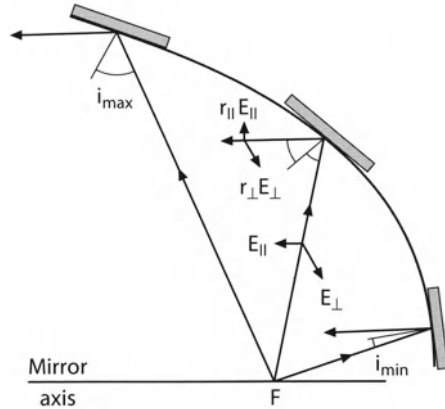


Fig. 8. Optical reflectance on a metallic surface and range of angles of incidence from a parabolic mirror



As shown in Fig. 7, the reflectance coefficient $R_{//}(\theta)$ (and consequently the average coefficient R) passes through a minimum value at incidence angle θ_p , the principal angle of incidence. The position of the principal angle of incidence, θ_p , depends on the incident wavelength. For the aluminium mirror, the principal angle of incidence shifts from 75° to 82° as the incident wavelength increases from 300 to 700 nm. At θ_p , the reflectance coefficient, R_{\perp} , remains approximately constant (0.98) as a function of wavelength and the reflectance coefficient ratio $R_{\perp}(\theta_p) / R_{//}(\theta_p)$ is equal to 1.15, 1.31, and 1.53 for the 300, 550 and 700 nm, respectively.

For a parabolic mirror, the situation is slightly more complicated since the reflectance coefficient at each wavelength must be determined by integrating over all angles of incidence on the mirror surface. The range of angles of incidence is determined by the geometrical parameters of the paraboloid (see Fig. 8).

A paraboloidal mirror will therefore reflect s polarised light more efficiently than p polarised light with $R_{//} > R_{\perp}$. The magnitude of the reflectance anisotropy will depend on: (1) the wavelength of the incident light and (2) the range of angles of incidence at the mirror surface which is determined by the dimensions of the paraboloid. The degree of polarisation, R_{pol} , can be calculated using:

$$R_{pol} = (R_{\perp} - R_{//}) / (R_{\perp} + R_{//}) \tag{28}$$

CL contrast in polycrystalline specimens can therefore result from polarised emission from grains with different crystallographic orientation with respect to the mirror axis. The observation of variation in CL intensity as the specimen is rotated with respect to the mirror confirms the presence of polarised CL emission (Cesbron et al. 1995; Stevens Kalceff et al. 1999 in this book).

4.2.3 The Diffraction Grating

A prism, or more frequently a reflection diffraction grating, is used to spatially separate panchromatic light. The grating consists of a surface with a large num-

ber of equally spaced rulings coated with aluminium to improve the reflectivity. When parallel light is incident on the surface, light is scattered according to the grating equation:

$$m\lambda = 2d \sin\theta \sin\phi \quad (29)$$

where λ is the wavelength, m specifies the order of the reflection with $m=0, \pm 1, \pm 2, \dots$, d is the spacing between the rulings, θ is half the angle between the incident and reflected ray at the grating and ϕ is the grating angle relative to the zero order position. (see Fig. 9). In CL spectroscopy the first ($m=1$) order is generally used for spectral measurement. However as the second order overlaps with the first, second order spurious CL peaks can be observed at twice the wavelength of the primary emission band. Edge filters can be used to confirm the presence of second order peaks (Fig. 10).

When the grating is rotated to the zeroth order ($m=0$) specular reflection occurs and the grating acts as a mirror. Due to the large light throughput at $m=0$, the zeroth order position is generally used for initial lateral alignment of the paraboloidal mirror and height adjustment of the specimen, especially when the CL peak positions are unknown.

The transmission efficiency of the grating is non-linear with wavelength due to light scattering and absorption processes. The position of maximum reflectivity is known as the blaze wavelength and its location is determined by shape and depth of the rulings. Peaks and/or dips in the transmission curve result from grating artefacts known as Wood's anomalies due to grazing angle light scattering in and out of the various orders (Fig. 11). These artefacts can produce spurious peaks in CL spectra that have not been corrected for system response. The transmission efficiency and magnitude of the Wood's anomalies are highly dependent on the polarisation state of the incident light, both being more pronounced when the electric vector is perpendicular (s polarised) to the rulings. The position of the Wood's anomalies can be determined for s -polarised light using equations given in Stewart and Gallaway (1962).

Fig. 9. The sign convention for the angle of incidence, angle of diffraction and grating angle

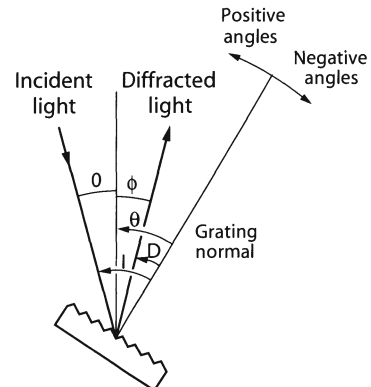
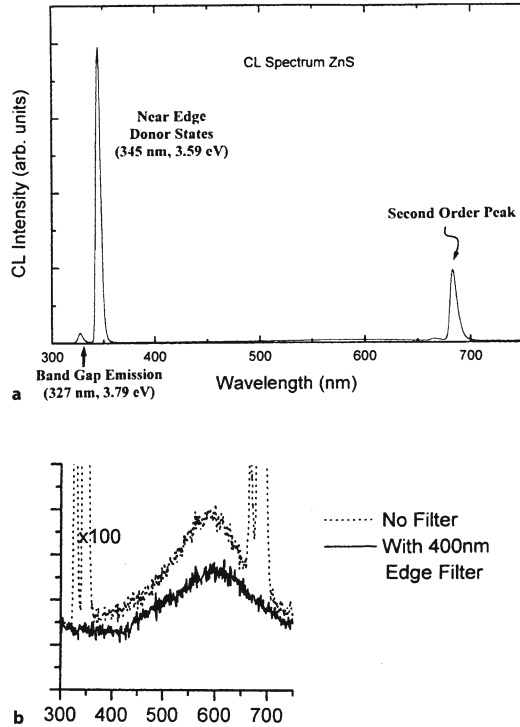


Fig. 10. CL spectra from ZnS with and without an edge filter confirming the presence of second-order peaks



The angular dispersion of the incident light can be simply determined by differentiating the grating equation,

$$\frac{d(\theta - \phi)}{d\lambda} = \frac{n}{d \cos(\theta - \phi)} = \frac{1}{\sqrt{\frac{d^2}{n^2} - \lambda}} \quad (30)$$

For the first order, $n=1$ and $d^2 > \lambda$, $\frac{d(\theta - \phi)}{d\lambda} \approx \frac{1}{d}$.

Therefore for a larger number of rulings per mm, d decreases and the angular dispersion increases. The dispersion of a grating is generally given as the reciprocal linear dispersion, RLD, where,

$$RLD = \frac{d\lambda}{dw} = \frac{1}{f} \frac{d\lambda}{d(\theta - \phi)} \approx \frac{d}{f} \quad (31)$$

where f is the focal length of the monochromator and dw is the width of the exit slit. The bandpass is the width of spectrum passed by the monochromator. The smallest bandpass of the monochromator defines its spectral resolving capabilities or resolution. The bandpass of the monochromator is given by the product of

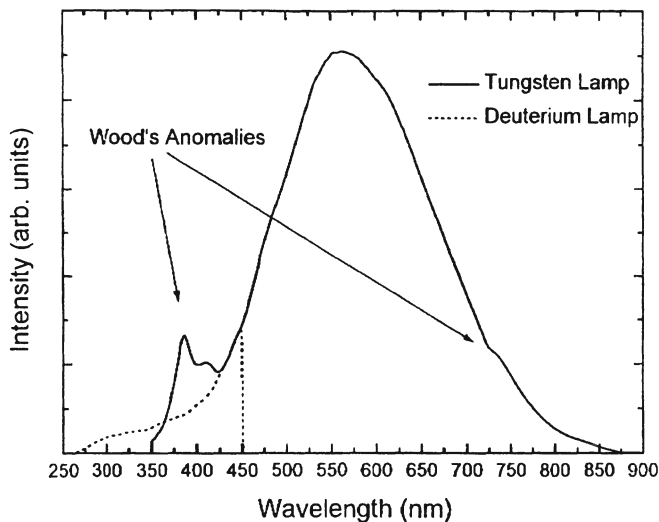


Fig. 11. Wood's anomalies in the transmission response of a 1200 lines/mm diffraction grating. The dark Wood's anomaly can be removed using a system response correction. The magnitude of the bright Wood's anomaly in the blue is dependent on the intensity in the red. Both strength of both anomalies is highly polarisation dependent

the RLD and the slit width. Therefore for a fixed exit slit width and focal length the resolution of the monochromator improves as the number of rulings per mm increases (as d decreases).

4.2.4 Sequential and Parallel Cathodoluminescence Spectroscopy Measurement

There are two basic parts to the CL spectrometer, the dispersive unit (grating or prism monochromator) used to produce a monochromatic light output from a panchromatic input, and the photon detector to measure the CL intensity at each wavelength. CL spectra can be measured either sequentially (as with a wavelength dispersive X-ray spectrometer, WDS) or in parallel detection mode (as with an energy dispersive X-ray spectrometer, EDS).

4.2.4.1 Serial Data Measurement

A sequential CL spectrometer consists of the dispersive device with a single channel detector placed behind the exit slit of the monochromator. The system developed by Semo (1974) consists of a flint prism, a condenser lens and a PMT as a detector. The analysed wavelength is sequentially selected by moving a slit in the focal plane of the optical condenser placed behind the monochromator. The prism has a very high transmission efficiency. However a non-linear relationship exists between the slit position and the measured wavelength which leads to inaccurate spectral analysis in the long wavelength, NIR region (Fig. 12).

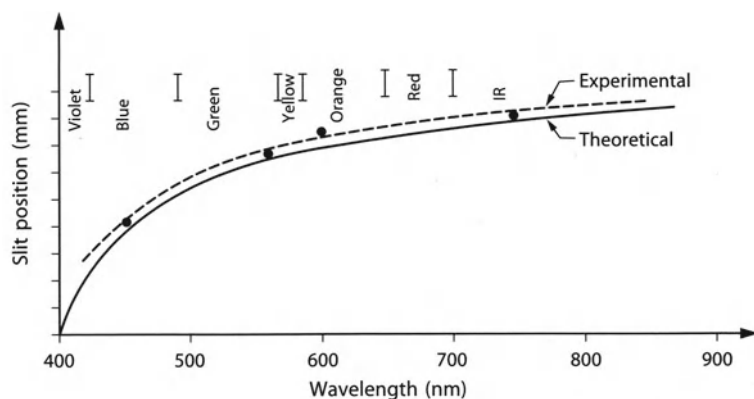


Fig. 12. Transmission response for a flint prism as a function of wavelength

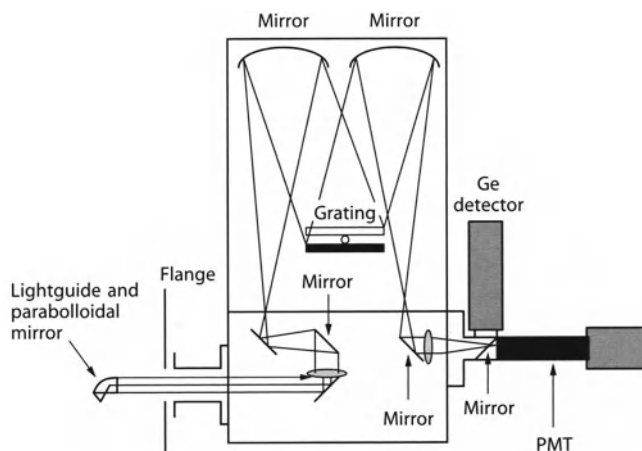


Fig. 13. Czerny-Turner monochromator arrangement used with the equipment at UTS

For high spectral resolution CL spectroscopy, diffraction grating monochromators are generally preferred to a prism based spectrometer system. The Czerny-Turner monochromator arrangement (shown in Fig. 13) is the most popular monochromator design. The wavelength is scanned by simply rotating a reflection diffraction grating on its axis. The grating is rotated using a sine drive to provide a linear scan in wavelength space. Alternatively, a cosecant drive will provide a linear scan in energy space, $E(\text{eV})=1239/\lambda(\text{nm})$. The CL signal at the exit of the CL collector can either be focused on the entrance slit of the grating monochromator or be directed to the spectrometer by means of an optical fibre bundle.

CL is measured with a light sensitive, single channel detector positioned behind the exit slit. The choice of photon detector will ultimately determine both the spectral and spatial resolution of CL spectra and images, respectively. Higher sensitiv-

ity detectors enable the use of narrow exit slit widths for high resolution spectroscopy and low beam powers ($E_o I_B$) for high resolution CL microscopy. PMT detectors have a rapid response time and high sensitivity in the visible making these detectors an ideal choice for CL microscopy and microanalysis. The wavelength detection range of the PMT depends on: (1) the type of photocathode material which sets the long wavelength (NIR) limit and (2) the optical transmission characteristics of the PMT front window which determines the short wavelength (UV) cut off. Cooling the PMT to -30°C via a Peltier device can significantly reduce the thermal noise in the detector improving the sensitivity and detection range.

In the NIR region, SS detectors are more efficient than PMTs. With SS detectors, the incident light is chopped and measured in phase in order to reduce measurement noise (phase sensitive detection method). The optical chopping speed is determined by the peak frequency response of the detector, but multiples of the local power supply frequency should be avoided (50 or 60 Hz).

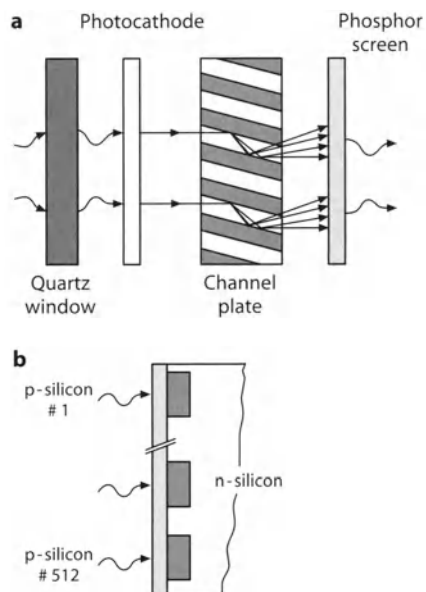
At low CL light levels individual photons can be measured using photon counting techniques. The main advantage of this technique is that noise pulses can be eliminated by using a pulse height discriminator.

4.2.4.2

Parallel Data Measurement

A parallel CL spectrometer utilises an optical multichannel analyser (OMA) as described by Löhnert et al. (1979). The exit slit of the grating spectrometer is removed and replaced by a multichannel solid state detector to analyse the CL emission in parallel over a wavelength range of 300–1100 nm. The multichannel detector used is either an intensified linear photodiode array (ILPDA) or a charge coupled device (CCD) camera.

Fig. 14a,b. Intensified linear photo-diode array consisting of **a** the intensifier and **b** the photodiode array



The ILPDA (Fig. 14) consists of the light intensifier and of the linear photodiode array (LPDA) with 1024 or 512 silicon photodiodes. All diodes are simultaneously illuminated and each diode is read sequentially leading to a simultaneous detection mode of the emitted photons. Wavelength information is determined by the position of the diode within the array. The height of the charge pulse collected at each diode is proportional to the amount of light absorbed. An intensifier (proximity focused image intensifier type) consists of a quartz window placed in front of a photocathode, an accelerating grid, a micro-channel plate and a luminescent screen. The electrons released from the photocathode by the incident photons are accelerated and directed towards the micro-channel plate providing a gain in the number of electrons. These electrons interact with a phosphor screen producing luminous photons, which are measured by the LPDA.

A CCD camera consists of an array, 1024 columns \times 256 rows of 27 \times 27 μm square, silicon photodiodes positioned at the exit focal point of the monochromator. The CCD is positioned so that the long axis of the array is aligned to the dispersion direction of the grating (i.e. long axis perpendicular to the rulings). The charge stored in all 256 pixels in each column is summed and measured (vertical binning) sequentially giving the CCD sensitivity equivalent to a PMT. When the CCD is cooled to liquid nitrogen temperatures the read noise per column is less than a few electrons making the CCD ideal for measuring low light levels. In addition, the CCD is a perfect detector for CL kinetics studies using parallel spectroscopy with moderate light levels in short (>50 ms) acquisition times.

4.3

Comparison of Optical (Stationary Beam) and Scanning Cathodoluminescence Microscopy

Optical CL microscopy has a number of advantages over scanning CL microscopy:

1. CL images can be measured from an insulating specimen without the need for a conductive coating which is generally required in EPMA or SEM CL analysis performed under high vacuum ($<10^{-5}$ Torr). The absence of this coating significantly increases the CL signal emitted from the surface. Cold cathode electron guns require a low vacuum (10^{-2} Torr) to operate efficiently. Leakage of surface trapped charge through the gas phase eliminates the electric field at the surface of the specimen. It should be mentioned that the neutralisation of electrostatic charge in the flood gun optical CL microscope provides similar operating conditions to the environmental scanning electron microscope (ESEM).
2. Large field of view CL images can be measured with low magnification optics and
3. Real colour images can be viewed and recorded using colour photographic film.

However there are a number of disadvantages with flood gun optical CL microscopy when compared with scanning CL microscopy on an EPMA or SEM:

1. A conventional flood gun bathes the specimen with electrons and so is not capable of providing laterally resolved CL spectroscopy.
2. The intensity versus wavelength response of colour photographic film mimics the human eye response and so is highly non-linear with limited wavelength sensitivity range, 400–700 nm.
3. The long working distance glass optics used in flood gun CL systems strongly absorbs short wavelength CL emission and in addition limits the image spatial resolution to the micron scale.
4. The poor vacuum of the flood gun can lead to: (a) iono-luminescence via high energy negative ions impinging on the specimen and (b) the deposition of a thin surface film of light absorbing hydrocarbon contamination.
5. Variation in colour film processing, optical microscope lens system and the poorly defined energy of the electron irradiation of the conventional flood electron gun makes it difficult to compare CL images measured on different flood CL systems.
6. The poor vacuum used in optical CL systems rules out CL imaging at low temperatures.
7. The low current density of the flood electron gun makes it difficult, if not impossible, to investigate materials exhibiting weak CL emission. Long exposure times can compensate to some extent but will decrease spatial resolution (vibration) and exclude investigations where the emission signal intensity varies rapidly as a function of irradiation time, for example quartz (Stevens Kalceff and Phillips 1995a,b; Stevens Kalceff et al. 1996, 1999). High brightness electron guns have been developed (Ramseyer 1989) but are not generally used in optical CL microscopy.

Many of the above problems could be resolved by replacing the colour film plate with a high sensitivity colour CCD camera with digital image store capabilities. Alternatively, for low light and UV or NIR applications a Si photodiode (1024×1024), liquid nitrogen cooled, CCD with the appropriate optical edge filters could be utilised to provide CL images which could be then corrected for system response.

4.4

Cathodoluminescence Lateral Spatial Resolution in Wide Band Gap Materials

4.4.1

Scanning Cathodoluminescence Microscopy

The CL spatial resolution in scanning CL microscopy of wide bandgap materials is determined by the CL generation volume (Fig. 15). The diameter of this volume depends on the two factors, the electron probe diameter and the spatial dimensions of the electron/hole pair distribution. In wide bandgap materials, the contribution to the emission spot size via electron / hole pair diffusion is negligible, and so the recombination length, L , is small ($L^2 = \tau D$). Note that this is not the case in semiconductors in which the magnitude of L and D can be significant. However, the spatial contribution to d_{CLvol} as a result of diffusion is small in semicon-

ductors as the electron/hole pair concentration $[N_{eh}]$ decreases rapidly with distance, r , from the generation point (Yacobi and Holt 1990) as

$$[N_{eh}] \propto r^{-1} \exp(-r/L) \tag{32}$$

Therefore, for most minerals where D and L are small, the CL generation volume is determined by $g(r)$, $g(z)$ and d_p

$$d_{CLgen\ vol} = f(g(r), g(z), d_p) \tag{33}$$

where the lateral $g(r)$ and depth $g(z)$ components arise from the spatial distribution of electron-hole pairs, and d_p is the probe diameter (Holt and Napchan 1994).

The depth component $g(z)$ is given by Eq. (6) (Sect. 3.1). According to Shea et al. (1978), the lateral, r , electron-hole pair distribution can be estimated using

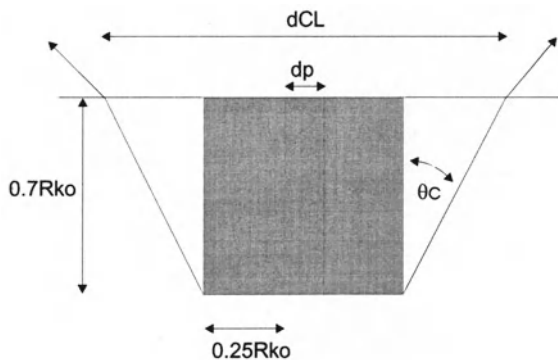
$$g(r) = \exp[-4r/R_{KO}] \tag{34}$$

Laterally, the effective CL probe diameter can be estimated to be approximately $0.5R_{KO}$ when the probe diameter is small compared with $d_{CLgen\ vol}$. With large beam currents the CL probe diameter can be estimated by

$$d_{CL} = d_{CLgen\ vol} + d_{probe} \tag{35}$$

In scanning CL microscopy, the spatial resolution improves with decreasing E_0 (as $R_{KO} \propto E_0$) and i_{probe} (as $i_{probe} \propto d_{probe}^{8/3}$). However, a trade off exists between image resolution and image quality (resulting from signal to noise ratio, S/N) as $I_{CL} \propto E_0 \cdot I_{probe}$. Decreasing E_0 to improve resolution is accompanied by a corresponding decrease in I_{CL} and the CL image S/N level. In order to offset the I_{CL} decrease at low E_0 there must be an equivalent increase in either: (1) the dwell time per pixel which increases the dose and may cause beam damage in irradiation sensitive material or (2) the probe current, I_{probe} , with an increase in d_{probe} which decreases the spectral resolution. Therefore, for best CL resolution there is an optimum E_0 incident energy, probe current and dwell time per pixel. It is

Fig. 15. CL emission volume $d_{cl\ vol}$ where R_{KO} is the electron range, θ_c is the critical angle (see text) and d_p is the probe diameter. The shaded region represents the CL generation volume



important to note that for specimens with long decay time fluorescence or phosphorescence the spatial resolution can be significantly reduced with fast scan speeds. If the excited state lifetime is longer than the dwell time per pixel then smearing in the direction of scan will be observed in the CL image. The length of the left to right streak can be used to estimate the lifetime of the emission as the line scan speed is well defined.

Scanned CL images are generated by scanning a beam of electrons with a well-defined energy, probe size, beam current and dwell time per measurement point (pixel) over the surface of the specimen. Longer dwell times will increase the signal to noise ratio (S/N) and eliminate image smearing when measuring CL from long lifetime emission centres. One disadvantage of using a large current density, stationary (long dwell time) electron probe to excite CL is that under these conditions phenomena such as specimen heating, electromigration and mass loss can occur. However, short dwell times combined with frame store recursive image capture techniques can be used to minimise these effects yet maintain the CL image quality (S/N).

4.4.2

Optical Cathodoluminescence Microscopy

With optical CL microscopy the spatial resolution is limited by the use of light optics which record the CL image directly on the photographic plate. Refraction at the specimen vacuum interface and total internal reflection of the CL emission further reduce the measured spatial resolution.

A detailed discussion and illustration on CL images as a function of the experimental conditions with a flood gun attached to an optical microscope is found in Marshall (1988).

5

Data Acquisition and Processing

5.1

Instrumental Characteristics of the Cathodoluminescence Spectrometers Used in This Work

A variety of photon detectors, diffraction gratings and light collectors are currently available to construct specific attachments to EPMA or SEM and optical microscopes for the detection and the analysis of CL emission. Two CL systems, one located at Microstructural Analysis Unit in University Technology Sydney (UTS), Australia, and the other at the Ecole Nationale de Mécanique et des Microtechniques (ENSM) in Besançon (France), are used to illustrate the merits, limitations and measurement artefacts of a number of components in the CL analysis system.

5.1.1

Scanning Cathodoluminescence Microscopy and Microanalysis System Located at UTS

At UTS, an Oxford Instruments MONOCL system (see Fig. 13) has been attached to a JEOL JSM 35 C type SEM. An optical paraboloidal mirror is used as the photon collector providing a parallel CL beam output incident on a quartz lens at the exit window. Initially a silver plated mirror, manufactured by depositing a thin Ag film on a paraboloidal shaped substrate, was used to collect CL. The Ag mirror was later replaced by an Al paraboloidal mirror, constructed by precision diamond machining of a bulk piece of aluminium to improve the light throughput and wavelength transmission efficiency. A front surface plane mirror allows the CL beam to be directed towards the PMT detector in order to obtain a panchromatic CL image or to be focused on the entrance slit of a grating spectrometer for spectral analysis. This system provides spectral analysis and imaging from 250 to 1800 nm with a Hamamatsu R2228 red extended PMT (300–900 nm), a Hamamatsu R943–02 Peltier cooled high sensitivity PMT and a North Coast Optical liquid nitrogen cooled Germanium detector (700–1800 nm). Oxford Instruments liquid nitrogen and liquid helium stages allow analysis over a temperature range of –268 to 500 °C. CL is collected with a diamond machined paraboloidal collection mirror which provides a large solid angle of collection and is retractable for BSE and SE imaging as well as wavelength dispersive X-ray microanalysis. A liquid nitrogen cooled, Photometrix UV enhanced, 1024×256, ultra-fast CCD plate connected to the MONOCL system via a silica fiber optic cable enables parallel collection of CL spectra for kinetics studies. A monochromator with 600 and 1200 lines/mm diffraction gratings disperses the CL for spectroscopy and monochromatic imaging. A series of mirrors and shutters within the MONOCL allows for panchromatic imaging for studying specimens with weak CL.

5.1.2

Scanning Cathodoluminescence Microscopy and Microanalysis System Located at ENSMM

The CL system located at ENSMM consists of a CL detection system attached to a CAMECA MS46 type EPMA. The CL emission was observed and measured at the ocular lens of the optical microscope equipped with a Cassegrain type objective. The ocular is linked to a spectrometer system by means of an optical fibre bundle. The optical spectrometer manufactured by the Tracor Northern company consists of a grating monochromator with three diffraction gratings 150, 300 and 600 grooves/mm and an ILPDA with 512 photodiodes. The wavelength transmission efficiency of the spectrometer and the silica fibre bundle allows for detection of CL emission within a 250–900 nm interval. However, in practice, UV absorption by glass components in the EPMA optical microscope reduces the CL measurement range to 400–900 nm.

5.2 Spectral Calibration and System Response Correction

5.2.1 Wavelength Calibration

Wavelength calibration must be carried out on a routine basis to ensure accurate measurement of the CL peak position. Measuring emission spectra from well characterised standard emission sources such as a Hg lamp or a HeNe laser (632.8 nm) provides the most reliable wavelength calibration procedure. The high intensity of the laser source enables high spectral resolution (0.1 nm) data acquisition and accurate calibration. The slit width should be set to provide a 0.1 nm resolution and the CL data collected from 635 to 640 nm with a 0.1 nm step size. Laser light should only enter the monochromator system via: (1) a diffuse reflectance target and (2) narrow slits to minimise possible PMT damage. Calibration is achieved by either software or hardware spectral tuning to obtain an exact agreement between the measured and expected emission peak positions.

Luminescent centres such as REE ions in crystalline hosts do not provide reliable standards for wavelength calibration. The trivalent REE peak position in these specimens can vary significantly due to: (1) concentration pairing effects, (2) clustering with charge compensating defects, (3) temperature and (4) strain (Henderson and Imbush 1989). In many synthetic REE doped crystals the REE concentration and distribution is not homogenous and the peak position of the sharp REE CL emission will shift according to the REE concentration and local strain (see Sect. 6).

5.2.2 Correction of Cathodoluminescence Spectra for System Response

The ability of the CL collector, monochromator and detection system to measure the intensity of the CL emission as a function of wavelength is known as the system response. In order to measure the true CL intensity at each wavelength the spectral data must be corrected for the system response. Once the CL spectra have been corrected for system response, the CL peak parameters position, half-width and intensity can be accurately measured and then compared with corrected CL data published in the literature.

Data are corrected for system response at each measurement wavelength using the following expression:

$$I_{corrected} = \frac{(I_{measured} - I_{dark\ counts})}{F_{system\ response}} \pm \frac{\sqrt{I_{measured}} + \sqrt{I_{dark\ counts}}}{F_{system\ response}} \quad (36)$$

where $I_{measured}$ is the intensity measured by the CL system, $I_{dark\ counts}$ is the intensity measured with no light entering the CL measurement system and $F_{system\ response}$ is the normalised system response.

The system response curve is measured from 200 to 2500 nm using deuterium (ultra-violet) and quartz halogen (visible and near infrared) 30 W standard light sources of spectral radiance. These calibrated lamps can be purchased from a number of optics suppliers. Tables of spectral irradiance ($\mu\text{W cm}^{-2} \text{nm}^{-1}$) as a function of wavelength at a distance of 50 cm are provided with each lamp. PMT detectors measure the number of photons per second per wavelength measurement interval but not spectral irradiance. The number of photons per μW ($\mu\text{J s}^{-1}$) of monochromatic light can be simply calculated as the energy in each photon is given by $E=hc/\lambda$ where h is Planck's constant ($6.626\times 10^{-34} \text{ J s}^{-1}$), c is the speed of light in a vacuum ($2.998\times 10^8 \text{ ms}^{-1}$) and λ is the wavelength. Therefore the number of photons per second per cm^2 emitted at each wavelength, $N_{\text{photon}}(\lambda)$, can be calculated from the spectral irradiance data using

$$N_{\text{photon}}(\lambda)=5.03\times 10^{15}\times\lambda \text{ (nm)}\times\text{spectral irradiance} \quad (37)$$

where the wavelength unit is nm and the spectral irradiance is expressed in $\mu\text{W cm}^{-2} \text{nm}^{-1}$. Note that there is no need to calculate the absolute number of photons entering the monochromator system.

The system response curve for each detector/grating combination can be measured using the following procedure: (1) set up the supply voltage and source to collector distance of the spectral irradiance source following the manufacturer's instructions, (2) place a 1 mm diameter aperture at the focal plane of the light collector, (3) illuminate the aperture with the calibrated source at a distance greater than 50 cm to prevent a thermal contribution to the measurement, (4) set PMT gain (high voltage) at the standard working value, (5) adjust collector to achieve a maximum count rate, (6) adjust slits to give 1 nm spectral resolution, (7) measure emission spectrum, I_m , over the full detection wavelength range with a 1 nm step, and (8) calculate response curve, F_{resp} , using:

$$F_{\text{resp}}=I_m/N_{\text{photon}} \quad (38)$$

The system response curve for a the paraboloidal mirror, Hamamatsu R2228 PMT and 1200 lines/mm 550 blaze diffraction grating is shown in Fig. 16. Notes:

1. Measurement errors can be significant at the low sensitivity tails of the response curve. In practice do not use $F_{\text{resp}} < 0.01$.
2. The system response curve is measured using unpolarised light. F_{resp} cannot be used to correct polarised CL emission, which can be observed when irradiating highly oriented single crystals. A variation in CL signal intensity as the specimen is rotated with respect to the collector indicates that CL emission is polarised (see Sect. 4.2.1.1; Stevens Kalceff et al., this Vol.).
3. Any contribution due to scattering with the monochromator of NIR emission must be eliminated when measuring blue tail end emission of the quartz-halogen lamp.
4. Intensity data measured around the bright Wood's anomaly is dependent on the intensity and polarisation of the calibration source.

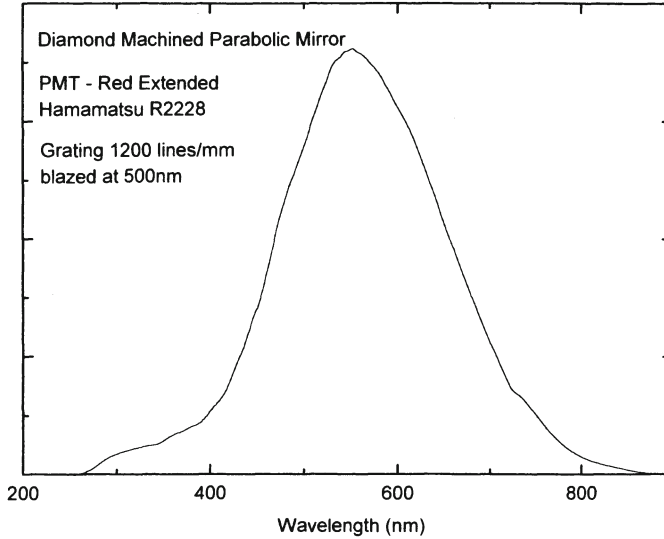


Fig. 16. System response curve for the CL measurement system at UTS

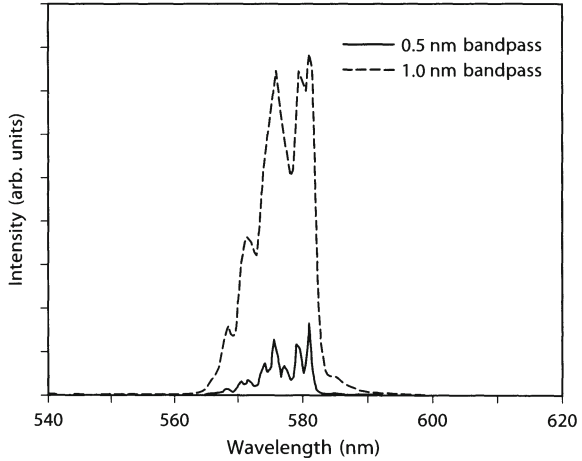
5.3 Spectral Resolution

Spectral resolution is a measure of peak sharpness, the ability of the spectrometer to separate two or more spectral lines that are close together. Resolving CL spectral fine structure greatly assists in unravelling the origin of emission (see Sect. 3.4). In both serial and parallel measurement systems, the natural CL peak width and spectral measurement conditions, assuming adequate CL intensity, determine the spectral resolution.

5.3.1 Serial Spectral Measurement

The spectral resolution of serially collected CL data is determined by the signal intensity (RC concentration, E_0 , I_B , specimen temperature and system response) and the monochromator slit width. The resolution is often expressed in terms of band-pass, which is the width spectrum passed by the spectrometer. Decreasing the slit width increases the spectral resolution but lowers the signal throughput (see Fig. 17). CL signal loss with reduced slit width can be offset by increasing the excitation power ($I_B \times E_0$). However high power density focused electron probes can produce heating materials with a low thermal conductivity, phase separation and strong subsurface electric fields which induce defect diffusion as well as mass loss in some cases. For homogeneous specimens high spectral resolution data (<0.1 nm) can be measured using the minimum slit width (the instrument resolution) with a defocused probe in order to increase signal and minimise electron beam induced damage. Measuring spectral data at low temperature can also improve the resolution by reducing the natural peak width (see Sect. 3.2.1).

Fig. 17. CL spectral resolution as a function of slit width with serial collection



5.3.2 Parallel Spectral Measurement

The spectral resolution of CL data measured with an optical multichannel analyser (OMA) is determined by the number of pixels (ILPDA) or rows (CCD) and the spectral coverage of the OMA:

wavelength resolution(nm)=spectral coverage(nm)/number of diodes (39)

and the spectral coverage is given by

spectral coverage(nm)=grating dispersion (nm/mm)×length of OMA(mm). (40)

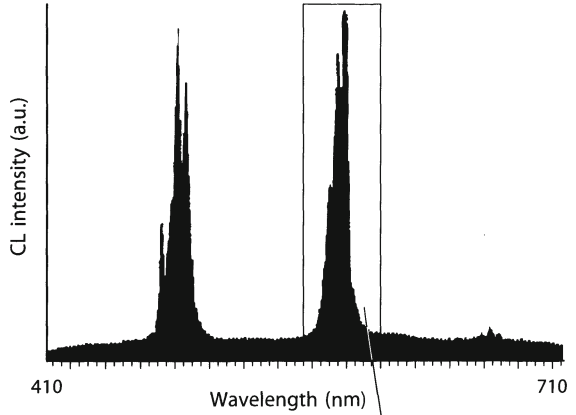
In practice, the spectral resolution is a function of the diffraction grating dispersion as the number of pixels and the length of the OMA [pixel size×pixel (or row) number]. Therefore the spectral resolution can be improved by increasing the number of rulings per mm (Fig. 18) or using higher diffraction orders (see Sect. 4.2.3).

6 Case Study – Identification of Cathodoluminescence Peaks in Natural and Synthetic Zircons

6.1 Peak Identification

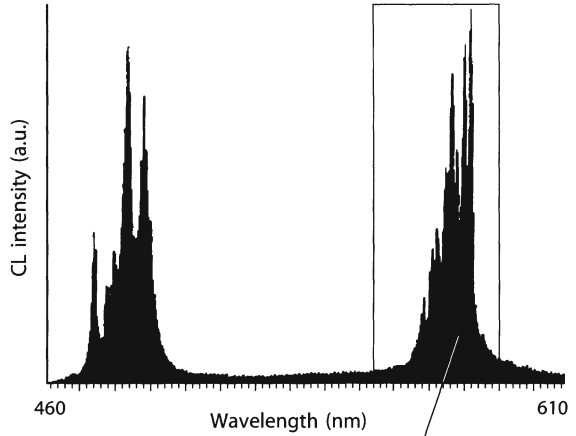
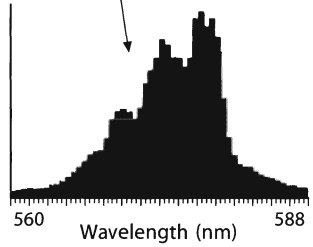
A panchromatic CL image of a natural zircon grain obtained with the CL scanning microscope is shown in Fig. 19a. The specimen was rotated by 90° around the electron beam direction in order to verify a possible contrast change related to

Fig. 18a,b. CL spectral resolution as a function of spectral coverage with parallel collection using **a** a 150 lines/mm grating and **b** a 300 lines/mm grating (synthetic Dy³⁺ doped zircon specimen)



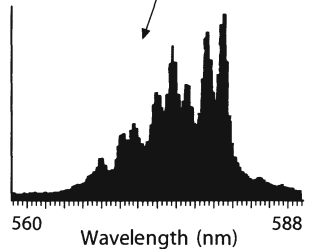
Grating: 300 lines/mm
Spectral range: 300 nm
0.6 nm per channel

a



Grating: 300 lines/mm
Spectral range: 150 nm
0.3 nm per channel

b



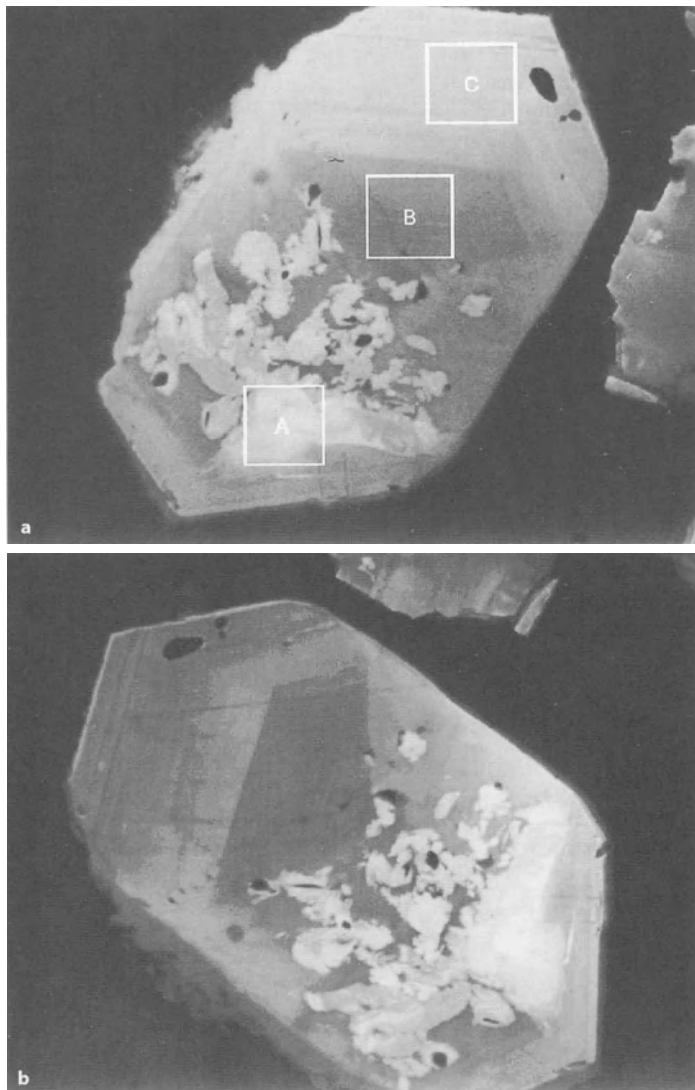


Fig. 19a,b. Panchromatic scanning CL image of a natural zircon and b after the specimen was rotated 90°

polarisation effect as previously mentioned (see Sect. 4.2.1.1). The panchromatic image in Fig. 19b did not reveal significant changes in contrast with respect to Fig. 19a. Three areas (100×100 μm) were selected for spectral analyses and are labelled A, B and C as indicated on the CL image presented in Fig. 19a. From these three locations, the CL spectra shown in Fig. 20 were measured with the serial spectrometer (equipment at UTS). The accelerating voltage was 15 kV, the resolution was 2 nm with a 5 nm step.

All spectra are characterised by narrow emission lines superimposed on top of broad emission bands centred at about 300, 380 and 550 nm with a long tail on the long wavelength side.

The broad emission bands are probably associated with defect centres, while the narrow lines are characteristic of rare earth ions that are frequently present in most of the natural zircon crystals. There is still considerable debate over the nature of the recombination centres associated with the broad emission bands. Based on CL and TL studies of natural zircons (Iacconi and Caruba 1984; Iacconi et al. 1980; Kirsh and Townsend 1987) the band near 430 nm results from bond breaking of the SiO_4^{4-} groups. According to Nicholas (1967), the broad band centred near 600 nm in the photoluminescence (PL) spectrum of natural zircons is associated with lattice defects resulting from radioactive decay of the uranium present at trace levels.

Natural zircon often contains REE impurities at a trace (part per million) level. CL spectra measured from natural zircon are characterised by sharp line REE emission peaks (see Sect. 3.4.1.1) in the visible and a broad emission band in the ultraviolet.

The REE peak position and relative intensity data presented by Dicke (1968) were measured from REE doped fluorites (CaF_2) and at best can only be used as a guide to the REE peak position in zircon. From these data, the CL lines shown on the CL spectra of the natural zircon (Fig. 20) can be tentatively assigned to Dy and Er CL emission lines. A more rigorous approach is to measure the REE peak parameters from a set of flux grown REE doped zircon standards (Cesbron et al. 1995) with *identical* excitation and measurement conditions.

The synthetic Dy^{3+} and Er^{3+} doped zircons were analysed with the same instrumental and experimental conditions as those used for recording the natural zircon spectra shown in Fig. 20, i.e. 15 keV incident energy, a 2 nm spectrometer resolution and a 5 nm step size. The data for the synthetic Dy or Er doped zircons in Fig. 21 are in good agreement with the wavelength positions of the narrow luminescent lines measured at the surface of the reference materials and the natural zircon specimen. However in the wavelength domain around 485 nm high overlap exists between the characteristic lines of Er and those of Dy.

All REE peaks in an unknown natural zircon specimen can be confidently assigned to REE impurities using CL spectra collected from the synthetic doped zircon crystals. This simple qualitative CL analysis confirms that small amounts of Dy and Er are present as impurities in the natural zircon specimen. However, the changes in the relative REE CL intensity may depend on the relative concentration of other radiative and non-radiative recombination centres rather than variations in the REE concentrations.

CL spectra were measured with a higher magnification ($20 \times 20 \mu\text{m}$) and a 25 keV incident energy inside the areas A, B and C (Fig. 19a). The spectra (1 nm resolution, 5 nm step) are shown in Fig. 22. The intensity of the narrow peaks relative to that of the broad emission bands strongly decreased with respect to spectra measured at lower magnification (Fig. 20). The differences between spectra in Figs. 20 and 22 may indicate either an inhomogeneity in the spatial distribution of the recombination centres or preferential excitation via saturation effects of these centres associated with the narrow and broad emission features as a func-

tion of the incident electron dose. These results indicate that reliable qualitative identification of all spectral components can only be obtained from several CL spectra measured under different excitation conditions.

**6.2
Spatial Distribution of the Dy and Er Impurities
Within the Natural Zircon Specimen**

In order to relate the changes in contrast in the panchromatic CL images in Fig. 19 with the local variations of the Dy and Er concentrations, CL images at several wavelengths with a 10 nm band-pass were recorded.

For each selected wavelength associated with the Dy or Er impurity, the measured intensity (i.e. the brightness of the CRT used for imaging) is the sum of the

Fig. 20. CL emission spectra (corrected for instrumental response) measured ($E_p=15$ keV) with a serial spectrometer from regions ($100 \times 100 \mu\text{m}$) in a natural zircon marked A, B and C in Fig. 19

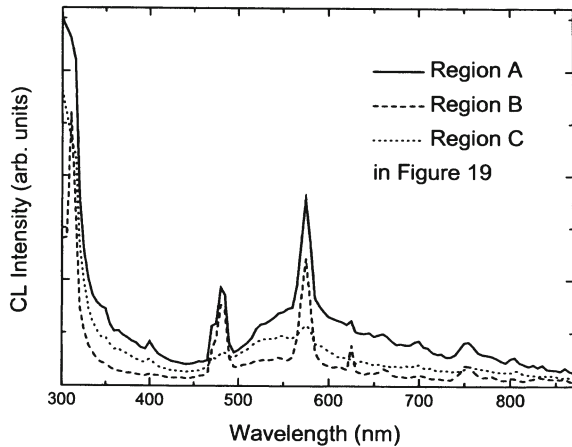


Fig. 21. CL emission spectra (corrected for instrumental response) measured with a serial spectrometer from Dy and Er doped synthetic zircon

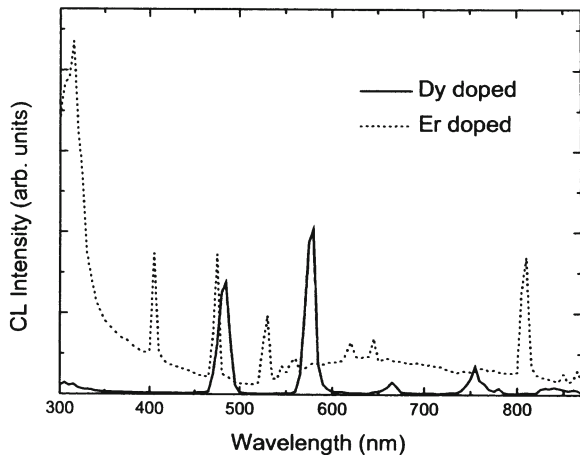
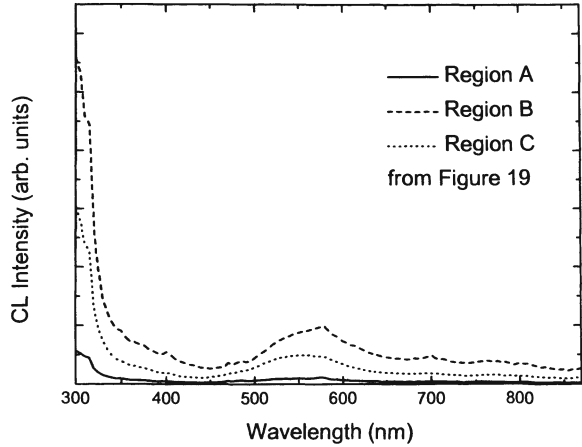


Fig. 22. CL emission spectra (corrected for instrumental response) measured ($E_p=25$ keV) with a serial spectrometer at high magnification inside the regions (20×20 μm) marked A, B and C in Fig. 19



intensity of the luminescent ion and that of the underlying broad emission band. In order to evaluate the relative contribution of both intensities to the contrast of the CL images, two images were recorded successively, the first one corresponding to the characteristic wavelength λ of the luminescent ion, the second one corresponding to the wavelength $\lambda-\Delta\lambda$.

For the Dy impurity, the CL images were measured at $\lambda=575$ nm (Dy line) and at $\lambda=540$ nm (emission band) successively. For the Er impurity, the CL images were measured at $\lambda=350$ nm (Er emission line) and $\lambda=330$ nm (broad emission band) successively.

The selected wavelength CL images are shown in Fig. 23. The image at $\lambda=540$ nm (Fig. 23a₂) was subtracted from that at $\lambda=575$ nm (Fig. 23a₁) in order to illustrate the spatial distribution of the Dy intensity corrected for the underlying broad emission band. The resulting image labelled (575–540 nm) in Fig. 23a₃ shows that the highest concentration of Dy recombination centres are present in some of the bright spots and within the central area (area B in Fig. 19). The image at $\lambda=330$ nm, corresponding to a defect related emission band, showed similar contrast to that measured at $\lambda=350$ nm corresponding to an Er³⁺ emission line (Fig. 23b₁). The image at $\lambda=330$ nm was subtracted from that at $\lambda=350$ nm in order to image the spatial distribution of the Er recombination centres. The resulting image labelled (350–330 nm) in Fig. 23b₂ shows a preferential localisation of Er in the bright areas shown in Fig. 19.

Even after subtracting the images measured from a characteristic REE CL emission line and those measured from the underlying broad emission band, it is still difficult to accurately relate the resulting contrast only to the presence or not of the REE impurity. These examples demonstrate that the contrast in a monochromatic CL image can only be confidently interpreted when these images are supplemented with CL spectral data.

Spectra (1 nm resolution, 2 nm step) were measured at high magnification within a bright CL area (area A) and outside the bright patch (area B) shown in Fig. 24. Spectra in Fig. 25 show that the two areas are characterised by a large dif-

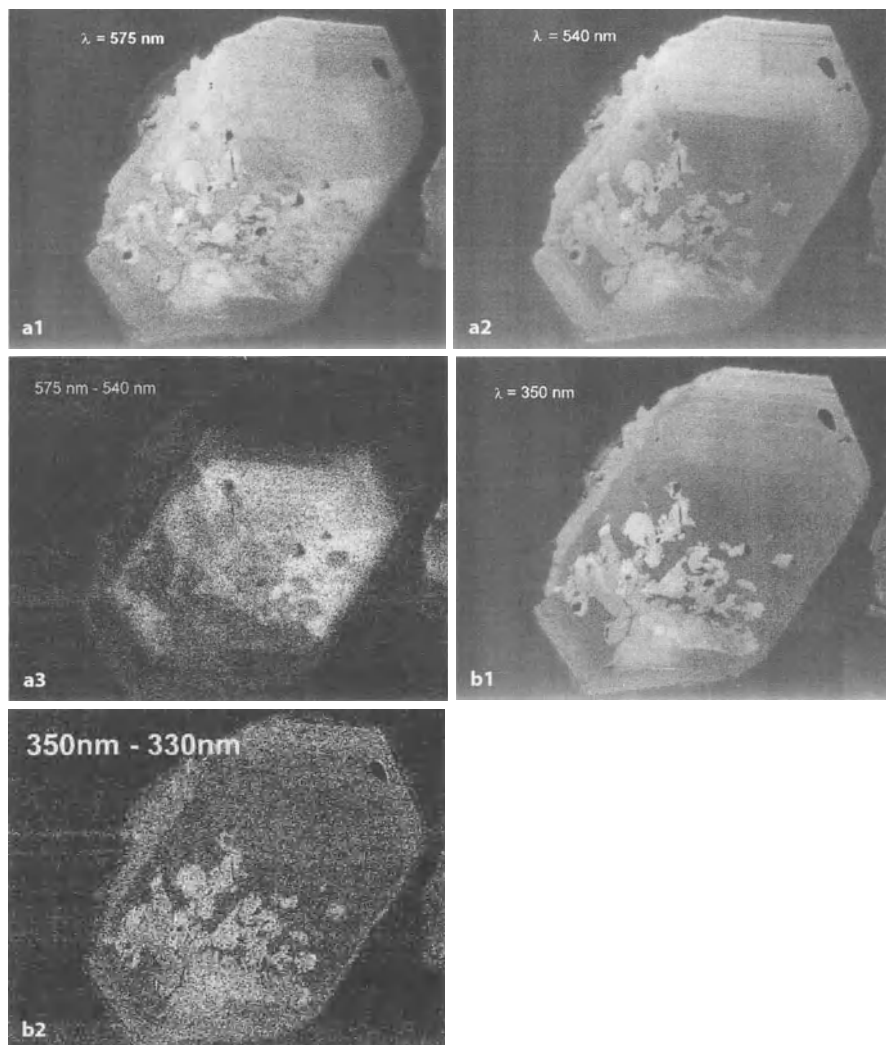


Fig. 23a,b. Scanning CL images from the natural zircon specimen measured at selected wavelength (**a**₁) $\lambda=575$ nm corresponding to a Dy^{3+} emission line, (**a**₂) $\lambda=540$ nm associated with a defect related emission band, (**a**₃) distribution of the Dy^{3+} centres after subtracting the image (**a**₂) from image (**a**₁), (**b**₁) $\lambda=350$ nm corresponding to a weak Er^{3+} emission line and (**b**₂) resulting image after subtracting the image measured at $\lambda=330$ nm associated with a defect recombination centre

ference in the intensity of the broad emission bands and these variations probably dominate the contrast of the CL images. However, as also shown in the spectra in Fig. 25, both areas exhibit a group of lines occurring near 485 and 580 nm which are consistent with those measured from the Dy^{3+} doped zircon standard. It is difficult to determine in which area the Dy signal is the strongest because the

intense broad emission band on the spectra of area A does not allow an estimate of the relative height of the Dy CL lines in both analysed areas. Characteristic Er³⁺ CL peaks are more clearly shown on the spectrum measured from the bright region than that measured outside the bright area. As a consequence, the contrast in the panchromatic CL image which is dominated by the intensity of the broad emission band also reveals the distribution of the Er ions which are preferentially located within the bright CL spot. However, no change in the Dy concentration can be derived from these analyses.

When areas A and B on the Fig.24 were analysed under identical excitation conditions and measured with an equivalent band-pass, a large difference in the CL yield was observed (Fig. 25). In order to study the fine structure of the Dy³⁺ and Er³⁺ whose lines near 485 nm partly overlap, the electron beam power must be increased as the band-pass (slit width) is reduced. However the beam intensity must remain below a certain threshold level to minimise beam induced damage. In practice, with serial collection of CL spectra, it is often difficult to use identical CL excitation and collection conditions when analysing specimens where there are large differences in CL emission intensity.

The CL collection problems can be resolved by measuring the CL data using a parallel spectrometer equipped with an intensified LPDA detector. Such a possibility is illustrated in Fig. 26, showing part of the spectra around 485 nm measured at areas A and B (Fig. 24) at the surface of the natural zircon. The difference in the CL yield between the two regions is accounted for by increasing the gain of the intensifier while maintaining constant the excitation conditions (25 keV beam energy and a 50 nA beam current). By only adjusting the gain of the ILPDA without changing the beam excitation conditions, spectral data can be measured with the same spatial resolution. In addition, the same gain setting can be used with all available gratings enabling an improvement in the wavelength resolution by increasing the number of grooves per mm while maintaining a constant electron dose.

While the presence of characteristic Er emission lines (partly interfering with some lines of the Dy CL emission lines) is confirmed in the spectrum in Fig. 27a, the presence or absence of Er at area B can only be established by comparing the relative intensity of the CL emission lines measured at area B (Fig. 27b) with the relative intensity of the same lines measured from the synthetic Dy doped zircon in Fig. 27c. It is important to note that the width of the CL multiplets for the Dy ions differs for the natural (Fig. 27a,b) and the synthetic (Fig. 27c) zircon specimens and that such a difference must be accounted for when measuring the CL line intensities (see next section).

Contrast of CL images, either panchromatic or at selected wavelengths, can only be associated with a particular recombination centre when CL spectra are measured from a number of areas exhibiting different brightness. In addition, CL images only reflect the local variations in the number of emitted photons and not the variations of the number of generated photons. From a selected wavelength image it is thus possible to illustrate the spatial distribution of a given recombination centre, but in order to relate the change in intensity with a change in the density of recombination centres, quantitative analyses must be performed.



Fig. 24a,b. Scanning CL images measured with a 5 keV (a) and 15 keV (b) incident energy from an area exhibiting bright luminescent spots at the surface of the natural zircon. Note the change in the spatial resolution as a function of the accelerating voltage (see Sect. 4.4)

Fig. 25. CL spectra (corrected for instrumental response) measured with a serial spectrometer from the bright region in natural zircon marked (a) in Fig. 24 and outside the bright spot (b) in Fig. 24

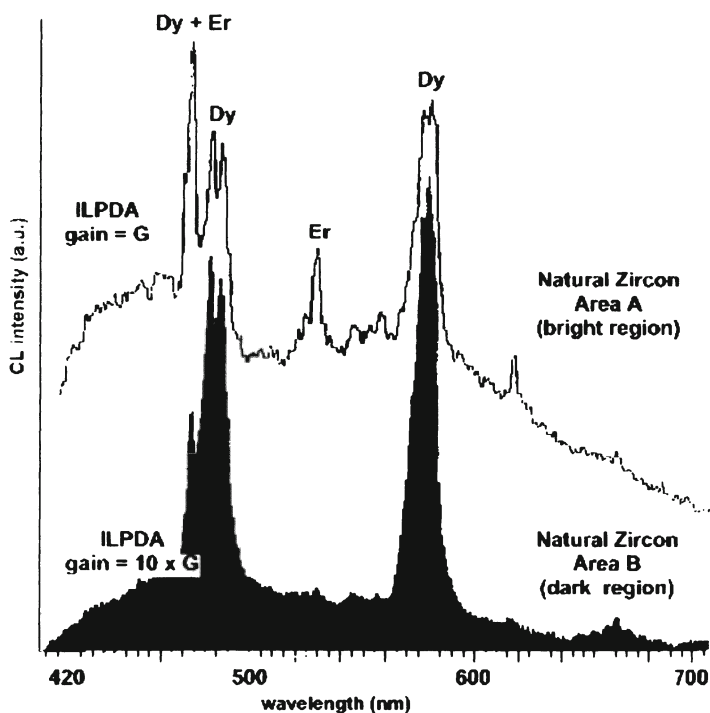
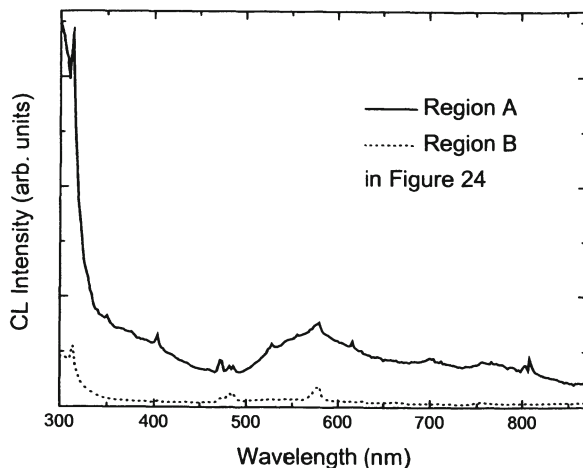


Fig. 26a,b. CL spectra (not corrected for instrumental response) measured with a parallel spectrometer from the bright region in natural zircon marked (a) in Fig. 24 and outside the bright spot (b) in Fig. 24. Note that adjusting the gain of the intensifier of the photodiode array (ILPDA) allows us the measurement of the CL spectra from areas A and B exhibiting very different signal levels without changing the excitation conditions

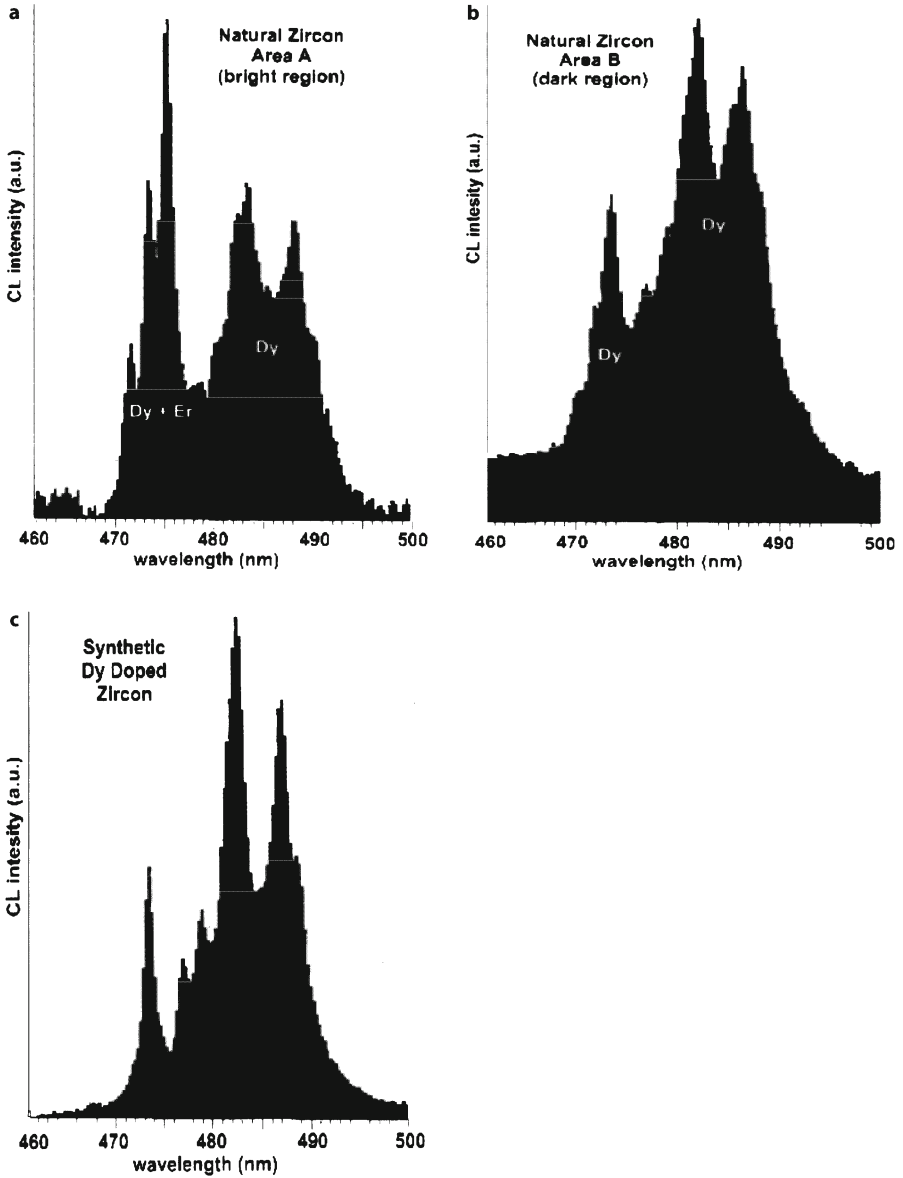


Fig. 27a–c. High resolution spectra (not corrected for instrumental response) measured with the parallel spectrometer equipped with a 300 g/mm, within the 460–500 nm interval from a a bright area CL area (area A in Fig. 24), b outside the bright spot (area B in Fig. 24) at the surface of the natural zircon and, c from Dy doped synthetic zircon. Note the difference in the line shape for the 483 and 488 nm Dy lines as a function of the analysed specimens

6.3 The Quantitative Procedure

The aim of quantitative CL analysis is to establish a relationship between the intensity of the signal and the concentration of the photon emitters. In order to achieve this goal, it is necessary to consider both the primary excitation of the luminescent centres by the incident electrons and the secondary excitation resulting from the absorption of all energies produced in the specimen (see Sect. 3.3.1).

Since the primary and secondary emissions originate from different depths below the specimen surface, the intensity emitted at the specimen surface is in the form:

$$I_{em} = C [I_p f(\chi)_p + \sum I_f f(\chi)_f] \quad (41)$$

where C is the concentration of recombination centres, I_p and I_f are the intensities produced in the specimen by the direct and the fluorescence mechanisms, respectively, and $f(\chi)_p$ and $f(\chi)_f$ are the corresponding correction factors for absorption of the generated photons by the matrix along the CL escape path length.

Only a fraction of the total emitted intensity, I_{mea} , will be measured by the spectrometer with a solid angle Ω of capture and a response function f_D . Therefore I_{mea} can be expressed as

$$I_{mea} = (\Omega/4\pi) f_D I_{em} \quad (42)$$

The concentration of radiative recombination centres involved in the analysed CL peak can be derived from the comparison of the measured intensity with a theoretical calculation of the CL intensity. In practice, in order to reduce the uncertainty in the calculation of the instrumental factor, f_D , a standards based approach can be used similar to the quantitative X-ray analysis procedure with the EPMA. The intensity ratio (k -ratio) between the CL intensity measured at the surface of the specimen and a reference compound gives a first approximation of the concentration of recombination centres. The exact concentration being obtained by applying to the experimentally measured concentration a set of correction factors accounting for the photon generation and emission in the unknown and reference materials.

$$C = k f_z f_A f_F \quad (43)$$

where k is the intensity measured at the specimen surface relative to that measured from the reference material, f_z expresses the differences in the number of generated photons in the analysed and reference specimens, f_A is the absorption correction factor and f_F the fluorescence correction term.

6.3.1 Cathodoluminescence Intensity Measurement: Curve Fitting

Identification of the REE elements in a wide band gap host is often difficult especially when a number of different REE impurities are present due to peak overlap,

polarisation artefacts and REE coordination effects (peak shift and broadening as well as intensity variations). The CL emission spectrum of a luminescent rare earth ion exhibits several lines of different energies each of these lines consisting of multiplets. Comparison of the relative peak height of the CL emission lines is a sufficient approximation for a qualitative analysis as illustrated above for Er and Dy impurities in zircon. However these overlaps cannot be neglected with a quantitative interpretation of the CL data and spectral decomposition must be applied using curve fitting techniques.

The observed line shape as a function of the energy, $P(E)$, of any spectroscopic feature is given by the convolution product of the physical width of the analysed phenomenon $L(E)$ with the instrumental broadening function $G(E)$ according to

$$P(E) = \int L(E-E') G(E) dE \quad (44)$$

which assumes that both the physical energy width of the emitted lines and the response function of the equipment over the full analysis energy range must be known.

In practice, a least squares fitting technique of the observed data to an analytical description of the spectroscopic features is more often applied rather than a rigorous mathematical deconvolution procedure. Such least squares fitting techniques are used on a routine basis for EDS X-ray spectra and have been applied by Rémond et al. (1993, 1996) to WDS X-ray spectra.

The Gaussian peak parameters of a CL emission band can be determined using

$$I_{CL}(E_i) = I_{peak} \exp \left[-2.773 \left(\frac{E_{peak} - E_i}{FWHM} \right)^2 \right] \quad (45)$$

where I_{CL} is the intensity at energy E_i , I_{peak} is the intensity at the Gaussian peak, and FWHM is the energy width of the peak at half the peak height.

Spectral peak fitting should only proceed: (1) once the data has been corrected for the system, and (2) after the spectral data have been converted from wavelength space into energy space using

$$I(E) = I(\lambda) \lambda^2 \quad \text{and} \quad E(eV) = \frac{1239}{\lambda(nm)} \quad (46)$$

This conversion is required as CL intensity is conventionally measured as photons per wavelength interval, $\Delta\lambda$, not energy interval,

$$\Delta E = \frac{hc}{\lambda^2} \Delta\lambda \quad (\text{which is obtained by differentiating } E = \frac{hc}{\lambda}).$$

In many cases CL emission peaks overlap and fitting procedures are required to determine the Gaussian peak parameters for each CL emission peak. The “goodness of fit” is generally given in terms of a χ^2 value

$$\chi^2 \approx \sum_i \frac{(I_m - I_{fit})^2}{I_{fit}} \quad (47)$$

where I_m is the measured CL intensity and for N peaks

$$I_{fit}(E_i) = \sum_N I_{peak}^N \exp \left[-2.773 \left(\frac{E_N - E_i}{FWHM_N} \right)^2 \right] \quad (48)$$

Equation (48) may not yield a unique solution due to the large number of fitting parameters ($3 \times N$) when Gaussian peaks are fitted to a single CL spectrum. However, a unique solution can often be obtained by tying peak parameters together and simultaneously fitting a number of CL spectra measured with a range of beam currents giving different integrated peak intensities.

Depending on the resolution of the spectrometer and the physical width of the CL emission, the CL peak profile may be intermediate between a Gaussian and a Lorentzian distribution. Rather than a pure Gaussian profile (Eq. 48) the use of a pseudo-Voigt distribution as a fitting function should be preferred, i.e., a linear combination of a Gaussian and a Lorentzian in proportion C_G and C_L successively.

$$P(E) = C_G G(E) + C_L L(E) \quad (49)$$

where $G(E)$ and $L(E)$ are Gaussian and Lorentzian distributions centred at the same position and having the same width.

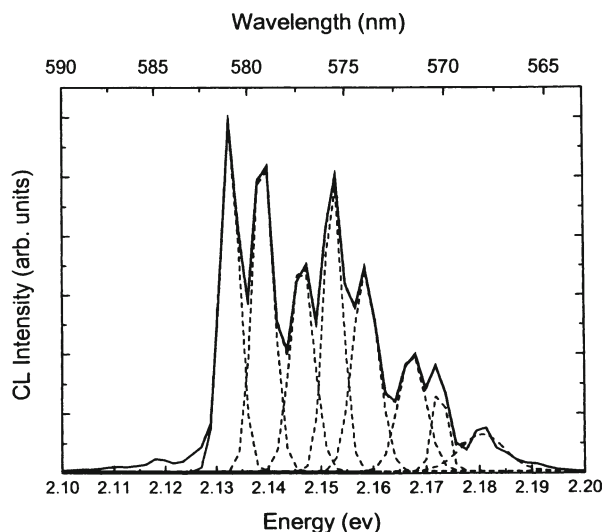
The CL emission spectra from the REE doped zircon standards can be used to generate REE peak parameters (position, FWHM and relative intensities of the complex lines) and enable accurate REE peak deconvolution in natural specimens with a number of REE present. It is tempting to develop a data base of these parameters derived from the spectral analysis of the synthetic doped zircon crystals, as shown in Fig. 28, for a high resolution CL spectrum from a synthetic Dy doped zircon. The parameters can be used in the fitting function (Eq. 48 or Eq. 49) when applying the least squares fitting technique to the CL spectrum of an unknown specimen. However, there are a number of practical limitations if generating such a data bank:

1. The reference peak parameters can only be used with spectral data measured under identical spectral resolution conditions, slit width, as the REE peaks are generally a multiplet comprised a number highly overlapped narrow emission peaks. Therefore, the unknown specimen must have a CL emission yield with the same order of magnitude compared to that of the reference materials. Unfortunately this situation is not generally the case when analysing natural and synthetic standard specimens.
2. In the fitting procedure, *all spectroscopic features* present in the CL spectrum to be processed must have a corresponding fitting function. Spectral analysis

of synthetic REE doped crystals show that a Gaussian peak profile is a sufficient approximation for describing the CL peak shape. However it is often difficult to obtain CL peak parameters either theoretically or experimentally. Theoretical models require a detailed knowledge of: (1) the vibrational properties of the matrix, and (2) the degree of electron-phonon coupling between the electronic states of the luminescent centre and the vibrating lattice. Experimental peak values require well-characterised synthetic crystals with a pre-determined defect structure. High temperature crystal growth using controlled atmosphere furnaces can be used to produce synthetic crystal. However, crystal fabrication procedures are often experimentally demanding and time consuming. For these reasons, curve fitting broad CL emission by adding a number of Gaussian (Eq. 45) or pseudo-Voigt profiles (Eq. 46) can produce erroneous results.

3. A large numbers of parameters are involved in the analytical description of all features present in a complex experimental spectrum. In order to reduce the number of variables in the fitting procedure, some of the variables must be coupled together, as discussed by Rémond et al. (1993, 1996) for processing X-ray spectra. However, in order to use such constraints in the fit, it is essential that the parameters that are coupled together remain independent of the experimental conditions used. However, this condition is difficult to maintain. In REE doped zircon for example, the use of constraints is not possible as the CL lines consist of complex multiplets with different polarisation characteristics peak width and relative intensities in natural and synthetic crystals (Fig. 27). There is little doubt that the type of structural defect and/or impurities, which provide charge compensation for the Dy^{3+} , leads to the observed differences in the Dy^{3+} emission characteristics.

Fig. 28. Gaussian peak fit for the sharp CL emission from a Dy doped zircon



For the reasons mentioned above, no attempt has been made to process the CL spectra measured from the natural zircon specimen using the results derived from the spectral analysis of the synthetic doped zircon crystals. In addition, the relative intensities are expected to also depend on instrumental factors such as the polarisation effect induced by optical reflection from the metallic light collector (see Sect. 4.2.2).

6.3.2

K-Ratio Determination:

Choice of Reference Materials

There is often a number of suitable reference compounds for quantitative X-ray analysis using high energy X-ray photons involving transitions on core levels. There is less choice for the case of soft X-ray emission bands involving valence electrons, as the shape of the X-ray bands is dependent on the chemical environment. As also reported by Bastin and Heijlinger (1991a) for the case of the B K α emission band the intensity of the emission depends on the polarisation effect induced by the monochromator. Furthermore, the intensity of soft X-ray emission bands measured from strongly insulating materials depends on the internal electrical fields which develop within the material as a result of charge trapping mechanisms. In addition to the change in intensity due to the change in the ionisation distribution function compared to that occurring for an electrical conductive material, some additional features may appear on the X-ray peak, as reported by Fialin et al. (1994, 1995). These authors observed that high energy satellite lines were present in the O K α emission spectrum of a synthetic α -alumina crystal but were absent in a natural sapphire crystal. The authors attributed the satellite peak to transitions from discrete states located in the band gap to the O 1 s vacancies. For quantitative analysis using soft X-ray emission band it is thus essential that both the analysed specimen and the reference materials have the same physical properties (defects) and not only similar composition.

It is evident from the previous comparisons between CL properties of natural and synthetic zircons that the CL peak shape and the relative intensities of the CL lines will vary as: (1) a function of the chemical environment and (2) the polarisation effect resulting from the CL generation mechanisms and from instrumental factors. In addition the CL emission of a particular trivalent rare earth ion depends on the host crystal lattice, as illustrated by Blanc et al. (this Vol.).

As a consequence, the same restrictions apply in the choice of reference materials for CL quantitative analysis as those mentioned above for quantitative analyses using soft X-rays.

Presently, quantifying CL emission spectra from crystals randomly orientated in a natural sample is impossible. Quantitative analysis from synthetic crystals grown under controlled conditions is still difficult as will be illustrated by the following example.

In order to investigate the feasibility of quantitative CL analysis, CL and X-ray spectra were measured from several areas within a single synthetic Dy doped zircon. Phosphorous has been added to these crystals to provide charge compensation (Cesbron 1995).

For these investigations the SEM installed at UTS equipped with both the CL spectrometer and a wavelength dispersive X-ray spectrometer was used. This combined CL and WDS spectrometer allowed the CL and WDS data to be rigorously measured from the same locations at the zircon surface.

The analysed synthetic crystal exhibits spatial variations in its CL emission properties as shown on the panchromatic CL image in Fig. 29. The CL emission spectra measured from the three areas labelled 1,2 and 3 are given in Fig. 30. The Dy LX X-ray peaks measured at the same three areas are shown in Fig. 31.

From the CL emission spectra it appears that the intensity of the Dy lines at 485 and 585 nm as a function of the analysis location is consistent with the brightness changes observed in the panchromatic image, i.e. the higher the intensity of the Dy line the higher the brightness of the CL emission. This result contrasts with the variations of the Dy $L\alpha$ X-ray intensities indicating that:

1. The Dy $L\alpha$ intensity is the highest in area 3 which corresponds to an intermediate brightness on the panchromatic CL image.
2. Areas 1 and 2 which exhibit a large difference in CL yield on the panchromatic image do not show significant variations in the Dy $L\alpha$ peak height.

From the comparisons between CL and X-ray data acquired in the same instrumental conditions, it becomes apparent that:

1. The brightness variations on the panchromatic CL image are consistent with the variations in the CL intensity of the Dy CL lines.

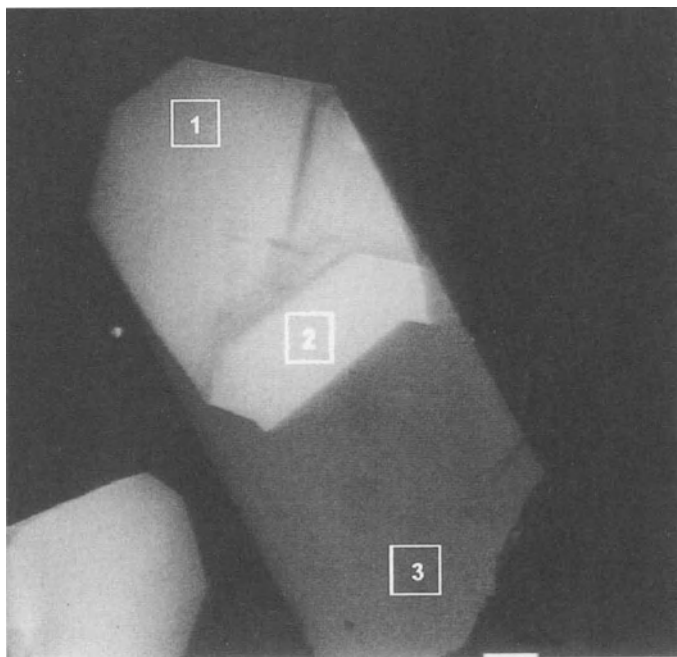


Fig. 29. Panchromatic CL image (700×700 μm) of a synthetic Dy doped zircon

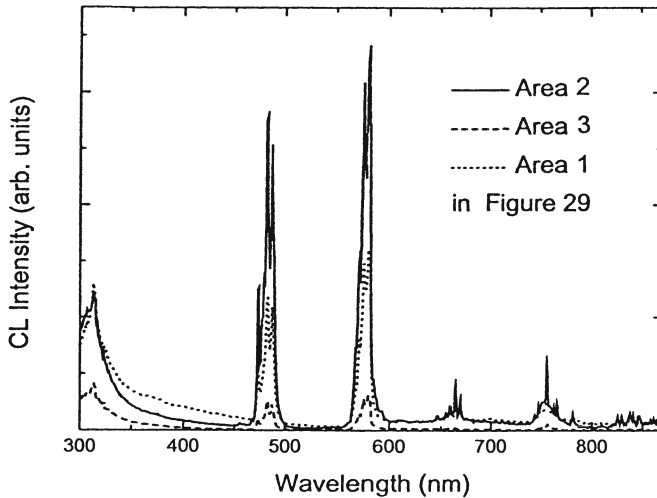


Fig. 30. CL emission spectra (corrected for instrumental response) measured from areas marked 1, 2 and 3 in Fig. 29

2. The contrast of the panchromatic CL image are dominated by the intensity variations of the characteristic lines rather than by the UV emission bands of lower intensity.
3. Identical contrast should be obtained for the panchromatic and selected wavelength images corresponding to the Dy emission lines.
4. The contrast of the CL images does not correspond to the variations in the mass concentrations of the Dy impurity incorporated in the synthetic zircon.

In order to explain the discrepancies between CL and X-ray data, several tentative explanations can be proposed:

1. The Dy $L\alpha$ X-ray emission lines result from transitions on core levels and are not sensitive to the chemical environment as observed with the Dy CL emission lines. Consequently, only a part of the total fraction of the Dy concentration measured from X-ray data may contribute to the CL emission, depending upon the crystallographic localisation of the Dy ions.
2. The role which the phosphorus plays in the CL emission process.
 - Quenching of the CL due to the high concentration of Dy ions inducing the formation of Dy cation pairs.
 - An increase in defect related recombination centres as suggested by the change in the shape and intensity of the UV emission band (see Fig. 30). The higher the P concentration, the more intense the UV band near 330 nm with the presence of a new band near 370 nm. This defect centre could have a high probability of radiative recombination leading to a decrease in the CL intensity.

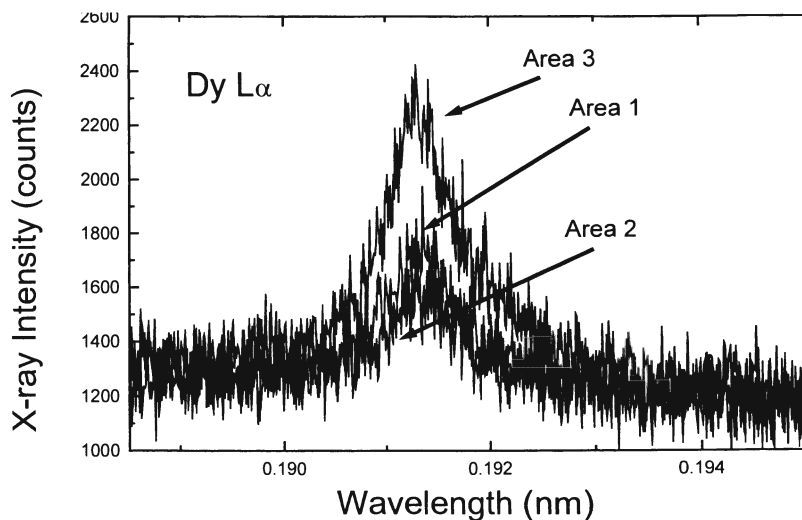


Fig. 31. Dy $L\alpha$ X-ray peaks measured from areas 1, 2 and 3 marked in Fig. 29

A third possible explanation for the observed difference between CL and X-ray data could be a crystallographic effect between the three different analysed areas resulting in intensity variations due to polarisation effect or to a difference in internal reflections on differently orientated crystallographic planes.

The polarisation effect was investigated by measuring the CL Dy lines for two successive positions of the specimen rotated by 90° . From the data in Fig. 32 it is shown that the emission measured from area 2 remained independent of the specimen orientation while spectra from areas 1 and 3 revealed relative intensity changes of some of the Dy multiplets around 585 nm.

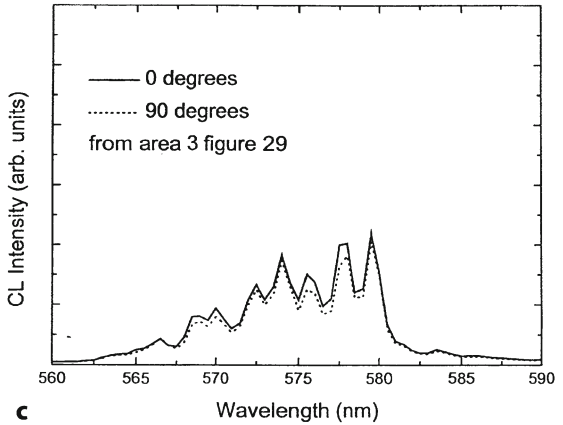
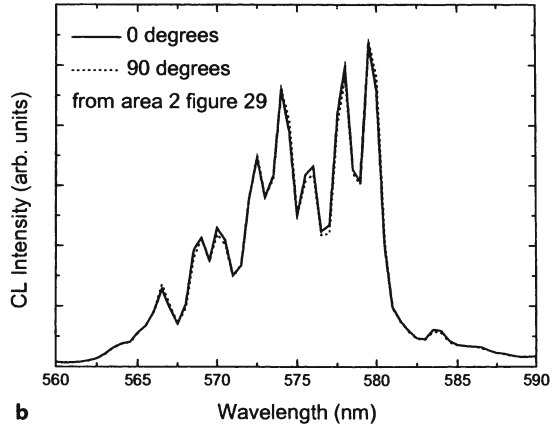
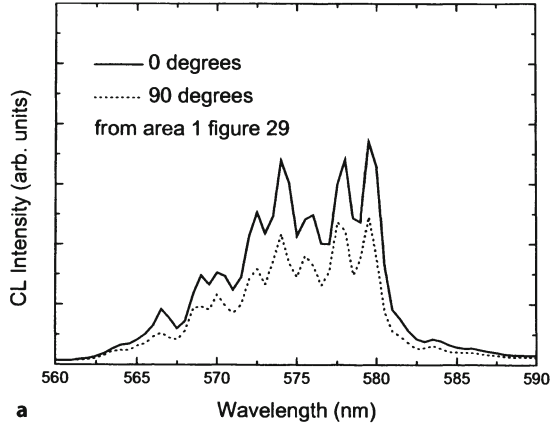
Based on these observations, the bright area in Fig. 29 may correspond to a crystal habit where the optical axis is parallel to the direction of the incident beam while areas 1 and 3 have different crystallographic orientations.

As shown in Fig. 32 the highest polarisation effect occurs in area 1 which corresponds to the highest density of structural defects. This may lower the symmetry of the recombination centre and consequently the increase of the magnitude of the polarisation effect.

In summary, for Dy doped zircon, the intensities of the UV and blue emission bands are low compared to those of the characteristic lines. For this reason the contrast in the panchromatic image corresponds to the local changes in the intensity of the Dy CL emission lines which however do not correspond to the changes in the concentration of that ion.

The interpretation of the contrast of a CL image in terms of the local variations of a particular trivalent rare earth ion is impossible when broad emission bands have a larger contribution to the contrast of the image than that of the characteristic line as is the case for natural zircons.

Fig. 32a–c. Polarisation effect resulting from rotation of the specimen by 90° between two measurements taken from areas 1, 2 and 3 in Fig. 29



In addition, CL measurement and interpretation problems are also encountered when comparing CL images obtained using an optical CL microscope with those collected with a scanning CL system. The wavelength response of these systems is often significantly different especially in the UV region and CL images measured from the same region of a specimen can result in major differences in CL contrast. For example, Rémond et al. (1995a) have reported contrast reversal around the perimeter and core of Ce-doped zircon crystals in panchromatic CL images measured with an optical and SEM CL system. This effect is due to the fact that the measured CL intensity results from the integrated CL emitted intensity convoluted with the response function of the CL equipment. With an optical CL system the photons are measured through a glass isolation plate which strongly absorbs in the UV region whereas the SEM system efficiently measures the UV CL emission. These effects are particularly important when investigating CL emission from wide band gap materials.

6.3.3

The Matrix Effect

According to Eq. (43), the concentration of the recombination centres can be derived from the experimental concentration by means of correction factors expressing the number of generated photons and the interactions between the generated photons and the matrix. The number of generated photons resulting from the primary excitation by the incident electrons is given by Eq. (5) (Sect. 3.1) which has been established for the case of semiconductors. The validity of such an equation for an insulating material will be discussed in Sect. 7 below. For wide band gap materials the absorption correction factor can, in a first approximation, be neglected. In optically transparent materials, the extinction coefficient is small relative to that for a semiconductor so the absorption effect over the optical path-length within the escape cone is small. For wide band gap materials, the direct recombination of charges through the band gap and the emission associated with deep level crystal lattice imperfections occurs in the UV. These short wavelength photons have a sufficient energy to produce a secondary photoluminescence emission and in certain circumstances can be dominant over the primary emission in wide band gap materials.

Photoluminescence excitation spectra for Dy^{3+} photo-emission in zircon, shown in Fig. 33, reveal that the UV CL around 300 nm overlaps with the Dy^{3+} optical absorption bands. Optical absorption by Dy^{3+} impurities reduces the UV CL signal increasing and delocalising the characteristic Dy^{3+} emission. The UV signal can be strongly attenuated when high Dy^{3+} concentrations are present. In addition, the UV induced Dy^{3+} luminescence increases the CL emission generation volume reducing the CL spatial resolution. More investigation in the mechanisms of production of CL photons in wide band gap materials are required before any attempt at quantitative interpretation of CL spectra.

In wide band gap insulating materials, thermal effect and charging phenomena must also be accounted for, but it is impossible in the present state of the art to propose an experimental procedure allowing one to evaluate these effects.

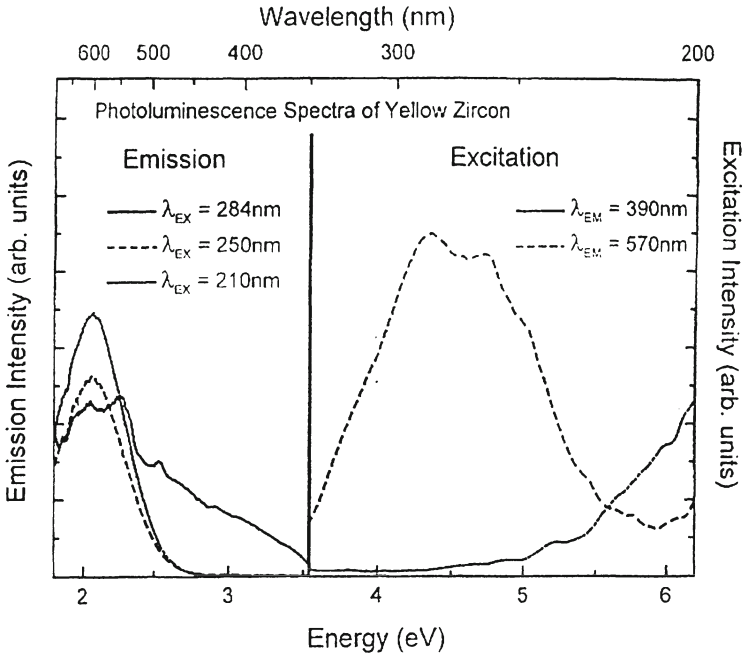


Fig. 33. Excitation and emission photoluminescence spectra from a natural zircon

7

Future Developments: Combining Cathodoluminescence and X-ray Data

7.1 Analogies Between Cathodoluminescence and X-ray Photons

There are a number of analogies between CL and X-ray emission even though there is a significant difference between the energy of the respective types of photon emission:

1. Electron beam induced X-ray and CL photons result from the dissipation of the primary beam energy via the creation of electron-hole pairs followed by electronic rearrangement and emission of photons. For both types of emission, the energy of the emitted photon is dependent on the energy levels involved in the radiative transitions.
2. Electronic transitions between electron-hole pairs on core levels lead to narrow atomic X-ray lines whose energies are characteristic of the emitting atoms and whose intensities are proportional to the concentration of the atoms. Likewise electron-hole pair recombination on energy levels of incompletely filled 3d or 4f shells of a luminescent ion produces CL photons whose energy is characteristic of that ion (quasi-atomic emitting system).

3. Electronic transitions between electron-hole pairs involving valence electrons produces broad X-ray bands whose energy positions and shapes depend on the chemical environment and chemical state of the emitter, e.g., O K α or the L X-ray emission series of first order transition elements. Similarly electronic rearrangement involving valence electrons and holes on recombination centres leads to CL emission bands whose energy and shapes depend on the chemical state (oxidation state and coordination) of the emitter.

These similarities between X-ray and CL emission strongly suggest that CL microscopy and microanalysis could complement X-ray microanalysis in: (1) trace element analysis of ions with incompletely filled subshells and (2) chemical environment studies. In addition, CL spectral analysis as a function of the excitation conditions and irradiation time should contribute to a better understanding of electrostatic charging phenomena resulting from charge trapping on point defects in wide band gap materials subjected to the electron irradiation.

Quantitative X-ray microanalysis using electron probe techniques is widely recognised as a routine method for the microanalysis of minerals. Detailed analytical models have been developed over the past 30 years which allow the mass concentrations of the analysed elements to be determined from the measured X-ray intensities. The versatility of these models permits the use of reference materials with different composition and crystallographic properties from the analysed specimens. However, there are still difficulties in obtaining accurate quantitative analysis when soft (low energy) X-ray emission bands are added in the analytical procedure. This situation is very similar to that encountered when studying the CL properties of wide band gap materials. For wide band gap minerals CL microanalysis is not routine and the interpretation of spectra and images remains difficult. Therefore it is clear that improvement in the analytical models are required for both soft X-ray and CL microanalytical studies and that concurrent CL and soft X-ray studies could provide a significant contribution to the progress of both analytical techniques.

7.2

Problems To Be Investigated

7.2.1

Strategy for Obtaining Reliable Cathodoluminescence Intensities

There have been significant advances in both soft X-ray WDS and CL instrumentation over the past few years which both involve improved sensitivity ranges via detectors in CL and synthetic multilayer diffraction monochromators in WDS. However, it must be stressed that enhanced detection (i.e. measurement efficiency of the instrumentation) does not imply enhanced analysis and in both techniques reliable interpretation methods are still to be fully developed. A major difficulty with both techniques is the accurate measurement of the absolute emitted photon intensity especially when the photon emission is polarised. In CL microanalysis intensity measurement problems arise from paraboloidal mirror collector due to: (1) difficulties in precise, reproducible collector alignment and (2) the

dependence of the reflectance efficiency on the polarisation state of the incident light. The magnitude of the polarisation effect depends on the emission wavelength and the type of diffraction grating (see Sect. 4.2.3).

It is still difficult to derive accurate intensities from an experimental CL spectrum. More frequently broad emission bands and narrow fine structures are simultaneously present. In order to measure the intensity of each feature by means of a least squares fitting techniques, the shape of the spectral component must be known to be described by an appropriate analytical function. Such a description must account for both the generation mechanism and the instrumental factors. An emission line given by a grating monochromator is mostly Gaussian but the physical width of a CL emission component depends on many factors and varies as a function of the chemical environment so that the convolution product of both effects may lead to complex peak shapes

Warwick (1987) has suggested that an analysis procedure similar to the X-ray ZAF technique could be developed for CL analysis of semiconductors. The procedure is based on the assumption that the CL intensity associated with a given recombination centre in a semiconductor is approximately proportional to the product of the concentration of the luminescent centre and the minority carrier lifetime. However Warwick (1987) noted that it will be necessary to include a factor related to the recombination time of the luminescent centre in order to apply a correction procedure similar to that used for X-ray spectrometry.

7.2.2

Prediction of the Number of Generated Photons

The generated intensity per incident electron is proportional to the number of ionisations, n_A , of a given energy level of an atom A, resulting from the interactions of an incident particles with the atoms A present.

7.2.2.1

X-ray Emission

For X-ray emission, the number of generated photons resulting from the inelastic scattering events, n_x , is

$$n_x = \omega n_A \quad (50)$$

where ω is the fluorescence yield and n_A is the number of ionisations of a given energy level of atoms A present in weight concentration C_A in the specimen given by:

$$n_A = C_A (N^0/A) Q(E) F \quad (51)$$

with N^0 Avogadro's number, E_0 the incident energy, $Q(E)$ the ionisation cross section of the energy level involved in the transition (probability per unit path length of an electron with a given energy causing ionisation of a particular inner shell) and with F given by:

$$F = \int \varphi(\rho z) d\rho z \quad (52)$$

The function $\varphi(\rho z)$ is the distribution of the number of generated photons as a function of depth, i.e. the ratio between the X-rays generated within a thin layer of thickness $\Delta\rho z$ at mass depth ρz in the specimen normalised to that generated within a free unsupported layer of equal thickness, $\Delta\rho z$.

The emitted intensity at the specimen surface is thus given by:

$$I_{em} = \int \varphi(\rho z) \exp(-\mu/\rho z \cos\theta) d\rho z = f(\chi) I_{gen} \quad (53)$$

and the absorption correction factor $f(\chi)$ can be derived from the ionisation distribution function.

For X-rays, analytical expressions of $\varphi(\rho z)$ have been proposed by Merlet (1992a,b), Packwood and Brown (1981) or by Pouchou and Pichoir (1984, 1991).

Pouchou and Pichoir (1984, 1991) used a polynomial analytical description of the $\varphi(\rho z)$ curve for describing the shape of the distribution of the ionisation as a function of depth due to the elastic and inelastic scattering of the incident electrons. The area, F , below the curve gives the number of ionisations (proportional to the number of generated photons) and is calculated theoretically by an evaluation of the atomic number correction

$$F = (R/S)Q(E) \quad (54)$$

where R is the fractional energy loss due to BSE (i.e., the ratio between the total number of photons actually generated in the sample and the total number of photons which should be generated in absence of backscattering effect) and $1/S$ is the stopping power

$$S = (-1/\rho)(dE/dx) \quad (55)$$

where dE/dx is the energy loss per elementary electron trajectory dx given by the Bethe's law

$$\frac{dE}{dx} = \left(\frac{2\pi N Z e^4}{E_x} \right) \log \left[\frac{E_x}{J(0.5e)^{1/2}} \right] \quad (56)$$

where E_x is the energy of the electron after traversing a path length, x , and J is the mean ionisation potential.

Packwood and Brown (1981) proposed an analytical parametric description of the $\varphi(\rho z)$ curve according to a model called modified surface Gaussian (MSG) expressed as:

$$\varphi(\rho z) = \gamma_0 e^{-(\alpha\rho z)^2} [1 - \{(\gamma_0 - \varphi(0)e^{-\beta\rho z})/\gamma_0\}] \quad (57)$$

The coefficients included in the above relation have been discussed by Packwood and Brown (1981). These parameters reflect the electron-matrix interactions and depend on the electron energy, the absorption edge energy, the mean ionisation potential, the backscatter electron coefficient and the surface ionisation $\varphi(0)$.

The advantage of the above expression is that numerical integration is straightforward, which allowed the authors to propose a general formula for the generated and emitted intensities from a homogeneous bulk specimen, a thin unsupported layer, a buried layer in the matrix or a gradient of composition as a function of depth (Packwood 1991; Packwood and Rémond 1993; Rémond et al. 1995b).

7.2.2.2

Cathodoluminescence Emission

For CL emission, the concept of expressing the intensity of the generated CL photons within the excitation volume (see Eq. 5 in Sect. 3.1) is similar to that use for the X-ray emission, i.e., a term expressing the depth dependence of the CL emission and a term expressing the proportionality between the number of generated photons and the number of ionisations. This proportionality is expressed by the fluorescence yield ω for X-ray photons (Eq. 50) and by the recombination rate RR (Eq. 8) for the case of CL.

For CL, most of the parameters are derived from experimental observations in contrast to those used for X-ray analysis, which are derived from theoretical studies of the energy loss mechanisms for the incident electrons travelling into the solid. Future developments to improve the quantitative interpretation of CL data will depend on developing a theoretical model for CL generation as a function of depth.

Measurements of light generation have been used to determine two-dimensional energy loss profiles in luminescent materials. The depth dependence of the CL emission is often expressed in terms of the universal Everhart-Hoff depth dose function $g(z)$ which is normalised to the R_{KO} depth penetration of the electrons (Eq. 6) and the area below the $g(z)$ curve is equal to unity.

The depth distribution of the CL emission results from empirical observations showing: (1) a correlation between the isocontours of energy dissipation (Evehart et al. 1972) and, (2) the isocontour of luminous intensity as revealed by the experiments in which the trace of the CL volume was photographed (Ehrenberg and Franks 1953; Ehrenberg and Kings 1963). The Gaussian form for the universal normalised depth dose function (Eq. 6 in Sect. 3.1) results from a curve fitting procedure and does not contain any physical parameters like those included in the $\varphi(\rho z)$ function developed for X-ray photon emission. Consequently, the CL intensity given in Eq. (5) as the product of two independent terms, the generation factor term (G) and the energy (E_{eh}) required to produce an electron/hole pair, should be merged into a single expression analogous to the $\varphi(\rho z)$ expressions for X-ray spectrometry.

Equation (5) in Sect. 3.1 expresses the CL intensity as the product of a depth function $g(z)$ and a generation factor G . The generation factor, G , is equivalent to the term R/S (atomic number correction) in Eq. (54) for X-ray generation. However, the generation factor includes the loss energy factor R due to backscattering. Note that the term $(1-R)$ in the CL generation factor (Eq. 6) is often estimated as half of the backscatter coefficient (Holt and Yacobi 1990; Leamy 1982.). A more rigorous estimation of the energy loss due to backscattering should be used, such as the expression for X-ray analysis with the EPMA derived by Duncumb and

Reed (1968) considering the energy distribution of backscattered electrons and not only the number of BSE. Another parameter to be optimised to model CL generation is the ionisation cross section of the energy level involved in the CL transition. In Eq. (2), the amount of energy required for the production of an electron/hole pair is approximated as $\approx 3 E_g$. This approximation is only valid for the intrinsic emission resulting from recombination of electrical charges across the band gap, E_g . A more accurate definition of this parameter is required when considering the excitation of a luminescent ion.

As for X-ray generation, the CL emission results from the recombination of the electrical charges created as a result of inelastic scattering interactions of the incident electrons with the solid. The creation of electron/hole pairs results from all mechanisms of dissipation of the energy of the incident electron beam. Bethe's formula for the stopping power expresses a continuous slowing down of the electron energy into the specimen and is the sum of theoretical stopping power for conduction electrons, plasmon formation, inner shell ionisation and valence electron excitation (Shimizu and Ding Ze Ju 1992; Ding Ze Ju and Shimizu 1996).

A difficulty in modelling the depth distribution of the generated CL photons is to determine which of the energies produced in the specimen during the multiple inelastic scattering events contribute to the CL emission. The electron/hole pairs involved in the radiative CL transitions produced by the highly energetic electrons, which suffer only a few inelastic collisions with the atoms, by the low energy secondary electrons, by the Auger electrons, plasmon decay and/or by the photoelectrons resulting from the interactions between the generated X-ray photons and the matrix. In order to develop a theoretical model for CL depth generation the relative contribution of each of these generation mechanisms must be determined as each process has a different spatial distribution.

Future improvement in the quantitative interpretation of CL data strongly depends on developing a physical description of the depth distribution of the CL photons generation. Experimental measurements using the tracer method and theoretical Monte-Carlo calculations must be carried out to develop a model similar to the $\phi(\rho z)$ curve for X-rays. A theoretical model for the X-ray depth distribution has been developed by using a known element embedded in a matrix at various depths emitting characteristic X-ray radiation. For CL, the use of a tracer approach is more complicated due to charge trapping at the embedded layer interface. In addition, the use of CL reference materials doped under controlled conditions with known impurities remains questionable. Intrinsic defects with short recombination times produced during fabrication may have a significant effect on the CL emission. Subsurface charging due to charge trapping at intrinsic and extrinsic defects as well as dislocations and grain boundary can modify the depth distribution of electron/hole pairs. Monte-Carlo calculation accounting for charging effect leading to distortions in the spatial and energy distribution, as discussed by Jbara et al. (1997), should be extended to the case of CL production and emission.

7.2.3

Effect of Charge Trapping on Cathodoluminescence and X-ray Spectra of Insulators

Charge trapping mechanisms are responsible for the development of retarding potentials reducing the kinetic energy of the incident electrons as a function of the irradiation time leading to a time dependence of the number of generated events during the inelastic scattering processes. In addition, the presence of these electrical fields modifies the depth distribution of the electrons scattered into the solid during the inelastic scattering processes.

In a study of the CL properties of natural ZnS crystals, Rémond (1977) observed a change in the colour of the CL emission as a function of the electron beam diameter. A natural ZnS specimen containing Cu and Ga as impurities exhibited a red CL emission when the incident electron beam was a few hundred microns in diameter. However when the beam diameter was reduced a blue-green hue was observed. The change in the CL colour observed at the surface of the natural specimen was postulated to result from an electroluminescence effect which is dependent on the irradiation dose. The dependence of the CL spectral distribution on the excitation conditions can tentatively be associated with the build-up of internal electrical fields due to charge trapping on some of defects which lead to electroluminescence mechanisms. Similar spectral changes between photoluminescence and electroluminescence of synthetic Cu and (Mn, Cu) doped ZnS crystals have been reported by Mattler and Ceva (1963).

The electrostatic fields produced by charge trapping at lattice defects produces a complex relationship between the CL intensity (Eq. 12 in Sect. 3.2) with the primary beam current, the beam diameter and the irradiation time.

The presence of surface and bulk charging phenomena in insulators can be confirmed by examining the X-ray spectral and intensity changes as a function of the irradiation condition. In a conductive specimen the maximum energy of emitted continuum X-ray photons, the Duane-Hunt limit, is equal to the energy of the primary electron beam. In uncoated insulating specimens a lower Duane-Hunt cut-off with respect to the incident energy indicates the presence of a retarding potential. The difference between the energy of the primary beam and the Duane-Hunt limit can be used to measure the retarding potential generated by the subsurface trapped charge (Bastin and Heijlingers 1991b; Rémond et al. 1994). The time dependence of the Duane-Hunt limit measured on X-ray spectra and the time dependence of the CL emission with the irradiation time should contribute to a better understanding of surface and bulk charging phenomena.

As reported by Cazaux and Le Gressus (1991), macroscopic charging phenomena result from microscopic causes i.e., the presence of structural defects acting as charge traps. Charging phenomenon is a time dependent effect resulting from trapping and detrapping mechanisms which will affect the measured intensity as a function of the irradiation time. Time dependence analysis should be used to extrapolate the CL intensity which should be measured at zero irradiation time, i.e., in the absence of charging effect. Time resolved analysis should also be used in order to identify the defects acting as traps. Combining CL and thermoluminescence studies in the same equipment should also lead to a better understanding of the CL mechanisms.

7.2.4

The Absorption Factor

Although the absorption of CL is weak due to the low absorption coefficient of transparent materials, its effect cannot be completely neglected. The absorption factor $f(\chi)$ is the Laplace transform of the depth distribution of the CL photons and a better description of this depth generation factor should also be accompanied by an improved correction for the absorption effect. This correction is most relevant for secondary excitation by UV photons which can propagate at much greater distances than the electrons responsible for the direct excitation of the CL photons. The absorption correction factor takes the form

$$I_{gen} \sum_0^{\theta_c} \exp(-\alpha z \csc \theta_c)$$

where α is the absorption coefficient for the analysed radiation by the matrix, z is the linear depth below the specimen surface and θ is the take-off angle of the detector. As previously discussed, the angle of the cone for the emitted CL rays depends on the refractive index and may vary to a large extent (see Table 1 in section 3.3). As a consequence, the value of the take-off angle to be used in the absorption factor has to be investigated.

7.2.5

Specimen Preparation: Defects Induced by Mechanical Polishing

A well-defined detector, specimen and electron beam geometry are essential for qualitative CL and X-ray microanalysis. With identical geometry, variations in the photon emission can then be attributed to changes in local chemistry rather than variations in the surface topography of the specimen. Therefore the surface of the specimen must be polished to an optical finish. Mechanical polishing is carried out using successively smaller abrasive particles until surface scratches are no longer optically visible. The grinding mechanism depends on the nature of the substrate to be polished, the pH of the fluid (used to lubricate and disperse the abrasive) and on the properties of the polishing disc. In order to penetrate into the disc material and to create a scratch at the surface of the specimen, the grain of abrasive must be solidly fixed to the polishing disc. Thus for a given load on the grains, the penetration depth will depend on the hardness of the disc material and on the physical properties of the materials to be polished. During and following mechanical polishing of solids, subsurface damage result from fissure propagation. Subsurface composition changes may also result from high energies deposited within a small volume of material leading to, production of highly localised heat, creation of excitations and defects in the material, production of dangling bonds and trapped electrons, emission of excited and reactive species into the gas phase and separation of charges leading to the creation of intense electric fields for many insulating materials. The creation of charge trap defects resulting from mechanical polishing has been illustrated by Rémond et al. (1994) by studying the Duane-Hunt limit changes on EDS spectra from uncoated ZnS crystals polished using several polishing procedures. The

effect of polishing in terms of both topography and induced defects has to be investigated for both X-ray and CL emissions.

In-depth analysis by varying the incident energy should provide the depth distribution of structural defect centres created during specimen preparation or during electron irradiation (Stevens Kalceff and Phillips 1995a,b; Stevens Kalceff et al. 1996, 1999). Depth concentration profiles $C(z)$ of recombinations centres can also be derived from the CL measured and calculated intensities using an analytical model describing the number of CL photons generated as a function of depth, as is done for the case of X-ray spectrometry applied to the study of layered or ion implanted specimens (Rémond et al. 1995b).

The future in the improvement of CL quantitative analysis is the development of an analytical description of the depth generation of CL photons analogous to the depth distribution of ionisation (known as the $\varphi(\rho z)$ function) in X-ray spectrometry.

8

Conclusion

In the 1960s, Curie, in his text book, *Luminescence in Crystals* (1963), wrote "Among the various kinds of luminescence, that excited by cathode rays would appear to have been the subject of most practical applications in recent years (e.g. cathode-ray tubes for oscilloscope, monochrome and colour television, radar, etc.). In contrast to the large amount of experimental effort in such applications relatively little attention has been given to a better understanding of the mechanism of the phenomenon". Forty years later this statement is still valid, especially regarding insulating materials and when compared with developments in the quantitative interpretation of X-ray spectra generated with SEM and EPMA techniques. For small band gap semiconductors, quantitative interpretation of CL data has been developed based on the solution of the diffusion equation for electron/hole pairs and the normalised depth-dose distribution of the dissipated energy. However, for wide band gap materials, such as natural and synthetic silicate minerals, this type of quantitative approach is still speculative. For an accurate description of the mechanisms of production and emission of CL photons it is important to account for the ionisation cross sections of all energy loss processes occurring during the inelastic scattering interactions. Experiments using the tracer method and theoretical Monte-Carlo calculations should provide a more accurate description of the CL generation depth function that is the basis of quantitative interpretation of CL data. For wide band gap materials more rigorous investigations are needed to understand and account for the secondary CL emission induced by the energy transfer from intrinsic and defect related UV emissions to other luminescent centres. Furthermore, a correction for electrostatic charging phenomena must be developed and included into either the experimental or analysis procedure when using CL and soft X-ray emission bands to analyse wide band gap materials. This correction procedure is required to account for differences in the spatial and energy distribution of the electrons in insulators when compared with conductive materials. The slow development

in the quantitative interpretation of CL spectra from insulators is mainly due to the fact that the CL emission has often been considered as a nuisance, interfering with the conventional (SE, BSE and X-ray) signals used for the microcharacterisation of materials in the EM and EPMA. Over the past 30 years most of the efforts have centred on CL optical microscopy although the interpretation of the images still remains contentious due to the absence of a fundamental understanding of the observed contrast. The current status of CL is similar to the early years of energy dispersive X-ray spectrometry and mapping with a SEM. Innovative solutions were eventually found for a number of problems which seemed insurmountable at the time and the EDS technique has now developed into a reliable, accurate and routine quantitative microanalysis technique. It is possible that CL microanalysis will also develop into a conventional microanalysis technique, but as with EDS many problems must be solved. Future developments will ultimately depend on developing a detailed model that can describe the spatial distribution of electron/hole pairs as a function of mass depth and excitation conditions. Fundamental studies of CL and soft X-ray emission performed simultaneously with a range of temperatures and excitation conditions should elucidate the main energy loss mechanisms involved in CL emission and enable these models to be developed and refined.

Acknowledgements. One of us, MRP, would like to acknowledge the contribution to this work by other members of the CL group at UTS, Prof. A.R. Moon and Dr. M.A. Stevens Kalceff. Thanks are due to F. Ngijoi for collecting some of the data with the CL spectrometer installed at ENSMM in Besançon (France).

References

- Bastin GF, Heijligers HJM (1991a) Quantitative electron probe microanalysis of ultra-light elements (Boron-Oxygen). In: Heinrich KFJ, Newbury DE (eds) *Electron Probe Quantitation*. Plenum Press, New York, pp 145-162
- Bastin GF, Heijligers HJM (1991b) Non conductive specimens in the electron probe microanalyser. A hitherto poorly discussed problem. In: Heinrich KFJ, Newbury DE (eds) *Electron Probe Quantitation*. Plenum Press, New York, pp 163-175
- Blanc Ph, Baumer A, Cesbron F, Ohnenstetter D, Panczer G Rémond G (1999) Systematic cathodoluminescence spectral analysis of synthetic doped minerals: Anhydrite, apatite, calcite, fluorite, scheelite and zircon. In: Pagel M, Barbin V, Blanc P, Ohnenstetter D (eds) *Cathodoluminescence in the Geosciences*, Springer-Verlag, Berlin (this Vol.)
- Bond EF, Haggis GH, Beresford D (1974) Improved cathodoluminescence microscopy. *J. Microscopy* 100:271-280
- Bresse JF, Rémond G, Akamatsu B (1996) Cathodoluminescence microscopy and spectroscopy of semiconductors and wide bandgap insulating materials. *Mikrochimica Acta Supp* 13:135-166
- Buschbeck F, Horl EM (1978) Electronic adding-up and storing of SEM color images. *Scanning Electron Microscopy I*: 835-839
- Cazaux J, (1986) Electrostatics of insulators charged by incident electron beams. *J Microsc Spectrosc Electron* 11:293-312
- Cazaux J (1996) Electron probe microanalysis of insulating materials: Quantification problems and some possible solutions. *X-ray Spectrometry* 25(6): 265-280
- Cazaux J, Le Gressus C (1991) Phenomena relating to charge in insulators: Macroscopic effects and microscopic causes. *Scanning Microscopy* 5:17-27

- Cesbron F, Blanc P, Ohnenstetter D, Rémond G, Rouer (1995) Cathodoluminescence of rare earth doped zircons. I. Their possible use as reference materials. *Scanning Microscopy Supp.* 9: 35–56
- Curie D (1963) *Luminescence in Crystals* (translated by GFJ Gartick) Methuen and Co Ltd, London, England
- Dicke GH (1968) *Spectra and Energy Levels of Rare Earth Ions in Crystals*. McGraw Hill, New York
- Ding ZJ, Shimizu R (1996) A Monte Carlo modeling of electroninteraction with solid including cascade secondary electron production. *Scanning* (18): 92–113
- Duncumb P, Reed SJB (1968) The calculation of stopping power and backscatter effect in electron probe microanalysis. In : KFJ Heinrich (ed) *Quantitative electron probe microanalysis*. NBS Spec. Publ. 298 pp 133–154.
- Ehrenberg W, Franks (1953) The penetration of electrons in luminescent materials. *J. Proc. Phys. Soc.* 66: 1057–1066
- Ehrenberg W, King DEN (1963) The penetration of electrons in luminescent materials. *Proc. Phys. Soc.* 81: 751–766
- Everhart TE, Hoff PH (1971) Determination of kilovolt energy dissipation vs penetration distance in solid materials. *J. Appl. Phys.* 42(13): 5837–5846
- Everhart TE, Herzog RF, Chung MS, Devore WJ (1972) Electron energy dissipation measurements in solids. In: Shinoda G, Kohra K, Ichinokawa T (eds) *Proc. 6th International Conference on X-Ray Optics and Microanalysis*. University of Tokyo Press, Tokyo, Japan pp 81–88.
- Fialin M, Rémond G, Bonnelle C (1994) New developments in electron probe microanalysis of oxygen in wide band gap oxides. *Microbeam Analysis* 3:211–224
- Fialin M, Bonnelle G, Rémond G, Blanc P (1995) Contribution of beam induced states to the O K α peak of alumina: Consequences for electron probe microanalysis. In: Etz ES (ed) *Proc. of the 29th Annual Conference of the Microbeam Society*, VCH Publishers, New York, 199–2000
- Fielding PE (1970) The distribution of uranium, rare-earth and color centers in a crystal of a natural zircon. *Am. Miner.* 55:428–440
- Goldstein JI Newbury DE, Echlin P, Joy DC, Fiori C, Lifshin E (1992) *Scanning Electron Microscopy and X-ray Microanalysis*. Plenum Press, New York and London
- Goni J, Rémond G (1969) Localization and distribution of impurities in blende by cathodoluminescence. *Miner. Mag.* 37(86): 153–156
- Henderson B, Imbush GF (1989) *Optical Spectroscopy of Inorganic Solids*. Clarendon Press, Oxford
- Holt DB, Napchan E (1994) Quantitation of SEM EBIC and CL signals using Monte Carlo electron-trajectory simulations. *Scanning* 16: 78–86
- Hörl EM, Roschger P (1980) CL SEM investigations of biological material at liquid helium and liquid nitrogen temperatures. *Scanning Electron Microsc.* I: 285–292
- Iacconi P, Caruba R (1984) Trapping and emission centres in X irradiated zircon. Characterisation by thermoluminescence. *Phys. Chem. Minerals* 11: 195–203
- Iacconi P, Deville A, Gaillard B (1980) Trapping and emission centres in X irradiated zircon. (II); Contribution of the SiO₄⁴⁻ groups. *Phys. Stat. Sol. (a)* 59: 639–646
- Jbara O, Cazaux J, Rémond G, Gilles C (1996) Halogen ion electric field assisted diffusion in fluorite and polyvinyl chloride during electron irradiation. *J. Appl. Phys.* 79: 2309–2313
- Jbara O, Potron P, Mouze D, Cazaux J (1997) EPMA of insulating materials X-Ray Spectrometry 26: 291–302
- Kanaya K, Okyama S (1972) In: Goldstein JI Newbury DE, Echlin P, Joy DC, Fiori C, Lifshin E (1992) *Scanning Electron Microscopy and X-ray Microanalysis*. Plenum Press, New York and London p89
- Kirsh Y, Townsend PD (1987) Electron and hole centres produced in zircon by irradiation at room temperature. *J. Phys. C: Solid State Phys.*, 20, 967–980
- Koyama H (1980) Cathodoluminescence study of SiO₂. *J. Appl. Phys.* 51(4): 2228–2235
- Leamy HJ (1982) Charge collection scanning electron microscopy. *J. Appl. Phys.* 53(6): R51–R67
- Le Poole JB, Bok AB, Boogerd WJ (1968) An electron luminescence microscope. *Geologie en Mijnbouw* 47:443–450

- Löhnert K, Hastenrath M, Kubalek E (1979) Spatially resolved cathodoluminescence studies of GaP LED's in the scanning electron microscope using optical multichannel analysis. *Scanning Electron Microsc.* I:229–233
- Long JVP, Agrell SO (1965) The cathodoluminescence of minerals in thin section. *Miner. Mag.* 34(268): 318–326
- Marfunin ASO (1979) Spectroscopy, Luminescence and Radiation Centers in Minerals. (Translated by W Schiffer). Springer-Verlag, Berlin Heidelberg New-York
- Marshall DJ (1988) Cathodo-luminescence of Geological Materials. Unwin Hyman, Boston
- Marshall DJ, Kopp OC (1999) The status of the standards program of the Society for Luminescence Microscopy and Spectroscopy. In: Pagel M, Barbin V, Blanc P, Ohnenstetter D (eds) *Cathodoluminescence in the Geosciences*, Springer-Verlag, Berlin (this Vol.)
- Mattler J, Ceva T (1961) In: *Luminescence in Crystals*, D. Curie (translated by G F J Garlick), Methuen and Co Ltd, 1963, p 244
- Merlet C (1992a) Quantitative electron probe microanalysis: New accurate phi-ro-z description. *Mikrochimica Acta* 12: 107–115
- Merlet C (1992b) Accurate description of surface ionisation in electron probe microanalysis: An improved formulation. *X-Ray Spectrometry* 21: 229–238
- Nicholas JV (1967) Origin of the luminescence in natural zircon. *Nature* 215: 1476–1482
- Packwood RH (1991) A comprehensive theory of electron probe microanalysis. In: Heinrich KFJ, Newbury DE (eds) *Electron Probe Quantitation*. Plenum Press, New York, pp 83–104
- Packwood RH, Brown JD (1981) A Gaussian expression to describe $\phi(\rho z)$ curves for quantitative electron probe microanalysis. *X-Ray Spectrometry* 10: 138–146
- Packwood RH, Rémond G (1993) The interpretation of x ray and electron signals generated in thin or layered targets. *Scanning Microscopy* 6: 367–384
- Pouchou JF, Pichoir F (1984) Un nouveau modele de calcul pour la microanalyse quantitative par spectrometrie de rayons x. Partie I: Application a l'analyse d'échantillons homogenes. *La Recherche Aérospatiale* 3: 167–192
- Pouchou JF, Pichoir F (1991) Quantitative analysis of homogeneous or stratified microvolumes applying the model PAP. In : Heinrich KFJ, Newbury DE (eds) *Electron Probe Quantitation*. Plenum Press, New York, pp 31–76
- Ramseyer K, Fischer J, Matter A, Eberhardt P, Geiss JJ (1989) A cathodoluminescence microscope for low intensity luminescence. *J. Sedimentary Petrology* 619–622
- Reimer L (1985) *Scanning Electron Microscopy, Physics of Image Formation and Microanalysis*. Springer-Verlag
- Rémond G (1977) Applications of cathodoluminescence in mineralogy. *J. of Luminescence* 15:121–155
- Rémond G, Kimoto S, Okuzumi H (1970) Use of the SEM in cathodoluminescence observations in natural specimens *Scanning Electron Microsc.* 33–40
- Rémond G, Kimoto S, Okuzumi H (1972) Applications du microscope électronique a balayage a l'étude de la cathodoluminescence de quelques minéraux: Limites de resolution et de sensibilité. In: Shinoda G, Kohra K, Ichinokawa T (eds) *Proc. 6th International Conference on X-Ray Optics and Microanalysis.*, University of Tokyo Press, Tokyo, Japan, pp 611–617
- Rémond G, Le Gressus C, Okuzumi H (1979) Electron beam effects observed in cathodoluminescence and Auger electron spectroscopy in natural minerals: Evidence for ionic diffusion. *Scanning Electron Microsc.* I:237–244
- Rémond G, Cesbron F, Chapoulie R, Ohnenstetter D, Roques-Carmes C, Schvoerer M (1992) Cathodoluminescence applied to the microcharacterization of mineral materials: A present status in experimentation and interpretation. *Scanning Microscopy* 6:23–68
- Rémond G, Campbell JL, Packwood RH, Fialin M (1993) Spectral decomposition of wavelength dispersive X-ray spectra: Implications for quantitative analysis in the electron probe microanalyser. *Scanning Microscopy Suppl* 7: 89–132
- Rémond G, Cazaux J, Fialin M (1994) X-ray spectrometry with electron probe microanalysis: The problem of soft peaks emitted from insulators. In: Jouffrey B., Colliex C. (eds) *Proc. 13th*

- International Conference on Electron Microscopy, vol.1, Interdisciplinary Developments and Tools. Les Editions de Physique, 91944 Les Ullis, France, pp 785-786
- Rémond G, Cesbron F, Blanc P, Ohnenstetter D, Rouer O (1995a) Cathodoluminescence of rare earth doped zircons. II: Relationship between the distribution of the doping elements and the contrasts of images. *Scanning Microscopy Supp.* 9: 57-76
- Rémond G, Packwood RH, Gilles C (1995b) Trace element standards for the electron microanalyser using layered and ion implanted materials. *The Analyst* 120:1247-1260
- Rémond G, Gilles C, Fialin M, Rouer O, Marinenko R, Myklebust R, Newbury D, (1996) Intensity measurement of wavelength dispersive X-ray emission bands: Applications to the soft X-ray region. *Mikrochimica Acta Supp* 13: 61-86
- Semo J (1974) Spectroscopie optique en cathodoluminescence au microscope électronique à balayage. *Revue de Physique Appliquée* 9: 355-359
- Shea SP, Partain LD, Warter PJ (1978) Resolution limits of the EBIC technique in the determination of diffusion lengths in semiconductors. *Scanning Electron Microscopy I*: 435-444
- Shimizu R, Ding ZJ (1992) Monte Carlo modelling of electron-solid interactions. *Rep. Prog. Phys.* 487-531
- Sippel RF (1965) A simple device for luminescence petrography., *Review of Scientific Instruments* 36(1): 556-558
- Stevens Kalceff, MA, Phillips MR (1995a) Electron irradiation induced outgrowths from quartz. *Appl. Phys.* 77(8): 4125-4127
- Stevens Kalceff MA, Phillips MR (1995b) Cathodoluminescence microcharacterization of the defect structure of quartz. *Phys. Rev. B.* 52: 3122-3134
- Stevens Kalceff MA, Phillips MR, Moon AR (1999) Cathodoluminescence micro-characterisation of silicon dioxide polymorphs. In: Pagel M, Barbin V, Blanc P, Ohnenstetter D (eds) *Cathodoluminescence in the Geosciences*, Springer-Verlag, Berlin (this Vol.)
- Stevens Kalceff MA, Phillips MR, Moon AR (1996) Electron irradiation-induced changes in the surface topography of silicon dioxide. *J. Appl. Phys.* 80(8): 4308-4314
- Stewart JE, Gallaway WS (1962) Diffraction anomalies in grating spectrophotometers. *Appl. Optics* 1(4): 421-429
- Steyn JB, Giles P, Holt DB (1976) An efficient spectroscopic detection system for cathodoluminescence mode scanning electron microscopy (SEM). *J. Microscopy* 107(2): 107-128
- Trigg AD (1985) A high efficiency cathodoluminescence system and its application to optical materials *Scanning Electron Microsc.* III: 1011-1022
- Vigouroux JP, Duraud JP, Le Gressus C, Petite G, Agostini P, Boiziau C (1985) Study by scanning electron microscopy and electron spectroscopy of the cascade of electron multiplication in an insulator submitted to an electrical field. *Scanning Electron Microscopy (I)*: 179-182
- Warwick CA (1987) Recent advances in scanning electron microscope cathodoluminescence assessment of GaAs and InP. *Scanning Microscopy (1)*: 51-61
- Yacobi BG, Holt DB (1990) *Cathodoluminescence Microscopy of Inorganic Solids*. Plenum Press, New York, London

Systematic Cathodoluminescence Spectral Analysis of Synthetic Doped Minerals: Anhydrite, Apatite, Calcite, Fluorite, Scheelite and Zircon

PHILLIPE BLANC, ALAIN BAUMER, FABIEN CESBRON,
DANIEL OHNENSTETTER, GÉRARD PANCZER, GUY RÉMOND

1

Introduction

As the geochemical behavior of the rare earth elements (REE) is of increasing interest in geology (see the reviews edited by Lipin and McKay 1989 and Jones et al. 1996), the main REE minerals in most igneous, metamorphic and sedimentary rocks are now being studied in detail. REE are major or trace constituents in many minerals (Burt 1989). Besides the specific REE mineral assemblages which occur in alkaline, peralkaline and carbonatitic rocks (Vlassov 1966; Burt 1989; Mariano 1989; Larsen 1996; Taylor and Pollard 1996; Wall and Mariano 1996; Khomyakov 1996), more common accessory minerals such as zircon, apatite, anhydrite, carbonates and fluorites are also REE carriers and play an important role in petrologic processes. The major application of the REE studies is the melt mineral partition coefficient, used to model igneous petrogenetic processes. This will depend on the compatibility of the REE in major minerals occurring in late differentiated stages such as apatite and zircon (McKay 1989). Most of the REE are well known to be luminescence activators (Pringsheim 1949; Levrenz 1950; Monod-Herzen 1966; Diecke 1968; Marfunin 1979; Marshall 1988, Waychunas 1988). In order to interpret the cathodoluminescence (CL) emissions of natural REE bearing minerals, it is essential to compare their CL spectra to those of synthetic minerals.

2

Present Status of the Problem

Luminescence may be produced by a wide variety of processes; such as chemiluminescence, electroluminescence, thermoluminescence (TL), photoluminescence (PL) and cathodoluminescence (CL). TL, PL and CL are techniques mostly used by earth scientists. PL involves the selective excitation of electronic levels of luminescent centers by photons while CL involves excitation via high energy electrons. CL has several advantages over PL; the greater energy density, the possibility to focus the microprobe beam of the scanning electron microscope (SEM) to less than 1 μm as well as high sensitivity CL mapping (Warwick 1987). Impulsed lasers used as excitation sources combine high power, focusability (through an optical microscope objective) and precise selective excitation of luminescent centers.

Laser induced microluminescence (LIL) provides the opportunity to use not only spectral but also kinetic studies of luminescence through a time range of few nanoseconds (ns) to milliseconds (ms), as shown by Rémond et al. (this Vol.). High energy CL often induces luminescent defects which can mask details or provide erroneous interpretations, whereas PL avoids these artifacts.

CL imagery has been used since the 1960s in mineralogy and petrology (Long and Agrell 1965; Smith and Stenstrom 1965; Sippel and Glover 1965; Rémond 1977) and is an efficient tool especially when combined with back scattered electron (BSE) imagery obtained via SEM or electron probe microanalyser (EPMA) (Henry and Toney 1987; Rémond et al. 1992; 1995, Blanc et al. 1994 b; Hanchar and Miller 1993; Hanchar and Rudnik 1995). However, only few CL spectra from natural REE-bearing minerals have been published (Mariano 1978; 1988; 1989; Mariano and Ring 1975; Roeder et al. 1987; Marshall 1988; Diaz et al. 1991; Ohnnetetter et al. 1991; Yang et al. 1992; Koberski and Keller 1995). In addition, CL spectra measured from doped synthetic analogues are scarcer and often fragmented, for example, apatite (Portnov and Gorobets 1969), fluorite (Mariano 1988; Barbin et al. 1996), calcite (Mason and Mariano 1990; Machel et al. 1991) and zircon (Hanchar and Marshall 1995). Spectra of apatites doped with individual REE were previously given by Morozov et al. (1970), Blanc et al. (1995) and Mitchell et al. (1997), for zircon by Cesbron et al. (1993; 1995) and Hanchar et al. (submitted), and for apatite by Baumer et al. (1997). In this chapter, a general study on synthetic REE-bearing minerals, anhydrite, apatite, calcite, fluorite, scheelite and zircon, all doped with REE, were obtained by different experimental procedures and their CL corrected spectra were recorded to provide a database of REE in a variety of crystalline hosts.

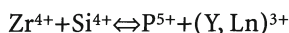
3

Experimental Procedure

3.1

Flux-Growth Method

Flux growth was selected to obtain zircon $ZrSiO_4$ -(REE): the crystals were grown from a flux consisting of equal proportions of Li_2MoO_4 and MoO_3 , in which stoichiometric quantities of SiO_2 and ZrO_2 were dissolved after careful mixing; the quantity SiO_2+ZrO_2 represented 1.34% of the flux mass (Cesbron et al. 1993; 1995). Spectrographically pure REE were introduced as oxides, more rarely as carbonate, and were accompanied with ammonium phosphate in order to take into account the xenotime-type substitution:



Later, almost all these syntheses were repeated but without the introduction of phosphorus.

The mixture, placed in a platinum crucible, was initially heated at 1125 °C during 48 h in order to ensure a good homogenization, then it was cooled to 900 °C

with a cooling rate of 1 °C/h and subsequently from 900 to 750 °C with a cooling rate of 2 °C/h. Zircons doped with Y, La, Ce, Pr, Nd, Sm, Eu, Gd, Tb, Dy, Ho, Er, Tm and Lu, with or without phosphorus, were thus obtained. The solubility of zircon at 1200 °C in such a flux is only 1.55% (Darmarajan et al. 1972) and the synthetic zircons can reach a maximum size of 3 mm.

3.2

Hydrothermal Method

Chlorapatite $\text{Ca}_5(\text{PO}_4)_3\text{Cl}-(\text{REE})$ was synthesized from an acid solution (Argiolas and Baumer 1978) corresponding to the composition $10 \text{ CaCl}_2 + 6 \text{ H}_3\text{PO}_4 + 143 \text{ H}_2\text{O}$, with 0.3–1% of the doping element (usually as oxide) added as hydrochloric solution. In other experiments corresponding to a basic environment, 1000 μl of a 200 g/l NH_4Cl solution were added to 100 mg of mixtures corresponding to $\text{Ca}_5(\text{PO}_4)_3(\text{OH}) + n\text{REE}_2\text{O}_3$. In order to facilitate the incorporation of trivalent ions, mixtures of $\text{Ca}_5(\text{PO}_4)_3(\text{OH}) + 1.5\% (\text{REE}_2\text{O}_3 + 2\text{NaCl})$ were also used. In both cases, the reactants were placed in sealed gold vessels and then submitted to the following conditions: 72 h at 700 °C and under 10^8 Pa (Blanc et al. 1995).

Fluorite $\text{CaF}_2-(\text{REE})$ was obtained using the same experimental conditions (Baumer et al. 1990), according to the reaction $\text{CaCl}_2 \cdot 2\text{H}_2\text{O} + 2\text{NaF} + \text{REE}$ (traces) $\rightarrow \text{CaF}_2-(\text{REE}) + 2\text{NaCl} + 2\text{H}_2\text{O}$. Crystals were euhedral, translucent to white, ranging in size from 20 to 400 μm .

3.3

Precipitation Method

Synthetic anhydrite $\text{CaSO}_4-(\text{REE})$ samples were obtained indirectly by precipitation of gypsum, which was subsequently transformed into anhydrite by dehydration in air at 800 °C for 3 h. Gypsum was precipitated by addition of 5 ml of a calcium chloride solution (0.2 mol/l), doped with a rare-earth element introduced as a hydrochloric solution, to 5 ml of a sodium or potassium sulfate solution with the same concentration of 0.2 mol/l. The precipitate was washed with distilled water and dried at 60 °C for 1 h (Baumer et al. 1997). The obtained crystals were very fine grained with no zonations related to REE concentration gradients.

Scheelite $\text{CaWO}_4-(\text{REE})$ and members of the solid solution scheelite-powellite (CaMoO_4) were synthesized by the same method using Na_2WO_4 and Na_2MoO_4 as reactants; precipitates were dried at 100 °C. The same experimental procedure, with $(\text{NH}_4)_2\text{CO}_3$ as starting material, was used to precipitate calcite $\text{CaCO}_3-(\text{REE})$.

The purity of the starting products such as Na_2SO_4 , K_2SO_4 , $\text{CaCl}_2 \cdot 6\text{H}_2\text{O}$, Na_2WO_4 , Na_2MoO_4 and $(\text{NH}_4)_2\text{CO}_3$ is in the order of 99.99% (Alfa “puratronic”); the purity of the rare-earth oxides is 99.9%.

3.4

Characterization Methods

Infra-red spectrometry and X-ray diffractometry were both utilized for identification and purity control of the synthetic minerals. IR-spectra were recorded on

a Perkin Elmer 225 IR spectrometer, using 13 mm diameter pellets with 300 mg of KBr; X-ray diffraction spectra were obtained with a CGR Theta-60 diffractometer.

CL spectra (Cesbron et al. 1993, 1995; Blanc et al. 1994a, 1995) were recorded from 200 to 900 nm with a CL spectrometer attached to a JEOL JSM 840 A scanning electron microscope, equipped with:

- An aluminum plated parabolic mirror *collector*.
- A cooled stage specially built in the laboratory, allowing a base temperature of 205 K when the crystals were deposited on top of a metallic specimen holder. Temperatures are measured by means of two carbon resistances.
- Silica lens UV quality.
- A Jobin-Yvon H10.UV grating *spectrometer*.
- A Hamamatsu R636 AsGa photomultiplier with a 650 U curve.

Operating conditions were: voltage: 25 kV; beam intensity: usually 1×10^{-7} A; spectrometer slits: 1 mm (allowing a 1 nm resolution at 500 nm, with a linear dispersion of 8 nm); scan step: 1 nm; integration time: 0.2 s. As our goal is to qualitatively interpret CL spectra of natural minerals, these conditions provide adequate signal for high resolution spectral measurement as well as minimizing the production of defects in the crystals. CL spectra were corrected for the response function of the whole system; they were processed with the Spectramax software (Jobin-Yvon and Spex).

Microcrystalline powders (anhydrite, apatite, calcite, fluorite and scheelite) were spread on a graphite coated adhesive (Link Analytical), carbon coated and analyzed with fast TV scanning under a 400 magnification ($300 \times 200 \mu\text{m}$). Spectra of pure REE oxides also were recorded to check their possible presence in the anhydrite powder resulting from gypsum calcination. Zircons were set with epoxy on an aluminum plate, with their *c*-axis parallel to the revolution mirror axis (Cesbron et al. 1993): after carbon coating, analyses were performed on 100 faces.

LIL investigations were undertaken by using microspectrometer equipment such as a micro-Raman microprobe, with which a monochromatic continuous wave (c.w.) Ar laser beam (from 514 to 458 nm) is focused on the sample and a stage range emission is collected on a CCD (charge coupled device). A double monochromator and dispersive grating of 1800 grooves/mm enable high spectral resolution spectroscopy. An additional advantage of using micro-Raman equipment is the possibility to run simultaneously Raman and LIL spectra. This is especially important when dealing with geomaterials in which additional phases may be present and induce erroneous interpretations. New detectors such as ICCD (intensified charge coupled device), triggered synchronously with a pulse laser, allow measurement of time resolved luminescence induced by a wide range of selective excitation, from UV to visible, provided by pulsed dye lasers and frequency doubling or tripling crystals.

In some synthetic minerals, the REE were analyzed by ICPS-MS (Perkin Elmer ELAN 5000) at the CRPG-CNRS of Nancy, France, using international geostandards; the precision can be estimated to ± 1 ppm in the concentration range of 10–50 ppm, and 10% relative to lower values. When investigating synthetic min-

erals doped with a specific REE, traces of other REE, usually in concentrations below 1 ppm, could be detected. The appearance of the spectrum was not affected by their presence, except for low concentrations of the doping element (Baumer et al. 1997).

4 Cathodoluminescence Spectra

4.1 The Undoped Crystals

All undoped minerals in this study show broad emission bands in the near UV wavelength region (Table 1), where the position of these bands depends on the nature of each mineral. This broad band is considered as the self-activated luminescence or “intrinsic band” of each mineral species. The intrinsic luminescence consists of an emission band centered at an energy $h\nu = E_g$ (Yacobi and Holt 1990; Rémond et al. 1992), where h is the Planck’s constant, ν the frequency and E_g is the absorption edge which is often determined by structural defects in the host lattice of the mineral. In zircon it has been shown (Cesbron et al. 1995) that there is possibly a relation between the energies of the self activated peaks and the lengths of the different atomic bonds. The same group has also shown that the crystal orientation with respect to the electron beam and to the mirror axis, as well as the excitation conditions, significantly influences the relative intensities of the different self activated emission spectra. In anhydrite the 343 nm band could be attributed to the lattice due to the presence of SO_4^{2-} (Gaft et al. 1985); the band at 390–425 nm in scheelite could be attributed to WO_4^{2-} (Curie 1960; Tarashchan 1978) and the peak at 281 nm to the $V \kappa$ center in fluorite (Banerjee and Ratnam 1973; Tarashchan 1978; Barbin et al. 1996). In fluorite, the presence of impurities enhances the formation of $V \kappa$ centers (self-trapped hole), aligned along the [100] direction, since these impurities provide effective electron traps (Merz and Pershan 1967). This $V \kappa$ center can be characterized as a F^{2-} complex (Kiessling and Scharmann 1975). In chlorapatites the self activated band centered at 360–380 nm could be attributed to the PO_4^{3-} group corresponding to the wide emission band observed with TL at 3.1–3.6 eV (Lapraz and Baumer 1981). The same lattice emis-

Table 1. Lattice emissions at 8 nm spectral resolution

Mineral	
Fluorite	281
Zircon	280
Calcite	363
ClApatite	360 380
Anhydrite	343 389
Scheelite	393 406–430

Conditions 25 kV, 10^{-7} A and PMT bias acceleration: 1025 V.

sion is also observed in synthetic fluorapatites (Lapraz and Baumer 1983). In calcite, the self activated peaks observed by CL at 363 nm and 380 nm are close to the absorption bands at 290 and 350 nm (Kolbe and Smakula; 1961; Medlin 1964; 1967; Visocekas et al. 1973). The emission in the UV could result from lattice defects (Nakagawa et al. 1988) due to CO_3^{3-} centers (Lapraz and Iacconi 1976; Calderon et al. 1983 1984) stabilized by structural crystal defects (Lapraz and Iacconi 1976) such as dislocations and twinning (Calderon et al. 1983).

4.2

Comparison of Cathodoluminescence Spectra of Tb^{3+} , Dy^{3+} and Tm^{3+} in Different Minerals

The purpose of this work is to provide a database of all the CL spectra produced by the different REE in mineral hosts such as fluorite, zircon, calcite, chlorapatite, anhydrite and scheelite (classified according to the increasing position – decreasing energy – of the maximum of their respective self activated emission band or “intrinsic” band; see paragraph on undoped crystals). Only luminescence induced by Tb^{3+} (Fig. 1a–f), Dy^{3+} (Fig. 2 a–f) and Tm^{3+} (Fig. 3a–f) will be given as examples; emissions given by other REE in doped minerals can be found in the literature for chlorapatites (Blanc et al. 1995), zircons (Cesbron et al. 1993, 1995) and anhydrites (Baumer et al. 1997). Absolute emissive power (photons/s) will not be considered here as these minerals do not contain the same concentration of doping elements; however scheelite and anhydrite by far are the most luminescent for these three REE. All the spectra were recorded under the same analytical conditions, with a linear dispersion of 8 nm which allows the recovering of a maximum of energy and permits observation of the weak emissions of natural samples.

4.2.1

Tb^{3+} Related Cathodoluminescence Emission

In all minerals studied, there was generally good agreement between the positions of the CL peaks (see Table 8), corresponding to the two transitions $^5\text{D}_3 \rightarrow ^7\text{F}_{6-2}$ and $^5\text{D}_4 \rightarrow ^7\text{F}_{6-0}$ (see Tables 8, 13), but some marked differences can be observed concerning their respective intensities. The major peak in fluorite (Fig. 1a), chlorapatite (Fig. 1d) and anhydrite (Fig. 1e) results from the strongly allowed transition $^5\text{D}_3 \rightarrow ^7\text{F}_6$ (Tarashchan 1978) at 382–383 nm while the intensity of the other strongly allowed transition $^5\text{D}_4 \rightarrow ^7\text{F}_6$ at 543–548 nm only represents 55–30% of the 382 nm peak. In fluorite and hydroxylapatite, the more intense peak is located at 382 nm. However in zircon (Fig. 1b) calcite (Fig. 1c) and scheelite (Fig. 1f), the 543–548 nm peak is predominant. Another interesting observation is the complete disappearance in calcite (Fig. 1c) of peaks at 382–383, 413–417, 436–438, 457–459 and 472–475 nm, corresponding to the transitions $^5\text{D}_3 \rightarrow ^7\text{F}_{6,5,4,3,2}$ and (covering an energy range from 3.25 to 2.60 eV). The most likely explanation of this effect is an absorption by the calcite self activated emission band which covers all of this energy range (see Table 1). This explanation is plausible for scheelite in which all of the first five peaks overlap with the self activated emission band (Fig. 1f): the intensity of the peak at 382 nm represents only 17% of the intensity of the major emission at 547 nm. In powellite, CaMoO_4 , the

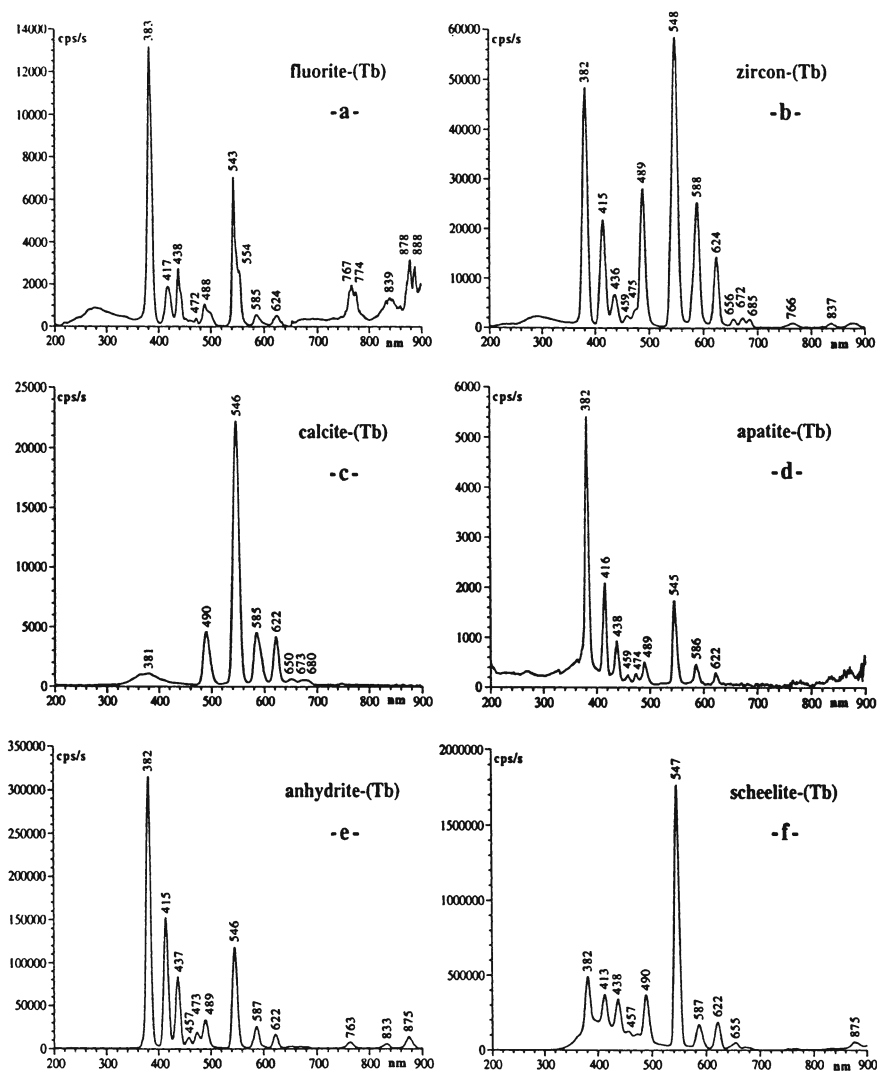


Fig. 1a-f. CL spectra of Tb³⁺ in: fluorite (a), zircon (b), calcite (c), chlorapatite (d), anhydrite (e) and scheelite (f)

Mo equivalent of scheelite, the self activated emission band shifts towards 538 nm, and the $^5D_4 \rightarrow ^7F_6$ at 543–548 nm emission peaks reappear. Tyson et al. (1988) has shown by fluorescence spectrometry that an addition of 10 mol% powellite in synthetic scheelite shifts the peak from 425 nm to 530 nm, the decrease in intensity of the scheelite peak at 425 nm occurs with the addition of 0.2 mol% powellite and is due to nonradiative energy transfer from tungstate to molybdate orbitals. These changes in intensity will be explained later in the discussion.

4.2.2

Dy³⁺ Related Cathodoluminescence Emission

The main feature of Dy³⁺ emissions in these minerals (Fig. 2a–f and Tables 9, 13) is the presence of four peaks respectively located at 478–487 ($^4F_{9/2} \rightarrow ^6H_{15/2}$), 573–586 ($^4F_{9/2} \rightarrow ^6H_{13/2}$), 660–673 ($^4F_{9/2} \rightarrow ^6H_{11/2}$) and 751–761 nm ($^4F_{9/2} \rightarrow ^6H_{9/2}$); the second of them is the most intense, with the exception of fluorite (Fig. 2a). Another small emission, almost missing in the scheelite spectrum (Fig. 2f), also occurs around 833–840 nm and could correspond to the $^4F_{9/2} \rightarrow ^6H_{7/2}$; it is usually accompanied by another one around 857–864 nm.

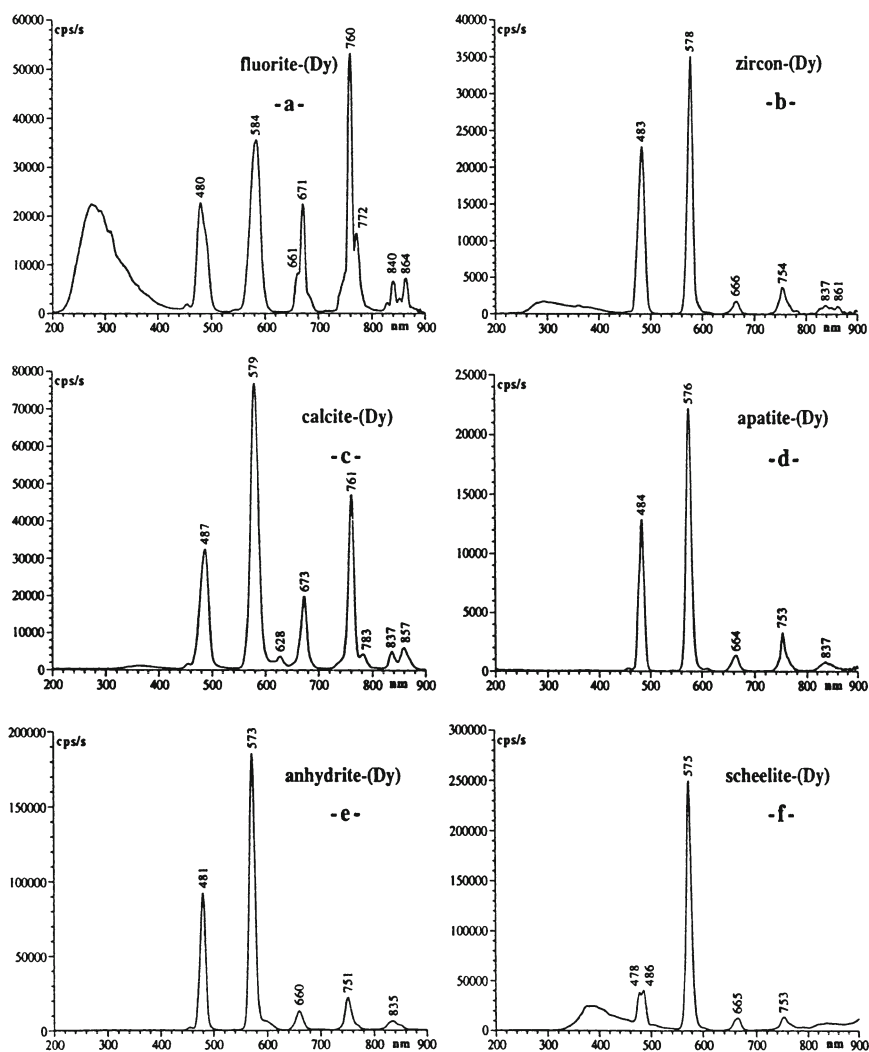


Fig. 2a–f. CL spectra of Dy³⁺ in: fluorite (a), zircon (b), calcite (c), chlorapatite (d), anhydrite (e) and scheelite (f)

4.2.3

Tm³⁺ Related Cathodoluminescence Emissions

As for Tb³⁺, Tm³⁺-doped minerals display a close agreement between their different emission peaks (Fig. 3a–f, Table 12). The most intense emission corresponds to a doublet at 348–364 nm, with the exception of fluorite (Fig. 3a) and scheelite (Fig. 3f) which exhibit strong CL emissions in the near IR domain. As for Tb³⁺-doped minerals, this change in intensity will be explained in the discussion. These two minerals, and also anhydrite (Fig. 3e) and calcite (Fig. 3c), seem to exhibit another IR emission beginning just before 900 nm; unfortunately the detection range of the spectrometer precluded further analyses.

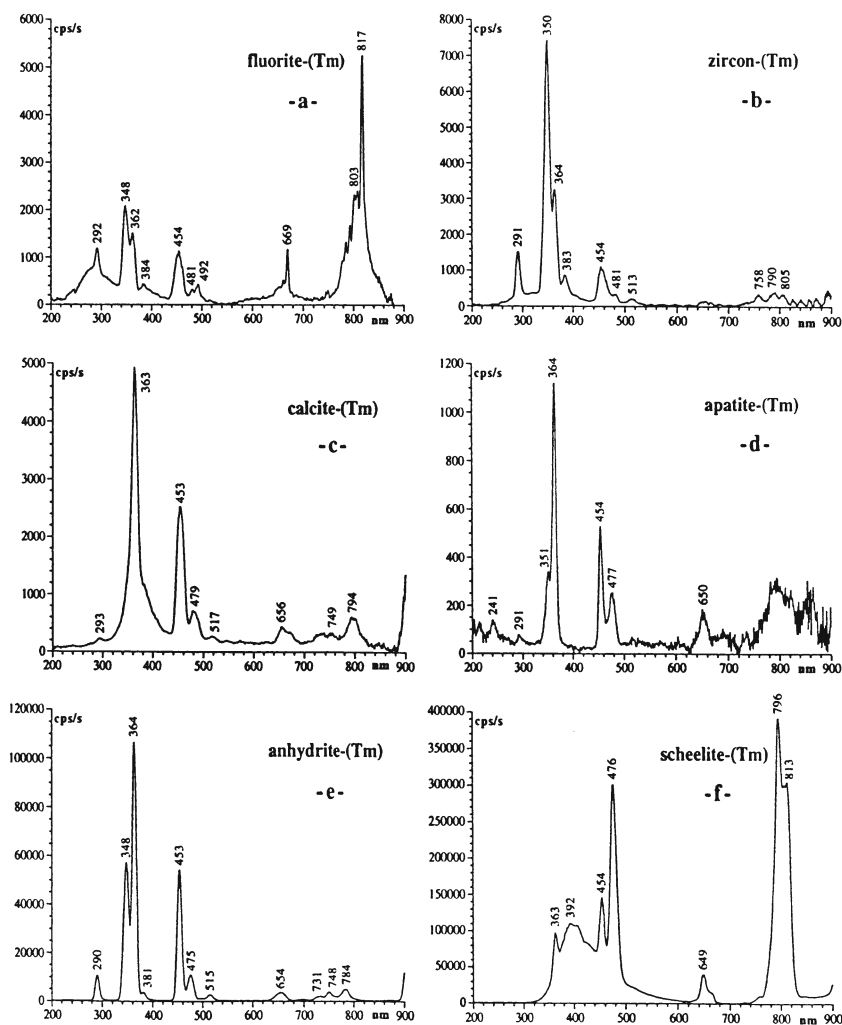


Fig. 3a–f. CL-spectra of Tm³⁺ in: fluorite (a), zircon (b), calcite (c), chlorapatite (d), anhydrite (e) and scheelite (f)

4.2.4

Multiplets

Some spectra, like those of fluorite-(Dy) (Fig. 2a), scheelite-(Dy) (Fig. 2f) fluorite-(Tm) (Fig. 3a), apatite-(Tm) (Fig. 3d), show a more or less partially resolved fine structure for several of their main emissions which are multiplets (see for instance Tarachan 1978 and Marfunin 1979). As it is our intention to present the spectral signatures of these minerals obtained under standard conditions in order to identify the different impurities, it would be out of our scope to describe these fine structures in detail. However, some experiments with a 0.1 mm slit allowing a much better linear dispersion lead to the following conclusions:

- The number of observed multiplets of Dy^{3+} emission change with each mineral host: around 480 nm, they are three for fluorite, seven for zircon (Fig. 4a), five for anhydrite and six in scheelite for only one single peak in calcite. There are at least eight components in the 580 nm band for the zircon-(Dy) (Fig. 4b).
- When a single crystal, initially with its *c*-axis parallel to the mirror axis, is rotated so that its *a*-axis becomes parallel to the mirror axis, there is no variation in the position of these multiplets. However, there is a change in the relative intensity, which can affect the position of the maximum of the envelope of the fine components (unresolved peak) when analyzing crystals with a 1 mm or larger slit, which allows resolution of the positions of the different multiplets of the radiative transition. The orientation related multiplet intensity variations are reported in the literature (see Rémond et al., this Vol.).
- With a linear dispersion of 8 nm the spectra are often complex with doublets, and the relative intensity of each peak may change with the polarization effect. Thus the envelope of the peak is moved and the peak position depends on the complex fine structure of the multiplets.

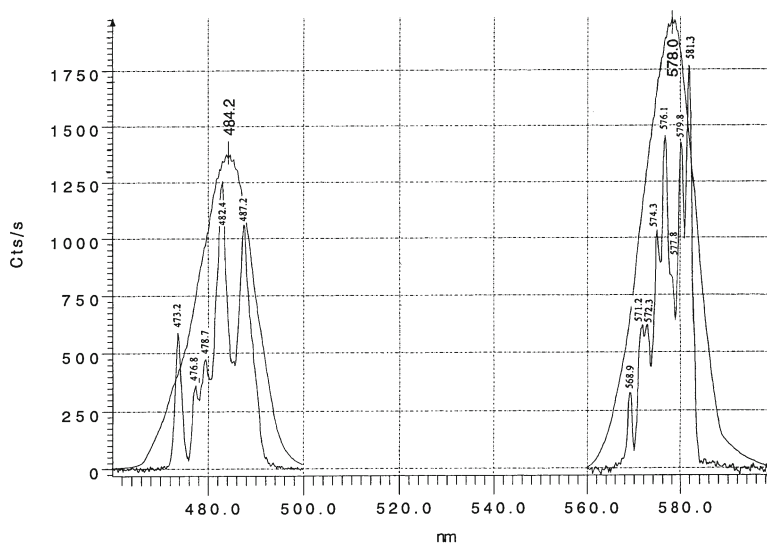


Fig. 4a,b. Fine structure, obtained with a 0.1 mm slit, of the CL emissions in zircon-(Dy) corresponding to the ${}^4F_{9/2} \rightarrow {}^6H_{15/2}$ (a) and the ${}^4F_{9/2} \rightarrow {}^6H_{13/2}$ (b) transitions

5 Reference Spectra from Doped Synthetic Minerals for Identification of Rare Earth Element Activators

5.1 Tables of Cathodoluminescence Emissions of Rare Earth Element and Related Transitions

The positions of the CL emissions peaks for each REE in each mineral studied are given in Tables 2–12. According to Monod-Herzen (1966), the REE from Pr^{3+} to Tm^{3+} exhibit narrow emissions peaks and lines, while Ce^{3+} exhibits a broad emission band. In our experiments La^{3+} and Yb^{3+} gave no significant emission and Lu^{3+} displayed only very low intensity peaks (Baumer et al. 1997).

In REE, the emission spectra are associated with two types of transitions, i.e. $f-f$ and $f-d$ transitions. The $f-d$ transitions are broad (Imbusch 1978) and occur in the UV region and the $f-f$ are responsible for the narrow lines (Marfunin 1979). The $f-f$ electronic transitions occur with REE from Pr^{3+} to Yb^{3+} , and the $f-d$ transitions are observed for Ce^{3+} , Sm^{2+} , Eu^{2+} and Yb^{2+} (Tarashchan and Waychunas 1995). Thus, transitions corresponding to the characteristic emissions lines of most of the REE (Table 13) could be indexed by comparison with TL, PL and LIL spectra (Merz and Pershan 1967; Morozov et al. 1970; Blase and Bril 1967; Blase 1973; Nambi et al. 1974; Kiessling and Scharmann 1975; Jain 1978; Tarashchan 1978; Marfunin 1979; Iaconi and Caruba 1980; Caruba et al. 1983; Blase and Aguilar 1984; Gaft et al. 1985; Kirsh and Townsend 1987; Kempe et al. 1991; Burrus et al. 1992; Burrus et al. 1992; Gorobets and Walker 1995; Tanabe et al. 1995; Tarashchan and Waychunas 1995, Reisfeld et al. 1996; Gaft et al. 1997 a and b). The energy levels and ground states for REE are given in Van Uitert and Iida (1962); Wybourne (1965); Diecke and Crosswhite (1963); Diecke (1968) and Imbusch (1978).

Table 2. Emissions of Ce^{3+}
at 8 nm spectral resolution

Mineral		
Fluorite	318	340
Zircon		
Calcite	350	363
ClApatite	353	360
Anhydrite	304	327
Scheelite	408	428
Conditions 25 kV, 10^{-7} A and PMT bias acceleration: 1025 V.		

Table 3. Emissions of Pp^{3+} at 8 nm spectral resolution

Fluorite	226-237-254-267-286	(362)	399	488	607-642-656	708-719	767	795	811	863
Zircon	Non-excited									
Calcite	Non-excited									
ClApatite	247-277			(475)-488	528-544	588-601-613-626-648	731			870
Anhydrite	222-232-249-260-282	350	411	490	591-602-606-(643)	697-731-743	776	813	837-849-858	
Scheelite			(393)	478-489	532-557	605-620-651	688-710-735	819-	833-857	874

Conditions 25 kV, 10^{-7} A and PMT bias acceleration: 1025 V.

Table 4. Emissions of Nd³⁺ at 8 nm spectral resolution

Fluorite	(274)	382	488	602	809	850–863–875–887
Zircon					809	874–882–892
Calcite						
ClApatite		391			806	874–
Anhydrite	313	391	426–448–523–539	600–647	803–826	868–874–879
Scheelite		(393)			802–808–814	834 875–882–892

Conditions 25 kV, 10⁻⁷ A and PMT bias acceleration: 1025 V.

Table 5. Emissions of Sm²⁺ and Sm³⁺ at 8 nm spectral resolution

Fluorite	(281)	560–568	588	607– 612–620	643– 654–663	671–676
Zircon	(342– 361)	559–570		597– 605–615	646–661	702– 710–725
Calcite	(370)	566		605	652	710 785–802
ClApatite		565		600	647	699–710
Anhydrite		562		600	644	691– 769 820 702–732
Scheelite	(393)	564		598–604	646	706 783–796 812– 858–881–891

Conditions 25 kV, 10⁻⁷ A and PMT bias acceleration: 1025 V.

Table 6. Emissions of Eu²⁺ and Eu³⁺ at 8 nm spectral resolution

Fluorite	Eu ²⁺	422	510	577–591–616–628		
Zircon	(302– 363–386)		560	595–616–632	652–656	692–704
Calcite	(363)	486		578–592–618	654	685–703 763
ClApatite	Eu ²⁺	459		593–620		693–697
Anhydrite	Eu ²⁺	385		593–618	660	697
Scheelite	(393–417)	537		593–615	654	702

Conditions 25 kV, 10⁻⁷ A and PMT bias acceleration: 1025 V.

Table 7. Emissions of Gd³⁺ at 8 nm spectral resolution

Fluorite	278	306–314
Zircon	(30–360)	308–313
Calcite		312–326 (365)
ClApatite		308–313–324
Anhydrite		306–312–318–322
Scheelite		306–312–317–320 (393)

Conditions 25 kV, 10⁻⁷ A and PMT bias acceleration: 1025 V.

Table 8. Emissions of Tb³⁺ at 8 nm spectral resolution

Fluorite	383	417	438-443	472	488-499	543-554	585	624	655	675	685	767-774	839	878-888
Zircon	382	415	436	459	475	548	588-596	624	666	672	685	766	837	878
Calcite	(363)-381			490	490	546	585	622	650	673	680			
ClApatite	382	416	438	459	474	545	586	622						
Anhydrite	382	415	437	457	473	546	587	622	652	670	680	763	833	875
Scheelite	382	413	438	457	490	547	587	622	655	672	682	752-760-766	832	875

Conditions 25 kV, 10⁻⁷ A and PMT bias acceleration: 1025 V.

Table 9. Emissions of Dy³⁺ at 8 nm spectral resolution

Fluorite	(281)	364	456	481-490	543	578-586		662-672-685	744-761	774	830-840-853-965
Zircon	(280)	362	456	483	542	578	609	646-666	754	780	810-828-845-861
Calcite	(364)	(364)	455	487	579	579	614-626	673	761	783	837-857
ClApatite	(364-377)	(364-377)	456	483	543	576	609	665	735	753	838
Anhydrite	303	303	456	481	540	573	601	660	701	751	834-850
Scheelite	(377)	(377)	454	478-486	539	575	602	665	738	753	820-836-854

Conditions 25 kV, 10⁻⁷ A and PMT bias acceleration: 1025 V.

Table 10. Emissions of Ho³⁺ at 8 nm spectral resolution

Fluorite	(277)	315	532-541-550	657	682	756-762
Zircon						
Calcite						
ClApatite		360	545	652		
Anhydrite	213	362	541	654		
Scheelite		(393)	504-542	646-659	753-755	822

Conditions 25 kV, 10⁻⁷ A and PMT bias acceleration: 1025 V.

Table 11. Emissions of Er³⁺ at 8 nm spectral resolution

Fluorite	321	381	405	473	527-542-549-552-561	651-671 679	760	777	792	810	830-839-850-859-867-874-874
Zircon	323		405	474	530	619					
Calcite											
ClApatite	319	378	402	471	527-545-549	618					
Anhydrite	290-318-	364-382	402	471	527-544-549	617					
Scheelite		(393)			505-523-528-543-552		734			820	844-857

Conditions 25 kV, 10⁻⁷ A and PMT bias acceleration: 1025 V.

Table 12. Emissions of Tm³⁺ at 8 nm spectral resolution

Fluorite	292	348–362	384	454	481–492	669		803–817
Zircon	291	350–364	383	454	481	513	656–679	758
Calcite	293	363		453	479	517	656–679	731–749
ClApatite	241	291	351–364	454	475		650	765
Anhydrite	290	348–364	381	453	475	515	654	731–748
Scheelite		363	(392)	454	476		649–666	796–813

Conditions 25 kV, 10⁻⁷ A and PMT bias acceleration: 1025 V.

Table 13. Rare earth element emissions lines and their related energy transitions

Ce ³⁺	Peak at 318 nm in fluorite	$^2D_{3/2} \rightarrow ^2F_{5/2}$
	Peak at 350 nm in calcite	$^2D_{3/2} \rightarrow ^2F_{5/2}$
	Peak at 353 nm in apatite	$^2D_{3/2} \rightarrow ^2F_{5/2}$
	Peak at 304 nm in synthetic anhydrite	$^2D_{3/2} \rightarrow ^2F_{5/2}$
	Peak at 318 nm in natural anhydrite	$^2D_{3/2} \rightarrow ^2F_{5/2}$
	Peak at 340 nm in fluorite	$^2D_{3/2} \rightarrow ^2F_{7/2}$
	Peak at 363 nm in calcite	$^2D_{3/2} \rightarrow ^2F_{7/2}$
	Peak at 360 nm in apatite	$^2D_{3/2} \rightarrow ^2F_{7/2}$
	Peak at 327 nm in synthetic anhydrite	$^2D_{3/2} \rightarrow ^2F_{7/2}$
Pr ³⁺	Peak at 488 nm	$^3P_1 \rightarrow ^3H_4$
	Doublet at 528–557 nm	$^3P_0 \rightarrow ^3H_4$
Nd ³⁺	Multiplet at 591–613 nm	$^1D_2 \rightarrow ^3H_4$
	Peak at 426 nm in anhydrite	$^2P_{1/2} \rightarrow ^4I_{9/2}$
	Peak at 488 nm in fluorite	$^4G_{1/2} \rightarrow ^4I_{9/2}$
	Peak at 523 nm in anhydrite	$^2G_{9/2} \rightarrow ^4I_{9/2}$
	Peak at 600 nm in fluorite and in anhydrite	$^4G_{5/2} \rightarrow ^4I_{9/2}$
Sm ³⁺	Peak at 803–809 nm	$^4F_{5/2} \rightarrow ^4I_{9/2}$
	Peak at 875 nm	$^4F_{3/2} \rightarrow ^4I_{9/2}$
	Doublet close to 568 nm	$^4G_{5/2} \rightarrow ^6H_{5/2}$
	Doublet close to 615 nm and doublet close to 660 nm	$^4G_{7/2} \rightarrow ^6H_{7/2}$
		$^4G_{5/2} \rightarrow ^6H_{7/2}$
Sm ²⁺	Doublet close to 671–676 nm	$^5D_0 \rightarrow ^7F_0$
	Doublet close to 700–710 nm	$^5D_0 \rightarrow ^7F_1$
	Peak at 725–732 nm	$^5D_0 \rightarrow ^7F_2$
	Doublet close to 785 nm	$^5D_0 \rightarrow ^7F_4$
	Peak at 820 nm	$^5D_0 \rightarrow ^7F_6$

Eu ³⁺	Peak close to 560 nm	$^5D_0 \rightarrow ^7F_0$
	Multiplet close to 592 nm	$^5D_0 \rightarrow ^7F_1$
	Multiplet close to 615 nm	$^5D_0 \rightarrow ^7F_2$
	Multiplet close to 654 nm	$^5D_0 \rightarrow ^7F_3$
Eu ²⁺	Multiplet close to 692–704 nm	$^5D_0 \rightarrow ^7F_4$
	Peak at 422 nm in fluorite	$4f^6_5d \rightarrow ^8S_{7/2}$
Gd ³⁺	Peak at 459 nm in apatite	$4f^6_5d \rightarrow ^8S_{7/2}$
	Peak at 385 nm in anhydrite	$4f^6_5d \rightarrow ^8S_{7/2}$
	Peak at 278 nm in fluorite	$^6I_{7/2} \rightarrow ^8S_{7/2}$
Tb ³⁺	Doublet close to 306–308 nm	$^6P_{5/2} \rightarrow ^8S_{7/2}$
	Doublet close to 312–314 nm	$^6P_{7/2} \rightarrow ^8S_{7/2}$
	Peak at 382 nm	$^5D_3 \rightarrow ^7F_6$
	Peak at 415 nm	$^5D_3 \rightarrow ^7F_5$
Dy ³⁺	Peak at 436–438 nm	$^5D_3 \rightarrow ^7F_4$
	Peak at 457 nm	$^5D_3 \rightarrow ^7F_3$
	Peak at 474 nm	$^5D_3 \rightarrow ^7F_2$
	Peak at 490 nm	$^5D_4 \rightarrow ^7F_6$
	Peak at 548 nm	$^5D_4 \rightarrow ^7F_5$
	Peak at 588 nm	$^5D_4 \rightarrow ^7F_4$
	Peak at 622 nm	$^5D_4 \rightarrow ^7F_3$
	Peak at 650 nm	$^5D_4 \rightarrow ^7F_2$
	Peak at 670 nm	$^5D_4 \rightarrow ^7F_1$
	Peak at 680 nm	$^5D_4 \rightarrow ^7F_0$
Ho ³⁺	Triplet at 481–487 nm	$^4F_{9/2} \rightarrow ^6H_{15/2}$
	Doublet at 575–579 nm	$^4F_{9/2} \rightarrow ^6H_{13/2}$
	Peak at 670 nm	$^4F_{9/2} \rightarrow ^6H_{11/2}$
	Peak at 753–761 nm	$^4F_{9/2} \rightarrow ^6H_{9/2}$
Er ³⁺	Peak at 541–550 nm	$^5S_2 \rightarrow ^5I_8$
Tm ³⁺	Peak at 405 nm	$^2H_{9/2} \rightarrow ^4I_{15/2}$
	Multiplet at 528–561 nm	$^4S_{3/2} \rightarrow ^4I_{15/2}$
Tm ³⁺	Doublet at 348–364 nm	$^1D_2 \rightarrow ^3H_6$
	Doublet at 454 nm	$^1D_2 \rightarrow ^3H_4$
	Doublet at 476 nm	$^1G_4 \rightarrow ^3H_6$
	Peak at 679 nm	$^1D_2 \rightarrow ^3F_2$
	Doublet at 796–813 nm	$^3F_4 \rightarrow ^3H_6$

The peaks of the self activated (Fig. 5a) and for the different REE are compared in Figs. 5b–5 l to show their relative position. Peak shift is also observed with Ce³⁺, Sm²⁺ and Eu²⁺ peaks which corresponds to the *f-d* transition. The emission of the Ce³⁺ ion originates often from the lowest *5d* level to the ²F ground state, which is a doublet ²F_{5/2} and ²F_{7/2} (Blasse and Brill 1967). In calcite the Ce³⁺ peaks are close to the self activated bands (see Table 1). For the REE from Pr³⁺ to the Tm³⁺, the main emission peaks, which correspond to the *f-f* transition, are approximately at

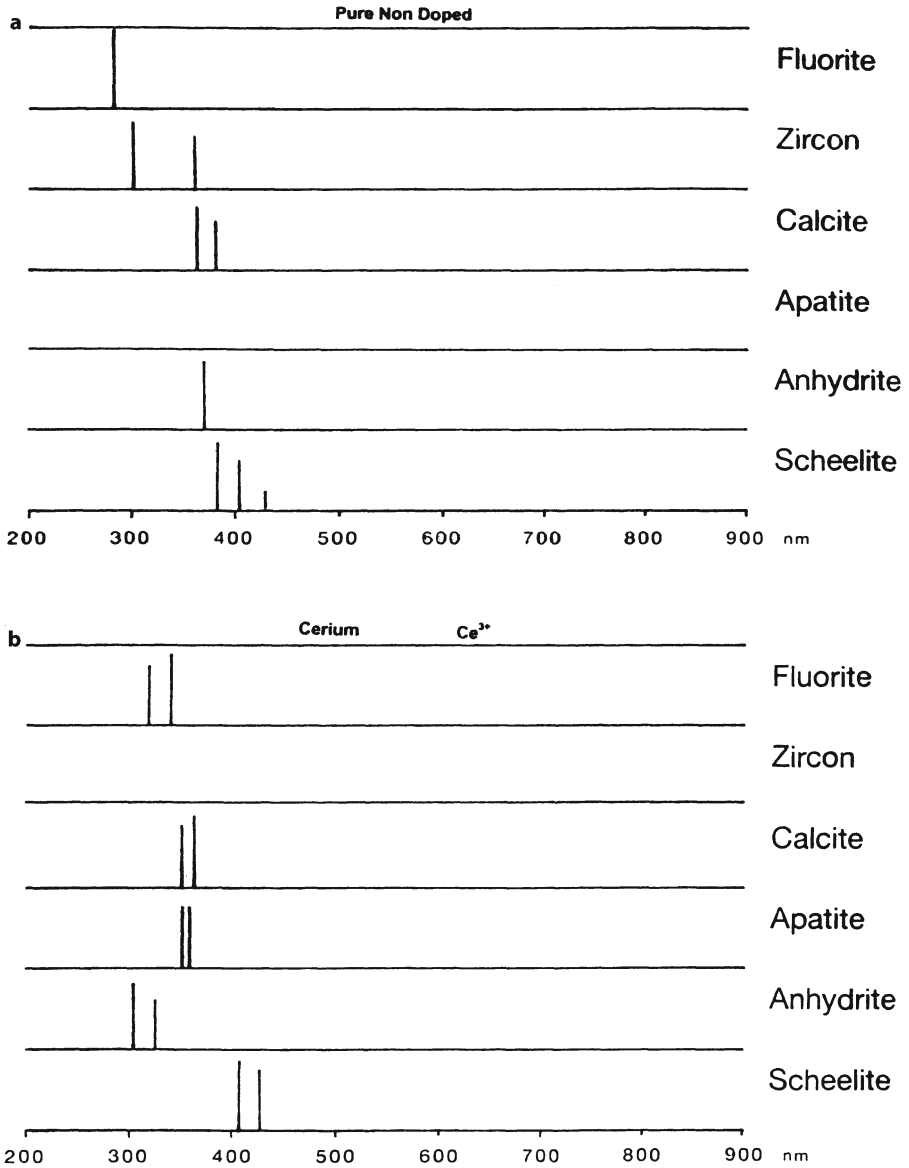


Fig. 5a-l. Peak shifts for the emission spectra of the lattice emissions (a) and the emissions of Ce^{3+} (b), and positions of the peaks of Pr^{3+} (c), Nd^{3+} (d), Sm^{3+} (e), Eu^{2+} and Eu^{3+} (f), Gd^{3+} (g), Tb^{3+} (h), Dy^{3+} (i), Ho^{3+} (j), Er^{3+} (k), Tm^{3+} (l) for fluorite, zircon, calcite, chlorapatite, anhydrite and scheelite

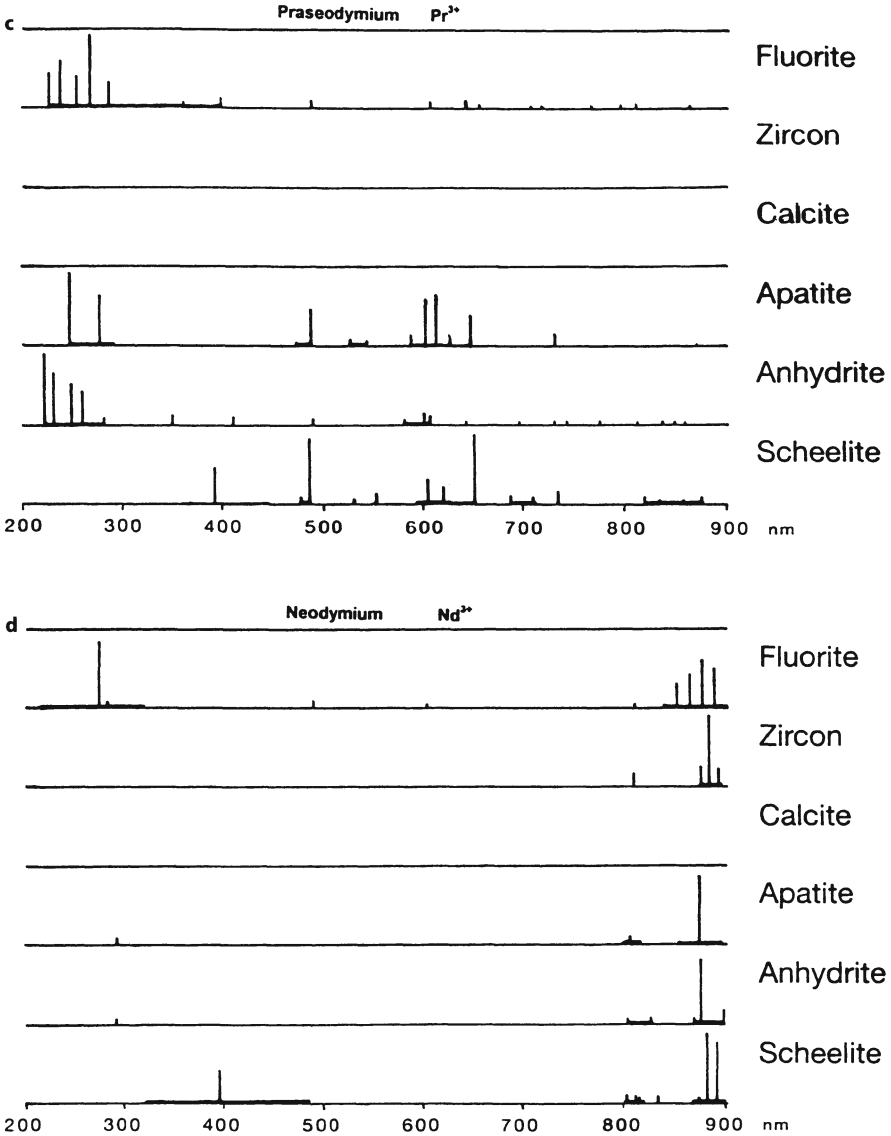


Fig. 5c, d.

the same wavelength, sometimes with inversion in emission intensity from one host to another, for example Tb^{3+} (Fig. 1 and Fig. 5g) for which the 382 ± 1 nm emission is the main peak in fluorite, chlorapatite and anhydrite, whereas in zircon, calcite, scheelite, fluorapatite and hydroxylapatite the 547 ± 1 nm is the more intense peak. In addition some peaks are missing from one host to another, for example the Pr^{3+} (Fig. 5c) emission at 237–267 nm which exists in fluorite, chlo-

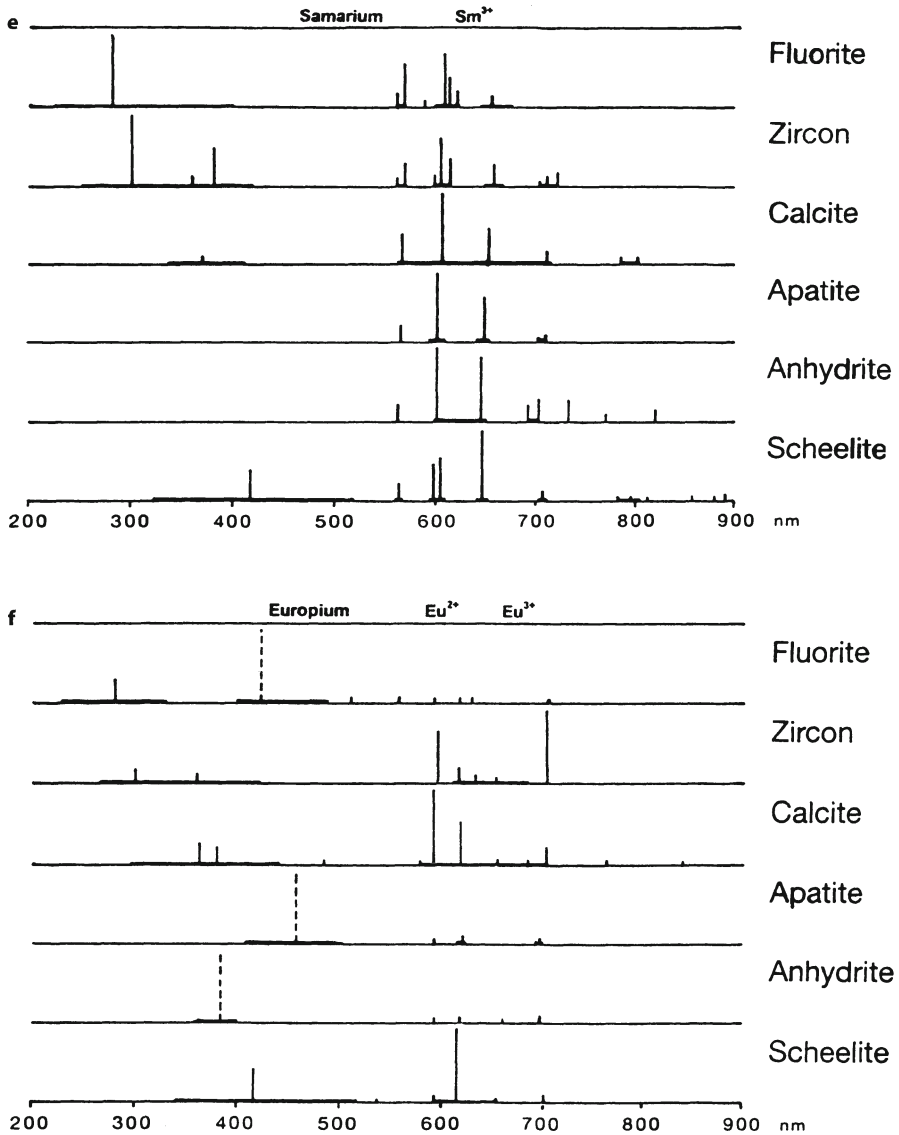


Fig. 5e, f.

apatite and anhydrite is not excited in zircon and calcite and scheelite. This may be due to energy transfer towards the self activated band. In apatite, the REE^{3+} occupy the CaII sites with charge compensation provided by replacement of F^- by O^{2-} (Morozov et al. 1970). The presence of these charge compensating impurities could affect the site symmetry and therefore the transition probability for the emission line.

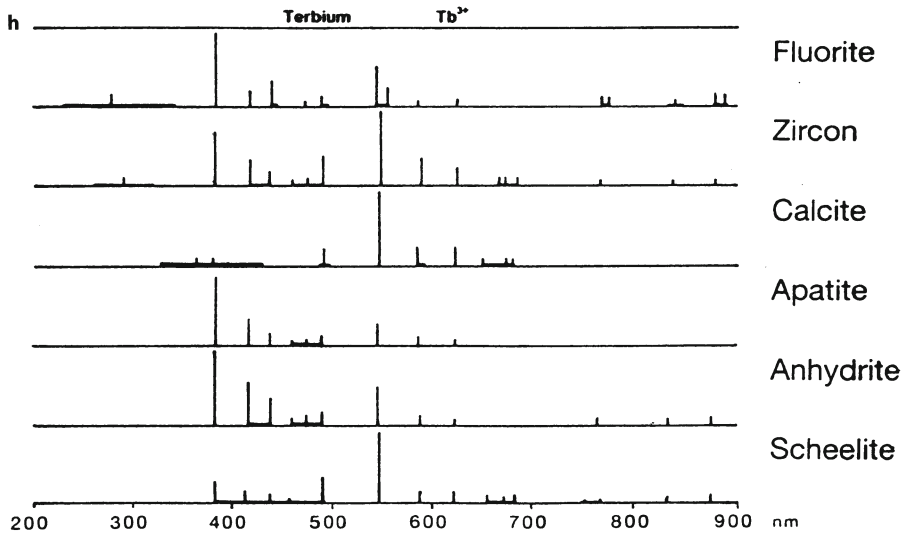
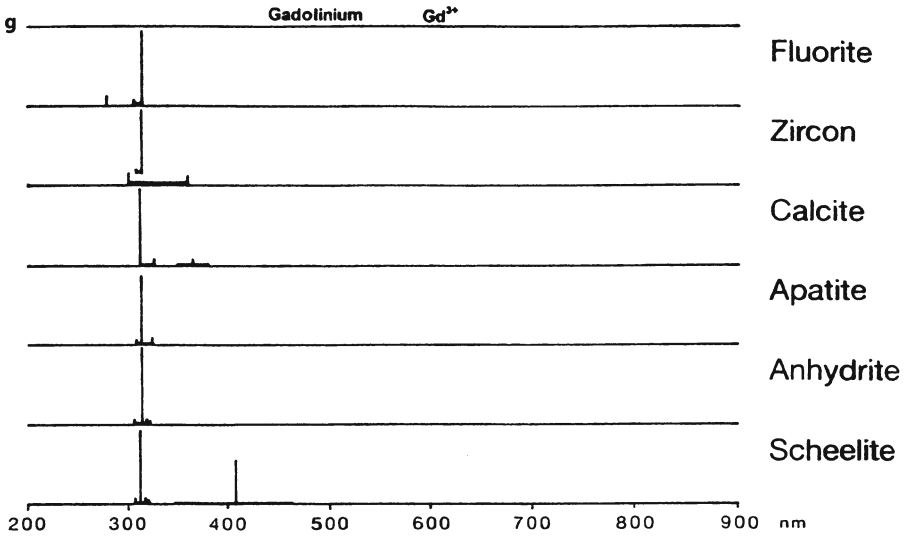


Fig. 5g, h.

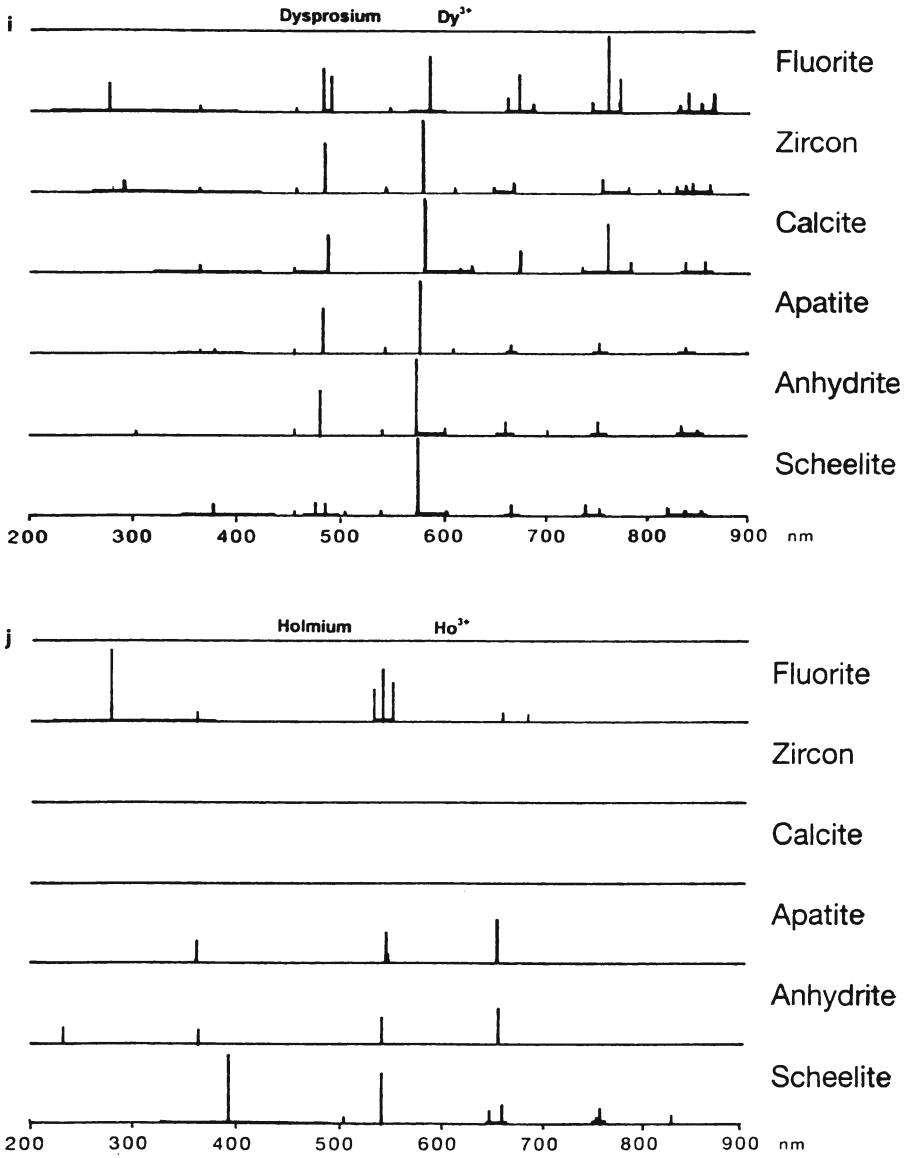


Fig. 5i, j.

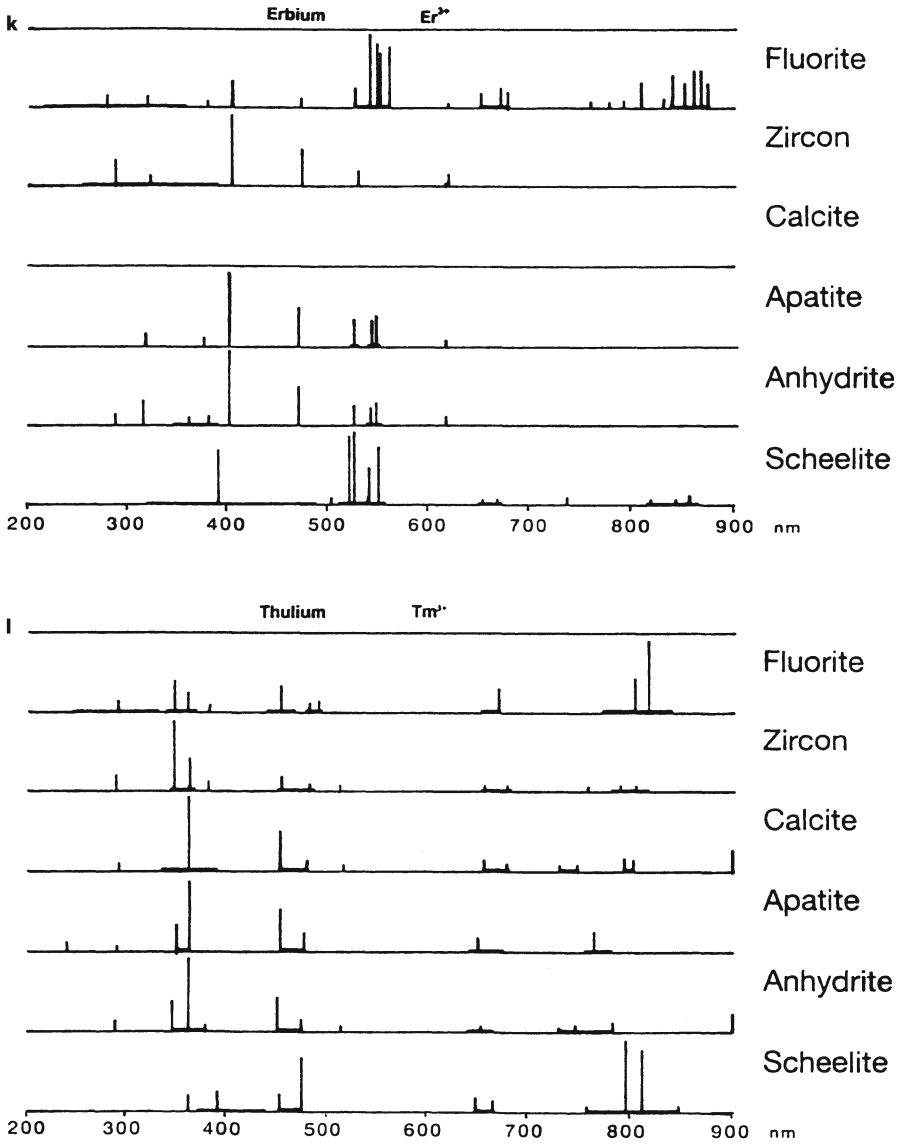


Fig. 5k, l.

5.2

Comparative Investigation of Natural and Synthetic Minerals by Laser Induced Luminescence and Cathodoluminescence

Laser induced luminescence spectra of dysprosium (Dy) doped Ca-phosphate (chlorapatite, $\text{Ca}_5(\text{PO}_4)_3\text{Cl}_2$), Ca-sulfate (anhydrite, CaSO_4) and Ca-tungstate (scheelite, CaWO_4) excited by the 458 nm c.w. Ar beam are shown for different spectral regions (Fig. 6). The characteristic emission bands of Dy substituted in the Ca site(s) are observed. The spectral resolution enables differentiation of some specific radiative transitions associated with the different crystallographic environment for each host. The Dy-chlorapatite spectrum shows broad bands while Dy-anhydrite and scheelite spectra exhibit characteristic well resolved emissions lines. The low crystallinity of the chlorapatite sample as well as the presence of two Ca sites of substitution for Dy explains the less informative spectrum. All spectra present a reabsorption line at 746.8 nm (Gaft et al. 1997). The power analytical of selective excitation is shown (Fig. 7). The emission from a sample of natural yellow fluorapatite was recorded under four different excitations in the UV and the violet part of the visible region: 308, 354, 360 and 460 nm. For each excitation, only selected radiative transitions of rare-earths are induced. Such experiment enables to discrimination of the different REE, which in high excitation CL, would have been observed as complex overlapping bands. Time-resolved luminescence of Eu^{3+} doped hydroxyapatite, implanted with Eu and thermally treated at 500 °C, shows variation in the emission patterns from short decay record (delay (d)=400 ns and gate width (w)=400 ns), to intermediate time (d=400 ns and w=2 ms) up to long decay (d=10.4 μ s and w=2 ms) record (Fig. 8). An order of magnitude variation in the intensity of these bands reveals the corresponding radiative electronic transitions which can be related to the different crystallographic environment of each substitution site (Ca1 and Ca2 sites).

These few examples emphasize the importance of complementary information that photoluminescence and CL can provide. While CL provides rapid general information on all luminescent centers, PL allows the selective excitation of specific luminescent centers.

6

Discussion and Future Developments

The CL spectra measured with a 8 nm wavelength resolution from synthetic doped minerals (Figs. 1–4) show that the wavelength position of each set of narrow CL emission lines is independent of the host crystal. This relationship between the emission line positions and the nature of the rare-earth doping ions can be used for a qualitative interpretation of the CL emission spectrum from a natural specimen. A similar approach is used in the qualitative interpretation of a X-ray spectrum based on the Moseley's law relating the energy of the X-ray photon with the atomic number of the emitting element. With X-rays, the characteristic resulting emission lines from transitions involving core electrons have their

relative intensities in a constant ratio, regardless of the composition of the specimen containing the constant ratio which is independent of the specimen containing the analyzed element (this property remains valid only when no secondary fluorescence effect occurs). However, a constant intensity ratio does not exist for CL emission spectra characteristic of rare-earth ions. The relative intensities of the CL emission lines of a given REE varies with the host crystal. In addition, the shape of the CL emission lines or bands depend on the chemical environment as it is the case for low energy X-ray photons (soft X-ray emission bands) involving valence electrons transitions.

Qualitative identification of a REE at trace levels from the CL emission spectrum of the specimen can only be accurately performed when both the wavelength peak position and the relative intensities of all lines are considered, accounting for the nature of the analyzed specimen. For this purpose, reference data used for the qualitative interpretation of CL spectrum must include both the position and the relative intensities of the emission lines. Such reference data can only be obtained from spectra corrected for the instrument response function, as is the case for the data presented here (Fig. 5). Reference CL spectra can be used for qualitative interpretation of a CL spectrum of an unknown specimen when the spectra have been measured with the same excitation conditions (beam energy, incident dose, temperature of measurements) and the same wavelength resolution of the spectrometer as used for the measurement of the reference spectra (e.g. 8 nm resolution in the present study). The same experimental conditions must be used in order to resolve spectral overlap by using a least squares fitting technique of the experimental spectrum with the measured or theoretical reference spectra, as discussed by Rémond et al. 2000 (this Vol.). Each REE activator produces several peaks (each of them comprised of multiplets easily observed with a 1 nm bandpass) which can be described by a Gaussian or a pseudo-Voigt profile in which peak position, peak height and peak width are the variables in the fitting procedure. When several REE activators are present in a specimen, many CL overlapping lines may occur and the least squares fitting technique may lead to a non-unique solution due to the large number of variables required in the fitting procedure. In order to reduce the number of variables, some parameters must be coupled to each other, such as the wavelength separation or the relative intensities of the lines for each activator. Therefore, it is essential to add the intensity ratios to the list of peak positions of the CL emission lines corresponding to each REE activator/host mineral system.

The intensity ratios of a set of CL lines associated with a given recombination center (after correction for the response function of the system) can be used for a quantitative interpretation of the CL emission spectrum. Based on analogies between the X-ray and CL mechanisms (as reported by Rémond et al., this Vol.), a possible quantitative approach consists of: (1) comparing the intensity measured from the unknown specimen and the reference minerals successively, and (2) applying to the measured intensity ratios a set of correction factors accounting for the mechanisms of energy transfer to the luminescent ion within the different compounds. In practice, as a result of the complex nature of the CL photon generation and emission mechanisms, it is important to define what measured signal is characteristic of the number of luminescent ions in the emitting volume.

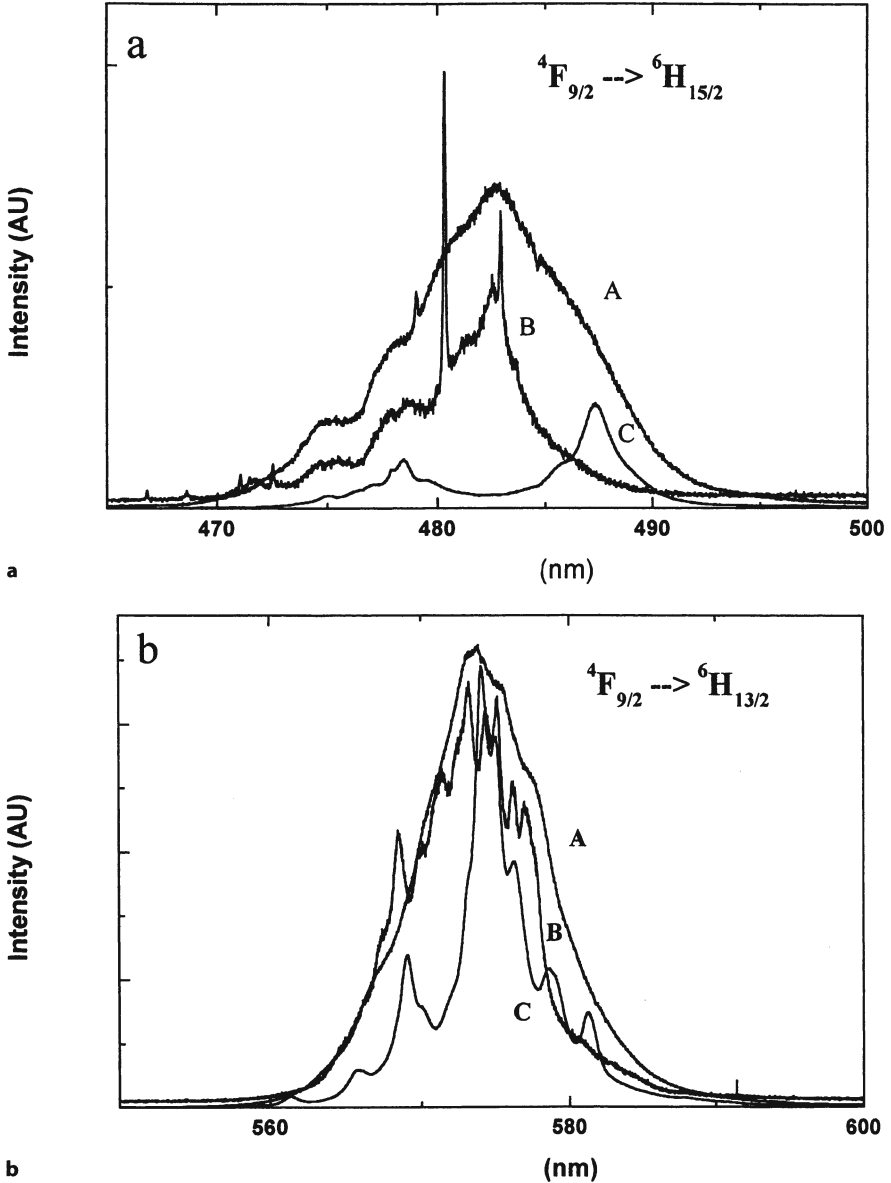


Fig. 6a,b. Emission spectra of Dy doped-chlorapatite (A), scheelite (B), anhydrite (C) in different spectral regions: a excitation 458 nm, b 578 nm, c 665 nm, d 753 nm

For semiconductors, Warwick (1987) showed that the concentration C_i of a given recombination center (i), is proportional to the I_{i0}/τ , where I_{i0} is the dynamic equilibrium intensity and τ is the decay constant which depends on all emission processes. In addition, quantitative analysis based on a comparative method using

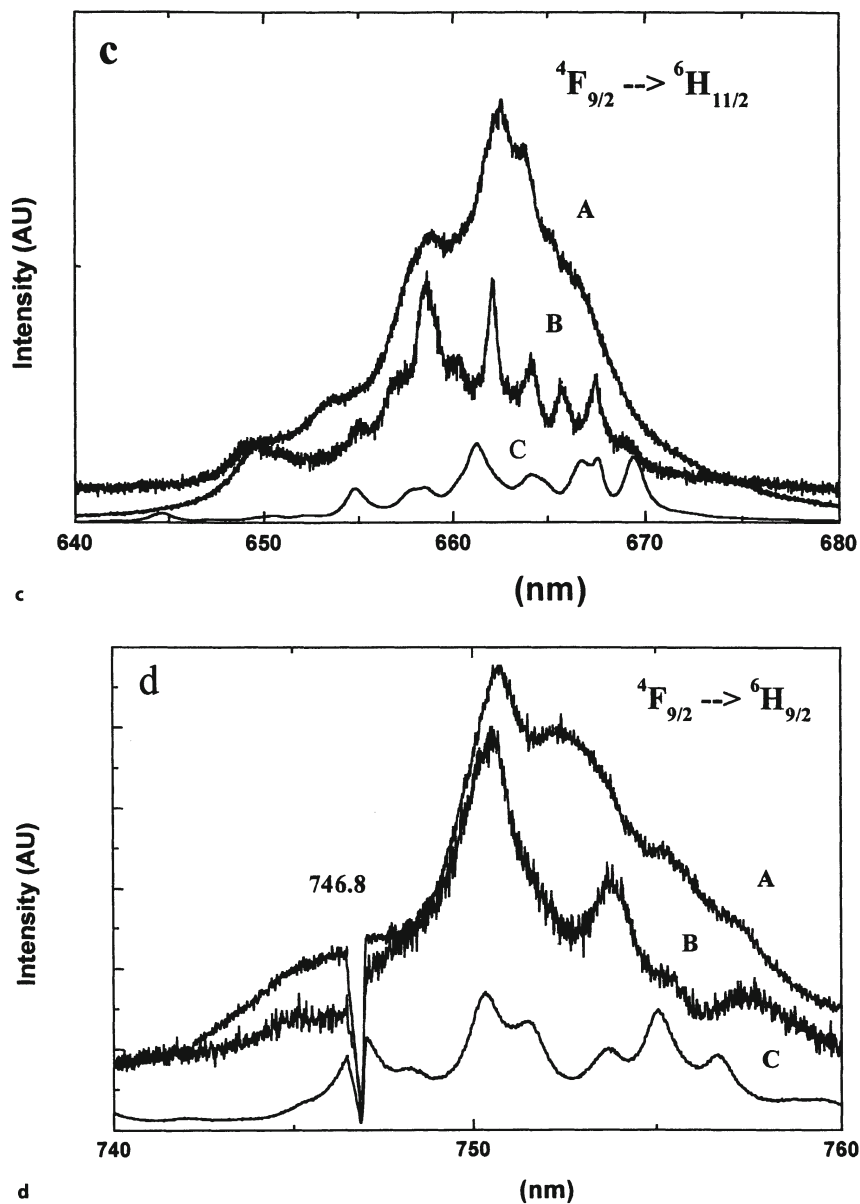


Fig. 6c, d.

reference compounds has more constraints with CL emission analysis than with X-ray spectrometry. A major difficulty is the choice of the reference materials. For a given REE activator incorporated into a particular mineral, the intensity ratios of the CL lines will depend on both the concentration of the analyzed activator

and the presence of all other impurities and defects. As a consequence, reference materials cannot be selected based only on the similarity of their crystallographic properties and chemical composition with respect to those of the analyzed specimen, but must also account for the presence of all impurities and defects (naturally pre-existing or induced defects during specimen preparation and beam irradiation) which can modify the CL properties of the crystal. As reported by Rémond et al. (this Vol.), the CL emission is a competitive process. The CL intensity depends on both the radiative and non-radiative transition probabilities, (photons versus Auger electrons), the capture cross-section of the energy levels involved in the transitions for the various energies participating to the excitation and the transfer of energy from an excited centre to another one. The measured CL intensity, I_{CL} , the number of photons emitted at the specimen surface per unit time can be expressed by the following equation

$$I_{CL} = \sum_i \Omega / 4\pi F_A^i F_R^i F_I^i I_{gen}^i$$

where i refers to each separate CL generation process (electron, X-ray and optical photon), $\Omega/4\pi$ is the solid angle of collection at which the fraction of emitted photons actually enter the detector, F_I is a factor accounting for instrumental parameters (collection and transmission efficiency of the detection system), F_A is a factor to account for optical absorption along the escape path length and F_R is factor

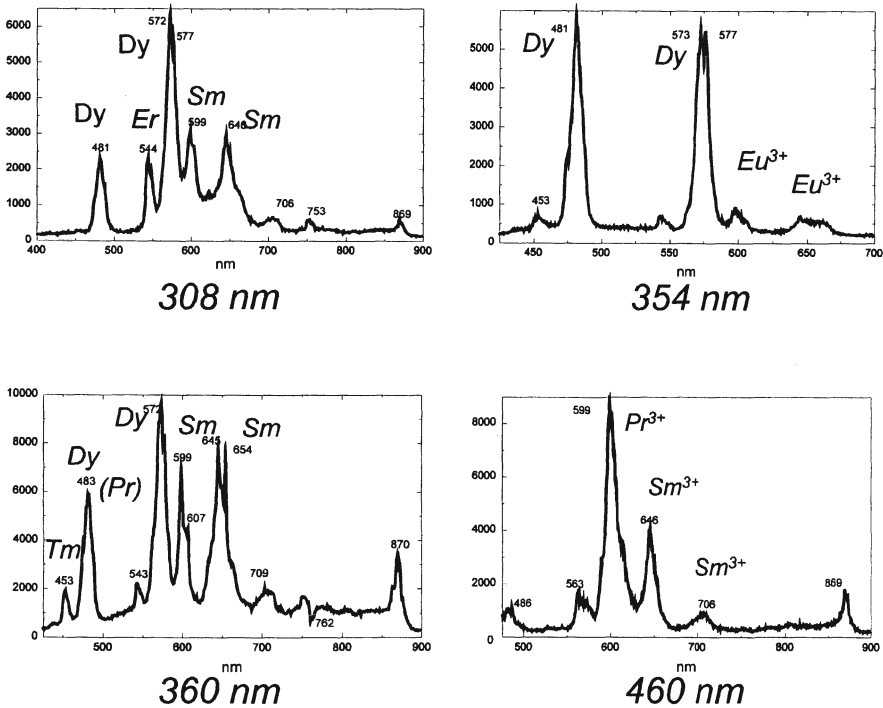


Fig. 7. Emission spectra of natural fluorapatite for different excitations (308, 354, 360 and 460 nm)

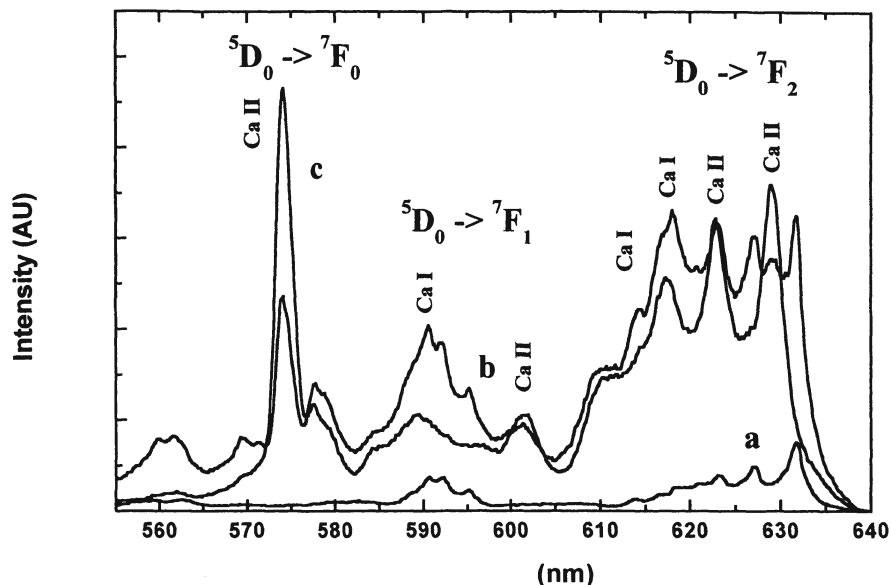


Fig. 8. Emission spectra at different recording times of synthetic hydroxyapatite (Biorad) implanted with Eu and thermally treated at 500 °C. *a* Short time, delay (d)=400 ns and gate width (w)=400 ns; *b* intermediate time, d =400 ns and w =2 ms; *c* long time, d =10.4 μ s and w =2 ms

which corrects for internal reflection and refraction at the specimen surface. The above expression is close to the usual ZAF expression used in the quantitative analysis scheme with the EPMA. The generated intensity, I_{gen}^i , is a function of the depth distribution of the energies participating in the emission and in the radiative recombination probabilities.

For transparent wide band gap materials, the absorption coefficient is very small and the absorption term can be neglected in a first approximation. However it is not as yet clear which of the electron energy loss mechanisms released in the matrix are responsible for the total observed CL yield (fast or slow secondary electrons, phonons, plasmons, etc.). It is however well established in some specimens that an important part of the CL emission results from a secondary emission process due to the absorption of CL photons originating from the de-excitation of another center, such as those associated with lattice defects. This secondary emission resulting from the energy transfer is equivalent to secondary fluorescence for X-ray spectrometry with the EPMA. Such a phenomenon can obviously only occur if the CL photon characteristic of a center have an energy slightly higher than the absorption edge of the center emitting the secondary emission. Secondary CL emission processes are efficient in wide band gap material with REE³⁺ and have a high probability of occurring. The so-called intrinsic CL emission (self activated or near edge emission) extends into the UV or blue region of the spectrum. The absorption bands of REE³⁺ ions exhibit a high oscil-

lator strength in the UV, as illustrated by Rémond et al. (this Vol.) especially for Dy bearing zircon. The CL emission of a REE³⁺ ion resulting from a secondary excitation by CL photons associated with lattice defects is a tentative explanation for the changes in intensity of the REE CL emission as a function of the host mineral.

In order to support such an assumption further experiments are needed:

- 1 For a given mineral REE concentration study: intensity ratio of REE lines as a function of defect concentration by adding different amounts of impurities to the REE
- 2 Studying the intensity ratios between several group of lines, and between fine structures by varying the energy of an incident UV line

7

Conclusion

For an accurate interpretation of the CL emission spectrum from a natural REE bearing mineral, reference spectra for a given REE activator incorporated in a particular host crystal lattice must be acquired with different wavelength resolutions, depending on whether a quantitative analysis is required. Low resolution emission spectra (such as those presented in Figs. 6–8) showing the envelope of the complex fine structure of the CL lines of a REE activator are a sufficient approximation for qualitative interpretation (direct identification of peaks or spectral decomposition) of an unknown spectrum. For a better understanding of the generation mechanisms of CL spectra, needed for a quantitative interpretation of experimental data, high resolution spectra must be obtained. With this objective, we propose in Tables 2–12 a preliminary description of the peak positions and relative intensities of the fine structures of the CL lines for the RE³⁺ ions in several minerals. It must be emphasized that these data do not provide an universal database but must be considered as a first step in a future quantitative interpretation of CL spectra. The next step will be a systematic comparison of CL characteristics (relative intensities of the multiplets, peak widths, decay times) with those of spectra generated with UV photons using the LIL. These comparisons should add to knowledge of the generation mechanisms of CL photons and, more particularly, to the contribution of the secondary excitation of the luminescent ion by the CL photons resulting from the intrinsic and related defects emissions.

Acknowledgements. This work was initiated and partly financed by the CNRS-INSU DBT grant n°4/6–4.15, and by the funds of the different laboratories at CRPG-Nancy, ESEM-Orléans, Université de Paris VI, Université de Nice and Université de Lyon. We thank Dr. Matthew R. Phillips from the University of Technology of Sydney and Prof. G. Calas from the University of Paris for improving the manuscript.

References

- Argiolas R, Baumer A (1978) Synthèse de chlorapatite par synthèse hydrothermale: étude de l'influence de la sursaturation sur l'évolution des faciès des cristaux. *Canad Mineral* 16, 285–290
- Banerjee HD, Ratnam VV (1973) Trapped holes and trapped-hole diffusion in CaF_2 crystals irradiated by cathode rays. *Physica* 65, 97–108
- Barbin V, Jouart JP, D'Almeida T (1996) Cathodoluminescence and laser-excited luminescence spectroscopy of Eu^{3+} and Eu^{2+} in synthetic CaF_2 : a comparative study. *Chem Geol* 130, 77–86
- Baumer A, Blanc Ph, Cesbron F, Ohnenstetter D (1997) Cathodoluminescence of synthetic (doped with rare-earth elements) and natural anhydrites. *Chem Geol* 138: 73–80
- Blanc Ph, Arbey F, Cros P, Cesbron F, Ohnenstetter D (1994 a) Applications de la microscopie électronique à balayage et de la cathodoluminescence à des matériaux géologiques (sulfates, carbonates, silicates). *Bull. Soc. géol. Fr.* 165: 341–352
- Blanc Ph, Baumer A, Cesbron F, Ohnenstetter D (1995) Les activateurs de cathodoluminescence dans des chlorapatites préparées par synthèse hydrothermale. *C R Acad Sci Paris, sér II* 321: 1119–1126
- Blanc Ph, Roger G, Couto H (1994 b) Recherche de signatures magmatique et hydrothermale dans des apatites du Nord du Portugal: étude par cathodoluminescence, microscopie électronique à balayage et microsonde électronique. *Bull Soc géol Fr* 165: 329–339
- Blase G, Bril A (1967) Investigation of some Ce^{3+} - activated phosphors. *J Chem Phys* 47, 5139–5145
- Blase G (1973) Crystal chemistry and rare-earth luminescence of mixed metal oxides. *Rev Chimie minér* 10, 39–46
- Burrus RC, Ging TG, Eppinger RG, Samson IM (1992) Laser-excited fluorescence of rare earth elements in fluorite: Initial observations with a laser Raman microprobe. *Geochim Cosmochim Acta* 56, 2713–2723
- Burt DM (1989) Compositional and phase relations among rare earth element minerals. In: Lipin BR, McKay GA (eds.) *Geochemistry and Mineralogy of rare earth elements*. Mineral Soc Amer, *Rev Mineral* 21, pp 259–307
- Calderon T, Aguilar M, Coy-Yill R (1983) Relationship between blue color and radiation damage in calcite. *Radiation Effects Lett* 76, 187–191
- Calderon T, Aguilar M, Jaque F, Coy-Yill R (1984) Thermoluminescence from natural calcites. *J Phys C/ Solid State Phys* 17, 2027–2038
- Caruba R, Iacconi P, Cottrant JF, Calas G (1983) Thermoluminescence, fluorescence and electron paramagnetic resonance properties of synthetic hydrothermal scheelites. *Phys Chem Minerals* 9, 223–228
- Cesbron F, Blanc Ph, Ohnenstetter D, Rémond G (1995) Cathodoluminescence of rare earth doped zircons. Part I: their possible use as reference materials. *Scanning Microscopy, suppl.* 9: 35–56
- Cesbron F, Ohnenstetter D, Blanc Ph, Rouer O, Sichere MC (1993) Incorporation des terres rares dans des zircons de synthèse: étude par cathodoluminescence. *C R Acad Sci Paris, sér II* 316: 1231–1238
- Curie D (1960) *Luminescence cristalline*. Dunod, Paris, pp 209
- Darmarajan R, Belt RE, Puttbach RC (1972) Hydrothermal and flux growth of zircon crystals. *J Crystal Growth* 13/14: 535–539
- Diaz MA, Luff BJ, Townsend PD, Wirth KR (1991) Temperature dependence of luminescence from zircon, calcite, iceland spar and apatite. *Nucl Tracks Radiat. Meas* 18: 45–51ZZ
- Dieke GH (1968) *Spectra and energy levels of rare earth ions in crystals*. John Wiley, New York, pp 401
- Gaft ML, Bershov LV, Krasnaya AR, Yaskolko VY (1985) Luminescence centers in anhydrite, barite, celestine and their synthesized analogs. *Phys Chem Minerals* 11, 255–260
- Gaft M, Reissfeld R, Panczer G, Boulon G, Shoval S, Champagnon B (1997 a) Reabsorption lines of molecular oxygen and water in natural apatite. *Optical Materials* 8: 149–157

- Gaft M, Reisfeld R, Panczer G, Shoval S, Champagnon B, Boulon, G (1997 b) Eu³⁺ luminescence in high-symmetry sites of natural apatite. *J Lumin* 72–74: 572–574
- Gorobets BS, Walker G (1995) Origins of luminescence in minerals: a summary of fundamental studies and applications. In: Marfunin AS (ed.) *Advanced Mineralogy*. Springer Verlag, Berlin, 2, pp 124–135
- Hanchar JM, Miller CF (1993) Zircon zonation patterns as revealed by cathodoluminescence and backscattered electron images: implications for interpretation of complexes crustal histories. *Chem Geol* 110: 1–13
- Hanchar JM, Marshall DJ (1995) Multi-laboratory results for the cathodoluminescence emission spectrum from a synthetic zircon standard. *Scanning Microscopy*, suppl. 9:
- Hanchar JM, Rudnik RL (1995) Revealing hidden structures: The application of cathodoluminescence and backscattered electron imaging to dating zircons from lower crustal xenoliths. *Lithos* 36: 289–303
- Hanchar JM, Watson EB, Cherniak DJ, Finch RJ, Mariano AN (1997) Rare-earth elements in zircons: synthesis and rare-element doping. *Amer Mineral* (submitted)
- Henry DJ, Toney JB (1987) Combined cathodoluminescence/backscattered electron imaging and trace element analysis with the electron microprobe: applications to geological materials. In: Geiss R.H. (ed.) *Microbeam Analysis*: pp. 339–342
- Iaconi P, Caruba R (1980) Trapping and emission centres in X-irradiated natural zircon. III. Influence of trivalent rare earth impurities. *phys stat sol (a)* 62, 589–596
- Iliev M, Sendova-Vassileva M (1995) Selective laser excited of rare-earth luminescence spectra. In: Marfunin AS (ed.) *Advanced Mineralogy*. Springer Verlag, Berlin, 2, pp 136–138
- Imbusch MD (1978) Inorganic luminescence. In: Lumb MD (ed.) *Luminescence Spectroscopy*. Academic Press, London, pp 1–92
- JainVK (1978) Thermoluminescence glow curves and spectrum of zircon (sand). *Bull Minéral* 101, 358–362
- Jones AP, Wall F, Williams CT (1996) *Rare Earths Minerals: Chemistry, origin and ore deposits*. Chapman & Hall, London, Mineral Soc Ser 7, pp 372
- Kempe von U, Trinkler M, Wolf D (1991) Yttrium und die Seltenerdphotolumineszenz natürlicher Scheelite. *Chem Erde* 51, 275–289
- Kirsk Y, Townsend PD (1987) Electron and hole centers produced in zircon by X-irradiation at room temperature. *J Phys C: Solid State Phys* 20, 967–980
- Kiessling J, Scharmann A (1975) Thermally stimulated effects of rare-earth doped CaF₂. *phys stat sol (a)* 32, 459–466
- Khomyakov AP (1995) *Mineralogy of Hyperagpaitic alkaline Rocks*. Clarendon Press, Oxford, pp 223
- Koberski U, Keller J (1995) Cathodoluminescence observations of natrocarbonatites and related peralkaline nephelinites at Oldoinyo Lengai. In: Bell K, Keller J (eds.) *Carbonatite Volcanism. Oldoinyo Lengai and the petrogenesis of natrocarbonatites*. Springer Verlag, Berlin, pp. 87–99
- Kolbe WF, Smakula S (1961) Anisotropy of color centers in calcite. *Phys Rev* 124, 1754–1757
- Lapraz D, Baumer A (1981) Chloroapatite, Ca₅(PO₄)₃Cl: Thermoluminescent properties. *phys stat sol (a)* 68, 309–319
- Lapraz D, Baumer A (1983) Thermoluminescent properties of synthetic and natural fluoroapatite, Ca₅(PO₄)₃F. *phys stat sol (a)* 80, 353–366
- Lapraz D, Iaconi P (1976) On some luminescent and optical properties of synthetic calcite single crystals: *phys stat sol (a)* 36, 603–616
- Larsen AO (1996) Rare earth minerals from the syenite pegmatites in the Oslo region, Norway. In: Jones AP, Wall F, Williams CT (eds) *Rare Earths Minerals: Chemistry, origin and ore deposits*. Chapman & Hall, London, Mineral Soc Ser 7, pp 151–166
- Levrenz HW (1950) *An introduction to luminescence of solids*. John Wiley, New York, pp 559
- Lipin BR, McKay GA (1989) *Geochemistry and Mineralogy of rare earth elements*. Mineral Soc Amer, *Rev Mineral* 21, pp 348
- Long JVO, Agrell O (1965) The cathodo-luminescence of minerals in thin section. *Mineral Mag* 34: 318–326

- Machel HG, Mason RA, Mariano AN, Mucci A (1991) Causes and emission of luminescence in calcite and dolomite. In: Baker CE, Kopp OC (eds.) Luminescence microscopy and spectroscopy: qualitative and quantitative applications. Soc. Sedim. Geol., Short course, Dallas, 25, pp 9–25
- Mariano AN (1978) The application of cathodoluminescence for carbonatite exploration and characterization. Proc 1st Inter Symp Carbonatites Juhno 1976, Poços de Caldas, Brasil, pp 39–57
- Mariano AN (1988) Some further geological application of cathodoluminescence. In: Marshall DJ (ed.) Cathodoluminescence of geological Materials. Unwin Hyman, Boston, pp 94–123
- Mariano AN (1989) Cathodoluminescence emission spectra of rare earth element activators in minerals. In: Lipin BR, McKay GA (eds.) Geochemistry and Mineralogy of rare earth elements. Mineral Soc Amer, Rev Mineral 21, pp 339–348
- Mariano AN, Ring PJ (1975) Europium activated cathodoluminescence in minerals. Geoch Cosmochim Acta 39, 649–660
- Mariano AN, Roeder PL (1989) Wöhlerite: chemical composition, cathodoluminescence and environment of crystallization. Can Mineral 27, 709–720
- Marfunin AS (1979) Spectroscopy, luminescence and radiation centers in minerals. Springer-Verlag, Berlin, pp 352
- Marshall DJ (1988) Cathodoluminescence of geological Materials. Unwin Hyman, Boston, pp 146
- Mason RA, Mariano AN (1990) Cathodoluminescence activation in manganese bearing and rare earth bearing synthetic calcites. Chem Geol 88 191–208
- McKay GA (1989) Partitioning of rare earth elements between major silicate minerals and basaltic melts. In: Lipin BR, McKay GA (eds.) Geochemistry and Mineralogy of rare earth elements. Mineral Soc Amer, Rev Mineral 21, pp 45–77
- Medlin WL (1964) Trapping centers in thermoluminescent calcite. Phys Rev 135, A1770–A1779
- Medlin WL (1967) Color center growth curves in calcite. J Phys Chem Solids 28, 1725–17333
- Merz JL, Pershan PS (1967) Charge conversion of irradiated rare-earth ions in calcium fluoride. Physic Review 162, 217–247
- Mitchell RH, Xiong J, Mariano AN, Fleet ME (1997) Rare-earth-activated cathodoluminescence in apatite. Can Mineral 35, 979–998
- Monod-Herzen G (1966) Luminescence. Dunod, Paris, pp 278
- Morozov AM, Morozova LG, Trefimov AK, Feofilov PP (1970) Spectral and luminescent characteristics of fluoroapatite single crystals activated by rare earth ions. Optika i spektroskopia 29, 590–596
- Nakagawa M, Fukunaga K, Okada M, Atobe K (1988) Lattice defects in thermoluminescent calcite. J Lumin 40&41, 345–346
- Nambi KSV, Bapat VN, Ganguly AK (1974) Thermoluminescence of CaSO₄ doped with rare earths. J Phys C: Solid State Phys 7, 4403–4415
- Ohnenstetter D, Cesbron F, Rémond G, Caruba R, Claude JM (1991) Emissions de cathodoluminescence de deux populations de zircons naturel: tentative d'interprétation. C R Acad Sci Paris 313, 641–647
- Pringsheim P (1949) Fluorescence and phosphorescence. Wiley, New York, pp 479
- Rémond G (1977) Applications of cathodoluminescence in mineralogy. J Lumin 15: 121–155
- Rémond G, Blanc Ph, Cesbron F, Ohnenstetter D, Rouer O (1995) Cathodoluminescence of rare earth doped zircons. Part II: relationship between the distribution of the doping elements and the contrasts of CL images. Scanning Microscopy, suppl. 9: 57–76
- Rémond G, Cesbron F, Chapoulièr R, Ohnenstetter D, Roques-Carmes C, Schvoerer M (1992) Cathodoluminescence applied to the microcharacterization of mineral materials: a present status in experimentation and interpretation. Scanning Microscopy 6: 23–68
- Rémond G, Phillips M, Roques-Carmes C Importance of instrumental and experimental factors on the interpretation of CL data from wide band gap materials. (this Vol.)
- ReisfeldR, Gaft M, Boulon G, Panczer G, Jørgensen CK (1996) Laser-induced luminescence of rare-earth elements in natural fluor-apatites. J Lumin 69: 343–353
- Roeder PL, Mac Arthur D, Ma XP, Palmer GL, Mariano AN (1987) Cathodoluminescence and microprobe study of rare-earth elements in apatite. Amer Mineral 72: 801–811

- Sippel RF, Glover ED (1965) Structures in carbonate rocks made visible by luminescence petrography. *Science* 167: 677–679
- Smith JV, Stenstrom RC (1965) Electron-excited luminescence as a petrologic tool. *J Geol* 73: 627–655
- Tanabe S, Suzuki K, Soga N, Hanada T (1995) Mechanics and concentration dependence of Tm^{3+} blue and Er^{3+} green up-conversion in codoped glasses by red-laser pumping. *J Lumin* 65, 247–255
- Tarashchan AN (1978) Luminescence of minerals. Nauk Dumka, Kiev, pp 296 (in russian)
- Tarashchan A, Waychunas G (1995) Interpretation of luminescence spectra in terms of band theory and crystal field theory. In: Marfunin AS (ed.) *Advanced Mineralogy*. Springer Verlag, Berlin, 2, pp 124–135
- Taylor RP, Pollard PJ (1996) Rare earth element mineralization in peralkaline systems: the T-zone REE-Y-Be deposit, Thor Lake, Northwest Territories, Canada. In: Jones AP, Wall F, Williams, CT (eds) *Rare Earths Minerals: Chemistry, origin and ore deposits*. Chapman & Hall, London, Mineral Soc Ser 7, pp 167–192
- Tyson RM, Hemphill WR, Theisen AF (1988) Effect of the W:Mo ratio on the shift of excitation and emission spectra in the scheelite-powellite series. *Amer Min* 73, 1145–1154
- Van Uitert LG, Iida S (1962) Quenching interactions between rare-earth ions. *J Chem Phys* 37, 986–992
- Visocekas R, Ceva T, Lapraz D, Iaconni P, Lefaucheux F (1973) Cathode-ray-excited luminescence and thermoluminescence of a synthetic calcite monocrystal. *phys stat sol (a)* 15, 61–66
- Vlassov KA (1966) Geochemistry and mineralogy of rare elements and genetic types of their deposits. vol II mineralogy of rare elements. Israel Program of Sci Translations, Jerusalem, pp 916
- Wall F, Mariano AN (1996) Rare earth minerals in carbonatites: a discussion centred on the Kangankunde carbonatite, Malawi. In: Jones AP, Wall F, Williams, CT (eds) *Rare Earths Minerals: Chemistry, origin and ore deposits*. Chapman & Hall, London, Mineral Soc Ser 7, pp 193–225
- Warwick CA (1987) Recent advances in scanning electron microscope cathodoluminescence assessment of GaAs and InP. *Scanning Microscopy* 1: 51–61
- Waychunas GA (1988) Luminescence, X-ray emission and new spectroscopies. In: Hawthorn FC (ed.) *Spectroscopic methods in mineralogy and geology*. Mineral Soc Amer, *Rev Mineral* 18, pp 639–698
- Wybourne BG (1965) *Spectroscopic properties of rare earths*. Wiley, New York, pp 236
- Yaccobi BG, Holt DB (1990) *Cathodoluminescence microscopy of inorganic solids*. Plenum Press, New York, pp 292
- Yang B, Luff BJ, Townsend PD (1992) Cathodoluminescence of natural zircons. *J Phys Condens Matter* 4: 5617–5624

The Status of the Standards Program of the Society for Luminescence Microscopy and Spectroscopy

DONALD J. MARSHALL, OTTO C. KOPP

1

Introduction

The use of the cathodoluminescence (CL) technique is now routine in a large number of laboratories in the earth sciences and related fields. The investigators use a variety of systems for producing the CL and for recording the results, either as photographs or as spectra. Differences exist and the time seemed appropriate to begin to exchange standard samples on a large scale. Any interchange of standards in the past has been only among a small group of investigators.

2

Society for Luminescence Microscopy and Spectroscopy Committee

The Society for Luminescence Microscopy and Spectroscopy (SLMS) formed a Standards Committee whose purpose was to develop a standards program. The results of the work of this committee have been disseminated in two unpublished reports (SLMS 1994, 1995) which have been circulated in limited numbers to those SLMS members who participated in the standards program and to others who have purchased them. A paper has been presented on a portion of this work (Hanchar and Marshall 1995).

The committee decided that two types of standards were required for the initial phase: (1) a standard for CL systems with spectral acquisition capability; (2) a standard for CL systems with photographic recording.

3

Standard for Cathodoluminescence Systems with Spectral Acquisition Capability

The importance of obtaining spectra of CL emission has been well documented and there are many examples in the literature (Mariano 1989; Walker and Burley 1991; Ponahlo 1989; Hemming et al. 1989). The major elements of each of the systems are:

- The method of generating the CL
- The means of coupling the CL emission to the spectral analyzer
- The type of spectral analyzer
- The type of photon detector
- Any correction used for the system spectral response

There are a large number of options for each of these elements and none of the laboratories participating in the survey had identical or even closely similar systems.

The performance characteristics that are generally of interest include resolution, wavelength accuracy, transmission and detection variation with wavelength, signal-to-noise ratio, and total spectral acquisition time. At this stage of the program, comparisons of absolute signal strengths among the participating laboratories was not considered.

A useful standard for comparing/evaluating these characteristics is one whose spectrum includes both peaks with multiplets and peaks covering a wide range of the spectrum. We were fortunate to obtain a satisfactory sample in the form of a synthetic zircon doped with dysprosium. The CL emission spectrum from this sample contains multiplets in the 485 and 575 nm regions and has a number of other peaks extending to 750 nm and higher. These zircons were prepared by Dr. John Hanchar at Rensselaer Polytechnic Institute (Hanchar 1996).

Circulation of a single sample was not considered practical so instead we circulated individual crystals from a large batch, grown at the same time under identical conditions. They contain about 1.4 wt% Dy. The crystals are approximately 1 mm in maximum dimension. Spectra were obtained by Hanchar on four of the crystals under nearly identical conditions and portions of these are reproduced as Figs. 1 and 2. The agreement of peak wavelengths among these four crystals is excellent (within 0.04 nm for the 579.8 nm peak), even though the absolute intensities varied by more than a factor of 10. On the basis of this, we concluded that the crystals from this batch had the requisite uniformity.

A total of eleven laboratories returned spectra in the initial phase. Two examples of the spectra are shown in Figs. 3 and 4, and all of the spectra are reproduced in the SLMS report referenced. Four additional laboratories returned spectra later and these results will be issued as an addendum.

The SLMS does not presume to say what the "correct" values are for the wavelengths of the various peaks observed or for any other aspects of the results. Our function is simply to report the data in a format which facilitates interlaboratory comparisons.

Some laboratories showed data recording down to 300 nm but the lowest peak wavelength actually reported is 414 nm. The highest peak wavelength reported is 761 nm, although some laboratories showed data recording to 850 and even 900 nm. The principal Dy peaks at approximately 485 and 575 nm were observed by all.

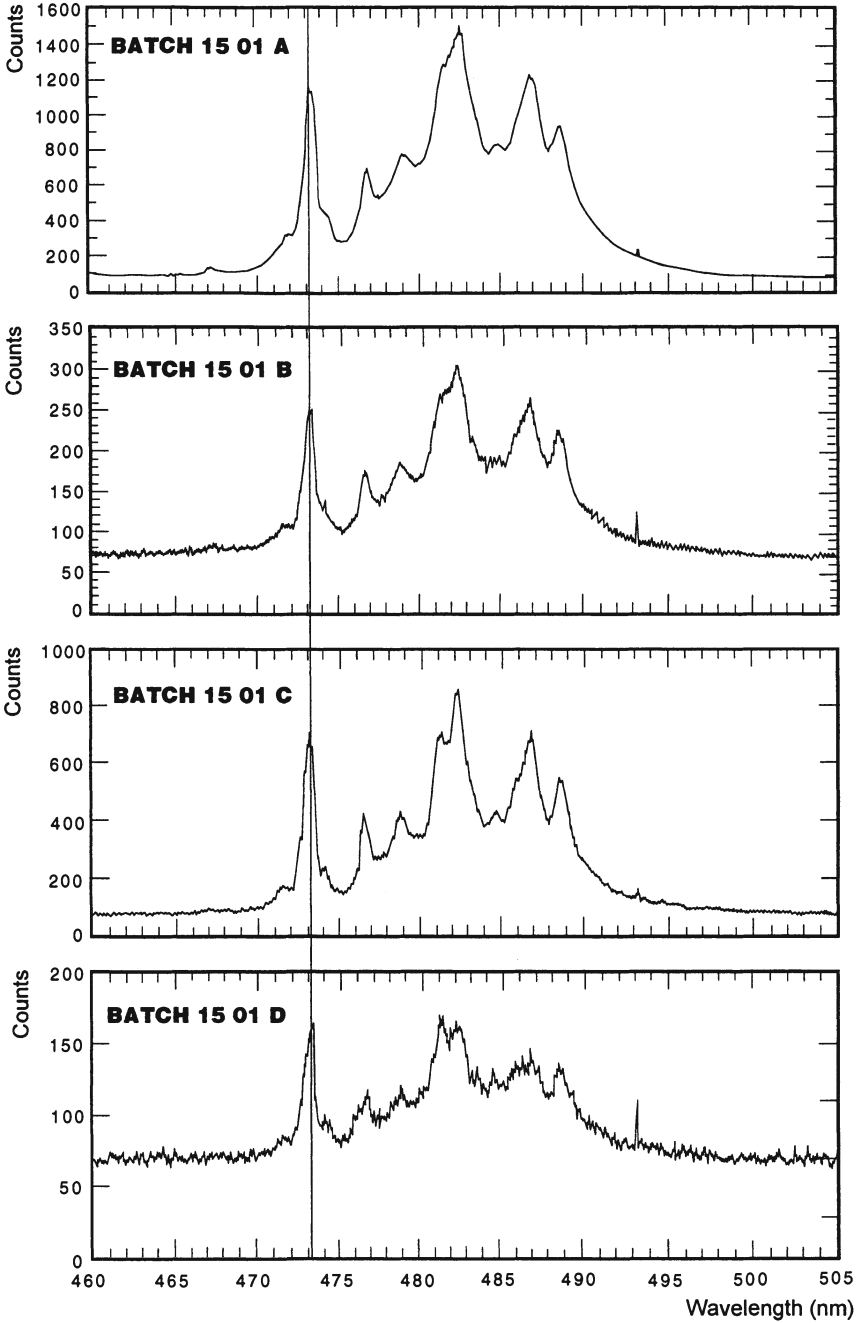


Fig. 1. Horizontal expansion of the spectrum in the 485 nm region for four of the synthetic zircons, selected at random, showing the uniformity of the spectral pattern, even at widely differing signal intensities

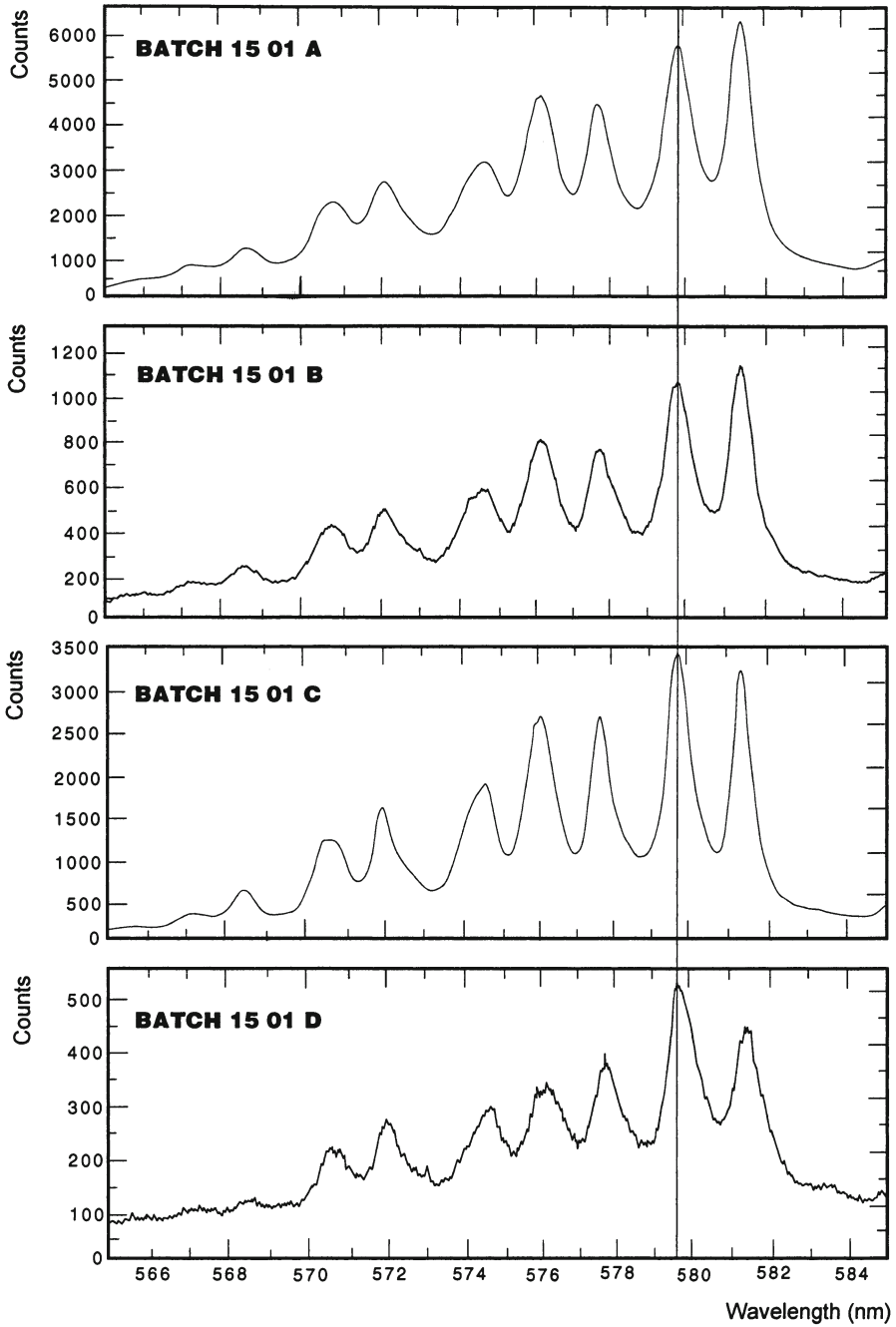


Fig. 2. Horizontal expansion of the spectrum in the 575 nm region for four of the synthetic zircons, selected at random, showing the uniformity of the spectral pattern, even at widely differing signal intensities

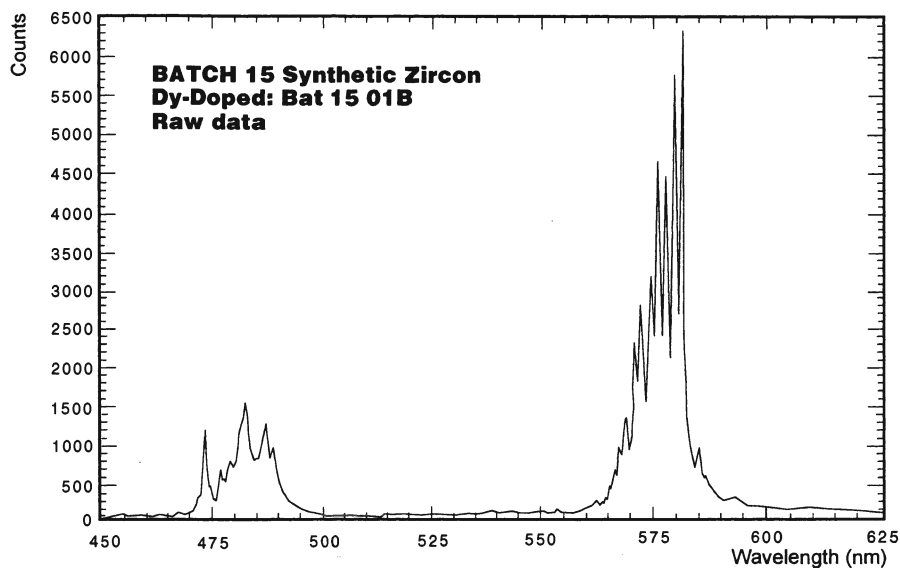


Fig. 3. Example of Dy-doped zircon spectrum on instrument with high resolution

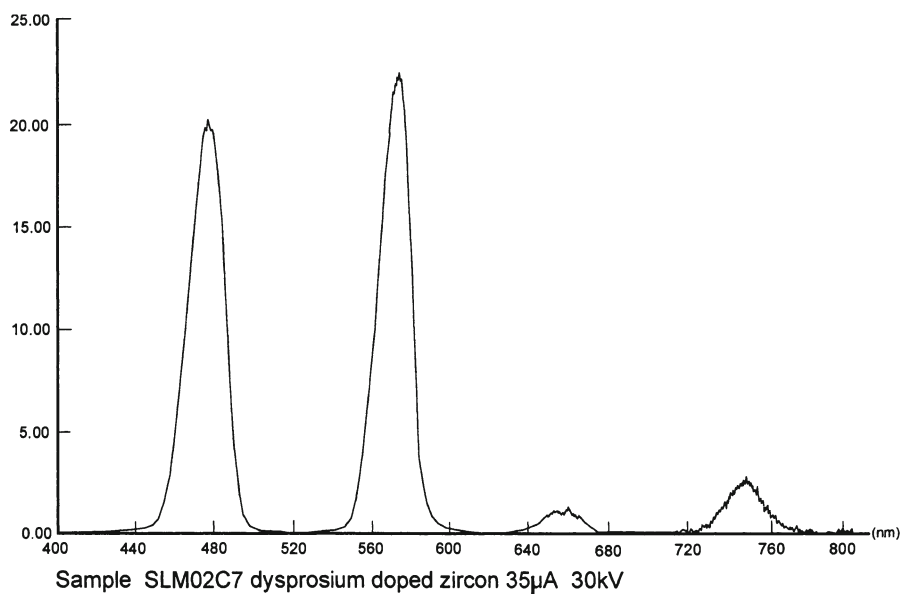


Fig. 4. Example of Dy-doped zircon spectrum on instrument operated at low resolution, showing peaks at longer wavelengths

3.1 Results

The results with respect to the five important performance characteristics are as follows.

3.1.1 Resolution

This characteristic was judged qualitatively on the basis of how well the major narrow bands at approximately 485 and 575 nm were resolved. Two of the participants identified eight separate peaks in the multiplet at 485 nm and either eight or nine peaks in the 575 nm multiplet. Four of the participants provided spectra which showed only one peak in each of these regions and no evidence of a multiplet. The remaining five participants provided spectra which showed evidence of a multiplet.

The signal-to-noise ratio of all of the submitted spectra with only one peak in the 485 and 575 nm regions was high enough that it appeared that participants might have changed their operating parameters (decreasing slit sizes) to obtain better resolution at a reduced sensitivity if their systems allowed for this.

3.1.2 Wavelength Accuracy

The wavelengths for the most intense signal in the two major narrow bands were compared. For the 485 nm band, the peak wavelength varied between 476 and 489 nm, a difference of 13 nm. This is a large variation, considering the wavelength accuracies presumed by the individual laboratories. There was no obvious correlation of these differences with resolution. The two systems with the highest resolution reported wavelengths of 481 ± 1 nm for the most intense peak. The two extreme values – 476 and 489 nm – were obtained on systems that showed only a single peak in the multiplet.

3.1.3 Transmission and Detection Variations

The systems contain many optical elements including the viewing window on the CL system (usually leaded glass with the possibility of contaminant coating of the surface on the vacuum system side), the microscope with its lenses, mirrors, prisms, etc., the coupling to the spectral analyzer (fiber optics in most cases but direct projection in two instances), the elements of the spectral analyzer, and the detector. Each of these has a transmission function (intensity vs wavelength) or detector function and the overall response is a superposition of all of these. We tested for variations in overall relative response by tabulating the ratio of the peak maxima for the 575 and 485 nm narrow bands (Table 1). This ratio varied between 0.6 and 3.9 for the 11 participants.

Table 1. Relative peak heights for peak maxima in 485, 575, and 660 nm regions

Laboratory	Detector	485	575	660	575/485
A	PMT	1	0.9	0.02	0.9
B	ARRAY	1	0.6	0.01	0.6
C	ARRAY	0.7	1	0.04	1.4
D	PMT	0.9	1	0.04	1.1
E(raw)	PMT	0.96	1	0.02	1.04
E(corr.)	PMT	0.8	1	0.04	1.25
F	ARRAY	1	0.9	0.03	0.9
G (raw)	PMT	1	0.76	0.03	0.76
G (corr.)	PMT	0.66	1	0.04	1.5
H	ARRAY	0.25	1	(*)	3.93
I	PMT	0.89	1	0.05	1.12
J	PMT	0.72	1	0.04	1.38
K	PMT	0.72	1	0.03	1.38

(*)This region was not recorded; PMT, photomultiplier tube; ARRAY, intensified diode array or unintensified CCD array; (raw), raw data; (corr.), data corrected for transmission function.

3.1.4

Signal-to-Noise

Absolute signal intensities are not comparable from the information provided. The noise levels on the spectra were less than 2% of the maximum peak intensity for all spectra and less than 1% for the majority of the spectra.

3.1.5

Spectral Acquisition Time

Spectral acquisition times ranged from a low of 0.24 s to a high of 4.2 min. One laboratory reported that the intensity decreased appreciably within the first 100 ms of electron bombardment and then became stable. No other laboratory commented on this aspect of performance. There are many examples of materials which exhibit CL which decays or fades with time, so a system with a short acquisition time is an asset.

3.1.6

Discussion

3.1.6.1

Calibration

Two different types of calibration are considered, transmission function and wavelength.

Transmission function calibration is used here in the sense of relative transmission, i.e., how does the transmission at wavelength "x" compare with that at

wavelength “y”? In an ideal system, they would be equal and variations in peak intensities in recorded spectra would reflect real differences in the emission from the sample at these various wavelengths. In an actual system, the transmission may vary widely over the recorded spectrum and the relative peak intensities would reflect this.

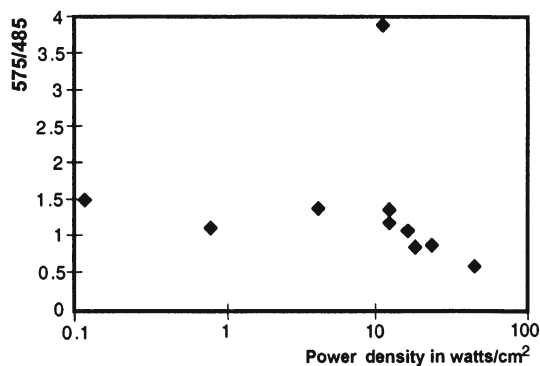
Transmission calibration involves use of a light source in which the relative intensities are known over a broad range of wavelengths. When this same source is measured on a candidate instrument, the observed spectrum, divided by the known spectrum, provides a relative transmission function. Three investigators reported the use of a tungsten lamp for making such a calibration.

Transmission function variations are normally associated with the optical system/detector components; but Steele (1994) has stated that relative peak intensities can also be a strong function of current density and he refers to unpublished data for olivine in which three peaks are seen at lower currents and only two at higher currents. This is clearly a different effect from transmission function variations but if it is present it might be misinterpreted in this way. No theory for this correlation has been presented to our knowledge and no evidence has been cited that this effect is important in the synthetic zircons; but allowance must be made for the possibility that there are apparent variations in transmission function which are actually associated with differing current densities. Power densities were calculated from the data provided in this program and ranged from 0.11 to 106 W/cm². There is no apparent correlation between power density and transmission for these data (Fig. 5).

Relative peak heights may also be a function of the crystal orientation in some minerals. No attempt was made to control this parameter but this will be addressed in future work.

Wavelength calibration is the calibration of the wavelength scale itself and would ideally be done with a series of very narrow peaks located across the spectrum. A mercury lamp makes a very convenient source for wavelength calibration and two investigators reported the use of such a lamp for calibration. It is possible that other investigators did either wavelength or transmission function calibrations but did not report it.

Fig. 5. Plot of ratio of peak maxima in 575 nm region to peak maxima in 485 nm region versus power density. There is no apparent correlation



CORRELATION OF 575/485 INTENSITY RATIO WITH POWER DENSITY

3.1.6.2

Other Considerations on Wavelength Accuracy

We considered that another possible reason for this difference in the peak wavelength of a complex multiplet might be due to the resolution differences. A test of this was made by mathematically degrading the resolution of the spectra provided by one of the participants with the highest resolution (Fig. 2). The original data was available for intensity at 0.05 nm intervals. We averaged these data points, using a 3 point, 9 point, 27 point, and 81 point average, and replotted the spectra. This is roughly equivalent to increasing the slit sizes by these amounts. Even for the convolved spectra using the 81 point average, which gives only an indication of a multiplet being present, the peak wavelength shift is only about 1 nm.

There will also be a wavelength shift associated with transmission differences. To estimate the magnitude of this effect, we assumed a relative transmission function that decreased linearly from a value of 1 at 700 nm to a value of 0.5 at 400 nm and multiplied the data for the 81 point average by this. When the convolved spectra were replotted, the shift in the peak maximum was less than 0.05 nm. This effect may be important for very broad band peaks but appears not to be an explanation for the wavelength differences observed in this sample.

So we conclude that the peak wavelength variations reported are not due to resolution differences and do truly represent significant wavelength scale calibration differences among the 11 participants.

3.1.6.3

Need for Wavelength Accuracy

One need not generally make an argument for the intrinsic value of having correct wavelength values. In practical terms, however, identification of major activator impurities such as Sm and Dy in zircon can usually be done even with incorrect calibrations. And the need for wavelength accuracy may be less for observing broad bands such as Mn produces in carbonates and feldspars. But there are situations, even with broad band peaks, where wavelength accuracy is needed for interpretation. As an example, Mariano et al. (1975) showed that both Fe²⁺ and Mn²⁺ can be activators in synthetic feldspars. Both elements produce CL spectra in the green region (Fe²⁺ 550±5 nm; Mn²⁺ 570±5 nm) and the wavelength accuracy needs to be much better than 20 nm to distinguish between these two possibilities. Furthermore, Sommer (1972) showed that the peak wavelength of Mn²⁺ emission in the calcite-magnesite solid solution series varies by almost 100 nm between the extremes. Future advances in these areas and in the use of CL for other studies in crystal physics will place a higher demand on wavelength accuracy.

3.2

Absolute Intensities and Signal-to-Noise Ratio

Absolute signal intensities depend on the experimental conditions of beam power density, etc., the efficiency of the coupling of the CL emission to the spectral analysis system, the duration of the signal collection, and the detector efficiency. All of the systems differed in these details. Absolute signal intensities are not directly comparable from the information supplied. However, the signal-to-noise

ratio of the raw spectra is a qualitative indicator of this – a poor signal-to-noise ratio being indicative of low signal intensities. Noise levels were less than 2% of the maximum peak intensity for all of the spectra submitted.

One of the reasons for resolution differences among different systems may be differences in the absolute signal intensities, necessitating the use of larger slits on those systems with lower sensitivity. With all spectrometer systems, there is a tradeoff between resolution and sensitivity.

3.3 Ionoluminescence

One investigator provided spectra obtained with ion bombardment (Yang et al. 1994). The multiplets are excellently resolved and the pattern of intensities of the 485 and 575 multiplets are closely similar to those obtained by Hanchar on the four crystals referred to previously. The wavelengths match to within 1.4 nm in the 575 multiplet and to within 1 nm in the 485 multiplet. Multiplet structure is quite apparent in the 650 and 750 nm peaks also. These spectra will be reproduced as part of the addendum that will be issued by the SLMS.

3.4 Suggestions for Future Work

Zircon is tetragonal and there may be some variation in spectra, depending on the direction of the emission (Cesbron et al. 1995). No provision was made for controlling this factor in this first round of investigation.

Steele's comment that the olivine spectrum depends on the power density should be further explored for the case of zircon.

Blanc (1996) has proposed the use of a YAG as a standard and has provided a large sample which is under evaluation at this time. The spectrum of this sample extends from at least 244 to 893 nm and higher.

Kihle (1996) has suggested that a cubic sample of YOS would also be a good choice and would minimize any possible orientation effects.

4 Limestone Standard and Cathodoluminescence Photography

Probably a majority of the CL practitioners in the earth sciences use CL for studying carbonates and results are reported via color photographs. There appear to be significant color variations among different laboratories and the exposure times differ widely. Some authors have stated that faintly luminescing specimens have only been observed with the hot cathode type of CL instrument (Barbin et al. 1989).

Some of the questions that arise in CL photography include:

1. Are the actual CL colors faithfully reproduced?
2. Are the colors a function of the exposure time?

3. What are the reasons for the differences in exposure time from laboratory to laboratory?

We decided to circulate a limestone standard to be photographed by participating laboratories in their normal fashion. Each laboratory furnished a full set of operating conditions and the final report provided comparisons of the features observed, the colors, and the exposure conditions.

In selecting the standard, we considered the following items to be important:

- The standard should exhibit large variations in CL intensity over the area of a thin section.
- The specimen CL should not be susceptible to rapid fading.
- The specimen, if possible, should be representative of real world specimens.

Several possibilities were considered and we finally selected a sample of a Mississippian limestone from the Burlington Formation in Iowa. The sample exhibits bright CL with elaborate cement zonation similar to that described by Meyers (1974). Professor William Meyers, SUNY Stony Brook, provided a hand specimen and from this we had about 20 thin sections prepared and distributed.

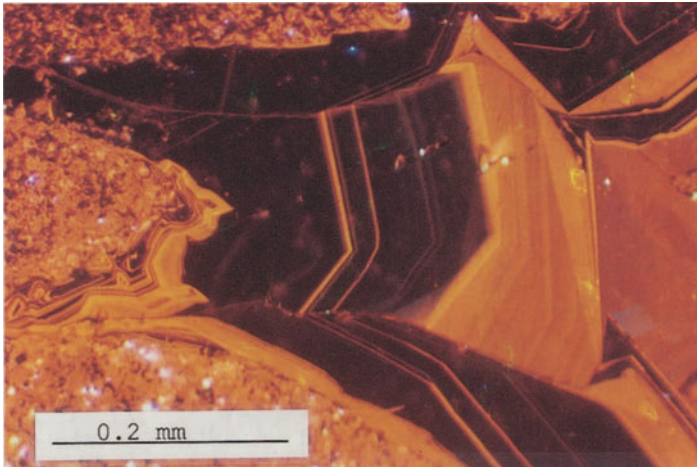
4.1 Results

Eleven responses, in the form of either color prints or color transparencies, were received. Each was accompanied by a full set of data on instrumentation used and on operating conditions.

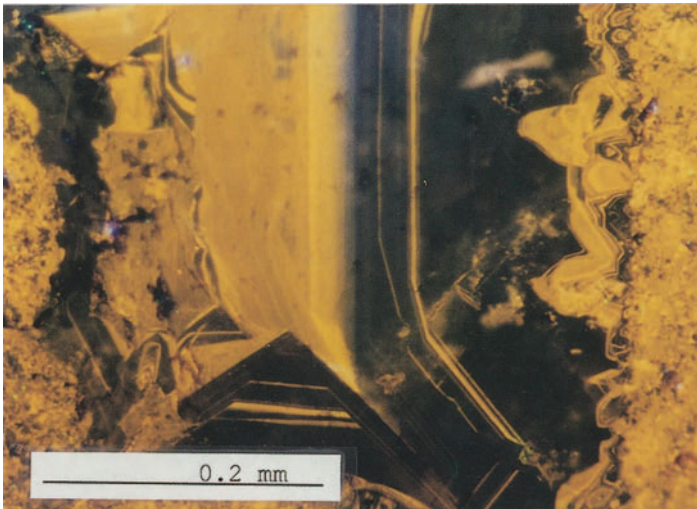
There has been informal discussion among CL investigators that different CL instruments with different beam parameters and different angles of incidence reveal different details. Dr. William Meyers examined most of the color prints submitted during this project and concluded that there were no significant differences among them with respect to the cement details that are revealed. However, there are obvious differences in the color recorded and in the exposure times.

Two examples of the photographic results are included herein (Fig. 6), illustrating the results from two different types of cold cathode instrument. (For the complete set of photos, please refer to the SLMS publication referenced previously.)

The color differences between these two examples are quite apparent. (It should be noted that both of these examples were furnished by the investigator as color prints and they were then mounted on the same sheet and copied by a conventional color copier. Some color shifts are inevitably introduced by the copying process but they are not significant in the opinion of the authors of this paper.) Yet it is presumed that the submitters would have approved these color reproductions if they had been submitted as part of a journal article. The present limitations of using conventional color photography to report CL results is illustrated by this pair of photos. The reasons for the color differences are not obvious.



Eric Hiatt
 U.Colorado at Boulder
 Technosyn, 8200 MKII
 Leitz
 Nikon M Plan ELWD
 210/0
 20X; 0.4
 Kodak Ektar Print
 ASA 1000
 Normal (C41)
 13.5 kV; 0.516 mA; 10 mm
 33.1 seconds



Michael Wagreich
 University of Vienna
 Luminoscope, ELM-2
 Leitz Orthoplan
 UM20; 20X; 0.33
 Kodak Gold Print
 200 ASA
 Normal development
 15 kV; 0.4 mA; 5 mm
 240 seconds

Fig. 6. Examples of color photographs from two authors using two different cold cathode instruments

4.2 Figure of Merit

The exposure times reported by the 11 participants varied from a short exposure time of 2.9 s to an exposure time as long as 10 min. The exposure time is a general indicator of the overall system transmission or system sensitivity. But part of the reason for the variations in exposure time is the variation in the experimental conditions selected by the various laboratories. Beam voltages ranged from 8 to 30 kV. Beam currents varied from 0.07 to 7 mA. Beam areas varied from 0.8 to 80 mm². Overall magnifications varied from 4× to 20×, and the film speeds

ranged from 160 to 1600 ASA. Because of these differing experimental conditions, a simple comparison of the exposure time is not too meaningful.

However, since we know how the exposure time is expected to vary with many of these parameters, we can develop an expression for the exposure time which includes the known variable parameters and the unknown factor, K , proportional to system transmission, which we refer to as a *figure of merit*. This expression is: (Please see the SLMS Report No. 2, 1995 for the detailed development of this equation.):

$$t = (1/K) * A * \left[\frac{M^2}{\{ASA * NA^2 * (V - 5000) * I\}} \right] \quad (1)$$

where t is the exposure time, V is the beam voltage, I is the beam current, NA is the numerical aperture of the objective lens, M is the overall magnification between the sample and the color print negative, ASA is the film speed, and A is the beam area on the sample.

As expected, the required exposure time decreases with higher beam current or beam voltage, larger ASA , and higher numerical aperture of the objective lens. The required exposure time increases with higher magnification and larger beam area.

The unknown quantity in this calculation is the figure of merit, K , which is proportional to the overall system transmission. K will be a function of many factors including window cleanliness, transmission of microscope objective and other elements of the microscope and camera, the number of surfaces that the beam must negotiate in traveling from the sample to the film, and others.

We rewrite Eq. (1) as

$$K = \left(\frac{A}{t} \right) * \left[\frac{M^2}{\{ASA * NA^2 * (V - 5000) * I\}} \right] \quad (2)$$

Since we know all the parameters on the right side of the equation, and since the exposure time is measured, we can use this equation to solve for K . When we do, we find a range of K from the lowest value of 0.00012 to the highest value of 0.28. This highest value is exhibited by the hot cathode system of Ramseyer (Ramseyer et al. 1989). The ratio of the highest to the lowest value among these 11 participants is 2300! This implies that if all the basic experimental parameters were identical, then the range in exposure times observed between the two extremes would be 2300 to 1.

There are some complications in this analysis. One is that the calculation of the figure of merit requires knowledge of the actual beam current to the sample. Beam current measurement is an inherent problem in a CL instrument, especially a cold cathode instrument, since current is usually measured in the current return line to the high voltage power supply and not at the sample itself. There are various loss processes such as aperture interception which can cause significant differences between the sample current and the total current. So a better estimate

of the figure of merit would be obtained if beam current to the sample itself could be measured. This is a difficult measurement to make because of the effects of secondary electrons, positive and negative ions in the discharge, and other factors. Some preliminary measurements indicate that the actual electron beam current reaching the sample in cold cathode instruments may be only a small portion of the total apparent beam current and this accounts, at least in part, for the differences observed in the figure of merit.

With the cold cathode systems, there will also be both low energy and high energy electrons and these will count equally in the measured beam current even though the high energy electrons are those primarily responsible for the observed CL.

Many investigators have noted that there is a fairly large latitude in exposure time for most films. Sometimes a factor of 2 difference in exposure time does not produce a striking difference in the photographs, especially with relatively brightly luminescing samples. As pointed out by Dr. Ramseyer, one of the reviewers of this paper, reciprocity is very important to consider. An Eastman Kodak publication (1996) states "Most color films require more than the normally calculated exposure when the lighting is unusually low. Also, the sensitivity difference between the many layers of color films can cause a color-balance shift," For some of their black and white films, at exposures of 10 s or more, the recommended adjustment for reciprocity is a factor of five to ten, i.e., the film sensitivity is reduced by this amount for the longer exposures. For many Kodak color films, actual reciprocity information is not presented but their use for exposures in the 10 s range or greater (Kodachromes and Ektachromes) or the 100 s range or longer (Gold and Royal Gold) is not recommended. Six of the 12 investigators reported exposure times greater than 10 s so the reciprocity correction would be important and it would reduce the apparent differences in transmission by a large factor. However substantial differences, greater than a factor of 100, would still remain in the figure of merit.

One investigator (Mindszenty) provided a set of four photographs, taken under identical conditions, but with different exposure times (5, 15, 30, and 60 s; Fujichrome 1600 ASA with push processing). The 30- and 60-s exposures revealed some details that were not apparent on the shorter exposures but the more significant fact is that the color of the brightly luminescing areas shifted from a red to a yellow with increasing exposure time. However, this shift was not so great as the differences seen in Fig. 1.

The importance of the correct reporting of color photograph type information will become increasingly apparent as more and more investigators adopt various color scanning/digitizing schemes.

4.3 Suggestions for Future Work

We hope to obtain one of the faintly luminescing carbonate samples that has been referred to (Barbin et al. 1989). It would also be of interest to obtain CL emission spectra from a standard carbonate sample. The wavelengths for calcite stated in the literature range from about 590 to 640 nm. For this purpose, a more

uniform, brightly luminescing sample with a known Mg concentration may be the best choice.

Acknowledgements. Scott Carpenter, U. Texas, Richardson, TX furnished one of the preliminary carbonate samples.; Ray Lund, Quality Thin Sections, Tucson, AZ, prepared the limestone thin sections; William Meyers, SUNY, Stony Brook, NY, furnished the limestone standard finally selected and reviewed all of the color photographs; John Hanchar provided the Dy-doped zircon standards. Dr. Karl Ramseyer emphasized the importance of film reciprocity.

References

- Barbin V, Ramseyer K, Decrouez D, Herb, R (1989) Marbres blancs: caractérisation par cathodoluminescence. C. R. Acad. Sci. Paris, t. 308, Série II, p. 861–866
- Blanc P (1996) Personal communication
- Cesbron F, Blanc P, Ohnenstetter D, Remond G (1995) Cathodoluminescence of rare earth doped zircons: Part I: Their possible use as reference materials. Scanning Microscopy Supplement 9, pp 35–56.
- Eastman Kodak Co (1966) Reciprocity and special filter data for Kodak films. Technical data sheet, E-31, 6 pages
- Hanchar JM (1996) A geochemical investigation of zircon. Ph.D. thesis, Rensselaer Polytechnic Institute, Troy, New York . 210 pages
- Hanchar JM, Marshall DJ (1995) Multi-laboratory results for the cathodoluminescence emission spectrum for a synthetic zircon standard. Scanning Microscopy Supplement 9, 1995. pp269–276
- Hemming NG, Meyers WJ, Grams JC (1989) Cathodoluminescence in diagenetic calcites: the roles of Fe and Mn as deduced from electron probe and spectrophotometric measurements. J. Sed. Pet., v. 59, p. 404–411
- Kihle J (1996) Personal communication
- Mariano AN (1989) Cathodoluminescence emission spectra of rare earth element activators in minerals In: Geochemistry and Mineralogy of Rare Earth Elements, Lipin, B.R., McKay, G.A. (eds.). Mineralogical Society of America (Washington, DC), Rev. Mineral. Vol. 21. p.45
- Meyers WJ (1974) Carbonate cement stratigraphy of the Lake Valley Formation (Mississippian) Sacramento Mountains, New Mexico. J. Sed. Pet., v. 44, p. 837–861
- Ponahlo J (1989) Mikrospektralphotometrie der Edelstein-Kathodolumineszenz. Zeitschrift der Deutschen Gemmologischen Gesellschaft, v. 18, 2/3, 63–84
- Ramseyer K, Baumann J, Matter A, Mullis J (1989) A cathodoluminescence microscope for low intensity luminescence. J. Sed. Pet., v. 59, 619–622
- Sommer SE (1972) Cathodoluminescence of carbonates, 1. Characterization of cathodoluminescence from carbonate solid solutions. Chemical Geology, v. 9, 257–273
- Standards Committee, Society for Luminescence Microscopy and Spectroscopy (1994) The CL emission spectrum of a Dy-doped zircon. Report of Investigation No. 1. 37 pages
- Standards Committee, Society for Luminescence Microscopy and Spectroscopy, 1995. Photography of the cathodoluminescence of a standard limestone. Report of Investigation No. 2. 26 pages
- Steele I (1994) Personal communication
- Walker G, Burley S (1991) Luminescence petrography and spectroscopic studies of diagenetic minerals. In: Luminescence microscopy and spectroscopy: qualitative and quantitative applications. Barker, C. E. and Kopp, O.C. (eds.). SEPM Short Course No 25 text
- Yang C, Homman NP-O, Johansson L, Malmquist KG (1994) Microcharacterizing zircon mineral grain by ionoluminescence combined with PIXE. Nuclear Instruments and Methods in Physics Research B 85 p. 808–814

Geologic Application of Cathodoluminescence of Silicates

KARL RAMSEYER, JOSEF MULLIS

1

Introduction

Cathodoluminescence from silicates has been known since the end of last century and early in this century, when Crookes (1879) and Goldstein (1907) observed that certain minerals, like zircon and quartz, emit light during bombardment with cathode-rays in evacuated glass tubes. Since then, a large number of silicates have been found to emit visible light during electron bombardment (Marshall 1988).

The application of cathodoluminescence (CL) in geology started in the 1960s when Long and Agrell (1965), Sippel (1965) and Smith and Stenstrom (1965) published articles on the possibilities of using CL for the characterization and better distinction of minerals and mineral modifications. Similarly, Geake and Walker (1966) and later Geake et al. (1972, 1973, 1977) used CL in studies of lunar rocks and meteorites. A major impact of CL in silicates was the observation by Sippel (1968) that authigenic quartz precipitated as cement in sandstones is non-luminescent and is thus clearly distinguishable from the blue- to red-luminescing, detrital quartz grains. Additional impact regarding the use of CL in silicates evolved continuously, with increasing knowledge of the causes of CL in different minerals, newer, more sophisticated instruments for spectral analyses (e.g., computer-assisted spectrometers with multichannel analyzers) and excellent CL detector systems for electron microscopes (e.g., higher resolution, lower detection limits). In the future, important developments for expanding the application of CL in silicates will come from several directions:

1. A major need is better knowledge of the cause of the most common “UV to bluish” CL color found in most silicates. Here, the difficulty centers around the characterization and quantification of defect centers such as oxygen vacancies, oxygen hole centers associated with substitutional elements and dangling oxygen bonds (Gorodec 1981; Marfunin 1978; Stevens Kalceff and Phillips 1995; Stevens Kalceff et al. 2000; Walker 1985).
2. In addition to the study of these poorly understood causes of CL, a more profound knowledge of the implications of trace element and other defect center concentrations and distributions deduced from CL observations is necessary (Machel and Burton 1991). This point is very important because CL provides a powerful opportunity to unravel the growth conditions and possible later alterations of minerals that are not recognizable at the micron

scale by other techniques. Otherwise, only qualitative descriptions of the CL characteristics are possible.

3. Similarly it would be of great importance to understand the physico-chemical factors that determine the distribution of CL activator elements in minerals that contain more than one structural position for a specific activator element. Again, this knowledge would help to determine more precisely the growth conditions and possible later alterations.

Generally speaking, it is not only necessary to unravel the causes of the different CL peaks in the minerals, which is the first step in understanding the CL characteristics, but, for a successful quantitative application of CL in mineral growth and recrystallization, the implications of the observed trace element and other defect center concentrations and distributions have to be better understood (Machel and Burton 1991).

At present, the most successful applications of CL in silicates are those cases in which differences in the CL appearance, or distribution, is adequate to solve a particular problem. This implies not only that a quantitative separation of different mineral species, or genetic groups of a specific mineral, is possible (e.g., Sears et al. 1990; Steele 1990), but also that paragenetic sequences, deformational effects (e.g., brittle-ductile) (Milliken and Laubach 2000; Mora and Ramseyer 1992), metamorphic grade (Steele 1990), low-high temperature modifications and polymorphism (Marshall 1988), crystal growth dynamics (Ramseyer and Mullis 1990; Steele 1990; Vavra 1990), reaction processes during firing of synthetic products (Mumenthaler et al. 1995) and radioactive fluid flow (Meunier et al. 1990; Ramseyer et al. 1989) are recognizable.

In this chapter selected examples are presented in which the use of CL is an integral part of understanding and/or recognizing precipitation/alteration processes not detectable at the micron scale/ppm level with any other technique. In order to decide whether CL may be adequate for a given problem, a short summary of the known causes of CL in silicates, including their spectral ranges and likely restrictions from the host chemical composition, will precede the presentation of the selected examples.

2

Causes of Cathodoluminescence in Silicates – Present Day Status

The search for the causes of CL in silicates started as early as the beginning of this century and is still under way. Numerous researchers were involved in this search, first with natural samples, then with experimentally grown, doped crystals, and only in the last few decades on an experimental-theoretical basis. CL caused by trace elements at cation position(s) in silicates is known, since these materials were tested for the use in luminescence screens and fluorescent lamps. A brief summary of these data is given (Tables 1, 2).

The difficulty in determining the cause of CL in silicates is that it may result from any of a combination of many factors, including: a large set of possible acti-

vator elements, variable chemistry (solid solutions), polymorphism, non-identical structural sites for an element, substitution of silica by hydrogen and defect structures such as broken Si-O bonds, oxygen vacancies and radiation-induced defects generated naturally or by the mode of observation, e.g., energetic radiation or heavy particle bombardment (Ramseyer et al. 1988; Stevens Kalceff and Phillips 1995). Most of these parameters are difficult to quantify on a micron scale at ppm concentrations (e.g., trace elements), are only detectable using bulk crystals (e.g., defect structures such as oxygen vacancies), or are difficult to produce in synthetic minerals.

As in carbonates, the transition-metal ion Mn^{2+} is a very prominent activator element in silicates, such as the plagioclases, amphiboles, pyroxenes, olivine, garnets and epidote. These minerals contain cations of the alkaline earth metals, e.g. Mg^{2+} , Ca^{2+} , Sr^{2+} and Ba^{2+} , in which the activator element Mn^{2+} substitutes easily for any of these ions. In cases in which more than one, non-identical crystallographic or structural site exists for the alkaline earth element, then various sites

Table 1. Cation position of common luminescence centers in silicates

Cation position	Luminescence center	Emission (nm)	n
K ⁺	Tl ⁺	280–285	2
	Pb ²⁺	285–295	2
	Mn ²⁺	570	1
Na ⁺	Tl ⁺	285	2
	Pb ²⁺	285	2
Cs ⁺	Tl ⁺	290–300	1
Ca ²⁺	Tl ⁺	280	1
	Pb ²⁺	280	1
	Mn ²⁺	550–640	18
	Cr ³⁺	745	1
Mg ²⁺	Mn ²⁺	580–665	6
	Ti ³⁺	630	1
	Cr ³⁺	680–698	4
Zn ²⁺	Mn ²⁺	510–540	3
Al ³⁺	Mn ²⁺	560–605	5
	Fe ³⁺	670–760	11
	Cr ³⁺	682–689	3
		860–880	1
	Ti ⁴⁺	390–440	3
Si ⁴⁺	Fe ³⁺	670–760	17
Zr ⁴⁺	Ti ³⁺	620	1
	Ti ⁴⁺	450–480	2
Sn ⁴⁺	Ti ⁴⁺	500–580	2

Data from Gorobec (1981), Marfunin (1979) and Boroznovskaya and Zhukova (1987). n, Number of silicates that show this luminescence center.

Table 2. Cation position of rare earth element luminescence centers in silicates

Cation position	Luminescence center	Emission (nm)	n	Reference
Ca ²⁺	Ce ³⁺	320–355	6	a,b
		340–380	7	a
		490	1	b
	Nd ³⁺	385	1	a
		Sm ³⁺	566–597	4
	600–641		4	a
	Eu ²⁺	395–470	10	a,c
		Eu ³⁺	616	1
	Gd ³⁺		312	3
		Tb ³⁺	440	1
	Dy ³⁺		546	1
		481	1	a
	Er ³⁺	575	1	a
		556	1	a
	Yb ³⁺	520–535	2	a
		Sm ³⁺	580–640	1
Tb ³⁺	430		1	a
	Dy ³⁺	540	1	a
Zr ⁴⁺		490	1	a
	Sm ³⁺	590	1	d
605		1	d	
Eu ²⁺	615	1	d	
	625	1	d	
Eu ³⁺	630	1	d	
	390	1	e	
Eu ³⁺	570	1	d	
	605–625	1	d	
Gd ³⁺	655–660	1	d	
	313	2	a,d	
Tb ³⁺	405	1	a	
	545–560	1	d	
Dy ³⁺	585	1	d	
	590	1	d	
Dy ³⁺	615–630	1	d	
	475–490	1	a,d,f	
Ho ³⁺	568.2	1	f	
	571.5	1	f	
Ho ³⁺	575	1	d,f	
	576	1	f	
Ho ³⁺	577.5	1	f	
	579.5–580	2	d,f	
Ho ³⁺	581.5–582	12	d,f	
	590	1	d	
Ho ³⁺	575–595	1	d	
	580	1	d	
Ho ³⁺	585	1	d	
	605	1	d	

n, Number of silicates that show this luminescence center.

^aGorobec (1981). ^bLaud et al. (1971). ^cMarfunin (1979). ^dTrofimov (1962). ^eOdin et al. (1991).

^fOhnenstetter et al. (1991).

exist also for the activator element and the CL signal may contain as many peaks as different sites exist (e.g., diopside, Walker 1985). In addition, different compositions of solid solutions, e.g., plagioclases (Geake et al. 1973), or polymorphic structures of the same mineral such as low- and high-temperature phases, e.g., wollastonite (Lange and Kressin 1955) may show different CL peak positions. In most alkaline earth metal containing silicates, the Mn^{2+} -activated CL emission peak is in the range of 510–665 nm (Table 1; Marshall 1988; Walker 1985; Gorobec 1981).

Two other transition metal ions, Fe^{3+} and Cr^{3+} , are known activator ions in silicates when substituting for Al^{3+} (Table 1; Marshall 1988; Walker 1985; Gorobec 1981). The most prominent silicates are the feldspar group (e.g., Telfer and Walker 1978; White et al. 1986), garnets (Walker 1985) and aluminosilicates (Marfunin 1979). In feldspars, ferric iron is located at the tetrahedral sites replacing Al^{3+} (Walker 1985; White et al. 1986), whereas in garnets and aluminosilicates, Cr^{3+} substitutes for octahedrally coordinated Al^{3+} . Both the ordering of the Al/Si distribution as well as the major element composition of the feldspar (Ab-An-Or) affect the position of the CL peak or peaks (e.g., Mora and Ramseyer 1992; Telfer and Walker 1978). Both Fe^{3+} - and Cr^{3+} -activated CL emission peaks in plagioclase and garnets, respectively, are in most cases at longer wavelengths and are often in the near-infrared region (Table 1).

A less common type of CL in silicates is caused by host elements of the mineral, like transition metals Ti^{4+} , Ti^{3+} and Mn^{2+} or the UO_2^{2+} -complex (Gorobec 1981; Marfunin 1979).

Heavy metal elements that can substitute for alkaline earth metals in silicates, such as copper, tin, thallium or lead, may also act as CL activators. Usually, however, either their occurrence and/or concentration is restricted to specific environments or the CL is in the non-visible part (UV) of the electromagnetic spectrum (Table 1; Boroznovskaya and Zhukova 1987; Gorobec 1981; Marfunin 1979; Mariano et al. 1973).

As in the case of carbonates and apatite, a number of rare earth ions, e.g., Ce^{3+} , Pr^{3+} , Nd^{3+} , Sm^{2+} , Sm^{3+} , Eu^{2+} , Eu^{3+} , Gd^{3+} , Tb^{3+} , Dy^{3+} , Er^{3+} or Ho^{3+} are CL activators in silicates such as zircon and feldspars (Table 2; Gorobec 1981; Marshall 1988 and references therein). In silicates with alkaline earth metals, the CL of rare earth element activation is often masked by the intense CL of Mn^{2+} . Silicates without alkaline earth metals, such as zircon, show a large variety of rare earth ion-activated CL (Blanc et al. 1994; Mariano 1989; Trofimov 1962). The emission of such CL is variable and found in the UV, visible and IR range of the electromagnetic spectra (Table 2; Blanc et al. 1994; Kirsh and Townsend 1988; Gorobec 1981; Laud et al. 1971; Marfunin 1979; Mariano 1989; Trofimov 1962).

In addition to these three groups of clearly defined activator elements, other causes must exist for CL colors in silicates in which no known or measurable trace element can be related to the CL signal, e.g., quartz, K-feldspar, kaolinite and zircon. Non-bridging oxygen hole centers or dangling Si-O bonds (Ramseyer et al. 1988; Stevens Kalceff and Phillips 1995), self-trapped excitons (Stevens Kalceff and Phillips 1995), aluminum substitution for silica (Speit and Lehmann 1982; Stevens Kalceff and Phillips 1995), lattice order (Zinkernagel 1978), or other point defects related to substitutional-interstitial element pairs (Demars et al. 1996;

Pagel et al. 1996; Stevens Kalceff and Phillips 1995), are proposed and/or have been proven as causes of CL in silicates.

Generally speaking, the CL of silicates is caused either by trace activator ions substituting for an element of the mineral, by defect centers involving oxygen or in a few cases by cations of the host mineral. Non-luminescence of silicates, by contrast, may be caused by a low concentration of activator elements or other defect centers, e.g., the activator element/defect center concentrations are below the detection limits of the instrument and/or applied technique, or the host minerals contain appreciable amounts of Fe^{3+} , Fe^{2+} , Ni^{2+} and Co^{2+} which act as a quencher of CL at room temperature (Marfunin 1979; Walker 1985), or the activator element is part of the host mineral, or present in an appreciable amount in the mineral, e.g., concentration quenching (Marfunin 1979).

3 Applications of Cathodoluminescence in Silicates – Examples

In silicates, CL can be used at different levels:

1. From a purely descriptive viewpoint without knowledge of the cause of CL. This application is adequate for a large number of studies in which phases or mineral generations need to be detected or distinguished, such as for quantification of minerals or the recognition and quantification of authigenic quartz, feldspar and kaolinite cement in sandstones or cataclastic systems, detection of trace element concentrations in zircon, recognition of brittle or ductile deformation, pressure solution or relict structures and recrystallization (Bjørkum 1996; Burley et al. 1989; Evans et al. 1994; Finch 1991; Finch and Walker 1991; Hearn 1987; Hopson and Ramseyer 1990; Houseknecht 1991; Marshall 1988; Matter and Ramseyer 1985; Milliken 1994; Odin et al. 1991; Owen 1991; Sippel 1968; Ramseyer et al. 1992a,b; Remond et al. 1992; Wenzel and Ramseyer 1992; Zinkernagel 1978).
2. Based on the causes and the concentration of the CL centers. Knowing the cause(s) of the CL and the activator concentrations may help to better determine the physico-chemical conditions of crystal formation and alteration, such as in the case of chemical zonations in zircons or forsterite (Halden et al. 1993; Steele 1995), the trace element signature of feldspars in plutonic metamorphic and sedimentary rocks (Götze et al. 2000), or the fenitization of igneous rocks, i.e. alkali metasomatism (Marshall 1988).
3. Based on results from artificially generated CL centers in synthetic or natural material under well defined physico-chemical conditions. Knowing the causes of the CL and its physico-chemical implications for crystallization or alteration are without any question the best and most valuable information which can be deduced from CL. Unfortunately, there exist only a few cases with such well-known causes of CL and clear indications for their occurrence, like the generation of CL in quartz and feldspar by radionuclides (Meunier et al. 1990; Owen 1988; Ramseyer et al. 1988), or the low intensity of Fe^{3+} -activated CL in lunar feldspars (Geake et al. 1977; Sippel and Spencer 1970).

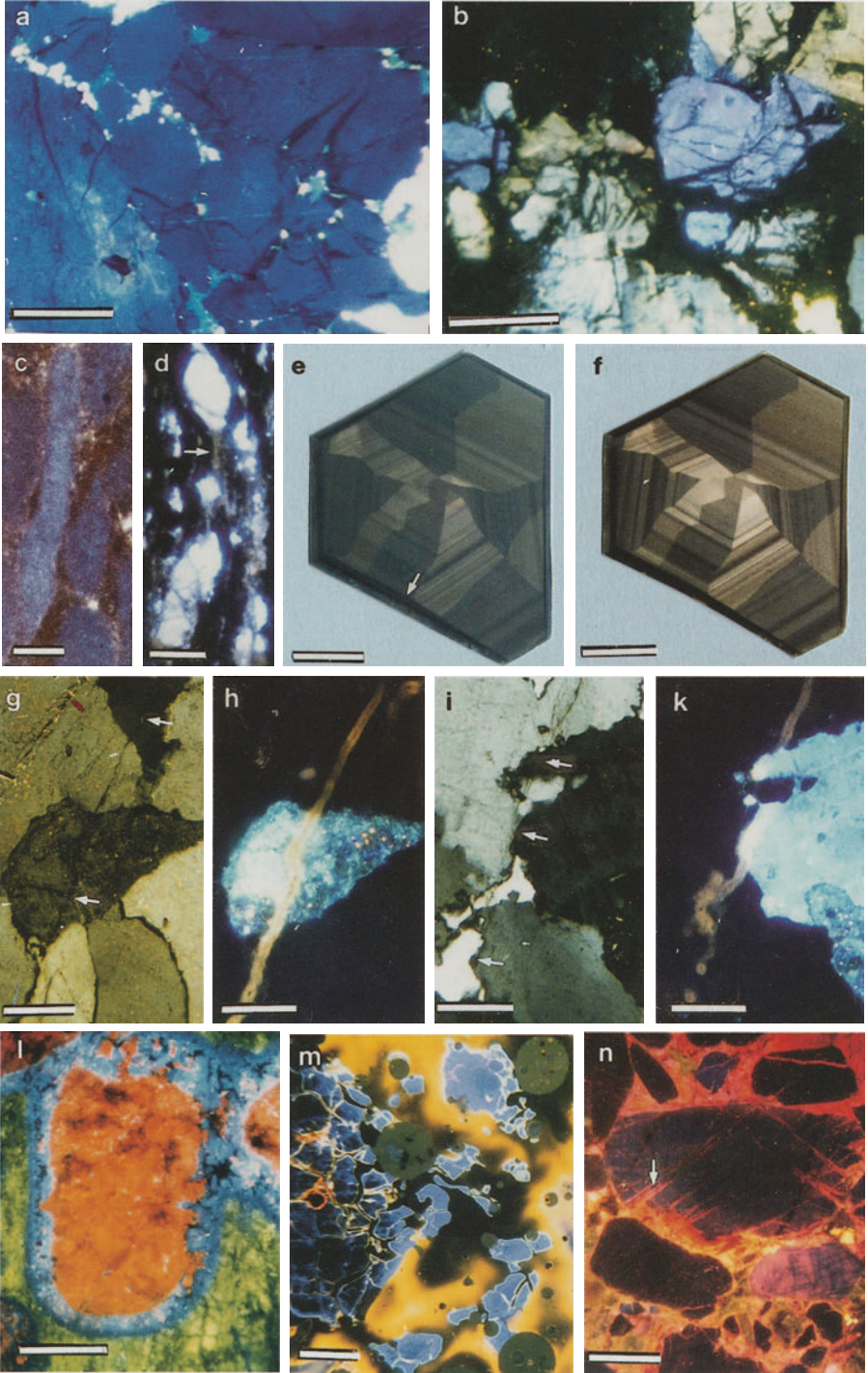
In most cases, either the cause of the CL or the implication of the occurrence and concentration of the activator element(s)/defect center(s) is unknown. The following typical examples of the application of CL to silicates will be presented with emphasis on the wide variety of studies in which CL may provide new insights. All of the photographs shown were made with the CL instrument at the Geological Department University of Bern, Switzerland (Ramseyer et al. 1989). This instrument is a "hot-cathode" instrument, which uses electrons generated by heating a tungsten filament. The operating conditions were 30 keV electron energy and 0.2–0.4 $\mu\text{A}/\text{mm}^2$ beam-current density. Luminescence characteristics were recorded on Ektachrome 400 color slide film and developed at 800 ASA. Exposure times ranged from 1 to 200 s depending on the magnification and CL intensity.

The most important application of CL is still in the field of clastic diagenesis to determine quantitatively the detrital composition and the provenance of the sandstones (Matter and Ramseyer 1985; Owen 1991; Richter and Zinkernagel 1975; Zinkernagel 1978; Zinkernagel 1992), the amount of quartz and feldspar cement (Burley et al. 1989; Houseknecht 1991; Milliken 1989; Ramseyer et al. 1993), the degree of pressure solution and compaction (Bjørkum 1996; Houseknecht 1991; Milliken 1994), and to visualize the albization process (Milliken et al. 1989; Ramseyer et al. 1992b) or the effect of brittle deformation on the destruction of porosity (Milliken and Laubach 2000; Fig. 1a,b). Good photomicrographs and quantitative assessments of the CL patterns on the above mentioned topics are given in the literature quoted and in Fig. 1.

Less commonly, CL is used in metamorphic petrology to unravel the deformation history and fluid migration during prograde and retrograde conditions. Deformation at higher P-T conditions may either be a brittle or a ductile process whereby the deformation generates either cracks or it is accomplished by grain boundary migration and recrystallization, respectively. CL is an excellent tool to distinguish these two deformation styles, which may act simultaneously, but independently, for different minerals. This latter effect is nicely shown in a sample from the Arnaball thrust, Scotland, in which quartz behaves ductilely (Fig. 1c) and K-feldspar brittlely (Fig. 1d).

Hydrothermal alteration of crystalline rocks is often more widespread and occurs at deeper levels than is easily recognized by normal petrography or chemical analyses of the minerals. Using CL, it is often easy to recognize the post-intrusion alteration sequence down to late stage hydrous alterations. The depth of these alterations may be greater than normally assumed, and in the case of the meteorite impact structure at Siljan (Sweden), CL shows that K-feldspar and plagioclase alteration occurs down to a depth of 4 km (Aldahan et al. 1988; Ramseyer et al. 1992a).

Not only are host rock alterations detectable with CL (Mora and Ramseyer 1992), but fluid migration pathways, fractures, etc., may record a complex paragenetic history of mineral growth and replacement. Detailed CL study of vein-quartz crystals in conjunction with other techniques (e.g., fluid inclusion microthermometry, stable isotope analyses of oxygen, trace element microchemical analyses) enabled Ramseyer and Mullis (1990) to relate the growth dynamics (Mullis 1991; Mullis et al. 1994) to the CL pattern found in individual quartz crystals from Alpine fissures (Fig. 1e,f). The most interesting points were that differ-



ent growth modes, i.e. continuous slow, discontinuous slow and discontinuous rapid, gave distinct CL patterns, which directly correlate with the activity of tectonic deformation in the Alpine region during crystal growth (Mullis et al. 1994). The example shown in Fig. 1e and 1f is a quartz crystal cut normal to the c-axis, showing oscillatory, sectoral and intrasectoral zonation, photographed at the beginning (Fig. 1e) and after 105 s (Fig. 1f) of electron bombardment. In addition, monochromatic CL photographs from a similar crystal from the same fissure revealed that the observed intensity variation is only present at 600 nm and not at 425 nm in the blue range (Barbin and Schvoerer 1997). The observed types of zonations are, based on Reeder's (1991) study of carbonate minerals, the result of a spatial difference in the luminescence center formation during crystal growth in a system far from equilibrium with high growth rates. This interpretation for quartz, in analogy to carbonates, fits well with the discontinuous slow growth of



Fig. 1. a CL photomicrograph of brittlely deformed quartz grains in a sandstone from the San Joaquin basin, California (Wildcat-well, Tenneco Schutte #1, 14589 ft). *Scale bar is 500 μm .* b CL photomicrograph of brittlely deformed K-feldspar (*blue*) and plagioclase (*white-yellow*) with non-luminescent fracture filling K-feldspar and albite, respectively, in a sandstone from the San Joaquin basin, California (Lakeside oil field, Tidewater KCL 36–35, 8452 ft). *Scale bar is 200 μm .* c CL photomicrograph of a ductilely deformed quartz in a sandstone, Arnaball thrust, SE Heilam, Scotland (UK). Note that the originally spherical grains are now elongated. *Scale bar is 100 μm .* d CL photomicrograph of a brittlely deformed K-feldspar in the same sandstone as shown in c. Note that the whitish luminescing K-feldspar is brittlely deformed and surrounded by low temperature authigenic K-feldspar (*arrow*). *Scale bar is 100 μm .* e CL photomicrograph of a fissure quartz from Gigerwald (Switzerland), with cut surface normal to the c-axis. The growth conditions deduced from fluid inclusion microthermometry are 300 °C, 170 MPa and a low-saline, aqueous, CO₂-containing solution. Note that growth is after the positive and negative rhombohedra and only the outermost part (*arrow*) of the crystal shows growth after the prisms. In addition, oscillatory and intrasectoral zoning is visible in the crystal grown after the rhombohedra. The cause of this intrasectoral zoning is twinning after the Brazil law. *Scale bar is 500 μm .* f CL photomicrograph of the same crystal as in e, but after 105 s of electron bombardment. Note that the CL color changed to gray-brown, but the CL intensity distribution is identical with that of the blue CL color in e. *Scale bar is 500 μm .* g Crossed-polarized photomicrograph of fractured Dala granite (*arrows*) from the Siljan impact structure (Central Sweden). *Scale bar is 250 μm .* h CL photomicrograph of the same field of view as in g. Note that the brown-luminescing zone engulfing the fracture is due to radiation damage and is visible in quartz (*black*) and plagioclase (*bluish-white*). *Scale bar is 250 μm .* i Crossed-polarized photomicrograph of fractured Dala granite (*arrows*) from the Siljan impact structure (central Sweden). *Scale bar is 250 μm .* k CL photomicrograph of the same field of view as in i. Note that the brown-luminescing zone engulfing the fracture is due to radiation damage and is visible in quartz (*black*) and K-feldspar (*light blue*). *Scale bar is 250 μm .* l CL photomicrograph of an alkali-feldspar granite shocked by a meteorite impact to 20–25 GPa, Araguinha impact crater, Brazil (from Engelhardt et al. 1992). Note that quartz luminesces with the typical *red color* (630 nm), whereas plagioclase and K-feldspar luminesces *yellow* and *blue*, respectively. *Scale bar is 200 μm .* m CL photomicrograph of a granite partially melted by lightning, Gotthard, Switzerland. Note that the *yellow-* and *bluish-luminescing* areas were previously plagioclase and quartz, respectively. *Scale bar is 500 μm .* n CL photomicrograph of a quartz sandstone intruded by a plutonic dyke with high-temperature-authigenic, red-luminescing quartz cement, Dala Sandstone, central Sweden. Note that the CL color of the detrital quartz grains is also partially altered from a “plutonic” *dark blue* to *red* (*arrow*). *Scale bar is 250 μm .*

the crystal, e.g., each increment seen under CL is a tectonically induced growth event due to a change of the PVT-chemical composition of the fluid in the fissure. These zonations are only present in the 600 nm region, where CL centers related to non-bonding Si-O exist. This shows that the oscillatory zonation contains zones of high and low growth rates (Reeder 1991) and therefore also high and low densities of structural defects, respectively.

Similarly, fluid flow through fractures may not only be detected by mineral growth, but also by radiation damage of the surrounding minerals like quartz, plagioclase (Fig. 1g,h) or K-feldspar (Fig. 1i,k; Meunier et al. 1990; Owen 1988; Ramseyer et al. 1989). In all cases, the energy and particle type can be determined by calculating the penetration depth of these particles into the mineral (Marmier 1983) and comparing these results with measured penetration depths from CL photographs (Owen 1988). Again, the observed color change to brown (650 nm, 1.88 eV, half-width 150 nm; Ramseyer et al. 1989) reveals that CL centers related to non-bonding Si-O were generated. This interpretation is confirmed by Stevens Kalceff and Phillips (1995) who assigned a CL peak at 1.91 eV to a non-bonding oxygen hole center from a non-OH precursor. As the generation of this CL center is time dependent, age determinations of the fluid flow may be possible, as postulated by Owen (1991) in the case of quartz with radiation-damage zones around zircon inclusions.

Growth zoning in silicates (quartz, feldspars, etc.) is a common feature not only for crystals formed in aqueous solutions but also crystallized from silicate melts (D'Lemos et al. 1997; Watt et al. 1997; Halden et al. 1993; Schneider 1993; Wenzel and Ramseyer 1992; Zinkernagel 1978). The zonation visible under CL may represent diffusion-controlled crystallization, where euhedral crystals form, mineral-melt disequilibria (D'Lemos et al. 1997), a process of resorption and crystallization or rapid dendritic growth where rounded crystals and crystals with embayments are generated (Watt et al. 1997; Schneider 1993). Other igneous structures, like exsolution lamellae, myrmekite formation or graphic structures are easily recognizable using CL and also easily set into genetic relationships with the genesis of the plutonic rocks (Hopson and Ramseyer 1990). Zonations in zircons (see also chapters by Gruner et al. and Poller et al., this Vol.) may reveal the chemical conditions, variability and kinematics during growth (Halden et al. 1993; Vavra 1990), or the history of the mineral through different erosional and metamorphic cycles. Recognition of a relict core or growth zones in zircon is especially important for U/Pb-dating in which distinct metamorphic events or the primary origin of the zircon is the target of dating. In addition, the CL characteristics and the oscillatory zonation of meteoritic forsterite may reveal crystallization conditions (e.g. growth from a melt or condensation from a vapor) during forsterite formation, thermal processing after crystallization and/or irradiation effects (Benstock et al. 1997; Steele 1995).

Single, catastrophic events, such as meteorite impacts (Fig. 1l) or vitrification by lightening (Fig. 1m), are other recognizable effects. Quartz formed under such conditions is typically characterized by red CL (630 nm, 1.94 eV, half-width 100 nm; Ramseyer 1990). This red CL is also present in clastic rocks where authigenic quartz cement forms during emplacement of a nearby plutonic dike or sill (Fig. 1n; Krynauw et al. 1994; Ramseyer et al. 1988). Based on the findings of

Stevens Kalceff and Phillips (1995), the cause of this red CL is the non-bonding oxygen hole center generated from precursor hydroxyl defect centers. This interpretation is consistent with electrodiffusion experiments showing that red CL is directly related to negatively charged particles which may diffuse through the large c-channels in high-quartz.

By increasing the temperature above the melting point of the common silicates, silicate glasses may be generated. This is often the case when lightning hits the ground in crystalline areas. Here, melting of the rock generates a glassy varnish which still clearly show the former distribution of minerals such as quartz, K-feldspar and plagioclase (Fig. 1m). Thus, partial mixing of silicate melts may be revealed by CL.

4

Conclusions

The application of CL to silicate minerals has great potential for all disciplines of earth and planetary sciences to unravel deformational, mineral alteration and mineral precipitation processes. The main limitation of CL of silicates is due to CL quenching by Fe^{2+} (Ni^{2+} , Co^{2+}). Minerals containing these ions as minor or major constituents may not be favorable for CL work, but testing is always the best way!

Acknowledgements. This project was carried out with funding provided by Swiss National Foundation (Grant No. 20-43128.95). The authors thank Stephen J. Burns for his helpful comments on earlier drafts of the manuscript. Reviews by Otto C. Kopp and Jens Götze led to significant improvements.

References

- AlDahan AA, Ramseyer K, Morad S, Collini B (1988) Low temperature alterations in granitic rocks from the Siljan Ring structure, central Sweden. In: Bodén A, Eriksson KG (eds) *Deep Drilling in Crystalline Bedrock*. Springer, Berlin, 1, pp 209–216
- Barbin V, Schvoerer M (1997) Cathodoluminescence et Géosciences. *Comptes Rendu Académie des Sciences, Paris, Sciences de la terre et des planètes, Série IIa*, 325:1–13
- Benstock EJ, Buseck PR, Steele IM (1997) Cathodoluminescence of meteoritic and synthetic forsterite at 296 and 77 K using TEM. *American Mineralogist* 82:310–315
- Bjørkum PA (1996) How important is pressure in causing dissolution of quartz in sandstones? *Journal of Sedimentary Research* 66:147–154
- Blanc P, Arbey F, Cros P, Cesborn F, Ohnenstetter D (1994) Applications de la microscopie électronique à balayage et de la cathodoluminescence à des matériaux géologiques (sulfates, carbonates, silicates). *Bulletin de la Société géologique de France* 165:341–352
- Boroznorskaya NM, Zhukova IA (1987) X-ray luminescence characteristics of potash feldspar from Kazakhstan rare-metal granite pegmatites. *Geochemistry International* 24:47–53
- Burley SD, Mullis J, Matter A (1989) Timing of diagenesis in the Tartan reservoir (UK North Sea): constraints from combined cathodoluminescence microscopy and fluid inclusion studies. *Journal of Marine and Petroleum Geology* 6:98–120
- Crookes W (1879) Contributions to molecular physics in high vacua. *Philosophical Transactions of the Royal Society of London* 170:641–662

- Demars C, Pagel M, Deloule E, Blanc P (1996) Cathodoluminescence of quartz from sandstones: Interpretation of the UV range by determination of the trace element distribution and of fluid inclusion P,T,X properties in authigenic quartz. *American Mineralogist* 81:891–901
- D'Lemos RS, Kearsley AT, Pembroke JW, Watt GR, Wright P (1997) Complex quartz growth histories in granite revealed by scanning cathodoluminescence techniques. *Geological Magazine* 134:549–552
- Evans J, Hogg AJC, Hopkins MS, Howarth RJ (1994) Quantification of quartz cements using combined SEM, CL, and image analysis. *Journal of Sedimentary Research* A64:334–338
- Finch AA (1991) Conversion of nepheline to sodalite during subsolidus processes in alkaline rocks. *Mineralogical Magazine* 55:459–463
- Finch AA, Walker DL (1991) Cathodoluminescence and microporosity in alkali feldspars from the Blå Måne So perthosite, South Greenland. *Mineralogical Magazine* 55:583–589
- Geake JE, Walker G (1966) The luminescence spectra of meteorites. *Geochimica et Cosmochimica Acta* 30:929–937
- Geake JE, Walker G, Mills AA (1972) Luminescence excitation by protons and electrons applied to Apollo lunar samples. In: Runcorn SK, Urey HC (eds) *The Moon*. International Astronomical Union, Symposium 47, 22.-26.4.1971, University of Newcastle upon Tyne, Reidel Publishing Company, Dordrecht, pp 270–297
- Geake JE, Walker G, Telfer DJ, Mills AA, Garlick GFJ (1973) Luminescence of lunar, terrestrial and synthesized plagioclase, caused by Mn^{2+} and Fe^{3+} . *Proceedings of the 4th Lunar Science Conference*, *Geochimica et Cosmochimica Acta* 3:3181–3189
- Geake JE, Walker G, Telfer DJ, Mills AA (1977) The cause and significance of luminescence in lunar plagioclase. *Philosophical Transactions of the Royal Society of London* A285:403–408
- Goldstein E (1907) Über das Auftreten roten Phosphoreszenzlichtes an Geissler'schen Röhren. *Bericht der Deutschen Physikalischen Gesellschaft* 598–605
- Gorobec B (1981) *Spectra of Luminescence of Minerals*. (in Russian) Ministry of Geology of the USSR, Moscow, 149 p
- Götze J, Krbetschek MR, Habermann D, Wolf D (2000) High-resolution cathodoluminescence studies of feldspar minerals. (this Vol.)
- Gruner T, Kempe U, Wolf D (2000) Relevance of cathodoluminescence (CL) for the interpretation of U-Pb zircon ages: an example from the Saxonian Granulite Complex. (this Vol.)
- Halden NM, Hawthorne FC, Campbell JL, Teesdale WJ, Maxwell JA, Higuchi D (1993) Chemical characterization of oscillatory zoning and overgrowths in zircon using 3 MeV μ -PIXE. *Canadian Mineralogist* 31:637–647
- Hearn PP (1987) A quantitative technique for determining the mass-fractions of authigenic and detrital K-feldspar in mineral separates. *Scanning Microscopy* 1/3:1039–1043
- Hopson RF, Ramseyer K (1990) Cathodoluminescence microscopy of myrmekite. *Geology* 18:336–339
- Houseknecht DW (1991) Use of cathodoluminescence petrography for understanding compaction, quartz cementation and porosity in sandstones. In: Barker C, Kopp OC (eds) *Luminescence Microscopy and Spectroscopy*. Society for Sedimentary Geology, SEPM Short Course 25, pp 59–66
- Kirsh Y, Townsend PD (1988) Speculations on the blue and red bands in the TL emission spectrum of albite and microcline. *Nuclear Tracks and Radiation Measurements* 14:43–49
- Krynauw JR, Behr HJ, Van den Kerkhof AM (1994) Sill emplacement in wet sediments: fluid inclusion and cathodoluminescence studies at Grunehogna, western Dronning Maud Land, Antarctica. *Journal of the Geological Society of London* 151:777–794
- Lange H, Kressin G (1955) Der Einfluss der Kristallstruktur auf die Lumineszenz des Calciumsilikates (Mn, Pb). *Zeitschrift für Physik* 142:380–386
- Laud KR, Gibbons EF, Tien TY, Stadler HL (1971) Cathodoluminescence of Ce^{3+} and Eu^{2+} -activated alkaline earth feldspars. *Journal of the Electrochemical Society* 118:918–923
- Long JVP, Agrell S (1965) The cathodoluminescence of minerals in thin section. *Mineralogical Magazine* 34:318–326

- Machel HG, Burton EA (1991) Factors governing cathodoluminescence in calcite and dolomite, and their implication for studies of carbonate diagenesis. In: Barker C, Kopp OC (eds) *Luminescence Microscopy and Spectroscopy*. Society for Sedimentary Geology, SEPM Short Course 25, pp 37–57
- Marfunin AS (1979) *Spectroscopy, Luminescence and Radiation Centers in Minerals*. Springer Verlag, Berlin, 325 p
- Mariano AN, Ito J, Ring PJ (1973) Cathodoluminescence of plagioclase feldspars. Geological Society of America, Boulder, Colorado, Abstracts with Programs 5, 726
- Mariano AN (1989) Cathodoluminescence emission spectra of rare earth element activators in minerals. In: Lipin BR, Mckay GA (eds) *Geochemistry and mineralogy of rare earth elements*. Mineralogical Society of America, Review in Mineralogy 21, pp 339–348
- Marmier P (1983) *Kernphysik I*. Zürich, Verlag der Fachvereine, 325 p
- Marshall DJ (1988) *Cathodoluminescence of Geological Materials*. Unwin Hyman, Boston, 146 p
- Matter A, Ramseyer K (1985) Cathodoluminescence microscopy as a tool for provenance studies of sandstones. In: Zuffa GG (ed) *Provenance of Arenites*. NATO ASI Series, Boston, Reidel Publishing Company 148, pp 191–211
- Meunier JD, Sellier E, Pagel M (1990) Radiation-damage rims in quartz from uranium-bearing sandstones. *Journal of Sedimentary Petrology* 60:53–58
- Milliken KL (1989) Petrography and composition of authigenic feldspars, Oligocene Frio Formation, South Texas. *Journal of Sedimentary Petrology* 59:361–374
- Milliken KL (1994) Cathodoluminescent textures and the origin of quartz silt in Oligocene mudrocks, South Texas. *Journal of Sedimentary Research* A64:567–571
- Milliken KL, Laubach SE (2000) The role of brittle deformation in sandstone diagenesis and fracture in siliciclastic petroleum reservoirs. (this vol.)
- Milliken KL, McBride EF, Land LS (1989) Numerical assessment of dissolution versus replacement in the subsurface destruction of detrital feldspars, Oligocene Frio Formation, South Texas. *Journal of Sedimentary Petrology* 59:740–757
- Mora CI, Ramseyer K (1992) Cathodoluminescence of coexisting plagioclases, Boehls Butte Anorthosite: Cathodoluminescence activators and identification of fluid flow paths. *American Mineralogist* 77:1258–1265
- Mullis J (1991) *Bergkristall*. Schweizer Strahler 9:127–161
- Mullis J, Dubessy J, Poty B, O'Neil J (1994) Fluid regimes during late stages of a continental collision: Physical, chemical, and stable isotope measurements of fluid inclusions in fissure quartz from a geotransverse through the Central Alps, Switzerland. *Geochimica et Cosmochimica Acta* 58:2239–2267
- Mumenthaler Th, Schmitt HW, Peters Tj, Ramseyer K, Zweili F (1995) Tracing the reaction processes during firing of carbonate containing brick mixes with the help of cathodoluminescence. *Ziegeleiindustrie International* 5/95:307–319
- Odin GS, Barbin V, Hurford AJ, Baadsgaard H, Galbrun B, Gillot PY (1991) Multi-method radiometric dating of volcano-sedimentary layers from northern Italy: age and duration of the Priabonian stage. *Earth and Planetary Science Letters* 106:151–168
- Ohnenstetter D, Cesbron F, Remond G, Caruba R, Claude JM (1991) Émission de cathodoluminescence de deux populations de zircons naturels: tentative d'interprétation. *Comptes Rendu Académie des Sciences, Paris, Série II*, 313:641–647
- Owen MR (1988) Radiation-damage halos in quartz. *Geology* 16:529–532
- Owen MR (1991) Application of cathodoluminescence to sandstone provenance. In: Barker C, Kopp OC (eds) *Luminescence Microscopy and Spectroscopy*. Society for Sedimentary Geology, SEPM Short Course 25, pp 67–75
- Pagel M, Barbarand J, Blanc P, Demars C, Savary V (1996) Combined UV and visible cathodoluminescence, fluid inclusion and trace element studies of authigenic quartz in sandstones. Workshop "Quartz cement: origin and effects on hydrocarbon reservoirs" 13.-14. May, Belfast, 27
- Poller U, Liebetrau V, Todt W (2000) Cathodoluminescence controlled dating of zircons by TIMS: application to metamorphic rocks. (this Vol.)

- Ramseyer K (1990) Types of cathodoluminescence colours in α -quartz. GAC-MAC Annual Meeting, Vancouver, Abstracts A107
- Ramseyer K, Mullis J (1990) Factors influencing short-lived blue cathodoluminescence of α -quartz. *American Mineralogist* 75:791–800
- Ramseyer K, Baumann J, Matter A, Mullis J (1988) Cathodoluminescence colours of α -quartz. *Mineralogical Magazine* 52:669–677
- Ramseyer K, Boles JR, Lichtner PC (1992b) Mechanism of plagioclase albitization. *Journal of Sedimentary Petrology* 62:349–356
- Ramseyer K, Diamond L, Boles JR (1993) Authigenic K-NH₄-feldspar in sandstones: a fingerprint of the diagenesis of organic matter. *Journal of Sedimentary Petrology* 63:1092–1099
- Ramseyer K, AlDahan AA, Collini B, Landström O (1992a) Petrological modifications in granitic rocks from the Siljan impact structure: Evidence from cathodoluminescence. *Tectonophysics* 216:195–204
- Ramseyer K, Fischer J, Matter A, Eberhardt P, Geiss J (1989) A cathodoluminescence microscope for low intensity luminescence. *Journal of Sedimentary Petrology* 59:619–622
- Reeder RJ (1991) An overview of zoning in carbonate minerals. In: Barker C, Kopp OC (eds) *Luminescence Microscopy and Spectroscopy*. Society for Sedimentary Geology, SEPM Short Course 25, pp 77–82
- Remond G, Cesbron F, Chapoulie R, Ohnenstetter D, Roques-Carmes C, Schvoerer M (1992) Cathodoluminescence applied to the microcharacterization of mineral materials: a present status in experimentation and interpretation. *Scanning Microscopy* 6/1:23–68
- Richter DK, Zinkernagel U (1975) Petrographie des "Permoskyth" der Jaggl-Plawen-Einheit (Südtirol) und Diskussion der Detritusherkunft mit Hilfe der Kathodenlumineszenz-Untersuchung. *Geologische Rundschau* 64:783–807
- Schneider N (1993) Das lumineszenzaktive Strukturinventar von Quarzphänokristen in Rhyolithen. *Göttinger Arbeiten zur Geologie und Paläontologie* 60:1–81
- Sears DWG, DeHart JM, Hasan FA, Lofgren GE (1990) Induced thermoluminescence and cathodoluminescence studies of meteorites. In: Coyne LM, McKeever SWS, Blake DF (eds) *Spectroscopic characterization of minerals and their surfaces*. American Chemical Society, Symposium Series 415, pp 190–222
- Sippel RF (1965) Simple device for luminescence petrography. *Review of Scientific Instruments* 36:1556–1558
- Sippel RF (1968) Sandstone petrology, evidence from luminescence petrography. *Journal of Sedimentary Petrology* 38:530–554
- Sippel RF, Spencer AB (1970) Luminescence petrography and properties of lunar crystalline rocks and breccias. *Proceedings of the Apollo 11 Lunar Scientific Conference*, 3, *Geochimica et Cosmochimica Acta*, Supplement 1, 2413–2426
- Smith JV, Stenstrom RC (1965) Electron-excited luminescence as a petrological tool. *Journal of Geology* 73:627–635
- Speit B, Lehmann G (1982) Radiation defects in feldspars. *Physics and Chemistry of Minerals* 8:77–82
- Steele IM (1990): Mineralogy of meteorites revealed by cathodoluminescence. In: Coyne LM, McKeever SWS, Blake DF (eds) *Spectroscopic characterization of minerals and their surfaces*. American Chemical Society, Symposium Series 415, pp 150–164
- Steele IM (1995) Oscillatory zoning in meteoritic forsterite. *American Mineralogist* 80:823–832
- Stevens Kalceff MA, Phillips MR (1995) Cathodoluminescence microcharacterization of the defect structure of quartz. *Physical Review B* 52:3122–3134
- Stevens Kalceff MA, Phillips MR, Moon AR (2000) Cathodoluminescence microcharacterisation of silicon dioxide polymorphs. (this Vol.)
- Telfer DJ, Walker G (1978) Ligand field bands of Mn²⁺ and Fe³⁺ luminescence centres and their site occupancy in plagioclase feldspars. *Modern Geology* 6:199–210
- Trofimov AK (1962) The luminescence spectrum of zircon. *Geochemistry* 11:1102–1108
- Vavra G (1990) On the kinematics of zircon growth and its petrographic significance: a cathodoluminescence study. *Contributions to Mineralogy and Petrology* 106:90–99

- von Engelhardt W, Matthäi SK, Walzebeck J (1992) Araguainha impact crater, Brazil. I. The interior part of the uplift. *Meteoritics* 2:442–457
- Walker G (1985) Mineralogical applications of luminescence technique. In: Berry FJ, Vaughan DJ (eds) *Chemical Bonding and Spectroscopy in Mineral Chemistry*. Chapman & Hall, London, pp 103–140
- Watt GR, Wright P, Galloway S, McLean C (1997) Cathodoluminescence and trace element zoning in quartz phenocrysts and xenocrysts. *Geochimica et Cosmochimica Acta* 61:4337–4348
- Wenzel T, Ramseyer K (1992) Mineralogical and mineral-chemical changes in a fractionation-dominated diorite-monzodiorite-monzonite sequence: evidence from cathodoluminescence. *European Journal of Mineralogy* 4:1391–1399
- White WB, Matsumura M, Linnehan DG, Furukawa T, Chandrasekhar BK (1986) Absorption and luminescence of Fe³⁺ in single-crystal orthoclase. *American Mineralogist* 71:1415–1419.
- Zinkernagel U (1978) Cathodoluminescence of quartz and its application to sandstone petrology. *Contributions to Sedimentology* 8:1–69
- Zinkernagel U (1992) Vulkanogener Detritus in Sandsteinen des Oberkarbons in Norddeutschland. In: Frank F, Zinkernagel U, Füchtbauer H (eds) *Zur Liefergebietsfrage der Sandsteine des Nordwestdeutschen Oberkarbons*. DGMK Deutsche Wissenschaftliche Gesellschaft für Erdöl, Erdgas und Kohle 384–8:35–77

Cathodoluminescence Microcharacterisation of Silicon Dioxide Polymorphs

MARION A. STEVENS KALCEFF, MATTHEW R. PHILLIPS,
ANTHONY R. MOON, WALTER KALCEFF

1

Introduction

1.1

Cathodoluminescence Emission from Silicon Dioxide

Optical cathodoluminescence (CL) microscopy and CL microanalysis are useful characterization techniques in the geosciences (Yacobi and Holt 1990; Remond et al. 1992a, 1997; Hagni 1987): Information on the distribution of defects (e.g. impurities) in minerals, obtained from optical CL microscopy, may be complemented by CL microscopy and spectroscopy (i.e. microanalysis) in an electron microscope. The focused electron beam in the electron microscope is typically submicron in diameter. The diameter of the electron beam produced by the cold cathode electron gun in the optical CL microscope is typically of order 1–10 mm in diameter (Yacobi and Holt 1990), thus the power density delivered to the specimen is usually greater during CL microanalysis. In a scanning electron microscope (SEM), the CL spectra may be collected from a larger region by defocusing the beam or scanning the beam over an area of the specimen. This has the effect of reducing electron irradiation induced effects (i.e. irradiation damage, heating effects), and averaging submicron sized inhomogeneities. CL microanalysis in a SEM provides high sensitivity (parts per million, ppm) high resolution (μm), and detection of defect centers in luminescent materials (Yacobi and Holt 1990; Remond et al. 1992a). Following the identification of the defects associated with the emission bands in the CL spectrum, the distribution of each luminescent center may be imaged with high spatial resolution using monochromatic CL microscopy. CL microanalysis also complements defect structure information available from other spectroscopies such as photoluminescence (PL), thermoluminescence (TL or TSL), electron spin resonance (ESR), and optical absorption (OAS) spectroscopies. CL microanalysis is a powerful technique ideally suited for investigating the microscopic distribution of impurities and other defects in luminescent materials.

Crystalline and amorphous silicon dioxide polymorphs have useful physical properties which result in their extensive and diverse applications in science and technology (Heaney et al. 1994). The defect structure of pure specimens of crys-

talline SiO₂ (quartz) and amorphous SiO₂ (fused quartz) have been investigated using CL microanalytical techniques (Stevens Kalceff and Phillips 1995a; Stevens Kalceff 1997; Stevens Kalceff et al. 1997a). The luminescence emissions are correlated with particular defect structures. The defect structure of SiO₂ polymorphs is extremely sensitive to ionizing radiation (Griscom 1985, 1990a, 1991; Remond et al. 1992a, 1994; Stevens Kalceff and Phillips 1995a,b; Stevens Kalceff et al. 1996b), which has consequences for both the reliable interpretation of analyses using CL and other electron probe techniques, and for the design of many SiO₂ devices which operate in irradiation environments (Stevens Kalceff and Phillips 1995a). CL microanalysis also provides insight into the processes of defect formation and migration due to the influence of trapped charge induced electric field within the irradiated volume of the specimen (Cazaux 1986a,b; Stevens Kalceff et al. 1996b).

CL microanalysis enables mapping of the distribution of defects associated with impurities in various oxidation states, vacancies, etc. with high sensitivity and submicron resolution (Yacobi and Holt 1990). The energy positions, emission peak widths and emission response to continuous electron beam irradiation over a range of temperatures and excitation conditions may be determined. The CL spectra from crystalline and amorphous silicon dioxide polymorphs typically have broad overlapping emissions. The identification of impurity associated components of the emission spectra in natural specimens is aided by knowledge of the irradiation induced and/or intrinsic emissions, as typical CL emission from silicon dioxide polymorphs is associated with both intrinsic and extrinsic defects. CL results from competitive specimen dependent, radiative and nonradiative processes (Remond et al. 1992a). The presence of localized concentrations of impurities, charging of the irradiated volume of the specimen, changes in the specimen temperature, and dielectric response during irradiation, are all dependent on excitation conditions and will effect the nonradiative and radiative transition probabilities.

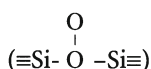
1.2

Defects in Silicon Dioxide

The normal defect free configuration of (low pressure) silicon dioxide polymorphs can be represented as ($\equiv\text{Si-O-Si}\equiv$) indicating that each silicon atom is surrounded by four tetrahedrally configured oxygen atoms and that adjacent silicon atoms are bridge bonded through a single oxygen atom. The silicon dioxide structure may be modified by the presence of defects (impurities, vacancies, etc.). The dominant observed defects occur in the short range order (Sigel and Marrone 1981) involving the slightly distorted SiO₄ tetrahedra which are common to both the crystalline and amorphous SiO₂ structures (Griscom 1990a). Hence, similar types of defects are found in crystalline and amorphous polymorphs of SiO₂. In irradiated silicon dioxide, point defects can be produced and/or modified by the electron beam (Griscom 1991; Stevens Kalceff and Phillips 1995a). Electron irradiation produces defects by the trapping of charge at the site of a pre-existing defect precursor. Alternatively, atomic displacements from the normal bonding (defect free) sites can result from either 'knock-on' (Griscom 1989; Griscom et al.

1983) (e.g. incident beam energies >70 keV for oxygen in silicon dioxide) or radiolytic (Vigouroux et al. 1985) processes (incident beam energies >5 keV in silicon dioxide; Griscom 1985)).

A number of preexisting and /or irradiation induced defects in high purity crystalline (Weil 1984) and high purity amorphous SiO₂ (Devine 1988b; Griscom 1991) have previously been identified, such as the well known E' center and variants (see in particular Griscom's extensive reviews: Griscom 1990a, 1985, 1991, 1984; Griscom 1980 and references therein). The general form of the E' center is usually represented as (≡Si·) which signifies an unpaired electron (·) associated with a single silicon atom bonded to only three oxygen atoms (≡) in the SiO₂ structure (i.e. a 'threefold coordinated' silicon atom). The E' center can be a component of the self trapped exciton, STE, which radiatively recombines to produce CL emission between ~2.2 and 3 eV, depending on the particular silicon dioxide polymorph structure (Luff and Townsend 1990; Itoh et al. 1990; Remond et al. 1992a; Khanlary et al. 1993; Stevens Kalceff and Phillips 1995a; Stevens Kalceff 1997; Stevens Kalceff et al. 1997a). The STE is an irradiation induced electron hole pair trapped by a self induced lattice distortion and is a consequence of the strong electron-phonon interactions in silicon dioxide (Itoh et al. 1988, 1994). Other defects include the nonbridging oxygen hole center (≡Si·O·) (Griscom and Friebele 1981; Skuja et al. 1984a; Griscom 1985; Nagasawa et al. 1986; Nishikawa et al. 1990), and oxygen excess centers including the peroxy radical (≡Si-O-O·) (Friebele et al. 1979; Griscom and Friebele 1981; Baker and Robinson 1983; Griscom 1990a; Griscom 1990b), the peroxy linkage (≡Si-O-O-Si≡) (Baker and Robinson 1983; Hanafusa et al. 1987; Imai et al. 1988b; Nishikawa et al. 1989; Griscom 1991), and the small peroxy linkage



(Edwards and Fowler 1982; Griscom 1990b, 1991). Oxygen-deficient centers (ODCs) include the twofold-coordinated silicon defect (=Si:) (Skuja et al. 1984b; Nagasawa et al. 1988; Trukhin et al. 1992; Skuja 1994), and the neutral oxygen vacancies including the unrelaxed oxygen vacancy (≡Si...Si≡; i.e. silicon atoms in normal lattice positions with separation of ~3.1 Å) and the relaxed oxygen vacancy (≡Si-Si≡; i.e. silicon atoms with separation of ~2.3 Å) (Nagasawa et al. 1988; Imai et al. 1988a; Tohman et al. 1989; Hosono et al. 1991; Griscom 1992; Dianov et al. 1992; Sulimov and Sokolov 1994). There are also two variants of the self trapped hole centers (STH; Pfeffer 1988a) (Griscom 1989, 1990a, 1991, 1992), which have only been observed in amorphous specimens at temperatures below 200 K (Griscom 1991). STH₁ is a hole trapped on a bridging oxygen (≡Si- $\overset{\cdot}{\text{O}}$ -Si≡), while STH₂ is a hole delocalized on two adjacent bridging oxygen atoms in the normal SiO₂ structure (Griscom 1989, 1992).

Interstitial mobile atoms, molecules and ions may also effect the defect structure of even ultrapure SiO₂ (Pfeffer 1988a). For example, in pure SiO₂ glasses, atoms, molecules and ions of hydrogen, chlorine, excess oxygen, etc. may be present depending on the method of synthesis (Pfeffer 1988b; Awazu and Kawazoe 1994) and /or may result from irradiation of the specimen (Awazu and Kawazoe

1990; Awazu and Kawazoe 1994). Mobile interstitial molecules and ions may act as charge traps and/or diffuse to and transform or eliminate other defect centers.

Tetrahedrally coordinated crystalline silicon dioxide is a relatively pure material, particularly in the crystal form. The substitution of impurity ions for silicon is limited by the high valency (Si^{4+}) and relatively small atomic radius of silicon (Sprunt 1981). Hydrogen associated defects (such as H^+ and OH^-) and substitutional Ti^{4+} , Ge^{4+} and Ti^{3+} , Al^{3+} , Fe^{3+} with charge compensating cations such as H^+ , Na^+ , K^+ , and Li^+ are frequently observed impurities in natural specimens (Sprunt 1981; Jani et al. 1983; Alonso et al. 1983; Maschmeyer and Lehmann 1983; Ramseyer and Mullis 1990; Weil 1994; Stevens Kalceff and Phillips 1995a; Stevens Kalceff et al. 1997b). Table 1 summarizes some commonly reported intrinsic and extrinsic luminescent emissions from pure synthetic and natural crystalline and amorphous silicon dioxide polymorphs, and proposed associations /identifications. Table 1 does not indicate the weight of evidence for each proposed identification. Some of the proposed associations are tentative, while others such as the association of the ~ 1.9 eV emission with a nonbridging oxygen defect is independently supported by a range of experimental investigations and theoretical calculations. It is noted that some of the proposed associations appear incompatible or contradictory. The inconsistencies in the literature may be due to a number of factors, such as the choice of electron beam parameters (i.e. beam energy, current and diameter), which is important in comparative work due to the irradiation sensitivity of silicon dioxide polymorphs. Different modes of irradiation (i.e. focused, defocused, stationary, scanned, continuous, etc.) enable some components of broad emissions with differing irradiation responses to be distinguished. In addition, the genesis of natural specimens/method of synthesis of synthetic specimens and their subsequent history will also influence the type, distribution and concentration of defects and defect precursors in each particular specimen. The presence of even trace amounts of impurities and defects will profoundly influence the CL emission. Sensitivity to the presence of small concentrations of (impurity) defects is the basis of the application of CL techniques in the geosciences. Specimen temperature may of course influence the energy position and peak width of some CL emissions due to the contraction and decreased thermal vibration of the lattice, as specimen temperature is decreased (Yacobi and Holt 1990). Low specimen temperatures will also reduce the rate of electron beam induced, thermally assisted damage and associated CL emission from irradiation sensitive silicon dioxide. The intensity of some CL emissions may also be influenced by the thermal diffusion limited annealing of defects directly associated with the CL emission or associated with competitive radiative and nonradiative processes. For example, at temperatures less than ~ 80 K, the thermal diffusion of hydrogen is negligible and CL emission associated with hydrogen stabilized defects is observed (e.g. the E_2' center in crystalline SiO_2 (Stevens Kalceff and Phillips 1995a)) (Table 2). The crystalline or amorphous nature of the silicon dioxide polymorph will also affect the CL spectra. For example, diffusion activation energies for interstitial impurities are lower in the less dense amorphous specimens, and particularly in those specimens with fine grain structure. In addition, luminescent emissions (Henderson and Imbusch 1989) from similar types of

Table 1. Commonly reported intrinsic and extrinsic luminescent emissions from crystalline and amorphous silicon dioxide polymorphs, and proposed associations /identifications

Energy (eV)	Specimen	Expt ^a	Association/identification	References ^e
1.65–1.8	Tin float glass, opal α -SiO ₂ , amethyst, citrine, sandstone	CL,TL	Associated with Fe ³⁺ impurity	1–6
1.8–2.5	P ⁺ , As ⁺ implanted α -SiO ₂	CL	Associated with structural changes /or P ⁺ , As ⁺ impurities	7
~1.9	a and α -SiO ₂ O rich SiO ₂	CL,P L	NBOHC (Si-O precursor) NBOHC (POL precursor) Oxygen vacancy Associated with O ₃	8–13 9,14 15 16 ^b ,17
1.93	SiO ₂	CL	Na impurity	8,18,19
1.95	Hydrated a and α -SiO ₂	CL	NBOHC (–OH precursor)	2,7,9,20
1.97	Tin float glass	CL	Sn ²⁺ impurity	3,18,19
2.0	Natural α -SiO ₂	TL	O-Al-O	21
~2–3	a-SiO ₂ , α -SiO ₂	CL	Fine structure due to O ₂	15,22,23
2.1–2.4	a-SiO ₂ , irradiated α -SiO ₂	CL	STE	9 ^b ,10 ^b ,13,24
2.14	Thin film a-SiO ₂	PL	Associated with B ₂ α center	25
2.15	Tin float glass	CL	Sn impurity	18,19
2.17	Ge doped α -SiO ₂	CL	STE associated with Ge	15
2.21	a-SiO ₂ thin film	CL	Electron irradiation induced	7
2.25–2.8	Natural α -SiO ₂	CL	Associated with interstitial cations	26
2.4	Synthetic Amethyst	CL	Fe impurity	27
2.5	α -SiO ₂	CL	Impurity	9,28
2.55	Smoky α -SiO ₂	CL	(Al ³⁺) ⁰ hole center	29
2.6–2.8	α -SiO ₂ Opal, rose quartz	CL,PL, TL,XL ^d	STE Ti ³⁺ , interstitial Ti ³⁺ , TiO ₂ ^c	8 ^b ,9 ^b , 15,24,30 1–3,31
2.64	a and α -SiO ₂	PL,TL	Al impurity	19 ^b
2.68	Tin float glass	CL	Sn ⁴⁺	3
2.74	a-SiO ₂	CL,PL	Oxygen deficient center	10,13,16,32
2.75	O implanted a-SiO ₂	CL	Oxygen related center	33
~2.9	Natural α -SiO ₂	CL	Substitutional Al and cation	26
~2.95	α -SiO ₂	CL	Intrinsic defect, not Al	9,30,34
2.99	C implanted a-SiO ₂ thin film	CL	C impurity	7
3.0	a-SiO ₂	CL	STEs associated with Ge, Al, H	18,19
3.1	α -SiO ₂ , a-SiO ₂	PL	–O–O–, O ₂	18 ^b ,19 ^b ,20
3.1–3.15	Sn or Ge doped a-SiO ₂ a-SiO ₂	PL	ODC associated with Sn or Ge ODC(associated with B ₂ β)	32 16

Table 1. Continued

Energy (eV)	Specimen	Expt ^a	Association/identification	References ^c
3.1-3.3	a and α -SiO ₂ , sandstone, opal	CL, TL XL	Ge ³⁺ Al ³⁺ -M ⁺ (where M ⁺ = H ⁺ , Li ⁺ , Na ⁺ , or K ⁺) Impurity incorporated during growth	32 2,8,9 ^b ,10,18, 26,30,34,35 13,36,15
3.25	Pure a-SiO ₂	TL	(H ₃ O ₄) ⁰ hole traps	37
~3.7	α -SiO ₂ in sandstone	CL	Associated with Al and Li impurities	38
4.3	α -SiO ₂	CL	Na impurity	1
4.2-4.5	N irradi. α -SiO ₂ , a-SiO ₂ , thin film a-SiO ₂	CL, PL	ODC, n and e irradiation induced, associated with B ₂ α center	16 ^b ,7,25,39,40

^aLuminescence experiment.

^bAlso see references therein.

^cSub-micron inclusions incorporated into the host lattice.

^dX-ray induced luminescence.

^eReferences: 1, Sprunt (1981); 2 Stevens Kalceff et al. (1997b); 3 Myhaljlenko et al. (1994); 4 Walker (1985); 5 Bruhn et al. (1996); 6 Zhang et al. (1994); 7 Koyama (1980); 8 Remond et al. (1992a); 9 Stevens Kalceff and Phillips (1995a); 10 Stevens Kalceff (1997); 11 Zinkernagel (1978); 12 Friebele et al. (1985); 13 Stevens Kalceff et al. (1997a); 14 Munekuni et al. (1990); 15 Luff and Townsend (1990); 16 Griscom (1991); 17 Awazu and Kawazoe (1990); 18 Khanlary et al. (1993); (19 Yang et al. (1994); 20 Nishikawa et al. (1992); 21 Hashimoto et al. (1994); 22 Gritsenko and Lisitsyn (1985); 23 Cazaux and Le Gressus (1991); 24 Itoh et al. (1990); 25 Awazu et al. (1993); 26 Ramseyer and Mullis (1990); 27 Ruppert (1987); 28 Itoh et al. (1988); 29 Nassau and Prescott (1975); 30 Gorton et al. (1996); 31 Marfunin (1979); 32 (1992); 33 Hagni (1987); 34 Alonso et al. (1983); 35 Jani (1983); 36 Skuja and Trukhin (1989); 37 Yang and McKeever (1990); 38 Demars et al. (1996); 39 Nishikawa et al. (1994); 40 Corazza et al. (1996).

defects may occur at different energies, because of slightly different structural configuration (producing slightly different crystal fields) in the vicinity of the defect. For example, CL emission associated with the radiative recombination of the STE is observed at ~2.7 eV in crystalline SiO₂ and at ~2.3 eV in amorphous SiO₂. The method of specimen preparation (i.e. polishing) can affect the concentrations of defects participating in radiative and nonradiative processes in the surface regions (Ruppert 1987). The influence of specimen preparation and surface roughness on the CL and X-ray signals has been demonstrated by Remond and coworkers (Remond et al. 1992b, 1996) and observed in CL from various silicon dioxide specimens (Sprunt 1981; Ruppert 1987 and references therein). In general, reported inconsistencies in CL measurements may be due to the failure to correct for total instrument response. This is particularly important for specimens such as silicon dioxide which typically have broad overlapping luminescence emissions even at lower temperatures (Stevens Kalceff and Phillips 1995a; Remond et al. 1996).

2 Electron Irradiation Induced Effects

2.1 Specimen Heating

CL emission from silicon dioxide polymorphs is strongly dependent on temperature, however, beam-induced sample heating is frequently overestimated (Cazaux and Le Gressus 1991). The electron beam induced sample heating has been estimated by Filippov (Filippov 1993), considering the electron irradiated volume, rather than the electron irradiated area at the surface only, as in the commonly used estimations of Castaing, etc. (Yacobi and Holt 1990; Castaing 1951; Reimer 1985). For example, for α -SiO₂ at 295 K, (the thermal conductivity of crystalline SiO₂, parallel to the c axis is $k_{295K}=0.113 \text{ W cm}^{-1} \text{ K}^{-1}$; Stevens Kalceff and Phillips 1995a), the maximum irradiation-induced temperature increase by an electron beam with energy of 30 keV, current of 0.25 μA and (focused) beam diameter of 0.6 μm is calculated to be $\sim 30 \text{ K}$ using Filippov's estimation, and $\sim 500 \text{ K}$ using Castaing's estimation. (It is noted that our investigation of the temperature response of the temperature sensitive sharp R line CL emission from Al₂O₃:Cr³⁺ is consistent with Filippov's estimation; Phillips et al. 1995). Filippov (1993) has also devised an analytical expression estimating the time taken for the irradiation induced temperature increase to stabilize. The temperature changes in silicon dioxide were predicted to stabilize within 10^{-3} s and therefore do not correlate with the development of the observed reproducible evolution of the CL images and spectra, which occurs at a much slower rate (of order 10^0 – 10^3 s (Stevens Kalceff and Phillips 1995a; Stevens Kalceff 1997; Stevens Kalceff et al. 1997a). The defect structure and therefore the CL from SiO₂ polymorphs is influenced by the irradiation induced, thermally assisted changes due to the irradiation induced electric field produced by the trapping of charges at pre-existing and/or radiolytically produced defects (Griscom 1985; Vigouroux et al. 1985; Stevens Kalceff and Phillips 1995a).

2.2 Specimen Charging

Electron irradiation of a grounded, conductively coated insulating material at normal incidence produces a symmetric charge distribution which induces an electric field. Cazaux (1986b, 1995) has characterized this electric field in terms of radial and axial components parallel and perpendicular (i.e. normal) to the surface, respectively. In the irradiated specimen, mobile pre-existing and irradiation induced negatively charged species will migrate towards the surface (Cazaux 1986b) while mobile positively charged species will migrate towards the region of maximum negative trapped charge, under the influence of the axial electric field (Fig. 1a). The radial field is zero along the axis defined by the normal incident electron beam and at the insulator specimen/conducting coating interface, and is only significant at μm depths below the coated surface (Cazaux 1986b). If the conductive coating is damaged or removed during the course of irradiation, the radial

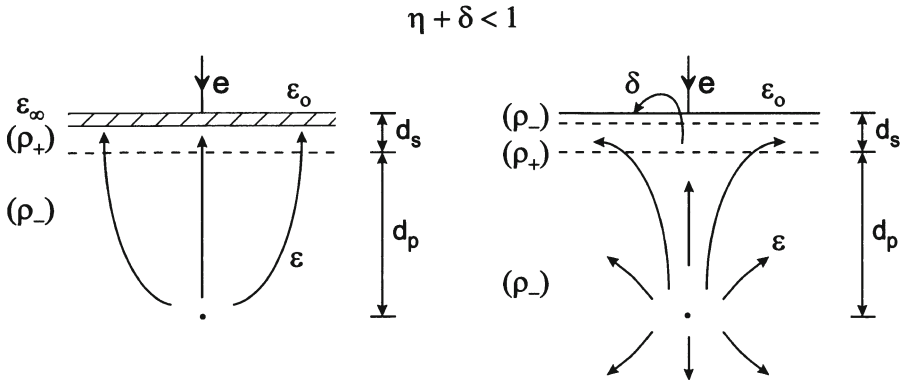


Fig. 1. The direction of migration of negatively charged mobile species due to the electric field induced by the trapping of charge in an electron irradiated insulator, as described by Cazaux and coworkers (Cazaux 1986a,b, 1995; Remond et al. 1992b)

field in the region of the surface becomes significant. The axial component of the trapped, charge induced electric field is influenced by the emission of secondary electrons from the areas of uncoated specimen, resulting in a positively charged surface layer and an increase in the magnitude of the radial component of the electric field at the surface (Cazaux 1986a,b) (Fig. 1b). Both natural and synthetic silicon dioxide polymorphs charge rapidly during irradiation (Vigouroux et al. 1985; Cazaux 1986a; Stevens Kalceff and Phillips 1995b; Stevens Kalceff et al. 1996b). No evidence of desorption from the SiO_2 surfaces, in the dendritic pattern typical of the damage due to dielectric breakdown (Blaise and Le Gressus 1991), was observed during any of the CL experiments (Stevens Kalceff and Phillips 1995a,b; Stevens Kalceff et al. 1996a,b; Stevens Kalceff 1997). When an insulator is continuously irradiated with an electron beam, the electric field produced by the trapped charge modifies the trajectories of the beam of electrons subsequently entering the specimen, resulting in reduced penetration depths into the specimen bulk (Blaise and Le Gressus 1991; Kotera and Suga 1988) and greater lateral diffusion of negative charge in the surface region (Blaise and Le Gressus 1991).

3 Experimental Details

3.1 Specimens

Premium, Q-grade, synthetic, high purity quartz (Sawyer Research Products Inc.) and anhydrous (type I) and hydrated (type II) fused silicon dioxide (National Scientific Company,) were investigated. The relative proportions of impurities and defects strongly influences the irradiation sensitive defect structure and therefore the CL from SiO_2 polymorphs. The impurity concentrations are well

characterized for these commercial materials. In Sawyer premium Q grade synthetic quartz, the impurities and their maximum concentrations were determined to be OH (<300 ppm), Al (<2 ppm), Na (<2 ppm), and Li (<2 ppm) with negligible amounts of common impurities such as Ge, K, Ca and Fe (Sawyer Research Products Inc.). In the amorphous, anhydrous, fused silicon dioxide specimen, the maximum concentrations of the major impurities were determined (National Scientific Company) to be Al (<15 ppm), -OH (<5 ppm) and Ti (<1 ppm), with <1 ppm of common impurities including Na, Li, K, Ca and Fe. In the hydrated fused silicon dioxide specimen, the maximum concentrations of the major impurities (National Scientific Company) include -OH (180 ppm), Al (<50 ppm) with <3 ppm of Ca, Fe, Na, K, and with <1 ppm of Li and Ti. Interstitial atomic and molecular hydrogen and/or oxygen may also be found, depending on the particular method of manufacture. The dissolved gases may be involved in the diffusion limited anneal of various defect centers. The concentration of dissolved gases is unknown in the as-received specimens (Pfeffer 1988a,b), although it is expected that irradiation with an electron beam will effect the local distribution and concentration of mobile species (Cazaux 1986b; Fialin and Remond 1990; Brow 1994).

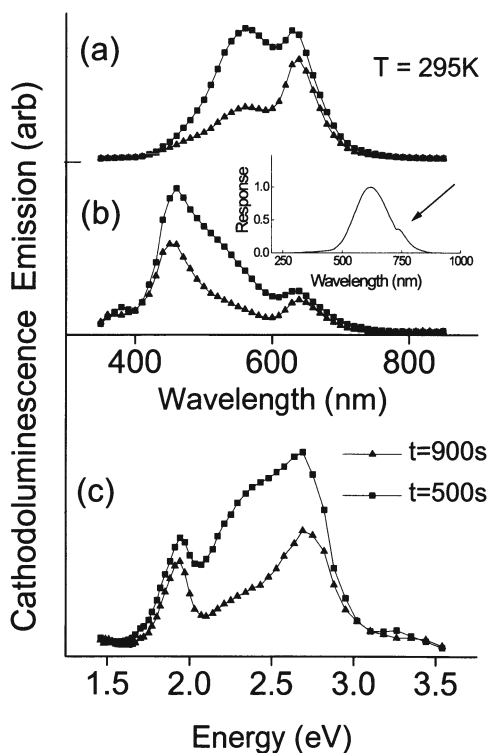
The stoichiometry of the SiO₂ polymorphs also has an important bearing on the native defects which may provide precursor states for defects produced during irradiation (Stevens Kalceff and Phillips 1995a,b; Nishikawa et al. 1990; Stevens Kalceff et al. 1996b; Friebele and Gingerich 1980). Optical absorption spectroscopy indicates the presence of oxygen deficient centers in the unirradiated ultrapure synthetic quartz and fused silicon dioxide specimens (Stevens Kalceff et al. 1996b; Itoh et al. 1988; Weeks et al. 1992). In addition, no optical absorptions associated with oxygen excess centers (Nishikawa et al. 1990; Weeks et al. 1992) have been observed from these specimens. Hence, it is concluded that the ultrapure specimens are nominally oxygen deficient (i.e., the pre-irradiation concentration of peroxy linkages is small, while the concentration of oxygen deficient defects is significant). This is an important distinction as the absolute and relative proportions of impurities and point defects influence the irradiation sensitive defect structure of silicon dioxide polymorphs.

For comparison, preliminary investigations of specimens of natural amorphous hydrated silicon dioxide (precious white and black opal from Australia) (Stevens Kalceff et al. 1996a, 1997b) and well crystallized specimens of rose quartz (Brazil), clear natural crystalline quartz (NSW, Australia), and amethyst (Brazil) (Martin et al. 1996; Cressy et al. 1993; Rossman 1994) are reported. The specimens were polished to an optical finish and coated with a thin grounded conducting layer of carbon or chromium prior to CL investigations to prevent deflection of the incident electron beam due to charging of the surface of the irradiated specimen. The thickness of the carbon and chromium films were determined to be 30 ± 4 and 6.0 ± 0.5 nm respectively, using a Park Scientific Autoprobe LS atomic force microscope. The specimens were not irradiated prior to the CL investigations.

3.2 Instrumentation

The CL experiments were performed in a JEOL JSM 35C SEM equipped for maximum versatility and sensitivity with Oxford Instruments liquid nitrogen (LN) and liquid helium (LHe) cryogenic stages, and an Oxford Instruments MonoCL cathodoluminescence imaging and spectral analysis system. The CL was excited using a continuous electron beam at normal incidence and measured using a retractable parabolic mirror collector. Spectra over the wavelength range 350–850 nm were collected by photon counting using a Hamamatsu R2228 photomultiplier tube (PMT) with a 1200 line/mm grating, blazed at 500 nm. CL spectra, collected as a function of wavelength λ (nm), were corrected for total instrument response (Devine 1988a) (Fig. 2) The total instrument response (see imbedded plot in Fig. 2b) was determined using Oriel calibrated standard lamps (tungsten and deuterium) and is a smoothly varying function between ~ 300 and 900 nm peaking at ~ 600 nm (~ 2.1 eV). The feature indicated by the arrow in Fig. 2 at ~ 720 nm is a Wood (or grating) anomaly (Hamilton et al. 1978; Stewart and Gallaway 1962). In energy space the CL emission bands generally have a Gaussian shape (Yacobi and Holt 1990). To transform the corrected CL spectra to energy space, the corrected wavelength λ (nm) data are converted to energy E (eV), and

Fig. 2a–c. CL spectra from α -SiO₂ following normal incidence stationary focused beam irradiation of energy 30 keV, current 0.25 μ A and diameter 0.6 μ m: a as collected, b corrected for total instrument response (*embedded plot*), and c converted to energy space. The Wood anomaly (Hamilton et al. 1978) is indicated by the arrow



the corrected CL intensities are multiplied by λ^2 (Hamilton et al. 1978). Spectra are collected between 350 and 850 nm such that the CL intensity is sufficient to ensure that the uncertainties in the low intensity emission are not magnified by the instrument response correction. The estimated maximum uncertainty in the CL emission intensities is $\sim 5\%$ at ~ 3 eV where the system response is poor, and $< 0.5\%$ at ~ 2 eV where the system response is optimized. The SiO_2 emissions are broad, with peak widths (full width at half-maximum, FWHM) greater than 0.15 eV; therefore failure to correct for instrument response can lead to errors in the band shapes and positions. This can lead to difficulties in fitting Gaussian components to the spectra and misinterpretation of the CL images (see Fig. 2). The majority of SiO_2 CL studies do not specify whether the spectra have been corrected for instrument response which may account for some of the inconsistencies between the published reports (Stevens Kalceff and Phillips 1995a).

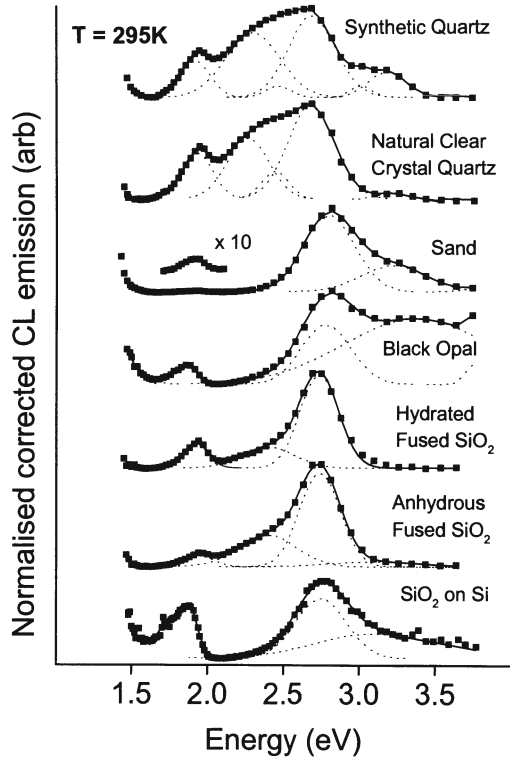
4 Cathodoluminescence Microanalysis

4.1 Spectroscopy and Microscopy

The majority of the CL emissions from the ultrapure specimens are associated with intrinsic point defects involving (SiO_4) tetrahedra common to the structure of low pressure silicon dioxide polymorphs (Stevens Kalceff and Phillips 1995a; Stevens Kalceff 1997; Stevens Kalceff et al. 1997a). In particular, the CL spectra from all specimens are similar over the energy (wavelength) range 1.8–2.1 eV (~ 590 –690 nm), despite different polymorph structure and impurity concentrations (Fig. 3).

In Fig. 4, 295 K CL spectra from pure synthetic crystalline quartz, collected as a function of increasing irradiation time, are presented. The CL emission was excited by continuous irradiation with a stationary electron beam of energy 30 keV and current 0.25 μA at normal incidence. The electron beam was focused with a incident beam diameter of ~ 0.6 μm (Yacobi and Holt 1990). The CL intensity from pure synthetic specimens of silicon dioxide polymorphs is relatively low, hence these beam parameters have been chosen to provide suitable low noise data. (The recent installation of a Hamamatsu R943-02 Peltier cooled high sensitivity photomultiplier tube, HSPMT, will enable lower beam currents to be used in future investigations.) When studying natural specimens, total CL emission can be increased, electron beam effects can be reduced and submicron inhomogeneities averaged using a scanning rather than a stationary electron beam. Monte Carlo simulations (Joy 1991) indicate that the penetration depth of 30 keV electrons in quartz is ~ 8 μm and is ~ 11 μm in less dense amorphous silicon dioxide. The resolution of the experimental spectral data ranges between 0.03 eV at 2 eV and 0.07 eV at 3 eV. The experimental spectral data, represented as scatter plots, were fitted with a multi-parameter Gaussian function using a non-linear least squares curve fitting algorithm (ORIGIN). The baseline offset and the position, width and integrated area under the peak were iteratively refined with the mini-

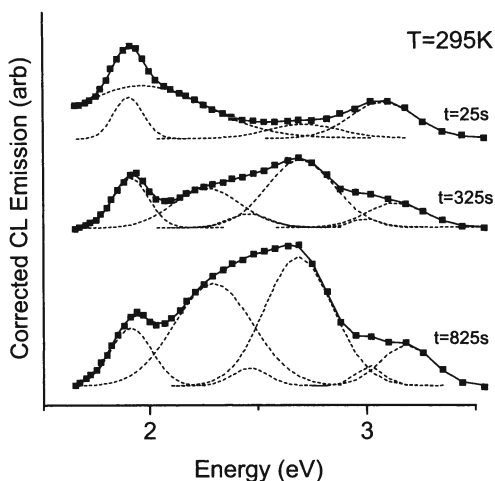
Fig. 3. CL spectra from silicon dioxide polymorphs following normal stationary focused beam irradiation of energy 30 keV, current 0.25 μ A and diameter 0.6 μ m are represented by scatter plots. The *dashed line plots* are calculated fitted Gaussian components, which when summed, result in the calculated fitted CL spectra represented as *solid line plots*



imum number of Gaussian emissions. The fitting procedure is described in more detail elsewhere (Stevens Kalceff and Phillips 1995a). In Fig. 4, the dashed line plots are the calculated fitted Gaussian components, which are summed to produce the calculated fitted solid line plots for direct comparison with the experimental scatter plots. Where necessary, statistical comparisons have been made to indicate the minimum number of Gaussian components required to provide a satisfactory fit. Commonly used numerical criteria of fit, generally known as reliability or R factors, allow this quantitative comparison. The R_{CL} factor provides merely a numerical comparison between fits and does not indicate whether a fit is correct or unique (Stevens Kalceff and Phillips 1995a). If fitting $(n+1)$ Gaussian components to the observed CL emission spectra results in a R_{CL} factor (Stevens Kalceff and Phillips 1995a) which does not significantly improve the fit achieved by (n) components, the fitting of more than (n) components to the spectral profile is not justified by the quality/resolution of the particular set of experimental spectra.

The characteristic response of CL emission associated with individual defects to changes in specimen temperature, specimen exposure to electron beam irradiation, (crystalline) specimen orientation, varying distribution and concentration of defects /impurities between different specimens provides useful opportunities to experimentally resolve the component peaks. In addition characteristics of

Fig. 4. CL spectra from α -SiO₂ following normal incidence stationary focused beam irradiation of energy 30 keV, current 0.25 μ A and diameter 0.6 μ m



luminescence centers such as the luminescence decay time and possible polarization of CL emission from crystalline specimens may be used to resolve components of the CL emission spectra, using time resolved techniques (Itoh et al. 1988; Haglund et al. 1988; Wang et al. 1988; Hayes et al. 1984) and polarization sensitive experiments (Itoh et al. 1988) such as polarized phase tuned techniques (Gorton et al. 1996).

4.2

Irradiation Response; Crystalline Silicon Dioxide

In Fig. 5, the integrated CL emission intensities of the resolved Gaussian components (a sample of which are shown in Fig. 4) are plotted as a function of irradiation time. The electron beam parameters may be varied to control the penetration depth and the power density of the electron beam enabling irradiation induced defects to be investigated. In Fig. 6, the experiments are repeated with the same beam power (energy, 30 keV and current, 0.25 μ A), but with a defocused beam of diameter 15 μ m. The electron irradiation induced changes occur at a slower rate, because of the reduction in the power density in the irradiated volume of specimen. This enables the growth and decay of the radiation sensitive CL emissions to be monitored. In Fig. 7, the integrated CL emission intensities of the resolved Gaussian components in Fig. 6 are plotted as a function of irradiation time. These irradiation response plots aid the characterization of the emission components, as each defect center has a characteristic response to electron irradiation (Stevens Kalceff and Phillips 1995a; Stevens Kalceff 1997; Stevens Kalceff et al. 1997a). Note in particular that the 1.95 eV CL component associated with the nonbridging oxygen hole (NBOHC) with nonbridging hydroxyl precursor (i.e., $\equiv\text{Si}-\text{OH} \rightarrow \equiv\text{Si}-\text{O} \cdot + \text{H}^0$) (Stapelbroek et al. 1979; Stevens Kalceff and Phillips 1995a) is rapidly attenuated by focused beam irradiation. This allows the overlapping 1.91 eV intrinsic emission component due to the NBOHC (i.e., $\equiv\text{Si}-\text{O}-\text{Si} \equiv \rightarrow \equiv\text{Si}-\text{O} \cdot \cdot \text{Si} \equiv$) to be

Fig. 5. The integrated CL intensities of the resolved calculated fitted Gaussian components of the CL spectra, produced by focused beam irradiation of α -SiO₂ (see Fig. 4) are plotted as a function of irradiation exposure

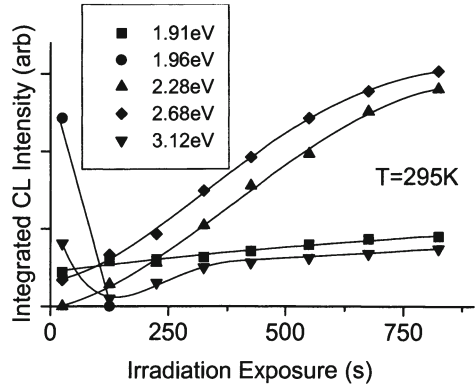


Fig. 6. CL spectra from α -SiO₂ following normal incidence stationary defocused beam irradiation of energy 30 keV, current 0.25 μ A and diameter \sim 15 μ m

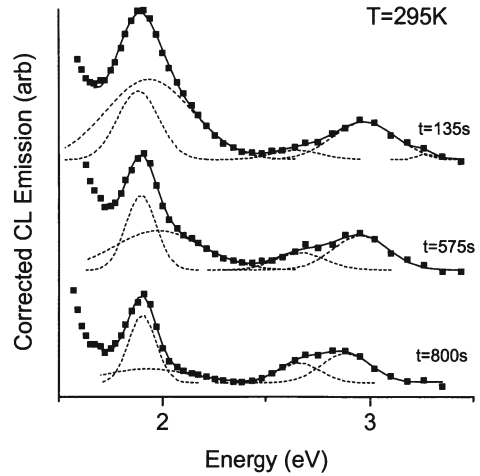
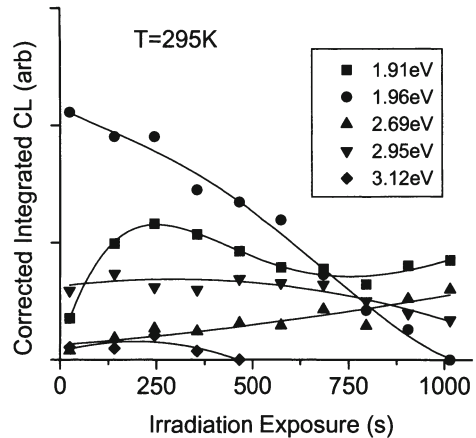


Fig. 7. The integrated CL intensities of the resolved calculated fitted Gaussian components of the CL spectra, produced by defocused beam irradiation of α -SiO₂ (see Fig. 6) are plotted as a function of irradiation exposure

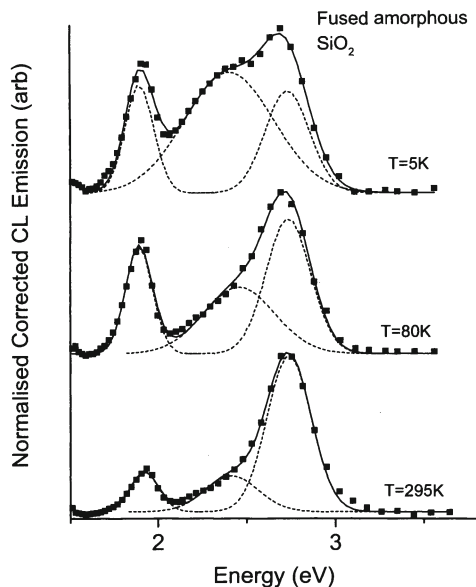


resolved. Conversely, the 1.95 eV emission is better observed by irradiating with a defocused electron beam as the rate of irradiation induced attenuation is reduced. Note also that the irradiation induced 2.3 eV emission, which is due to the radiative recombination of the STE in the irradiation damaged (amorphized) surface regions of the crystal specimen (Stevens Kalceff and Phillips 1995a,b), is more easily observed in CL spectra produced by the more powerful focused beam irradiation.

4.3 Temperature Response; Amorphous Silicon Dioxide

In Fig. 8 the normalized, corrected CL spectra from amorphous SiO_2 (fused quartz) irradiated by a 30 keV, 0.25 μA focused electron beam for ~ 600 s at $T \sim 295$ K, $T \sim 80$ K and $T \sim 5$ K are shown. As the specimen temperature increases there is a decrease in the intensity of the ~ 2.4 eV emission which is associated with the radiative recombination of the STE, relative to the ~ 2.7 eV emission which is associated with an oxygen deficient defect. A possible mechanism for the production of the oxygen deficient defects is the thermally activated nonradiative conversion of STEs to complementary defect pairs (e.g. oxygen deficient and oxygen excess defects) as temperature increases (Itoh and Tanimura 1990; Song and Williams 1992). The observed anticorrelation of the relative intensities of the temperature responses of the 2.4 and 2.7 eV CL emissions is consistent with a contribution from this mechanism. It is noted that nonradiative decay of STEs may also be facilitated by dynamic factors such as local disorder and structural asymmetry, even at very low temperatures (Itoh and Tanimura 1990; Song and Williams 1992).

Fig. 8. CL spectra at $T=5$ K, 80 K and 295 K from a- SiO_2 following normal incidence stationary focused beam irradiation of energy 30 keV, current 0.25 μA and diameter 0.6 μm



Resolved CL emissions from silicon dioxide polymorphs have been associated with various defect centers with reference to the dependence of the CL spectra and images on temperature, irradiation, polymorph structure, concentration and distribution of preexisting defect precursors. Comparisons were made with information from complementary techniques, such as ESR, OAS, PL, TSL, etc. (Weil 1984, 1994; Griscom 1991; Stevens Kalceff and Phillips 1995a; Stevens Kalceff 1997; Stevens Kalceff et al. 1997a, and references therein). In addition, identifications were aided by comparison with theoretical calculations such as predictions of local states introduced into the band structure by defects (O'Reilly and Robertson 1983; Robertson 1988; Dianov et al. 1992). In Table 2, the mean CL emission position and mean FWHM of the resolved Gaussian bands from ultrapure quartz and pure anhydrous and hydrated amorphous silicon dioxide (type I and II fused quartz) are summarized. The maximum deviation from the mean peak position and mean FWHM is estimated to be ± 0.06 eV (Stevens Kalceff and Phillips 1995a; Stevens Kalceff 1997; Stevens Kalceff et al. 1997a).

Table 2. Possible identifications of Cathodoluminescence emissions from ultrapure amorphous and crystalline silicon dioxide

Position (eV)				Suggested identifications
FWHM				
Crystalline	SiO ₂	Amorphous	SiO ₂	
295 K	80 K	295 K	5 K	
1.91 (0.20)	1.88 (0.17)	1.92 (0.19)	1.89 (0.18)	Associated with NBOHC with Si-O, and in crystalline SiO ₂ post irradiation peroxy linkage precursors or \equiv Si : center
1.95 (0.42)	1.95 (0.32)			In hydrated specimens, attenuates during irradiation associated with NBOHC with Si-OH precursor
2.28 (0.39)				Radiative recombination of a STE from amorphous SiO ₂ outgrowth on irradiated crystalline SiO ₂
		2.40 (0.35-0.44)	2.40 (0.3-0.5)	Radiative recombination of the STE, multiple components when strongly irradiated.
	2.69 (0.65)			Radiative recombination of a STE from crystalline SiO ₂ associated with an E ₂ ' center (stabilized by immobile H ^o)
2.68 (0.35)	2.72 (0.33)			Radiative recombination of a STE from crystalline SiO ₂ associated with an E ₁ ' center and either a peroxy radical, peroxy linkage or NBOHC
		2.74 (0.30)	2.73 (0.30)	Oxygen deficient center; twofold coordinated silicon and/or oxygen vacancy defect
2.93 (0.33)				Intrinsic emission?
3.12 (0.37)		3.12 (0.7)	3.15 (0.7)	Low intensity broad emission associated with the charge compensated, substitutional [Al ³⁺ -M ⁺] center where M ⁺ is Li ⁺ , Na ⁺ or H ⁺ and attenuates during irradiation.

4.4

Polarized Cathodoluminescence; Crystalline Silicon Dioxide

The ~ 2.7 eV emission attributed to the radiative relaxation of the STE in quartz is strongly polarized along the *c* axis (Itoh et al. 1988; Gorton et al. 1996; Fisher et al. 1990). The scatter plot in Fig. 9 shows the degree of polarization of the visible CL emission spectra of natural clear crystal quartz comparing the emission from polished faces cut perpendicular to the *c* axis and parallel to the *c* axis (i.e. perpendicular to the *a* axis). The degree of polarization, *P*, is defined (Itoh et al. 1988)

$$P = \frac{I_z - I_x}{I_z + I_x}$$

where I_z and I_x are the intensities of the components parallel to the *c* and *a* axes respectively. Thus Fig. 9 shows a significant degree of polarization of $\sim 0.4 \pm 0.1$ for the ~ 2.7 eV emission. In contrast, the line plot shows the negligible degree of polarization in the CL spectra also oriented at 90° with respect to each other, but collected from the polished face perpendicular to the *c* axis. The maximum uncertainty in the estimation of the degree of polarization is indicated by the error bar in Fig. 9. The uncertainty at the ends of the range is greater because of the poorer instrument response at these wavelengths (see Fig. 2b). The specimen orientation with respect to the *E* (electric) vector of the incident electron beam may influence the intensity of certain emissions and therefore must be considered when investigating the CL emission from SiO_2 crystals or polycrystalline specimens.

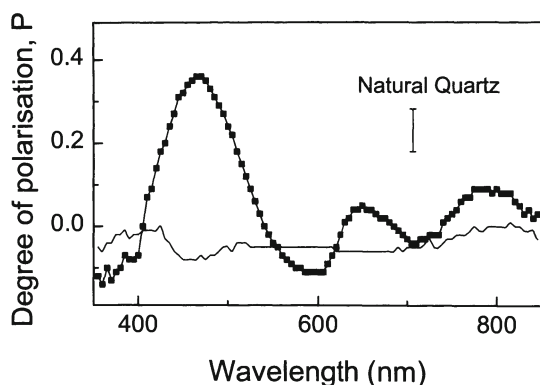


Fig. 9. The degree of polarization (see text) of the visible CL emission spectra of natural clear crystal quartz comparing the emission from polished faces cut perpendicular and parallel to the *c* axis is represented by a scatter plot. The *line plot* shows the negligible degree of polarization in CL spectra oriented at 90° with respect to each other, but collected from the polished (*z*) face perpendicular to the *c* axis

4.5

Bulk vs Microanalytical Techniques; Amorphous Silicon Dioxide

4.5.1

Precious Opal

Defect centers in natural hydrated amorphous silicon dioxide (opal) have been identified and imaged with high sensitivity and high spatial resolution using CL microanalysis (Stevens Kalceff et al. 1996a,b). Color in precious gem opal is due to diffraction effects from regularly stacked, three dimensional arrays of uniformly sized, close packed microspheres of amorphous silica (150–400 nm in diameter) (Darragh et al. 1976). Water, silica, air, etc. may fill the voids between the spheres. Desirable diffraction effects are optimized in grains with regular, distinct, unfilled intersphere voids (Segnit et al. 1965). TEM imaging confirms the amorphous nature of sedimentary opal (Rossman 1994).

Four typical Australian natural precious opal specimens mined from sedimentary host rocks (McOrist et al. 1995) from widely separated regions were investigated, including two specimens of white opal from Coober Pedy (central South Australia) and two specimens of black opal from Lightning Ridge (northern NSW). The concentration of impurities in common opal specimens obtained from the same deposits associated with the precious opal were determined using neutron activation analysis (NAA) by McOrist et al. (1995). The major impurities are similar in all specimens and include principally Al (7000–8000 ppm) with significant concentrations (500–2000 ppm) of Fe, Ti, Na and K. In general impurity concentrations are greater in the black opal specimens. Physically absorbed water molecules (4–9% by weight) (Darragh et al. 1966, 1976; Segnit et al. 1965; Graetsch et al. 1990) or chemically bonded single or twin non-bridging hydroxyl (terminal -OH) groups (Segnit et al. 1965) in concentrations of order 1000 ppm, are also present.

High sensitivity, high spatial resolution detection of local defect centers by CL microanalysis provides information which complements bulk analyses of precious opal. CL images of the black opal are distinguished by distinct 'bright' mottled regions which are absent in CL micrographs of white opal. 'Dark' regions intersected with bright narrow features are typical of the CL images of both types of opal. The boundaries between 'dark' and 'bright' features in the CL micrographs are well defined (see Fig. 10) and correspond to the grain boundaries between the common opal intergrain regions and the precious opal grains of the black opal and white opal specimens. CL spectra (e.g. Fig. 11) between 1.5–3.5 eV (i.e. ~850–350 nm) were collected at 295 K in scan mode for the common opal intergrain regions (Fig. 11a) and the precious opal grains of the black opal (Fig. 11b) and white opal (Fig. 11c) specimens. Figure 11 shows that characteristic intrinsic defects may contribute to the CL emission from opal (Stevens Kalceff et al. 1997b). A spectrum from pure hydrated amorphous silicon dioxide is included for comparison (Fig. 11d). The intensity of the CL emission is particularly low from white opal and from the precious grains of black opal. The intergrain regions are characterized by bright CL indicating a relatively higher concentration of impurities /defects than in the precious grains. The CL spectra from the bright intergrain

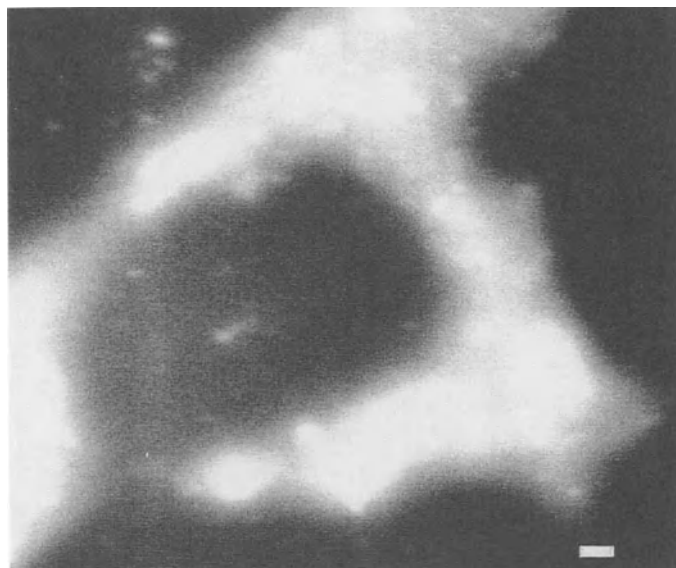
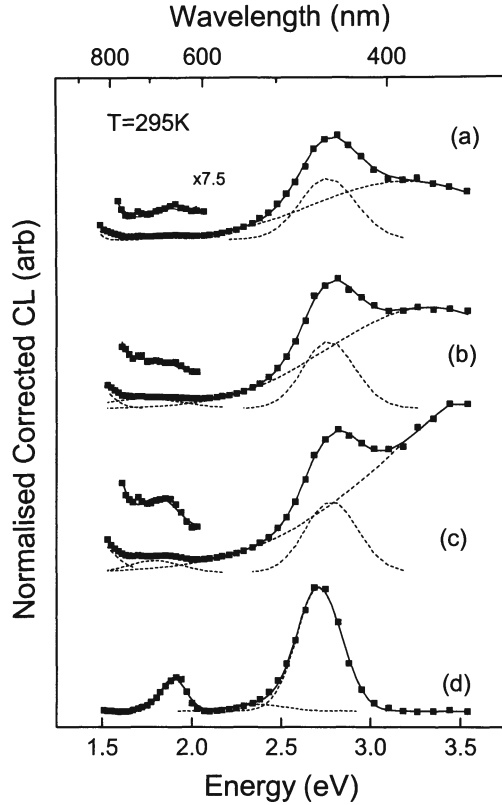


Fig. 10. Panchromatic CL micrograph of Australian precious black opal showing grain boundaries between 'bright' intergrain regions and 'dark' precious grain regions. The dimension marker indicates 10 μm

and dark precious grain regions are similar although the intensities are typically an order of magnitude less from the precious grains. CL microanalysis indicates the intergrain region is composed predominantly of amorphous silicon dioxide, with submicron sized light absorbing particles (e.g. titanium and iron oxides and carbon) which provide the desirable high contrast in black opal specimens (Stevens Kalceff et al. 1997b).

The CL spectra were also collected as a function of specimen temperature (between ~ 5 and 295 K) and exposure to stationary and scanned electron irradiation, which provide additional valuable information assisting identification of the defects. Corrected CL spectra were fitted and identified with particular defect centers with reference to CL analyses of ultrapure specimens of silicon dioxide (Stevens Kalceff et al. 1997b). The relative intensities of the CL emissions from impurity defects are not necessarily related to the relative concentrations of the impurities. Impurities may be present in nonluminescent configurations (e.g. Fe^{2+} , uncompensated substitutional Al^{3+}). The intensity of particular CL emissions may be reduced by competitive nonradiative de-excitation processes, in particular specimens or regions of specimens. Additionally, as a consequence of multiple mechanisms of energy transfer of varying efficiency, competitive radiative and nonradiative processes may exist for each defect center, influenced by the concentration and distribution of other defect centers (e.g. impurity ions) found in each particular specimen (Remond et al. 1992a). The lack of correlation between the CL intensities from microscopic volumes and bulk element concentration may also reflect the inhomogeneity of the natural specimens, although it

Fig. 11. CL spectra (30 keV, 0.25 μA) of a 'bright' inter-grain and **b** 'dark' precious grain regions in Australian black opal, and **c** white opal at 295 K. The CL intensities are normalized to the 2.8 eV emission and the intensity scale has been expanded for easier comparison of the lower intensity emissions below 2 eV. The CL spectrum of pure amorphous silicon dioxide is included for comparison (**d**)



is noted that typical CL spectral profiles are similar for all the opal specimens (see Fig. 11). Bulk analyses identify the major impurities present which assists with possible identification of the CL emissions (Stevens Kalceff et al. 1997b). Table 2 summarizes the proposed possible identification of the resolved CL emissions from precious opal.

4.6

Irradiation Kinetics of the 1.9 eV Cathodoluminescence Emission; SiO_2 Polymorphs

If the CL emission is continuously monitored as a function of irradiation exposure, the CL emission kinetics may be determined. Typical irradiation response spectra of the 1.9 eV CL emission are shown in Fig. 12. The normalized 1.9 eV CL emission intensity is plotted as a function of electron beam irradiation exposure. The natural crystalline silicon dioxide specimen was continuously irradiated with an scanning electron beam of energy 30 keV and current 0.25 μA at normal incidence. Each spectrum was obtained from a previously unirradiated area of the specimen. While the electron beam parameters were maintained for each

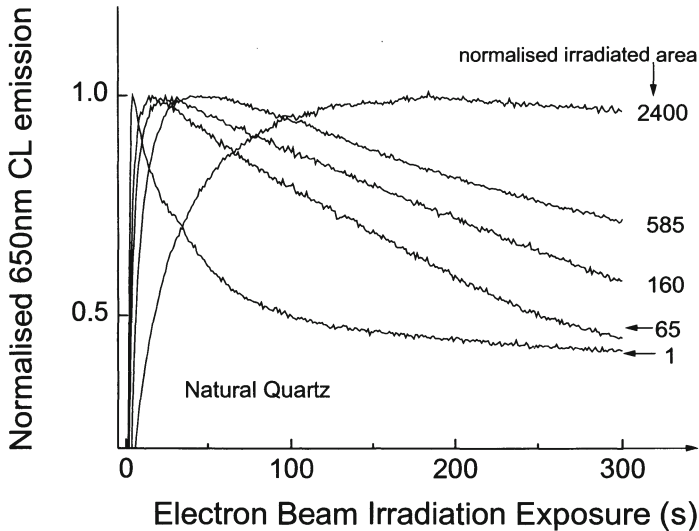


Fig. 12. Normalized irradiation response of the ~ 1.9 eV emission as a function of the normalized area scanned by the 30 keV, 0.20 μA focused electron beam from (a) z cut $\alpha\text{-SiO}_2$ at 295 K

spectrum, the power density delivered to each new interaction volume was varied by changing the area over which the specimen was irradiated. The 1.9 eV CL irradiation response in hydrated specimens is characterized by an initial increase and maximizing of the luminescence, after which the emission decays until approximately stabilizing (slow decay) after longer irradiation times. Thus Fig. 12 shows that the 1.9 eV CL intensity varies in a characteristic manner during irradiation time and is correlated with the power density in the interaction volume and the beam induced electric field. The rate of evolution of the characteristic CL emission response depends on the power density delivered to the interaction volume.

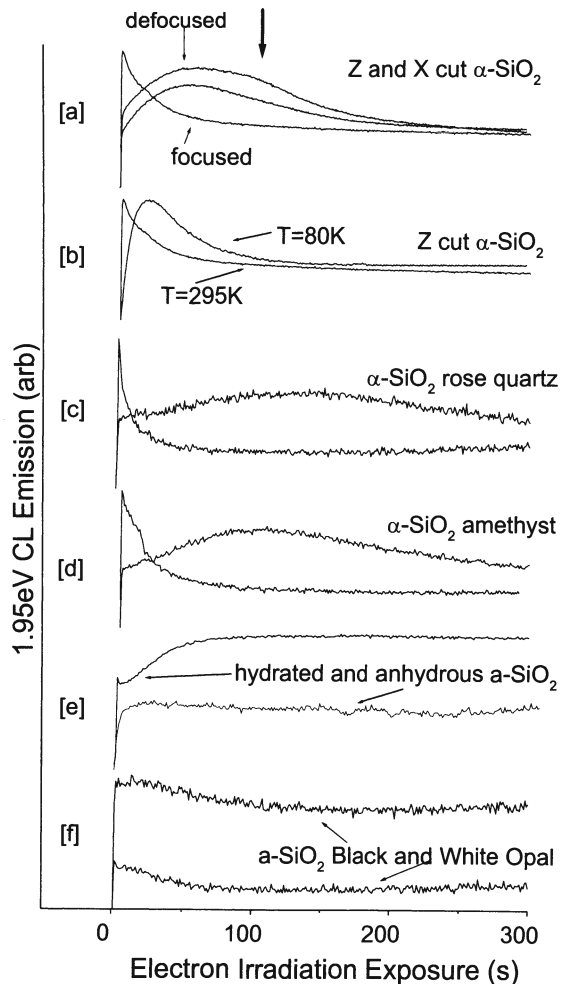
Figure 13 shows the irradiation kinetics of the ~ 1.9 eV CL emission from a range of silicon dioxide polymorphs. The ~ 1.9 eV emission from silicon dioxide consists of at least two overlapping emissions associated with the NBOHC with bridging Si-O bond precursor, while the ~ 1.95 eV emission is associated with the nonbridging hydroxyl Si-OH precursor (Stevens Kalceff and Phillips 1995a). As has been shown (Stevens Kalceff and Phillips 1995a), the 1.95 eV emission attenuates due to the radiolysis of the O-H bond and subsequent migration of the hydrogen associated defects such as H^+ and OH^- (see Figs. 4–7) to the periphery of the irradiated volume (see Fig. 1). The overlapping 1.91 eV emission saturates and reaches equilibrium within the specimen interaction volume.

The ~ 1.9 eV emission from crystalline silicon dioxide, resulting from focused and defocused beam irradiation of the polished face perpendicular to the c axis (i.e. z cut) and defocused beam irradiation of the polished face perpendicular to the a axis (i.e. x cut), are compared in Fig. 13a. There is an extra irradiation sensitive component in CL from the z face (indicated by the arrow), which also atten-

uates with continuing irradiation. Thermal and electro-migration of mobile defect species is enhanced along the *c* axis channels in quartz (Ramseyer and Mullis 1990; Kats 1962a,b; Halliburton et al. 1981; Markes and Halliburton 1979; Edwards and Beall Fowler 1982). It is possible that this extra component is the result of radiolysis of nonbridging oxygen precursors other than Si-OH which is the defect precursor associated with the major attenuating component resolved at 1.95 eV (see Figs. 4-7). In the *z* cut specimen, the *c* axis channels allow the electric field induced migration of ions, away from the resultant NBOHC. These NBOHCs may then recombine with holes in the valance band edge and produce CL emission at ~ 1.9 eV.

In Fig. 13b, the 1.9 eV irradiation response spectra of *z* cut α -SiO₂ at T=295 K and T=80 K are compared. Figure 13b shows that the irradiation induced migra-

Fig. 13a-f. Irradiation response of the ~ 1.9 eV emission from silicon dioxide polymorphs: a *z* and *x* cut α -SiO₂ at 295 K; b *z* cut α -SiO₂ at 80 K and 295 K; c rose quartz at 295 K; d amethyst at 295 K; e hydrated and anhydrous α -SiO₂; f black inter-grain and white precious opal irradiated in scan mode at 295 K



tion of the hydrogen associated mobile defect species produced by the radiolysis of the nonbridging hydroxyl center is thermally assisted. The irradiation response spectra produced by focused and defocused irradiation of the crystal growth faces of rose quartz and amethyst perpendicular to the *a* axis are shown in Fig. 13c,d respectively. The spectral response (Fig. 13), CL images and CL spectra (not shown) indicate the presence of NBOHC with nonbridging impurity (e.g. hydroxyl) center precursors, as well as a contribution from the intrinsic NBOHC with Si–O bond precursor.

The 1.95 eV component is absent in the irradiation response spectrum for anhydrous fused amorphous silicon dioxide plotted in Fig. 13e. In contrast the irradiation response spectrum from the hydrated specimen shows a component that attenuates within seconds. Migration in amorphous SiO₂ specimens is enhanced through the relatively open lattice structure, along grain boundaries, and at the surface (Devine et al. 1987; Kingery et al. 1975). For example, the oxygen diffusion coefficient in α -SiO₂ ($\rho=2.2$ g cm⁻³) is greater than in α -SiO₂ ($\rho=2.7$ g cm⁻³) as diffusion is inhibited in the more dense polymorphs (Itoh et al. 1990; Devine et al. 1987). In α -SiO₂, charges trapped by defects at grain boundaries produce enhanced electric fields, which result in efficient electromigration of charged mobile defect species, such as the highly mobile hydrogen defect species (Griscom 1985).

The irradiation response spectra in Fig. 13f have been obtained at 295 K during the scanned irradiation of areas of specimen ($\sim 30 \times 20$ μm^2) of intergrain regions of black opal and precious opal grains of white opal specimens. The spectra were obtained in scanned mode to average local inhomogeneities and to enable the initial stages of the irradiation response to be investigated by reducing the rate of evolution of the irradiation response, which depends on the power density delivered to the interaction volume. It can be seen that although the intensity of the emission is greater from the black intergrain region, consistent with a higher defect concentration, the irradiation response spectra are very similar in form. The irradiation sensitive component attenuates during the initial stages of irradiation. It is noted that with continuing irradiation, the ~ 1.9 eV emission intensity from opal continues to increase, rather than saturate like the 1.9 eV emission from other SiO₂ polymorphs shown in Fig. 13. This increase in CL emission is likely to be associated with impurity defects.

4.7

Electron Irradiation Induced Damage of Silicon Dioxide

Silicon dioxide polymorphs are sensitive to the effects of electron irradiation as indicated by the irradiation response spectra in Fig. 13. Electron beam irradiation produces characteristic, reproducible permanent changes in the surface topography, CL images and CL spectra of silicon dioxide polymorphs. Topographical, compositional and electronic defect structure analysis considering the effects of polymorph structure, temperature, and beam irradiation time has enabled the beam induced changes and their development to be characterized (Stevens Kalceff and Phillips 1995b; Stevens Kalceff et al. 1996b).

4.7.1

Crystalline Silicon Dioxide

The electron beam induces outgrowths on α -SiO₂ which have previously been characterized for ultrapure specimens using atomic force microscopy and CL microscopy and spectroscopy (Stevens Kalceff and Phillips 1995a,b; Stevens Kalceff et al. 1996b). These characteristic outgrowths are also observed on the different crystal faces of ultrapure and natural clear quartz, rose quartz, and amethyst specimens. The development of the outgrowths is strongly correlated with reproducible, characteristic changes in the spatial distribution of the monochromatic CL images resulting from stationary electron beam irradiation at normal incidence. CL microanalysis indicates that the processes involved in the volume changes correlate with defect center formation and/or migration. CL microanalysis suggests that the development of the outgrowths is associated with rapid and substantial local migration of oxygen which diffuses as O₂⁻ in silicon dioxide (see Fig. 1; Edwards and Beall Fowler 1982). Thus electron irradiation of quartz results in oxygen enrichment of the surface regions, which has also been observed during EPMA (Fialin and Remond 1990) and XPS (Brow 1994) experiments on SiO₂ (see also Cazaux 1986b). It has been proposed (Stevens Kalceff and Phillips 1995a,b) that a proportion of the excess oxygen accumulating at the surface is incorporated in the α -SiO₂ (quartz) structure in the form of peroxy linkages in which there are two rather than one bridging oxygen atoms between adjacent silicon atoms (Griscom 1985, 1991; Edwards and Beall Fowler 1982). As oxygen is incorporated into the α -SiO₂ structure, the formation of peroxy linkages may cause an expansion of the surface region and some disruption of the crystalline order, resulting in amorphous outgrowths. Electron, ion and neutron irradiation induced amorphization of α -SiO₂ has been reported (Reimer 1985; Itoh et al. 1994; Corazza et al. 1996 and references therein).

The expansion of the α -SiO₂ surface damages the conductive coating during irradiation which results in the increase in the magnitude of the radial component of the localized irradiation induced electric field at the surface (see Fig. 1) (Cazaux 1986a,b). This effect is illustrated in Fig. 14a,b which shows atomic force micrographs and secondary electron images (SEI) of an annular outgrowth on the α -SiO₂ surface produced by continuous irradiation with a 30 keV, 0.250 μ A defocused electron beam. The annular profile of the outgrowth in Fig. 14, produced by defocused irradiation of the crystalline specimens, is the result of oxygen accumulating at the surface region, and then migrating to the periphery of the beam induced charge distribution (Cazaux 1986b) under the influence of the radial component of the electric field (see Fig. 1).

In Fig. 14c,d the monochromatic CL images associated with the outgrowth produced by the defocused irradiation of quartz are shown: In Fig. 14c the \sim 2.7 eV CL (blue) emission associated with the radiative recombination of the STE is imaged. In Fig. 14d, the \sim 1.9 eV (red) emission associated with the NBOHC is imaged. The reproducible characteristic evolution of the monochromatic CL gives insight into processes that are responsible for changes in the surface topography (Stevens Kalceff et al. 1996b). Similar AFM, SEI and CL images are seen from irradiated natural clear quartz, rose quartz and amethyst. For

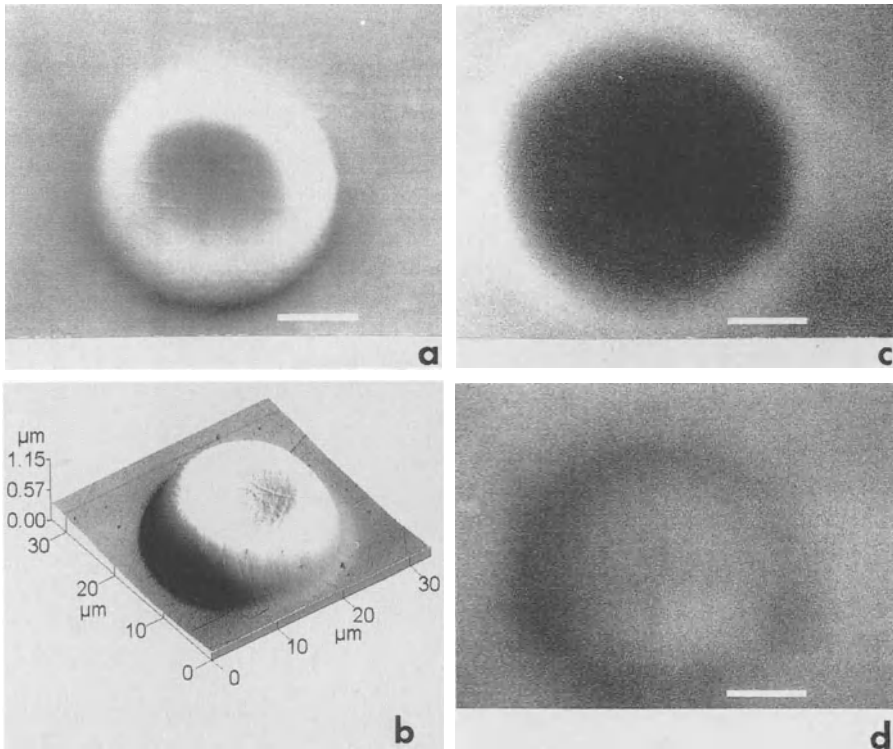


Fig. 14. **a** SEM secondary electron image; **b** atomic force micrograph (unprocessed image); **c** ~ 1.9 eV monochromatic CL image; **d** ~ 2.7 eV monochromatic CL image of α -SiO₂ irradiated with a defocused 30 KeV, 0.25 μ A, ~ 15 μ m diameter electron beam for 600 s. The dimension marker indicates 10 μ m

example, Fig. 15 shows the CL image of well crystallized rose quartz (see Rossman's review: Rossman 1994 and references therein) from the unpolished crystal growth face perpendicular to the *a* axis. The origin of the (red) luminescent vein feature in Fig. 14 is unknown, but is likely to be related to an inclusion of foreign material or immobile impurity associated defects, rather than NBOHC with Si-OH precursor, as the CL emission from the vein is relatively insensitive to electron beam irradiation. It is believed that possibly interstitial impurity defects (P, Ti) are associated with the color of the rose quartz crystal (Rossman 1994).

The 1.9 eV CL image is attributed to the migration of mobile hydrogen defects to the edge of the irradiated volume, resulting in an increase in the concentration of nonbridging hydroxyl defects, which are precursors for the ~ 1.9 eV emission. It is noted that the 1.9 eV emission is quenched within the irradiated volume and that the ~ 1.9 eV CL ring is not observed in irradiated anhydrous crystalline silicon dioxide specimens. The attenuation of the 2.7 eV emission is due to the increase in the concentration of O₂⁻ just within the boundary of the interaction

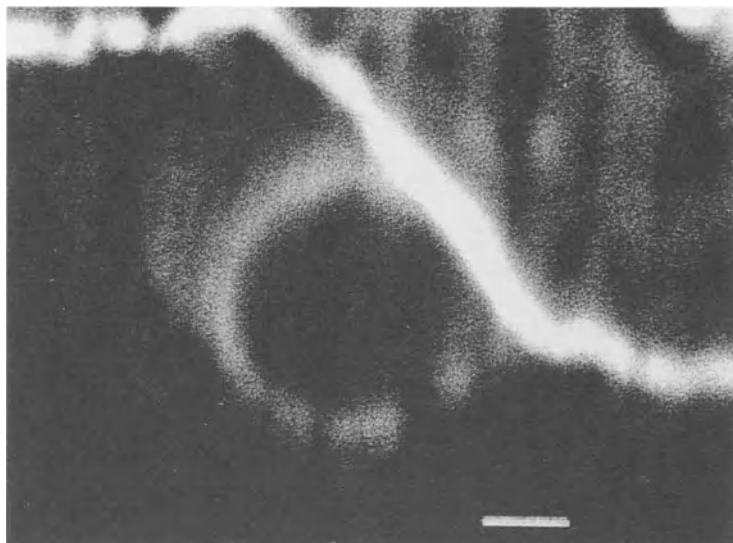


Fig. 15. Panchromatic image of CL from the unpolished (x) crystal growth face of rose quartz perpendicular to the a axis. Note the CL ring image produced by stationary defocused 30 keV, 0.25 μ A electron beam irradiation (see Fig. 14c). The dimension marker indicates 10 μ m

volume, which provides a competitive nonradiative alternative for the relaxation of the STE responsible for the ~ 2.7 eV emission in crystalline polymorphs of silicon dioxide.

The significance of charging effects and their relation to the development of defect migration and radiation damage in SiO_2 have important implications in the application and interpretation of CL and other electron probe techniques.

5 Conclusions

Cathodoluminescence microanalysis enables high resolution, high sensitivity defect structure determination (Yacobi and Holt 1990; Remond et al. 1992a; Stevens Kalceff and Phillips 1996; Steeds 1992). Cathodoluminescence investigations of pure synthetic quartz, hydrated and anhydrous (amorphous) fused silicon dioxide, opal, amethyst, rose quartz and natural clear crystal quartz show that intrinsic defects make a significant contribution to the CL emission from SiO_2 , and in particular irradiated SiO_2 . It is necessary to characterize possible intrinsic contributions to prevent misinterpretation of the CL images, as the CL spectra from silicon dioxide polymorphs are typified by broad overlapping emissions. In Table 1, proposed associations of commonly reported CL emissions from silicon dioxide polymorphs are listed. It is important to note that many of the proposed identifications are tentative and further work is needed to resolve the inconsistencies (Walker 1997) in the silicon dioxide literature.

Some of the results of the present work are listed in Table 2. The mean CL emission positions and mean FWHM of the resolved Gaussian bands from ultrapure quartz and pure anhydrous and hydrated amorphous silicon dioxide are summarized and possible identifications and/or associations suggested. In addition the determination of the irradiation and temperature response of crystalline and amorphous silicon dioxide CL emissions has enabled processes of defect formation and subsequent electrodiffusion of mobile species due to the influence of a localized electric field induced by trapped charges within the interaction volume to be investigated.

The characteristic changes in the surface topography of ultrapure synthetic and natural SiO₂ during irradiation are highly correlated with the changes observed in the CL micrographs, and therefore CL microanalysis gives insight into the microscopic diffusion processes contributing to the changes in irradiation damaged SiO₂ polymorphs. The irradiation induced electromigration of charged species has consequences for the choice of beam parameters and interpretation of electron probe techniques. CL microanalysis and optical CL microscopy are powerful complementary techniques in the geosciences.

Acknowledgements. M.A. Stevens Kalceff gratefully acknowledges financial support from In-search Ltd. and the Australian Research Council.

References

- Alonso, P.J., Halliburton, L.E., Kohnke, E.E., and Bossol, R.B. (1983) X-ray induced luminescence in crystalline SiO₂. *J. Appl. Phys.*, 54(9), 5369
- Awazu, K., and Kawazoe, H. (1990) O₂ molecules dissolved in synthetic silica glasses and their photo chemical reactions induced by ArF excimer laser radiation. *J. Appl. Phys.*, 68, 3584
- Awazu, K., and Kawazoe, H. (1994) Gaseous species and their photochemical reaction in SiO₂. *J. Non-Cryst. Sol.*, 179, 214
- Awazu, K., Watanabe, K., and Kawazoe, H. (1993) Study of oxygen-deficient centers in SiO₂ films using photoluminescence spectra. *Jap J. Appl. Phys.*, 32(6 A), 2746
- Baker, J.M., and Robinson, P.T. (1983) EPR of a new defect in natural quartz: possibly O₂⁻. *Solid State Communications*, 48, 551
- Blaise, G., and Le Gressus, C. (1991) Charging and flashover induced by surface polarization relaxation process. *J. Appl. Phys.*, 69, 6334
- Brow, R. (1994) Electron beam reduction of sodium-containing glass surfaces. *J. Non-Cryst. Sol.*, 175, 155
- Bruhn, F., Bruckenschen, P., Meijer, J., Stephan, A., Richter, D.K., and Veizer, J. (1996) Cathodoluminescence investigations and trace-element analysis of quartz by micro-pixe – implications for diagenetic and provenance studies of sandstones. *Can. Miner.*, 34(6), 1223
- Castaing, R. (1951) These' Electron beam based techniques for spatially resolved chemical and crystallographical analyses. Universite' de Paris, Paris France
- Cazaux, J. (1986a) Electrostatics of insulators charged by incident electron beams. *J. Microsc. Spectr. Electr.*, 11, 293
- Cazaux, J. (1986b) Some considerations on the electric field induced in insulators by electron bombardment. *Journal of Applied Physics.*, 59(5), 1418
- Cazaux, J. (1995) The role of the Auger mechanism in the radiation damage of insulators. *Microsc. Microanal. Microstruct.*, 6, 345

- Cazaux, J., and Le Gressus, C. (1991) Phenomena relating to charge in insulators: Macroscopic effects and microscopic causes. *Scan. Micro.*, 5(1), 17
- Corazza, A., Crivelli, B., Martini, M., Spinolo, G., and Vedda, A. (1996) Photoluminescence and optical absorption in neutron-irradiated crystalline quartz. *Phys. Rev. B.*, 53, 9739
- Cressy, G., Henderson, C.M.B., and Vanderlaan, G. (1993) Use of L-edge x-ray absorption spectroscopy to characterize multiple valence states of 3D transition metals – a new probe for mineralogical and geochemical research. *Phys.Chem.Min.*, 20, 111
- Darragh, P.J., Gaskin, A.J., and Sanders, J.V. (1976) Opals. *Scientific American*(April), 84
- Darragh, P.J., Gaskin, A.J., Terrell, B.C., and Sanders, J.V. (1966) Origin of precious opal. *Nature.*, 209(5018), 13
- Demars, C., Pagel, M., Deloule, E., and Blanc, P. (1996) Cathodoluminescence of quartz from sandstones – interpretation of the UV range by determination of trace element distributions and fluid-inclusion P-T-X properties in authigenic quartz. *Am.Miner.*, 81, 891
- Devine, R.A.B. (1988a) Ion implantation and ionizing radiation effects in thermal oxides. In C.R. Helms, and B.E. Deal, Eds. *The Physics and Chemistry of SiO₂ and the Si-SiO₂ Interface.*, p. 519. Plenum Press, New York
- Devine, R.A.B. (1988b) *The Physics and Technology of Amorphous SiO₂*. Plenum Press, New York
- Devine, R.A.B., Capponi, J.J., and Arndt, J. (1987) Oxygen-diffusion kinetics in densified amorphous SiO₂. *Phys.Rev.B.*, 35, 770
- Dianov, E.M., Sokolov, V.O., and Sulimov, V.B. (1992) Semiempirical calculations of point defects in silica. Oxygen vacancy and twofold coordinated silicon atom. *Journal of Non-Crystalline Solids.*, 149, 5
- Edwards, A.H., and Beall Fowler, W. (1982) Theory of peroxy-radical defect in a-SiO₂. *Phys.Rev.B.*, 266, 6649
- Fialin, M., and Remond, G. (1990) Electron probe microanalysis of oxygen in strongly insulating oxides. *Microbeam Analysis*, 2, 179
- Filippov, M.N. (1993) Evaluation of electron probe thermal action in scanning electron microscopy and electron probe microanalysis. *Izvestiya Akademii Nauk Seriya Fizicheskaya*, 57(8), 165
- Fisher, A.J., Hayes, W., and Stoneham, A.M. (1990) Structure of the self-trapped exciton in quartz. *Phys.Rev.Lett.*, 64, 2667
- Friebele, E.J., and Gingerich, M.E. (1980) Radiation -induced optical absorption bands in low loss optical fiber waveguides. *J.Non Cryst. Sol.*, 38&39, 245
- Friebele, E.J., Griscom, D.L., and Marrone, M. (1985) The optical absorption and luminescence bands near 2 eV in irradiated and drawn synthetic silica. *J.Non-Cryst.Sol.*, 71, 133
- Friebele, E.J., Griscom, D.L., Stapelbroek, M., and Weeks, R.A. (1979) Fundamental defect centers in glass: the peroxy radical in irradiated, high-purity, fused silica. *Phys.Rev.Lett.*, 42(20), 1346
- Gorton, N.T., Walker, G., and Burley, S.D. (1996) Experimental analysis of the composite blue CL emission in quartz – is this related to Aluminium content. International conference on Cathodoluminescence and related techniques in the Geosciences, p. 59, Nancy, France
- Graetsch, H., Mosset, A., and Gies, H. (1990) XRD and ²⁹Si MAS-NMR study on some non-crystalline silica minerals. *J.Non-Cryst.Sol.*, 119, 173
- Griscom, D.L. (1980) E' center in glassy SiO₂: ¹⁷O, ¹H, and 'very weak' ²⁹Si superhyperfine structure. *Phys.Rev.B.*, 22, 4192
- Griscom, D.L. (1984) Characterization of three E''-center variants in X- and γ-irradiated high purity a-SiO₂. *Nucl.Inst.Meth.Phys.Res.*, B1, 481
- Griscom, D.L. (1985) Defect structure of glasses. *J. Non-Cryst.Sol.* 73 1985 51
- Griscom, D.L. (1989) Self trapped holes in amorphous silicon dioxide. *Phys.Rev.B.*, 40, 4224
- Griscom, D.L. (1990a) Electron Spin Resonance Investigations of defects and defect processes in amorphous silicon dioxide. *Reviews of Solid State Science*, 4, 565
- Griscom, D.L. (1990b) Growth and decay kinetics of defect centers in high-purity fused silicas irradiated at 77 K with x-rays or 6.4 eV laser light. *Nucl.Instr.Meth.Phys.Res.*, B46, 12

- Griscom, D.L. (1991) Optical properties and structure of defects in silica glass. *Jour. Cer.Soc.Japan*, 99, 923
- Griscom, D.L. (1992) Electron Spin Resonance characterization of self-trapped holes in amorphous silicon dioxide. *J.Non-Cryst.Sol.*, 149, 137
- Griscom, D.L., and Friebele, E.J. (1981) Fundamental defect centers in glass:²⁹Si hyperfine structure of the non bridging oxygen hole center and the peroxy radical in a-SiO₂. *Phys.Rev B.*, 24, 4896
- Griscom, D.L., Stapelbroek, M., and Friebele, E.J. (1983) ESR studies of damage processes in X-irradiated high purity a-SiO₂:OH and characterization of the formyl radical defect. *J.Chem.Phys.*, 78, 1638
- Gritsenko, B.P., and Lisitsyn, V.M. (1985) Intrinsic short-lived defects in quartz. *Sov.Phys.Sol.Stat.*, 27, 1330
- Haglund, R.F., Kinser, D.L., Mogul, H., Tolk, N.H., Wang, P.W., and Weeks, R.A. (1988) Effects of processing on irradiation damage thresholds in silica glasses. *The Physics and Technology of Amorphous SiO₂*, p. 215. Plenum Press, New York
- Hagni, R.D. (1987) *Process Mineralogy VI. The Metallurgical Society of AIME*
- Halliburton, L.E., Koumvakalis, N., Markes, M.E., and Martin, J.J. (1981) Radiation effects in crystalline SiO₂: The role of aluminum. *Journal of Applied Physics.*, 52, 3565
- Hamilton, T.D.S., Munro, I.H., and Walker, G. (1978) Luminescence instrumentation. In M.D. Lumb, Ed. *Luminescence Spectroscopy*. Academic Press, London
- Hanafusa, H., Hibino, Y., and Yamamoto, F. (1987) Formation mechanism of drawing-induced defects in optical fibers. *J.Non-Cryst Sol.*, 95, 655
- Hashimoto, T., Sakaue, S., Aoki, H., and Ichino, M. (1994) Dependence of TL-property changes of natural quartzes on aluminium contents accompanied by thermal annealing treatment. *Rad. Measurements.*, 23, 293
- Hayes, W., Kane, M.J., Salminen, O., Wood, R.L., and Doherty, S.P. (1984) ODMR of recombination centers in crystalline quartz. *J.Phys.C.*, 17, 2943
- Heaney, P.J., Prewitt, C.T., and Gibbs, G.V. (1994) *Silica*. In P.H.Ribbe, Ed. *Reviews in Mineralogy*, 29. Mineralogical Society of America, Washington DC
- Henderson, B., and Imbusch, G.F. (1989) *Optical Spectroscopy of Inorganic Solids*. Clarendon, Oxford
- Hosono, H., Abe, Y., Imagawa, H., Ima, H., and Arai, K. (1991) Experimental evidence for the Si-Si bond model of the 7.6-eV band in SiO₂ glass. *Phys.Rev.B.*, 44, 12043
- Imai, H., Arai, K., and Imagawa, H. (1988a) Two types of oxygen-deficient centers in synthetic silica glass. *Phys.Rev.B.*, 38, 12772
- Imai, H., Arai, K., Saito, T., Ichimura, S., Nonaka, H., Vigouroux, J.P., Imagawa, H., Hosono, H., and Abe, Y. (1988b) UV and VUV optical absorption due to intrinsic and laser induced defects in synthetic silica glasses. In R.A.B. Devine, Ed. *The Physics and Technology of Amorphous SiO₂*, p. 153. Plenum Press, New York
- Itoh, C., Suzuki, T., and Itoh, N. (1990) Luminescence and defect formation in undensified and densified amorphous SiO₂. *Physical Review B*, 41, 3794
- Itoh, C., Tanimura, K., and Itoh, N. (1988) Optical studies of self trapped excitons in SiO₂. *J.Phys.C.*, 21, 4693
- Itoh, N., Shimizu-Iwayama, T., and Fujita, T. (1994) Excitons in crystalline and amorphous SiO₂: formation, relaxation and conversion to Frenkel pairs. *J.Non-Cryst.Sol.*, 179 194
- Itoh, N., and Tanimura, K. (1990) Formation of interstitial-vacancy pairs by electronic excitation in pure ionic crystal. *J.Phys.Chem.Sol.*, 51, 717
- Jani, M., Halliburton, L.E., Kohnke, E.E. (1983) Point defects in crystalline SiO₂: thermally stimulated luminescence above room temperature. *J.Appl.Phys.*, 54, 6321
- Jani, M.G., Bossoli, R.B., and Halliburton, L.E. (1983) Further characterization of the E'₁ center in crystalline SiO₂. *Phys.Rev.B.*, 27, 2285
- Joy, D.C. (1991) An introduction to Monte Carlo simulations. *Scanning Microscopy*, 5, 329

- Kats, A. (1962a) Hydrogen in alpha-quartz. Philips Research Reports, 17, 133
- Kats, A. (1962b) Hydrogen in alpha-quartz. Philips Research Reports, 17, 201
- Khanlary, M.R., Townsend, P.D., and Townsend, J.E. (1993) Luminescence spectra of germanosilicate optical fibres. 1: radioluminescence and cathodoluminescence. *J.Phys.D*, 26, 371
- Kingery, W.D., Bowen, H.K., and Uhlmann, D.R. (1975) Introduction to Ceramics. John Wiley and Sons., New York
- Kotera, M., and Suga, H. (1988) A simulation of keV electron scattering in a charged up specimen. *J.Appl.Phys.*, 63(2), 261
- Koyama, H. (1980) Cathodoluminescence study of SiO₂. *J.Appl.Phys.*, 51, 2228
- Luff, B., and Townsend, P. (1990) Cathodoluminescence of synthetic quartz. *J.Phys. Cond. Matter*, 2, 8089
- Marfunin, A.S. (1979) Spectroscopy, Luminescence and Radiation Centers in Minerals ch6., Springer-Verlag, Berlin
- Markes, M.E., and Halliburton, L.E. (1979) Defects in synthetic quartz: Radiation-induced mobility of interstitial ions. *J.Appl.Phys.*, 50, 8172
- Martin, B., Florke, O.W., Kainka, E., and Wirth, R. (1996) Electron irradiation damage in quartz, SiO₂. *Phys.Chem.Min.*, 23, 409
- Maschmeyer, D., and Lehmann, G. (1983) New hole centers in natural quartz. *Phys.Chem.Minerals*, 10, 84
- McOrist, G.D., Smallwood, A., and Fardy, J.J. (1995) Trace elements in Australian opals using neutron activation analysis. *Journal of Radioanalytical and Nuclear Chemistry*, 2(185), 293
- Munekuni, T., Yamanaka, Y., Shimogaichi, Y., Tohmon, R., Olike, Y., Nagasawa, K., and Hama, Y. (1990) Various types of nonbridging oxygen hole center in high purity silica glass. *J. Appl. Phys.* 68 1990 1212
- Myhaljlenko, S., Puechner, R.A., Edwards, J.L., and Davito, D.B. (1994) Can photo- and cathodoluminescence be regarded as complementary techniques? Proc.13 Pfefferkorn Meeting on Luminescence 1994. (obtained from internet), Niagara, Canada
- Nagasawa, K., Hoshi, Y., Ohki, Y., and Yahagi, K. (1986) Radiation effects on pure silica core optical fibers by γ -rays: Relation between 2 eV band and non-bridging oxygen hole centers. *Jap J. Appl. Phys.*, 25(3), 464
- Nagasawa, K., Mizuno, H., Yamasaka, Y., Tohmon, R., Ohki, Y., and Hama, Y. (1988) . In R.A.B. Devine, Ed. *The Physics and Technology of Amorphous SiO₂*, p. 193. Plenum Press, New York
- Nassau, K., and Prescott, B.E. (1975) A reinterpretation of smoky quartz. *Phys.Stat.Sol(a)*, 29, 659 National Scientific Company, Quakertown, PA 18951 USA
- Nishikawa, H., Nakamura, R., Tohmon, R., Ohki, Y., Sakurai, Y., Nagasawa, K., and Hama, Y. (1990) Generation mechanism of photoinduced paramagnetic centers from preexisting precursors in high-purity silicas. *Phys.Rev.B*, 41, 7828
- Nishikawa, H., Shiroyama, Y., Nakamura, R., Ohki, Y., Nagasawa, K., and Hama, Y. (1992) Photoluminescence from defect centers in high purity silica glasses observed under 7.9 eV excitation. *Physical Review B*, 45(2), 586
- Nishikawa, H., Tohmon, R., Ohki, Y., Nagasawa, K., and Hama, Y. (1989) Defects and optical absorption bands induced by surplus oxygen in high-purity synthetic silica. *J.Appl.Phys.*, 65, 4672
- Nishikawa, H., Watanabe, E., Ito, D., and Ohki, Y. (1994) Decay kinetics of the 4.4 eV photoluminescence associated with the 2 states of oxygen-deficient-type defect in SiO₂. *Phys.Rev.Lett.*, 72, 2101
- O'Reilly, E.P., and Robertson, J. (1983) Theory of defects in vitreous silicon dioxide. *Phys.Rev.B*, 27, 3780
- ORIGIN. . MicroCal Software Inc., 22 Industrial Drive E. Northhampton MA 01060 USA
- Pfeffer, R.L. (1988a) Molecular diffusion in a-SiO₂: its role in annealing radiation-induced defect centers. In C.R. Helms, and B.E. Deal, Eds. *The Physics and Chemistry of SiO₂ and the Si-SiO₂ Interface*, p. 169. Plenum Press, New York
- Pfeffer, R.L. (1988b) Transformation of radiation induced defect centers as a probe of molecular diffusion in a-SiO₂. In R.A.B. Devine, Ed. *The Physics and Technology of Amorphous SiO₂* ., p. 181. Plenum Press, New York

- Phillips, M.R., Moon, A.R., and Stevens Kalceff, M.A. (1995) Identification of Radiative Recombination Centres in Ti: α -Al₂O₃ using Cathodoluminescence Irradiation Kinetics. In E.S. Etz., Ed. *Microbeam Analysis-1995*, p. 95. VCH Publishers, New York
- Ramseyer, K., and Mullis, J. (1990) Factors influencing short-lived blue cathodoluminescence of alpha-quartz. *American Mineralogist*, 75, 791
- Reimer, L. (1985) SEM: Physics of Image Formation and Microanalysis. Springer Verlag, Berlin
- Remond, G., Cesbron, F., Chapoulie, R., Ohnenstetter, D., Rouques-Carmes, C., and Schvoerer, M. (1992a) Cathodoluminescence applied to the microcharacterization of mineral materials: present status in experimentation and interpretation. *Scanning Microscopy*, 6(1), 23
- Remond, G., Fialin, M., and Gilles, C. (1992b) The use of L X-ray spectra of the first-series transition elements for quantitative analysis with the electron microprobe. In G.W. Bailey, J. Bentley, and J.A. Small, Eds. *Proc 50th Annual Meeting of EMSA*, p. 1626. San Francisco Press
- Remond, G., Millot, C., and Roques-Carmes, C. (1996) Les techniques de preparation et de caracterisation des etats de surface: implications en microanalyse. Ecole d'ete de Microanalyse et Microscopie a Balayage. ANRT, Juillet 8-13 1996, Louvain la Neuve, Belgique
- Remond, G., Phillips, M.R., and Rouques-Carmes, C. (2000) Importance of instrumental and experimental factors on the interpretation of CL data from wide bandgap materials. In M. Pagel, V. Barbin, P. Blanc, and D. Ohnenstetter, Eds. *Cathodoluminescence in the Geosciences*. Springer-Verlag, Berlin
- Robertson, J. (1988) Electronic structure of defects in amorphous silicon dioxide. In R.A.B. Devine, Ed. *The Physics and Technology of Amorphous SiO₂*, p. 91. Plenum Press, New York
- Rossmann, G.R. (1994) Colored varieties of the silica minerals. In P.J. Heaney, C.T. Prewitt, and G.V. Gibbs, Eds. *Silica*, 129, p. 433. Mineralogical Society of America., Washington DC
- Ruppert, L.F. (1987) Applications of cathodoluminescence of quartz and feldspar to sedimentary petrology. *Scanning Microscopy*, 1, 63
- Sawyer Research Products Inc., Eastlake Ohio 44095 USA
- Segnit, E.R., Stevens, T.J., and Jones, J.B. (1965) The role of water in opal. *Journal of the Geological Society of Australia*, 12, 211
- Sigel, G.H., and Marrone, M.J. (1981) Photoluminescence in as-drawn and irradiated silica optical fibers: An assessment of the role of nonbridging oxygen hole centers. *J.Non-Cryst.Sol.*, 45, 235
- Skuja, L. (1994) Direct singlet-to-triplet optical absorption and luminescence excitation band of the twofold-coordinated silicon center in oxygen-deficient glass. *J.Non-Cryst.Sol.*, 167, 229
- Skuja, L., and Trukhin, A. (1989) Comment on the "Luminescence of fused silica: Observation of the O₂⁻ emission band". *Phys.Rev. B.*, 39, 3909
- Skuja, L.N., Silin, A.R., and Boganov, A.G. (1984a) On the nature of the 1.9 eV luminescence centers in amorphous SiO₂. *J.Non.Cryst.Sol.*, 63, 431
- Skuja, L.N., Streletsky, A.N., and Pakovich, A.B. (1984b) A new intrinsic defect in amorphous SiO₂ twofold coordinated silicon. *Sol.Stat.Comm.*, 50, 1069
- Song, K.S., and Williams, R.T. (1992) *Self-Trapped Excitons*. Springer-Verlag, Berlin
- Sprunt, E.S. (1981) Causes of quartz cathodoluminescence colors. *Scan.Electr.Micros.*, 525
- Stapelbroek, M., Griscom, D.L., Friebele, E.J., and Sigel, G.H. (1979) Oxygen-associated trapped-hole centers in high-purity fused silicas. *J. Non-cryst. Sol.*, 32, 313
- Steeds, J. (1992) Cathodoluminescence. In G. Trigg, Ed. *Ency. Appl. Phys.* V3, p. 121
- Stevens Kalceff, M.A. (1997) Cathodoluminescence microcharacterization of the defect structure of irradiated hydrated and anhydrous fused silicon dioxide. *Physical Review B* 57(10) 5674-5683
- Stevens Kalceff, M.A., and Phillips, M.R. (1995a) Cathodoluminescence microcharacterization of the defect structure of quartz. *Phys.Rev.B.*, 52, 3122
- Stevens Kalceff, M.A., and Phillips, M.R. (1995b) Electron irradiation induced outgrowths from quartz. *J.Appl.Phys.*, 77(8), 4125-4127
- Stevens Kalceff, M.A., and Phillips, M.R. (1996) Cathodoluminescence Microcharacterization of Silicon Dioxide Polymorphs. *International Conference on Cathodoluminescence and Related Techniques in Geosciences*, (Sept. 1996), p. 149, Nancy, France

- Stevens Kalceff, M.A., Phillips, M.R., and Moon, A.R. (1996a) Cathodoluminescence Microcharacterization of Opal. International Conference on Cathodoluminescence and Related Techniques in Geosciences, (Sept. 1996), p. 151, Nancy, France
- Stevens Kalceff, M.A., Phillips, M.R., and Moon, A.R. (1996b) Electron Irradiation Induced Changes in the Surface Topography of Silicon Dioxide. *J.Appl.Phys.*, 80(8), 4308
- Stevens Kalceff, M.A., Phillips, M.R., and Moon, A.R. (1997a) Cathodoluminescence microcharacterization of the irradiation sensitive defect structure of amorphous silicon dioxide. *Microscopy and Microanalysis*, 3, 751
- Stevens Kalceff, M.A., Phillips, M.R., Moon, A.R., and Smallwood, A. (1997b) Cathodoluminescence Microanalysis of Natural Hydrated amorphous SiO₂; Opal. *J.Phys.Chem.Min.*, 24, 131
- Stewart, J., and Galloway, W. (1962) Diffraction anomalies in grating spectrophotometers. *Appl.Optics*, 1, 421
- Sulimov, V.B., and Sokolov, V.O. (1994) Cluster modeling of the neutral oxygen vacancy in pure silicon dioxide. *J.Non-Cryst.Sol.*179, 260 1994
- Tohman, R., Mizuno, Y., Ohki, K., Sasagane, K., Nagasawa, K., and Hama, Y. (1989) Correlation of the 5.0- and 7.6-eV absorption bands in SiO₂ with oxygen vacancy. *Phys.Rev.B.*, 39, 1337
- Trukhin, A.N., Skuja, L.N., Boganov, A.G., and Rudenko, V.S. (1992) The correlation of the 7.6 eV optical absorption band in pure fused silicon dioxide with twofold-coordinated silicon. *J.Non-Cryst.Sol.*, 149, 96
- Vigouroux, J.P., Durad, J.P., Le Moel, A., Le Gressus, C., and Griscom, D.L. (1985) Electron trapping in amorphous SiO₂ studied by charge buildup under electron bombardment. *Journal of Applied Physics*, 57, 5139
- Walker, G. (1985) Mineralogical applications of luminescence techniques. In F.J. Berry, and D. Vaughan, Eds. *Chemical Bonding and Spectroscopy in Mineral Chemistry*. Chapman and Hall, London
- Walker, G. (1997) Physical parameters for the identification of luminescence centers in minerals. In M. Pagel, V. Barbin, P. Blanc, and D. Ohnenstetter, Eds. *Cathodoluminescence in the Geosciences*. Springer-Verlag, Berlin
- Wang, P.W., Hagland, R.F., Kinser, D.L., Mendenhall, M.H., Tolk, N.H., and Weeks, R.A. (1988) Luminescence induced by low energy electron deposition in Suprasil and Spectrosil glasses. *J.Non Cryst. Sol.*, 102, 288
- Weeks, R.A., Magruder III, R.H., and Wang, P.W. (1992) Some effects of 5 eV photons on defects in SiO₂. *J.Non.Cryst.Sol.*, 149, 122
- Weil, J.A. (1994) EPR of iron centers in silicon dioxide. *Appl.Mag.Reson.*6,1 1994
- Weil, J.A. (1984) A review of electron spin spectroscopy and its application to the study of paramagnetic defects in crystalline quartz. *Phys.Chem. Minerals* 10 149 1984
- Yacobi, B., and Holt, D. (1990) *Cathodoluminescence Microscopy of Inorganic Solids*. Plenum Press, New York
- Yang, B., Townsend, P.D., and Holgate, S.A. (1994) Cathodoluminescence and depth profiles of tin in float glass. *J.Phys.D.*, 27, 1757
- Yang, X.H., and McKeever, S.W.S. (1990) The pre-dose effect in crystalline quartz. *J.Phys D.*, 23, 237
- Zhang, Q., Yang, B., Wood, R.A., White, D.R.R., Townsend, P.D., and Luff, B.J. (1994) Thermoluminescence spectra of amethyst. *Rad Measure.*, 23, 423
- Zinkernagel, U. (1978) Cathodoluminescence of Quartz and its application to sandstone petrology. *Contrib. Sedimentology*, 8, 1
- Journal of Non Crystalline Solids (1992) vol. 149, and references therein
- Journal of Non Crystalline Solids (1994) vol. 179, and references therein

Brittle Deformation in Sandstone Diagenesis as Revealed by Scanned Cathodoluminescence Imaging with Application to Characterization of Fractured Reservoirs

KITTY L. MILLIKEN, STEPHEN E. LAUBACH

1

Introduction

The stable observing conditions, high magnifications, and sensitive light detection that are characteristic of scanning electron microscope-based cathodoluminescence (scanned-CL) imaging overcome several of the disadvantages of conventional light microscope-based CL systems, allowing more routine application of this petrographic method for description of micron-scale textural relationships between detrital grains, cements, and fractures in sandstones. Scanned-CL imaging has great utility for documenting the interrelation between deformation and diagenesis at the micrometer scale in siliciclastic rocks. A survey of sandstone units of widely varying age, location, and burial history suggests that quartz-lined and quartz-filled microfractures are nearly ubiquitous in lithified quartzose sandstones. Because fractures formed in association with quartz precipitation are prevalent in quartz-cemented siliciclastic hydrocarbon reservoir rocks, scanned-CL imaging of microfractures can potentially yield important information on subsurface fracture populations that have economic significance.

2

Methods

Images described here were produced using Oxford Instrument's photomultiplier CL detectors CL302 and P2 installed on JEOL T330A and T300 SEMs. Light is collected with the parabolic mirror inserted about 1 mm above an epoxy-impregnated, carbon-coated, polished thin section. Panchromatic images are observed on the CRT of the SEM and recorded on Polaroid film. An accelerating voltage of 10 kV with sample current set near 90% of the maximum for the SEM provides adequate photon emission for examining the luminescence variations in authigenic (relatively dark luminescent) and detrital quartz (relatively bright luminescent). Many of the CL photomicrographs in our studies are taken after several minutes of beam exposure, thus taking advantage of the beam-induced enhancement of CL emission in quartz to achieve higher contrast in the image. Because this chapter reviews interpretations of deformation history as

revealed by the CL contrast between detrital and authigenic quartz, quantitative assessment of emission intensity and color, and the variables affecting these parameters, are not critical.

3 Previous Cathodoluminescence Applications in Siliciclastic Rocks

In a now-classic paper, R. F. Sipple (1968) used light microscope-based CL to show that many apparent sutured boundaries in sandstones arise by quartz cementation rather than by pressure solution. Sipple also described quartz-filled fractures in sand grains and recognized the implications of this observation for the interpretation of polycrystallinity in quartz. Routine use of the methods described in Sipple's paper was difficult (restricted to relatively low magnifications and requiring long exposure times for photographic recording of the luminescence) and significant applications of this pioneering study were not immediately forthcoming.

Since the late 1970s, CL microscopy has been used to address several important issues in sandstone petrology. CL has particular utility for examining features in detrital and authigenic quartz. Quartz lacks the major compositional and textural variability that makes other major sandstone components, such as feldspars and lithic fragments, amenable to application of petrographic and chemical methods that depend on large degrees of chemical and textural variation (e.g., back-scattered electron imaging). Large variations in CL intensity, however, arise from the relatively slight variations in trace element content or defect structure that characterize quartz of various origins (Sipple 1968 and numerous subsequent publications). In the realm of chemical diagenesis, CL imaging clearly yields superior quantification of quartz cement volumes (Evans et al. 1988), and CL zoning in quartz cements has been used to study cement timing and paragenesis, in a manner analogous to CL studies of carbonate cementation (e.g., Hogg et al. 1992). As recognized by Sipple (1968), CL images are an important key to deciphering the role of local pressure solution vs silica import as a cause for quartz cementation (Houseknecht 1984, 1987, 1991).

It has also been suggested that CL colors (Matter and Ramseyer 1985; Owen 1991; Kennedy and Arikian 1990) and CL textures (Milliken 1994a) in detrital quartz grains might be useful as provenance indicators in siliciclastic rocks. With this goal in mind, a number of studies have focused on characterization of CL properties of quartz, especially in crystalline rocks that represent potentially significant sources of sediment (e.g., Zinkernagel 1978; Sprunt et al. 1978; Sprunt and Nur 1979; Ramseyer et al. 1988). Practical applications of this approach to provenance determination (e.g., Owen and Carrozzini 1986; Owen and Anders 1988) have been few, however, and additional basic studies on the systematics of quartz CL character in various igneous and metamorphic rocks and in modern sediments are clearly warranted.

Certain analysis methods in sandstone petrology can be used in combination with scanned-CL to overcome the uncertainties that result from the small-scale and sometimes cryptic mixing of authigenic and detrital quartz that occurs

through cementation and brittle deformation (see following section). For example, laser-extraction isotope analysis (Hervig et al. 1995) and fluid inclusion analysis (e.g., Burley et al. 1989) take advantage of scanned-CL to characterize with greater certainty the nature of the material analyzed.

Like Sipple, subsequent workers have recognized the utility of the CL contrast between detrital and authigenic quartz for documenting the mechanisms of grain-scale deformation in sandstones (Onash 1990, 1994; Morad et al. 1991; Hippler 1993; Dunn 1993; Fowles and Burley 1994; Milliken 1994b; Dickinson and Milliken 1995). This aspect of CL imaging is of interest because it provides a strong link between the chemical and deformational histories of sandstones, and, additionally, finds significant practical applications in the description of fractured reservoirs (Laubach 1997a).

4 Cathodoluminescence Evidence for Brittle Deformation at Small Scales in Sandstones

Survey of a wide variety of quartz-rich sandstones of different ages and burial histories (to date, 26 stratigraphic units ranging in age from Cambrian to Oligocene) reveals that brittle deformation of detrital grains occurs to some degree in many, perhaps most, sandstones. Perhaps because fractured surfaces present kinetically favored sites for quartz precipitation, small intragranular microfractures are prone to being filled in or 'healed' by authigenic quartz in optical continuity with the detrital grain. Such precipitation results in fractures that, commonly, are virtually invisible using conventional light microscopy as well as with secondary electron and back-scattered electron imaging. In some cases, intra- or transgranular microfractures correspond to planes of fluid inclusions that are visible to the trained eye (Laubach 1989). In other cases, quartz-filled fractures manifest virtually no overt evidence in light microscopy and are only revealed by CL imaging (Fig. 1).

Brittle deformation features in sandstones have a wide range of complexity and scale. Described in the following sections are some of the principal styles of brittle deformation that are commonly revealed by scanned-CL imaging of quartz in sandstones.

4.1 Simple Intragranular Fractures

Simple intragranular opening-mode (extension) fractures are the most common type of brittle deformation observed in sandstones. Clearly, some of these intragrain fractures are inherited. Distinguishing post-depositional fractures from those inherited from the sand source is a challenge that is partially resolved by panchromatic scanned-CL imaging. Examination of the fracture fill at high magnification may reveal either continuity or truncation of the cement where the fracture intersects the grain surface (Laubach 1997). Fractures identified as inherited based on textural relations also commonly are filled with quartz that differs

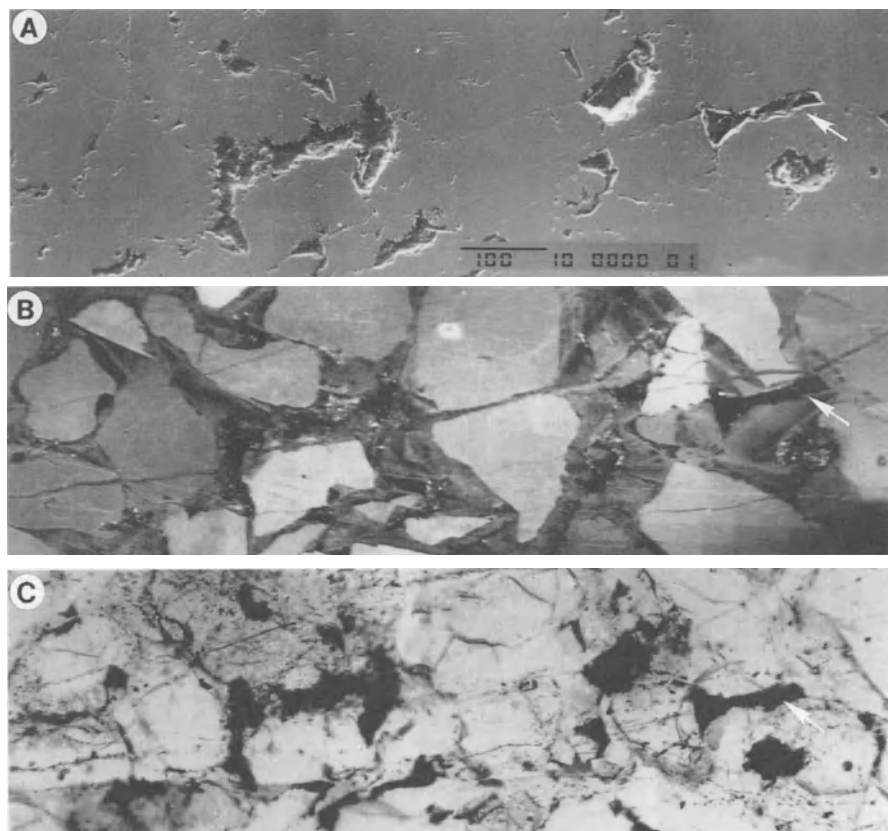


Fig. 1A–C. Quartz-cemented and microfractured sandstone as revealed by secondary electron imaging (A), scanned-CL-imaging (B), and plane light microscopy (C). *White arrows* in the right-center region of the images indicate equivalent locations at the edge of a quartz-lined pore. Travis Peak Formation, Cretaceous, East Texas. *Scale bars* are 100 μm

in luminescence brightness from adjacent cement. It is likely that color information obtained through the use of filters in the light collection system will in the future provide more straightforward discrimination of inherited vs in situ origins for simple intragranular fractures.

Another category of intragranular fracture has curved to straight traces arranged in simple to complex intersecting patterns, and commonly radiating from points of grain contact and displaying a wide range of orientations (Fig. 2). Such fractures commonly have distinctive triangular shapes and small length:width ratios (they are short and wide). The arrangement and shape of these microfractures are similar to that of microfractures produced in uniaxial compaction experiments on wet sand packs (Gallagher et al. 1974; Schutjens 1991; Zhang et al. 1990; Elias and Hajash 1992). These fractures probably represent deformation associated with sediment compaction (with or without a superposed tectonic stress field) at a time when significant intergranular porosity existed in the rock.

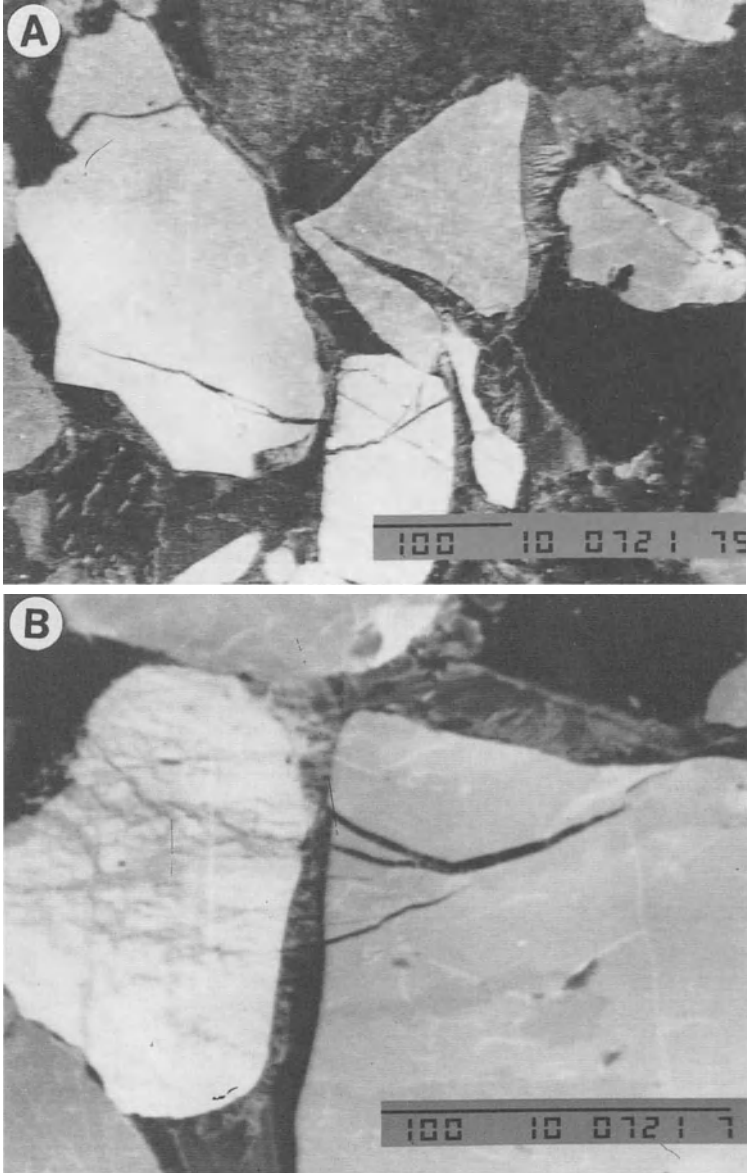


Fig. 2A,B. Grain interaction fractures. Canyon Sandstone, Permian, West Texas

A third category of intragrain fracture cuts indiscriminately across grains. These intragrain fractures have shapes and orientation patterns that match those of nearby large transgranular fractures. They are simply the smallest size fractions of fracture populations that grew after cementation and compaction made the sandstone relatively homogeneous mechanically.

Intragrain fractures in these three categories can be distinguished using criteria described by Laubach (1997). Using scanned-CL, point-counts from fine to medium sandstones in ten formations show that inherited fractures visible as cement-filled features make up about 10% of intragrain fractures, with the balance about equally split between the other two categories. Fluid-inclusion planes do not always correspond to cement-filled fractures, probably because many inherited fluid-inclusion planes were created or modified in a metamorphic environment and lack the compositional differences or defects that cause CL contrast (Sprunt et al. 1978).

One interesting aspect of these ubiquitous intragranular fractures is that they are a major cause of apparent polycrystallinity in detrital quartz grains and render the use of polycrystallinity questionable for provenance determination (e.g., Sipple 1968; Morad et al. 1991; Dickinson and Milliken 1995).

4.2 Fractures Affiliated with Concavo-convex and Sutured Grain Boundaries

In highly compacted, yet still-porous, sandstones, local concentration of simple intragranular fractures leads to the development of crushed grains (e.g. Dickinson and Milliken 1995; Fig. 3). Development of intragranular fractures tends to be spatially heterogeneous, with highly variable degrees of grain crushing even in adjacent grains of similar mineralogy. Controls on the distribution of intragranular fractures are not always apparent, but include factors such as the local packing arrangement and also pre-existing zones of weakness such as inherited frac-



Fig. 3. Crushed grain boundary from the subsurface Frio Formation Texas Gulf coast. Field of view is uniform quartz with only minor visible microporosity. Dark luminescing quartz is authigenic whereas the detrital grains and their fragments are bright

tures or crystal boundaries in polycrystalline grains. Propagation of cracks from pore-spaces and pre-existing cracks has been noted in compaction experiments (e.g., Adams and Sines 1978; Wong 1982). Thus, it is likely that intragranular fracturing in certain circumstances is a self-ramifying process on the micrometer-scale, because the initial fracturing of a grain leads to an increase in load to the point of failure on nearby grains and pores.

A significant number of interpenetrating grain boundaries, ranging in complexity from simple concavo-convex contacts described above, to stylolites, are associated with a prominent degree of brittle deformation. CL images reveal that many cases of apparently sutured boundaries arise almost entirely by spatial redistribution of grain fragments rather than volume loss. Many grains show a pronounced increase in intensity of brecciation immediately adjacent to the region of maximum curvature of the grain contact. In such areas, intense crushing of the indented grain produces a finely comminuted aggregate of $<5\text{-}10\ \mu\text{m}$ particles that are near the limit of the instrument's spatial resolution with CL imaging. This microns-wide region of highly comminuted and displaced grain debris suggests a history of repeated localized fracturing in what might be termed a "brittle process zone" (Fig. 4). Progressive evolution of crushing along such a zone typically leads to a triangular region of concentrated microfractures within the indented grain (Fig. 5).

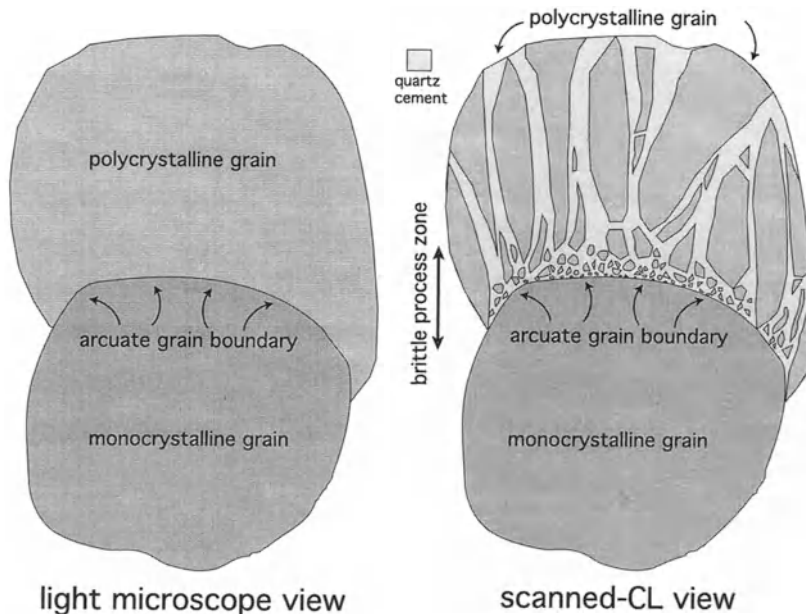


Fig. 4. Line drawings that contrast two petrographic views of sand grains having a concavo-convex contact. Conventional light microscopy, either with plane-polarized light or with crossed polars, reveals an arcuate grain boundary that is strongly suggestive of compaction through pressure dissolution and volume loss from the upper polycrystalline grain. Scanned-CL microscopy reveals that polycrystallinity in upper grain arises from brittle deformation including a zone of highly comminuted silt-size rubble along contact. Fragments of crushed grain have been cemented by authigenic quartz

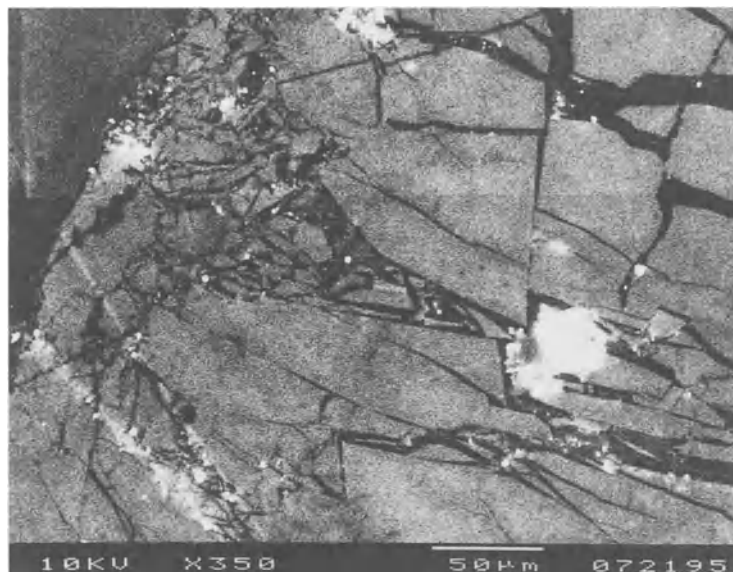


Fig. 5. Well-developed triangular crush zone, Hickory Formation, Cambrian, Central Texas. Field of view is uniformly quartz with only minor amounts of microporosity

Along more highly sutured contacts, finely crushed grain debris tends to be less abundant, and brittle deformation is instead manifested as microfractures localized on grain promontories (Fig. 6). In all cases of apparent pressure solution, from simple concavo-convex grain boundaries to stylolites, volume loss estimated from scanned-CL images is typically much less than that determined from conventional petrography. Although some actual volume loss may occur, estimating that loss is severely complicated by the complex, multidimensional particle rearrangement that accompanies the repeated heterogeneous deformation.

The association of microfractures with a range of apparent pressure solution features suggests that brittle deformation is integral in some way to the pressure solution mechanism (Milliken 1994b; Dickinson and Milliken 1995). A genetic association between brittle processes and pressure solution has been suggested by numerous workers (e.g., Gratz 1991), based upon theoretical models of stress (Fletcher and Pollard 1981; Wood 1981), observations from compaction experiments (e.g., Maxwell 1960), relationships between stylolites and macroscopic veins in outcrop and core (Choukroune 1969; Nelson 1981; Heydari and Moore 1993), and associated stylolites and microfractures at the thin section scale (Onash 1990; Morad et al. 1991; Raynaud and Carrio-Schaffhauser 1992).

It is possible that enhancement of quartz solubility at grain contacts occurs as a direct result of extreme particle size reduction (e.g., Petrovich 1981; Holdren and Speyer 1985). In this view, fracturing is the primary or initial process active in the pressure solution mechanism, followed by the secondary process of dissolution. This is consistent with observation of numerous microfractures in rocks that lack abundant stylolites.



Fig. 6. Fractures propagating from region of maximum curvature along sutured grain boundary. Field of view is entirely quartz. Breathitt Formation, Pennsylvanian, eastern Kentucky

4.3

Transgranular Fractures and Crack-Seal Deformation

Transgranular and transcement fractures, though less common than simple intra-granular fractures, are far more prevalent than previous optical microscopy or conventional CL observations suggested (Laubach 1997a,b). Based on scanned-CL observations, such fractures can be grouped into categories based on fracture shapes and fracture patterns with respect to detrital grains (Laubach 1997a; his Table 2, p. 612). Planar fractures that cut indiscriminately grains and cement most closely resemble large (i.e., visible without magnification) quartz-lined veins. They have similar internal mineral fill patterns, orientations (Laubach 1997a,b), and size distributions (Marrett and Laubach 1997). In many ways, these microfractures and associated macrofractures are simply different size fractions of the same fracture sets.

Displacement and fragmentation of wall-rock grains and CL-zoned cements attests to an episodic history of repeated fracturing and cementation, creating “crack-seal” microstructure (Ramsay 1980) (Fig. 7). Even in structural settings distant from folds and faults, quartz-cemented sandstones commonly contain large quartz-lined and -bridged fractures that have crack-seal microstructures that show that these fractures were opening as quartz cement precipitated (Laubach 1988). Interestingly, in large fractures the increase in fracture volume due to crack opening is typically greater than the decrease due to cement precipitation, such that fracture porosity is preserved (Laubach 1997a,b). In these fractures, quartz crystals precipitated locally in open fracture pore space preserve

crack-seal microstructures. The spatial distribution of contemporaneous CL cement zones and primary fluid inclusions within such veins can be exceedingly complex.

Images of the walls and tips of crack-seal veins show how crack-seal structure evolves in sandstones. Small cracks are not always precisely located parallel to those formed at earlier stages of fracture growth. Instead, on a small scale (1 to tens of micrometers), the paths of transgranular microfractures are influenced by local heterogeneities such as grain-cement boundaries or contacts between cement and pore space, leading to heterogeneous crack development and formation of complex intergrowths of detrital quartz and authigenic minerals of variable age (Fig. 7). Because some small fractures are not completely filled, they become the locus of repeated fracture. These observations show that, even in macroscopically undeformed rocks, complex structures can develop as a result of episodic fracture growth.

Information revealed by CL imaging allows distinction to be made among authigenic phases formed at different stages of the deformation history. CL imaging also shows that closed microfractures, which are locally marked by fluid inclusion planes, were sealed by precipitation of material transported over distances greater than grain scale, rather than healed by local-scale diffusive mass transfer.



Fig. 7. Complex grain/cement intergrowth in a crack-seal fracture fill. Repetitive fracturing has transported highly angular slivers of bright luminescing detrital quartz relatively large distances across the fracture. Luminescence variations that suggest complex intergrowths of different generations of authigenic quartz are indicative of fracture movement synchronous with quartz precipitation leading to fracturing and overgrowth of the earlier-formed cement. Frontier Formation, Wyoming. *Scale bar is 100 μm*

Thus, fluid inclusions associated with quartz-lined microfractures are primary rather than secondary and can be used for investigating evolution of fluid properties during diagenesis and deformation. Integrating fluid inclusion, geochemical, and structural data through the use of CL imaging is an intriguing avenue for future work.

4.4 Deformation Bands

Deformation bands are curvilinear millimeter to meter-scale zones where sandstone is more indurated and typically shows diminished porosity and permeability. Some deformation bands are zones where these changes in rock properties correspond to locally denser grain packing than in adjacent rock, whereas others show reduced particle size as a result of localized grain crushing.

Some deformation bands show no evidence of slip parallel to band surfaces and reflect localized compaction (Hill 1989) but others are clearly faults (Aydin and Johnson 1983; Fowles and Burley 1994; Antonellini et al. 1994; Antonellini and Aydin 1994, 1995; Milliken 1996a,b). Scanned-CL observations from the Cambrian Hickory Formation of central Texas help to clarify how such bands grow. In this example, a sequence of fabrics from edge to center probably represent progressive stages in band development. Band edges are relatively porous and contain sand-size grains with abundant quartz-filled intragranular fractures. In contrast, band centers display a bimodal particle size distribution with large, rounded, and virtually unfractured sand-size particles surrounded by a highly comminuted microrubble (gouge) of angular silt-size debris (Fig. 8). Band development apparently begins as a planar zone of localized grain crushing.

As particle shape heterogeneity increases, localized breakage leads to further particle size reduction. The sand-size, rounded grains in band centers probably survive simply because these particles avoided breakage up to the point that further displacement was accommodated entirely within comminuted silt-size rubble. Porosity and permeability reduction within the deformation band arise from a combination of particle size reduction and quartz cementation (Fig. 8). As in the case of apparent pressure solution, silica mobilization in deformation bands may be promoted by increase in surface area of detrital quartz through mechanical particle size reduction.

These microstructural observations are compatible with a process of fault-zone thickening at the grain scale that occurs as a diffuse front of brittle deformation that migrates laterally into the host rock, a pattern characteristic of many natural fault zones that become thicker as they accommodate greater displacement (Aydin and Johnson 1978; Martel 1990). Experiments within a variety of rock types show that artificial faults can increase in thickness as grains in the host rock adjacent to the fault become fractured then incorporated into the fault (see references in Martel 1990).

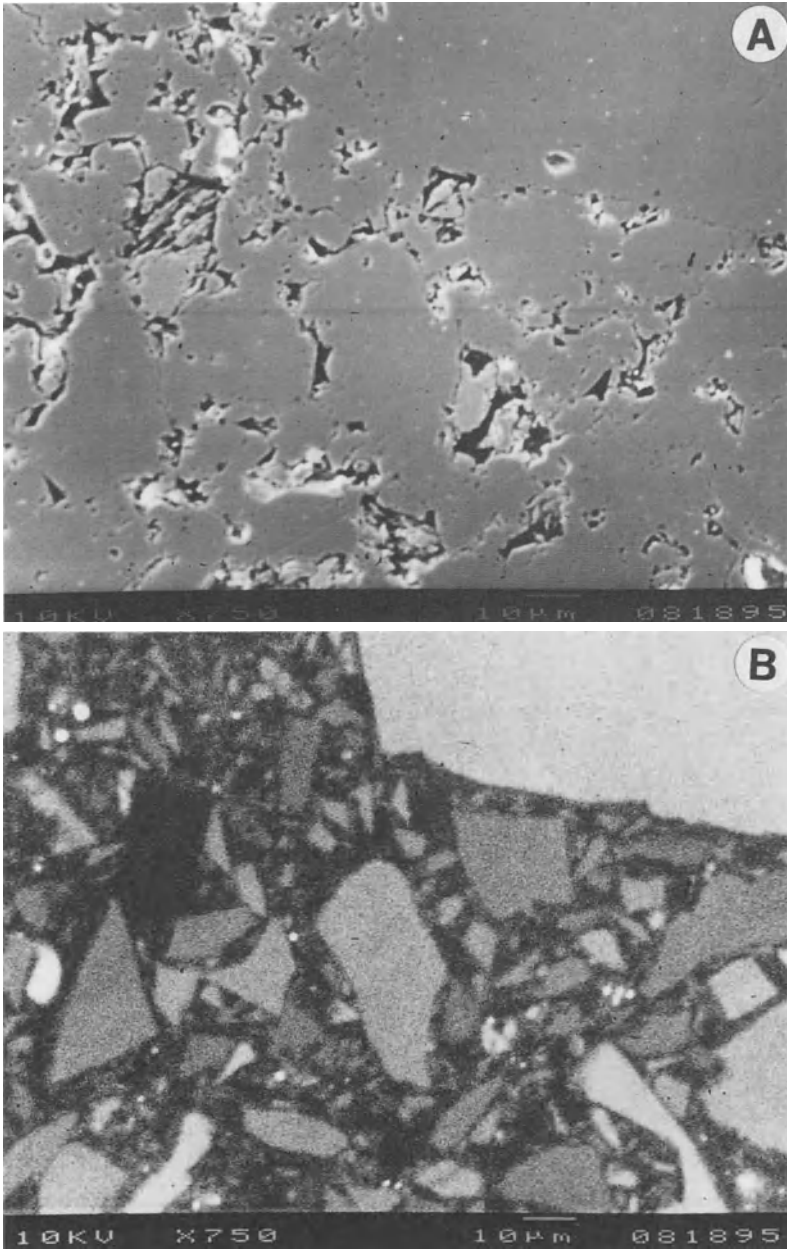


Fig. 8. Secondary electron image (A) and scanned-CL-image (B) of the central region of a deformation band in the Cambrian Hickory Sandstone Central Texas. Note the angular shapes of the quartz particles (bright-luminescing) which are cemented by a significant component of authigenic quartz (dark luminescence). Minor amounts of microporosity remain in the uncemented portions of the interparticle space

5 Application to Fractured Reservoirs

Improved understanding of diagenetic processes and petrophysical heterogeneities that result from deformation band development illustrate one way scanned-CL analysis can be applied to fractured reservoir studies. For example, bands have significant detrimental effects on sandstone reservoir continuity (Fowles and Burley 1994; Antonellini et al. 1994). Another approach is to use scanned-CL measurements of microfractures as a diagnostic tool for inferring the properties of large fractures (Laubach 1997).

Direct measurement of the attributes of large fractures is extremely challenging because such fractures rarely intersect wellbores where they can be observed. The consequence is an unacceptably high level of uncertainty about even the most basic fracture attributes critical for exploration and development success. As this review shows, in many siliciclastic petroleum reservoirs, microfractures, with sizes of microns to millimeters, are more common than large fractures and can be sampled effectively even in small volumes of rock. In some cases the properties of large fractures can be inferred from observation of microfractures and associated diagenetic minerals in the rock matrix.

Among the fracture attributes that can be inferred from observation of small fractures are size distribution (Marrett and Laubach 1997), degree of mineral fill (Laubach and Milliken 1996), and orientation (Laubach 1997a,b). Size distribution is one of the most useful parameters because of its influence on permeability and other rock properties (such as seismic velocity) (Marrett et al. 1997). Scanned-CL observation of microfractures extends the range of observational data on fracture populations by more than three orders of magnitude. This allows power-law scaling patterns of fracture populations to be deduced from small core samples that may not contain fractures visible to the unaided eye. This area of application of scanned-CL observations has great promise.

In concert with conventional paragenetic analysis, scanned-CL observations of microfractures can be used to estimate the degree to which fracture networks have been filled with authigenic cements (Laubach and Milliken 1996). This is accomplished by dividing cements on the basis of timing of cement precipitation relative to fracture growth (Fig. 9). Because large fractures are rarely encountered in core, scanned-CL observations of microfractures are used to fix the time(s) of fracture formation.

According to this classification, syn- and postkinematic cements are those available to fill fractures. However, because synkinematic quartz tends to incompletely fill fractures, preliminary and unpublished data from our laboratory suggest that it is postkinematic cement that best predicts the degree to which fracture are filled.

Such estimates can yield valuable predictions of well performance in areas where natural fractures are the dominant conduits for fluid flow to the well. For example, Fig. 10 shows comparisons of post-stimulation production outcomes for paired natural gas wells in East Texas and Wyoming. The geologic and engineering characteristics of these paired wells are similar in each region. The rocks contain reservoir storage volume and natural fractures provide intrareservoir flow

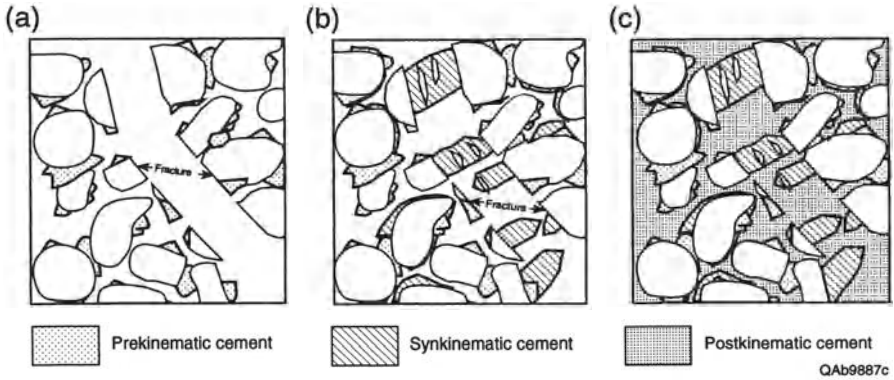


Fig. 9a-c. Classification of cement types according to time of cement precipitation relative to fracture opening (after Laubach and Milliken 1996). a Prekinematic, b Synkinematic. Note crack-seal structures and preservation of fracture porosity. c Postkinematic. Postkinematic cement is principally responsible for closing fractures

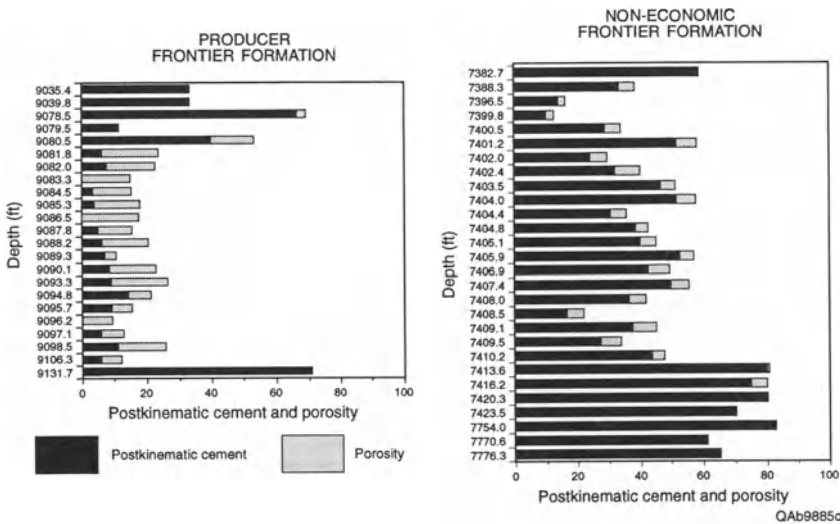


Fig. 10. Postkinematic cement and porosity at several depths in natural gas wells East Texas and Wyoming. Postkinematic cement is shown as a proportion of total cement. Timing of cement precipitation relative to fracture opening was determined using scanned-CL observation of microfracture patterns and conventional analysis of cement petrogenesis

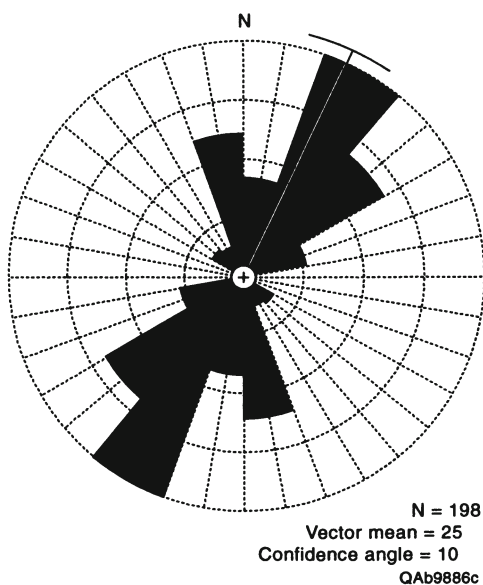
pathways. Key differences between wells are overall rate of fluid production (producer vs non-producer) and postkinematic cement volume. High values of postkinematic cement imply that natural fractures are cemented shut, and in this case uniformly high values of postkinematic cement accurately predict low fluid production and vice versa.

Scanned-CL observations also can be used directly to measure fracture orientations. Fluid-inclusion planes have been used as structural markers in metamorphic rocks since Tuttle (1949). Laubach (1989) identified post-depositional microfractures in macroscopically undeformed sedimentary sandstones using optical microscopy and showed that they formed at the same time as large quartz-lined fractures. CL equipment available then did not resolve the authigenic quartz surrounding the fluid inclusions. Without a capability to image cross-cutting relations between cement and microvein fill, such microstructural observations were of limited value, because of the possibility that many of the microfractures observed were inherited (Laubach 1989; Anders and Wiltschko 1994).

Scanned-CL observations allow measurements of a large number of microfractures to be rapidly compiled, making practical the use of microfractures as guides to the strike of larger fractures (Laubach 1997b). Scanned-CL not only allows inherited fractures to be identified, but also reveals cross-cutting relations among fractures, so that the sequence of fracture formation can be deduced. Scanned-CL observations also reveal fracture shapes and patterns, so that the smallest but most abundant microfractures can be used as proxies for large fractures.

For example, Fig. 11 shows microfracture orientation data from a major fractured oil reservoir in Texas (S. Laubach, unpublished report 1997). Microfractures used in this plot are all intragranular. The main microfracture trend matches exactly the orientation of large fractures measured independently in horizontal core. Cross-cutting relations, visible using scanned-CL, show that the subsidiary microfracture trend represents a younger fracture set. Such information is a highly cost effective and powerful guide to oil- and gas-field development practices.

Fig. 11. Microfracture strikes in three samples from a major fractured Texas siliciclastic oil reservoir (from S. Laubach, unpublished report 1997). Independent measurement of large fractures in the same well shows strike of $N30E \pm 10$. All microfractures used are intragranular (category 1d Laubach 1997)



Scanned-CL is superior to other methods for microstructure characterization because the relation of fractures to diagenetic phases can be imaged. Although microfractures due to drilling, core expansion/contraction, core handling, and sample preparation are often present, scanned-CL reveals those that are partly filled with authigenic mineral precipitates and that reliably represent a sample of subsurface fracture populations.

6

Conclusions

Localization of quartz precipitation in microfractures in some cases produces sandstones that contain significant amounts of authigenic quartz within fractured detrital grains. Quantitative determination of this intragranular fracture-filling quartz is nearly impossible using conventional microscopy; thus, scanned-CL imaging of sandstones has important ramifications for understanding chemical as well as physical aspects of sandstone diagenesis.

Crack-seal structures visible with CL imaging also demonstrate that quartz cement precipitation and fracture development are intimately linked (Laubach 1988; Laubach 1997). This genetic association needs to be accounted for in models of quartz precipitation and fracture development.

Scanned-CL observations distinguish three categories of microscopic fractures. Some of these can be used to determine orientations of large fractures, significantly enhancing the value of core observations in siliciclastic reservoirs. Although large fractures play the most important role in performance of petroleum reservoirs, research in progress suggests that microstructural observations can also be used to infer the openness and size distribution of large fractures. Such information is vital to cost-effective development of many fractured siliciclastic hydrocarbon reservoirs.

Acknowledgements. This work was supported in part by the Donors of the Petroleum Research Fund of the American Chemical Society (ACF-PRF 22805-AC8), the U.S. Department of Energy under DOE Subcontract No. G4S51732, and by the following companies in the UT fracture research consortium: Chevron USA, Conoco, Inc., Exxon Production Research, Union Pacific Resources, and Oxford Instruments. KLM also acknowledges the Institut Français du Pétrole for its support during preparation of this manuscript. The many constructive suggestions from reviewers Anne Marie Boullier and Yves Bernabe are greatly appreciated.

References

- Adams M, Sines G (1978) Crack extension from flaws in a brittle material subjected to compression. *Tectonophysics* 49:97–118
- Anders MH, Wiltshcko DV (1994) Microfracturing paleostress and the growth of faults. *J Struct Geol* 16:795–815
- Antonellini MA, Aydin A, Pollard DD (1994) Microstructure of deformation bands in porous sandstones at Arches National Park Grand County Utah. *J Struct Geol* 16:941–959

- Antonellini, Aydin A (1994) Effect of faulting on fluid flow in porous sandstones. Petrophysical properties. *Amer Association of Petroleum Geologists Bull* 78:355–377
- Antonellini M, Aydin A (1995) Effect of faulting on fluid flow in porous sandstones. Geometry and spatial distribution. *Amer Association of Petroleum Geologists Bull* 79:642–671
- Aydin A, Johnson AM (1983) Analysis of faulting in porous sandstones. *J Struct Geology* 5:19–31
- Burley SD, Mullis J, Matter A (1989) Timing diagenesis in the Tartan reservoir (UK North Sea): constraints from combined cathodoluminescence microscopy and fluid inclusion studies. *Mar Petrol Geol* 6:98–102
- Choukroune P (1969) An example of mesoscopic analysis of concentric folding in limestone series. *Tectonophysics* 7 57–70
- Dickinson WW, Milliken KL (1995) The diagenetic role of brittle deformation in compaction and pressure solution Etjo Sandstone Namibia. *J Geol* 103:339–347
- Dunn TL (1993) Early quartz grain fracturing and annealing, an important brittle deformation mechanism of early compaction in first cycle orogenic sandstones revealed by scanning electron cathode luminescence microscopy. *Geol Soc Amer Abstr, Annual Mtg* 25:6:A335
- Elias B, Hajash Jr A (1992) Changes in quartz solubility and porosity due to effective stress. An experimental investigation of pressure solution. *Geology* 20:451–454
- Evans J, Hogg AJ, Hopkins MS, Howarth R J (1994) Quantification of quartz cements using combined SEM CL and image analysis. *J Sed Res* 64 A:334–338
- Fletcher RC, Pollard DD (1981) Anticrack model for pressure solution surfaces. *Geology* 9:419–424
- Fowles J, Burley SD (1994) Textural and permeability characteristics of faulted high porosity sandstones. *Mar Petrol Geol* 11:608–623
- Gallagher JJ, Friedman M, Handin J, Sowers GM (1974) Experimental studies relating to microfractures in sandstone *Tectonophysics* 21:203–247
- Gratz AJ (1991) Solution-transfer compaction of quartzites. Progress toward a rate law. *Geology* 19:901–904
- Hervig RL, Williams LB, Kirkland IK, Longstaffe F J (1995) Oxygen isotope microanalysis of diagenetic quartz, possible low temperature occlusion of pores. *Geochimica Cosmochimica Acta* 59:2537–2543
- Heydari E, Moore CH (1993) Zonation and geochemical patterns of burial calcite cements. *J Sed Petrology* 63:44–60
- Hill RE (1989) Analysis of deformation bands in the Valley of Fire State Park Nevada Master's Thesis Univ Nevada Las Vegas
- Hippler SJ (1993) Deformation microstructures and diagenesis in sandstone adjacent to an extensional fault. implications for the flow and entrapment of hydrocarbons. *Amer Association of Petroleum Geologists Bull* 77:625–637
- Hogg AJC, Sellier E, Jourdan AJ (1992) Cathodoluminescence of quartz cements in Brent Group sandstones Alwyn South UK North Sea in Morton A C, Haszeldine R S Giles MR, Brown S, eds *Geology of the Brent Group*. *Geol Soc London Special Pub* 61:421–440
- Holdren GR, Speyer PM (1985) Reaction rate–surface areas relationships during the early stages of weathering—I Initial observations. *Geochimica Cosmochimica Acta* 49:675–681
- Houseknecht DW (1984) Influence of grain size and temperature on intergranular pressure solution quartz cementation and porosity in a quartzose sandstone. *J Sed Petrology* 54:348–361
- Houseknecht DW (1987) Assessing the relative importance of compaction processes and cementation to reduction of porosity in sandstones. *Amer Assoc Petrol Geol Bull* 71:633–642
- Houseknecht DW (1991) Use of cathodoluminescence petrography for understanding compaction quartz cementation and porosity in sandstones. in Barker CE, Kopp OC, eds, *Luminescence microscopy and spectroscopy. quantitative and qualitative applications Society for Sedimentary Geology Tulsa Oklahoma* pp 59–75
- Kennedy SK, Arikian F (1990) Spalled quartz overgrowths as a potential source of silt. *J Sed Petrology* 60:438–444
- Laubach SE (1988) Subsurface fractures and their relation to stress history in East Texas Basin sandstone. *Tectonophysics* 156 no 4 495–503

- Laubach SE (1989) Paleostress directions from the preferred orientation of closed microfractures (fluid-inclusion planes) in sandstone East Texas basin USA *J Struct Geology* 11 no 5 603–611
- Laubach SE (1997a) A method to detect natural fracture strike in sandstones. *AAPG Bull* 81 no 4 604–623
- Laubach SE (1997b) Determination of natural fracture orientation using scanned CL. The University of Texas at Austin, Bureau of Economic Geology, Contract Report, 7 p
- Laubach SE, Milliken KL (1996) New fracture characterization techniques for siliciclastic rocks. in Aubertin M, Hassani F, Mitri H (eds) *Proc 2nd North Amer Rock Mechanics Symp*, Balkema. Rotterdam 1209–1213
- Marrett R, Laubach SE (1997) Diagenetic controls on fracture permeability and sealing. *Int J Rock Mech Min Sci* 34 no 3–4
- Marrett R, Ortega O, Reed R, Laubach S (1997) Predicting macrofracture permeability from microfractures *AAPG Annual Convention Official Program* p A76
- Martel SJ (1990) Formation of compound strike-slip fault zones Mount Abbot quadrangle California. *J Struct Geol* 12 no 7:869–882
- Matter A, K Ramseyer (1985) Cathodoluminescence microscopy as a tool for provenance studies of sandstones in GG Zuffa ed *Provenance of Arenites Dordrecht Reidel*, pp 191–212
- Maxwell JC (1960) Experiments on compaction and cementation of sand in Griggs DT, Handin J, eds, *Rock Deformation. Memoir Geological Society of America* pp 105–132
- Milliken KL (1994a) Cathodoluminescent textures and the origin of quartz silt in Oligocene mudrocks South Texas. *J Sed Res* 64 A:567–571
- Milliken KL (1994b) The widespread occurrence of healed microfractures in siliciclastic rocks. Evidence from scanned cathodoluminescence imaging. pp 825–832 in Nelson P, Laubach SE, eds, *Rock Mechanics. Models and Measurements Challenges from Industry*, 1st North Amer Rock Mech Symp, A A Balkema, Rotterdam, pp 825–832
- Milliken KL (1996a) Deformation bands formed by interrelated cementation and brittle fracture in porous sandstones Hickory Formation Central Texas. *Synkinematic diagenesis revealed by cathodoluminescence imaging*. *AAPG annual meeting San Diego California*, p A98
- Milliken KL (1996b) Polyphase emplacement of authigenic quartz in quartzose sandstones during fracturing. *South-central GSA meeting Abstracts with Programs* 28:1:53–54
- Morad S, Bhattachayya A, Al-Aasm IS, Ramseyer K (1991) Diagenesis of quartz in the Upper Proterozoic Kaimur Sandstone Son Valley central India. *Sed Geol* 73:209–225
- Nelson RA (1981) Significance of fracture sets associated with stylolite zones. *Amer Assoc Petroleum Geologists Bull* 65:2417–2425
- Onash CM (1990) Microfractures and their role in deformation of a quartz arenite from the central Appalachian foreland. *J Struct Geol* 12:883–894
- Onash CM (1994) Assessing brittle volume-gain and pressure solution volume-loss processes in quartz arenite. *J Struct Geol* 16:519–530
- Owen MR (1991) Application of cathodoluminescence to sandstone provenance. in Barker E, Kopp OC, eds, *Luminescence microscopy and spectroscopy. quantitative and qualitative applications*. Society for Sedimentary Geology Tulsa Oklahoma p 67–75
- Owen MR, Anders MH (1988) Evidence from cathodoluminescence for non-volcanic origin of shocked quartz at the Cretaceous-Tertiary boundary. *Nature* 334:145–147
- Owen MR, Carozzi AV (1986) Southern provenance of Upper Jackfork Sandstone southern Ouachita Mountains. *cathodoluminescence petrology*. *Geol Soc Amer Bull* 97:110–115
- Petrovich R (1981) Kinetics of dissolution of mechanically comminuted rocks-forming oxides and silicates– I Deformation and dissolution of quartz under laboratory conditions. *Geochimica Cosmochimica Acta* 45:1665–1674
- Ramsay JG (1980) The crack-seal mechanism of rock deformation *Nature* 284:135–139
- Ramseyer K, Baumann J, Matter A, Mullis J (1988) Cathodoluminescence colours of α -quartz. *Min Mag* 52:669–677
- Raynaud S, Carrio-Schaffhauser R (1992) Rock matrix structures in a zone influenced by a stylolite. *J Struct Geol* 14:973–980

- Schutjens P (1991) Experimental compaction of quartz sand at low effective stress and temperature conditions *J Geol Soc London* 140:725–740
- Sipple RF (1968) Sandstone petrology. evidence from luminescence petrography *J Sed Petrology* 38:530–554
- Sprunt E S, Dengler L A, Sloan D (1978) Effect of metamorphism on quartz cathodoluminescence. *Geology* 6:305–308
- Sprunt ES, Nur A (1979) Microcracking and healing in granites: new evidence from cathodoluminescence. *Science* 205:495–497
- Tuttle OF (1949) Structural petrology of planes of liquid inclusions. *J Geol* 57:331–356
- Wong T-F (1982) Micromechanics of faulting in Westerly Granite. *Int J Rock Mech Min Sci* 19:49–64
- Wood JR (1981) Fracture pressure solution: Experiment and theory. *GAC-MAC Abstracts* 5:43
- Zhang J, Wong T-F, Davis TM (1990) Micromechanisms of pressure-induced grain crushing in porous rocks *J Geophys Res* 95 no B1:341–352
- Zinkernagel U (1978) Cathodoluminescence of Quartz and Its Application to Sandstone Petrology. *Contributions to Sedimentology* 8. Stuttgart E Schweizerbart'sche Verlagsbuchhandlung (Nägele und Obermiller)

High-Resolution Cathodoluminescence Studies of Feldspar Minerals

JENS GÖTZE, MATTHIAS R. KRBETSCHKE,
DIRK HABERMANN, DIETER WOLF

1

Introduction

Feldspars are the most important rock-forming minerals occurring in igneous, metamorphic and sedimentary rocks. Cathodoluminescence (CL) of feldspars is an important tool in interpreting genetic conditions of rock formation and alteration (Marshall 1988). Furthermore, feldspars are widely used as dosimeters in dating geological and archaeological materials by thermally or optically stimulated luminescence (TL, OSL).

Feldspars formed under different conditions may show different luminescence emission characteristics, depending on crystallization environment and trace-element uptake during growth or recrystallization. Thus, different CL colors permit rapid visual distinction of different feldspar phases, compositional zoning, fine-scale structures, and mineral intergrowth (Fig. 15A–C). Usually it is quite easy to distinguish the distribution of alkali feldspars and plagioclases using CL. Furthermore, variations in color and intensity, which probably represent variations in the concentration of activators or defects, can be used to distinguish different feldspar generations or to provide useful information in provenance evaluation of clastic sediments. Within single feldspar grains, alteration, exsolution, zoning, and related phenomena are often revealed by CL. Moreover, the sharp contrast between detrital and authigenic feldspars enables authigenic overgrowths on detrital feldspar grains to be detected (Kastner 1971). Several studies have illustrated the usefulness of CL investigations in the study of authigenic feldspar in sandstones or carbonate rocks (Marshall 1988 and references therein).

In the present study CL characteristics of terrestrial feldspar samples covering the Or-Ab-An ternary system of lunar plagioclases and of Ba-feldspar (celsian) were analyzed by optical and high-resolution spectral CL to investigate the causes of the different luminescence behavior of feldspar and to identify possible activator elements.

2 Analytical Procedure

In the present study CL spectra of 30 feldspar samples were measured covering the Or-Ab-An ternary system (Fig. 1). The samples were characterized by CL and optical microscopy, X-ray diffraction, major- and trace-element analysis. Additional samples of lunar plagioclases from Luna 20 and Luna 24 and Ba-feldspar (celsian) were also investigated.

Monomineralic feldspar fractions were separated from mineral pieces and rocks. After careful crushing and manual separation under a microscope, the material was milled and sieved. Heavy-liquid density separation was carried out on the 100–200 µm grain size fraction followed by HCl etching (10%). Combined X-ray diffraction analysis and quantitative analysis of major elements were used to characterize the feldspar samples. Difficulties of measuring the concentrations of trace elements in feldspar minerals at low levels by electron probes often prevent a correlation between CL intensity and the concentration of possible activator elements. Therefore, trace element contents were measured using ICP-MS and atomic emission spectrometry, although these methods allow no spatial resolution of the element distribution within the analyzed crystals.

Optical and CL microscopy were carried out on polished thin sections of the samples using a “hot cathode” CL microscope at 14 kV and with a current densi-

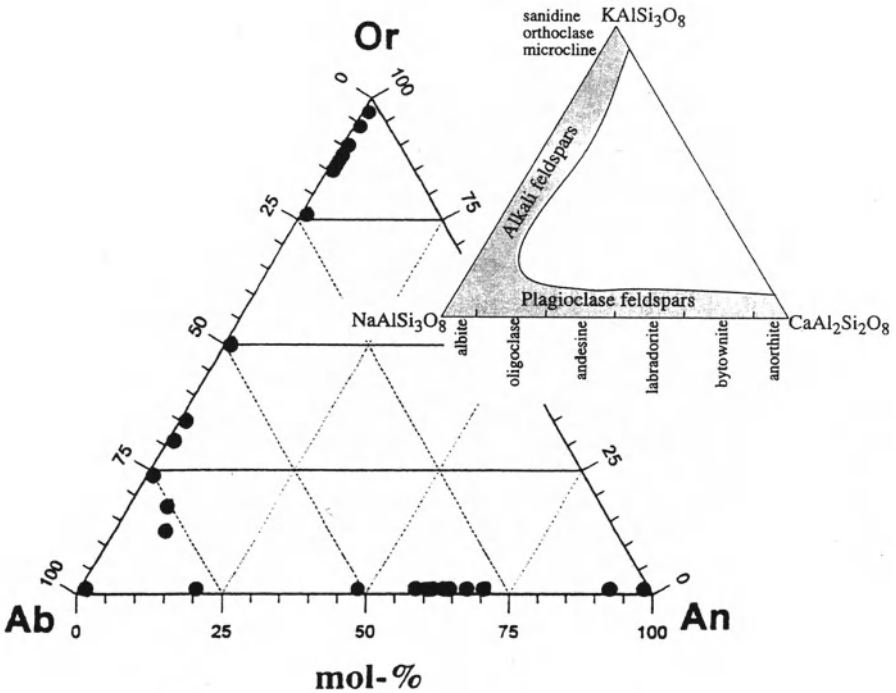


Fig. 1. The ternary Or-Ab-An feldspar system showing the position of the samples investigated

ty of ca. 10 $\mu\text{A}/\text{mm}^2$. To prevent the build-up of electrical charge during CL operations, the thin sections were coated with carbon. Color slides were taken with Kodak Ektachrome 400 HC.

CL spectra were obtained using an EG&G digital triple-grating spectrograph with liquid nitrogen cooling and a Si-based charge-coupled (CCD) detector. The CCD camera was attached to the CL microscope by a 1.5 m quartz fiber guide (Neuser et al. 1995). CL spectra were measured in the range 320–1100 nm using standardized conditions (accumulation time 10 s, spot width 30 μm) and were corrected for the spectral response of the instrument.

3

Crystal Structure and Chemistry of Feldspar Minerals

Feldspars are MT_4O_8 aluminosilicates whose structures are composed of corner-sharing AlO_4 and SiO_4 tetrahedra (T site) linked in an infinite three-dimensional array (Ribbe 1983). Charge compensating cations (K^+ , Na^+ , Ca^{2+} , Ba^{2+}) occupy large, irregular cavities in the tetrahedral framework (M site; Fig. 2). Most natural feldspars occur in the Or-Ab-An ternary with the general formula $\text{K}_x\text{Na}_y\text{Ca}_{1-(x+y)}\text{Al}_{2-(x+y)}\text{Si}_{2+(x+y)}\text{O}_8$. Feldspars with K and Na in the M site form solid solutions of the alkali feldspar series, whereas a complete range of composition is observed between Na and Ca in the plagioclase series (Fig. 1). Feldspars of the K-Ba series (“hyalophane”), K-Na-Ba ternaries, NaBSi_3O_8 (reedmergnerite), or $\text{NH}_4\text{AlSi}_3\text{O}_8$ (buddingtonite) are rarely observed. If boron substitutes for Al in tetrahedral coordination, the mineral reedmergnerite (NaBSi_3O_8) can occur, especially in authigenic feldspar in sediments (Smith and Brown 1988) or sodic feldspar from peralkaline environments (Černý 1994). Furthermore, a wide variety of compounds with feldspar topology has been synthesized with Rb, NH_4 , Sr, Ba, and Pb in M sites, and Fe^{3+} , B, Ga, Ge, and AlSiP in T sites (Bruno and Penttinghaus 1974).

At high temperatures feldspars form more extensive solid solutions. During cooling alkali feldspars segregate because of the differences in cation size of K^+ (1.33 Å) and Na^+ (0.97 Å) into separate phases and form perthite (albite in orthoclase) or antiperthite (orthoclase in albite). The similar ionic radii of Na^+ and Ca^{2+} (0.99 Å) cause a complete range of composition within the plagioclase series. However, perfect long-range Al,Si order within the plagioclase structure is only achievable in pure albite and anorthite. In the intermediate plagioclase composition range incommensurate structures e_1 and e_2 are formed which result in the existence of a miscibility gap between them (Putnis 1992). Thus, compositions around An_{50} exsolve into two phases, e_1+e_2 , which coexist as lamellar intergrowths.

Numerous elements can substitute for K, Na, Ca, Si and Al in feldspar, including B, Ba, Be, Cs, Fe, Ga, Ge, Li, Mg, Mn, P, Pb, Rb, (rare-earth elements) REE/Y, Sn, Sr, Ti (e.g. Heier 1962; Rhodes 1969; Lyakhovich 1972; Bruno and Penttinghaus 1974; Ribbe 1983; Smith and Brown 1988; Parsons 1994). Factors governing the incorporation of the different elements into feldspar are ionic characteristics, structural aspects and physico-chemical conditions during mineral formation.

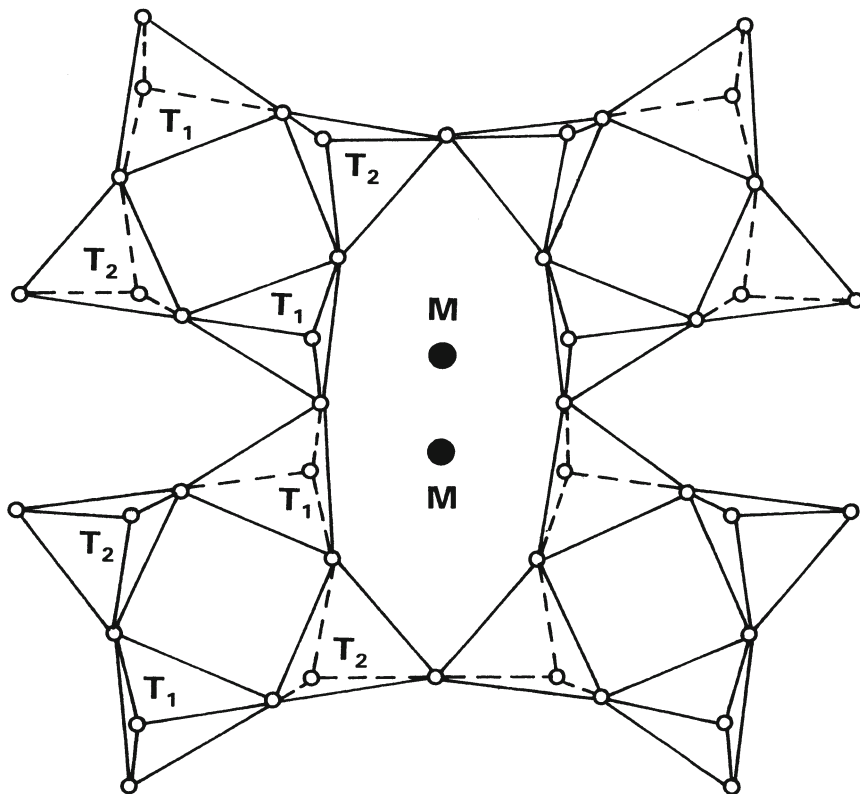


Fig. 2. Schematic feldspar structure with four-fold rings of individual T_1 and T_2 tetrahedra (T-site) with a pair of tetrahedra pointing up and a pair pointing down. Cations occupy the large cavities (M-site) between the rings

In K-feldspar large cations enter the M sites (e.g. compatible Ba, Sr and incompatible Li, Rb, Cs, Tl, Pb, and NH_4), whereas the number of substituents in plagioclases is limited (Sr, Ba, Li, Eu and negligible contents of the large compatibles Rb, Cs, Tl) because of the smaller cations in the M site. Small cations are incorporated into the tetrahedral T sites (mainly Fe^{3+} , Ga, P, B, Ti, Ge, and Be). Some of these substituting elements in natural feldspars can act as luminescence activators depending on the crystallographic position, valence and bonding state.

Petrov (1994) compiled 20 paramagnetic centers in alkali feldspar which were detected by EPR measurements. He distinguished between thermally stable paramagnetic centers (cations Fe^{3+} and Mn^{2+} with d^5 electron configuration) and thermally metastable centers which generally can be reactivated by natural or artificial irradiation. Petrov (1994) summarized the thermally metastable paramagnetic centers into four main groups: (1) cations with unusual valence (Ti^{3+} , $[\text{Pb}-\text{Pb}]^{3+}$), (2) anions with unusual valence ($\text{O}^{1-}/\Sigma\text{M}_i$ and $\text{O}^{1-}/\Sigma\text{Y}_i \times \Sigma\text{Z}_i$), with $\text{Y} = \text{Al, Na, Ag, Pb, Z} = \text{Na}$ and $\text{M} = \text{e.g. Si}^{4+}, \text{Mg}^{2+}$ (3) BO_m^n radicals (SiO_3^{3-} , $\text{SiO}_3^{3-}/^{27}\text{Al}$, PO_3^{2-} , NO_2), and (4) organic radicals (C_2H_5 , CH_3). The most widely distributed

centers in natural feldspars are O^- defects as well as Ti^{3+} and Fe^{3+} impurities (Marfunin et al. 1967; Ioffe and Yanchevskaya 1968; Marfunin and Bershov 1970; Weeks 1973; Matyash et al. 1981; Petrov 1994).

4 Cathodoluminescence

4.1 General

Most of the feldspars in samples from igneous and metamorphic rocks exhibit CL colors of bright blue, greenish-yellow, violet, and red. The CL emissions of both terrestrial and lunar feldspars generally consist of three broad emission bands: a strong blue emission (420–500 nm), one emission band in the green (540–570 nm), and one red band on the edge of the infra-red (690–760 nm). The overall emission color depends on the relative intensities of the three main emission bands. The variable incorporation of divalent and trivalent activator elements in the crystal causes plagioclase to exhibit practically all CL colors, whereas alkali feldspars dominantly luminesce in blue and red. In many plagioclases the infrared band is dominant but, since only the tail of this band is in the visible range, it often has little effect on the visual color. Accordingly, blue and green luminescing feldspars with an intense red-infrared emission band can occur. Smith and Stenstrom (1965), Görz et al. (1970) and Sippel (1971) found a polarization of the CL emission in all feldspars except adularia and sanidine.

Authigenic feldspars are often described as either non-luminescent or darkly luminescent (Kastner 1991; Kastner and Siever 1979). Authigenic feldspar, which is assumed to form at low temperature, seems to have low concentrations of trace elements (<100 ppm Mn, Ti, Fe; Escobar and Mariano 1976) and lattice defects. Walker and Burley (1991) and Götze et al. (1996) observed both white and brown luminescing orthoclase overgrowths and low albite in sandstones using high-sensitivity CL microscopes. Although the causes of the dull or absent CL in authigenic feldspar are still unknown, the fact alone was still put to good use in detecting their presence (Fig. 15D)

Although variations in CL color recorded by optical CL give important textural information, CL spectroscopy was used to record CL colors and emission intensities quantitatively and to provide information on the nature of luminescence centers. The comparison of the CL spectra of the different feldspars shows significant differences between the samples investigated. The emission bands and peaks can be related to defects as well as activator elements incorporated in the feldspar structure (Table 1). The incorporation of activator elements in the feldspar seems to be determined by the P, T and redox conditions during formation of the parent rocks (Rokatschuk et al. 1989). Therefore, typomorphic luminescence properties are caused by the structural incorporation of, e.g., Eu^{2+} , Fe^{3+} , Tl^+ , Ce^{3+} , Mn^{2+} (e.g., Gorobets et al. 1989).

The blue emission occurring in almost all feldspars has been related to structural defects (electron-hole recombinations at various hole centers) similar to

Table 1. Characteristic luminescence emission peaks and associated activators in feldspars

Activator	Color	Peak	Method	Reference
Tl ⁺	UV	280 nm	PL	Gorobets et al. (1989)
Pb ²⁺	UV	280 nm	RL	Tarashchan et al. (1975)
?	UV	330 nm	TL	Huntley et al. (1991)
			TL, IR-OSL	Krbetschek et al. (1996)
Ce ³⁺	UV	355 nm	CL	
	Bluish-green	490 nm	CL	Laud et al. (1971)
Eu ²⁺	Blue	420 nm	CL	Mariano and Ring (1975)
			TL, RL	Jaek et al. (1996)
Cu ²⁺	Blue	420±5 nm	CL	Mariano et al. (1973)
			TL, RL	Jaek et al. (1996)
Al-O ⁻ -Al	Blue	450-480 nm	TL, RL	Marfunin (1979)
			CL	Walker (1985)
Ti ³⁺	Blue	460±10 nm	CL	Mariano et al. (1973)
		450 nm	CL	Geake et al. (1973)
Ga ³⁺	Bluish-green	500 nm	CL	De St. Jorre and Smith (1988)
O ⁻ -Si...M ⁺	Bluish-green	500-510 nm	TL, RL	Marfunin and Bershov (1970)
Mn ²⁺	Greenish-yellow	559 nm	CL	Sippel and Spencer (1970)
		570±5 nm	CL	Mariano et al. (1973)
		540-561 nm	CL	Mora and Ramseyer (1992)
		550-565 nm	CL, TL	Götze et al. (1996)
Fe ³⁺	Red/IR	700±10 nm	CL	Mariano et al. (1973)
		705-730 nm	CL	Sippel and Spencer (1970)
		700-780 nm	CL	Geake et al. (1973)
		690-760 nm	RL	Boroznovskaya et al. (1982)
		680-745 nm	CL	Mora and Ramseyer (1992)
		688-740 nm	CL, TL	Götze et al. (1996)
Sm ³⁺	Red	Several peaks	CL	Mariano et al. (1973)
	Blue-IR	See Fig. 13	CL	Götze et al. (1996)
Dy ³⁺ , Eu ³⁺	Blue-IR	Several peaks	CL	
Tb ³⁺ , Nd ³⁺		See Fig. 13	CL	Götze et al. (1996, 1999)
?	IR	860 nm	CL	Götze et al. (1996)
				Krbetschek et al. (1998)
Cr ³⁺	IR	880 nm	RL	Boroznovskaya et al. (1996)

those in quartz and other silicates. It has a much shorter decay time at room temperature than the other bands (Walker 1985). Variabilities in position and shape of the blue peak indicated that there is more than one luminescence center involved in the blue emission. Finch and Klein (1996), for instance, detected Al-O⁻-Al as well as Si-O⁻-Si paramagnetic defects in blue luminescing alkali feldspar.

4.1.1

Al-O⁻-Al

The CL emission band between 450 and 480 nm which occurs in both alkali feldspars and plagioclases is caused by the substitution of Al³⁺ for Si⁴⁺ in feldspar (e.g. Marfunin 1979). Speit and Lehmann (1982) ascribed TL emission bands between 400 and 475 nm in various feldspars to this center. The O⁻/2²⁷Al (or Al-O⁻-Al) center forms with two Al atoms, one of which is “structural Al” and the other “impurity Al”. This oxygen hole center adjacent to two Al ions is the most common center in feldspars, except in those with very high An content (Speit and Lehmann 1982). The formation of short-range disordered domains is due to Al-O-Al clustering associated with structural defects in their local environment (Petrov et al. 1993). The O⁻/2²⁷Al centers are preferentially formed in feldspar with large M cations (K, Ba), e.g. orthoclase, sanidine, and hyalophane. Therefore, the intensity of the blue CL emission is generally higher in alkali feldspars than in plagioclases. Variations in the peak position are caused by different types of Al-O⁻-Al centers, associated with two non-equivalent sites for the impurity Al (Kirsh et al. 1987).

4.1.2

Copper

Another emission in the blue at 420 nm due to Cu²⁺ was detected in synthetic and natural feldspars (Mariano et al. 1973; Jaek et al. 1996). Since copper is distributed in feldspars as divalent ion in the Ca-site, the CL can be assigned to a hole trapped near a Cu²⁺ impurity (Matyash et al. 1982). Cu contents were measured in feldspars generally between 1 and 30 ppm (Smith and Brown 1988).

4.1.3

Titanium

Mariano and Ring (1975) suggested that the blue emission (460 nm) in feldspars is due to Ti³⁺ activation. Titanium is incorporated in natural and synthetic feldspars in concentrations of a few hundreds ppm up to 0.1 wt-%. Generally, the Ti concentrations in alkali feldspars are higher than in plagioclases and Ti content tends to be higher in volcanic than in low-temperature rocks (Smith and Brown 1988). The Ti³⁺ electron center (Ti^{3++e⁻}) was detected in various ordered and disordered feldspars assuming that titanium was initially incorporated as Ti⁴⁺ in Al sites (Marfunin and Bershov 1970; Speit and Lehmann 1982). According to Mariano (1973) it is not clear yet whether Ti³⁺ is an activator or a sensitizer enhancing intrinsic CL. Kirsh et al. (1987) concluded that the Ti⁴⁺ ion or TiO₄⁴⁻ group forms an electron trap from which electrons can be released during heating.

4.1.4

Si-O⁻...M²⁺

An additional emission band is situated at 500–510 nm in the CL spectra of almost all alkali feldspars investigated (Fig. 3). From EPR measurements it was concluded that this luminescence emission is associated with a hole on an oxygen adjacent to a divalent impurity ion (Si-O⁻...M²⁺; Marfunin and Bershov

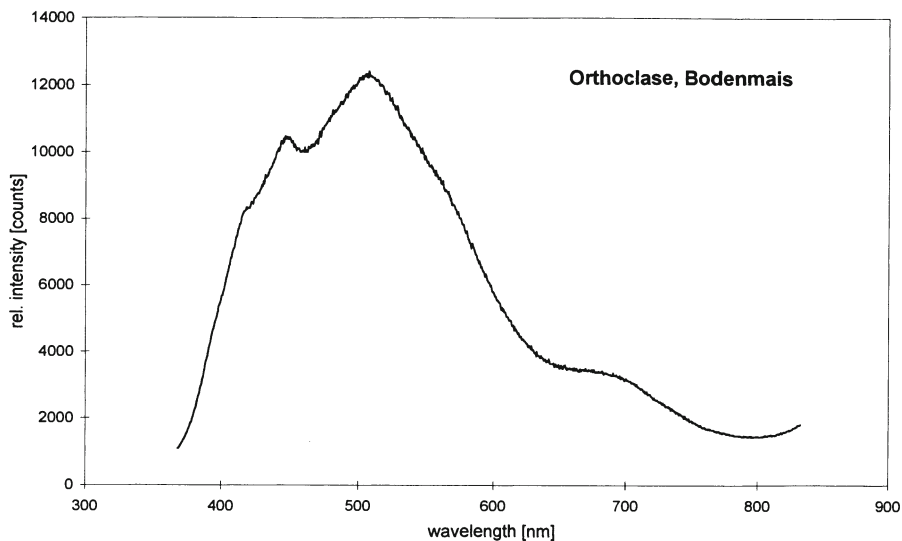


Fig. 3. CL emission spectrum of a bright blue luminescing orthoclase sample from Bodenmais, Germany. The spectrum is dominated by two emission bands at 450 nm (Al-O⁻-Al center) and 500 nm (Si-O⁻...M²⁺ center) which are the most common in K-feldspars

1970; Matyash et al. 1982). It was suggested that this center must be stabilized by the divalent metal ion M²⁺ in a T site adjacent to the oxygen (most likely Mg²⁺, Zn²⁺ or Be²⁺; Marfunin and Bershov 1970; Speit and Lehmann 1982; Petrov 1994).

4.1.5 Gallium

De St. Jorre and Smith (1988) reported gallium enriched albite (up to 4000 ppm Ga) from rare metal deposits in Canada showing bright blue CL with a similar spectrum as obtained from a Ga-doped plagioclase with a maximum emission around 500 nm. They concluded that probably a minimum concentration of 800 ppm Ga triggers the blue CL color in albite. It is uncertain whether Ga behaves as a CL activator or enhances the formation of lattice defects. In most of the samples investigated the Ga content was too low (generally <200 ppm) to correlate with the CL intensity of the 500 nm peak.

4.1.6 Manganese

The green emission band centered around 560 nm is due to Mn²⁺ in M sites (most probably Ca²⁺ sites) and is especially detected in plagioclases. The Mn²⁺ emission is less common in K-feldspars because of the difficulty of the Mn²⁺-K⁺ substitution. Generally, feldspars contain between 2 and 200 ppm manganese with a tendency for a tenfold increase from K-feldspar (5–50 ppm) to anorthite (Smith and Brown 1988). Most of the investigated alkali feldspars have

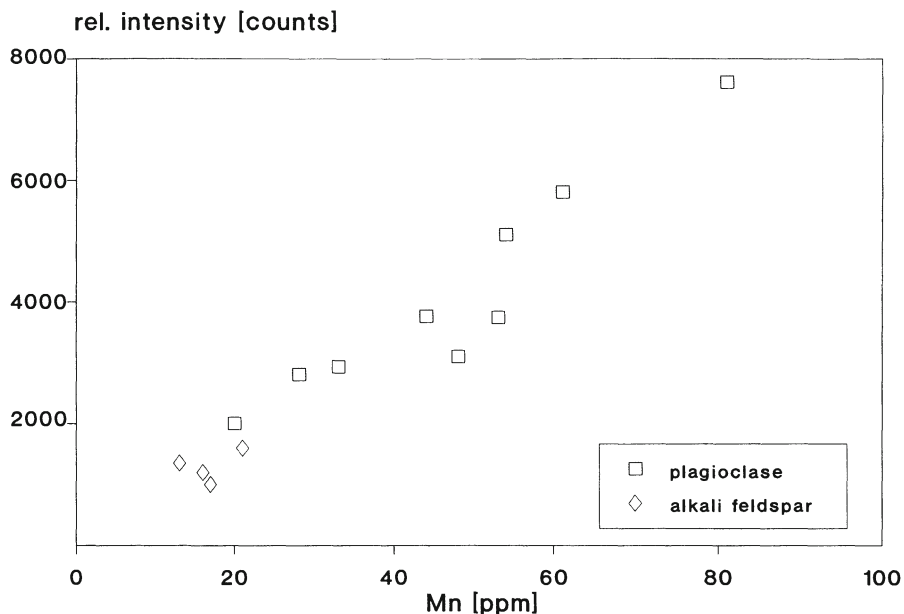


Fig. 4. Intensity of the green peak (550–565 nm) in relation to the Mn concentration of the feldspars investigated

Mn concentrations <10 ppm. There is no spectroscopic evidence to show which of the four calcium sites Mn^{2+} occupies in anorthite (Geake et al. 1971; Telfer and Walker 1978). Although the position of the green peak changes (compare with Table 1), the wavelength of this peak cannot be correlated directly with the feldspar composition. Mora and Ramseyer (1992) reported a shift of the green peak toward shorter wavelengths with increasing anorthite content. Measurements on synthetic anorthites (Telfer and Walker 1978) and natural plagioclases (Mora and Ramseyer 1994; Götze et al. 1996) have shown a clear correlation between the intensity of the green emission band and the manganese content up to a critical self-quenching value of about 1 mole-% Mn^{2+} (Fig. 4). The suggestion that Mn contents below 20 ppm can act as CL activators was confirmed.

An intense yellow emission with a maximum at 571 nm was observed in celsian (Fig. 15E and Fig. 5). In general, alkali feldspars contain 10^3 – 10^4 ppm Ba whereas the Ba contents in plagioclases are considerably lower (100–3000 ppm). In various occurrences (e.g., Mn deposits), Ba contents increase through the hyalophane series towards the end member celsian (Smith and Brown 1988). The results suggest that Mn^{2+} is the dominant activator in Ba-feldspar.

Furthermore, Mn^{2+} activation is always common in extraterrestrial plagioclases. In all lunar plagioclases investigated the emission due to Mn^{2+} is the most intensive (Fig. 6). This confirms results of Geake et al. (1973), who reported Mn-activated luminescence in plagioclases from Apollo samples and meteorites.

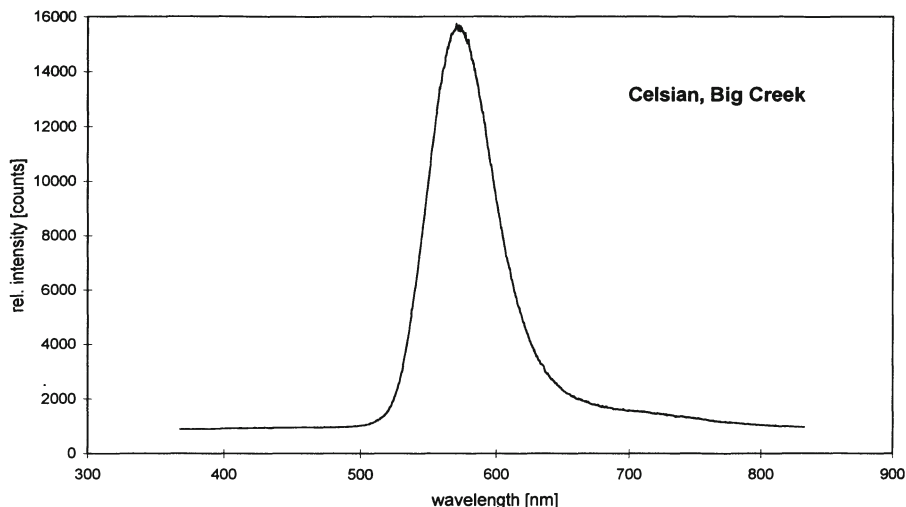


Fig. 5. Bright yellow-greenish luminescing Ba-feldspar (celsian) from Big Creek, California (compare with Fig. 15E) showing a strong Mn^{2+} -activated CL emission band with a maximum at 571 nm

4.1.7 Iron

Smith and Stenstrom (1965) first observed a red emission of feldspars in CL. Geake et al. (1973), Telfer and Walker (1975, 1978), and White et al. (1986) showed that the red emission band around 700 nm is due to Fe^{3+} which occupies Al^{3+} tetrahedral sites in the feldspar. The deep-red luminescence is due to the ${}^4\text{T}_1 \rightarrow {}^6\text{A}_1$ transition of Fe^{3+} (Geake and Walker 1975; White et al. 1986). Reddish-orange emission in feldspars may also result from vitrification of plagioclase by shock waves (Sippel and Spencer 1970) or lattice damage due to impact events (Ramseyer et al. 1992).

Generally, the Fe^{3+} emission is present in all terrestrial feldspar types. An absorption spectrum for Fe^{3+} in orthoclase published by White et al. (1986) is identical to the excitation spectrum observed by Walker (1985) in bytownite. In most natural feldspars the intensity of the red peak is governed by the incorporation of Fe^{3+} and the maximum CL intensity in feldspar samples, doped with Fe^{3+} , was found at 1.5% (Telfer and Walker 1978). A strong temperature dependence of the integrated intensity of the Fe^{3+} luminescence band was observed by White et al (1986), who reported a rapid increase of the luminescence intensity with decreasing temperature.

Fe^{3+} substitutes for Al^{3+} in the T10 position in ordered alkali feldspars (e.g. low albite) and in the T1 and T2 positions, as well as in tetrahedra of type TO_3OH , in disordered ones (Petrov et al. 1989; Petrov 1994). In plagioclases three lattice positions of trivalent iron are still under discussion. With increasing total Fe_2O_3 concentration the substitution of Fe^{3+} at tetrahedral positions increases whereas the concentration of Al-O^- -Al centers decreases (Petrov 1994). Natural feldspars con-

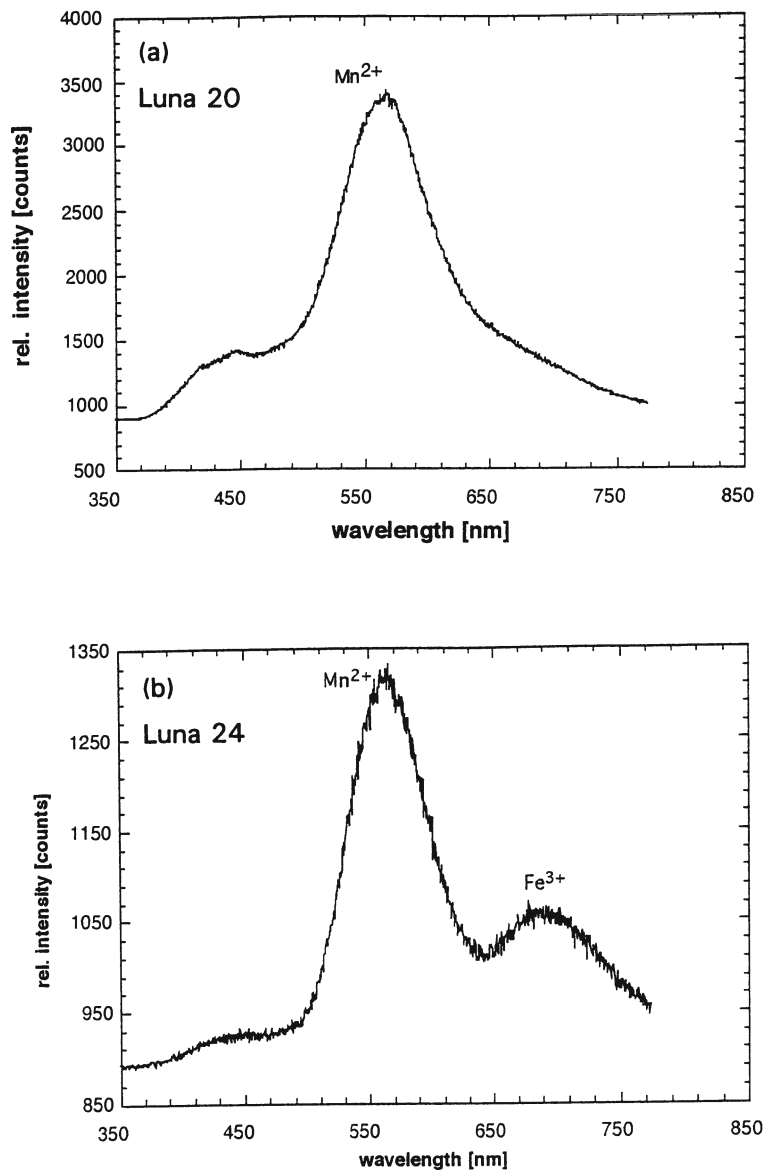


Fig. 6a,b. CL emission spectra of green luminescing lunar plagioclases from Luna 20 (a) and Luna 24 (b) (see Fig. 15I,K). Both spectra are dominated by the Mn²⁺-activated emission band. In the Luna 24 sample Fe³⁺ is clearly detectable by the red emission band at 690 nm

tain a maximum of 4 wt-% iron (Smith and Brown 1988). A few hundred up to 10⁴ ppm of Fe is fairly common. Generally, total iron increases with An-content from An₀ to An₉₀ with the highest values (ca. 1 wt-%) in volcanic bytownite and

the lowest (<100 ppm) in pegmatitic albites (Smith 1983). However, much of the iron chemically measured as traces in feldspar is probably not structurally incorporated but is instead present in an accessory phase such as hematite (Marshall 1988; Mora and Ramseyer 1992).

An intense red CL emission is especially reported from feldspars of alkaline rocks or carbonatite localities. Red luminescing feldspars typically characterize fenitization processes since the fenitization solutions contain Fe^{3+} which can be incorporated into the feldspar (Mariano 1978; Rae and Chambers 1988; Kempe et al. 1999). The red color of Fe^{3+} in albite is a characteristic feature of albitization in rare-metal deposits (Fig. 15F, Fig. 7). In contrast, the red emission band is weak or absent in lunar plagioclases (Fig. 15I, Fig. 6a) which has been ascribed to low oxygen partial pressure ($f\text{O}_2$) during plagioclase crystallization (Geake et al. 1971, 1973). Nevertheless, the occurrence of the CL emission band at ca. 700 nm (Fig. 15K, Fig. 6b) indicates that Fe^{3+} activated CL is common in lunar plagioclases. Although this emission is generally less intense in lunar than in most terrestrial feldspars, the results indicate that at least some of the iron in lunar plagioclases is ferric iron (Götze et al. 1999a).

In calcic plagioclases iron occurs as both Fe^{2+} in the large-cation sites and Fe^{3+} in tetrahedral sites depending on the oxidation state of the host rock. The role of Fe^{2+} as CL activator (emission band at 550–570 nm, Mariano et al. 1973) or quencher (Geake et al. 1972, 1973) was controversially discussed. Mariano (1978) published a CL spectrum of a synthetic plagioclase with 2 wt-% FeO. Generally, such high concentrations of iron are assumed to quench the luminescence. Possibly, the peak detected at 550 nm is caused by minor concentrations of Mn^{2+} which were incorporated as traces in the iron sample used for doping. Mora and Ram-

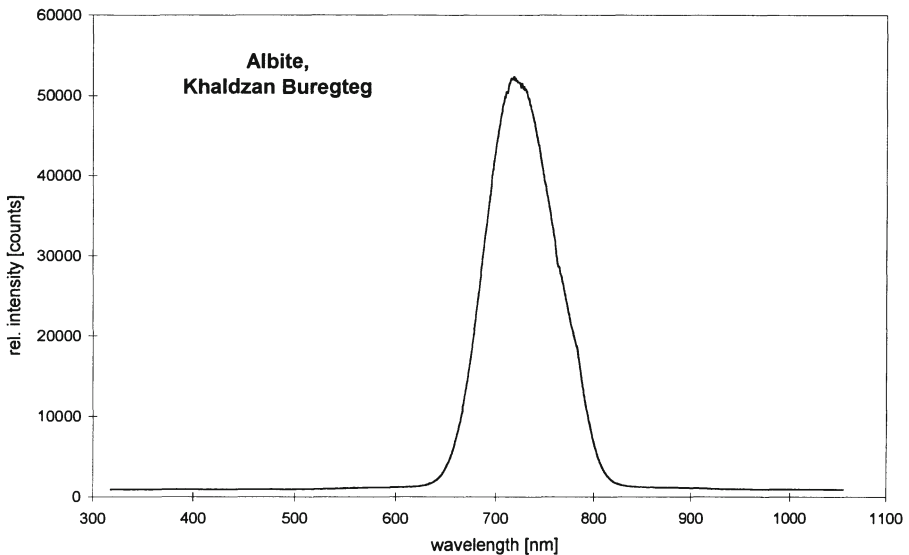


Fig. 7. CL emission spectrum of red luminescing albite from Khaldzan Buregte, Mongolia (compare Fig. 15F) which has formed during albitization of a granite

seyer (1992) and Götze et al. (1996) showed that Mn^{2+} activation already occurs at concentrations as low as 20 ppm.

The sensitivity of the red peak position to anorthite content has been previously reported (e.g. Sippel and Spencer 1970; Geake et al. 1973; Telfer and Walker 1975; Mora and Ramseyer 1992). In Fig. 8 the dependence of the red peak position on An content for investigated plagioclases is illustrated. There is a shift from 688 nm to 740 nm over the range An_{98} – An_5 . Both the structural state of the plagioclase and the tetrahedral site occupancy of Fe^{3+} can also affect the position of the red peak (Telfer and Walker 1982; Petrov et al. 1989). Boroznovskaya et al. (1982) distinguished different structural sites of Fe^{3+} in calcic plagioclase by ESR, one of which should be especially responsible for the red luminescence peak. Considering this fact, the intensity and position of the red peak could not be directly correlated with the bulk content of structural Fe^{3+} in plagioclase. Furthermore, the existence of incommensurate structures within the plagioclase series can influence the position of the red peak. In the intermediate composition around An_{50} plagioclases exsolve into two phases, $e_1 + e_2$, which coexist as lamellar intergrowths (Putnis 1992). Probably, these structural peculiarities can explain the existence of a slight splitting of peaks around 700 nm (see Fig. 9) or gaps within the shift of the red peak position.

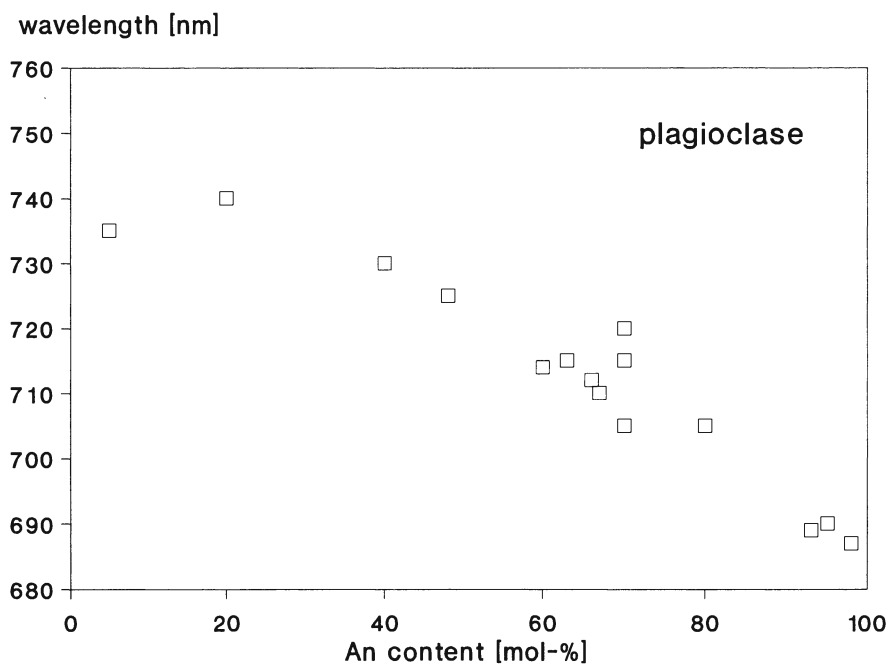


Fig. 8. Position of the red peak (ca. 700 nm) in the CL emission spectra of the investigated plagioclases in relation to An content

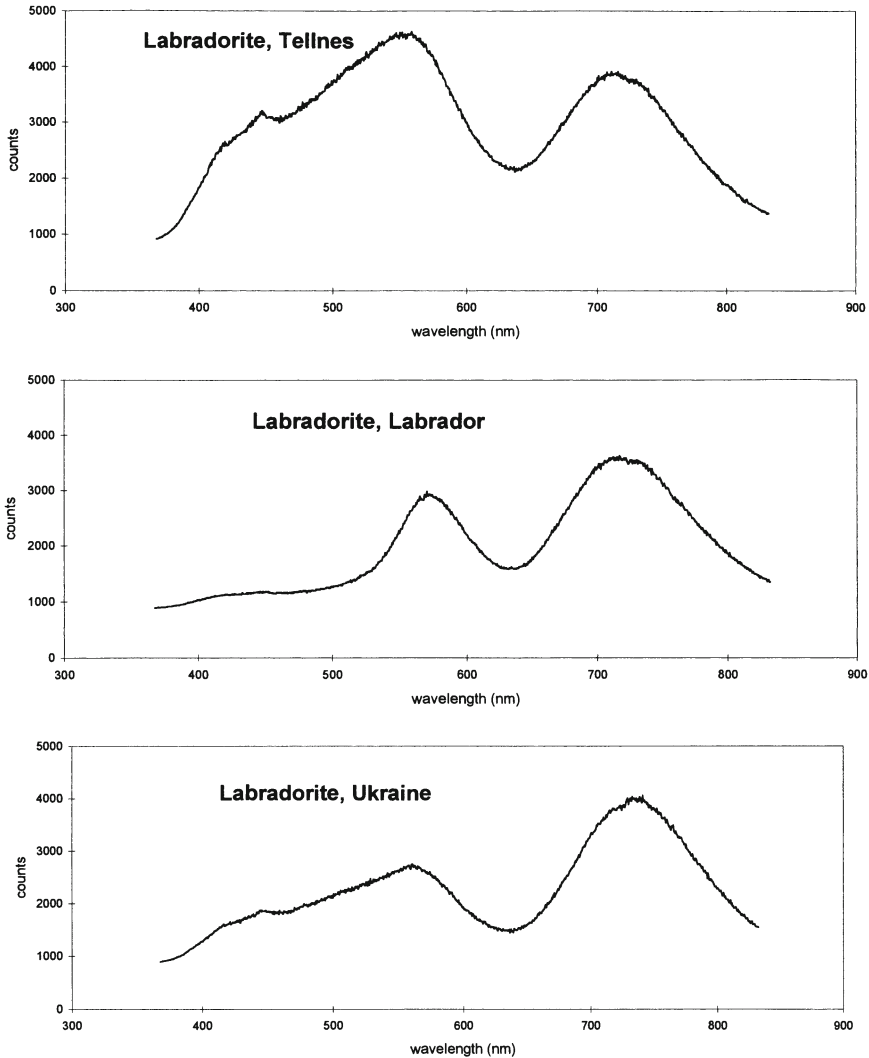


Fig. 9. CL emission spectra of three labradorite samples from different localities. The shape of the red emission bands indicates two maxima within a composite peak

A shift of the red peak in alkali feldspars depending on the Or content is shown in Fig. 10. This correlation is similar to that observed in phosphorescence spectra of alkali feldspars (Dütsch and Krbetschek 1997; Fig. 11). The monoclinic feldspar varieties (sanidine, orthoclase) show the same behavior as the triclinic ones (microcline, anorthoclase). A possible explanation of this effect could be the influence of the K^+-Na^+ substitution on the crystal field (Schläfer and Gliemann 1980). The incorporation of the larger potassium ion causes a stretching of the lattice resulting in non-linear variations of the cell dimensions and thus, a shift of the red peak.

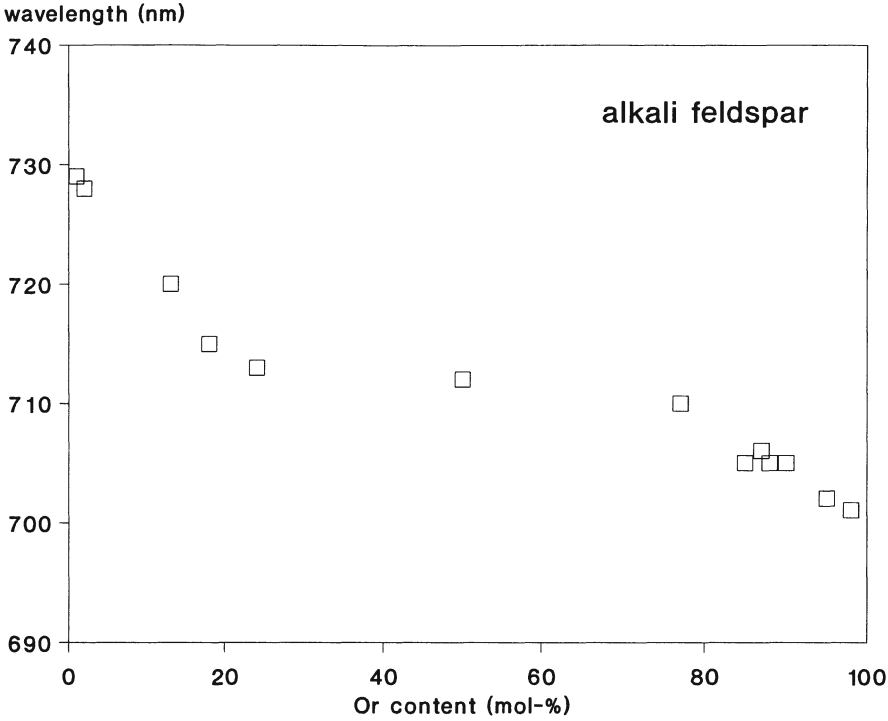


Fig. 10. Position of the red peak (ca. 700 nm) in the CL spectra of investigated alkali feldspars in relation to Or content

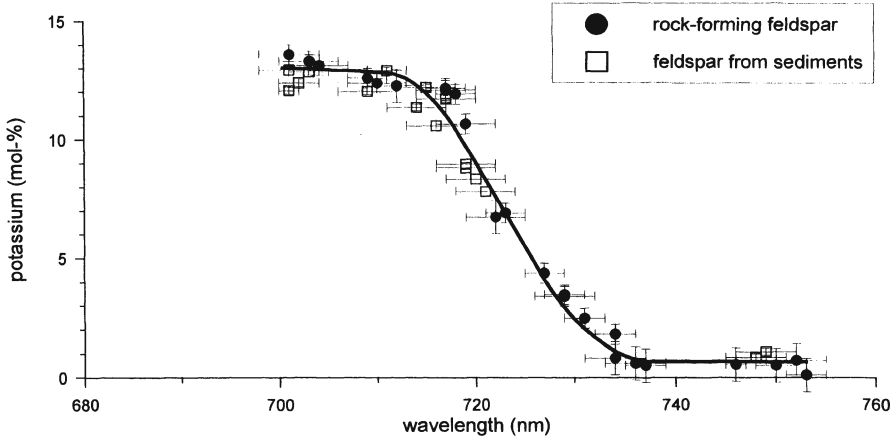


Fig. 11. Relation between the position of the red radio-phosphorescence peak and the potassium content of alkali feldspars. (Modified after Dütsch and Krbetschek 1997)

4.1.8

Rare-Earth Elements

Some other substituting trace elements in feldspars can act as luminescence centers. Rare-earth element activation responsible for CL is known since Mariano et al. (1973) synthesized doped plagioclase. The REE ions Eu^{2+} , Sm^{3+} , and Ce^{3+} were found to be effective as activators in synthetic feldspar samples (Mariano and Ring 1975; Laud et al. 1971; Jaek et al. 1996), whereas these elements occur rarely in sufficient amounts in natural feldspars to be activators (Marshall 1988). The REE and Y occur as trivalent ions in feldspars except Ce^{4+} and Eu^{2+} . The partition of Eu^{2+} into plagioclases is more efficient than the trivalent REE because of the similarity to Sr^{2+} . The contents of REE and Y are significantly higher in plagioclases (up to 10 ppm, La, Ce, Eu up to 100 ppm) than in K-feldspar (Smith and Brown 1988).

CL investigations of magmatic, metamorphic and sedimentary feldspars indicate that, in contrast to previous assumptions, REE activated CL in feldspars is common (Götze et al. 1999b). The blue-violet Eu^{2+} activated luminescence at 420 nm was detected in plagioclases of hydrothermal and Greisen deposits, and regional metamorphic rocks (amphibolite facies). It is uncommon in plagioclases of granitoids, crustal pegmatites and REE formations (Gorobets et al. 1989). Ce^{3+} activation was reported from plagioclase of regional metamorphic rocks showing variations in dependence on P, T conditions of rock formation (Rokatschuk et al. 1989; Kusnetsov and Kramarenko 1995).

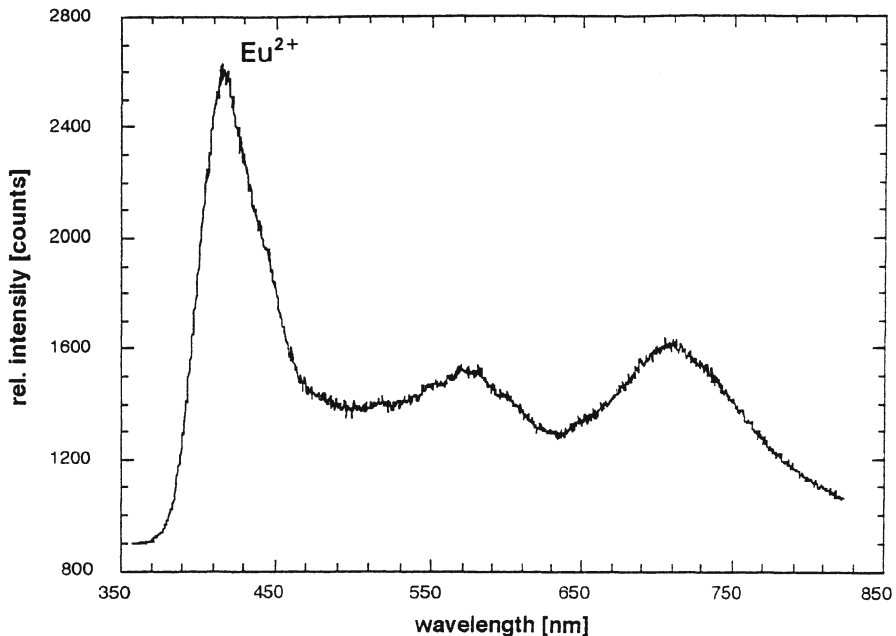


Fig. 12. CL emission spectrum of a labradorite sample from Bautzen, Germany (compare with Fig. 15G). The blue-violet luminescing outer rim of the plagioclase crystal shows a strong emission band at 420 nm which can be related to Eu^{2+} activation

Table 2. Contents of REE (ppm) detected in an albite sample from Spruce Pine, USA, by ICP-MS (compare with Figs. 13, 15H)

Element	Content (ppm)
La	27.4
Ce	49.5
Pr	6.02
Nd	18.4
Sm	3.28
Eu	0.06
Gd	2.01
Tb	0.26
Dy	0.98
Ho	0.14
Er	0.38
Tm	0.06
Yb	0.43
Lu	0.07

The influence of the crystal field on shape and position of REE luminescence spectra significantly differs for divalent and trivalent REE ions. Mariano et al. (1973) reported a broad band emission of Eu^{2+} at approximately 420 nm in a doped (200 ppm Eu^{2+}) synthetic anorthite showing deep blue luminescence (Fig. 15G). This emission band (Fig. 12) is caused by the transition between the $4f^6-5d$ state configuration and the $^8S_{7/2}$ level of the $4f^7$ ground state configuration (Mariano and Ring 1975). In contrast, trivalent ions of the rare-earth show narrow emission lines which reflect the transitions between excited state wave functions lying inside closed electronic shells. These transitions are more or less shielded from the local crystal field and thus, the positions of the emission lines are relatively constant (Fig. 13). In selected samples, strong REE activated CL was observed (Fig 15H, Table 2) which could be related to Sm^{3+} , Dy^{3+} , Nd^{3+} , and Tb^{3+} . In these feldspars REE accordingly play an important role in controlling CL and thus, variations in the REE distribution within single feldspar crystals can be detected.

4.1.9

Thallium and Lead

The substitution of K^+ in alkali feldspars by Tl^+ or Pb^{2+} results in luminescence around 280 nm in the UV (Marfunin 1979; Gorobets et al. 1989). However, Krbetschek et al. (1996) reported a 280 nm emission in IRSL in samples with no determinable lead content, which is contrary to this finding. Garcia-Guinea et al. (1996) suggested that an emission band in TL at 290 nm is associated either with the presence of crystalline phases of albite or with Na/K exsolution interfaces.

Lead is probably one of the elements which is preferentially incorporated in feldspar and not as microinclusions of minerals. The data compiled by Smith and

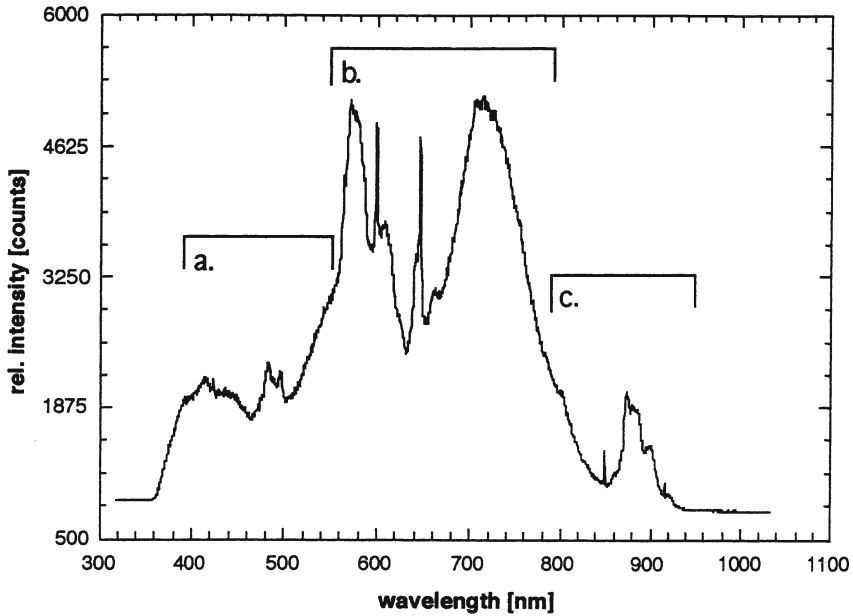


Fig. 13a–c. Strong REE activated CL emissions of blue-violet luminescing zones within an albite from Spruce Pine, USA (compare with Fig. 15H). a–c Narrow emission lines which reflect the transitions between excited states inside the closed electronic shells of the REE. (Modified from Götze et al. 1999b)

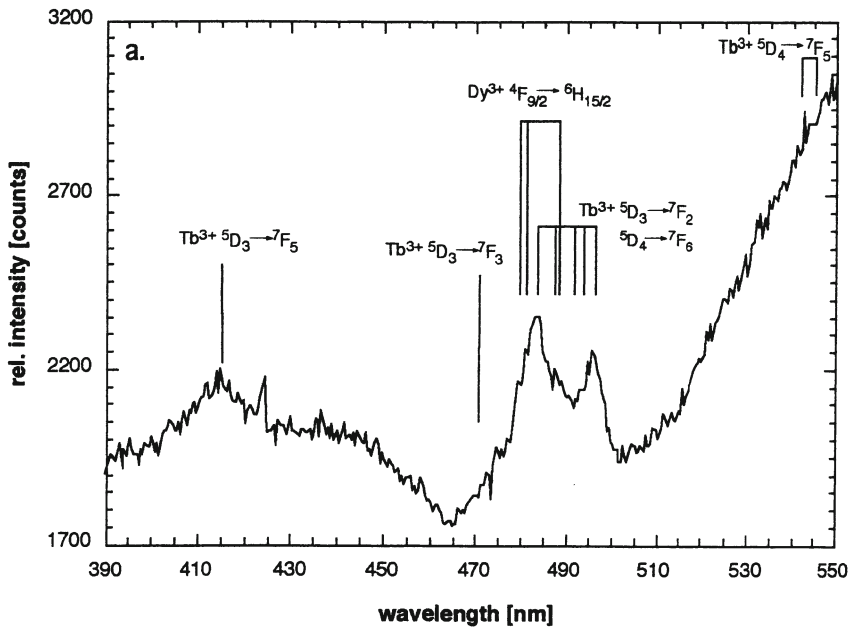


Fig. 13a

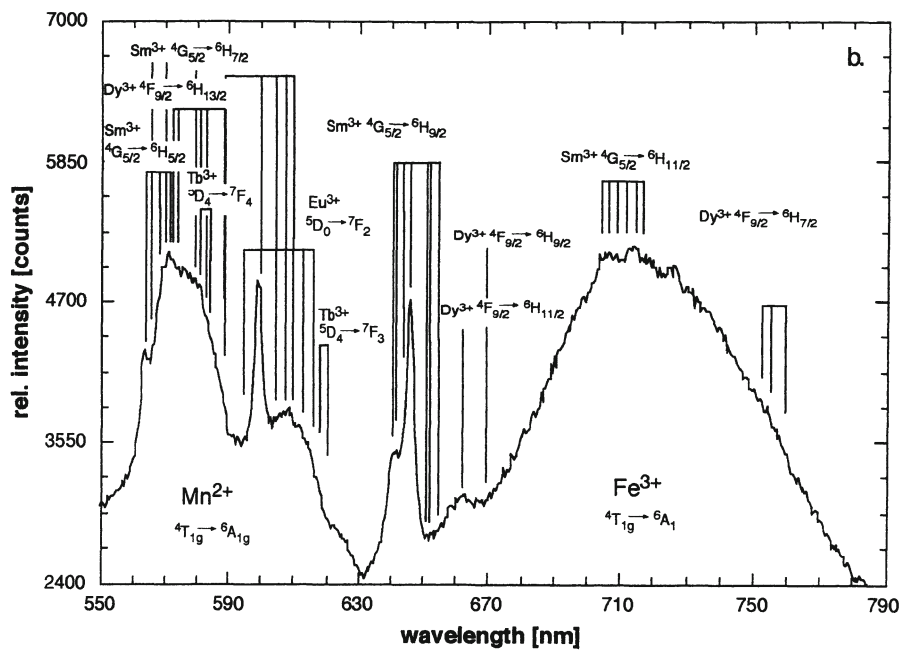


Fig. 13b

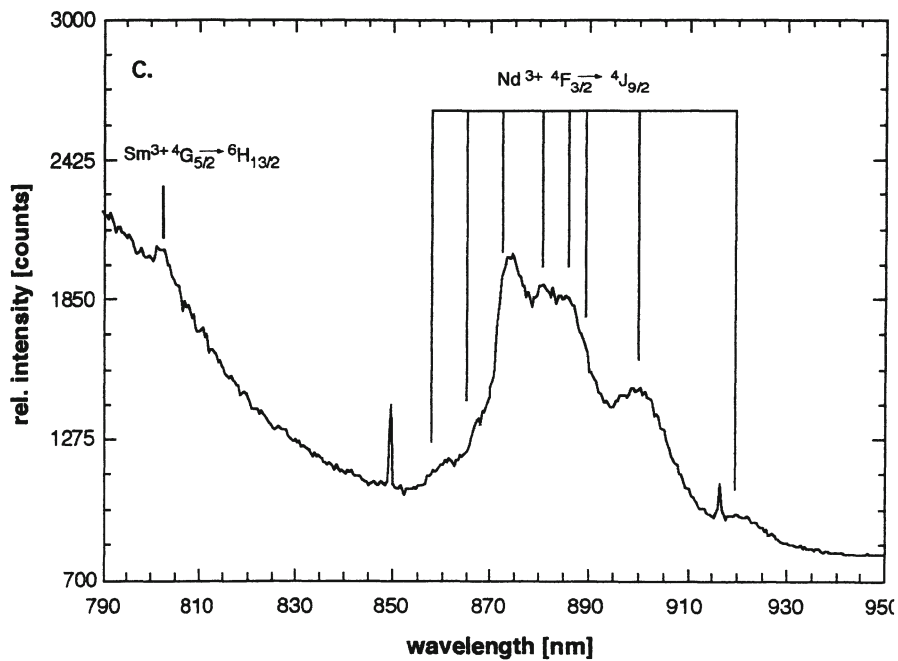


Fig. 13c

Brown (1988) illustrate that most alkali feldspars contain 10–1000 ppm Pb and plagioclases 1–100 ppm. The highest values were measured in amazonites of pegmatites (ca. 1000 ppm Pb). Tarashchan et al. (1973) and Marfunin (1979) reported a luminescence band in the UV at 280 nm in amazonites and other feldspars which they related to Pb^{2+} . Pb^{2+} can produce the paramagnetic center Pb^{1+} by capture of an electron. If this electron is delocalized at two Pb^{2+} ions, a $[Pb-Pb]^{3+}$ center arises charge compensated by Al,Si exchange at adjacent tetrahedral position. The $[Pb-Pb]^{3+}$ dimetric center was described by Petrov et al. (1993) as a chromophore of the blue-green color of microcline (amazonite). Unlike K-feldspar, plagioclases are less commonly colored because of the lack of lead in the large-cation site. High concentrations of Pb in amazonite can also lead to the formation of a $Pb-O^{\dots}X$ center, where the divalent ion X is likely Mg^{2+} (Speit and Lehmann 1982). The Pb content in other feldspars is probably too low to cause detectable concentrations of this center. Only in amazonite was Pb^{2+} observed, substituting for K^+ and O^- -Pb on the oxygen (Marfunin and Bershov 1970).

Thallium tends to concentrate in residual fluids, e.g. in rare-metal pegmatites. Therefore, the highest Tl contents were measured in rare-element granitic pegmatites with up to 3000 ppm (Shmakin 1979). In feldspars of granitic rocks most values lie below 10 ppm (Smith and Brown 1988). Boroznovskaya et al. (1996) detected enhanced Tl^{1+} activated luminescence (280 nm) in feldspar of rare-metal mineralizations and proposed the ratio of the Mn^{2+}/Tl^{1+} emission intensity to determine the relative acidity-alkalinity in rare-metal pegmatites.

4.1.10

Other Bands

During the present study an emission band was firstly detected in the IR around 860 nm (Fig. 14). This emission was observed in two samples of an adularia and an orthoclase. The energy (1.45 eV) is identical to the excitation energy used for optically stimulated luminescence (IR-OSL). This emission is also visible in induced radioluminescence of microcline and orthoclase (Trautmann et al. 1998), where it is much more intensive than the emission bands in the visible and UV region. The signal decreases with irradiation time, which can be interpreted as luminescent trapping of electrons. No link to a specific type of defect or activator could be found, accordingly the 860 nm emission needs to be further investigated. Boroznovskaya et al. (1996) reported an emission at 880 nm which they related to the presence of Cr^{3+} . However, their published RL spectra do not show any emission band in this region.

An emission band was detected at 330 nm in TL, IRSL and phosphorescence spectra of feldspars (e.g. Luff and Townsend 1993; Huntley et al. 1991; Krbetschek et al. 1996) but has not been reported yet from CL spectra. This emission was found as dominant in the albite corner of the feldspar ternary and has also been measured as the main emission in mid- to high-Na feldspar fractions from sediments. Spectral measurements have shown this emission often as a prominent high-temperature TL emission. However, Prescott et al. (1994) did not detect the 330 nm emission in any of their samples covering the whole feldspar ternary. Although the relation to a specific defect type is still under discussion, this emission was found to be suitable for luminescence dating (Krbetschek et al. 1998).

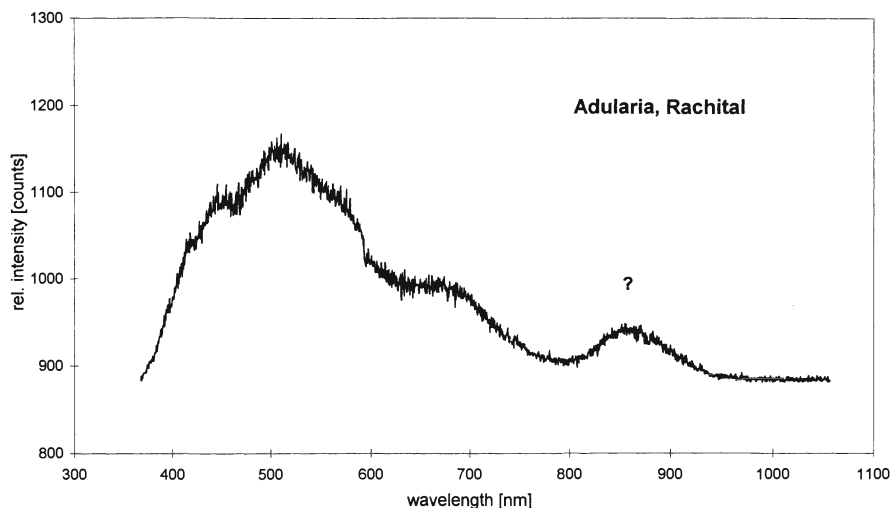


Fig. 14. Adular from Rachital, Switzerland showing a CL emission band of unknown origin in the IR at 860 nm

5 Conclusions

The research on spectral information of the CL emission from feldspar minerals can be dated back to the 1960s (Smith and Stenstrom 1965). Up to now numerous studies have led to important knowledge about the CL behavior of feldspars and its relation to specific types of crystal defects and trace-element activators. The present study summarizes results of systematic CL investigations within the ternary feldspar system Or-Ab-An. Although the samples investigated show significant differences in CL colors and CL spectra, some general conclusions were drawn. The most common CL emission bands in feldspars are caused by defects of the type Al-O⁻-Al (450 nm, especially in K-feldspar), O⁻-Si...M⁺ (around 500 nm in alkali feldspars) and the incorporation of Mn²⁺ into the M-position (ca. 560 nm) and Fe³⁺ into the T-position (around 700 nm) of the feldspar structure, respectively. Mn²⁺ is the main activator in most terrestrial and lunar plagioclases as well as in Ba-feldspar (celsian). Other elements which can act as activators of CL emission in feldspars are Tl, Pb, Cu, some REE and probably Cr. The incorporation of these activator elements into the feldspar structure is mainly determined by the element supply and the P, T and redox conditions during formation of the parent rocks. Therefore, the evaluation of the CL emission spectra can provide important information concerning physico-chemical conditions of rock and mineral formation and alteration. The comparison of the CL spectra with results of other luminescence techniques illustrates that the main emission bands in CL spectra were also detected in TL, IR-OSL and phosphorescence spectra (Krbetschek et al. 1998). Differences in the relative intensities of the emission bands however show very different mechanisms of luminescence production.

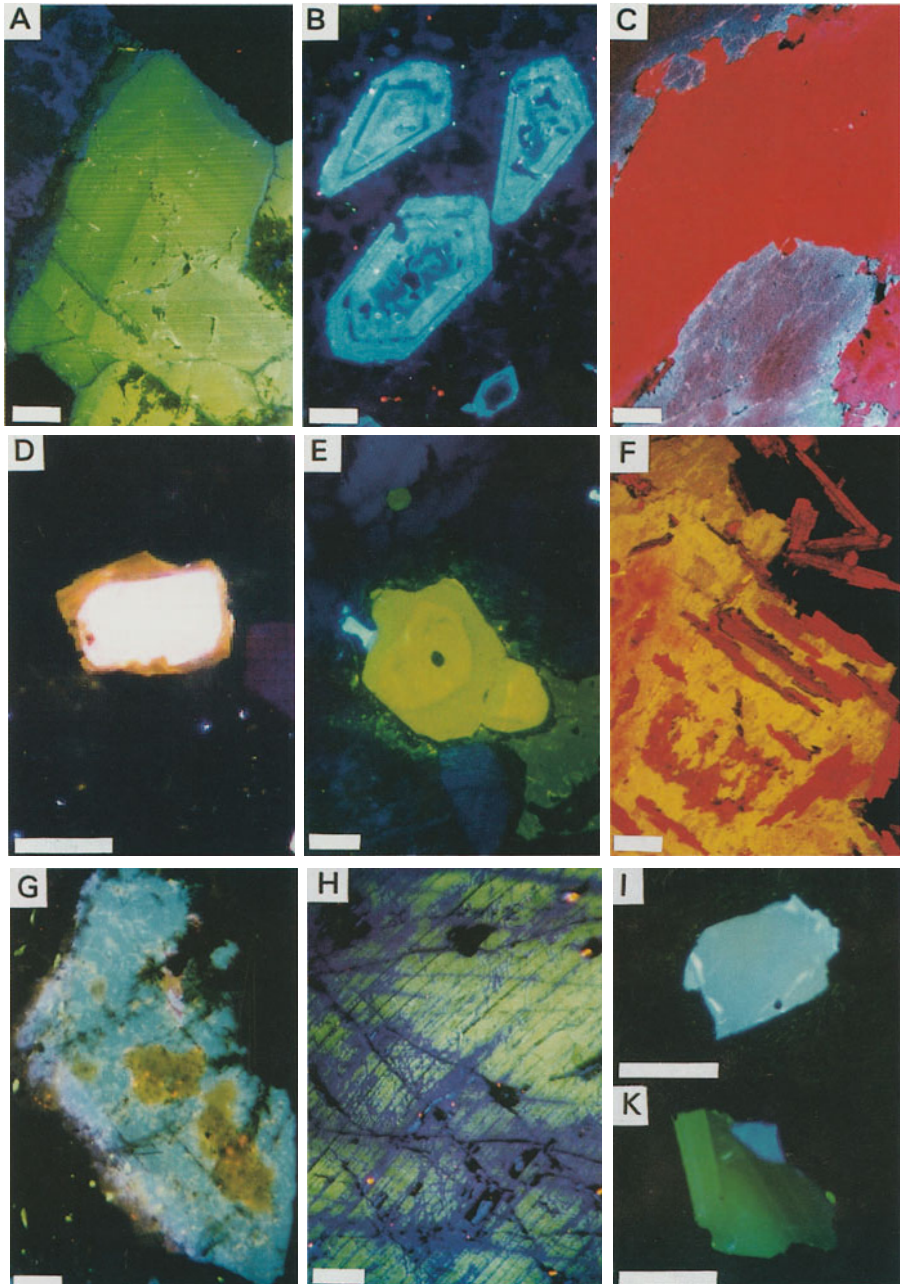


Fig. 15A–K. CL micrographs of selected feldspar samples. *Scale bar* is 200 μm . **A** Plagioclase sample of a granite sample from Eibenstock, Germany showing zoning under CL which is not discernible by polarizing microscopy. The twin lamellae are visible due to intensity variations which are caused by the orientations of the subcrystals. **B** Zoned blue luminescing K-feldspar (paradoxite) crystals from Euba, Germany. **C** Intergrowth of blue-violet luminescing microcline

and red luminescing albite in a perthite sample from Årendal, Norway. D Detrital K-feldspar ($K_{0.9}Na_{0.1}AlSi_3O_8$ with traces of Ti, Nb) with authigenic overgrowth of nearly pure K-feldspar from a fluvial sediment (Oder River, Germany). E Bright yellow-greenish luminescing Ba-feldspar (celsian) from Big Creek, Fresno, California in a matrix of complex Ba-silicates (for spectrum see Fig. 5). F Deep red luminescing albite (spectrum see Fig. 7) replacing K-feldspar during albitization of a granite from Khaldzan Buregte, Mongolia. G Labradorite crystal from Bautzen, Germany showing a violet luminescing rim which is caused by Eu^{2+} activation (compare with Fig. 12). H Green luminescing albite from Spruce Pine, USA, with violet luminescing alteration zones which are caused by strong REE activation (compare with Fig. 13). I Green luminescing anorthite clast from lunar soil (Luna 20). K Green luminescing anorthite grain from lunar soil (Luna 24) showing zoning under CL

Acknowledgements. We thank U. Kempe, T. Trautmann, P. Beuge, A. Massanek (Freiberg) and R.D. Neuser, D.K. Richter (Bochum) for their support during the investigations and their helpful discussions. We are very grateful to W.L. Brown for critical reading of the manuscript. The mineralogical collection of the TU Bergakademie Freiberg kindly provided samples for the present study. D. Dettmar (Bochum) is gratefully acknowledged for the careful sample preparation.

References

- Borosnovskaya NN, Lesnov FP, Scherbakova MYa (1982) On the X-ray luminescence of Fe^{3+} in calcic plagioclase (in Russian). *Geokhimiya* No 9:129–131
- Boroznovskaya NN, Makagon VM, Zhukova AI (1996) Luminogen generation in rare-metal pegmatite K-feldspar as affected by geochemical and crystal-chemical factors (in Russian). *Geokhimiya* No 12:1202–1209
- Bruno E and Pentinghaus H (1974) Substitution of cations in natural and synthetic feldspars. In: MacKanzie WS and Zussman J (eds) *The feldspars*. Manchester University Press, Manchester, pp 574–609.
- Černý P (1994) Evolution of feldspars in granitic pegmatites. In: Parsons I (ed) *Feldspars and their reactions*. NATO ASI Ser. C 421, Kluwer Acad Publ, Dordrecht-Boston-London, pp 501–540
- De St. Jorre L and Smith DGW (1988) Cathodoluminescent gallium-enriched feldspars from the Thor Lake rare-metal deposits, Northwest territories. *Can Miner* 26:301–308
- Dütsch C and Krbetschek MR (1997) New methods for a better internal ^{40}K dose rate determination. *Radiat Meas* 66:407–412
- Escobar R and Mariano AN (1976) On the origin of Colombian emeralds. 2nd biannual meeting of the Mineralogical Society of America, Tucson, Abstract
- Finch A and Klein J (1996) EPR and the cathodoluminescence of alkali feldspars. International conference on cathodoluminescence and related techniques in geosciences and geomaterials, Nancy, Abstracts, pp 45–46
- García-Guinea J, Rendell HM, Sanchez-Muñoz L (1996) Luminescence spectra of alkali feldspars: Some relationships between structural features and luminescence emission. *Rad Prot Dosim* 6:395–398
- Geake JE and Walker G (1975) Luminescence of minerals in the near infrared. In: Karr C (ed) *Infrared and Raman spectroscopy of lunar and terrestrial minerals*. Academic Press, New York, pp 73–89
- Geake JE, Walker G, Mills AA, Garlick GFJ (1971) Luminescence of Apollo lunar samples. In: *Proceedings 2nd Lunar Science Conference* 3, pp 2265–2275

- Geake JE, Walker G, Telfer DY, Mills AA, Garlick GFJ (1973) Luminescence of lunar, terrestrial, and synthesized plagioclase, caused by Mn^{2+} and Fe^{3+} . In: Proceedings 4th Lunar Science Conference 3, pp 3181–3189
- Gorobets BS, Gaft ML, Podolskiy AM (1989) Luminescence of minerals and ores (in Russian). Ministry of geology USSR, Moscow
- Gorz H, Bhalla RJRSB, White EW (1970) Detailed cathodoluminescence characterization of common silicates. In: Weber JW and White EW (eds) Space applications of solid state luminescent phenomena, pp 1–12
- Götze J, Krbetschek MR, Habermann D, Rieser U, Wolf D (1996) Investigation of feldspars by spectral TL, CL, and (IR)OSL. In: Third European Meeting Spectroscopic Methods in Mineralogy, Kiev, Programme and Abstracts, p 21
- Götze J, Habermann D, Kempe U, Neuser RD, Richter DK (1999a) Cathodoluminescence microscopy and spectroscopy of plagioclases from lunar soil (Luna 20, Luna 24). *Amer Miner* 84:1027–1032
- Götze J, Habermann D, Neuser RD, Richter DK (1999b) High-resolution spectrometric analysis of REE-activated cathodoluminescence (CL) in feldspar minerals. *Chem Geol* 153:81–91
- Heier KS (1962) Trace elements in feldspars – A review. *Norsk Geol Tid* 42:415–454
- Huntley DJ, Godfrey-Smith DI, Haskel EH (1991) Light induced emission spectra from some quartz and feldspars. *Nucl Tracks Radiat Meas* 18:127–131
- Ioffe VA and Yanchevskaya IS (1968) EPR and thermoluminescence study of irradiated $NaAl-Si_3O_8$ and $LiAlSiO_4$ single crystals (in Russian). *Phys tverd tela* 10:472–477
- Jaek I, Hütt G, Vasilchenko E (1996) Luminescence of the natural alkali feldspars artificially doped by Eu- and Cu-ions. In: Third European Meeting Spectroscopic Methods in Mineralogy, Kiev, Programme and Abstracts, pp 23
- Kastner M (1971) Authigenic feldspars in carbonate rocks. *Amer Miner* 56:1403–1442
- Kastner M and Siever RS (1979) Low temperature feldspars in sedimentary rocks. *Amer J Sci* 279:435–479
- Kempe U, Götze J, Dandar S, Habermann D (1999) Magmatic and metasomatic processes during formation of the Nb-Zr-REE deposits from Khaldzan Buregte (Mongolian Altai): indications from a combined CL-SEM study. *Miner Mag* 63: 165–167
- Kirsh Y, Shoal S, Townsend PD (1987) Kinetics and emission spectra of thermoluminescence in the feldspars albite and microcline. *Phys Stat Sol (a)* 101:253–262
- Krbetschek MR, Götze J, Dietrich A, Trautmann T (1998) Spectral information from minerals relevant for luminescence dating. *Radiat Meas* 27: 695–748
- Krbetschek M, Götze J, Habermann D, Rieser U, Wolf D (1996) High resolution luminescence studies of alkali feldspars and plagioclases. In: International conference on cathodoluminescence and related techniques in geosciences and geomaterials, Nancy, Abstracts, pp 79–80
- Krbetschek MR, Rieser U, Stolz W (1996) Optical dating: Some luminescence properties of natural feldspars. *Rad Prot Dosim* 66:407–412
- Kusnetsov GV and Kramarenko NK (1995) Kinetic luminescence characteristics of Ce^{3+} in plagioclases as a guide for facial classification of granitoids (in Russian). *Miner Zhurn* 17, No 2, 86–90
- Laud KR, Gibbons EF, Tien TY, Stadler HL (1971) Cathodoluminescence of Ce^{3+} and Eu^{2+} -activated alkaline earth feldspars. *J Electrochem Soc* 118:918–923
- Luff BJ and Townsend PD (1992) High sensitivity thermoluminescence spectrometer. *Meas Sci Technol* 3:65–71
- Lyakhovich VV (1972) Trace elements in rock-forming minerals of granitoides (in Russian). *Izd Nedra, Moscow*
- Marfunin AS (1979) Spectroscopy, luminescence and radiation center s in minerals. Springer-Verlag, Berlin Heidelberg New York
- Marfunin AS and Bershov LV (1970) Electron-hole center s in feldspars and their possible crystalchemical and petrological significance (in Russian). *Dokl Akad Nauk* 193:412–414
- Marfunin AS, Bershov LV, Meilman ML, Michoulier J (1967) Paramagnetic resonance of Fe^{3+} in some feldspars. *Schweiz Mineral Petrogr Mitt* 47:13–20

- Mariano AN (1978) The application of cathodoluminescence for carbonatite exploration and characterization. In: Braga CJ (ed) Proceedings of the 1st Intern Sympos on Carbonatites, Brasil Departamento Nacional da Producao Mineral, Brasilia, pp 39–57
- Mariano AN and Ring PJ (1975) Europium-activated cathodoluminescence in minerals. *Geoch Cosm Acta* 39:649–660
- Mariano AN, Ito J, Ring PJ (1973) Cathodoluminescence of plagioclase feldspars. *Geol Soc Amer, Abstr Progr* 5:726
- Marshall DJ (1988) Cathodoluminescence of geological material. Allen & Unwin, London
- Matyash IV, Bagmut NN, Litovchenko AS, Proshko VYa (1982) Electron paramagnetic resonance study of new paramagnetic centers in microcline-pegmatites from pegmatites. *Phys Chem Miner* 8:149–152
- Matyash IV, Brik AB, Zayak AP, Masykin VV (1981) Radiospectroscopy of feldspar (in Russian). *Naukova Dumka, Kiev*
- Mora CI and Ramseyer K (1992) Cathodoluminescence of coexisting plagioclases, Boehls Butte anorthosite: CL activators and fluid flow paths. *Amer Miner* 77:1258–1265
- Neuser RD, Bruhn F, Götze J, Habermann D, Richter DK (1995) Cathodoluminescence: method and application. *Zbl Geol Paläont Teil I, H. 1/2*:287–306
- Parsons I (1994) Feldspars and their reactions. NATO ASI Ser. C 421, Kluwer Acad Publ, Dordrecht Boston London
- Petrov I (1994) Lattice-stabilized CH₃, C₂H₅, NO₂, and O¹⁻-radicals in feldspar with different Al-Si order. *Amer Miner* 79:221–239
- Petrov I, Yude F, Bershov LV, Hafner SS, Kroll H (1989) Order-disorder of Fe³⁺ ions over the tetrahedral positions in albite. *Amer Miner* 74:604–609
- Petrov I, Mineeva RM, Bershov LV, Agel A (1993) EPR of [Pb-Pb]³⁺ mixed valence pairs in amazonite type microcline. *Amer Miner* 78:500–510
- Prescott JR, Fox PJ, Robertson GB, Hutton JT (1994) Three-dimensional spectral studies of the bleaching of the thermoluminescence of feldspars. *Radiat Meas* 23:367–375
- Putnis A (1992) Introduction to mineral sciences. University Press, Cambridge
- Rae DA and Chambers AD (1988) Metasomatism in the North Qoroq centre, South Greenland; cathodoluminescence and mineral chemistry of alkali feldspars. *Trans Royal Soc Edinb: Earth Sci* 79:1–12
- Ramseyer K, AlDahan AA, Collini B, Landström O (1992) Petrological modifications in granitic rocks from the Siljan impact structure: evidence from cathodoluminescence. *Tectonophysics* 216:195–204
- Rhodes JM (1969) On the chemistry of potassium feldspars in granitic rocks. *Chem Geol* 4:373–392
- Ribbe PH (1983) Feldspar Mineralogy. *Rev Miner* 2, 2nd edition, Miner Soc Amer, Chelsea, Michigan
- Rokatschuk TA, Tscherbakov IB, Steschin VA (1989) Genetic interpretation of the distribution of centres in plagioclases. *Miner Zhurn* 11, No 5, 60–67
- Schläfer A and Gliemann S (1980) Einführung in die Ligandenfeldtheorie. 2. Aufl, Akad Verlagsgesell, Wiesbaden
- Shmakin BM (1979) Composition and structural state of K-feldspars from some U.S. pegmatites. *Amer Miner* 64:49–56
- Sippel RF (1971) Luminescence petrography of the Apollo 12 rocks and comparative features in terrestrial rocks and meteorites. In: Proc 2nd Lunar Sci Conf 1, pp 247–263
- Sippel RF and Spencer AB (1970) Cathodoluminescence properties of lunar rocks. *Science* 167:677–679
- Smith JV (1983) Some chemical properties of feldspars. In: Ribbe PH (ed) Feldspar Mineralogy. *Rev. Miner.* 2, pp 281–296
- Smith JV and Brown WL (1988) Feldspar Minerals. 1 Crystal structures, physical, chemical, and microtextural properties. 2nd edition, Springer Verl, Heidelberg New York London Paris Tokyo
- Smith JV and Stenstrom RC (1965) Electron-excited luminescence as a petrologic tool. *J Geol* 73:627–635

- Speit B and Lehmann G (1982) Radiation defects in feldspars. *Phys Chem Miner* 8:77–82
- Tarashchan AN, Serebrennikov AI, Platonov AN (1973) Features of lead ions luminescence in amazonite (in Russian). In: *Constitution and properties of minerals* 7, pp 106–111
- Telfer DJ and Walker G (1975) Optical detection of Fe³⁺ in lunar plagioclase. *Nature* 258:694–695
- Telfer DJ and Walker G (1978) Ligand field bands of Mn²⁺ and Fe³⁺ luminescence centres and their site occupancy in plagioclase feldspars. *Mod Geol* 6:199–210
- Trautmann T, Krbetschek MR, Dietrich A, Stolz W (1998) Investigations on radioluminescence of feldspar: potential for a new dating technique. *Radiat Meas* 29: 421–425
- Walker G (1985) Mineralogical applications of luminescence techniques. In: Berry FJ and Vaughan DJ (eds) *Chemical bonding and spectroscopy in mineral chemistry*. Chapman & Hall, London, pp 103–140
- Walker G and Burley S (1991) Luminescence petrography and spectroscopic studies of diagenetic minerals. In: Barker CE and Kopp OC (eds) *Luminescence microscopy and spectroscopy: Qualitative and quantitative applications*. SEPM, Tulsa, pp 83–96
- Weeks RA (1973) Paramagnetic resonance spectra of Ti³⁺, Fe³⁺, and Mn²⁺ in lunar plagioclases. *J Geophys Res* 78:2393–2401
- White WB, Masako M, Linnehan DG, Furukawa T, Chandrasekhar BK (1986) Absorption and luminescence of Fe³⁺ in single-crystal orthoclase. *Amer Miner* 71:1415–1419

Application of Cathodoluminescence to Carbonate Diagenesis

HANS G. MACHEL

1

Introduction

Cathodoluminescence (CL) petrography is a popular tool in investigations of carbonate rocks and their diagenesis. The most widespread use of CL in carbonate studies is in cement stratigraphy using zoned cements. Visual CL colors and intensities are commonly correlated with analyzed Mn^{2+} and Fe^{2+} contents and then used, often in conjunction with other geochemical data (such as stable and radiogenic isotope data, fluid inclusion and paleomagnetic data, etc.), to interpret salinity, temperature, and Eh of the paleo-formation waters, and possibly paleo-fluid flow directions. Such applications of CL have great potential for applied research, e.g., via establishing porosity evolution in hydrocarbon reservoirs (e.g., several articles in Barker and Kopp 1991). Another popular use of CL is to identify marine components (cements or biochems, mainly brachiopods) that are unaltered or least altered by recrystallization, in order to determine the isotopic composition of paleo-ocean water (e.g., Popp et al. 1986; Lohmann and Walker 1989; Tobin et al. 1996).

In a comprehensive analysis of the factors that govern CL in calcite and dolomite, Machel and Burton (1991) identified 26 factors in five groups, which govern the CL color, intensity, and zonation of diagenetic carbonates (Fig. 1). On the basis of a critical literature analysis, Machel and Burton (1991) further claimed that, although some of the above factors had been considered in conventional CL work, many previously unconsidered factors also can have significant effects on CL. For example, at invariant pH/Eh, CL zonation in diagenetic carbonates can be generated solely from changes in Ca^{2+} activity, precipitation rate, or temperature. CL zonation may also result from changes in salinity or pH/Eh. On the other hand, determining pH and Eh at the time of precipitation from observed CL and corresponding Mn^{2+} and Fe^{2+} concentrations, which has been common practice, is impossible with the present state of knowledge. Furthermore, data from modern groundwater aquifers indicate that it is unlikely that diagenetically coeval calcite cements form over more than a few kilometers to a few tens of kilometers of flow distance, let alone over several tens of kilometers, except under very uncommon circumstances. Hence, standard cement stratigraphic correlations may not be valid or only on a relatively small scale.

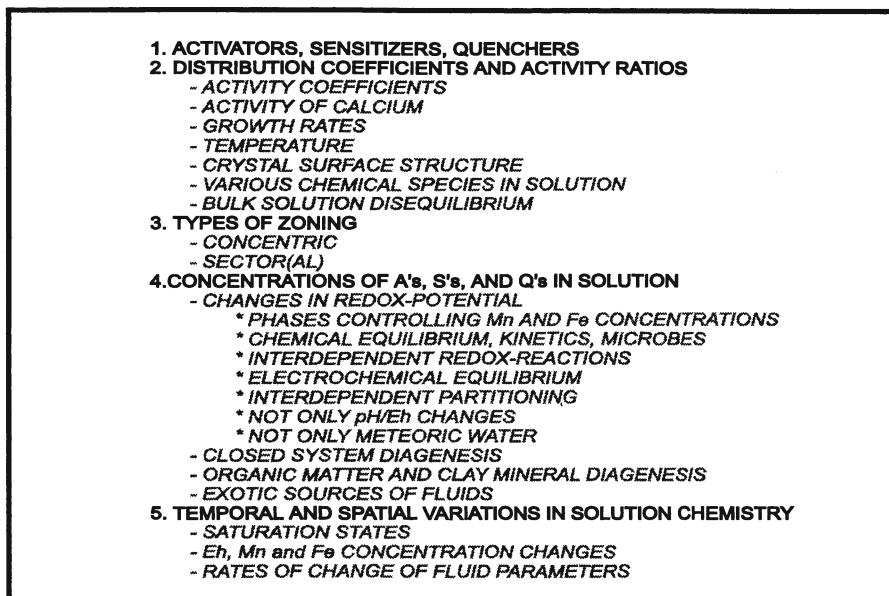
- 
1. **ACTIVATORS, SENSITIZERS, QUENCHERS**
 2. **DISTRIBUTION COEFFICIENTS AND ACTIVITY RATIOS**
 - ACTIVITY COEFFICIENTS
 - ACTIVITY OF CALCIUM
 - GROWTH RATES
 - TEMPERATURE
 - CRYSTAL SURFACE STRUCTURE
 - VARIOUS CHEMICAL SPECIES IN SOLUTION
 - BULK SOLUTION DISEQUILIBRIUM
 3. **TYPES OF ZONING**
 - CONCENTRIC
 - SECTOR(AL)
 4. **CONCENTRATIONS OF A's, S's, AND Q's IN SOLUTION**
 - CHANGES IN REDOX-POTENTIAL
 - * PHASES CONTROLLING Mn AND Fe CONCENTRATIONS
 - * CHEMICAL EQUILIBRIUM, KINETICS, MICROBES
 - * INTERDEPENDENT REDOX-REACTIONS
 - * ELECTROCHEMICAL EQUILIBRIUM
 - * INTERDEPENDENT PARTITIONING
 - * NOT ONLY pH/Eh CHANGES
 - * NOT ONLY METEORIC WATER
 - CLOSED SYSTEM DIAGENESIS
 - ORGANIC MATTER AND CLAY MINERAL DIAGENESIS
 - EXOTIC SOURCES OF FLUIDS
 5. **TEMPORAL AND SPATIAL VARIATIONS IN SOLUTION CHEMISTRY**
 - SATURATION STATES
 - Eh, Mn and Fe CONCENTRATION CHANGES
 - RATES OF CHANGE OF FLUID PARAMETERS

Fig. 1. Factors that govern CL in diagenetic carbonates

Indent in the years since, progress has been made in some of the areas mentioned above, but not in others. Moreover, the paper by Machel and Burton (1991) has not only clarified the subject matter but also, and regrettably, caused some confusion. As Bruckschen et al. (1997, p. 89) pointed out: "The overinterpretation of luminescence patterns in carbonate cements on one hand, but also the overcritical objections against these studies by another group of researchers [sic] resulted in a somewhat confusing discussion about the value of the concept of cement stratigraphy." These thoughts provide the basis for the present chapter. Its objectives are twofold: (1) to discuss the factors that govern CL in calcite and dolomite, focussing on those that are especially important for diagenetic studies; and (2) to point out the most important implications of these factors to applied studies of carbonate diagenesis. This chapter, although based on Machel and Burton (1991), presents not only a review but also some important new findings and thoughts that are based on several salient studies that have been published since 1991.

2

Factors That Govern Cathodoluminescence in Diagenetic Calcite and Dolomite

Almost all CL in carbonates is caused by trace elements, including rare earth elements (REEs), in solid solution, which act as activators, sensitizers, and quenchers (Fig. 2). These elements respond in the same capacities, i.e., as activators, sensitizers, and quenchers, respectively, to different types of excitation (electron

ACTIVATORS	SENSITIZERS	QUENCHERS
> 10-20 ppm	> 10 ppm	> 30-35 ppm
Mn ²⁺	Pb ²⁺	Fe ²⁺
Sm ³⁺	Ce ³⁺	Fe ³⁺
Tb ³⁺	etc..?	Ni ²⁺
Dy ³⁺		Co ²⁺
Eu ²⁺		etc..?
Eu ³⁺		
etc..?		

Fig. 2. Possible activators, sensitizers and quenchers of luminescence, and their effective minimum concentrations, in calcite and dolomite

beams, UV-excitation=photoluminescence, X-rays, etc.), as governed by principles of crystal physics (e.g., Marfunin 1979). Hence, it is admissible to compare the results of electron excitation with those of other methods of excitation. In particular, comparison of CL and photoluminescence are made further below when necessary. In addition, some carbonates exhibit an intrinsic luminescence ('intrinsic blue' in the case of calcite) that is very weak and visible only when activators are essentially absent (e.g., Mason and Mariano 1990; Mason 1994).

Mn²⁺ appears to be the most important activator and Fe²⁺ the most important quencher in diagenetic calcites and dolomites because, of all known elements, they are most abundant and/or most effective, and they appear to be positively correlated to observed or measured luminescence intensities (e.g., Machel et al. 1991). For this reason, much of the discussion that follows will use Mn²⁺ and Fe²⁺ as the principal trace elements. However, the other elements may well be dominant in certain settings.

2.1

Activators, Sensitizers, Quenchers

2.1.1

Manganese

As little as 10–20 ppm Mn²⁺ in solid solution is sufficient to produce visually detectable luminescence, if total Fe contents are below about 150 ppm (Machel et al. 1991; Neuser et al. 1996). Mn²⁺-activated CL in calcite and dolomite (for Ca²⁺-

substitution) emits in a band from about 570 to 640 nm, which appears yellow to orange/red (Machel et al. 1991). Conversely, CL emission can be used, with suitable calibration using other methods, as an analytical tool to detect activator elements. For example, concentrations as low as 10 ppm (5 ppm for some elements; Fraser 1990) can be detected with proton induced X-ray emission (PIXE) (Bruckschen et al. 1993; Habermann et al. 1996a). Even lower concentrations of 0.1 ppm Mn^{2+} can be detected with high resolution spectrometric analysis of CL (HRS-CL) and/or quantitative high resolution analysis of CL (QHRS-CL) (Habermann 1997; Habermann et al. 1996a,b, and this volume). However, such low concentrations do not produce CL that is visible in standard luminescence microscopes.

Recent experimental work has shown that the intensity and wavelength of Mn^{2+} -activated CL in calcite varies with temperature, the type of medium in which heating takes place, and with the magnesium content. This is understandable in light of the fact that CL of Mn^{2+} occurs via transitions of outer electrons whose energy states and transitions depend on lattice coordination (Marfunin 1979; Machel et al. 1991). In particular, heating in H_2O -vapor generally promotes greater CL intensity than heating in CO_2 , and the wavelength increases or the band width decreases or increases with heating, depending on the Mg^{2+} -content (Mason 1994, 1997, 1998). Mason explained the effect of heating on CL intensity as the results of the annihilation of lattice defects, and the changes in wavelength and band width as results of local redistribution of the activator ions. Apparently, the concentration dependence of CL on Mn^{2+} is not as simple as previously thought. The significance of these findings for studies of carbonate diagenesis has yet to be determined.

2.1.2

Rare Earth Elements

Several REEs are activators of CL in carbonates (Mason and Mariano 1990; Machel et al. 1991). The most important and best known REE activators are Sm^{3+} , Eu^{2+} and Eu^{3+} , Tb^{3+} , Dy^{3+} , and perhaps Ho^{3+} and others. Sm^{3+} -activated luminescence can be visually indistinguishable from that activated by Mn^{2+} , emission from Eu-containing calcite is red or blue and also can be similar to Mn-activated CL, whereas Tb^{3+} and Dy^{3+} activate green and cream-white luminescence, respectively (Mason and Mariano 1990; Machel et al. 1991; Habermann et al. 1996a,b). Spectral analysis shows that REEs almost invariably go in pairs or in groups, and that REE-activated luminescence is outshone by the much stronger Mn-activated CL, if Mn^{2+} is present at >10 ppm (Habermann et al. 1996a,b). Visual luminescence detection limits for rare earths are on the order of 10 ppm, and calculated detection limits by HRS-CL/QHRS-CL are in the ppb range (Habermann 1997; Habermann et al. this volume).

Most CL of REEs is caused by energy transitions of inner electrons (e.g., Marfunin 1979; Machel et al. 1991). Hence, most CL of REEs is not dependent on lattice defects and/or coordination and/or physical processes that change them (such as heating). In some cases, however, outer f-electrons are involved in CL, such as in Ce^{3+} and Eu^{2+} . This leads to some influence of the crystal field in Ce^{3+} and Eu^{2+} CL in some silicates (Goetze, 1999), and perhaps also in some carbonates.

2.1.3

Major Sensitizers

Pb²⁺ and Ce³⁺ are important sensitizers of Mn²⁺-activated luminescence in carbonates. In photoluminescence, where sensitization is particularly effective (relatively little activation of the activator elements), sensitizers appear to be effective at concentrations as low as 10 ppm (Gies 1976).

2.1.4

Major Quenchers

Quenchers of Mn²⁺-activated luminescence in carbonates are Fe²⁺, Co²⁺, Ni²⁺, and Fe³⁺. Ferrous iron, Fe²⁺, commonly is considered to be the only quencher in natural carbonates, but Fe³⁺ and Ni²⁺ probably are important in at least some cases (Machel et al. 1991). The concentrations at which quenchers appear to be effective may vary from element to element. Effective minimum concentrations as low as 30–35 ppm have been reported in studies of photoluminescence (Gies 1976), and quenchers may be effective at similarly low concentrations in CL.

The interplay of Mn²⁺ and total Fe (divalent and trivalent) in determining the luminescence characteristics of natural carbonates is not well understood. It appears possible that the Fe²⁺/Mn²⁺ ratio exerts a control on at least the intensity of carbonate luminescence. However, it is more likely that the absolute concentrations of Mn²⁺ and Fe²⁺ (self-quenching and quenching, respectively) determine the CL intensity (Habermann, personal communication, 1997). In either case, log Fe/log Mn plots are a useful way of illustrating the CL behavior of carbonates as a function of Mn and Fe concentrations in solid solution (Fig. 3; from Machel et al. 1991). Recent analytical data show that some calcites plot in “wrong” fields, e.g., some bright samples plot in the dull field (Neuser et al. 1996). In such samples factors other than Mn and Fe contents, probably the presence of sensitizers, are involved in CL. Also, the effective concentrations of quenchers and effects of quencher/Mn-ratios may well depend on temperature, as indirectly suggested by the studies by Mason (1994, 1997, 1998). Effects of heating on quenchers have not been investigated experimentally.

2.2

Distribution Coefficients and Activity Ratios

The recognition that CL in carbonates is governed by trace elements in solid solution necessitates a discussion of the factors that govern CL in calcite and dolomite in the context of the distribution law(s) of aqueous trace element geochemistry. The same laws can be used to express REE concentrations in diagenetic carbonates, and similar laws are used in igneous systems where element partitioning takes place in melts rather than in water.

Trace element incorporation into solids from aqueous solution commonly is described by one of two relationships (e.g., McIntyre 1963), i.e., the Homogeneous Distribution Equation or the related Heterogeneous Distribution Equation. In the first case the distribution of trace elements is uniform throughout the whole solid or growth zone, either because the trace/major ion ratios in the fluid do not change during precipitation (“open system”), or because the solid continuously

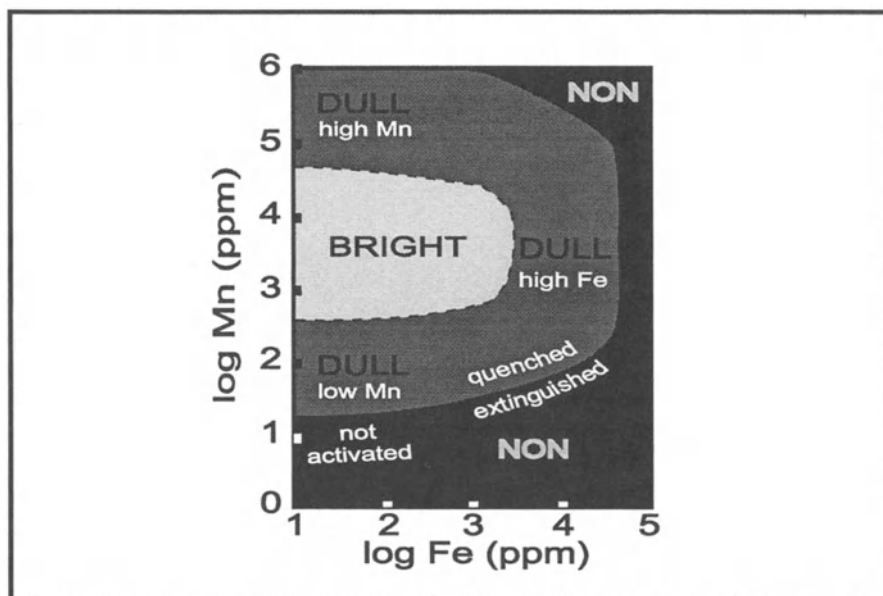


Fig. 3. Fields for CL in calcite and dolomite. (After Machel et al. (1991). Non-luminescence is due to low Mn (activator) concentrations (*lower left*), and extinction is due to Fe-quenching (*lower right*) as well as self-quenching by Mn (*right and upper right*)

recrystallizes during crystal growth. In the second case, the solid does not reequilibrate with the solution, and the trace element concentration in the solid changes continuously as the solution concentration changes with crystal growth (“closed system”).

For carbonates, the Homogeneous Distribution Law is used most often, as expressed in the following equation:

$$D_{\text{Me}}^* = \frac{(X_{\text{Me}^{2+}} / X_{\text{Ca}^{2+}})_s}{(m_{\text{Me}^{2+}} / m_{\text{Ca}^{2+}})_l} \quad (1)$$

where D_{Me}^* is the distribution coefficient, $X_{\text{Me}^{2+}}$ and $X_{\text{Ca}^{2+}}$ are the mole fractions of a trace element Me^{2+} (substituting for calcium) and calcium Ca^{2+} , respectively, in the solid, *s*; $m_{\text{Me}^{2+}}$ and $m_{\text{Ca}^{2+}}$ designate molal concentrations in the liquid, *l*. D_{Me}^* is also called the “effective distribution coefficient” or “partition coefficient” (Morse and Bender 1990), in order to indicate that the measured D_{Me}^* values are non-thermodynamic and valid only under the specific experimental conditions used. If element incorporation is defined thermodynamically, activities rather than concentrations are used in the equation for the Homogeneous Distribution Law:

$$D_{\text{Me}} = \frac{(X_{\text{Me}^{2+}} / X_{\text{Ca}^{2+}})_s}{(a_{\text{Me}^{2+}} / a_{\text{Ca}^{2+}})_l} \quad (2)$$

where D_{Me} is the thermodynamic distribution coefficient; the activity of an ion, a_i , is the product of the activity coefficient, γ_i , and the molal concentration, m_i . D_{Me} and D_{Me}^* are related by

$$D_{Me} = D_{Me}^* (\gamma_{Ca^{2+}} / \gamma_{Me^{2+}}) \quad (3)$$

where $\gamma_{Ca^{2+}}$ and $\gamma_{Me^{2+}}$ are the total activity coefficients which include ionic strength and ion pairing effects for Ca^{2+} and Me^{2+} in solution, respectively. The advantage of thermodynamic distribution coefficients is that they can be applied to solutions of widely different compositions, and thermodynamic distribution coefficients are used in all quantitative discussions below.

According to the Homogeneous Distribution Law, a crystal is enriched or depleted in trace elements relative to the liquid by the factor of D_{Me} , depending on whether D_{Me} is greater or smaller than 1, respectively. Furthermore, the trace elemental concentrations in solid solution are identical throughout the crystal in an open system or where the crystal constantly recrystallizes during growth (Fig. 4,

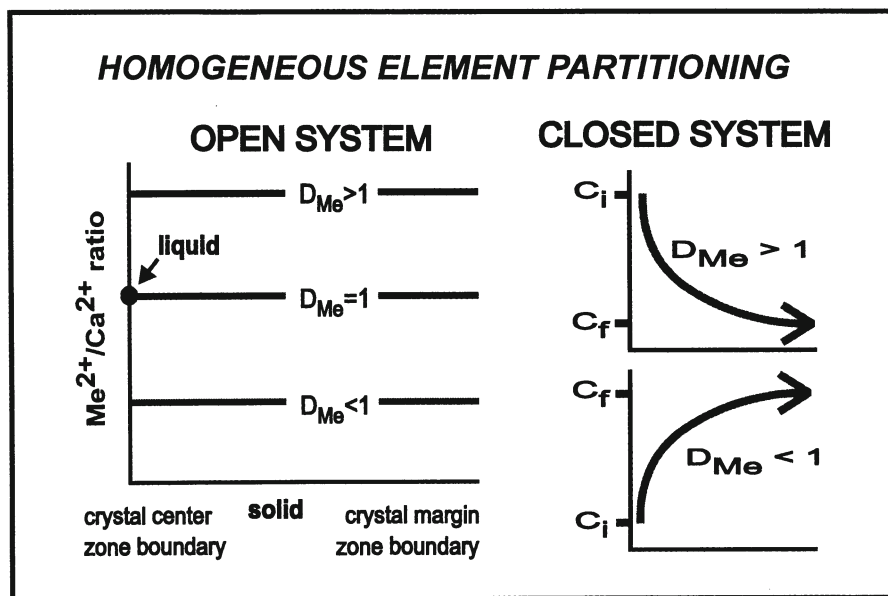


Fig. 4. Homogeneous element partitioning between solid and liquid with constant Me^{2+}/Ca^{2+} ratio for a trace element, Me^{2+} , substituting for Ca^{2+} . *Left* For an open system, the liquid composition is marked by a circle. The solids are illustrated as horizontal lines of constant composition with distance from crystal center to margin, or between boundaries of a (concentric) growth zone. For $D_{Me}=1$, the Me^{2+}/Ca^{2+} ratio in the solid is equal to the Me^{2+}/Ca^{2+} ratio in the liquid. For $D_{Me}<1$, the solid is depleted relative to the liquid by a factor of D_{Me} ; for $D_{Me}>1$, the solid is enriched relative to the liquid by a factor of D_{Me} . *Right* In a closed system, C_i and C_f represent concentrations of trace elements in carbonates in equilibrium with initial and final solution compositions, respectively. Directions of arrows show trends in solid compositions with fluid evolution over time. Such element distribution can be represented using the Heterogeneous Distribution Law (McIntyre 1963)

left). On the other hand, the trace element concentrations in solid solution decrease (increase) from an initial value, c_i , to a final value, c_f , depending on whether D_{Me} is smaller (greater) than one (Fig. 4, right), when the system is closed and/or recrystallization is inhibited. If growth of such a crystal is episodic, it will be zoned.

The fundamental value of the Homogeneous Distribution Law is that the fluid (aMe^{2+}/aCa^{2+})_l ratio can be back-calculated from the measured (XMe^{2+}/XCa^{2+})_s ratio in calcite or dolomite. Accurate back-calculation of the (aMe^{2+}/aCa^{2+})_l ratio depends on: (a) activity coefficients, which are functions of ionic strength and ion pairing; (b) concentrations of elements in solution; and D_{Me} values, which depend on (c) kinetics, (d) temperature, and (e) surface structure of the solid (see Machel and Burton 1991 for a more detailed discussion).

A number of D_{Me} values are known experimentally or from calculations based on laboratory experiments. Accordingly, D_{Mn} values of calcite range from 2.5 to 1700, D_{Fe} values range from 1 to >20; other transition metals, including Co, Ni, probably are incorporated similarly to Mn and Fe and, hence, their D_{Me} values probably are greater than 1; calculated D_{REE} values are $D_{Ce}=1500$, $D_{Sm}=1400$, $D_{Tb}=700$, $D_{Dy}=600$, $D_{Eu}=900$. D_{Me} values for dolomite are higher by factors of about 1.2 for Mn^{2+} and 2.5 for Fe^{2+} relative to those for calcite (see Machel and Burton 1991 for literature sources).

There are several important points that have to be considered when back-calculating fluid compositions from solid compositions. These points are implicit in the above equations and include the roles of the activity coefficients, activity of calcium, growth rates, temperature, crystal surface structure, various chemical species in solution, and bulk solution disequilibrium.

2.2.1

Activity Coefficients

Concentrations of trace elements in the solids are governed by the (aMe^{2+}/aCa^{2+})_l ratio rather than by the absolute cation activities or concentrations in aqueous solution. For example, calcite with 4125 ppm Mn^{2+} , corresponding to a particular CL color and intensity, can precipitate from a near-surface meteoric water or from a deep subsurface brine, as long as both fluids have the same (aMe^{2+}/aCa^{2+})_l ratio (Fig. 5). Thus, only the (aMe^{2+}/aCa^{2+})_l ratio can be back-calculated.

2.2.2

Activity of Calcium

Machel and Burton (1991) calculated the effects of variations in aCa^{2+} on trace element incorporation and CL in diagenetic calcite, using typical diagenetic conditions and limits for Mn^{2+} and Fe^{2+} . One of their examples was a solution with $aCa^{2+}=10^{-2.5}$, aMn^{2+} and $aFe^{2+}=10^{-7}$, which precipitates calcite with dull CL (x in Fig. 6). Once the solution aCa^{2+} decreases from $10^{-2.5}$ to 10^{-3} , calcite with bright CL forms (y in Fig. 6). These considerations show that CL zonation in diagenetic carbonates can be generated at invariant aMn^{2+} and aFe^{2+} (i.e., invariant pH/Eh), solely as a result of changes in aCa^{2+} .

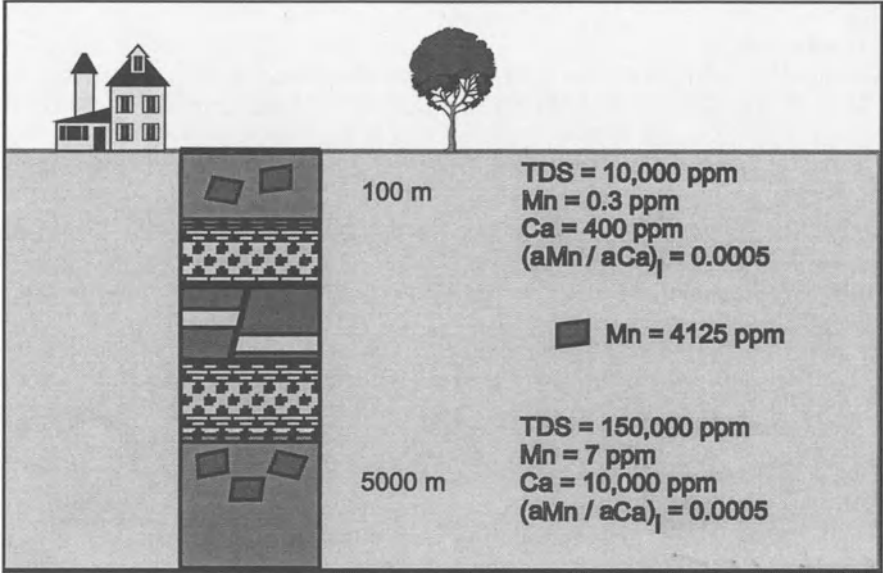


Fig. 5. A shallow freshwater aquifer and a deep brine with widely different bulk solution chemistries (TDS=total dissolved solids) produce calcite with the same Mn²⁺ composition because ($a_{Mn^{2+}}/a_{Ca^{2+}}$), are equal in both solutions. Calculations were done for $D_{Mn}=15$, $\gamma_{Mn}=\gamma_{Ca}=1$ for freshwater and $\gamma_{Mn}=\gamma_{Ca}=0.2$ for brine (γ values were calculated using SOLMINEQ, Kharaka et al. 1988). The values chosen for solution Mn²⁺ and Ca²⁺ concentrations and TDS represent average fresh waters and brines (Veizer (1983)

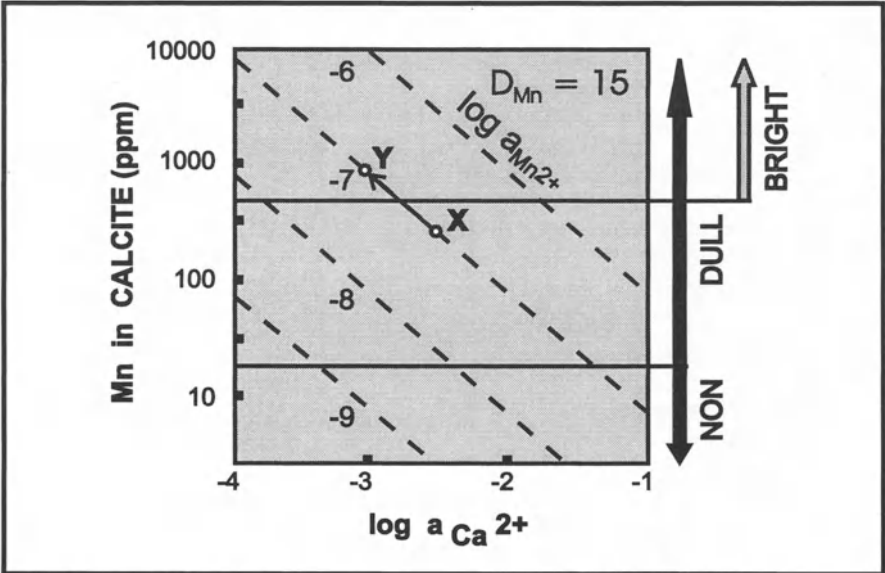


Fig. 6. Dependence of Mn²⁺ in calcite on solution log aCa²⁺ for $D_{Mn}=15$. Dashed lines show calculations for solutions with log aMn²⁺=-6 to -9. (After Machel and Burton 1991, their Fig. 3 A)

2.2.3

Growth Rates

Distribution coefficients for both Mn and Fe depend on crystal growth rate. Generally D_{Me} values are at their maxima (for $D > 1$) and minima (for $D < 1$) at low growth rates and approach unity for very high rates (McIntyre 1963). For calcite, D_{Mn} values were determined experimentally at 25°C to vary from $D_{Mn}=5$ to 60 over precipitation rates from 12000 to 12 $\mu\text{mol m}^{-2} \text{h}^{-1}$; $D_{Mn}=1.33$ to 18.8 over rates from 300,000 to 60 $\mu\text{mol m}^{-2} \text{h}^{-1}$; $D_{Mn}=3.8$ to 16 over rates from 45,000 to 450 $\mu\text{mol m}^{-2} \text{h}^{-1}$; and D_{Fe} values at 25°C vary from 1.9 to 3.7 over rates from 50,000 to 800 $\mu\text{mol m}^{-2} \text{h}^{-1}$ (see Machel and Burton 1991 for literature sources).

In another example, Machel and Burton (1991; their Fig. 3C,D) used a solution with $a\text{Mn}^{2+}=10^{-8}$ and $a\text{Fe}^{2+}=10^{-7}$ that precipitates calcite at a rate equivalent to $\log D_{Mn}=0.7$ and $\log D_{Fe}=0.2$. These D_{Me} values correspond to a rate of 20,000 $\mu\text{mol m}^{-2} \text{h}^{-1}$ at 25°C. Such calcite is non-luminescent. With decreasing precipitation rate to 1,000 $\mu\text{mol m}^{-2} \text{h}^{-1}$, the D_{Me} values increase to $\log D_{Mn}=1.2$ and $\log D_{Fe}=0.5$, forming calcite with dull CL. These calculations demonstrate that CL zonation in diagenetic carbonates can be generated at invariant $a\text{Mn}^{2+}$ and $a\text{Fe}^{2+}$ (i.e., invariant pH/Eh) solely as a result of changes in precipitation rate.

Changes in precipitation rate from 20,000 to 1,000 $\mu\text{mol m}^{-2} \text{h}^{-1}$ may occur close to recharge areas of confined carbonate aquifers (typically a few kilometers) where the calcite saturation state decreases relatively rapidly downflow. Farther downflow the precipitation rates will continue to decrease as the solution approaches equilibrium for calcite. Thus, the effects of precipitation rate in producing CL zonation will be even more pronounced from a few kilometers to tens of kilometers downflow. Also, precipitation rates and $a\text{Ca}^{2+}$ will decrease concomitantly in closed systems, and their combined effects will magnify changes in Mn^{2+} or Fe^{2+} incorporation.

2.2.4

Temperature

Experimental data by Bodine et al. (1965) and Dromgoole and Walter (1990) indicate that temperature has the potential to change trace element contents even if no other fluid parameters vary (Machel and Burton 1991). In many natural aquifers, temperature will increase downflow concomitantly with increases in salinity and decreases in precipitation rate. Therefore, $a\text{Ca}^{2+}$, rate and temperature all act on CL sympathetically.

2.2.5

Crystal Surface Structure

During crystal growth, crystallographically non-equivalent faces may incorporate elements to different degrees, which commonly leads to sector(al) zonation (further discussed below). The magnitude of the involved processes can be expressed with D_{Me} values. For example, Reeder and Paquette (1989) calculated a multiplication factor of 7 to 8 variation for D_{Mn} and D_{Mg} associated with sector(al) zoning in natural calcite, and they consider the surface structure effect to be of the same order of magnitude as the rate and temperature effects. In fact, these factors are

interdependent and all affect D_{Me} values by influencing ion adsorption and incorporation on crystal surfaces.

**2.2.6
Various Chemical Species in Solution**

Various chemical species in solution (e.g., H^+ , SO_4^{2-} , PO_4^{3-}) influence the incorporation of Mn^{2+} and Fe^{2+} in carbonates. There are no systematic investigations of the dependence of D_{Mn} and D_{Fe} values on fluid composition, but factors such as the activity of SO_4^{2-} and P_{CO_2} (pH) have significant effects on D_{Mg} , and may also be important in determining D_{Mn} and D_{Fe} (e.g., Burton and Walter 1988; Mucci et al. 1989). The significance of these effects for carbonate CL is not known.

**2.2.7
Bulk Solution Disequilibrium Partitioning**

Application of the thermodynamic Homogeneous Distribution Equation (Eq. 2) assumes that trace element incorporation occurs by bulk solution equilibrium partitioning, i.e., crystal compositions are homogeneous and proportional, by a factor of D_{Me} , to bulk solution ($a_{Me^{2+}}/a_{Ca^{2+}}$). In nature, however, element incorporation during precipitation, recrystallization, or replacement may occur via bulk solution disequilibrium partitioning (Machel 1990). Thereby, trace element incorporation during crystal growth takes place from thin, surface-adsorbed or surface-bonded fluid layers with compositions different from the solution occupying the bulk of the pore space (Fig. 7). The elemental (and isotopic) composi-

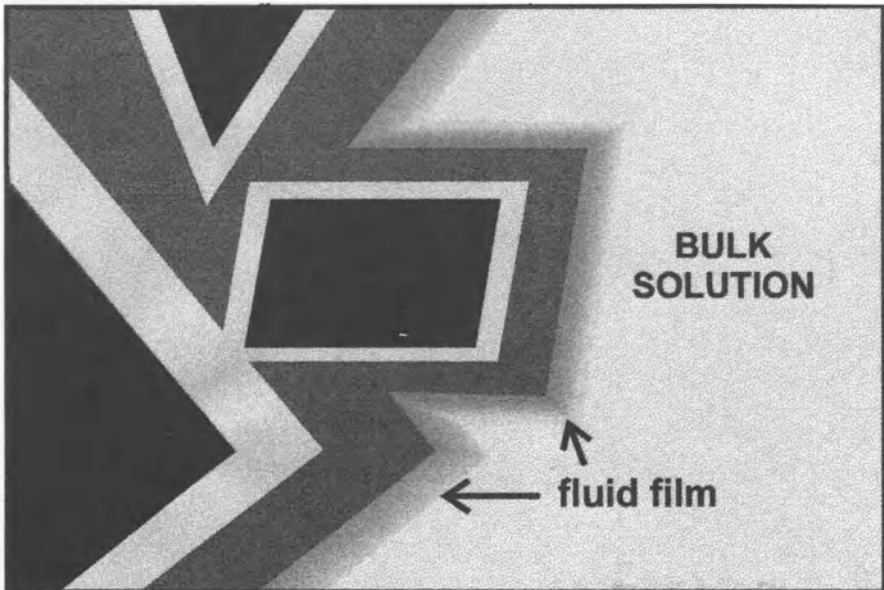


Fig. 7. Bulk solution disequilibrium partitioning between a cement and a liquid. Patterns in the solids designate different CL. Element partitioning takes place between the solid and a fluid film with composition different from the bulk solution

tions of minerals formed in bulk solution disequilibrium are determined by the compositions of the surface fluid layers, as well as by crystal growth rates and temperature.

A special case of bulk solution disequilibrium element partitioning is crystals that form in restricted pore spaces (microenvironments) which have $(a_{\text{Me}^{2+}}/a_{\text{Ca}^{2+}})_i$ different from that of the bulk solution. Zonal sequences may be inconsistent within a single thin section, or consistent within one thin section but inconsistent between thin sections from different horizons at one locality, or between localities. Such cases are quite common in the geologic record (e.g., Emery and Dickson 1989; Horbury and Adams 1989; Tobin and Walker 1996). Cases of multichambered ammonites with cement patterns that vary from chamber to chamber can be purchased at almost any mineral-rock fair.

Another, hitherto almost entirely unknown phenomenon of potential importance to CL is the effect of bacteria on trace element partitioning. In a recent experimental study, Mortimer et al. (1997) showed that manganese and calcium incorporation in microbially formed siderite did not reflect bulk solution equilibrium. Rather, manganese and calcium were found to be inversely proportional to the rate of microbial activity. Similar effects must be expected for microbially formed calcites and dolomites and for other trace elements.

2.3

Types of Zoning

Several types of zoning (zonation) can be revealed by CL. This section addresses those types that form during crystal growth and, therefore, could potentially be used for correlation (sequence stratigraphy) and back-calculation of fluid compositions. Recrystallization and/or replacement generally disturbs or obliterates growth zones and results in crystals with unzoned, "mottled" or "blotchy" luminescence. Such patterns can be used to identify recrystallization but are not discussed in this chapter.

2.3.1

Concentric Zoning

Concentric zones are parallel to growth surfaces of crystals and commonly have widths between a few microns to several millimeters (Fig. 8 A). This zoning pattern is a record of crystal morphology during growth (Reeder 1991). A common succession of "simple" concentric zoning is non-, to bright-, to dull-CL, to-non. In some cases concentric zonation is cyclic, i.e., two or three CL colors and intensities occur repetitively, possibly reflecting a cyclic pore water evolution.

There are many factors causing concentric zoning, including changes in bulk solution composition, changes in growth rate, and changes in temperature. Crystals have concentric CL colors that fade into one another if one or more of these factors change gradually. If changes are rapid while a crystal is growing, or if changes occur while crystal growth is temporarily halted, sharp concentric zoning results. Hence, sharp zonal boundaries may or may not indicate a hiatus in crystal growth.

Oscillatory zoning is another type of concentric zoning. Oscillatory zones are rarely wider than a few microns, and typically there is a multiple alternation of

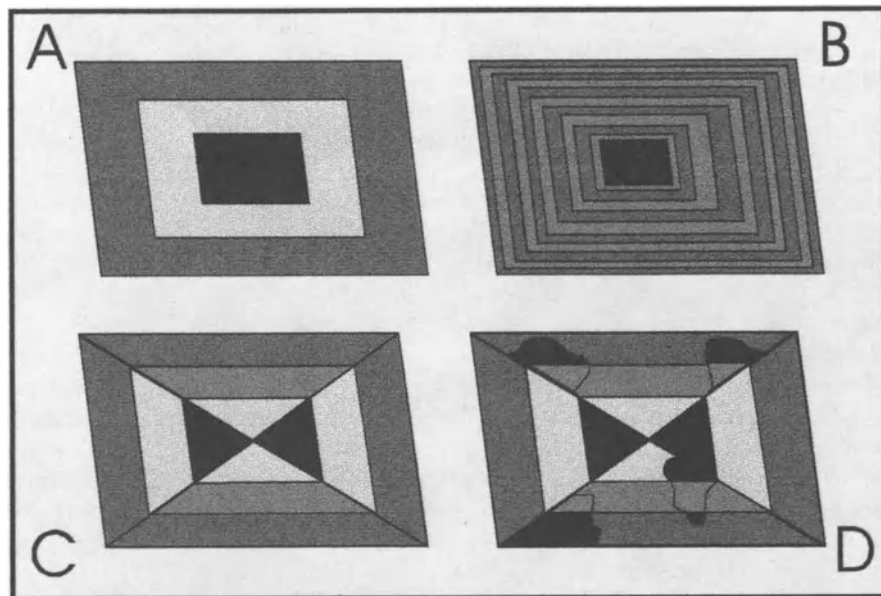


Fig. 8A–D. Common zoning types in carbonates. A Simple concentric zoning. B Oscillatory zoning. C Sector(al) zoning. D Intrasector(al) zoning

two zones about equally thick but with different CL colors/intensities (Fig. 8B). In many cases, oscillatory zoning occurs within simple concentric zones. Therefore, oscillatory zoning generally is easy to distinguish from simple concentric zoning but may be mistaken for cyclic zonation in some cases. Oscillatory zoning appears to form only in systems far from equilibrium as a result of certain diffusion-precipitation processes on growing crystal surfaces (“geochemical self-organization”) (e.g., Reeder 1991; Ortoleva 1994).

2.3.2

Sector(al) Zonation

Sector(al) zoning results from differences in cement composition that vary for time-equivalent, but crystallographically non-equivalent, growth sectors (e.g., Reeder and Paquette 1989; Reeder 1991), giving rise to different CL intensities of adjacent sectors (Fig. 8 C). Highly irregular sectors result when crystal morphology changes during growth. Triangular blocks, arrowhead blocks, and fir-tree arrays with sharply defined zigzag boundaries are special types of sector zoning. Intrasector(al) zoning is a special sub-type of compositional zoning of trace elements in time-equivalent regions within a single growth sector of synthetic and natural calcite (Fig. 8D). Sector zoning and intrasectoral zoning are types of disequilibrium partitioning because crystallographically non-equivalent faces, or parts of faces, that grew simultaneously have compositional differences, i.e., adjacent faces grow with different D_{Me} values (Reeder 1991; Fouke and Reeder 1992).

2.4

Concentrations and Activities of Activators, Sensitizers, and Quenchers in Diagenetic Fluids

There are four groups of processes that determine the trace element concentrations in diagenetic fluids, and hence in precipitating carbonates: changes in redox-potential, closed system element partitioning, organic matter maturation, and clay mineral diagenesis. In addition, exotic sources may contribute trace elements. These aspects are discussed below.

2.4.1

Changes in Redox-Potential

Changes in redox-potential (Eh) in solution affect concentrations of elements which have different valence states, including Fe and Mn. Such changes are caused by redox-reactions, which commonly are expressed as pH/Eh diagrams. A popular version of a pH/Eh diagram with superimposed fields of non, bright, dull, and non luminescence is shown in Fig. 9A. Similar diagrams have been in use in studies of carbonates, particularly in meteoric diagenesis, since the mid-1970s (Carpenter and Oglesby 1976; Oglesby 1976).

When computing and applying such pH/Eh diagrams, all authors explicitly or implicitly have made numerous assumptions, including: (1) the concentrations of Mn^{2+} and Fe^{2+} in aqueous solution are controlled by chemical equilibrium of redox-reactions including specific Mn-oxides and Fe-oxides, i.e., $Mn^{4+}O_2$, and $Fe^{3+}OOH$ or $Fe^{3+}(OH)_3$ or $Fe^{3+}_2O_3$ (depending on the author); (2) meteoric groundwater aquifers are in chemical equilibrium (i.e., they are devoid of any kinetic inhibition of redox-reactions, and are not microbially dominated); (3) the concentrations of Mn^{2+} and Fe^{2+} in aqueous solution are independently, rather than interdependently, controlled by reduction of the above oxides; (4) meteoric groundwater aquifers are in electrochemical equilibrium; (5) the amount of Mn^{2+} incorporation in calcite is not influenced by the amount of Fe^{2+} in solution, and vice versa; (6) changes in Eh (and/or minor pH changes) is/are the sole causes of CL zonation in diagenetic carbonates; and (7) the observed CL changes can only occur in meteoric groundwater systems. All of these assumptions can be shown to be incorrect in many, if not most, cases (Machel and Burton 1991). This, unfortunately, seriously limits the applicability of diagrams such as Fig. 9 A. It may well be that the rock with which one is dealing formed in an aqueous system whose pH/Eh characteristics were entirely different, perhaps like in the hypothetical example shown in Fig. 9B.

2.4.2

Closed System Diagenesis

Trace element variations in diagenetic fluids can be governed by the degree of "openness" of the system. In open systems (unlimited water supply, relatively high flow rates), carbonate cementation, recrystallization, and replacement have no noticeable effect on fluid composition. In "semi-closed" and "closed" systems that contain low contents of clay minerals and organics, carbonate cementation (and often recrystallization) will lead to increases in the fluid concentrations of ele-

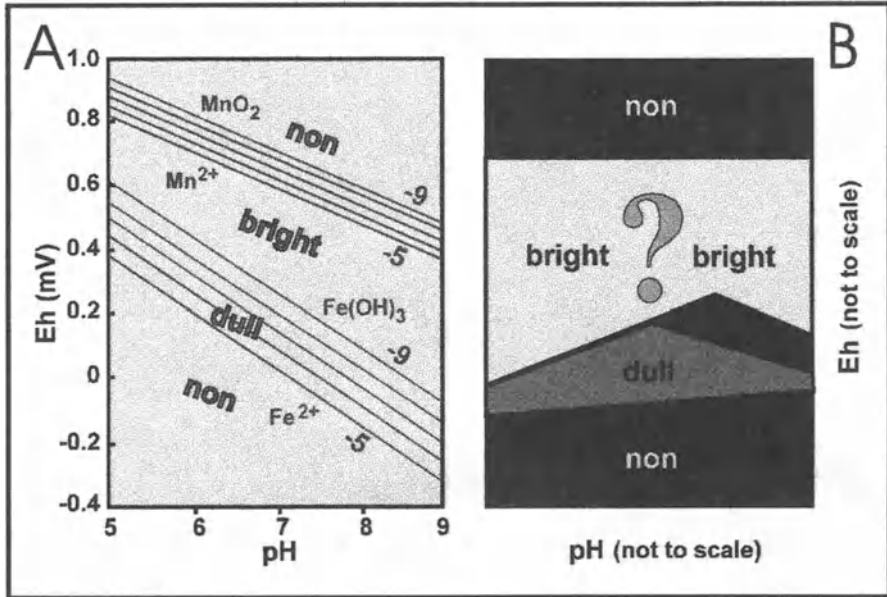


Fig. 9. A Superimposed stability fields for MnO₂ and Mn²⁺ (near top, less inclined lines) and Fe(OH)₃ and Fe²⁺ (below and center, more inclined lines) defined by Eh and pH. The lines labeled -5 and -9 show positions of equilibrium between the mineral oxides and specified activities, *a*, of Mn²⁺ or Fe²⁺ from $a_{Me^{2+}}=10^{-5}-10^{-9}$. B Hypothetical pH/Eh diagram for CL in diagenetic carbonates. The axes are not to scale. Other boundaries between CL fields are feasible, depending on which mineral and amorphous phases control pH/Eh in the system. The commonly observed CL sequence of non-bright-dull(-non) might be formed with decreasing Eh, as shown in left portion of diagram. Another possible CL sequence is non-bright-non-dull-non, as shown on the right. (After Machel and Burton 1991)

ments with $D_{Me} < 1$ and to decreases of element concentrations with $D_{Me} > 1$ (Fig. 4, right). The magnitudes of such concentration changes depend on the degree of openness of the system, and on D_{Me} values. These considerations imply that closed system precipitation can be the sole cause of variable CL color and intensities in carbonates. The changes in CL would be unidirectional as fluids become progressively depleted/enriched in the trace elements.

2.4.3

Organic Matter and Clay Mineral Diagenesis

Organic matter and clay mineral diagenesis are possible sources and sinks of many trace elements, including all known activators, sensitizers, and quenchers of CL in carbonates. Hence, diagenesis of clay minerals and organic matter can lead to CL zonation in diagenetic carbonates. Organic matter preferentially hosts Ag, [Co], Cr, Cu, [Eu], Ga, La, Mn, Mo, Ni, Pb, Te, U, V, Y, and [Zn], while other elements are associated mostly with clay minerals, e.g., B, Ba, Be, Co, Cs, Hf, [Mo], [Pb], Rb, Sc, Se, Th (e.g., Khawlie and Carozzi 1976; Parekh et al. 1977; Leventhal and Hostermann 1982; elements without square brackets are confirmed, those with

square brackets are suspected, by these authors to be associated with clay minerals and organic matter). Furthermore, iron compounds, such as siderite, pyrite, hematite, or limonite, also host Co and Ni, potentially important quenchers.

Many of the above elements are released into pore waters during compaction and concomitant burial diagenesis. Release of trace elements commonly takes place sequentially, because the various minerals and organic components react over extended intervals of burial depth rather than all at once. It is reasonable to conclude, therefore, that sequential elemental release is an important cause of zonation. Cases have been reported in which CL colors and intensities, and corresponding trace element contents, of carbonates are related to the proximity of terrigenous influence (e.g., Nelson et al. 1989).

2.4.4

Exotic Sources of Fluids

Large amounts of elements in dissolved or colloidal form can be supplied by continental runoff to shelf carbonates in coastal proximity (e.g., Kremling 1983), or to carbonates that are subaerially exposed. Many carbonates are dissected by tectonic or karstic fracture systems that act as conduits for hydrothermal and/or meteoric fluids, as exemplified by several case studies (e.g., Viau and Oldershaw 1984; Gregg and Hagni 1986; Amieux and Jeanbourquin 1989). CL zonation obviously can result from the gradual or sudden influx of exotic fluids.

2.5

Temporal and Spatial Variations in Solution Chemistry

In diagenetic environments, particularly in shallow meteoric (fresh water) aquifers, two or more fluid parameters usually vary spatially in a systematic pattern: salinity, activity coefficients, and temperature increase downflow, whereas precipitation rate (saturation state), Eh, and $a_{Ca^{2+}}$ increase upflow (Fig. 10) (e.g., Freeze and Cherry 1979). The groundwater commonly is supersaturated for calcite near the recharge area (except right at the point of recharge) and then becomes progressively less saturated through precipitation towards the discharge area, causing decreasing precipitation rates and decreasing $a_{Ca^{2+}}$ downflow. However, these trends may be highly variable spatially and/or temporally. For example, salinity and saturation states may vary on time-scales ranging from seasons to years, and in highly permeable systems even in response to very short-lived events such as heavy rainfall. Also, the effects of trace element partitioning in bulk solution disequilibrium, introduction of exotic fluids, clay mineral and organic matter diagenesis, electrochemical (dis)equilibrium, and bacteria, albeit nearly always present, vary less systematically and are nearly unpredictable (Fig. 10). Consequently, there is the potential for developing cyclic and/or erratic, non-correlatable zonation from fluctuating solution properties.

Of special importance are hydrocarbon traps located within local or regional groundwater systems, as they have a tendency to leak and, thereby, contaminate the groundwater with liquid and/or gaseous hydrocarbons (Fig. 11). The resulting strongly reducing plumes may be vertical or follow the groundwater flow pattern.

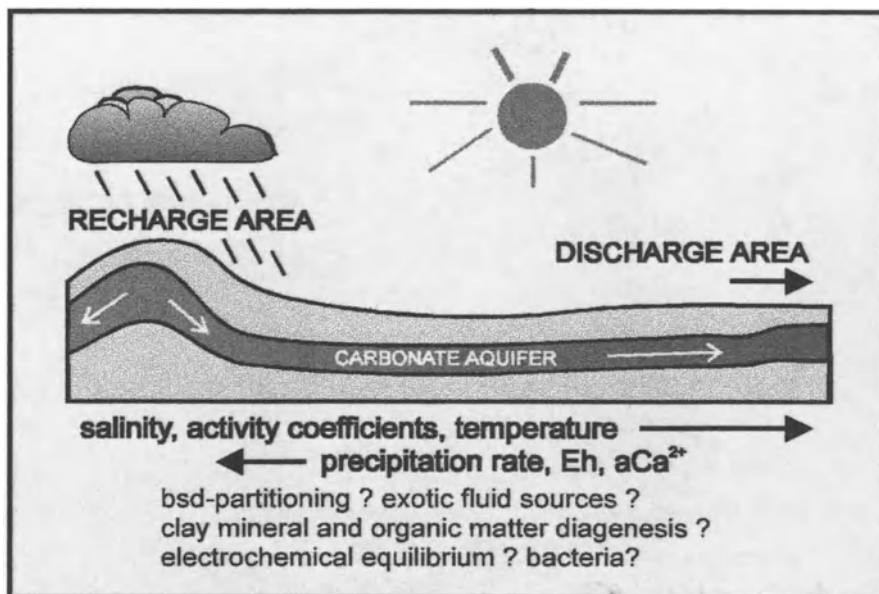


Fig. 10. Geochemical trends in an idealized, confined carbonate aquifer

They have diagenetic effects quite different from those in the surrounding, more oxidizing groundwater, with enhanced formation of magnetite, siderite, calcite, dolomite, Fe-sulfides, or other phenomena (Barker et al. 1991; Burton et al. 1993; Machel 1995).

Three spatial and temporal variations appear to be more common and/or important than the others mentioned above. These are changes in saturation state, Eh changes accompanied by changes in Mn and Fe concentrations (activities), and the rates of such changes.

2.5.1

Saturation States

The presence of carbonate cement(s) necessitates supersaturation with respect to the carbonate mineral(s) in question, i.e., most commonly calcite. The question arises, therefore, what governs calcite saturation states in carbonate aquifers, and where and when such aquifers are supersaturated with respect to calcite.

Studies of modern carbonate and siliciclastic aquifers show that the groundwaters are commonly not supersaturated for calcite but merely saturated or even undersaturated, in which case no carbonate precipitation or even carbonate dissolution occur. Several well-studied regional carbonate aquifers, located in very different climates and hydrologic settings, demonstrate this point, i.e., an aquifer of the humid Valley and Ridge Province in Pennsylvania, where 20% of the samples are saturated and 80% are undersaturated with respect to calcite (Jacobson and Langmuir 1970; Langmuir and Whittemore 1971; sample depths of 30–150 m); a tropical to subtropical limestone aquifer of central Florida, where

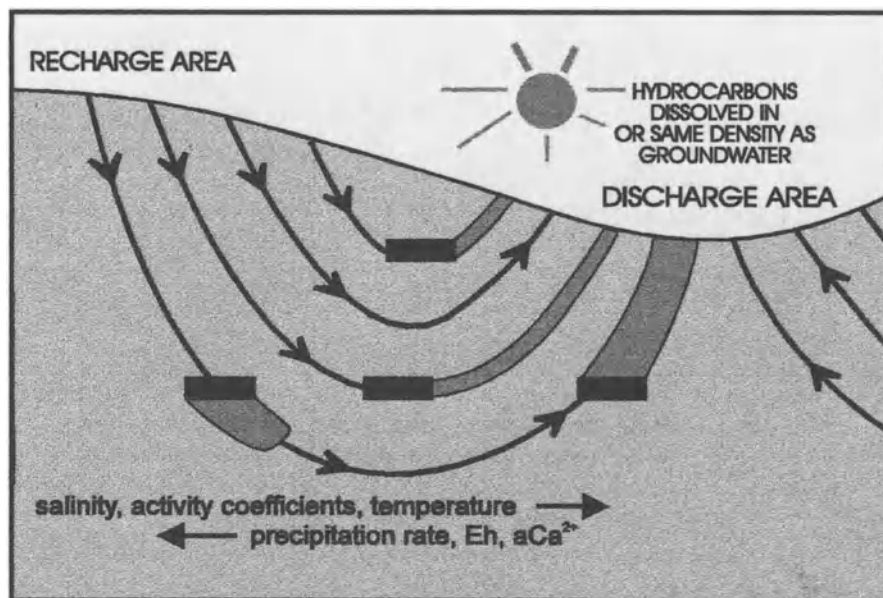


Fig. 11. Schematic illustration of four hydrocarbon traps embedded in an active topography-driven groundwater flow system. For simplicity, the flow domain is assumed to be isotropic and homogeneous except for the traps. Geochemical plumes form where hydrocarbons leak into the groundwater. In this particular example, the plumes follow the regional ground water flow because the leaking hydrocarbons are either dissolved in, or have the same density as, the groundwater. The plumes are nearly vertical when the hydrocarbons escape as a separate phase with densities lower than the ground water. (See Machel 1995)

66% of the samples are supersaturated with respect to calcite, 24% are saturated, and 10% are undersaturated (Back and Hanshaw 1970; Hanshaw et al. 1971; samples from depths of 50–400 m); a dolomite aquifer of Manitoba in a semihumid temperate climate, where 20% of the samples are supersaturated with respect to both calcite and dolomite, 62% are saturated, and 8% are significantly undersaturated (Render 1970; Goff 1971; samples from 10–50 m of depth); and the Chalk Aquifer of Berkshire, U.K., where 38 of 41 samples are undersaturated for calcite (Edmunds et al. 1987). In addition, there is indirect evidence for a lack of supersaturation from carbonate cement studies. In the Floridan Aquifer, for example, none of the calcite cements investigated by Budd et al. (1993) are in isotopic ($\delta^{18}\text{O}$ and $\delta^{13}\text{C}$) and trace element (Fe, Mn, Sr) equilibrium with the extant aquifer waters, suggesting that these rocks have been basically inert with respect to calcite cementation during the past 5–10 m.y.

These data indicate that shallow carbonate (as well as siliciclastic) aquifers contain relatively few and/or small areas of calcite supersaturation, and that carbonate cementation may be restricted to a fairly small (and distant) time interval in the history of an aquifer. This must be considered in studies of cement stratigraphy (see Sect. 3).

2.5.2

Eh, Mn²⁺ and Fe²⁺ Concentration Changes

Groundwater that travels from upland recharge to lowland discharge areas commonly exhibits a decline in the measured Eh if flow is under confined conditions (e.g., Freeze and Cherry 1979). Often there is a concomitant slight increase in pH. Such pH/Eh changes are inferred to increase Mn²⁺ and Fe²⁺ concentrations, as well as the concentrations of the reduced species of other elements with variable oxidation states. Measurements from recent carbonate and siliciclastic groundwater aquifers indicate, however, that Mn²⁺ and Fe²⁺ concentrations commonly do not increase concomitantly with a drop in Eh, or steady decreases in Eh are accompanied by erratic increases and/or decreases in Mn²⁺ and/or Fe²⁺. A case in point is the Chalk Aquifer of Berkshire, UK, where a relatively sharp decrease in Eh defines a redox boundary about 35 km downflow from the recharge area, and where the Mn and Fe concentrations in aqueous solution vary erratically, albeit sympathetically, in the reducing part of the aquifer (Fig. 12) (Edmunds et al. 1987). In other aquifers the redox boundary may be as close as 15 km to the recharge area, and the elemental compositions vary even more erratically (Edmunds 1973; Edmunds et al. 1982 1984). These data must also be considered in studies of cement stratigraphy.

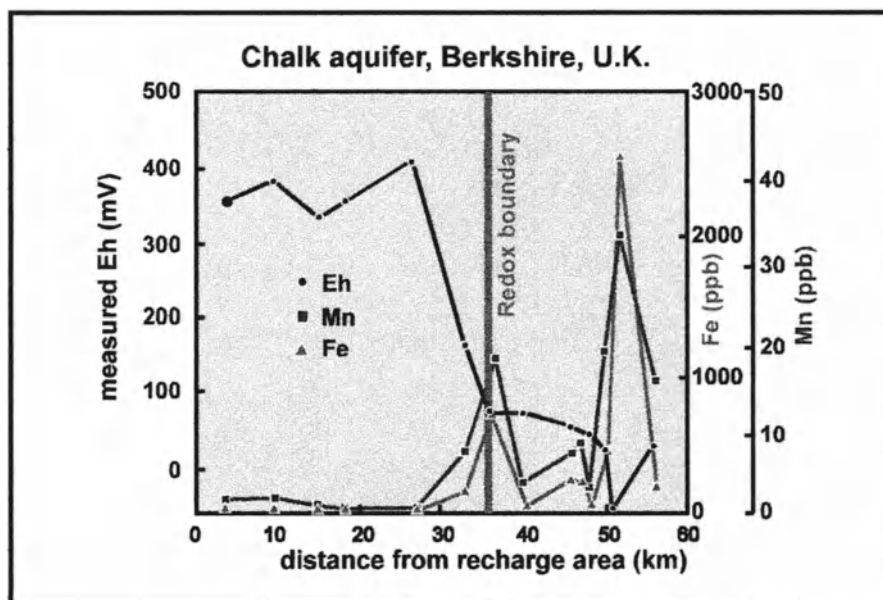


Fig. 12. Measured Eh, total Fe and Mn in the Berkshire Chalk aquifer (Edmunds et al. 1987). The redox boundary is defined by a sharp drop from values of Eh \geq 300 mV to values of Eh \leq 100 mV, separating more oxidizing conditions near the recharge area from more reducing conditions closer to the discharge area. There are erratic but sympathetic trends in Mn and Fe downflow. Mn and Fe values typical for the more oxidizing part also occur in the more reducing part

2.5.3

Rates of Change of Fluid Parameters

It is common practice to correlate natural water pH/Eh conditions and mineral stability fields in pH/Eh diagrams with the sizes of CL zones (e.g., Barnaby and Rimstidt 1989). However, the sizes of CL fields in pH/Eh diagrams do not correlate with cement abundances except when fluid Eh and pH values change steadily, either temporally or spatially. The relative amounts of bright or dull calcites are controlled mainly by the rates of pore water pH/Eh evolution, rather than by the size of stability fields. Similar arguments can be made with respect to rates of change in precipitation rate or other fluid parameters. Two examples illustrating this point are discussed in Machel and Burton (1991).

3

Implications for and Application to Studies of Carbonate Diagenesis

Many studies have demonstrated the terrific potential of CL to reveal textural details of cementation and recrystallization, and of complicated paragenetic relationships that otherwise would not be detectable, and CL has proved to be indispensable as a tool to identify geochemically distinct and internally homogeneous domains for microdrilling and various microbeam techniques (Meyers 1976; studies reviewed in Meyers 1991; Bruckschen et al. 1992; Pedone et al. 1994; Braithwaite and Rizzi 1997, and many others). On the other hand, interpretations of pore water evolution, especially in the 1970s and 1980s, were/are often based on oversimplified assumptions (Machel 1985; Machel and Burton 1991). Most recent studies have attempted to consider a number of the factors discussed in the previous sections. Admittedly, diagenetic studies are hampered by a limited knowledge of some of these factors, and the potential significance of others. For example, trace element disequilibrium partitioning due to microbes has not been recognized until relatively recently.

3.1

Activators, Sensitizers, Quenchers

The possible presence and/or concentrations in cements of all activators and sensitizers are best revealed by means of CL-spectrophotometry (e.g., Machel et al. 1991; Habermann et al. 1996a,b). This method is faster than other analytical procedures, it is non-destructive, there are no possibilities of contamination during sample preparation, and small (a few μm) spots can be analyzed. On the other hand, the presence and amounts of quenchers cannot be determined. Another approach is to compare CL intensities, measured photometrically, with element concentrations measured by atomic adsorption, inductively coupled plasma, microprobe analysis, etc. (e.g., Hemming et al. 1989; Lee and Harwood 1989). Visual inspection, leading to the well known classification of non, dull, and bright luminescence, as well as recognition of colors associated with certain activators, is still useful but only qualitatively and for textural investigations.

The role of REEs in diagenetic carbonates deserves special consideration because they are activators at very low concentrations (see above). For many years REE activation in diagenetic carbonates has been ignored. However, a number of studies have identified REE and/or REE-activated luminescence in carbonates. In general, diagenesis leads to a relative enrichment in the carbonates of the light REEs, and to a relative enrichment of the heavy REEs in organic components and clay minerals (Parekh et al. 1977; Schieber 1988). Other studies have shown that dolostones were enriched in REEs relative to limestones (Kubanek and Parhek 1976). REE-activated luminescence is known from samples that range from hydrothermal carbonates (e.g., Gies 1976) to Holocene and Pleistocene corals (Scherer and Seitz 1980). Further examples of REE-activated CL in marine sediments and limestones, sinter calcites and similar speleothems, and hydrothermal vein fillings are provided by Richter et al. (1995) and Habermann et al. (1996a,b).

3.2

Back-Calculation of Fluid Composition

The $(a\text{Me}^{2+}/a\text{Ca}^{2+})_i$ ratios of the bulk solution at the time of precipitation may be back-calculated from the measured $(X\text{Me}^{2+}/X\text{Ca}^{2+})_s$ of the concentric growth zones and a D_{Me} value, using the distribution equations 1 and 2, discussed previously. Distribution coefficients and activity ratios are related to activity coefficients, $a\text{Ca}^{2+}$, growth rates, temperature, crystal surface structure, fluid composition, and bulk solution disequilibrium partitioning, and several of these factors are interrelated. Ideally, these factors should be known in order to quantify the magnitudes of their effects on luminescence.

The obvious approach is to combine CL studies with other geochemical methods. For example, temperature and salinity can often be determined or estimated using oxygen isotope and/or fluid inclusion data (e.g., Braithwaite and Rizzi 1997). Growth rates, however, can be determined successfully in only some cases, i.e., in recent or geologically very young aquifers that are well-studied. For example, Handford et al. (1984) calculated aragonite cement growth rates from the thicknesses of cements precipitated in subaerially exposed carbonate sediment mounds, and Herman and Lorah (1988) conducted direct measurements of calcite precipitated onto seed crystals placed in travertine-depositing streams. In these well defined diagenetic environments, reasonable choices can be made for D_{Me} in order to back-calculate $(a\text{Me}^{2+}/a\text{Ca}^{2+})_i$ ratios of the bulk solution at the time of precipitation. Growth rates in most ancient aquifers, however, are next to impossible to estimate. Related to this point, saturation states must be known or estimated, and there are case studies that provide extensive data bases on saturation states in aquifers (see above).

3.3

Growth Rates

The fact that growth rates change distribution coefficients indicates that the rate of precipitation (as well as temperature) must be known or estimated for an accurate back-calculation of fluid composition from D_{Me} and $(a\text{Me}^{2+}/a\text{Ca}^{2+})_s$ values. In

order to estimate precipitation rates, however, both the saturation state for calcite (or dolomite) and the bulk fluid compositions must be well known, which usually is not possible (this is a classic Catch 22, as the fluid composition is what one wants to back-calculate originally).

Hence, all back-calculations of fluid composition using trace element distribution laws necessarily yield inaccurate results, the values obtained depend on the assumptions used for the fluid composition. Reasonable estimates of precipitation rates can be made only for recent aquifers whose composition and temperature can be measured. For ancient diagenetic carbonates, this is a nearly impossible task. In addition, changes in growth rate may lead to incorrect cement or zone correlations (see below).

3.4

Bulk Solution Disequilibrium

Bulk solution disequilibrium partitioning may be difficult to recognize but is most commonly represented by fairly large trace element variations, and erratic CL distribution (“blotchy”, irregular), between petrographically coeval phases over small distances (Machel 1990). Other textural indications of bulk solution disequilibrium are oscillatory and sector(al) zoning.

The fact that crystals may grow in bulk solution disequilibrium has several important implications. Firstly, crystals or crystal zones with different CL color and/or intensity are not necessarily formed from different bulk fluids but can be synchronous (see also Sect. 3.5). Secondly, back-calculations of $(a_{Me^{2+}}/a_{Ca^{2+}})_l$ from crystals or crystal zones identified by CL may merely determine the composition of surface-adsorbed or surface-bonded fluid films or of restricted pore spaces, rather than the bulk solution composition. In either case, the composition of the bulk solution cannot be back-calculated accurately in systems with pronounced and spatially variable bulk solution disequilibrium (Machel 1990). Thirdly, attempts have to be made to identify whether any of the carbonate cements under investigation may be formed by or with the mediation of bacteria (or other microbes). Lastly, and perhaps most importantly, crystals formed in bulk solution disequilibrium and/or restricted microenvironments should not be used for correlation in cement stratigraphy.

3.5

Zoning and Correlation

Conventional applications of correlation to cement stratigraphy have been reviewed by Meyers (1991) and will not be repeated here. This section discusses the potential and the pitfalls of using the various types of cements and zonation for correlation and back-calculation of fluid composition, as they appear in light of the factors discussed in Sect. 2 above.

Simple concentric zoning, especially of cements of one growth form, can be used for correlation and, in some cases, for back-calculation of the bulk fluid composition. Cyclic zoning, representing periodic changes in bulk fluid composition, can be utilized for the same purposes. However, there is one important

caveat, based on the recognition that different faces/sectors may have different effective D_{Mn} (see Sect. 2.3.2). In the humble opinion of this writer, this caveat may well be one of the most important yet usually ignored pitfalls in cement stratigraphy. The three examples shown in Fig. 13 (first presented in Machel and Burton 1991, but repeated here because of their importance) illustrate this point. Two growth forms of calcite, GF-1 and GF-2, with different D_{Mn} values, form simultaneously in a carbonate aquifer at three locations, A, B, and C. Differences in growth forms are due to subtle changes in fluid chemistry along the flow path (variations in SO_4^{2-} , temperature, Mg^{2+} , etc.). The conditions are such that GF-1 forms at A and C, and GF-2 forms at B. The $(aMn^{2+}/aCa^{2+})_i$ is identical at A and B but smaller at C. Cement zones at A and B have different CL due to different Mn contents. The differences in these cements result solely from their different growth forms and corresponding D_{Mn} values, even though the crystals formed simultaneously and from the same fluid (with respect to $(aMn^{2+}/aCa^{2+})_i$). Yet, according to conventional wisdom the zones at A and B would not be correlated as time-equivalent because the crystals have different growth forms and CL. This would be an incorrect interpretation. Furthermore, cement zones formed at B and C have the same Mn content and CL because their different growth forms and corresponding D_{Mn} values offset the effects of the change in fluid composition with respect to $(aMn^{2+}/aCa^{2+})_i$. According to conventional wisdom, correlation of zones with equal CL would indicate precipitation from the same fluid. However, this interpretation would be incorrect as well, as the fluid composition at B differs

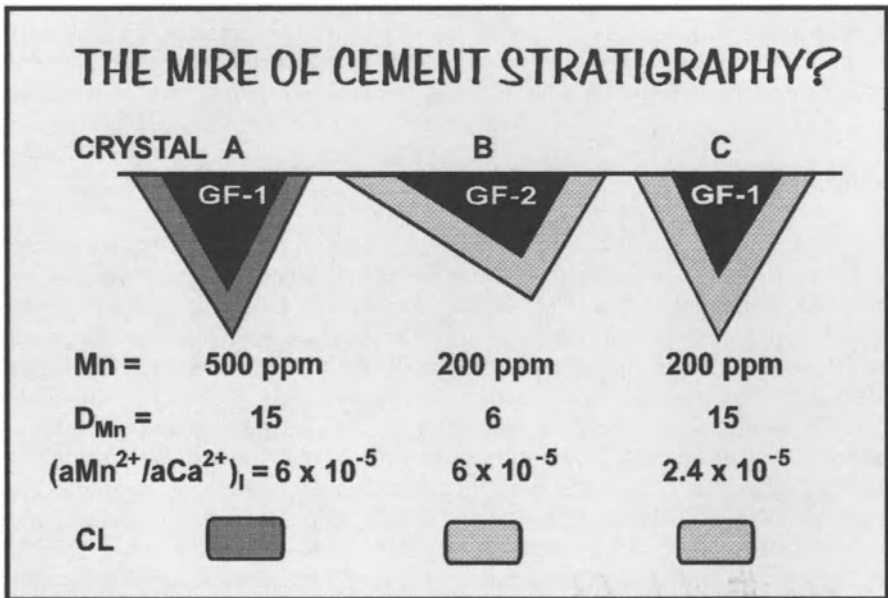


Fig. 13. Three concentrically zoned calcite cement crystals grown coevally at locations A, B, and C in an aquifer, showing the effect of growth forms on CL for two fluid compositions (after Machel and Burton 1991). GF-1 and GF-2 are two growth forms with different D_{Mn} values. The $(aMn^{2+}/aCa^{2+})_i$ is identical at A and B but smaller at C. See text for further explanation

from that at C. Thirdly, the concentric zones at A and C have different CL resulting from the change in fluid composition. Cements A and C normally would not be correlated as time-equivalent because they have different CL. This interpretation would also be incorrect because these crystals are coeval.

These examples illustrate that growth forms should be identified before correlations of cements or zones are attempted, and that spatial (and temporal) variations in fluid chemistry must be considered. Unfortunately, identification of growth forms commonly is difficult to impossible in thin section and usually is not done, unless the crystals face open spaces such as remaining primary voids, molds, and vugs. One has to wonder, therefore, how many of the published studies failed to correlate different growth forms from the same fluid as coeval or mistakenly correlated cements that are not coeval. Additional data, such as isotope ratios and fluid inclusion homogenization temperatures and freezing point depressions, should be used in connection with CL for unambiguous interpretations.

All crystals and zoning patterns that are formed by bulk solution disequilibrium partitioning and in restricted pore spaces, including oscillatory and sector(al) zoning, should be avoided for correlation and for back-calculation of fluid composition. These types of zones can seldom be correlated, and their composition clearly does not represent the bulk pore fluid(s). In rare cases, however, sector zones could be used for correlation, if crystallographically equivalent sectors are compared. A case in point is the study by Hendry and Marshall (1991) who found a regional consistency in the observed sector zone pattern in Jurassic sparry calcites (these crystals display an unusually complex combination of sector zonation and sector-specific lamellar or polygonal zonation). However, the trace element variations in these crystals bear no simple relationship with either the chemical evolution of the bulk pore fluid or the relative overall growth rates of the crystals.

3.6

Saturation States

It is common practice in cement stratigraphic interpretations to correlate calcite cements or cement zones over several tens to hundreds of kilometers (e.g., Meyers 1991; Bruckschen et al. 1992). Thereby, apparently correlatable cements have been interpreted as synchronous or diachronous precipitates, and zonal sequences such as non-bright-dull, or variations thereof, have been attributed routinely to decreases in Eh. Such interpretations assume, explicitly or implicitly, that the aquifers were supersaturated with respect to calcite over tens to hundreds of km of flow distance. Although these assumptions may be justified in some cases, they often are not. Rather, the geochemical data available from modern aquifers (see Sect. 2.5.1) indicate that one should expect carbonate cementation in carbonate aquifers to be localized in supersaturated areas or patches. Only in exceptional circumstances (presumably with very high permeability, correspondingly fast flow rates, and homogeneous rock composition without significant local anomalies) can carbonate cements be formed simultaneously over large distances. Even then the CL characteristics may not be identical in the simultaneously formed cements (Fig. 13).

3.7

Activity of Calcium and Salinity Gradients

Changes in $a\text{Ca}^{2+}$ ($=\gamma\text{Ca}^{2+}m\text{Ca}^{2+}$) in natural aquifers occur because of two processes: (1) variations in $m\text{Ca}^{2+}$ from precipitation and dissolution reactions, evaporation and dilution; or (2) changes in γCa^{2+} due to salinity variations. If $a\text{Me}^{2+}$ is constant, a downflow gradient in salinity, which is common in shallow aquifers (Fig. 10), is likely to cause a concomitant gradient in cement compositions via changes in γCa^{2+} . The magnitude of the latter can be calculated using SOLMINEQ and similar programs, and may be sufficient to generate changes in CL (Machel and Burton 1991).

These considerations indicate, once again, that it is very unlikely that carbonate cements or cement zones form with identical composition, and synchronously, over several tens to hundreds of kilometers in meteoric groundwater aquifers. For cements forming along a large salinity gradient to have the same composition, the $(m\text{Me}^{2+}/m\text{Ca}^{2+})_i$ ratio must precisely balance the gradient in $\gamma\text{Mn}^{2+}/\gamma\text{Ca}^{2+}$ and $\gamma\text{Fe}^{2+}/\gamma\text{Ca}^{2+}$ along the flow path. This is extremely unlikely where flow distances are large and many independent processes influence Mn^{2+} , Fe^{2+} and Ca^{2+} concentrations.

3.8

pH/Eh

Many studies of carbonate diagenesis have interpreted CL zonations to reflect changes in pH/Eh, especially in terms of identifying a change from more oxidizing to more reducing conditions (e.g., Meyers 1991, and references therein). The data discussed above and in Machel and Burton (1991) reveal, however, that the observed zonations may well have been caused by other processes, or that erratic CL patterns would have formed, had the paleoaquifer under investigation formed coeval carbonate cements.

The data from the Berkshire aquifer (Fig. 12) serve to prove this point. The total concentrations of Fe and Mn are such that calcites precipitating upflow from the redox boundary would be largely non-luminescent, and those precipitating downflow could range from non-luminescent to dull or bright luminescent (using reasonable distribution/partition coefficients and the CL fields shown in Fig. 3). Furthermore, it is important to recognize that non-luminescent cements (due to very low Mn and Fe concentrations) can precipitate even in the more reducing parts of a groundwater aquifers. Almost all conventional interpretations have placed such calcites near the recharge areas and/or in the oxidizing parts of the aquifers.

On the other hand, the CL and corresponding Mn^{2+} and Fe^{2+} contents of calcite and dolomite cements could be used to determine the Eh (and pH) conditions of the paleoaquifer. This is possible if the following criteria/parameters are known or can be met/estimated with reasonable accuracy: (a) no elements other than Mn^{2+} and Fe^{2+} are involved in the CL of the samples under consideration; (b) bulk solution equilibrium partitioning was established or closely approached during cement precipitation; (c) all phases (crystalline or amorphous) that determined the element concentrations and the redox-potential of the paleoaquifer are

known; (d) the paleoaquifer attained, or closely approached, electrochemical equilibrium between all redox-couples during precipitation; (e) the rate of change of Eh and/or the precipitation rate are known. With the present state of knowledge, most of these criteria/parameters cannot be constrained. Consequently, the orientations, positions, and sequence of CL boundaries cannot be defined unequivocally (Fig. 9B). The commonly observed CL sequence of non-bright-dull-non (Meyers 1991) might be formed with decreasing Eh, as shown in Fig. 9A. Similarly, Bruckschen et al. (1997) identified two recurrent CL patterns in various cement stratigraphic studies, i.e., pattern #1, consisting of four generations (generation 1: bright [yellow]-blotchy CL, with or without red-CL microdolomite inclusions; generation 2: homogeneous intrinsic CL terminated by a bright [yellow] CL zone; generation 3: a transition from moderate to dull orange CL; and generation 4: mainly intrinsic CL with a few bright yellow zones); and pattern # 2, similar to pattern # 1 but without the second generation [the zones addressed by Bruckschen et al. as “intrinsic CL” correspond to “non” above, as the weak intrinsic blue CL may or may not be visible]. Bruckschen et al. (1992 1997) interpreted both patterns to reflect decreasing Eh, with a return to oxidizing conditions during the formation of generation 4, and they contend that this pore water evolution reflects a complete basin evolutionary cycle from marine sedimentation via burial diagenesis to telogenetic meteoric diagenesis. Generation 2 is interpreted to reflect an early diagenetic influx of meteoric water. While this certainly is one possible interpretation for these patterns, it is not the only one.

3.9

The Problem of Scale

The previous discussion clearly showed that several of the factors that govern CL in carbonates are scale-dependent, i.e., saturation indices (sizes and locations of supersaturated parts of an aquifer), changes in the activity of calcium, changes in salinity (and concomitant changes in activity coefficients), changes in Eh (minor pH), and changes in growth forms (related changes in effective distribution coefficients). For example, significant parts of many aquifers are saturated or undersaturated with respect to carbonates, which prohibits carbonate cementation, and the redox-boundaries commonly inferred to cause concomitant increases in Mn^{2+} and Fe^{2+} concentrations typically are fairly close to the recharge areas, i.e., within about 15–36 km (Edmunds 1973; Edmunds et al. 1982, 1984, 1987). Consequently, it is highly unlikely that oxygenated groundwaters occur more than 100 km downflow from the recharge area in a confined aquifer.

Conversely, the geochemical patterns observed in modern groundwater aquifers may not change systematically downflow. The effects of bulk solution disequilibrium partitioning, exotic fluid sources, clay mineral and organic matter diagenesis, electrochemical disequilibrium, as well as reducing plumes caused by leaking hydrocarbon traps, are superimposed on the above “regional” trends, but cannot be generalized. The magnitudes of these trends, and their effects on CL in diagenetic carbonates, will vary among and within aquifers, depending on aquifer size, flow rate, rock composition, climate, rainfall, and, particularly in deeper settings, the degree of hydrologic isolation through aquitards.

These considerations lead to the general conclusion that cement stratigraphic correlations are more likely to be correct if the (paleo-)aquifer systems investigated are relatively small. This point is beautifully exemplified in Smackover oil and gas fields from Mississippi. Heydari and Moore (1993) showed that luminescence patterns of calcites are consistent within each field, but that calcites differ in the number of zones and CL intensity from field to field. Heydari and Moore (1993) noted that there is no compelling evidence that equivalent zones in separate fields precipitated simultaneously, and they correctly concluded (p. 44): "It is therefore unwise to correlate individual zones or groups of zones as time horizons from one field to another".

On the other hand, a number of the factors discussed in this paper are principally scale-independent. This includes the determination of the concentrations of activators, sensitizers, and quenchers, as well as bulk solution properties such as ionic composition, temperature, or flow direction, as determined from CL and/or from other methods used in conjunction (petrography, isotope geochemistry, fluid inclusion analysis, paleomagnetic data, etc.).

4

Conclusions

Many factors govern the CL color, intensity, and zonation of diagenetic carbonates. Most of these factors are reasonably well understood, but some have been recognized only relatively recently (e.g., the potential importance of microbially induced bulk solution disequilibrium). Studies of diagenetic carbonates using CL and corresponding trace element concentrations should consider as many as possible of these factors, many of which can have dramatic effects on trace element partitioning and CL. There are numerous pitfalls in correlation and back-calculation of fluid composition. In general, cement stratigraphic correlations are more likely to be correct if the (paleo-)aquifer system investigated is relatively small.

Acknowledgements. This paper is founded on the work of a multitude of colleagues who have shaped my understanding of CL through their publications, presentations, and in personal discussions. I gratefully acknowledge all these individuals, many of whom are cited in this paper. Special thanks go to E.A. Burton whose help was instrumental in furnishing an earlier synoptic paper on the same subject (Machel and Burton 1991). Editorial comments by P.A. Cavell and M. Pagel are much appreciated. Financial assistance was provided by the Natural Science and Engineering Research Council of Canada (NSERC) and by the Alexander von Humboldt Foundation.

References

- Amieux, P, Jeanbourquin, P (1989) Cathodoluminescence et origine diagénétique tardive des cargneules du massif des Aiguilles Rouges (Valais, Suisse). *Bulletin Société Géologique France*, v. 8, pp 123-132
- BackW, Hanshaw BB (1970) Comparison of chemical hydrogeology of the carbonate peninsulas of Florida and Yucatan. *Journal of Hydrology*, v. 10, pp 330-368

- Barker CE, Kopp OC (eds) (1991), Luminescence Microscopy and Spectroscopy - Qualitative and quantitative applications. SEPM (Society for Sedimentary Geology) Short Course, No. 25
- Barker CE, Higley DK, Dalziel MC (1991) Using cathodoluminescence to map regionally zoned carbonate cements occurring in diagenetic aureoles above oil reservoirs: initial results from the Velma oil fields Oklahoma. In: Barker CE, Kopp OC (eds) Luminescence Microscopy and Spectroscopy - Qualitative and quantitative applications. SEPM (Society for Sedimentary Geology) Short Course, No. 25, pp 155-160
- Barnaby RJ, Rimstidt DJ (1989) Redox conditions of calcite cementation interpreted from Mn and Fe contents of authigenic calcites. Geological Society of America Bulletin, v. 101, pp 795-804
- Bodine MW, Holland HD, Borczik M (1965), Coprecipitation of manganese and strontium with calcite. In: Problems of Postmagmatic Ore Deposition, Proceedings of Symposium, Prague, v. 2, pp 401-406
- Braithwaite CJR, Rizzi, G (1997) The geometry and petrogenesis of hydrothermal dolomites at Navan, Ireland. Sedimentology, v. 44, pp 421-440
- Bruckschen P, Neuser RD, Richter DK (1992) Cement stratigraphy in Triassic and Jurassic limestones of the Weserbergland (northwestern Germany). Sedimentary Geology, v. 81, pp 195-214
- Bruckschen P, Bruhn F, Höfert M, Richter DK, Veizer J (1993) Lumineszenz-Verhalten und Geochemie von Karbonaten und Quarzen in Sedimentgesteinen: erste Ergebnisse mit der Protonenmikrosonde (PIXE). Zentralblatt Geologie und Paläontologie Teil I (1992 (1/2)), pp 611-627
- Bruckschen P, Bruhn F, Richter DK (1997) Basic patterns in cement stratigraphy of Phanerozoic marine limestones: potential or pitfall? 18th IAS Regional European Meeting, Abstracts, GAEA heidelbergensis, pp 89-90
- Budd DA, Hammes U, Vacher HL (1993) Calcite cementation in the upper Floridan aquifer: a modern example for confined-aquifer cementation models? Geology, v. 21, pp 33-36
- Burton EA, Walter LM (1990), The role of pH in phosphate inhibition of calcite and aragonite precipitation rates in seawater. Geochimica et Cosmochimica Acta, v. 54, pp 797-808
- Burton EA, Machel HG, Qi J (1993) Thermodynamic constraints on anomalous magnetization in shallow and deep hydrocarbon seepage environments. In: Aïssaoui DM McNeill DF, Hurley, NF (eds), Applications of paleomagnetism to Sedimentary Geology. SEPM (Society for Sedimentary Geology) Special Publication, No. 49, pp 193-207
- Carpenter AB, Oglesby TW (1976) A model for the formation of luminescently zoned calcite cements and its implications. Geological Society of America Abstracts with Programs, v.8, pp 469-470
- Dromgoole E, Walter LM (1990) Iron and manganese incorporation into calcite: effects of growth kinetics, temperature, and solution chemistry. Chemical Geology, v. 81, pp 311-336
- Edmunds WM (1973) Trace element variations across an oxidation-reduction barrier in a limestone aquifer. In: Ingerson E (ed) Proceedings of Symposium on Hydrogeochemistry and Biogeochemistry, v. 1, pp 500-526
- Edmunds WM, Bath AH, Miles DL (1982) Hydrochemical evolution of the East Midlands Triassic sandstone aquifer. Geochimica et Cosmochimica Acta, v. 46, pp 2069-2081
- Edmunds WM, Miles DL, Cook JM (1984) Redox processes in aquifers. IAHS Publication No. 150, pp 3-70
- Edmunds WM, Cook JM, Darling WG, Kinniburgh DG, Miles DL, Bath AH, Morgan-Jones M, Andrews JN (1987), Baseline geochemical conditions in the Chalk aquifer, Berkshire, U.K.: a basis for groundwater management: Applied Geochemistry, v. 2, pp 251-274
- Emery D, Dickson JAD (1989) A syndepositional meteoric phreatic lens in the Middle Jurassic Lincolnshire Limestone, England, U.K.. Sedimentary Geology, v. 65, pp 273-284
- Foucke BW, Reeder RJ (1992) Surface structural controls on dolomite composition: evidence from sectoral zoning. Geochimica et Cosmochimica Acta, v. 56, pp 4015-4024
- Fraser DG (1990) Applications of the high-resolution scanning proton microprobe in the earth sciences: an overview. Chemical Geology, v. 83, pp 27-37

- Gies H (1976) Zur Beziehung zwischen Photolumineszenz und Chemismus natürlicher Karbonate. *Neues Jahrbuch für Mineralogie Abhandlungen*, v. 127, pp 1–46
- Goetze J.W. (1999) Cathodoluminescence microscopy and spectroscopy in applied mineralogy. Habilitationsschrift TU Bergakademie Freiberg (unpub.), 128 pp.
- Goff K.J. (1971) Hydrology and chemistry of the Shoal Lakes Basin, Interlake Area, Manitoba. M.S. thesis, Univ. Manitoba
- Gregg J.M, Hagni R.D. (1986) Irregular cathodoluminescent banding in late dolomite cements: evidence for complex faceting and metalliferous brines. *Geological Society of America Bulletin*, v. 98, p
- Habermann D (1997) Quantitative hochauflösende Kathodenlumineszenz-Spektroskopie von Calcit und Dolomit. Unveröff. Dissertation Ruhr-Universität Bochum, 152 pp
- Habermann D, Neuser RD, Richter DK (1996a) REE-activated cathodoluminescence of calcite and dolomite: high-resolution spectrometric analysis of CL-emission (HRS-CL). *Sedimentary Geology*, v. 101, pp 1–7
- Habermann D, Neuser RD, Richter DK (1996b) Hochauflösende Spektralanalyse der Kathodenlumineszenz (KL) von Dolomit und Calcit: Beispiele der Mn- und SEE-aktivierten KL in Karbonatsedimenten. *Zentralblatt Geologie und Paläontologie Teil I* (1995 (1/2)), pp 145–157
- Handford CR, Kendall AC, Prezbindowski DR, Dunham JB, Logan BW (1984) Salina-margin tepees, pisoliths and aragonite cements, Lake MacLeod, Western Australia: their significance in interpreting ancient analogs. *Geology*, v. 12, pp 523–527
- Hanshaw BB, Back W, Deike RG (1971) A geochemical hypothesis for dolomitization by ground water. *Economic Geology*, v. 66, pp 710–724
- Hemming NG, Meyers WJ, Grams JC (1989) Cathodoluminescence in diagenetic calcites: the roles of Fe and Mn as deduced from electron microprobe and spectroscopic measurements. *Journal of Sedimentary Petrology*, v. 59, pp 404–411
- Hendry JP, Marshall JD (1991) Disequilibrium trace element partitioning in Jurassic sparry calcite cements: implications for crystal growth mechanisms during diagenesis. *Journal of the Geological Society London*, v. 148, pp 835–848
- Herman JS, Lorah MM (1988) Calcite precipitation rates in the field: Measurement and prediction for a travertine-depositing stream. *Geochimica et Cosmochimica Acta*, v. 52, pp 2347–2355
- Heydari E, Moore CH (1993) Zonation and geochemical patterns of burial calcite cements: Upper Smackover Formation, Clarke County, Mississippi. *Journal of Sedimentary Petrology*, v. 63, pp 44–60
- Horbury AD, Adams AE (1989) Meteoric-phreatic diagenesis in cyclic late Dinurian carbonates, northwest England. *Sedimentary Geology*, v. 65, pp 319–344
- Jacobson, RL, Langmuir D (1970) The chemical history of some spring waters in carbonate rocks. *Ground Water*, v. 8, pp 5–9
- Kharaka YK, Gunter WD, Aggarwal PK, Perkins EH, Debraal JD (1988) SOLMINEQ.88. A computer program for geochemical modeling of water-rock interactions: U.S.G.S. Water Resources Investigations Report, v. 88–4227
- Khawlie MR, Carozzi AV (1976) Microfacies and geochemistry of the Brereton Limestone (Middle Pennsylvanian) of southwestern Illinois, U.S.A.. *Archives des Sciences, Geneve*, v. 29, pp 670–710
- Kremling K (1983) Trace metal fronts in European shelf waters: *Nature*, v. 303, pp 225–227
- Kubanek F, Parekh PP (1976) A study of trace element distribution in an interlaminated limestone-dolostone. *Geologisches Jahrbuch*, D-20, pp 23–39
- Langmuir D, Whittemore DO (1971), Variation in the stability of precipitated ferric oxyhydroxides. in HEM, J.D, ed, *Proceedings Symposium on Nonequilibrium systems in natural water chemistry: Advances in Chemistry Series #106*, American Chemical Society, Washington D.C, pp 209–234
- Lee MR, Harwood GM (1989) Dolomite calcitization and cement zonation related to uplift of the Raisby Formation (Zechstein Carbonate), northeast England. *Sedimentary Geology*, v. 65, pp 285–305

- Leventhal JS, Hostermann JW (1982) Chemical and mineralogical analysis of Devonian black shale samples from Martin County, Kentucky; Carroll and Washington Counties, Ohio; Wise County, Virginia; and Overton County, Tennessee, U.S.A.. *Chemical Geology*, v. 37, pp 239–264
- Lohmann KC, Walker JCG (1989) The $\delta^{18}\text{O}$ record of Phanerozoic abiotic marine calcite cements. *Geophysical Research Letters*, v. 16, pp 319–322
- Machel H.G. (1985) Cathodoluminescence in calcite and dolomite and its chemical interpretation. *Geoscience Canada*, v. 12, pp 139–147
- Machel HG (1990) Bulk solution disequilibrium in aqueous fluids as exemplified by diagenetic carbonates. In: Meshri, I.D. and Ortoleva, P.J. (eds.): Prediction of reservoir quality through chemical modeling. *American Association Petroleum Geologists Memoir*, No. 49, pp 71–83
- Machel HG (1995) Magnetic mineral assemblages and magnetic contrasts in diagenetic environments – with implications for studies of paleomagnetism, hydrocarbon migration and exploration. In: Turner, P. and Turner, A. (eds), *Paleomagnetic applications in hydrocarbon exploration and production*. Geological Society Spec. Pub, No. 98, pp 9–29
- Machel HG, Burton EA (1991) Factors governing cathodoluminescence in calcite and dolomite, and their implications for studies of carbonate diagenesis. In: Barker, C.E. and Kopp, O.C. (eds) *Luminescence Microscopy and Spectroscopy – Qualitative and quantitative applications*. SEPM (Society for Sedimentary Geology) Short Course, No. 25, pp 37–57
- Machel HG, Mason RA, Mariano AN, Mucci A (1991) Causes and emission of luminescence in calcite and dolomite. In: Barker, C.E. and Kopp, O.C. (eds) *Luminescence Microscopy and Spectroscopy – Qualitative and quantitative applications*. SEPM (Society for Sedimentary Geology) Short Course, No. 25, pp 9–25
- Marfunin AS (1979) *Spectroscopy, Luminescence and Radiation Centers in Minerals: Translated from the Russian by V.V. Schiffer*, Springer-Verlag, Berlin. 352 pp
- Mason RA (1994) Effects of heating and prolonged electron bombardment on cathodoluminescence emission in synthetic calcite. *Chemical Geology*, v. 111, pp 245–260
- Mason RA (1997) The influence of heating on cathodoluminescence emission from natural calcite. *Canadian Mineralogist*, v. 35, pp 723–733
- Mason RA (1998) The response of luminescence in synthetic calcite to laboratory heating. *Canadian Mineralogist*, v. 36, pp 1089–1104
- Mason RA, Mariano AN (1990) Cathodoluminescence activation in manganese -bearing and rare-earth bearing synthetic calcites. *Chemical Geology*, v. 88, pp 191–206
- Mcintyre WL (1963) Trace element partition coefficients—a review of theory and application to geology. *Geochimica et Cosmochimica Acta*, v. 27, pp 1209–1264
- Meyers WJ (1974) Carbonate cement stratigraphy of the Lake Valley Formation (Mississippian), Sacramento Mountains, New Mexico. *Journal of Sedimentary Petrology*, v. 44, pp 837–861
- Meyers WJ (1991) Calcite cement stratigraphy: an overview. In: Barker, C.E. and Kopp, O.C. (eds) *Luminescence Microscopy and Spectroscopy – Qualitative and quantitative applications*. SEPM (Society for Sedimentary Geology) Short Course, No. 25, pp 133–148
- Morse JW, Bender ML (1990) Partition coefficients in calcite: Examination of factors influencing the validity of experimental results and their application to natural waters. *Chemical Geology*, v. 82, pp 265–277
- Mortimer RJG, Coleman ML, Rae JE (1997) Effect of bacteria on the elemental composition of early diagenetic siderite: implications for paleoenvironmental interpretations. *Sedimentology*, v. 44, pp 759–765
- Mucci A, Canuel R, Zhong S (1989) The solubility of calcite and aragonite in sulfate-free seawater and the seeded growth kinetics and composition of the precipitates at 25° C. *Chemical Geology*, v. 74, pp 309–320
- Nelson CS, Harris GJ, Young HR (1989) Burial-dominated cementation in non-tropical carbonates of the Oligocene TeKuti Group, New Zealand. *Sedimentary Geology*, v. 60, pp 233–250
- Neuser RD, Bruhn F, Götze J, Habermann D, Richter DK (1996) *Kathodenlumineszenz: Methodik und Anwendung*. *Zentralblatt Geologie und Paläontologie Teil I* (1995 (1/2), pp 287–306.

- Oglesby TW (1976) A model for the distribution of manganese, iron, and magnesium in authigenic calcite and dolomite cements in the Upper Smackover Formation in eastern Mississippi. M.S. thesis, Columbia, Missouri, University of Missouri, 122 p
- Ortoleva PJ (1994) Geochemical self-organization. Oxford Monographs on Geology and Geophysics, No. 23, Oxford University Press, New York, 244 pp
- Parekh PP, Möller P, Dulski P, Bausch WM (1977) Distribution of trace elements between carbonate and non-carbonate phases in limestone. *Earth and Planetary Science Letters*, v. 34, pp 39–50
- Pedone V, Dickson JAD, Meyes WJ (1994) Intracrystalline alteration of low-magnesian calcite cement in the Devonian Pillara Formation, Canning Basin, Western Australia. *Journal of Sedimentary Research*, v. A64, No. 2, pp 160–173
- Popp BN, Anderson TE, Sandberg PA (1986) Brachiopods as indicators of original isotopic compositions in some Paleozoic limestones. *Geological Society of America Bulletin*, v. 97, pp 1262–1269
- Reeder RJ (1991) An overview of zoning in carbonate minerals. In: Barker, C.E. and Kopp, O.C. (eds) *Luminescence Microscopy and Spectroscopy – Qualitative and quantitative applications*. SEPM (Society for Sedimentary Geology) Short Course, No. 25, pp 77–82
- Reeder RJ, Paquette J (1989) Sector zoning in natural and synthetic calcites. *Sedimentary Geology*, v. 65, pp 239–247
- Render FW (1970) Geohydrology of the metropolitan Winnipeg area as related to groundwater supply and construction. *Canadian Technology Journal*, v. 7, pp 243–274
- Richter DK, Habermann D, Neuser RD, Oelze R (1995) Kathodenlumineszenz-Untersuchungen an Höhlensintern des nördlichen Sauerlandes. *Speläontlogisches Jahrbuch – Verein für Höhlenkunde in Westfalen*, v. 33, pp 33–37
- Scherer M, Seitz H (1980) Rare earth element distribution in Holocene and Pleistocene corals and their redistribution during diagenesis. *Chemical Geology*, v. 28, pp 297–289
- Schieber J (1988) Redistribution of rare-earth elements during diagenesis of carbonate rocks from the mid-Proterozoic Newland Formation, Montana, U.S.A.. *Chemical Geology*, v. 69, pp 111–126
- Shopov YY, Ford DC, Schwarcz HP (1994) Luminescent microbanding in speleothems: high-resolution chronology and paleoclimate. *Geology*, v. 22, pp 407–410
- Tobin KJ, Walker KR (1996) Ordovician low- to intermediate-Mg calcite marine cements from Sweden: marine alteration and implications for oxygen isotope in Ordovician seawater. *Sedimentology*, v. 43, pp 719–735
- Tobin KJ, Walker KR, Steinhauß DM, Mora CI (1996) Fibrous calcite from the Ordovician of Tennessee: preservation of marine oxygen isotopic composition and its implications. *Sedimentology*, v. 43, pp 235–251
- Veizer J (1983) Chemical diagenesis of carbonates: Theory and application of trace element technique. In: Arthur MA et al. (eds) *Stable isotopes in sedimentary geology: SEPM Short Course #10*, pp 3–1–3–100
- Viau CA, Oldershaw AE (1984) Structural controls on sedimentation and dolomite cementation in the Swan Hills Formation, Swan Hill Field, Central Alberta. In: Eliuk, L, ed, *Carbonates in subsurface and outcrop C.S.P.G. Core Conference, Calgary, Alberta*, pp 103–131

Cathodoluminescence of Carbonate Shells: Biochemical vs Diagenetic Process

VINCENT BARBIN

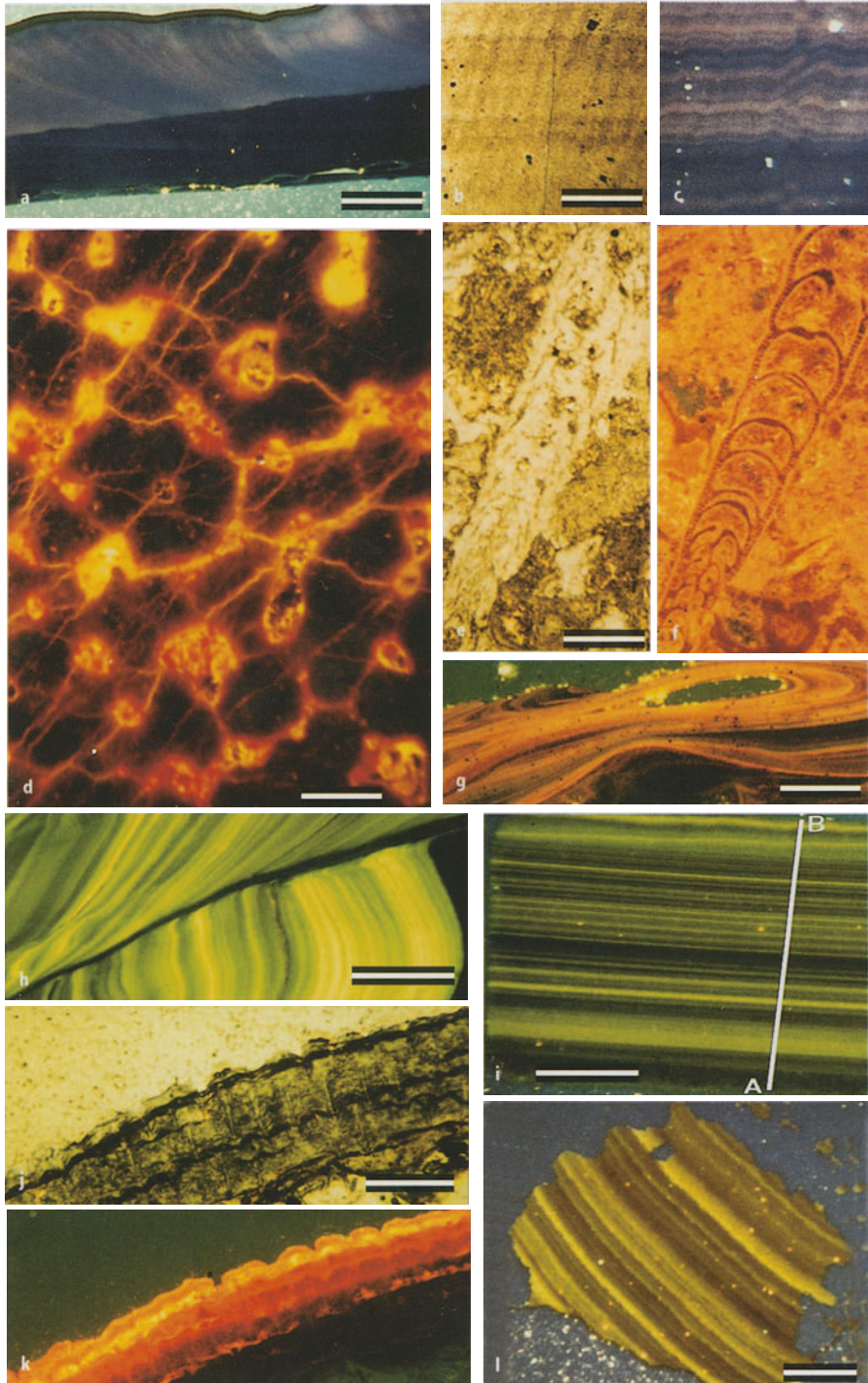
1

Introduction

Cathodoluminescence (CL), or the emission of photons in the visible range of the electromagnetic spectrum under cathodic excitation, is of increasing interest to geologists and is now routinely used in mineralogy, petrology and sedimentology (see reviews in Marshall 1988; Rémond et al. 1992; Neuser et al. 1996; Barbin and Schvoerer 1997). Presently, better knowledge of the physical causes of CL and the use of CL spectroscopy has widened the application of CL in the geosciences. This new generation of CL instruments in combination with micro-scale, trace-chemical analytical techniques has a great potential for improving CL interpretations.

Paleontological and paleoenvironmental applications of CL microscopy are less well developed. More than 60 minerals have been identified in different organisms, with the most common being phosphate and carbonate salts of calcium (Mann 1988; Lowenstam and Weiner 1989). It is well known that CL often reveals outlines and internal structures of fossils that are invisible in plane or polarized light microscopy (Fig. 1e,f). CL may also reveal textures more clearly, which aids the identification of poorly preserved fossils (Smith and Stenstrom 1965; Long and Agrell 1965, Martin and Zeegers 1969; Miller and Clarkson 1980; Richter and Zinkernagel 1980; Faupl and Beran 1983; Smith et al. 1984; Martini et al. 1987; Amieux 1987; Miller 1988; Barbin et al. 1989; Grant et al. 1991; Baumgartner-Mora and Baumgartner 1994; Kershaw 1994; Debenay et al. 1996a; Nöth et al. 1997).

This chapter deals with CL of biogenic carbonates. Since a decade ago, numerous, Recent, biogenic carbonates of different genera and environmental origins have been studied. Two aims were pursued: (1) to search for ontogenetic and paleoenvironmental records in skeletal organisms using CL emission, and (2) to investigate how CL patterns differ between biochemical and diagenetic CL emission.



2 Physical Fundamentals of Cathodoluminescence in Carbonates

2.1 Luminescence Centers

The luminescence in carbonate shells is caused by the same physical phenomena as those in abiogenically crystallized carbonate minerals. Luminescence centers are generally point defects in crystals such as free electrons, vacancies, and impurities. During energy dissipation of accelerated electrons within the crystal, these electrons may meet free electrons which can excite impurity centers and/or may be captured by gaps in the crystal structure. Among impurities, the ions of the transition group metals whose 3d electron configuration is partly filled (e.g. Mn^{2+} , Fe^{3+}) are very sensitive to external energy contributions. The emission of these centers depends strongly on the coordination polyhedra of the ions in the crystal and their nature.

In contrast, electron transitions of partly filled or unfilled inner shells (e.g. REE^{3+}) are not appreciably influenced by the atomic environment (e.g. Marshall 1988) and thus their emission is very similar in different crystals. Other, non-impurity related emissions may also contribute to the CL of natural crystals. These emissions are called intrinsic because they are caused by structural defects of the crystal lattice (e.g. Walker et al. 1989; Barbin and Schwoerer 1997 and references therein).

The most commonly observed CL emissions in biogenic carbonates are caused by substitution of Mn^{2+} and structural defects.

2.2 The Luminescence of Calcite and Aragonite

Calcite and aragonite, two polymorphs of $CaCO_3$, have only one possible substitution site for Mn^{2+} , the Ca^{2+} site. Substitution within the lattice in biogenic car-



Fig. 1a–l. a CL photomicrograph of *Bathymodiolus thermophilus* from a hydrothermal vent (84 PI), scale bar is 500 μm ; b plane-polarized light photomicrograph of a tangential section of *Bathymodiolus thermophilus*, from a hydrothermal vent, scale bar is 500 μm ; c same field of view as b but under CL; d CL photomicrograph of a Cretaceous dinosaur egg shell, Rocques-Hautes, Le Tholonet (France), tangential section, scale bar is 500 μm ; e plane-polarized light photomicrograph of a Middle Eocene foraminifera (Buliminidae), Avesa (Italy), scale bar is 100 μm ; f same field of view as e but under CL; g CL photomicrograph of balanidae, Ensenada Bay (Beagle Channel, Argentina), scale bar is 500 μm ; h CL photomicrograph of *Margaritifera margaritifera*, River Sörkedalselva (Sweden), scale bar is 500 μm ; i CL photomicrograph of *Nautilus pompilius* Cebu (Philippines), scale bar is 500 μm . Section A-B is the μ PIXE transect shown in Fig. 5. Note the close correlation between μ PIXE Mn distribution and yellow-green luminescence banding; j plane-polarized light photomicrograph of *Crania* sp., Josephine sea mount (Spain); k same field of view as j but under CL, scale bar is 250 μm ; l CL photomicrograph of Carboniferous *Comatoceras* sp., Boggy Formation (Oklahoma, USA). Note the similarity of the CL pattern with Recent *N. pompilius* shown in i, scale bar is 500 μm

bonates is well documented by electron paramagnetic studies (e.g. Wildman 1970; Blanchard and Chasteen 1976a,b; White et al. 1977). The difference in the observed CL color, orange in calcite vs green in aragonite, is due to changes of crystal field parameters (e.g. Henderson and Imbusch 1989; Yang et al. 1995). The free Mn^{2+} energy levels are modified and the emission occurs as a result of the transition from the ${}^4T_{1g}$ excited state to the ${}^6A_{1g}$ ground state. Calcite has a rhombohedral structure while aragonite is orthorhombic.

3 Biom mineralization of Shells

A brief summary on the biomineralization processes helps to better understand the CL observations of carbonaceous skeletons and their causes. Biominerals are formed either extracellularly or intracellularly. Two main processes of biomineralization are known: biologically induced, which is considered as the primitive stage of biomineralization, and biologically controlled (i.e. matrix mediated process), which is under genetic control (e.g. Lowenstam 1981; Dubois and Chen 1989). In the latter, a morphologically complex structure nucleates and grows (e.g. calcite or aragonite skeleton) together with a genetically controlled macromolecular matrix of protein, polysaccharides and lipids. For example, matrix macromolecules involved in regulating the biological growth of calcite are known to share a carboxylic-rich character that arises from the abundant amino-acids aspartate and glutamate. Aspartate causes preferential development of the $\{0001\}$ and possibly the $\{\bar{1}100\}$ crystal plane of calcite (Teng and Dove 1997). The mantle of a mollusk is directly responsible for the growth of the crystals and the secretion of the organic matrix of the shell. According to Wilbur and Saleuddin (1983), shell formation comprises four components: the external medium (e.g. seawater), the hemolymph and body tissues, the extrapallial fluid, and the shell. The extrapallial fluid lies between the mantle and the inner shell surface, the environment of shell deposition. The complex assemblage of macromolecular constituents at the mineralizing site may differ between different species and between different layers in the same shell (Mann 1998). Nevertheless, the organic shell matrix of mollusks is considered to be highly organized prior to the nucleation of the first crystals, which explains the mechanical and crystallochemical properties observed in shells (Mann 1988). The bicarbonate of the shell is derived from two sources: the external medium and metabolic CO_2 . Conversion of metabolic CO_2 to HCO_3^- is a reversible reaction catalyzed by carbonic anhydrase. Calcium ions then combine with HCO_3^- releasing a proton to form $CaCO_3$. These carbonate crystals are formed within the extrapallial fluid which is supersaturated with respect to $CaCO_3$. Opening and closing of mollusk valves correlate with significant variations in the O_2 , pH, calcium and succinic acid concentrations of the extrapallial fluid (Lowenstam and Weiner 1989). Carbonate saturation is attained either by a sufficient increase of the HCO_3^- concentration through transport by the outer mantle epithelium and/or by a sufficient decrease in the chelation of Ca^{2+} (Wilbur and Saleuddin 1983). The different shell layers are produced by individual palleal surfaces (ectostracum, mesostracum and endostracum). During the life of the shell, each epithelial cell changes and succes-

sively contributes to form different shell layers. Calcite forms the foliated structure and frequently the prismatic layers, while aragonite forms the myostracum, pseudoprismatic or cross lamellar and nacreous layers. Several other structures exist and mixed mineralogy is possible (e.g. Carter 1980).

Echinoderms secrete a mesodermal skeleton composed of high magnesium calcite plates which are composed of aligned crystallites to form polycrystalline aggregates. These aggregates act optically as single calcite crystals (Dubois and Chen 1989; Smith 1990).

The growth of calcite shells of articulate brachiopod is mainly controlled at the mantle margin of the valves (Williams 1968a,b). As in mollusk shells, at different periods of its life each cell of the outer epithelium secretes successively different layers (Fig. 2 in Barbin and Gaspard 1995).

Barnacle shell growth is of two types: (1) concrescent shells or (2) nonconrescent shells. Growth proceeds by secretion of calcite by the mantle epithelium (Bourget 1980). Internal growth bands have been observed. According to Bourget (1980), these bands are either formed during immersion or as doublets in continuously immersed animals. These bands are possibly of an endogenous rhythm kept in phase and reinforced by the semidiurnal tidal cycle. In addition, stress bands may also be caused by high temperature.

Processes of foraminifera test calcification are not yet totally understood. The mechanism seems to be different for porcelaneous vs hyaline tests. The porcelaneous foraminifera have a large stock of inorganic carbon in vesicles which may be used for calcification, while in hyaline foraminifera calcification takes place outside the cytoplasm in an organic membrane (for more details see Debenay et al. 1996a and references therein). Nevertheless, calcitic globular crystallites are recorded from all foraminiferal tests. These crystallites can be grouped into different shapes ranging from rows or needles to rhombohedral crystals (Debenay et al. 1996b). Formation of foraminiferal tests is probably the result of two processes: a physicochemical process under energetic control and a biological one under strict biological control (Debenay et al. 1996b).

Calcification processes in algae were mainly studied in Rhodophyta and especially in coralline algae. Two phases of mineralization are generally apparent: (1) acicular crystals probably of calcite form in the middle lamellae and outer cell walls, (2) more intense calcification occurs within the inner cell walls and perpendicular to the wall surface (e.g. Pentecost 1991). Calcification involves high magnesium calcite. The second radial layer has a higher magnesium content than the first, magnesium-poor layer (e.g. Flajs 1977a,b; Bosence 1991).

In avian eggshells, the calcite nucleation sites are spherulitic protein masses organized on the fibrous disulfide-linked proteins of the inner shell membranes. Oriented calcite nucleation occurs at these sites (Mann 1988).

4

Material and Methods

Cathodoluminescence emission was detected with a high sensitivity (hot cathode) CL microscope (Ramseyer et al. 1989) at 30 keV accelerating voltage and

0.4 $\mu\text{A}/\text{mm}^2$ beam current density. Luminescence images were recorded on Ektachrome 400 color slide film (developed at 800 ASA) with exposure time ranging from 4 to 180 s. Observations were made on non-etched, uncovered thin sections coated with an aluminium film. The CL emission was recorded using a PTI model 01-001 monochromator with a Hamamatsu R928 photomultiplier. Generally, the monochromator was set for 10 nm resolution and was linked to the CL microscope via a flexible quartz optic fiber bundle through a fused silica window. Multiple scans (mean of ten measurements at each wavelength position) were used in order to eliminate noise. The spectra were corrected between 270 and 740 nm for the spectral response of the instrument by means of a calibrated tungsten lamp. Intensity is expressed in arbitrary units of photon counts.

Particle induced X-ray emission (micro-PIXE) analyses were used to determine trace element concentrations in biogenic carbonates using the GEO-PIXE program (Ryan et al. 1990). PIXE allows nearly non-destructive trace element analysis with high accuracy and precision. The detection limit (LOD) is 10–100 ppm, depending on the analyzed element, and the spatial resolution 5 μm . The same thin-section was used for PIXE analysis and CL microscopy. This method provides in situ trace chemical analysis and is ideal for the quantitative evaluation of the trace element-induced CL emission (e.g. Habermann et al. 1997; Yang et al. 1995).

5 Sampling

Numerous carbonaceous skeletal organisms were studied. Recent shells were chosen to study ecological effects such as shallow marine conditions, deep sea environments with stable or unstable conditions, nektonic living habitat or fresh water conditions (Table 1).

All Recent shells were taken from living or freshly-killed organisms. Fossils were taken from environments such as asphalts or clays, where diagenetic alterations are slow.

6 Cathodoluminescence Detection Limit

The main trace element activator of CL in carbonate exoskeletal organisms is Mn^{2+} . In crystals, a concentration of 10 ppm allows a direct visual observation of the CL, while lower concentrations (<5 ppm) are still detectable with spectroscopic methods (e.g. Habermann et al. 1996, this Vol.; Machel, this Vol.; Marshall 1988; and personal observations). For concentrations above 400 ppm there is no longer a linear relationship between Mn^{2+} concentration and CL intensity (El Ali et al. 1993).

In biogenic calcite, Richter and Zinkernagel (1981) suggest that a Mn^{2+} concentration of up to 20–40 ppm is necessary for visible CL emission in calcite and less in aragonite. Other observations show that a concentration <15 ppm is suffi-

Table 1. Mineralogy, habitat, color and CL intensity of skeletal organisms

Organism	Mineralogy	Habitat	Main CL colour	CL intensity
Recent skeletal				
Foraminifera				
<i>Ammonia</i> spp.	Low Mg calcite?	Marine shelf	Orange or non-luminescent	Dull to medium
Planktonic foraminifera	Calcite	Open marine	Non-luminescent	-
Miliolidae	High Mg calcite	Marine shelf	Orange or non-luminescent	Dull to bright
Mollusk bivalvia				
<i>Pecten maximus</i> outer, inner layers myostracum	Calcite, aragonite	Marine shelf	Orange or non-luminescent	Dull to medium
<i>Ostrea edulis</i> prismatic and foliated layers chalky structure, myostracum	Calcite, aragonite	Saline pond	Orange, Non-luminescent with greenish bands	Medium to bright Medium to bright Medium to bright Non to medium
<i>Crasostrea gigas</i> , prismatic and foliated layers chalky structure ligament	Calcite	Marine farm	Orange	Medium to dull
<i>Mytilus edulis</i> outer layer inner layer	aragonite		green to yellow	Medium to dull
<i>Cardium edule</i> Solen sp.	Calcite aragonite	Saline pond	Orange or non-luminescent	Dull to bright
<i>Bathymodiolus thermophilus</i>	Aragonite	Marine endobenthic	Greenish bands	Medium to dull
<i>Margaritifera</i> sp.	Calcite aragonite	Hydrothermal vent	Greenish bands Orange or non-luminescent	Medium to dull Medium to dull
<i>Hyriopsis</i> sp.	Aragonite	River	Green to yellow	Medium to bright
<i>Anodonta</i> sp.	Aragonite	Lake	Green to yellow	Bright
Anadara senilis initial shell regenerated	Aragonite calcite	Freshwater pond Lagoon	Green to yellow Blue-green orange	Bright Bright Dull medium to bright

Table 1. Continued.

Organism	Mineralogy	Habitat	Main CL colour	CL intensity
Mollusc gastropoda				
<i>Patella</i> sp.	Aragonite + calcite	Shallow marine	Orange and blue-green	Dull to bright
<i>Lymnaea dyaphana</i>	Aragonite + regenerative calcite	freshwater	Green	Medium
<i>Helix</i> sp.	Aragonite	Terrestrial	Green-yellow	Medium to bright
Mollusc archaeogastropoda				
<i>Haliotis</i> sp.	Aragonite calcite	Marine shelf	Blue-green green orange	Dull to medium, medium to bright
Mollusc cephalopoda				
<i>Nautilus pompilius</i>	Aragonite	Open sea	Yellow-green	Medium to bright
<i>Nautilus macromphalus</i>	Aragonite	Open sea	Blue-green	Dull
Brachiopoda articulate				
<i>Aerothyris kerguelensis</i>	Calcite	Marine	Non-luminescent to Blue	Dull
<i>Waltonia inconspicua</i>	Calcite	Marine	Blue with orange luminescing bands	Medium to dull
<i>Macandrevia africana</i>	Calcite	Marine	Blue with orange luminescing bands	Medium to dull
<i>Notosaria nigricans</i>	Calcite	Marine	Blue with orange luminescing bands	Medium to dull
<i>Campages furcifera</i>	Calcite	Marine	Blue with orange luminescing bands	Medium to dull
<i>Terebratulina retusa</i>	Calcite	Marine	Blue with orange luminescing bands	Medium to dull
<i>Gryphus vitreus</i>	Calcite	Marine	Non-luminescent to blue	Dull
Brachiopoda inarticulate				
<i>Crania</i> sp.	Calcite	Marine	Orange to blue	Dull to bright
Echinoderms				
Echinoïds	Mg-calcite	Marine	Non-luminescent to blue	Very dull
Crinoïds	Mg-calcite	Marine	Non-luminescent to blue	Very dull

Table 1. Continued.

Organism	Mineralogy	Habitat	Main CL colour	CL intensity
Crustaceans				
Barnacle sp.	Calcite	Marine	Orange	Medium to bright
Corals				
<i>Porites</i> sp.	Aragonite	Marine	Blue to green	Dull
Algae				
Rhodophytes	Mg calcite	Lagoon	Orange	Dull to bright
Avian eggshells				
<i>Dromaius</i> sp.	Low Mg-calcite	Terrestrial	Dark blue	Dull
<i>Rhea</i> sp.	Low Mg-calcite	Terrestrial	Dark blue	Dull
<i>Struthio</i> sp.	Low Mg-calcite	Terrestrial	Dark blue	Dull
Fossil skeletal				
Mollusk cephalopods				
<i>Belemnitella</i> sp.	Calcite	Marine	Blue to orange	Dull to medium (orange lines)
<i>Euciphoceras</i> regale	Aragonite	Open sea, eocene	Yellow-green	Medium to bright
<i>Michelinoceras</i> sp.	Aragonite	Nearshore-deoxygenated habitat carboniferous	Yellow-green	Medium to bright
<i>Comatoceras</i> sp.	Aragonite	Open sea carboniferous	Non-luminescing to blue	Dull
Dinosaur eggshells				
Dinosaur eggshell	Calcite	Terrestrial	Blue with orange growth lines	Dull

Non-luminescent: no CL emission has yet been observed.

cient for visible CL emission and even less for spectroscopic detection (Yang et al. 1995; Barbin 1998). The amount of Mn^{2+} in biogenic carbonates is generally below 100 ppm and frequently less than 50 ppm (Milliman 1974; Morrison and Brand 1986). The previous assumption that biogenic carbonates are not luminescent is the result of technical problems: the first generation of CL microscopes were not able to detect low luminescence intensities, i.e. low Mn^{2+} concentrations. Similarly, the relative high detection limit of electron microprobes (≈ 150 ppm, 3σ -error) prevented studies of the relationship between Mn concentration and environmental conditions (e.g. Izuka 1988).

While El Ali et al. (1993) suggest that the quenching effect of Fe^{2+} is detectable only for concentrations >1000 ppm, Machel (1983, this Vol.) found effects for concentrations as low as 30–60 ppm. Apparently, the Fe^{2+}/Mn^{2+} ratio and not solely the Fe^{2+} concentration is more important, but this point is still under debate (Machel, this Vol.). The amount of Fe in biogenic carbonates is generally below 100 ppm (Milliman, 1974).

7

Cathodoluminescence of Biogenic Carbonates

7.1

Previous Work

7.1.1

Cathodoluminescence Observations on Recent Organisms

Few authors have studied CL emission of Recent skeletal organisms. Glover (1977) showed that with some exceptions, such as barnacles, oysters, sand dollars and some corals, the Mn level in calcareous marine organisms is considerably below 100 ppm and thus the exoskeletons show no or very weak CL emission. Sommer (1972) showed that regenerative calcite and vaterite in aragonitic bivalve shells (*Amblema* sp.) are locations with important fluctuations in the Mn concentration. Sommer (1972) also observed green luminescing aragonite in the marine gastropod *Achitectonica*. Richter and Zinkernagel (1980, 1981) performed the most important work on CL in Recent skeletal organisms. They described bright yellow-green luminescence in the marine aragonitic gastropod *Bittium* and a zoned orange luminescence in Recent echinoid tests. They mentioned that individual CL zones clearly did not represent annual growth stages but only a sequence of zones represent more likely annual growth stages. The authors also state that ecological parameters such as the life habitat, e.g. sediment surface vs in the sediment, has an important influence on luminescence (Richter and Zinkernagel 1980). They also observed the phenomenon that echinoid tests, which do not show luminescence during initial excitation, become blue-luminescing after prolonged electron bombardment. Friedman (1993) indicated that the bulk of skeletal particles in many reefs are composed of non-luminescent aragonite.

7.1.2

Cathodoluminescence Observations on Fossil Tests

Numerous authors described luminescence in fossil shells but generally attributed luminescence to be due to diagenetic alteration. Most authors still consider primary biogenic carbonates to be non-luminescent (e.g. Czerniakowski et al. 1984; Popp et al. 1986; Saelen 1989; Middleton et al. 1991). Baumgartner-Mora and Baumgartner (1994) discussed some aspects of the diagenesis of foraminiferal tests, and observed that most foraminiferal tests exhibit a partially or totally homogenized texture under CL. They proposed that the growth structure of larger hyaline benthic foraminifera will be preserved only when they were pencon-temporaneously displaced into deep water.

7.2

This Work

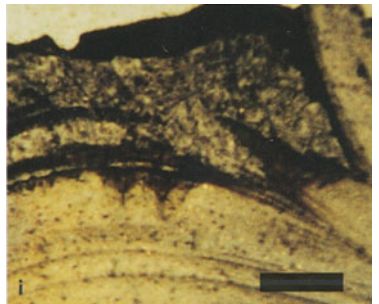
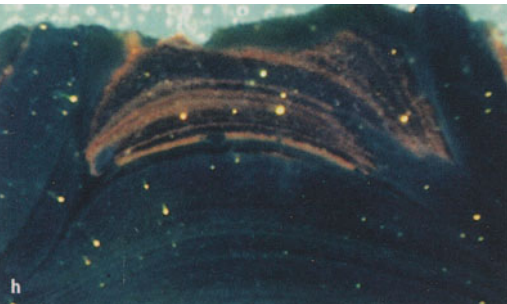
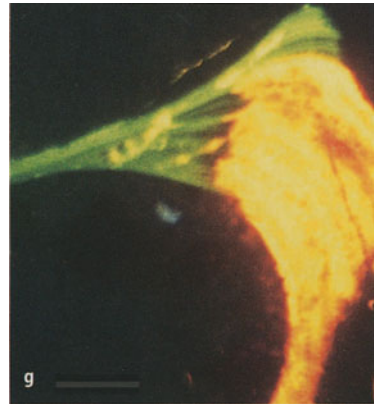
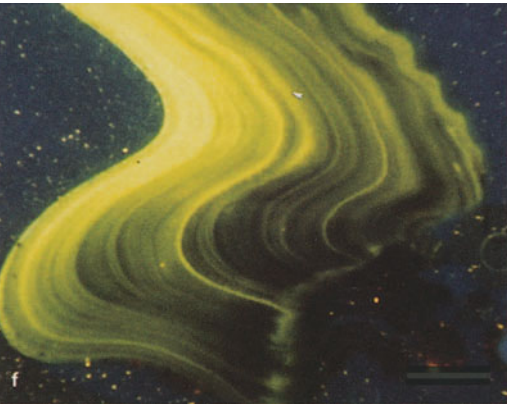
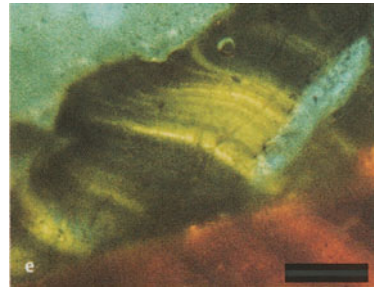
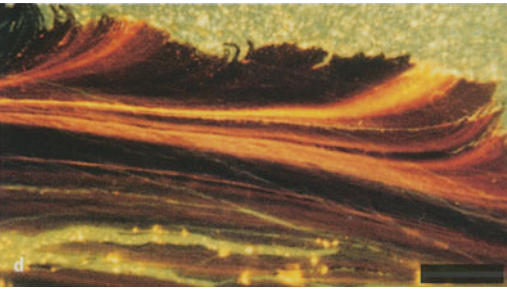
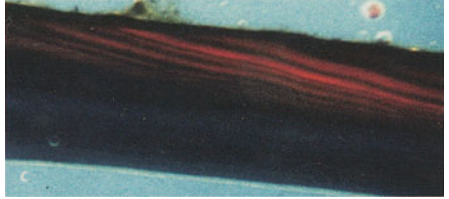
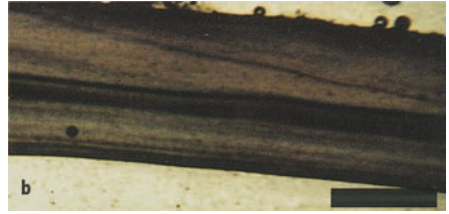
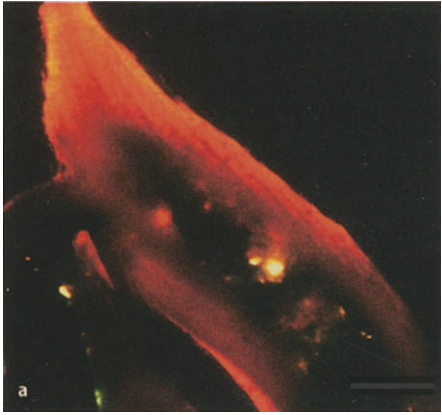
A large number of invertebrates secrete carbonate shells showing extremely rapid chemical fluctuations independent of mineralogy (aragonite or calcite), habitat (marine or continental), or environment. CL emission is thus likely in these carbonate skeletons and should not exclusively be the result of post-mortem diagenetic alterations. Our studies show a general relationship between CL intensity and growth rhythms, but also a likely influence of environment and seawater chemistry. The comparison with well preserved fossil shells shows that CL patterns are similar in fossil and recent shells.

7.2.1

Mollusk Shells

Fast growth of mollusk shells in shallow marine environments was illustrated by the study of a *Pecten maximus* grown in the Bay of Brest under precisely known conditions (Buestel et al. 1987; Barbin et al. 1991b; Schein et al. 1991). In this calcitic shell, winter growth increments are clearly marked by orange luminescing lines even when growth lines are hidden by the foliated microstructure (Fig. 2d). Juvenile parts of the shells show a weak blue luminescence, similar to shell parts surrounding the orange luminescing winter growth lines. In addition, the luminescence intensity is higher in the older adult parts of the shell when growth is slower. The maximum CL intensity is not directly related to the lowest growth rate, i.e. the winter stop, but more precisely during the continued low growth periods. The growth history of the shell is also found in the radial cross section of the resilifer. Other events such as summer storms or accidental stress are seen in CL emission but are generally not as intense as the winter growth increments. Bioeroded zones are often characterized by a bright luminescence and showing a palisade aspect due to the borrowing action of bacteria, sponges or algae (Barbin et al. 1991b). For example, the Mn^{2+} content in pristine *Mituhopecten yessoensis* shells may fluctuate between 3.5 and 12 ppm whereas the concentration is between 42 and 55 ppm in the external probably biocorroded surface (Masuda and Hirano 1980).

Other shells were studied from the natural shallow marine environment. In *Mytilus edulis* a calcitic outer layer and an aragonitic inner layer could be dis-



tinguished on the basis of weak orange luminescing lines in the outer calcitic part (Fig. 2b,c).

Oysters show luminescence in calcite and also sometimes in the aragonitic myostracum (Fig. 1; Fig. 3a,b in Barbin et al. 1991a). More interestingly, the luminescing lines can be followed at the umbo where the calcitic shell is linked with the ligament (mineralized in aragonite, Stenzel 1962) through the boundary of calcite and aragonite (Fig. 2e). CL spectroscopy of the calcitic oysters shows the characteristic emission of Mn^{2+} in calcite at 615 nm and a second broad band which may be due to an intrinsic emission (Fig. 3). The shoulder on the short wavelength side of the peak may correspond to CL emission of aragonite.

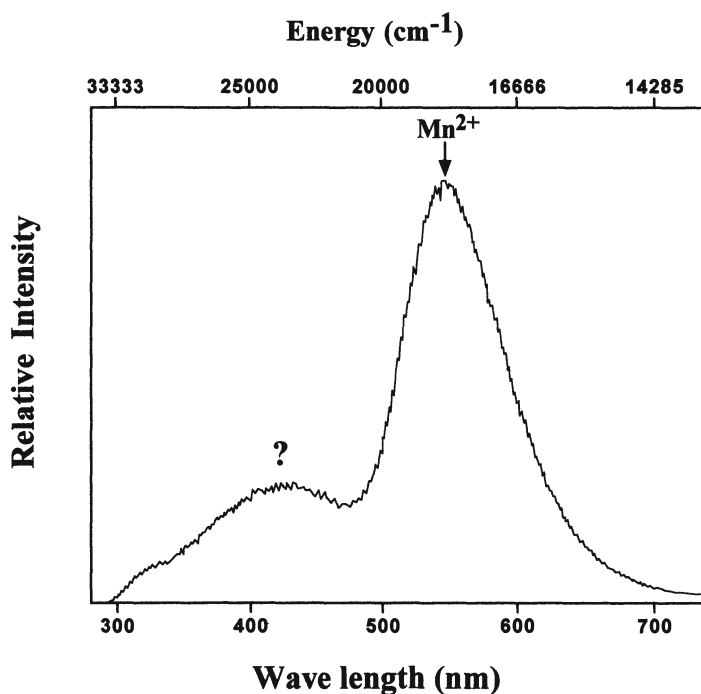


Fig. 3. CL spectrum of Mn^{2+} activated orange luminescing biogenic calcite (oyster, see Fig. 2f), 200 μm spot size

←
 Fig. 2a-i. a CL photomicrograph of Miliolidae, Marseille Bay (France); scale bar is 250 μm ; b plane-polarized light photomicrograph of *Mytilus edulis*, Leucate Pond (France); scale bar is 500 μm ; c same field of view as b but under CL; d CL photomicrograph of *Pecten maximus*, Brest Bay (France), scale bar is 500 μm ; e CL photomicrograph of *Crassostrea gigas*, Marennes-Oléron Basin (France), scale bar is 500 μm ; f CL photomicrograph of *Anodonta* sp., La Neuville en Hez fresh water pond (France), scale bar is 500 μm ; g CL photomicrograph of *Lymnaea dyaphana*, Tierra del Fuego National Park (Argentina), scale bar is 100 μm ; h CL photomicrograph of *Haliothis* sp., University collection, scale bar is 500 μm ; i same field of view as h but under plane-polarized light

In aragonitic marine bivalve shells, luminescence is very weak, nevertheless growth lines are detectable. In contrast, freshwater aragonitic bivalves, e.g. *Anodonta* sp. or *Margaritifera margaritifera*, show brighter green to yellow luminescence (Fig. 1h, Fig. 2f).

Gastropods (*Patella* sp.) and archaeogastropods (*Haliotis* sp.) from shallow marine environments have mixed mineralogies (calcite and aragonite). In both cases calcite generally shows bright orange luminescence while aragonite exhibits dull blue to green and rarely a yellow luminescence. In *Haliotis*, the mineralogy and ultrastructure of the external shell-layer may differ among species. In some, this layer is totally calcitic while others are pure aragonitic and at least some have a mixed mineralogy. Dauphin et al. (1989) suggested that in *Haliotis* with a mixed mineralogy, the mantle epithelium can simultaneously secrete the two polymorphs. The studied specimens clearly show orange luminescing bands typical for calcite. At present, these bands are difficult to interpret because they are not present in all parts of the shell. Possible explanations are an original structure, regenerative parts of the shell, or bacterial activity (Fig. 2h,i).

Cephalopods were studied in order to investigate shells of organisms living in the water column. Recent specimens of *Nautilus pompilius* and *Nautilus macromphalus* were investigated. A detailed description of shell luminescence found in *N. pompilius* and *N. macromphalus* are given in Barbin (1992). The luminescence in *N. macromphalus* is a very weak blue with greenish bands (Fig. 1a in Barbin et al. 1995), while the *N. pompilius* shell shows CL emission consisting of alternating yellow and green bands (Fig. 1i). The luminescence bands correlate in both specimens with growth lines. In *Nautilus*, the intensity of the luminescence increases with ontogeny. The CL spectrum of *N. pompilius* (Fig. 4; Figs. 2 and 3 in Barbin et al. 1995) confirms the optical observations that emission at 540 nm is mainly from Mn²⁺ substitution for Ca²⁺ in aragonite. An additional broad band in the blue range was detected which may be related to an intrinsic emission. PIXE analyses of the wall show a variable manganese concentration with values ranging from 10 ppm (i.e. LOD) to 85 ppm (Fig. 5; Barbin et al. 1995; Barbin 1998). The measured Mn²⁺ variation correlates with the intensity of the CL emission (Barbin 1998). Additional CL studies of cephalopod shells from Carboniferous (*Michelinoceras* sp.) and Eocene (*Euciphoceras regale*) were performed in order to test the continuity of shell biogeochemistry since Carboniferous times. CL emission of *E. regale* is similar to that of *N. pompilius*, which exhibits yellow and green bands (Fig. 1c in Barbin et al. 1995). The intensity pattern as well as the width of the luminescence bands in *E. regale* are comparable to those observed in the shell of the Recent *N. pompilius*. The *Michelinoceras* sp. shell shows the characteristic CL pattern of alternating yellow and green luminescence, similar to that observed in *N. pompilius* (Fig. 1l). The Carboniferous *Comatoceras* sp. shows essentially non- to bluish-luminescence comparable to the CL emission observed in Recent *N. macromphalus*.

The original mineralogy of belemnites is still under discussion. Nevertheless, it seems that the prismatic structure is primary and that most of the rostra are originally calcitic (Veizer 1974; Saelen 1989). Under CL, belemnites show orange lines on a dull blue luminescing background. These lines are parallel to growth increments and may have a biochemical origin.

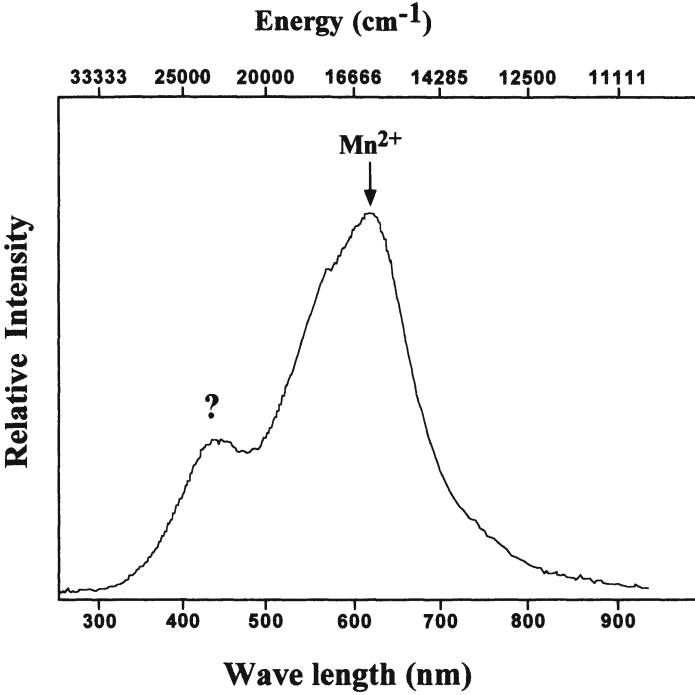


Fig. 4. CL spectrum of Mn²⁺ activated yellow-green luminescing biogenic aragonite (nautilus, see Fig. 2f), 200 μm spot size

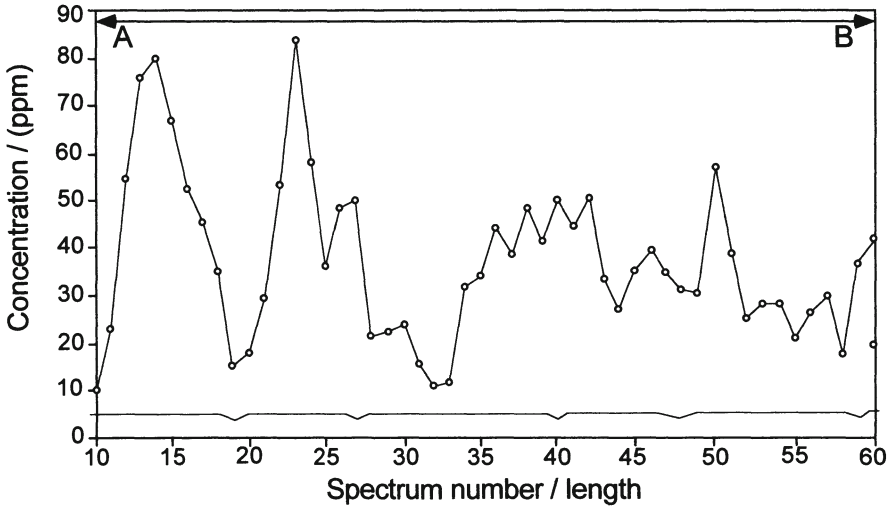


Fig. 5. PIXE analyses of Mn in the shell of *Nautilus pompilius*. The profile was taken along the A-B section shown on Fig. 1i. (Figure courtesy of C. Yang, for more details on PIXE analysis, see Yang et al. 1995)

The deep sea hydrothermal vent environment with chemosynthetic food supply was studied with *Bathymodiolus thermophilus* (Schein et al. 1991). The CL emission of the calcitic shell is orange with fine, irregular intensive and thick bands which correspond to a highly variable Mn^{2+} concentration in the external layer of the shell (Fig. 1b,c). Superimposed on this fine zonation is a broader, zonation due to long term changes (Fig. 1a).

7.2.2

Echinoderm Tests

Echinoïds or crinoïds did not show significant luminescence, which contradicts previous observations on sand dollars (Glover 1977) and other echinoïds (Richter and Zinkernagel 1980, 1981). As skeletal concentration of Mn, Fe and Ni may differ significantly between echinoïd species from the same community (Stevenson and Ufret 1966) our observations cannot be generalized.

7.2.3

Foraminifera Tests

Most Recent foraminifera are calcitic and only *Robertinina* is aragonitic. Porcelaneous foraminifera have high-Mg-calcite tests while some hyaline foraminifera have low-Mg-calcite tests. All studied planktonic foraminifera do not show CL emission, while almost all porcelaneous foraminifera have a more intensive orange emission (Fig. 2a) than hyaline foraminifera (Plate 1, Fig. 3 in Barbin et al. 1991a). Aragonitic foraminifera show a weak greenish luminescence.

7.2.4

Brachiopod Shells

Recent, living brachiopods from the four main superfamilies, Terebratulacea, Terebratellacea, Cancellothyridacea and Rhynchonellacea, from different environments and bathymetries were studied under CL. The ventral valve has generally been used for analysis. The inner parts of Recent brachiopod shells often show orange luminescing bands (Plate 1, Figs. 1–6 in Barbin and Gaspard 1995). These bands are similar to those found in *Pecten* and are related to periods of low growth rate. The width of the luminescent bands changes during ontogeny of the individual, reflecting changes in winter, spawning seasons and disturbances. Thus, using CL to determine the state of diagenetic alterations of a brachiopod shell is questionable (Barbin and Gaspard 1995). Preliminary observations on inarticulate brachiopods show that they are generally more luminescent than are articulate ones (Fig. 1j,k).

7.2.5

Corals

All studied corals are aragonitic and show dull blue-green luminescence, which does not provide more information than classical UV-light observations.

7.2.6

Crustaceans

The Mn^{2+} content of barnacle shells primarily reflects the Mn^{2+} content of the animal's aquatic environment (Gordon et al. 1970). Blanchard and Chasteen (1976b) found a good correlation between the Mn^{2+} content of the shell and the position of the animal in the intertidal zone.

Barnacle shells show orange luminescing bands ranging from low to bright intensity (Fig. 1g). These bands may be related to internal growth bands, but there are not enough data to relate the CL emission to environmental factors.

7.2.7

Algae

Encrusting coralline algae (*Neogoniolithon* sp.) from the shallow lagoon of Bahiret el Biban were used for this study. Under CL the *Melobesia* shows zones of orange luminescence (Plate 1, Figs. 1a,b and 2a,b in Barbin et al. 1991a), whereby the perithallium is more luminescent than the hypothallium. In a single microridge, successive layers may show different luminescence intensities, which may correspond to changes in the physicochemical conditions such as heavy rainfalls in the lagoon.

7.2.8

Eggshells

Avian eggshells were studied in order to have material for comparison with dinosaur eggshells. Calcitic Palaeognathae eggs from *Struthio* (ostrich), *Rhea* and *Dromaius* (emu) from a breeding farm were used. Details on the microstructure of these eggshells are given by Dauphin (1990a,b) and references therein. All eggshells show a weak bluish emission without evidence of zonation. In contrast, the CL of dinosaur eggshells is generally a bright orange in pores and in cracks between them now filled with diagenetic calcite (Fig. 1d). The rest of the eggshell is non- to dull luminescent with weak orange luminescing growth lines in some specimens. Thus, the use of CL may help to evaluate the degree of diagenetic alteration of dinosaur eggshells as well as the growth of the eggshells.

7.2.9

Shell Repair

Most of the previously studied invertebrates can repair damage inflicted to their shells by deposition of new shell material in the damaged area. Depending on phylum and even species, and environmental conditions, regeneration may be different in mineralogy (calcite, aragonite or vaterite) and time of precipitation (Wilbur and Saleuddin 1983). Because differentiation between calcite and aragonite is very difficult by optical mineralogy, areas with regenerative depositions may be overlooked. In addition, bulk analyses of the shell may erroneously indicate a mixed initial mineralogy. In CL the difference of calcite vs aragonite emission, orange vs green-yellow, respectively, makes discrimination very easy. Shell repair was observed in *Anadara senilis* from Mbodiène Lagoon (Plate 2 and Fig. 2a,b in Barbin et al. 1991a) and in *Lymnaea dyaphana* from Tierra del Fuego National Park (Fig. 2g and Plate 1, Fig. 6 in Barbin and Schvoerer 1997). The pres-

ence of some orange luminescing calcitic areas in aragonitic shells is thus not always evidence of post-mortem diagenetic alterations. These areas may well represent places of shell repair.

Another interesting observation visible only under CL is the effect of resorption during skeleton growth as in the case of echinoids in which luminescing zones are truncated (Richter and Zinkernagel 1980, 1981).

7.2.10

Summary

Stable oxygen and carbon isotope measurements on biogenic carbonates have become standard technique for reconstructing physico-chemical conditions of past oceanic waters. For these studies, CL is used as a tool to identify possible diagenetic modification. From our studies on modern biogenic carbonates, it appears that CL is a common phenomenon and that only juvenile parts with a higher growth rate of the shell are generally non-luminescent. In addition, it was shown by Rush and Chafetz (1990) that the practice of using fabric-retentive, non-luminescent brachiopods as indicators of their original chemistry is questioned. Thus, distinction between pristine mineralogy and diagenetic alteration remains difficult.

8

Causes of Variable Cathodoluminescence Emission of Biogenic Carbonates

8.1

Environmental Factors

The relationship between trace element content of shells and environmental conditions is still an open question despite much research on this topic. For CL studies, Mn²⁺ partitioning between shell and seawater is of crucial interest. It is well known that external growth lines, microstructural patterns or biogeochemical variations are tools to study environmental and ontogenic parameters in the shell (e.g. Schein et al. 1991).

Seasonal variations exist in minor and trace element content of modern and ancient brachiopod shells (see discussion in Grossman et al. 1996). In addition, Carriker et al. (1982) could show that an ontogenetic concentration of elements such as Mn is possible. Bradley (1910) suggests that the Mn content of mollusk shell is principally a function of diet. Similarly, Stevenson and Ufret (1966) showed that the Fe content in the stereom of regular echinoids is related to the Fe content in the algal food source. The problem remains why these algae have various Fe contents. Since these works, other parameters have been studied.

Salinity may be one of the dominant environmental control of the concentration of Mn²⁺ in invertebrate shells (e.g. Rucker and Valentine 1961; Pilkey and Goodell 1963, 1964; Gordon et al. 1970; Rosenberg 1980; Masuda 1981). Dunca and Nyström (1993) demonstrated that there is a seasonal periodicity of the accumulation of trace elements in freshwater bivalve shells. Using micro-PIXE analyses Dunca and Nyström (1993) observed in *Unio* shells that Mn has a low concentra-

tion in spring time when growth rate is high and as the growth decreases over the summer period the Mn concentration increases. In autumn, Mn decreases strongly and, finally, in winter, when growth ceases, the Mn level is again high. These results are similar to our observations on the relationship between the intensity of the CL emission and the ontogeny and growth rhythms. In addition, pH may influence the Mn content of shells (Dunca and Nyström 1993).

Surprisingly, *Margaritifera margaritifera* shows different Mn concentrations for specific seasons depending of the collection site. Decreased Mn concentration in *M. margaritifera* shells from the River Pauliströmsån (Sweden) is probably due to a lower growth rate during autumn and winter (Nyström et al. 1995). The same species from an other site has a high Mn concentration in the summer period, which correlates with a depletion in oxygen in the surrounding water (Nyström et al. 1996).

Evaporation, influx of fresh water or modification of Eh are the basic three ways to change the Mn^{2+} content of seawater. It is well known that the Mn^{2+} concentration in river and seawater is generally below 8–10 ppb and 0.3 ppb, respectively (Broecker and Peng 1982). Veizer (1983) considers that calcite directly precipitated from seawater would contain 1–2 ppm of Mn^{2+} . We have previously seen that the Mn^{2+} content in biogenic carbonates is between 2 and several hundred ppm. Metabolic and crystallochemical processes must be taken into account to explain the higher concentration of Mn^{2+} in biogenic carbonates. Nevertheless, the question if this increase represents chemical fluctuations of the water is still open. This question is not easy to solve because each family, genus and species control their own metabolism differently. The impact of solution chemistry on bivalve trace element composition (e.g. *Mytilus edulis*) was demonstrated for Mg, Sr, Na, Pb and Cd within calcitic and aragonitic layers (Lorens and Bender 1980; Sturesson 1976, 1978). It was shown that *M. edulis* can control the Mg activity of the outer extrapallial fluid. Environmental stress can have the impact of increasing sulfur as well as Mg content in biogenic carbonates. Interactions between seawater chemistry and the *Crassostrea virginica* shell, cultured in controlled and natural systems, were investigated by Carriker et al. (1980). They observed that Mn and Zn concentrations were higher in the prismatic calcite of shells from the flow-through system. The authors concluded that oysters have the capacity to concentrate several elements in their shells when the concentration of these elements increased in ambient seawater. In addition, they observed a heterogeneous distribution of these elements in major regions of the shells.

Presently, two possibilities exist: either (1) the flux of Mn^{2+} is constant in the environment and only the growth rate controls incorporation in the shell, or (2) the Mn^{2+} content of the extrapallial fluid is variable and environmental conditions lead the animal to release Mn in order to produce more shell material, e.g. under stress conditions. A general increase of CL intensity is seen with ontogeny. This may be related to growth rate, since growth rate decreases with age. It is reasonable to expect that the Mn/Ca ratio in biogenic carbonates is influenced by the seawater chemistry and by environmental stress, as was shown for other ions by Lorens and Bender (1980) or Sturesson (1976, 1978). A positive correlation between shell Mn content and water temperature can be explained because temperature is one of the main factors influencing shell growth (Nyström et al. 1996).

The possibility to easily distinguish under CL between aragonite and calcite is useful when studying specimens in which the aragonite/calcite ratio is determined by the environmental conditions. A relationship exists between sea surface temperature and the proportion of structural and mineralogical components in the shells of certain mollusk species. For example, in *Patella* shells, the width of the outer aragonitic layer increases relative to that of the outer calcitic layer with increasing sea surface temperature (Cohen and Branch 1992). Generally, the aragonite/calcite ratio is estimated from X-ray diffraction traces of whole shell powders, and Cohen and Branch (1992) could show that these measurements are less well correlated with sea surface temperature than the ratio of the widths of the outer lamellar and foliar layers. Thus, CL may improve these compositional analyses.

8.2 Diagenetic Evolution of Shells

Carbonate diagenesis commonly includes seven major processes: cementation, microbial micritization, neomorphism (recrystallization), dissolution, compaction and dolomitization. It operates in marine, near-surface meteoric and burial environments. Two of these processes concern carbonate skeletons: microbial micritization, which happens on the sea floor or just below, and neomorphism.

Micritization is due to the action of endolithic algae, fungi and bacteria. The surface of the shell is bored and holes are filled with carbonate mud or micritic cement. Micritization may start during the life of the organism, and CL is a useful technique to visualize such phenomena.

The process of neomorphism takes place in the presence of water and is a dissolution-precipitation process. At low temperatures, processes in which aqueous solutions are involved are much more frequent than solid-state processes, as in diagenetic environments water is mostly present (e.g. Tucker and Wright 1990). In the presence of diagenetic fluids, such as meteoric waters, burial waters and/or brines, aragonite and high-Mg-calcite are meta-stable and alter readily to diagenetic low-Mg-calcite, while low-Mg-calcite is relatively resistant to the dissolution-precipitation process (e.g. Brand and Morrison 1987 and references therein). During diagenesis, when biogenic carbonates are dissolved and diagenetic low-Mg-calcite precipitates, minor and trace elements are also involved. For example, the Sr content decreases whereas the Mn content increases (e.g. Brand and Morrison 1987, Brand 1989). In cases with an influx of more oxidizing meteoric waters, the paragenetic sequence of carbonate cements may record a gradual decrease in Mg, Fe and Mn content in the pore fluid during shallow burial (Carpenter et al. 1988). Richter and Zinkernagel (1980) consider that the transformation from high-Mg-calcite to low-Mg-calcite takes place as a single reaction and not along distinct zones because the Mg composition of altered echinoid tests is homogeneous. They suggest that the transformation causes chemical homogenization of the Mn distribution, and thus a probable former luminescence zonation will disappear. Diagenesis of high-Mg-calcite from miliolides may take place without any visible alteration in the crystal morphology. This observation and the

simultaneous change in Mg and $\delta^{18}\text{O}$ composition indicate that the transformation is a repetitive (tens to hundreds), incongruent recrystallization that involves dissolution-precipitation (Towe and Hemleben 1976; Budd and Hiatt 1993). Maliva and Dickson (1992) proposed that the replacement of aragonite by calcite in shells occurs along thin solution films (<10 nm) between the growing calcite crystals and the skeletal aragonite. The neomorphic reaction zone tends to have a negligible or low degree of chemical isolation from the bulk pore waters. The decrease in the intraskeletal pore water calcium carbonate ion activity product caused by calcite precipitation results in aragonite dissolution adjacent to aragonite-calcite contacts (Maliva and Dickson 1992 and references therein). CL microscopy is therefore useful in studies of neomorphism of aragonitic bivalves (Hendry et al. 1995). Hendry et al. (1995) showed that in the Blisworth Limestone Formation two separate stages of skeletal neomorphism exist.

The magnitude of the elemental shift in biogenic aragonite during diagenesis may be greatly influenced by the original biogeochemistry and microstructure of the organism (Brand and Morrison 1987). Walter and Morse (1984) have shown that most of the total surface area of biochemical particles is unavailable for reaction with aqueous solution. The dissolution rate is a function of grain size and microstructure and both can play an important role in controlling the reactivity of biogenic carbonates during diagenesis. High Mn content in fossil carbonate may not always be the result of alteration of the pristine carbonate material. Calcite precipitation in equilibrium with reducing seawater would contain more Fe and Mn than calcite crystallized from normal seawater (Veizer 1977).

Nevertheless, CL microscopy is often used to determine whether high Mn concentrations in a fossil are of diagenetic or of biochemical origin. It has also been shown, that the homogenization of the cathodomicrofacies starts at higher temperatures than solid state recrystallization. The study of the evolution from a limestone to a marble situated in the contact zone of a granitic pluton revealed that a temperature of 350°C was necessary to modify the cathodomicrofacies (Schmid and Ramseyer 1996). This might explain the persistence of fossil ghosts in some limestones.

Synsedimentary mixing from different environments may be documented by CL microscopy when specimens of the same species show different luminescence intensities in the same sample. If we assume that two individuals from the same species in the same environment likely exhibit similar luminescence, then individuals showing different luminescence are most likely from different origins or they were altered under different early diagenetic conditions. Both cases imply that they have been reworked (Barbin et al. 1989).

9

Conclusion

From these studies it is now evident that:

1. Most Recent biogenic carbonates show luminescence under cathodic excitation.
2. This luminescence is principally due to the presence of Mn^{2+} substituting for Ca^{2+} ions in the lattice.

3. Emission is orange in calcite and green to yellow in aragonite due to the crystallographic environment and its influence on physical phenomena generating CL.
4. CL microscopy is very useful for detecting changes in the mineralogy of shells, whether of diagenetic or biochemical origin.
5. Luminescence intensity is related to growth increments. In bivalve shells, bands of maximum emission intensity are frequently correlated with annual growth lines and lower growth rates. CL emission increases with ontogeny.
6. The amount of Mn^{2+} incorporated within carbonate is primarily controlled by metabolic activity. Nevertheless, environmental changes are recorded within the shell and may be revealed under CL.
7. Factors such as water chemistry, temperature, and depth may influence the CL signal.
8. As Rosenberg and Hughes (1991) proposed, it will be of evolutionary interest to know what the distribution of elements within skeletons is, even if skeletal composition proves to be so variable that regular, taxon-specific patterns cannot be confirmed. Observations on Recent and fossil cephalopods are in accord with these ideas (Barbin et al. 1995).

Thus, progress has been made during the last decade regarding the knowledge and cause of CL emission from biogenic particles and their different origins. CL microscopy is now a useful method for detecting minor changes in trace elements in shells, and thus can prove important information on ecological parameters. Further progress may require cultures of different organisms under controlled environmental conditions (e.g. pH, salinity, oxygen concentration, light).

Acknowledgements. I am indebted to my different co-authors with whom I have collaborated for over a decade, and especially to U. Brand, J.P. Debenay, D. Decrouez, D. Gaspard, R.A. Hewitt, K. Ramseyer, M. Roux, E. Schein and Ch. Yang. I should also thank G. Garcia, S. Gordillo and H. Mutwei for kindly sending shell material and the breeding farm "La Logerie Eurotruche" (Maché, Vendée, France) for kindly yielding Palaeognathae eggs. I thank S. Burns, K. Ramseyer, D.K. Richter and M. Roux for their useful comments on the manuscript.

References

- Amieux P (1987) Description pétrographique de foraminifères par combinaison d'images en lumière naturelle et en cathodoluminescence. C. R. Acad. Sci. Paris (II), 304: 741–744
- Barbin V (1992) Fluctuations in shell composition in *Nautilus* (Cephalopoda, Mollusca): evidence from cathodoluminescence. *Lethaia*, 25: 391–400
- Barbin V (1998) Cathodoluminescence microscopy and spectroscopy of carbonates: new applications in geology and archaeology. 13th Pfefferkorn conference on Luminescence. *Scann. Microsc.*, vol. spec. 9: 113–123
- Barbin V, Gaspard D (1995) Cathodoluminescence of Recent articulate brachiopod shells. Implications for growth stages and diagenesis evaluation. *Geobios*, M.S. 18: 39–45
- Barbin V, Ramseyer K, Decrouez D, Herb R (1989) Mise en évidence par la cathodoluminescence d'indices de remaniements synsédimentaires. *Geobios*, 22: 253–259

- Barbin V, Ramseyer K, Debenay JP, Schein E, Roux M, Decrouez D (1991a) Cathodoluminescence of Recent biogenic carbonates: an environmental and ontogenic fingerprint. *Geol. Mag.*, 128: 19–26
- Barbin V, Schein E, Roux M, Decrouez D, Ramseyer K (1991b) Stries de croissance révélées par cathodoluminescence dans la coquille de *Pecten maximus* récent de la rade de Brest (Pectinidae, Bivalvia). *Geobios*, 24: 65–70
- Barbin V, Brand U, Hewitt RA, Ramseyer K (1995) Similarity in Cephalopod shells biogeochemistry since Carboniferous: Evidence from cathodoluminescence. *Geobios*, 28: 701–710
- Barbin V, Schvoerer M (1997) Cathodoluminescence et géosciences. Point sur ... C. R. Acad. Sci. Paris. Sci. terre planètes, 325: 157–169
- Baumgartner-Mora C, Baumgartner PO (1994) Shell structure of fossil foraminifera studied by cathodoluminescence. *Europ. Microsc. Anal.*, Marsh: 29–32
- Blanchard SC, Chasteen ND (1976a) Electron paramagnetic resonance spectrum of sea shell *Mytillus edulis*. *J. Phys. Chem.*, 80: 1362–1367
- Blanchard SC, Chasteen ND (1976b) Determination of manganese (II) in powdered Barnacle shells by electron paramagnetic resonance. *Analyt. Chim. Acta*, 82: 113–119
- Bosence DWJ (1991) Coralline Algae: mineralization, taxonomy, and palaeoecology. In: Riding R. (ed.) *Calcareous algae and stromatolites*. Springer Verlag, Berlin Heidelberg New York, pp 98–113
- Bourget E (1980) Barnacle shell growth and its relationship to environmental factors. In: Rhoads DC and Lutz R (eds) *Skeletal growth of aquatic organisms*. New York: Plenum, pp.469–491
- Bradley HC (1910) Manganese in the tissues of lower animals. *J. Biol. Chem.*, 8: 237–249
- Brand U (1989) Aragonite-calcite transformation based on Pennsylvanian molluscs. *Geol. Soc. Am. Bull.*, 101: 377–390
- Brand U, Morrison JO (1987) Biogeochemistry of Fossil Marine invertebrates. *Geoscience Canada*, 14: 85–107
- Broecker WS, Peng TH (1982) *Tracers in the Sea*. Eldigio Press
- Budd DA, Hiatt EE (1993) Mineralogical stabilization of High-Magnesium calcite: geochemical evidence for intracrystal recrystallization within Holocene porcelaneous foraminifera. *J. sed. Petr.*, 63: 261–274
- Buestel D, Gerard A, Guenole A (1987) Croissance de différents lots de coquilles Saint-Jacques *Pecten maximus* en culture sur le fond dans la rade de Brest. *Haliotis*, 16: 463–477
- Carpenter SJ, Erickson JM, Lohmann KC, Owen MR (1988) Diagenesis of fossiliferous concretions from the upper cretaceous fox hills formation, north Dakota. *J. Sed. Petr.*, 58: 706–723
- Carriker MR, Palmer RE, Sick LV, Johnson CC (1980) Interaction of mineral elements in seawater and shell of oysters (*Crassostrea virginica* (Gmelin)) cultured in controlled and natural systems. *J. exp. Mar. Biol. Ecol.*, 46: 279–296
- Carriker MR, Swann CP, Ewart JW (1982) An exploratory study with the proton microprobe of the ontogenetic distribution of 16 elements in the shell of living oysters (*Crassostrea virginica*). *Mar. Biol.*, 69: 235–246
- Carter JG (1980) Guide to Bivalve shell microstructures. In: Rhoads DC and Lutz R (eds.), Appendix 2, Bivalve shell mineralogy and microstructure. New York: Plenum, pp.645–673
- Cohen AL, Branch GM (1992) Environmentally controlled variation in the structure and mineralogy of *Patella granularis* shells from the coast of southern Africa: implications for paleotemperature assessments. *Palaeogeog. Palaeoclim. Palaeoecol.*, 91: 49–57
- Czerniakowski LA, Lohmann K, Wilson JL (1984) Closed-system marine burial diagenesis: isotopic data from the Austin Chalk and its components. *Sedimentology*, 31: 863–877
- Dauphin Y (1990a) Microstructures et composition chimique des coquilles d'œufs d'oiseaux et de reptiles. *Palaeontographica Abt. A*, 214: 1–12
- Dauphin Y (1990b) Comparative microstructural studies of eggshells. 1-Dinosaurs of the southern France. *Rev. Paléobiol.*, 9: 121–137
- Dauphin Y, Cuif H, Mutvei H, Denis A (1989) Mineralogy, chemistry and ultrastructure of the external shell-layer in ten species of *Haliotis* with reference to *Haliotis tuberculata* (Mollusca: Archaeogastropoda). *Bull. Geol. Institut. Univ. Uppsala. N.S.*, 15: 7–38

- Debenay J-P, Pawlowski J, Decrouez D (1996a) Les foraminifères actuels. Masson, 329p
- Debenay J-P, Guillou J-J, Lesourd M (1996b) Colloidal calcite in foraminifer tests: crystallization and texture of the test. *J. Foram. Res.*, 26: 277–288
- Dubois Ph, Chen C-P (1989) Calcification in echinoderms. In: Jangoux M and Lawrence JM (eds) *Echinoderm studies*. A.A. Balkema. vol. 3, pp 109–172
- Dunca E, Nyström J (1993) Using the freshwater bivalve as an environmental indicator. *Biomining* 93. L'institut Océanographique de Monaco. Abstracts
- El Ali A, Barbin V, Calas G, Cervelle B, Ramseyer K, Bouroulec J (1993) Mn²⁺-activated luminescence in dolomite, calcite and magnesite: quantitative determination of manganese site distribution by EPR and CL spectroscopy. *Chem. Geol.*, 104: 189–202
- Faupl P (Von), Beran A (1983) Diagenetische Veränderungen and Radiolarien-und Schwamm-spicula-führenden Gesteinen der Strubergschichten (Jura, Nördliche Kalkalpen, Österreich). *N. Jb. Geol. Paläont. Mh.*, 3: 129–140
- Flajs G (1977a) Skeletal structures of some calcifying algae. In: Flügel E (ed) *Fossil algae: recent results and developments*. Springer Verlag, Berlin Heidelberg New York, pp 225–231
- Flajs G (1977b) Die Ultrastrukturen des Kalkalgenskeletts. *Palaeontographica*, 160: 69–128
- Friedman GM (1993) Discussion of cathodoluminescence of Recent biogenic carbonates: an environmental and ontogenetic fingerprint. *Geol. Mag.* (Barbin et al., 1991), 130: 269–270
- Glover ED (1977) Unpb. PhD thesis, Univ Wiscconsin
- Gordon CM, Carr RA, Larson RE (1970) The influence of environmental factors on the sodium and manganese content of Barnacle Shells. *Limno. Oceano.*, 15: 461–466
- Grant SWF, Knoll AH, Germs GJB (1991) Probable calcified metaphytes in the latest proterozoic nama group, Namibia: origin, diagenesis, and implications. *J. Paleont.* 65: 1–18
- Grossman EL, Mii HS, Zhang C, Yancey TE (1996) Chemical variation in Pennsylvanian brachiopod shells. diagenetic, taxonomic, microstructural, and seasonal effects. *J. Sed. Res.*, 66: 1011–1022
- Habermann D (1997) Quantitative hochauflösende Kathodolumineszenz-Spektroskopie von calcite und Dolomit. Unvorüf Dissertatin Ruhr-Universität Bochem 152p
- Habermann D, Neuser RD, Richter DK (1996) REE-activated cathodoluminescence of calcite and dolomite: high-resolution spectrometric analysis of CL emission (HRS-CL). *Sed. Geology*, 101: 1–7
- Henderson B, Imbusch GF (1989) *Optical Spectroscopy of Inorganic Solids*. Clarendon Press, Oxford
- Henfry JP, Ditchfield PW, Marshall JD (1995) Two-stage neomorphism of Jurassic aragonite bivalves: implications for early diagenesis. *J. Sed. Rech.*, A65: 214–224
- Izuka SK (1988) Relationship of magnesium and others minor elements in tests of *Cassidulina subglobosa* and *C. orianguata* to physical oceanic properties. *J. Foram. Res.*, 18: 151–157
- Kershaw S (1994) Cathodoluminescence of Silurian stromatoporoids from Gotland, Sweden. *Cour. Forsch. Inst. Senckenberg*, 172: 307–318, Frankfurt am Main
- Long JVP, Agrell SO (1965) The catho-doluminescence of minerals in thin section. *Min. Mag.*, 24: 2318–2326
- Lorens RB, Bender M (1980) The impact of solution chemistry on *Mytilus edulis* calcite and aragonite. *Geochim. Cosmochim. acta*, 44: 1265–1278
- Lowenstam HT (1981) Minerals formed by organisms. *Science*, 211: 1126
- Lowenstam HT, Weiner S (1989) *On biomineralization*. Oxford University Press
- Machel HG (1983) Cathodoluminescence in carbonates petrography: some aspects of geochemical interpretation. *Am. Assoc. Pet. Geol. Bull.*, 67: 507–508
- Maliva RG, Dickson JAD (1992) The mechanism of skeletal aragonite neomorphism: evidence from neomorphosed molluscs from the upper Purbeck Formation (Late Jurassic-Early Cretaceous), southern England. *Sed. Geol.*, 76: 221–232
- Mann S (1988) Molecular recognition in biomineralization. *Nature*, 332: 119–124
- Marshall DJ (1988) *Cathodoluminescence of geological materials*. Unwin Hyman Ltd, London

- Martin H, Zeegers H (1969) Cathodo-luminescence et distribution du manganèse dans les calcaires et les dolomies du Tournaisien supérieur au Sud de Dinant (Belgique). C. R. Acad. Sci. Paris (II), 269: 922–924
- Martini R, Amieux P, Gandin A, Zaninetti L (1987) Triassic foraminifers from Punta Tonnara (SW Sardinia) observed in cathodoluminescence. Rev. Paléobiol., 6: 23–27
- Masuda F (1981) Chemical composition in marine carbonates as an indicator of paleoenvironment. Report Grand-Aid, Sci. Res. (C), project N°454262: 1–44
- Masuda F, Hirano M (1980) Chemical composition of some modern marine pelecypod shells. Sci. Rep. Inst. Geosci. Univ. Tsukuba, sec. B, 1: 163–177
- Middleton PD, Marshall JD, Brenchley PJ (1991) Evidence for isotopic change associated with Late Ordovician glaciation from brachiopods and marine cements of central Sweden. Geol. Sur. Canada Paper, 90: 313–321
- Miller J (1988) Cathodoluminescence microscopy. In: Tucker M. (ed) Techniques in Sedimentology. Blackwell Sci. Publ Oxford, pp. 174–190
- Miller J, Clarkson ENK (1980) The post-ecdysial development of the cuticle and eye of the Devonian trilobite *Phacops rana milleri* Steward 1927. Phil. Trans. Royal Soc., 288: 461–480
- Milliman JD (1974.) Marines carbonates. Springer-Verlag, Berlin Heidelberg New York.
- Morrison JO, Brand U (1986) Geochemistry of Recent Marine invertebrates. Geoscience Canada, 13: 237–254
- Neuser RD, Bruhn F, Götze J, Habermann D, Richter DK (1996) Kathodolumineszenz: Methodik und Anwendung. Zbl. Geol. Paläont., Teil I, 1995, 1/2: 287–306
- Nöth S, Habermann D, Neuser RD, Richter DK (1997) Kathodolumineszenz und Diagenese triassischer Conodonten Nordwestdeutschlands. Zbl. Geol. Paläont, Teil I, 1996, 5/6: 533–545
- Nyström J, Dunca E, Mutvei H, Lindh U (1996) Environmental history as reflected by freshwater Pearl Mussels in the River Vramsån Southern Sweden. Report, Ambio, 25/5: 350–355
- Nyström J, Lindh U, Duncan E, Mutvei H (1995) A study of *M. margaritifera* shells from the River Pauliströmsån S. Sweden. NIMB, Beam Interactions with Materials & atoms, Nucl. Inst. and Meth. in Phys. Res., B104: 612–618
- Pentecost A (1991) Calcification processes in Algae and Cyanobacteria. In: Riding R (ed.) Calcareous algae and stromatolites. Springer Verlag, Berlin Heidelberg New York, pp.3–20
- Pilkey O, Goodell H.G (1963) Traces elements in Recent mollusk shells. Limn. Oceano., 8: 137–148
- Pilkey O, Goodell HG (1964) Comparison of the composition of fossil and Recent Mollusk shells. Geol. Soc. Am. Bull., 75: 217–228
- Popp BN, Podosek FA, Brannon JC, Anderson TF, Pier J (1986) ⁸⁷Sr/⁸⁶Sr ratios in Permo-Carboniferous sea water from the analyses of well-preserved brachiopods shells. Geochim. Cosmochim. Acta, 50: 1321–1328
- Ramsayer K, Fischer J, Matter A, Eberhardt P, Geiss J (1989) A cathodoluminescence microscope for low intensity luminescence. J. Sed. Petr., 59: 619–622
- Rémond G, Cesbron F, Chapoulière R, Ohnenstetter D, Roques-Carmes C, Schvoerer M (1992) Cathodoluminescence applied to the microcharacterization of mineral materials: A present status in experimentation and interpretation. Scann. Microsc., 6: 23–68
- Richter DK, Zinkernagel U (1980) Mn-activated cathodoluminescence in Echinoid tests. International Association of Sedimentologists, 1st European Regional Meeting 1980, Bochum, Abstracts: 172–176
- Richter DK, Zinkernagel U (1981) Zur Anwendung der Kathodolumineszenz in der Karbonatpetrographie. Geol. Rdsch., 70: 276–302
- Riding R (1991) Calcareous Algae and stromatolites. Springer Verlag, Berlin Heidelberg New York
- Rosenberg GD (1980) An ontogenetic approach to the environmental significance of bivalve shell chemistry. In: Rhoads DC and Lutz R (eds.), Skeletal growth of aquatic organisms. New York: Plenum, pp.133–139
- Rosenberg GD, Hughes WW (1991) A metabolic model for the determination of shell composition in the bivalve mollusc, *Mytilus edulis*. Lethaia, 24: 83–96

- Rucker JB, Valentine JW (1961) Salinity response of trace element concentration in *Crassostrea virginica*. *Nature*, 190: 1099–1100
- Rush PF, Chafetz HS (1990) Fabric-retentive, non-luminescent brachiopods as indicators of original $\delta^{13}\text{C}$ and $\delta^{18}\text{O}$ composition: a test. *J. Sed. Petr.*, 60: 968–981
- Ryan CG, Cousens DR, Griffin WL, Sie SH, Suter GF (1990) Quantitative PIXE microanalysis of geological material using the CSIRO proton microprobe. *Nucl., Instr. and Meth. B47*: 55–71
- Saelen G (1989) Diagenesis and construction of the Belemnite rostrum. *Palaeontology*, 32: 765–798
- Saleuddin ASM, Wilbur KM (1983) Physiology part 1. In: *The Mollusca*, Wilbur K.M. (Ed.), vol.4, Academic Press, New York
- Schein E, Roux M, Barbin V, Chiesi F, Renard M, Rio M (1991) Enregistrement des paramètres écologiques par la coquille des bivalves: approche pluridisciplinaire. *Bull. Soc. géol. Fr.*, 162: 687–698
- Schmid J, Ramseyer K (1996) Effect of static recrystallisation of calcite on its cathodoluminescence. *Résumé, Int. Conf. on cathodoluminescence and related techniques in geosciences and geomaterials*: 137–138, Nancy
- Smith AB (1990) Biomineralization in Echinoderms. In: Carter JG (ed.). *Skeletal biomineralization: patterns, processes and evolutionary trends*. Van Nostrand Reinhold New York, vol. 1, pp 413–443
- Smith MM, Boyde A, Reid SA (1984) Cathodoluminescence as an indicator of growth increments in the dentine in tooth plates of Triassic lungfish. *N. Jb. Geol. Paläont. Mh.*, 1: 39–45
- Smith JV, Stenstrom RC (1965) Electron-excited luminescence as a petrologic tool. *J. Geol.*, 73: 627–635
- Sommer SE (1972) Cathodoluminescence of carbonates, 2. Geological applications. *Chem. Geol.*, 9: 275–284
- Stenzel HB (1962) Aragonite in the Resilium of Oysters. *Science*, 136: 1121–1122
- Stevenson RA, Ufret SL (1966) Iron, manganese and nickel in skeletons and food of the sea urchins *Tripneustes esculentus* and *Echinometra lacunter*. *Limn. Oceanogr.*, 11: 11–17
- Sturesson U (1976) Lead enrichment in shells of *Mytilus edulis*. *Ambio*, 5: 253–256
- Sturesson U (1978) Cadmium enrichment in shells of *Mytilus edulis*. *Ambio*, 7: 122–125
- Teng HH, Dove PM (1997) Surface site-specific interaction as aspartate with calcite during dissolution: implications for biomineralization. *Am. Min.*, 82: 878–887
- Towe KM, Hemleben Ch (1976) Diagenesis of magnesian calcite: evidence from miliolacean foraminifera. *Geology*, 4: 337–339
- Tucker ME, Wright VP (1990) *Carbonate sedimentology*. Blackwell Scientific Publications, Oxford
- Veizer J (1974) Chemical diagenesis of belemnite shells and possible consequences for paleotemperature determinations. *N. Jb. Paläont. Abh.*, 147: 91–111
- Veizer J (1977) Geochemistry of lithographic limestones and dark marls from the Jurassic of southern Germany. *N. Jb. Paläont. Abh.*, 153: 129–146
- Veizer J (1983) Chemical diagenesis of carbonates: theory and application of trace element technique. In: Arthur MA, Anderson TF, Kaplan IR, Veizer J and Land LS (eds). *Stable isotopes in sedimentary geology*. Dallas: SEPM short course n°10, pp 3–100
- Walker G, Asumere OE, Kamaluddin B (1989) Luminescence spectroscopy of Mn^{2+} centre in rock-forming carbonates. *Min. Mag.*, 53: 201–211
- Walter LM, Morse JW (1984) Reactive surface area of skeletal carbonates during dissolution: effect of grain size. *J. Sed. Petr.*, 54: 1081–1090
- White LK, Szabo A, Carkner P, Chasteen ND (1977) An electron paramagnetic resonance study of manganese (II) in the aragonite lattice of a clam shell, *Mya arenaria*. *The J. Physic. Chemis.*, 81: 1420–1424
- Wilbur KM, Saleuddin ASM (1983) Shell formation. In: Saleuddin ASM. and Wilbur KM (Eds), *The Mollusca*, vol.4, Physiology part 1. Academic Press, New York, pp 235–287

- Wildman TR (1970) The distribution of Mn^{2+} in some carbonates by electron paramagnetic resonance. *Chem. Geol.*, 5: 167–177
- Williams A (1968a) A history of skeletal secretion among articulate brachiopods. *Lethaia*, 1: 268–877
- Williams A (1968b) The evolution of the shell structure of articulate brachiopods. *Palaeontology*, spec. paper.n°2: 55 p
- Yang C, Homman NP-O, Malmqvist KG, Johansson L, Halden NM, Barbin V (1995) Ionoluminescence – A new tool for the Nuclear Microprobe in Geology. *Scann. Microsc.*, 9: 43–62

Quantitative High Resolution Spectral Analysis of Mn²⁺ in Sedimentary Calcite

DIRK HABERMANN, ROLF D. NEUSER, DETLEV K. RICHTER

1

Introduction

Cathodoluminescence (CL) is used to detect trace element distribution in minerals. Thus, a possible quantitative analysis of activator elements based on their CL intensity has served as the incentive for numerous investigations. There is general agreement in the literature about the role of Mn²⁺ as the most important activator element, and of Fe²⁺, as the most efficient quencher element in calcites and dolomites (e.g. Richter and Zinkernagel 1975, 1981; Pierson 1981; Frank et al. 1982; Fairchild 1983; Grover and Read 1983; Machel 1985; Meyers and Lohmann 1985; ten Have and Heijnen 1985; Mason 1987; Walker et al. 1989; Mason and Mariano 1990; Machel et al. 1991). But the correlation of CL intensity and Mn concentration is controversially discussed. Frank et al. (1982) reported that CL intensity is controlled by the Fe/Mn ratio only. A much more complex correlation was revealed by Mason (1987) and Hemming et al. (1989), in which CL intensity is predominantly controlled by the absolute Mn content and the efficiency of Fe quenching, which increases with increasing Mn concentration. Fairchild (1983) and Pierson (1981), however, pointed out that Fe quenching is not affected by increasing Mn concentrations. Savard et al. (1995) suggested an "erratic" Mn²⁺-activated CL behavior for Mn concentrations below 225 ppm in calcite.

Not only the correlation between CL intensity and the activator concentration is a topic of discussion, but also the lower limit of activator concentrations above which CL occurs. There is a widespread assumption that a concentration level of 10–30 ppm is needed before Mn²⁺ activation in calcite is present (e.g. Savard et al. 1995; Bruhn 1995). However, Walker et al. (1989) pointed out that there is no reason why Mn²⁺ activation should be inhibited below this concentration level at low Fe concentrations. The only limitation is the sensitivity of the detector system. Habermann et al. (1996b, 1998) revealed a Mn²⁺-activated CL below 1 ppm Mn in calcite. It is obvious that one possible reason for these controversial interpretations is the variety of analytical methods, equipment and working conditions, as numerous studies are based on the subjective eye-detection of CL intensity (e.g. Richter and Zinkernagel 1981; Fairchild 1983; Savard et al. 1995; Bruhn 1995). Generally, spectroscopic investigations appear to be more reliable and consistent, as they provide measurable values (e.g. Mason 1987; Hemming et al. 1989; Walker et al. 1989; El Ali et al. 1993; Homman et al. 1994 [ionoluminescence]; Habermann 1997).

Quantitative X-ray fluorescence spectroscopy is based on the fact that, at a given energy, the amount of the characteristic X-ray photons is proportional to the element concentration (Smith 1976). The same correlation is attributed to CL. At a given beam energy the number of CL photons is proportional to the activator element content.

It is a fact that quantitative X-ray fluorescence spectroscopy, e.g. electron micro probe (EMP), proton-induced X-ray emission (PIXE), needs well defined analysis conditions and extensive knowledge of complex physical processes (e.g. the interaction between the particle beam and the solid). This is also valid for quantitative CL spectroscopy. So, in the following, principle necessities of the methodology, including examples of essential analyses and limitations and advantages of quantitative high resolution spectroscopy of CL emission (QHRS-CL; Habermann et al. 1996b) are documented and discussed.

2 Cathodoluminescence Microscopes and Spectroscopy: Instrumentation

Basically, constant analysis conditions are necessary to carry out QHRS-CL. This includes a high degree of constancy of the electron beam and an objective and sensitive detector system. It is well documented that the CL signal reacts very sensitively to variations in element distribution and concentration as well as changes in the crystal lattice (e.g. Mason 1987; Walker and Burley 1991; Habermann et al. 1996b). Therefore, estimating CL intensity visually is never suitable for quantitative investigations because there is always a subjective factor (Walker and Burley 1991). However, spectroscopic investigations are convenient, and thus low CL intensities will require a very sensitive detector system as well as an efficient excitation source.

Usually the CL spectra are obtained by dispersing the CL signal of the area of interest by a grating spectrometer. Most spectrometers in use are monochromators which project the light signal to a dispersion grating, transforming the polychromatic beam into a spectrum. This spectrum is moved along a narrow exit slit of the spectrometer by turning the grating, which allows detection of the intensity of separate (monochromatic) spectral bands by a photomultiplier. Newer high speed spectrographs use fixed gratings with different dispersion rates. The whole spectrum is collected at once by a highly sensitive charge-coupled device (CCD) array mounted to the exit port. This assembly and the associated electronic components are called an optical multichannel analyzer (OMA). Although OMA systems are still quite expensive, they have several advantages over monochromators:

1. The spectra can be stored in very short times (100 ms).
2. Low CL intensities can be detected correctly.
3. The wavelengths of the spectrum can be stored simultaneously.
4. Post-processing is easily done because the spectrum is obtained digitally.

For quantitative analyses this technique is a must. It is also advantageous but not essential to use a "hot" cathode CL microscope instead of a device equipped with

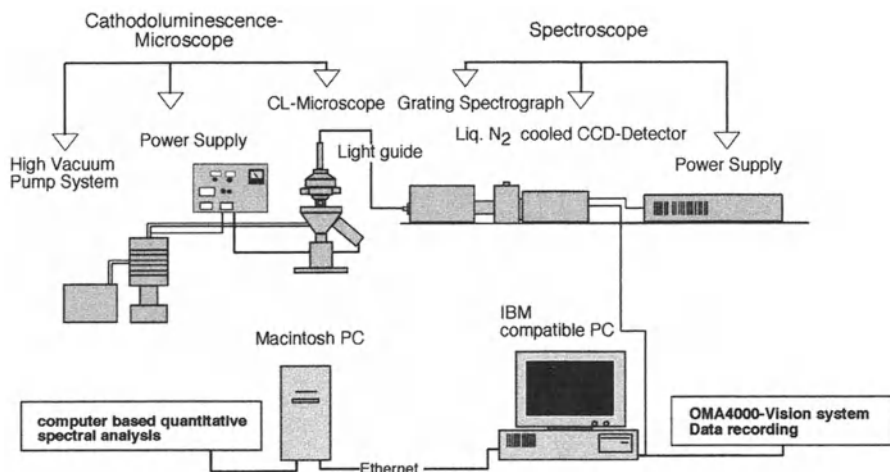


Fig. 1. Schematic view of the QHRS-CL (quantitative high resolution spectroscopy of CL emission) device developed at the Ruhr-University Bochum

a “cold” cathode. “Hot” cathode CL microscopes, as developed by Zinkernagel (1978), Neuser (1988, 1995), and Ramseyer et al. (1989), guarantee constant and well defined analysis conditions and a very efficient excitation. This is of particular importance when analyzing small amounts of Mn²⁺, rare-earth elements (REE) and investigating the intrinsic CL of carbonates and other minerals. The schematic view (Fig. 1) of the QHRS-CL device developed by the authors at the Ruhr-University Bochum shows a possible assembly for quantitative CL spectroscopy.

CL spectra can be very complex due to an overlapping of different emission bands, which are not only related to Mn²⁺-activated CL. These peaks can either be intrinsic or related to different activator elements. To separate the different peaks, it is necessary to fit these spectra using computer programs. The program we use has structure similar to that of commercial quantitative x-ray fluorescence spectroscopy (e.g. Guelph PIXE software package; Maxwell et al. 1995). However, such programs have to be adapted to the special needs of quantitative CL.

To estimate the correlation between CL intensity and activator concentration external analytical methods are needed. As CL intensity very sensitively documents small scale changes in the amount of activator elements and their distribution, it is necessary to employ a sensitive analytical method. This requires a highly sensitive microbeam technique offering detection limits much below 100 ppm. Today, only a few methods, e.g. PIXE, secondary ion mass spectrometry (SIMS), and laser ablation (LA)-ICP-MS, meet these requirements, each of which has its own limitations compared to the CL analysis method. The most important differences are the size of the analyzed spot and depth of penetration. PIXE or SIMS are suitable methods to calibrate quantitative CL spectroscopy. The spot size (10–50 μm) and depth of penetration (up to some μm) of these methods do not differ too much from that of CL spectroscopy. However, these common

microbeam analysis methods cannot distinguish between substituted elements and elements attributed to other phases or fluid inclusions. Nevertheless, in a first approximation, it may be supposed that Mn is still incorporated in the carbonate matrix.

3

Physics of Luminescence

When an electron beam strikes a surface, the bombarding electrons penetrate into the sample and cause different kinds of processes, including back-scattering of the projectile electrons, production of secondary electrons, characteristic X-rays, diffracted X-rays, X-ray continuum, CL and sample heating. These processes are dependent on the energy of the electron beam and thus decrease with decreasing electron beam energy and increasing depth of interaction with the solid.

In a simplified model, X-ray fluorescence and CL are caused by electron excitation of atomic shells to higher energetic states and their subsequent transition to lower energetic states (for more details see Walker, this volume).

The energy difference between the excited state and ground state (electron transition: ${}^4T_{1g} \rightarrow {}^6A_{1g}$) of the non-bonding 3d-electrons of Mn^{2+} ions (paramagnetic center) is proportional to the crystal field strength. Therefore the wavelength of the Mn^{2+} emission is a function of the host lattice structure. In contrast, REE^{3+} show only a very small interaction with the host crystal field and therefore, these elements have constant peak positions. For more details, see Marfunin (1979), Walker et al. (1989) and literature on crystal field theory (e.g. Burns 1993).

4

Characteristics of Luminescence Spectra of Carbonates

4.1

Estimating Mn^{2+} -Activated Cathodoluminescence in Calcite and Dolomite

Regarding Mn^{2+} -activated luminescence of carbonates and other minerals, there are still several questions concerning the correlation of wavelength of Mn^{2+} -activated emission and crystal structure crystal field of the mineral.

The wavelength of Mn^{2+} -activated CL is dominantly controlled by the symmetry and the interatomic distance of the central metal ion and ligands (Medlin 1968). In case of similar symmetries of the carbonate structures (e.g. calcite group (space group $R\bar{3}$)), the wavelength of Mn^{2+} -activated CL is dominantly controlled by the metal ion-oxygen distance (e.g. Sommer 1972a,b; Walker et al. 1989). While rhombic carbonates with decreasing metal ion-oxygen distances induce an increase in wavelength of Mn^{2+} -activated emission, trigonal carbonates show an inverse trend (Sommer 1972a).

In the structure of stoichiometric dolomite (space group $R\bar{3}$) Mg^{2+} and Ca^{2+} are ordered, whereas in calcian dolomites and in magnesian calcites the degree of order of the Mg^{2+} ions is lower. There is a linear-positive correlation between Mg content and average metal ion-oxygen distance in magnesian calcite (Althoff 1977). But this correlation does not induce an uniform shift in the wavelength of the Mn^{2+} -activated CL to higher values. Although Sommer (1972a) and Koberski (1992) described a nearly linear correlation between Mg content of calcite and the shift of the Mn^{2+} peak to higher wavelengths, there are other examples that differ in a wide range (10–~25 nm) from such a linear correlation (Fig. 2): The Mn^{2+} peaks in sedimentary Mg-calcite (>0.8 mol% MgCO_3) do not show only higher wavelengths but also higher values of the full width of the peak half height maximum (FWHM) compared to Mg-free calcite. Nearly Mg-free calcite only shows FWHM values of ~90 nm, whereas Mg-calcite shows values of ~95–128 nm. Recent results of high resolution CL spectroscopy (Habermann 1997) document that in magnesian calcite (>0.8–1 mol% MgCO_3) the Mn^{2+} -activated emission is composed of two peaks related to the Mn^{2+} substitution in two different lattice positions (Fig. 3). The first peak is located at around 605 nm with a FWHM value of 90 nm. This peak can be clear-

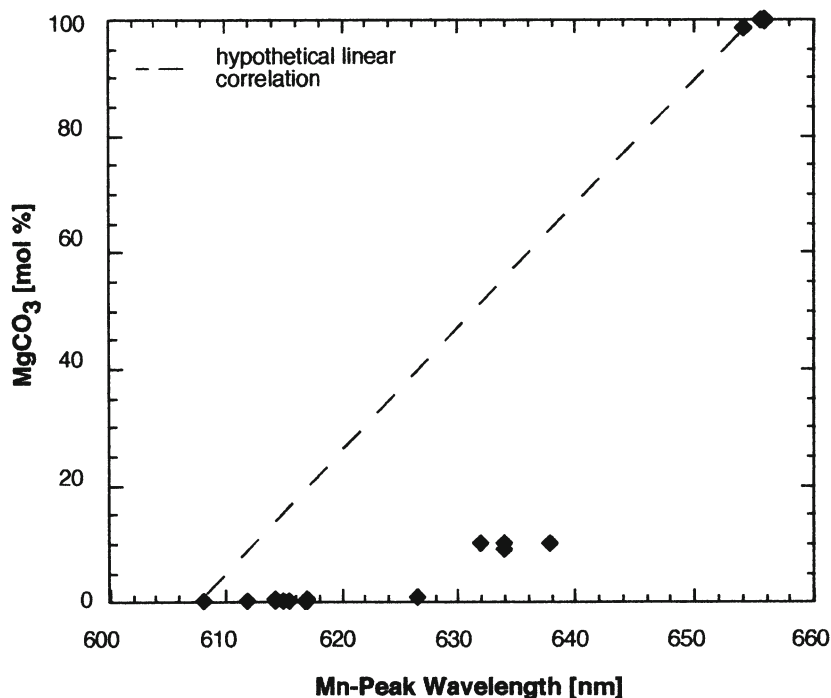


Fig. 2. Wavelength of Mn^{2+} -activated CL in calcite and magnesite. There is no linear correlation between the Mg content and Mn^{2+} -peak wavelength. The deviation from a hypothetical linear correlation is obvious. All samples have Fe and other trace element concentrations below 6000 ppm. Therefore this deviation can not be explained by substitution of these elements

ly attributed to Mn^{2+} -activated emission in a nearly Mg-free calcite structure ("main-structure") (crystal field splitting parameter $\Delta=7100\text{ cm}^{-1}\pm 200\text{ cm}^{-1}$) (Δ data from Walker et al. 1989). The second peak shows a maximum at 654 nm and an FWHM value of 90 nm. As such peaks are well known for Mn^{2+} incorporated in the Mg^{2+} position of magnesite (e.g. Spötl 1991), this peak can be attributed to the Mn^{2+} activation in a magnesite-like "(sub)-structure" of magnesian calcite.

Pure magnesite shows a peak maximum wavelength of 656 nm for Mn^{2+} , allowing a first approximation of Δ as $8450\text{ cm}^{-1}\pm 200\text{ cm}^{-1}$ (Habermann 1997).

The described two Mn^{2+} peaks in magnesian calcite can only be analyzed in samples containing more than $\sim 1\text{ mol}\%$ MgCO_3 . This coincides with high resolution transmission electron microscopy (HRTEM) analyses (Khan and Barber 1990) in which "ribbon microstructures" are determined at MgCO_3 contents above $\sim 0.8\text{ mol}\%$. These structures are interpreted as coherent Mg-dominated microstructures (Reeder 1992). Here, CL spectroscopy and HRTEM analysis reveal that Mg^{2+} is not strictly homogeneously distributed and three-dimensional MgCO_3 domains must occur in magnesian calcite.

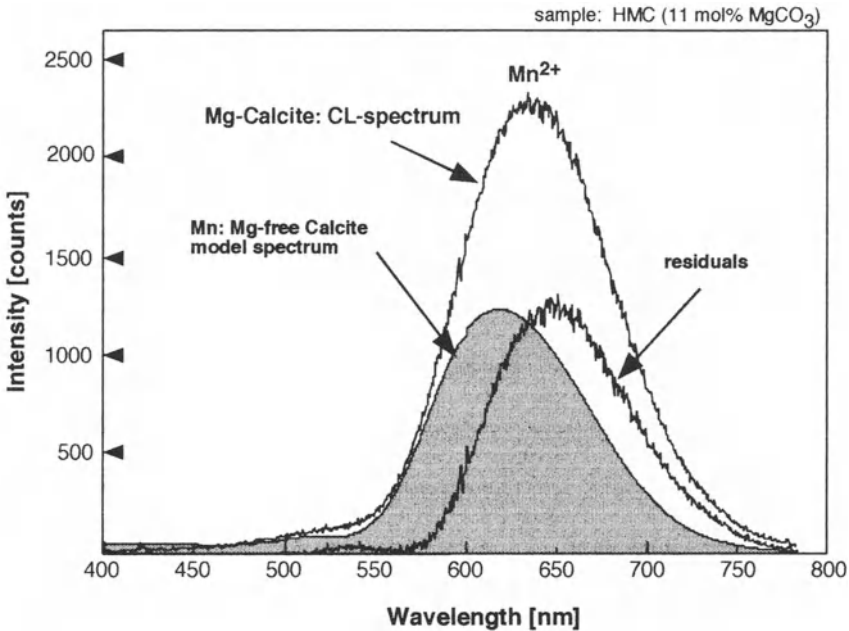


Fig. 3. Spectrum of Mn^{2+} -activated CL in Mg-calcite (sample: HMC, echinoderm skeleton fragment (11 mol% MgCO_3)). Peak position at 632 nm and the full width of the peak height (FWH) of 100 nm are both higher than in an assumed linear correlation between wavelength of Mn peak and Mg content. Two peaks can be established by subtracting a reference spectrum of Mn-activated CL in Mg-free calcite. The residuals clearly show the characteristics of Mn^{2+} -activated CL in a crystal field of a magnesite-like structure. This indicates that Mn^{2+} is substituted in two different lattice positions in Mg-calcite. (Habermann 1997)

The Mn²⁺ distribution quotient

$$K_D[Mn^{2+}] = \frac{Mn^{2+} \text{ Mg-Position}}{Mn^{2+} \text{ Ca-Position}}$$

of sedimentary magnesian calcites is regularly >5 (Habermann 1997). So with only a few mol % MgCO₃ incorporated into the calcite lattice and a high K_D value, a distinct part of the Mn²⁺-activated CL can be attributed to an intense Mn²⁺ peak at 654 nm. As the emission maxima of the two Mn²⁺ peaks (605 and 654 nm) are not in the same spectral region, the absolute CL intensity is the sum of the overlapping parts of these two Mn²⁺ peaks. But this is not equal to the intensity of both peak maxima separately. For that reason the integral of the Mn²⁺ peak(s), or estimating the intensity of the two Mn²⁺ related peaks, in a spectrum is necessary for exact determination of the Mn²⁺-activated CL intensity.

As described before, the complex correlation between the Mn²⁺-activated CL intensity and the lattice position is well known in dolomite. In the dolomite structure the Mn²⁺ ion may be incorporated in the Ca as well as the Mg position (e.g. Walker and Burley 1991; El Ali et al. 1993). From there, the Mn²⁺ peaks can emit at 575 nm (Mn²⁺ in Ca position) and 660 nm (Mn²⁺ in Mg position) (El Ali et al. 1993; Habermann et al. 1996c).

Clearly, the correlation between Mn content and CL intensity can only be determined correctly by analyzing the absolute intensity of all Mn²⁺ peaks or by integrating the Mn²⁺-activated emission.

4.2

Correlation Between Mn²⁺-Activated Cathodoluminescence Intensity and Mn Content of Calcite

The correlation between Mn²⁺-activated CL intensity and analyzed Mn and Fe content of sedimentary and hydrothermal calcite is shown in Fig. 4 (sample description see Table 1). The Mn and Fe concentrations vary between 16–1000 and 20–4000 ppm, respectively, with no or only minor inhomogeneities in CL. The linear correlation between Mn content and Mn²⁺-activated CL intensity reveals that the CL intensity is strongly correlated with the activator element concentration. This correlation is also the circumstantial evidence for the beginning of Mn²⁺ activation being in the sub-ppm range. The CL spectra of samples with Mn concentrations below 20 ppm analyzed with PIXE (detection limit of PIXE=10 ppm; Meijer et al. 1994) clearly show intense Mn²⁺ peaks in addition to the intrinsic bands (Fig. 5a–e). Thus, Mn²⁺ activation begins much below 20 ppm Mn. There is in fact no concentration level for Mn²⁺ activation in the range of 10–30 ppm Mn content, as published by numerous authors (e.g. Savard et al. 1995). The continuous linear increase in Mn²⁺-activated CL intensity with increasing Mn content – if not sensitized or quenched – is the circumstantial evidence that CL intensity is initially controlled by the Mn concentration. There is no physical reason why Mn²⁺ activation could not start at one atom of the irradiated crystal lattice volume if the Fe concentration is low (see Habermann et al. 1998). The latter fact is demonstrated by the linear correlation between CL intensity and Mn content (<1000 ppm Mn).

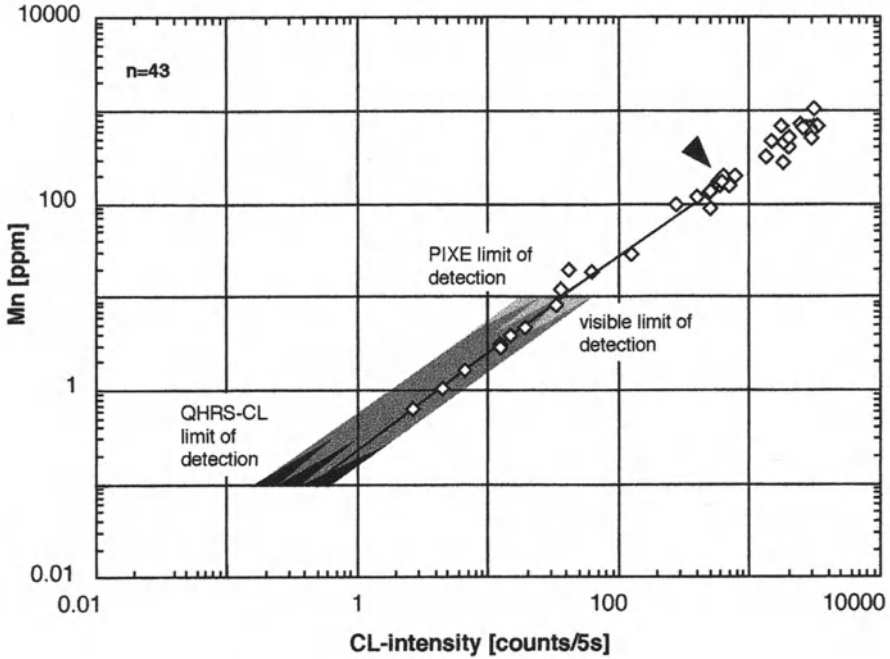


Fig. 4. Correlation between CL intensity (normalized to counts/5 s) and Mn and Fe content in visually homogeneously luminescent calcite (see Table 1). The data reveal an excellent linear correlation ($R=0.97$) in the range between 19–1000 ppm. Fe contents up to 2000 ppm have no influence on this relation. Mn contents below the detection limit of PIXE (10 ppm) were analyzed by QHRS-CL. The calibration of QHRS-CL is based on analytical data of an Iceland spar (sample I-SPAT). The plotted line (arrow) connects zero with the analyzed Iceland spar cluster. (Modified from Habermann et al. 1998)

Table 1. Fe and Mn analyses of sedimentary calcite

No.	Sample analyses	Concentration (ppm) (error $\pm 10\text{--}25\%$)		CL intensity (counts/5 s)	Description	Visually homogeneous	Method: QHRS-CL* PIXE**
		Mn	Fe				
1	K-SUR-P1	12	65	36	Hydrothermal calcite	*	**
2	K-SUR-P2	20	93	40	Hydrothermal calcite	*	**
3	DB142-1	3.1	-	12.2	Hydrothermal calcite	*	*/**
4	DB142-2	3.0	-	12	Hydrothermal calcite	*	*/**
5	DB143-P1	98	24	273	Burial calcite cement	*	**
6	DB143-P2	159	620	695	Burial calcite cement		**
7	DB143-P3	91	1333	609	Burial calcite cement		**
8	DB143-P4	29	641	125	Burial calcite cement	*	**
9	SINTER1-2	0.7	n.a.	2.5	Sinter calcite	*	*/**

Table 1. Continued.

No.	Sample analyses	Concentration (ppm) (error ± 10 –25%)		CL intensity (counts/5 s)	Description	Visually homogeneous	Method: QHRS-CL* PIXE**
		Mn	Fe				
10	GAP1-1	4.8	-	19	Sinter calcite	*	*
11	KAP HIRO1	4	n.a.	15	Pleistocene brachiopod shell	*	*
12	KAP HIRO23	8.2	n.a.	32	Pleistocene brachiopod shell	*	*
13	MALACH ^a	-	-	-	Sinter calcite	*	*
14	TREZ-1	1.7	n.a.	6.7	Recent brachiopod shell	*	*/**
15	I-SPAT-P1	159	241	700	Hydrothermal calcite	*	**
16	P2	168	212	726	Hydrothermal calcite	*	**
17	P3	159	186	592	Hydrothermal calcite	*	**
18	P4	198	248	644	Hydrothermal calcite	*	**
19	P5	173	130	571	Hydrothermal calcite	*	**
20	P6	136	57	504	Hydrothermal calcite	*	**
21	P7	117	42	399	Hydrothermal calcite	*	**
22	TRI-W-1	172	878	615	Burial calcite cement	*	**
23	2	156	629	582	Burial calcite cement	*	**
24	3	130	351	482	Burial calcite cement	*	**
25	4	171	377	567	Burial calcite cement	*	**
26	5	202	390	779	Burial calcite cement	*	**
27	Jt30 -3	56	393	25	Hydrothermal calcite		**
28	5	34	310	39	Hydrothermal calcite		**
29	Fb5 ^b -1	511	62	3488	Burial calcite cement		**
30	2	541	59	2667	Burial calcite cement		**
31	3	642	174	2603	Burial calcite cement		**
32	4	677	354	3233	Burial calcite cement		**
33	5	722	387	3328	Burial calcite cement		**
34	6	770	304	2927	Burial calcite cement		**
35	7	736	185	3173	Burial calcite cement		**
36	8	810	120	3666	Burial calcite cement		**
37	9	833	204	3206	Burial calcite cement		**
38	10	744	103	3175	Burial calcite cement		**
39	11	614	75	3669	Burial calcite cement		**
40	12	651	97	3334	Burial calcite cement		**
41	13	425	811	2708	Burial calcite cement		**
42	14	241	2331	943	Burial calcite cement		**
43	15	240	2942	851	Burial calcite cement		**
44	16	175	2942	604	Burial calcite cement		**
45	21	88	845	511	Burial calcite cement	*	**

Table 1. Continued.

No.	Sample analyses	Concentration (ppm) (error ± 10 -25%)		CL intensity (counts/5 s)	Description	Visually homogeneous	Method: QHRS-CL* PIXE**
		Mn	Fe				
46	22	64	633	578	Burial calcite cement		**
47	25	400	184	1980	Burial calcite cement	*	**
48	26	273	172	1784	Burial calcite cement	*	**
49	27	310	800	1331	Burial calcite cement	*	**
50	28	465	473	1460	Burial calcite cement	*	**
51	29	470	488	1782	Burial calcite cement	*	**
52	30	519	325	2006	Burial calcite cement	*	**
53	31	669	174	3204	Burial calcite cement	*	**
54	32	659	207	1767	Burial calcite cement	*	**
55	33	636	259	2668	Burial calcite cement	*	**
56	34	590	326	2668	Burial calcite cement	*	**
57	35	499	540	2981	Burial calcite cement	*	**
58	36	613	414	2865	Burial calcite cement	*	**
59	37	696	124	2458	Burial calcite cement	*	**
60	38	641	98	2770	Burial calcite cement	*	**
61	39	648	86	2934	Burial calcite cement	*	**
62	40	668	85	3091	Burial calcite cement	*	**
63	41	1011	51	3054	Burial calcite cement	*	**
64	Pb19 T -1 ²)	202	814	901	Burial calcite cement		**
65	2	400	747	871	Burial calcite cement		**
66	3	273	489	1326	Burial calcite cement		**
67	4	310	1745	899	Burial calcite cement		**
68	5	465	1777	823	Burial calcite cement		**
69	6	470	1368	885	Burial calcite cement		**
70	7	519	2394	800	Burial calcite cement		**
71	8	669	2274	588	Burial calcite cement		**
72	9	659	4035	662	Burial calcite cement		**
73	10	636	457	402	Burial calcite cement		**
74	11	590	153	305	Burial calcite cement		**
75	12	499	164	224	Burial calcite cement		**
76	13	613	194	3104	Burial calcite cement		**
77	14	696	126	2065	Burial calcite cement		**
78	15	641	n.a.	230	Burial calcite cement		**
79	16	648	1834	622	Burial calcite cement		**
81	17	668	1743	824	Burial calcite cement		**
82	18	1011	557	1038	Burial calcite cement		**
83	Pb19S-1 ^b	422	2628	1677	Burial calcite cement		**
84	2	449	2540	1661	Burial calcite cement		**

Table 1. Continued.

No.	Sample analyses	Concentration (ppm) (error ±10–25%)		CL intensity (counts/5 s)	Description	Visually homogeneous	Method: QHRS-CL* PIXE**
		Mn	Fe				
85	3	447	2459	1641	Burial calcite cement		**
86	4	415	2312	1648	Burial calcite cement		**
87	5	276	1632	2224	Burial calcite cement		**
88	6	304	1939	2203	Burial calcite cement		**
89	7	396	1927	1442	Burial calcite cement		**
90	8	428	2060	1734	Burial calcite cement		**
91	9	369	1731	1313	Burial calcite cement		**
92	10	435	2882	1545	Burial calcite cement		**
93	11	440	1856	1668	Burial calcite cement		**
94	12	423	1871	1623	Burial calcite cement		**
95	13	1131	2825	1362	Burial calcite cement		**
96	14	443	2938	1324	Burial calcite cement		**
97	15	515	1956	1926	Burial calcite cement		**
98	16	439	712	1147	Burial calcite cement		**
99	17	286	697	1147	Burial calcite cement		**
100	18	309	1006	1136	Burial calcite cement		**
101	19	309	1012	1311	Burial calcite cement		**
102	20	272	1052	1207	Burial calcite cement		**
103	OP1–19 ^b	19	4	60	Calcite: belemnite rostrum	*	**
104	OP1–21 ^b	1	28	5	Calcite: belemnite rostrum	*	*/**

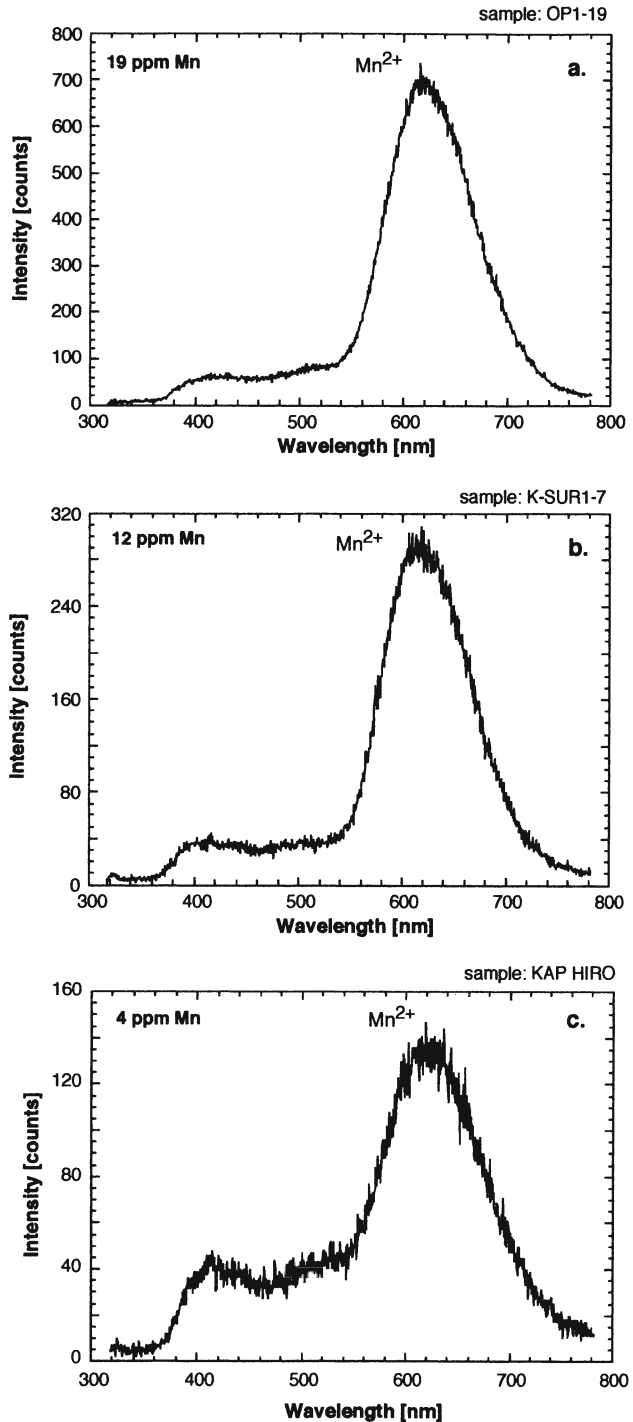
Mn contents >10 ppm analyzed by PIXE. Mn contents below the detection limit of PIXE (10 ppm) are analyzed by QHRS-CL (this work and Habermann et al. 1998). All mentioned CL analyses are data of this work or from Habermann (1997).

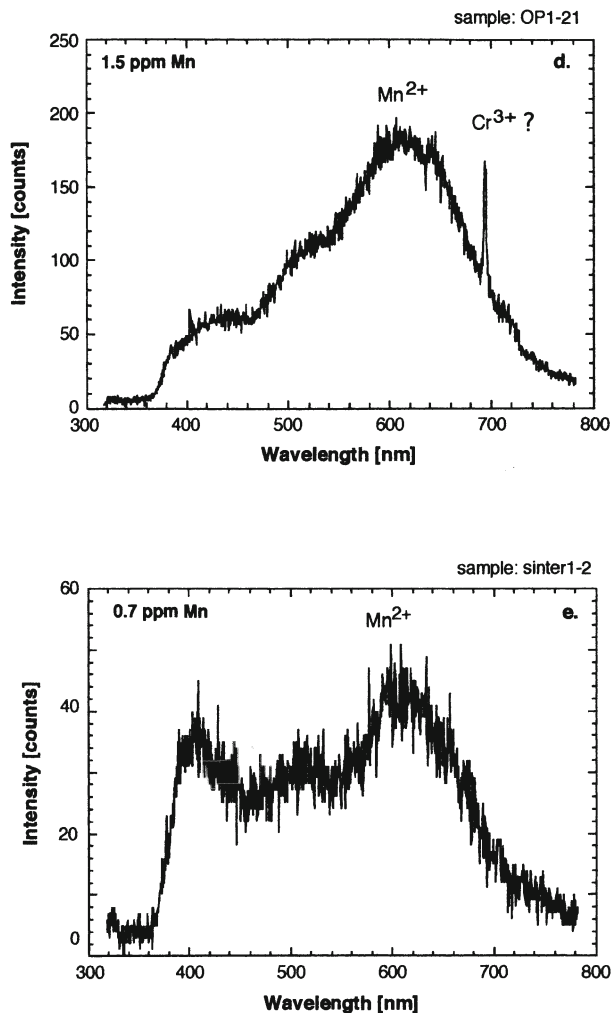
n.a., not analysed; –below detection limit.

^aNot plotted in Fig. 6. as no Mn²⁺-activated CL is detectable.

^bPIXE analyses from Bruhn (1995) (values of sample FB5 are mean of two PIXE analyses). All analyses of CL intensity are data from Habermann (1997).

Fig. 5a–e. CL spectra of calcite with Mn concentrations below 20 ppm (detection limit of PIXE=10 ppm) clearly show intense Mn peaks in addition to the intrinsic band. As the Mn^{2+} peaks are of low intensity there are only blue-violet to blue CL colors present (see Fig. 12a–c). **a** Sample: OP1-19, belemnite rostrum; recording time: 60 s; **b** sample: K-SUR, hydrothermal calcite cement; recording time: 30 s; **c** sample KAP-HIRO, brachiopod shell; recording time: 30 s; **d** sample: OP1-21, belemnite rostrum; recording time: 120 s; **e** sample: sinter1–2, stalagmite; recording time: 60 s. (Habermann et al. 1998)





As described before, a small scale inhomogeneity of the Mn distribution, and Fe- and self-quenching can also have a negative effect on estimating the Mn content using CL spectroscopy. This relation is shown in Fig. 6. The analysis results are highly consistent with those of Hemming et al. (1989; Fig. 1a).

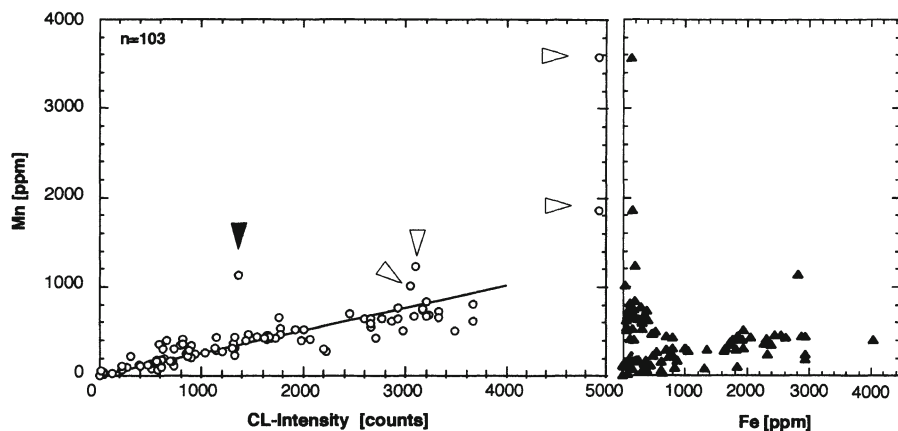


Fig. 6. Correlation between CL intensity and Mn and Fe content in visually homogeneous and slightly inhomogeneously luminescent calcites. The poor correlation ($R=0.75$) compared to the data in Fig. 4 is due to inhomogeneities in the Mn distribution and higher absolute Mn and Fe content (>1000 and >3000 ppm). However, a linear correlation is determinable (notice the high conformity with data of Hemming et al. 1989). The plotted line refers to the analyzed Iceland spar (sample I-SPAT) as a reference for, e.g., quenching effects. The *white arrows* mark samples with dominant Mn self-quenching. The *black arrow* indicates a sample with both Mn self-quenching and Fe quenching

4.2.1

Estimating the Detection Limit of Quantitative Cathodoluminescence Spectroscopy

The CL spectra (Fig. 5a–e) document that Mn and REE peaks are high, although the Mn and REE concentrations are below the detection limit of PIXE. A discriminated CL peak with a confidence level of 99.86% the smallest accepted CL peak area in a spectrum is $3\sqrt{Nb}$, where Nb is the background at the peak position (Homman et al. 1994). In view of the variations of analysis conditions the detection limit has to be fixed for each spectrum separately. In summary, at present the calculated detection limit of QHRS-CL is mostly in the range of 0.1–0.3 ppm for a recording time of 2 min. Using the scanning method to record the CL signal, this will be in the range of 1–3 ppm and also mostly below the limit of PIXE.

5

Quenching and Sensitizing of Mn^{2+} -Activated Cathodoluminescence

The influence of quenching is of particular importance with respect to CL intensity and acts to limit quantitative CL spectroscopy. There are four major sources of that effect CL intensity:

1. Self-quenching at high activator concentrations
2. Quenching by Fe and other quencher elements

3. Thermal quenching
4. Quenching by structural defects

5.1

Self-Quenching and Quenching by Fe and Other Quencher Elements

Self-quenching at high activator concentration plays the most important role. It is due to a transfer of excitation energy from the absorbing ion to another, similar ion which is more efficient than the emitted luminescence (e.g. Marfunin 1979; Machel et al. 1991). In the literature there are different opinions about the concentration level at which self-quenching occurs. Mason (1987) states a beginning of self-quenching at >500 ppm Mn, while our results (Fig. 6) reveal an occurrence at a slightly higher concentration level (>1000 ppm).

The second important quenching effect is attributed to Fe. Mn²⁺-activated CL is quenched at >3000–4000 ppm Fe and the degree of Fe quenching is controlled by the Fe and Mn content (Fig. 6). Here, the efficiency of Fe quenching increases with increasing Mn content according to decreasing average Fe²⁺ and Mn²⁺ ion distance.

In a first approximation the Fe content in carbonates can be attributed to the Fe²⁺ ion. Quenching abilities of Fe³⁺ cannot be excluded, but compared to Fe²⁺ the possible Fe³⁺ concentrations in sedimentary calcite and dolomite are too low to have a considerable influence.

Other quencher elements like Ni²⁺ or Co²⁺ are of no importance due to their low concentrations in sedimentary calcite and their much lower efficiency compared to Fe²⁺ (Marfunin 1979).

The Fe/Mn ratio can vary over a wide range without changes in CL intensity (Hemming et al. 1989; Mason 1987; Habermann 1997) and therefore has no effect on the CL intensity. The large amount of data showing low CL intensity and a relatively high Fe/Mn ratio – and also the reverse trend – are based merely on the crystal growth conditions of sedimentary and hydrothermal carbonates and not on a correlation of the Fe/Mn ratio.

5.2

Thermal Quenching

If a sample is bombarded with accelerated electrons or other radiation, heating of the surface is one important effect. In addition to CL, this heating may cause thermoluminescence if the temperature increases. Moreover, heating also causes a decrease in luminescence intensity. Figure 7 illustrates the decrease in CL intensity during electron bombardment. The strong increase in sample temperature depends on the electron energy, the beam density and the thermal conductivity of the sample. This effect is reversible by cooling down the sample to room temperature. As the analyzed samples were coated with a thin gold layer, a charging of the sample resulting in quenching can also be excluded. So, this temporary decrease in CL intensity can be clearly attributed to thermal quenching.

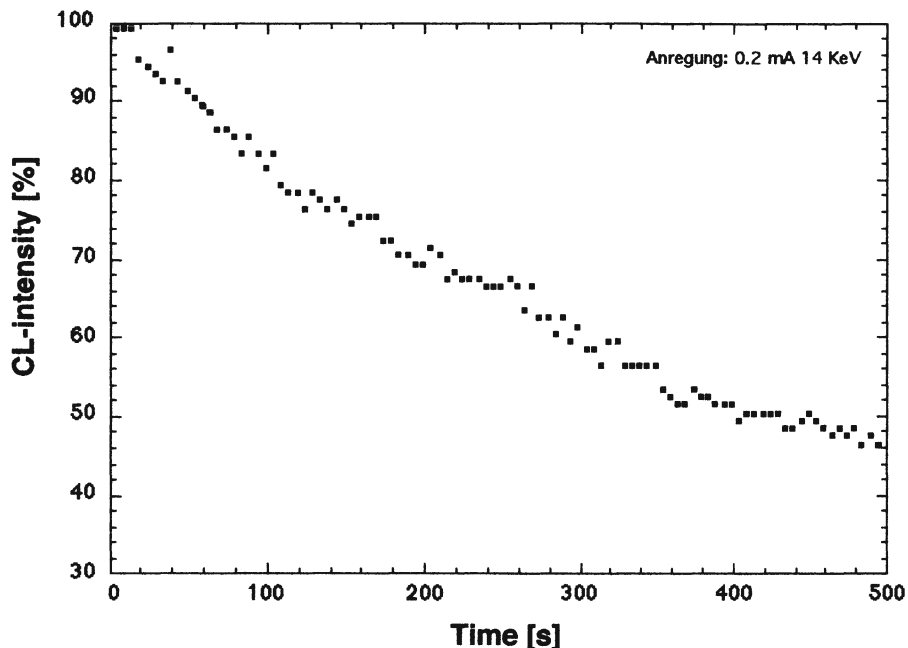


Fig. 7. Relation between CL intensity and time of irradiation by an electron beam. After 500 s the intensity is only about 50%

Thermal quenching is due to an increase of the efficiency of nonradiative electron transitions compared to radiative electron transitions at higher temperatures (Walker 1985). There are different opinions regarding to what extent the temperature is raised if a solid is bombarded with accelerated electrons. Ranges vary between ~ 50 and 100 °C (Weast and Astle 1981) and ~ 500 and 600 °C (Marshall 1988). However, for quantitative CL spectroscopy it is not necessary to estimate the sample temperature exactly. Measuring the relationship between duration and power of the electron bombardment and the decreasing CL intensity is sufficient, but this relationship has to be determined for each mineral group separately. As the thermal conductivity of coating materials is very different, the samples should always be covered with a conductive layer of the same kind and thickness.

5.3 Quenching by Lattice Defects

In contrast to thermal influences, quenching by lattice defects (e.g. Mason 1994) is of importance as the intensity of CL is reduced permanently. This is caused by growth defects, defects generated by intense deformation and radiation damage (Marshall 1988; Mason 1994). Investigations reveal that the first two reasons can be excluded when analyzing sedimentary and hydrothermal calcite (Habermann 1997).

To investigate defects generated by radiation, experiments with accelerated electrons (beam source: CL microscope) and protons (beam source: PIXE) were carried out. In our study we did not investigate the effect of long-term bombardment; rather, our main objective was short-term electron and proton irradiation, which is more similar to the spectroscopic analysis procedure. Figure. 8 shows the spectra of two samples (one calcite and one apatite) irradiated by an electron beam and proton beam, respectively.

The investigations reveal a slight increase in intrinsic CL at 520–700 nm wavelength (Fig. 8a) if pure calcite is irradiated by an electron beam of a current density of 15 $\mu\text{A}/\text{mm}^2$ for 15 min in a vacuum of $<10^{-7}$ Torr. Peaks are located at 580 and 660 nm. We propose a relationship between these peaks and intrinsic emission which is caused by radiation damage. As the intrinsic peaks at about 400 nm are attributed to Ca⁺ and CO₃⁻ centers (Calderón et al. 1984), the peaks at 580 and 660 nm can possibly be attributed to broken Ca-O bondings or oxygen vacancies (Habermann 1997). However, the increase in a CL intensity induced by this effect is very small.

No measurable decrease in CL intensity was detected after 15 min of irradiation of a Mn bearing calcite. However, Mason (1994) describes a permanent reduction of the initial CL intensity up to 71% if the sample is irradiated over several hours, whereas only a small decrease in the CL intensity is documented after 8–10 min of irradiation.

So, irradiation by accelerated electrons has no important effect on the permanent CL behavior of calcite if the duration of irradiation is short. But this is not the case for all minerals. For instance, the CL of quartz and fluorite is much more influenced by irradiation with electrons. This is also the case if minerals are irradiated by accelerated protons (acceleration: 3 MeV). The analysis of a REE containing apatite demonstrates a decrease in CL intensity up to 55% after 20 min of proton irradiation. Here, accelerated protons cause a permanent quenching of the extrinsic CL (Fig. 8b). Lattice defects can be produced by electron bombardment (Hobbs 1979; Marshall 1988; Mason 1994). This is even more valid for accelerated protons due to their higher energy and mass compared to accelerated electrons. If ionoluminescence is used for quantitative analysis (e.g. Homman et al. 1994) this point is of importance, but using CL radiation damage affecting the CL intensity is of minor importance.

5.4 Sensitizer

The sensitizing effect caused by sensitizer elements like Pb²⁺ (Gies 1976) and Ce³⁺ (Marfunin 1979) may play a role in photoluminescence studies. However, these elements do not seem to have an important influence on CL intensity. The analyzed samples in Fig. 6 show no effect that can be clearly related to a sensitizing of the Mn²⁺-activated CL. This does not mean that sensitizing is not present, but the possible amplitude of this effect is too low to be detected unequivocally. This is probably due to the low intensity of this effect and its being compensated for by the standard errors of the applied analyzing methods (e.g. PIXE, EMS for calibration of the quantitative CL spectroscopy) and spectrometric analyses. Additionally, a

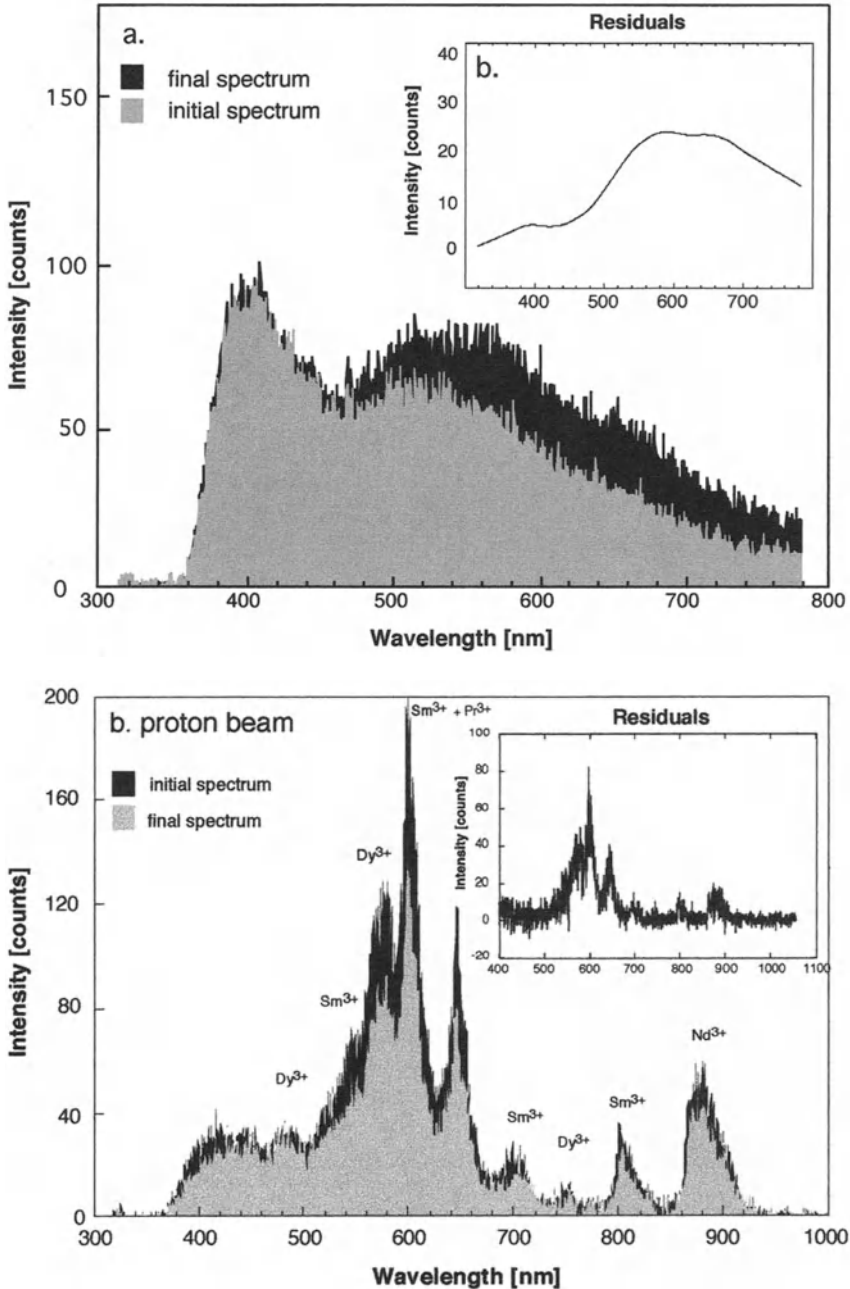


Fig. 8a,b. Spectra of two samples irradiated by an electron beam and proton beam. **a** Electron beam: the increase in the intrinsic CL between wavelengths of 200 and 700 nm, with peaks at 580 and 660 nm, is possibly attributed to broken Ca-O bondings or oxygen vacancies. **b** Proton beam: spectra of a REE-containing apatite document a decrease in CL intensity up to 35% after 20 min of proton irradiation. This can be clearly attributed to lattice defects (see dark spot in Fig. 12d)

small-scale inhomogeneity in trace element distribution may have a greater influence on the divergence between CL intensity and activator concentration analyzed by other methods than possible sensitizer elements. Conclusively, our studies on sedimentary calcite show no effect that can be clearly attributed to sensitizing.

6 Rare Earth Elements

The REE are some of the most important activator elements in natural minerals. REE include trace elements of the atomic numbers 21 (Sc), 39 (Y) and 57–71 (La–Lu). In the following, the term REE is exclusively used for the elements of the atomic numbers 57–71. Usually, these elements are in the trivalent ionic state, but some of the REE also occur in the divalent (Sm²⁺, Eu²⁺, Yb²⁺) and tetravalent (Ce⁴⁺, Pr⁴⁺, Tb⁴⁺) state.

Only Eu^{2+/3+}, Er³⁺, Tb³⁺, Dy³⁺, Sm³⁺, Pr³⁺, Ho³⁺ and Nd³⁺ (reabsorbed) emit in the visible spectral range. Nd³⁺ has peaks at 870–940 nm while Ce³⁺ emits in the UV (355 nm).

In contrast to Mn²⁺, the trivalent REE show nearly constant wavelengths. The term “nearly” is due to the fact that the structure of the REE related peaks in a spectrum are different depending on the symmetry and strength of the host crystal field (Marfunin 1979). Therefore, Ca²⁺ substituted by REE in calcite structures is unequivocally detectable using CL spectroscopy. Commonly, the REE-activated CL is hidden by dominant Mn²⁺-activated CL (Figs. 9, 10). We showed that the REE-activated CL of calcite and dolomite is still common in hydrothermal and sedimentary calcite (see Habermann et al. 1996a). As the REE content may exceed 100 ppm, the emission intensity caused by REE is of special importance, influencing the absolute CL intensity. Particularly, in case of low Mn content the additional REE-related CL emission can cause a significant increase in CL intensity. In this case digital spectral analysis is also indispensable for correctly estimating the CL intensity attributed to Mn²⁺ and REE (Figs. 9, 10).

In natural minerals REE are mostly incorporated in groups. Therefore, sensitization, quenching and absorption by other REE are dominant effects yielding strong variations in the correlation between the REE-activated CL intensity and the REE content (e.g. Marfunin 1979).

Only for a few REE is quantitative CL spectroscopy possible and an estimation of their CL intensity unequivocal. These elements are Dy³⁺, Eu³⁺ and Sm³⁺ because some of their peaks lie in a spectral region where no other REE have emission peaks and absorption bands, and no or only minor sensitization occurs.

It is hard to calibrate a quantitative REE-CL spectroscopy by an external analysis method as most microprobes like EMP and PIXE are often not sensitive enough for analyzing REE concentration in a low ppm range. However, in addition to the PIXE method, Homman et al. (1994) developed a quantitative ionoluminescence (IL)-spectroscopy for some REE. This method has a much higher sensitivity than PIXE, although it uses the scanning technique to record the IL spectra. But Homman et al. (1994) suggested using a CCD detector to lower the detection limit in the range of 0.1 ppm, which is much below other microprobe

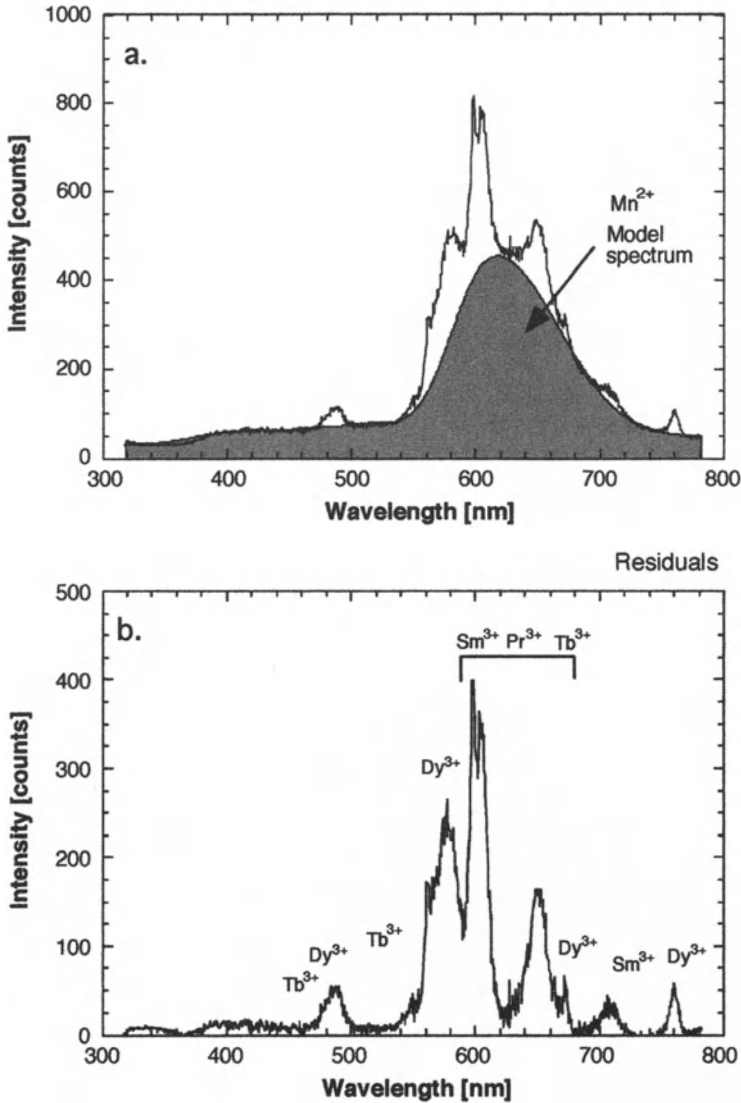


Fig. 9. Spectrum of Sm^{3+} - and Dy^{3+} -activated CL in calcite obtained by subtracting a reference spectrum of Mn-activated CL in Mg-free calcite; deep burial calcite cement, archaeocyathide limestone Cambrian, Morocco

analysis methods. It is indispensable to analyze small amounts (<10 ppm) of REE, and methods like SIMS or LA-ICP-MS work efficiently. But for analyzing small scale zoning these methods are not very useful. As small scale REE zoning is often observed in natural calcite (Habermann et al. 1996a), it is of importance to use a small spot size (below 50 μm in diameter).

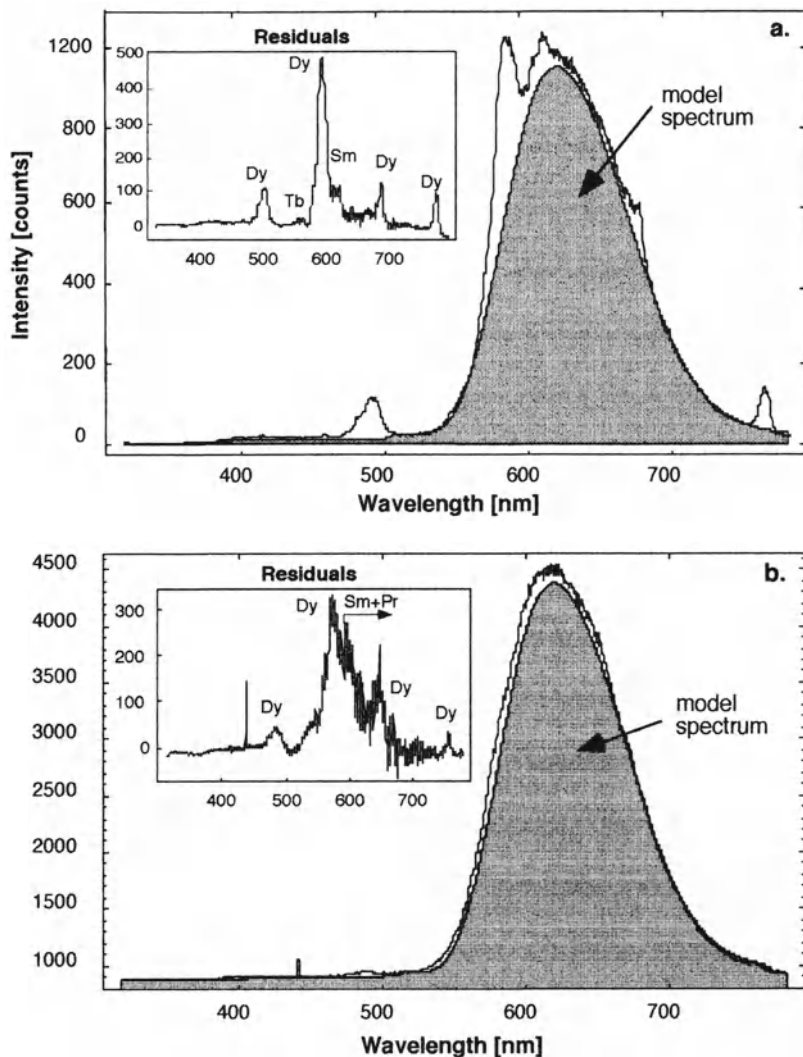


Fig. 10a,b. REE-activated CL in calcite detected by using HRS-CL. As REE-activated CL is mostly blotted out by Mn²⁺-activation, the REE content can only be revealed by further processing. **a** Calcite, pale violet CL (hydrothermal cement sequence; Triassic limestone, Perachora peninsula (Greece) QHRS-CL analyses: Mn=7 ppm; Dy=13±5.2 ppm; (see Fig. 12e). **b** Calcite, dull orange CL (deep burial cement sequence; Triassic limestone; Hydra, Greece); QHRS-CL analysis: Mn=152 ppm

However, at present the quantitative REE -CL spectroscopy has many limits. For future work it will be of importance to overcome these limits. Quantitative REE analysis using high resolution CL spectroscopy is one of potential method of the future.

7

Conclusion

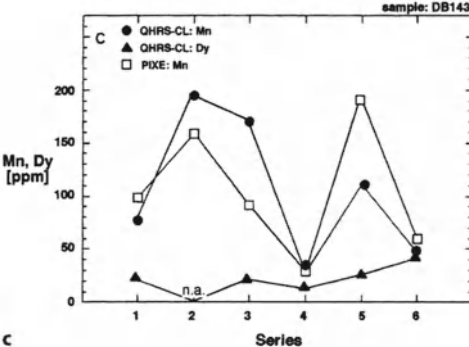
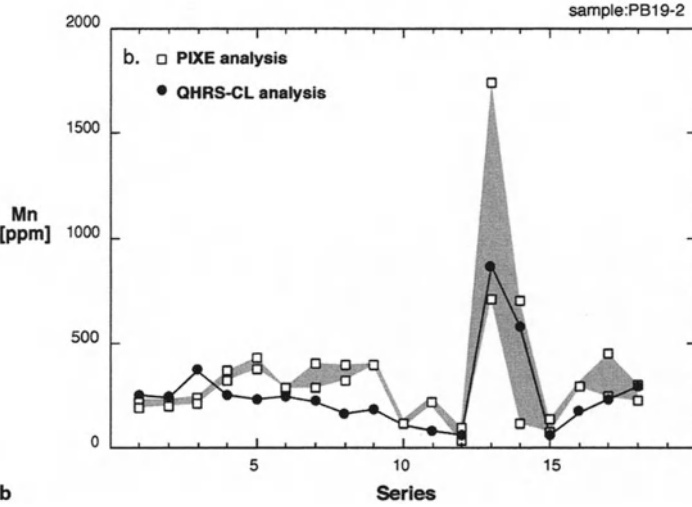
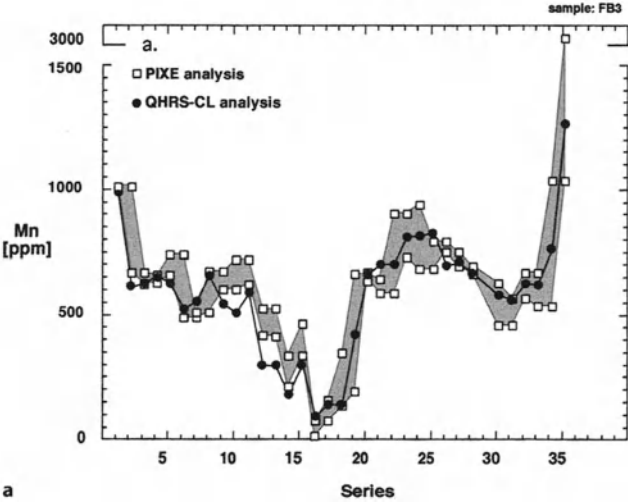
Our investigations reveal a positive and linear correlation between Mn content (up to 1000 ppm) and Mn²⁺-activated CL intensity in calcite. A comparable trend was also documented by Hemming et al. (1989), while Mason (1987) described a linear correlation up to 400–500 ppm Mn. These experimental data of a linear relationship between Mn content and CL intensity are not consistent with data presented by Savard et al. (1995), in which a field of “erratic” luminescence behavior is described in the range between ~20 and 200 ppm Mn. In this range of Mn content PIXE and QHRS-CL reveal a high conformity of analytical data (Fig. 11a). It is out of the question that the discrepancies between visible determination of the CL intensity and objective CL spectroscopy presumably are due to a subjective error caused by a visible determination (see also Hemming et al. 1989).

Quenching effects are the most limiting factors for quantitative CL spectroscopy. Here, self-quenching is more efficient than quenching by Fe. Fe quenching of Mn²⁺-activated CL starts at ~2000 ppm Fe depending on Mn concentration. At concentration levels with “Mn self-quenching” and “Fe quenching”, CL intensity is a complex function of both, making quantitative CL spectroscopy very problematic. This is consistent with the observations of Hemming et al. (1989), in which Fe concentrations less than ~1000–2000 ppm had no influence on Mn²⁺-activated CL intensity if the Mn content was low (<500 ppm). However, the absolute Mn²⁺ and Fe²⁺ concentrations control Mn²⁺-activated CL intensity of calcite.

It is not clear that Fe content in carbonates can only be attributed to the Fe²⁺ ion. There are no unequivocal data as to whether or not Fe³⁺ is an effective quencher in carbonates. Nevertheless, it cannot be excluded that Fe³⁺ may be an effective quencher, but compared to Fe²⁺ the possible Fe³⁺ concentrations are too low in the investigated samples.

The CL properties of carbonates are complex, but applying digital filters on a CL spectrum this complexity can be decoded. As shown, this is of importance when analyzing the Mn²⁺-activated CL intensity correctly. Particularly the Mn-distribution in different lattice positions in carbonates and thus the emission of sometimes more than one Mn band is a possible reason for a mismatch of the absolute CL intensity and the Mn content. But this is also of great potential in ana-

Fig. 11a–c. Comparison between PIXE analyses and QHRS-CL analyses, reflecting the conformity of these two methods. a Cement sequence of a Triassic limestone of Hydra (Greece). QHRS-CL analysis areas are mostly located between the PIXE analysis spots (sample: FB5; see Fig. 12f; PIXE analyses in Bruhn 1995, QHRS-CL analyses in Habermann 1997). b Calcite cement sequence, Triassic Trochitenkalk (Germany). Deviations are caused by small inhomogeneities in Mn distribution (QHRS-CL analyses spots are placed beside the PIXE analyses spots, only analyses of clear defined zones are plotted) (sample: PB19–2; see Fig. 12g; PIXE analyses from Bruhn 1995, QHRS-CL analyses from Habermann 1997). c Dysprosium is also proved by QHRS-CL below the detection limit of PIXE. At present, the error of Dy analyses is in the range of 30–40% (Habermann 1997) due to the lack of an appropriate calibration method in this low range of concentration; n.a., not analyzed; (sample: DB143). Analysis conditions: PIXE: time=20 min/spot, spot size=10 µm; QHRS-CL: time=5 s/spot, spot size=30 µm; Fe content is below 4000 ppm



lyzing the Mn^{2+} distribution quotient in the carbonate structure in thin sections (e.g. El Ali et al. 1993).

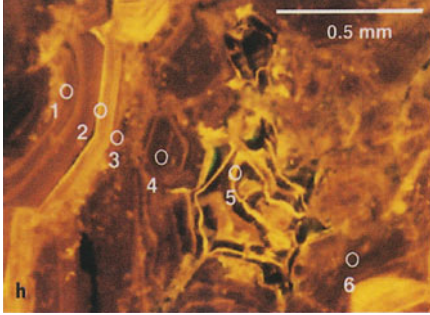
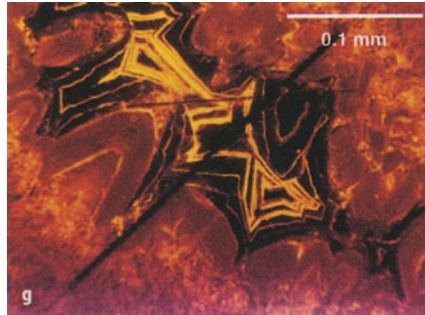
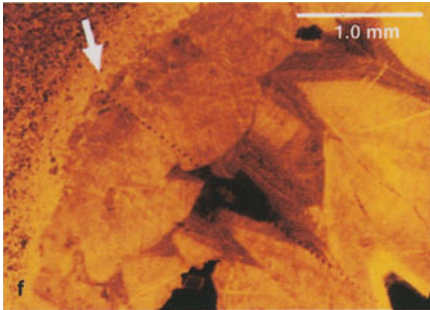
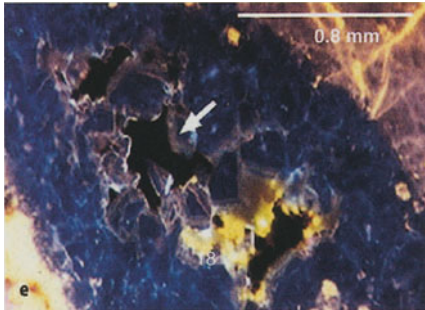
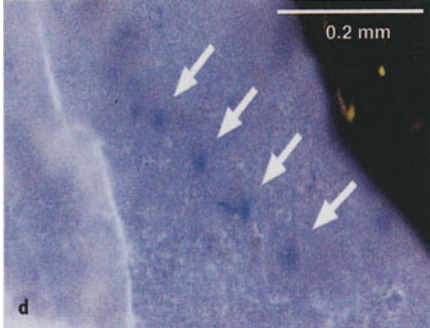
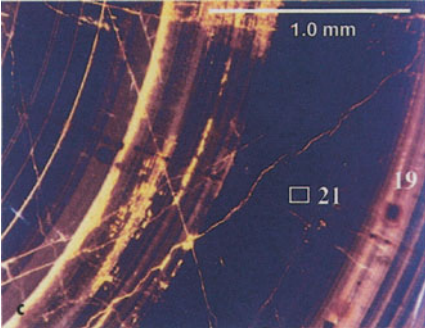
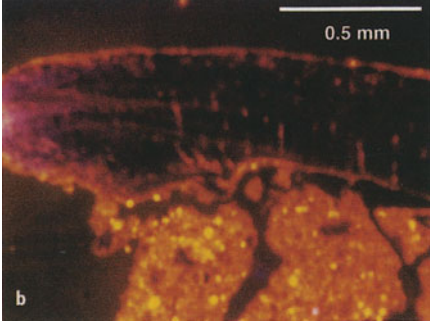
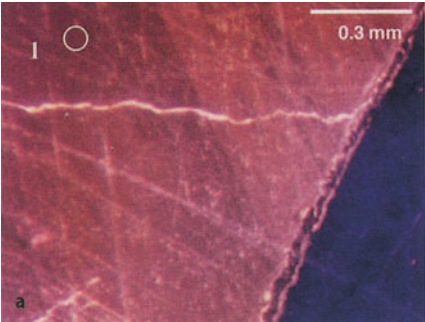
As REE are common in sedimentary calcite (Habermann et al. 1996a) these elements are also of importance considering CL intensity. In numerous minerals some of these elements (Sm^{3+} , Pr^{3+} , $Eu^{2+/3+}$, Er^{3+} , Nd^{3+} , Dy^{3+}) are easily analyzed using CL spectroscopy. At present, quantitative CL spectroscopy is also employed to analyze a range of REE in calcite and dolomite.

Quantitative CL spectroscopy is a powerful additional tool to EMP and PIXE or related methods. CL spectroscopy is sensitive for Mn analyses of calcites and dolomites below 3000 ppm and works very efficiently below 1000 ppm. In case of Mn concentrations below 10–50 ppm this method is a very powerful tool with calculated detection limits in the range of 100 ppb. It is remarkable that quantitative CL spectroscopy (apparatus described in Chap. 2, Fig 1) only takes a few minutes to analyze Mn concentrations in the ppb range. Additionally, both substituted Mn and the crystal structure can be evaluated.

As up to now there are only data on sedimentary and hydrothermal calcite and dolomite, we are not able to give more details on metamorphic carbonates. Here, more investigations are needed.

Mn^{2+} analyses using quantitative CL spectroscopy show a high coincidence compared to PIXE. Figure 11a–c show three samples of line scans through calcite cement generations of early stage to late stage of burial diagenesis and hydrothermal cements. In all samples the Fe content is below 4000 ppm. Some of the deviations are attributed to small scale inhomogeneities in the Mn distribution (see Fig. 12f, g).

Fig. 12a–h. All CL photographs were taken using a HC1-LM CL microscope at an electron beam density of approx. $15 \mu A/mm^2$; exposure time varies depending on CL intensity. The colors in the photographs represent the visible impression. Film: Kodak EL 135–36, 400 ASA. The samples of c, f, and g are described in Bruhn (1995), too. Figure parts a–c, e are from Habermann et al. (1998). a Mn^{2+} -activated hydrothermal calcite cement showing a violet CL, although the Mn content is only 12 ppm (I =analysis point, see spectrum Fig. 5b). Early diagenetic calcite cement is emitting dark blue, which is the intrinsic color of calcite (sample: K-SUR, Hydra/Greece). b Pleistocene brachiopod shell, calcite (sample: KAP HIRO, Corinth/Greece). In the internal part of the shell an Mn content of 4 ppm can be analyzed using QHRS-CL. c Belemnite (calcite) with a zoning of dark blue, violet and orange CL (sample: OPI-19 and -21). Calcite with 19 ppm Mn shows dull orange CL – point 19 (trace element analysis in Bruhn 1995). Zones containing only 1.5 ppm Mn (QHRS-CL analysis) are luminescing dark blue, e.g. point 21 (compare the spectrum in Fig. 5d; notice the Cr^{3+} peak, which is very uncommon in biogenic calcite). d REE-activated apatite with light violet CL (sample: Cerro de Merato, Mexico). PIXE analysis spots show a decreased CL intensity (*arrows*) due to quenching by lattice defects after irradiation with a proton beam (see Fig. 8b). e Hydrothermal calcite cement sequence (sample: DB14-2; Triassic limestone, Perachora peninsula, Greece). Violet CL (*arrow*) is due to Mn^{2+} and Dy^{3+} activation. The Mn^{2+} and the Dy^{3+} contents are below the detection limit of PIXE (Mn \sim 10 ppm, Dy \sim 23 ppm). QHRS-CL analyses reveal 7 ppm Mn and 13 ± 5.2 ppm Dy (see Fig. 10a). f Calcite cement sequence: Phreatic pore filling of a Triassic limestone (Hydra, Greece). Sample: FB5 (*Arrow*: starting point of the PIXE and QHRS-CL line scan; see Fig. 11a). g Phreatic calcite cement (Triassic Trochitenkalk, NW Germany, sample from Bruckschen et al. 1992). PIXE analysis spots are non-luminescent (see Fig. 11b). h Hydrothermal calcite cement sequence (sample: DB14-3; Triassic limestone, Perachora peninsula, Greece). *circles*: PIXE and QHRS-CL analysis spots (see Fig. 11c)



The great potential of quantitative CL spectroscopy is its high sensibility combined with a very low amount of damage to the sample. Compared to, e.g. SIMS and LA-ICP-MS, these are big advantages. Additionally, this method can also supply extensive information about crystal structure. Quantitative CL spectroscopy is not only applicable to carbonates. Other minerals such as feldspars, apatite and zircon can be analyzed too, which is one of the most important potentials of this new method.

Acknowledgements. This work was kindly supported by the Deutsche Forschungsgemeinschaft (DFG Ri 216/13-1). The assistance in PIXE analyses by the staff of the Dynamitron Tandem Laboratory of the Ruhr-University Bochum, especially by J. Meijer and A. Stephan, is kindly appreciated. Furthermore, we wish to thank F. Bruhn (CSIRO Exploration & Mining, North Ryde, Australia) for his cooperation at the beginning of our PIXE investigations. Thanks are also due to M. Pagel for his patience during the completion of this manuscript.

References

- Althoff PL (1977) Structural refinement of dolomite and a magnesian calcite and implications for dolomite formation in the marine environment. *Amer Mineral* 62: 772-783
- Bruckschen P, Neuser RD, Richter DK (1992) Cement stratigraphy in Triassic and Jurassic limestones of the Weserbergland (northwest Germany). *Sed. Geol* 81: 195-214
- Bruhn F (1995) Kombinierte Spurenelement-Mikroanalysen und Kathodolumineszenz-Untersuchungen: Entwicklung einer Meßmethodik für die Bochumer Protonenmikroskopie (PIXE) und Fallstudien aus der Sedimentologie. Diss. Ruhr-Universität Bochum
- Burns RG (1993) Mineralogical applications of crystal field theory. (2nd edition) Cambridge University, Cambridge
- Calderón T, Aguilar M, Jaque F, Coy-Yll R (1984) Thermoluminescence from natural calcite. *J Physics*, 17: 2038-2077
- El Ali A, Barbin V, Calas G, Cervelle B, Ramseier K, Bouroulec J (1993) Mn²⁺-activated luminescence in dolomite, calcite and magnesite: quantitative determination of manganese and site distribution by EPR and CL spectroscopy. *Chem Geol* 104: 189-202
- Fairchild IJ (1983) Chemical controls on cathodoluminescence of natural dolomites and calcites: new data and review. *Sedimentology* 30: 579-583
- Frank D, Carpenter AB, Oglesby TW (1982) Cathodoluminescence and composition of calcite cement in the Taum Sauk limestone (Upper Cambrian), Southeast Missouri. *J Sediment Petrol* 52: 631-638
- Gies H (1976) Zur Beziehung zwischen Photolumineszenz und Chemismus natürlicher Karbonate. *N Jb Miner Abh* 172: 1-46
- Grover Jr. G, Read JF (1983) Paleoaquifer and deep burial related cements defined by regional cathodoluminescence pattern, Middle Ordovician Carbonates, Virginia. *AAPG Bull* 67: 1275-1303
- Habermann D (1997) Quantitative hochauflösende Kathodolumineszenz-Spektroskopie von Calcit und Dolomit. Diss. Ruhr-Universität Bochum
- Habermann D, Neuser RD, Richter DK (1996a) REE-activated cathodoluminescence of calcite and dolomite: High Resolution Spectrometric analysis of CL emission (HRS-CL). *Sed Geol* 101: 1-7
- Habermann D, Neuser RD, Richter DK, Bruhn F (1996b) Quantitative analysis of Mn²⁺ in sedimentary calcite using cathodoluminescence spectroscopy. V.M Goldschmidt Conference 1996 (Heidelberg). *Journal of Conference Abstracts*, 1 (1) 226

- Habermann D, Neuser RD, Richter DK (1996c) Hochauflösende Spektralanalyse der Kathodolumineszenz (KL) von Dolomit und Calcit: Beispiele der Mn- und SEE-aktivierten KL in Karbonatsedimenten. *Zbl Geol Paläon*, Teil 1, 1995 (1/2) 145–157
- Habermann D, Neuser RD, Richter DK (1998) Low limit of Mn²⁺-activated cathodoluminescence of calcite: state of the art. *Sed Geol* 116: 13–24
- Hemming NG, Meyers WJ, Grams JC (1989) Cathodoluminescence in diagenetic calcites: The role of Fe and Mn as deduced from electron probe and spectrophotometric measurements. *J Sediment Petrol* 59: 404–411
- Hobbs LW (1979) Radiation effects in analysis of inorganic specimens by TEM. In: Hren JJ, Goldstein JI, Joy DC (eds) *Introduction to analytical electron microscopy*. Plenum, New York
- Homman NP-O, Yang C, Malmquist KG (1994) A highly sensitive method for rare-earth element analysis using ionoluminescence combined with PIXE. *Nuclear Instruments and Methods in Physics Research*, A353: 610–614
- Khan MR, Barber DJ (1990) Compositional-related microstructures in zinc-bearing carbonate assemblages from Broken Hill, New South Wales. *Mineralogy and Petrology* 41:229–245
- Koberski U (1992) Anwendung der Kathodolumineszenz auf Fragestellungen in der Petrologie. Diss. Albert-Universität Freiburg
- Machel H (1985) Cathodoluminescence in calcite and dolomite and its chemical interpretation. *Geoscience Canada* 12: 139–147
- Machel HG, Mason RA, Mariano AN, Mucci A (1991) Causes and emission of luminescence in calcite and dolomite. In: Barker CE, Kopp OC (eds) *Luminescence microscopy and spectroscopy: qualitative and quantitative applications*. SEPM Short Course 25: 9–25
- Marfunin AS (1979) Spectroscopy, luminescence and radiation centres in minerals: Translated from Russian by V.V. Schiffer. Springer Verlag, Berlin
- Marshall DJ (1988) Cathodoluminescence of geological materials. Unwin-Hyman, Boston
- Mason RA (1987) Ion microprobe analysis of trace elements in calcite with an application to the cathodoluminescence zonation of limestone cements from the Lower Carboniferous of South Wales, UK. *Chem Geol* 64: 209–224
- Mason RA (1994) Effects of heating and prolonged electron bombardment on cathodoluminescence emission from synthetic calcite. *Chem Geol* 111: 245–260
- Mason RA, Mariano AN (1990) Cathodoluminescence activation in manganese bearing and rare-earth bearing synthetic calcites. *Chem Geol* 88: 191–206
- Maxwell JA, Teesdale WJ, Campbell JL (1995) The Guelph PIXE software package II. *Nucl Inst Meth B95*: 407–421
- Medlin WL (1968) The nature of traps and emission centres in thermoluminescent rock materials. In: McDougall DJ (ed) *Thermoluminescence of geological materials*. Academic, New York, pp 193–223
- Meijer J, Stephan A, Adamczewski J, Bukow HH, Rolfs C, Pickart T, Bruhn F, Veizer J (1994) PIXE microprobe for geoscience applications. *Nucl Instr Meth B89*: 229–232
- Meyers WJ, Lohmann KC (1985) Isotope geochemistry of regional extensive calcite cement zones and marine components in Mississippian limestones, New Mexico. In: Schneidermann N, Harris PM (eds) *Carbonate Cements*. SEPM Spec Pap 36: 223–240
- Neuser RD (1988) Zementstratigraphie und Kathodolumineszenz des Korallenoolith (Malm) im Südniedersächsischen Bergland. *Bochumer geol. u. geotech. Arb* 32: 1–172
- Neuser RD (1995) A new high-intensity cathodoluminescence microscope and its application to weakly luminescing minerals. *Bochumer geol u. geotech Arb* 44: 116–118
- Pierson, B. J (1981) The control of cathodoluminescence in dolomite by iron and manganese. *Sedimentology* 28: 601–610
- Ramseyer K, Fischer J, Matter A, Eberhardt P, Geiss J (1989) A cathodoluminescence microscope for low intensity luminescence. *J Sediment Petrol* 59: 619–622
- Reeder RJ (1992) Carbonates: growth and alteration microstructures. In: Busek, P. R (ed.) *Minerals and reaction at the atomic scale: Transmission electron microscopy*. Review in *Mineralogy* 25: 381–424

- Richter DK, Zinkernagel U (1975) Petrographie des "Permoskyth" der Jaggl-Plawen-Einheit (Südtirol) und Diskussion der Detritusherkunft mit Hilfe von Kathodo-Lumineszenz-Untersuchungen. *Geol. Rdsch* 64: 783–807
- Richter DK, Zinkernagel U (1981) Zur Anwendung der Kathodolumineszenz in der Karbonat-petrographie. *Geol. Rdsch* 70: 1276–1302
- Savard MM, Veizer J, Hinton R (1995) Cathodoluminescence at low Fe and Mn concentrations: A SIMS study of zones in natural calcites. *J Sediment Res A* 65: 208–213
- Smith DGW (1976) Microbeam techniques. In: Short course in microbeam techniques. Min Ass Can Edmont
- Sommer SE (1972a) Cathodoluminescence of carbonates, 1. Characterisation of cathodoluminescence from carbonate solid solutions. *Chem Geol* 9: 257–273
- Sommer SE (1972b) Cathodoluminescence of carbonates, 2. Geological application. *Chem Geol* 9: 274–284
- Spötl C (1991) Cathodoluminescence of magnesite: Examples from the Eastern Alps. *Geology* 19: 52–55
- Ten Have T, Heijnen W (1985) Cathodoluminescence activation and zonation in carbonate rocks: An experimental approach. *Geologie en Mijnbouw*, 64: 297–310
- Walker G (1985) Mineralogical application of luminescence techniques. -In: Berry FJ, Vaughan DJ (eds) Chemical bonding and spectroscopy in mineral chemistry. Chapman and Hall, London, pp 103–140
- Walker G, Burley S (1991) Luminescence petrography and spectroscopic studies of diagenetic minerals. In: Barker CE, Kopp OC (eds) Luminescence microscopy and spectroscopy: Qualitative and quantitative applications. SEPM Short Course 25: 83–96
- Walker G, Abumere OE, Kamaluddin B (1989) Luminescence spectroscopy of Mn²⁺ centers in rock-forming carbonates. *Mineral Mag* 53: 201–211
- Weast RC, Astle MJ (eds) (1981) CRC Handbook of chemistry and physics. Chem. Rubber Co Cleveland, Ohio
- Zinkernagel U (1978) Cathodoluminescence of quartz and its application to sandstone petrology. *Contrib Sedimentol* 8: 1–69

Systems of Interacting Luminescence Centers in Natural Diamonds: Laser-Induced Time-Resolved and Cathodoluminescence Spectroscopy

GERARD PANCZER, MICHAEL GAFT,
ARNOLD S. MARFUNIN

1

Introduction

Luminescence is produced by a wide variety of processes, including photoluminescence (PL) and cathodoluminescence (CL), the types used by earth scientists. CL has several advantages over PL, namely, a greater energy density and the possibility to focus the microprobe beam to a few microns (Marfunin 1994). In addition, CL only stimulates the surface, whereas PL stimulates the whole crystal zone excited by the laser beam.

Pulsed lasers employed as excitation sources combine very high power and the ability to focus that power with a highly selective monochromatic excitation. Such lasers enable the determination of not only spectral but also kinetic parameters of luminescence in the time domain from ns to ms. In this chapter, laser-induced luminescence (LIL) will be compared with conventional PL and CL. Diamond is selected because it commonly displays luminescence and has been thoroughly studied by traditional methods.

Micro-Raman equipment, in which a monochromatic laser beam is focused on the sample, is the most suitable for micro-LIL investigation. Modern commercial dye lasers can achieve on the order of 1–2 W of power from the red region to the UV (260 nm) by the use of a range of dyes and frequency doubling crystals and are suitable for both Raman and luminescence spectroscopy. Double monochromators used in Raman spectroscopy also give a very high spectral resolution as well as a very low scattered light background. An additional advantage of micro-Raman equipment is the possibility of simultaneously obtaining Raman and luminescence spectra. This is especially important when dealing with geological materials because additional minerals may be present which can result in erroneous interpretations.

Luminescence spectroscopy is one of the most widely used techniques in the study of diamonds even when compared with optical absorption, ESR, IR and Raman spectroscopy. Hundreds of spectra have been obtained and fluorescence characteristics are important in the drawing up of diamond quality gemmological certificates. A wide range of electronic and laser applications are based on the optical properties of diamond. Nitrogen center aggregation is controlled by the residence time of diamond in the mantle but the distinction between natural and synthetic, irradiated, or enhanced diamonds and identification of any particular

diamond can be made by detailed luminescence studies. Furthermore, CL topography reflects the growth parameters.

Two approaches have been used for the determination and characterization of luminescence centers in natural diamonds: experimental laser-induced time-resolved spectroscopy and systematic analysis of the diamond structure related to center formation. Ten specimens have been chosen from the collection of approximately 200 characteristic crystals taken from some thousands of Yakutian diamonds.

2

Experimental Techniques

Steady state luminescence and excitation spectra at 300 and 77 K were obtained by 500 W Xe arc lamp excitation on an SLM spectrofluorimeter.

2.1

Time-Resolved Luminescence

The time-resolved luminescence spectra at 300 and 77 K were investigated under UV laser excitation (308, 354 and 384 nm) using 10 μ J pulses and were analyzed by a Hilger and Watts monochromator with a grating of 1200 grooves/mm blazed at 500 nm. Luminescence in the range of 400–900 nm was detected by a fast response GaAs photomultiplier (RCA 31034) and the signal was fed into a Canberra multichannel analyzer for the lifetime data. For short decay times (less than 1000 ns) time-resolved spectra were obtained using an SR250 Boxcar, the output of which was digitized, and decay times were measured by a Lecroy 9410 digital oscilloscope.

The lifetime analysis of the decay curves was carried out with an Origin computer program which allows the best fit to the experimental curve to be achieved by using several exponentials and adjusting their relative contributions.

2.2

Cathodoluminescence

The CL spectra were recorded with a CL spectrometer on a Jeol JSM-840 scanning electron microscope operated at 10 kV. The recording system consists of a parabolic mirror, a silica window allowing the passage of UV emission, a Jobin-Yvon H-10 spectrometer and a Hamamatsu R636 photomultiplier, which allows detection from 200 to 900 nm. The emission and excitation spectra are corrected for the spectral response functions of the system.

3 Experimental Results

3.1 Photoluminescence

3.1.1 N3, N3-Delayed and 2.96 eV Centers

Determination of the nature of the luminescence centers was undertaken by comparing the luminescence emission at 77 and 300 K on the “pure type” diamonds (Table 1) with certain types of defects. Usually the major differences between spectra at 77 and at 300 K are in decay times and the presence of zero-phonon lines at 77 K. The only luminescence with appreciable fine structure at 300 K is that from the N3 center; its zero-phonon line at 415 nm shows considerable variability in intensity and is sometimes almost undetectable (Fig. 1b). The decrease in the zero-phonon line intensity is accompanied by an increase of the 360 nm line in the excitation spectrum (Fig. 1a). The cause may be the formation of N3 clusters with the ensuing concentration quenching resulting from energy migration. The transfer is of the emission-reabsorption type, namely, emission by one

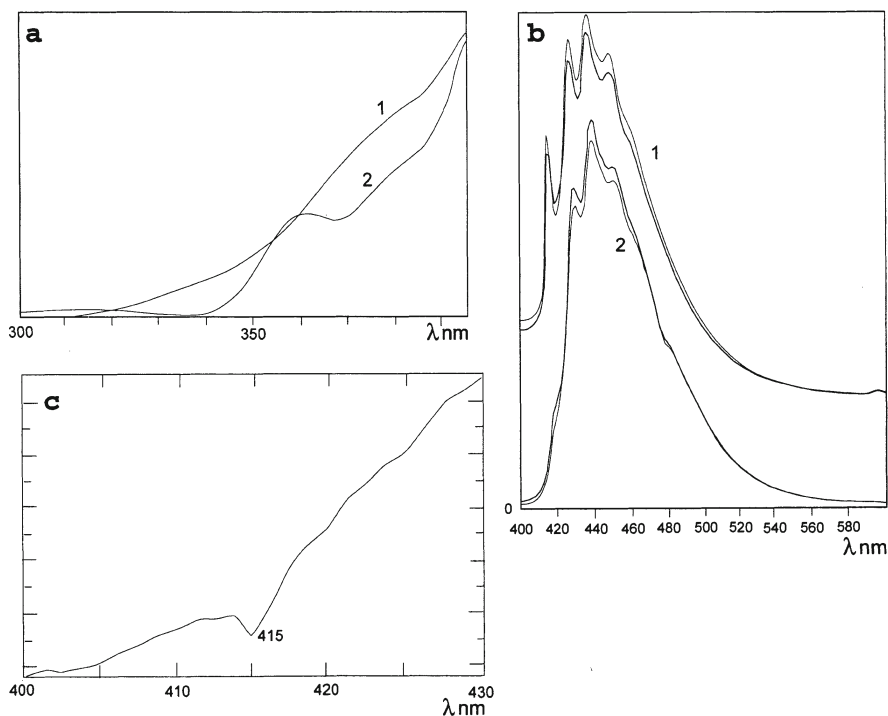


Fig. 1a-c. Excitation (a), luminescence (b) spectra of N3 centers. 1 Strong line at 415 nm; 2 without line at 415 nm; and reabsorption of the line at 415 nm (c)

Table 1. Luminescence centers in investigated diamonds

Center	λ_{lum} (nm)	λ_{ex} (nm)	τ (μ s)	T(°K)	Reference ^a	Description of diamond
N3	415, 428, 439, 452	308	0.04	77	1	Colorless
N3-delayed	415, 428, 439, 452	384	870	300	2	
2.96 eV	415, 428, 439, 452	308	38.7	77	3	
			4.6	300		
S2	489, 523, 530 (broad)	354	95	77	4	
?	463	354	312	77		
H3	525 (broad)	384	0.02,	300	5	Yellow-green
			11.2, 6000			
?	530 (broad)	308	126, 213	77		
S3	498, 545 (broad)	354	200	77	6	
GR1	794	308	0.02, 0.28	77	7	
?	635 (broad)	308	55, 280	300		Yellow
N3	415, 428, 439, 452	308	0.04	77	1	Colorless
S1	570 (broad)	308	3.0, 27, 200	300	4	
?	635 (broad)	308	55, 280	300		
	604, 700, 788	308	?	77	7	

^a1, Gaft (1994); 2, Bokii et al. (1986); 3, Pereira and Santos (1993); 4, Marfunin (1979); 5, Pereira and Monteiro (1991); 6, Davies (1994); 7, Marfunin (1997).

luminescence center and its reabsorption and emission by the other center. This is explained by the similarity of the energies of emission and reabsorption. In the luminescence of the sensitizer, only the intensity of the absorbed part decreases, the rest remaining unchanged (Gaft 1994).

This suggests the following explanation. A feature distinguishing the N3 center is that its absorption is similar to its excitation and presents a mirror reflection about the zero-phonon line of its photoluminescence emission spectrum. The line at 415 nm is present in the emission and absorption spectra subjected to concentration quenching. This is confirmed by the fact that this process is particularly prominent in the yellowish diamonds, which are characterized by a high N3 content (Pereira and Santos 1993). A strong reabsorption line at 415 nm in these diamonds is clearly seen in the spectrum which was recorded with a time delay of 1 μ s; under these circumstances N3 luminescence is no longer detected because of its short decay time (Fig. 1c).

Short-decay spectra usually show emission from N3 luminescence centers with a decay time of less than 40 ns. Despite such an extremely short decay time, the long-decay spectra of the same samples are sometimes characterized by zero-phonon lines which are very close in energy to those in N3 centers. At 77 K under 308 nm excitation the decay curve may be adjusted to a sum of two exponentials of $\tau_1=4.2$ μ s and $\tau_2=38.7$ μ s, while at 300 K only the shorter-lived component remains. Under 384 nm excitation an even longer decay component of $\tau_3=870$ μ s

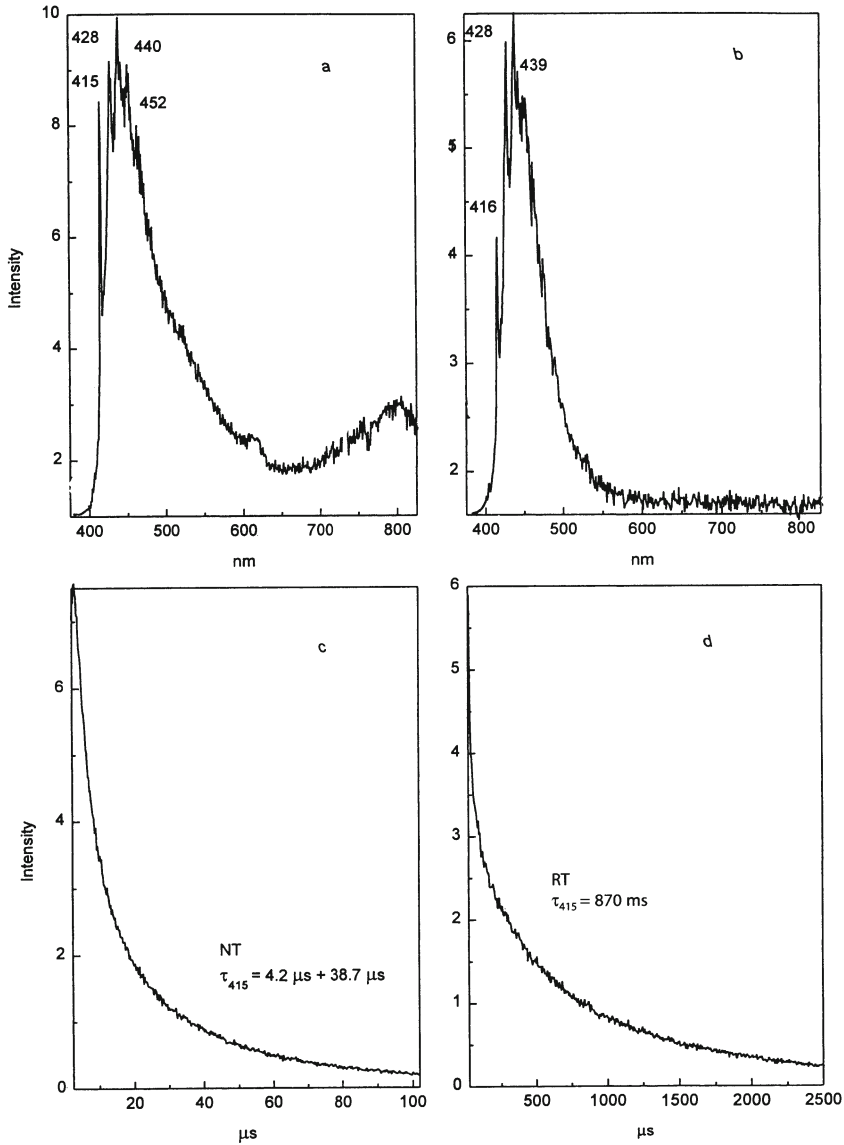


Fig. 2a–d. Luminescence (a, b) and decay (c, d) of 2.96 eV and N3-delayed centers (NT, 77 K; RT, 300 K)

may appear (Fig. 2). The first type of long-lived luminescence may be connected with a 2.96 eV center which is possibly correlated with Al presence (Pereira and Santos 1993). The second type of delayed N3 luminescence is ascribed to the presence of two metastable states identified as quartet levels at the N3 center (Pereira and Monteiro 1991).

3.1.2

H3, H4, S2 and S3 Centers

The H3, H4, S2 and S3 centers are characterized by relatively broad bands (max at 525–545 nm), sometimes accompanied by very weak zero-phonon lines at 489 and 523 nm (S2), 498 (S3) and 503 (H3) nm (Fig. 3). It is very difficult to distinguish between the centers of this group, especially when they present together.

Under pulsed-laser excitation the differences in decay times are more definitive. Different decay components (Fig. 4) in the green part of the spectrum allow us to establish the presence of H3 (12 μ s) and S3 (126 and 213 μ s) centers (Bokii et al. 1986; Davies 1994).

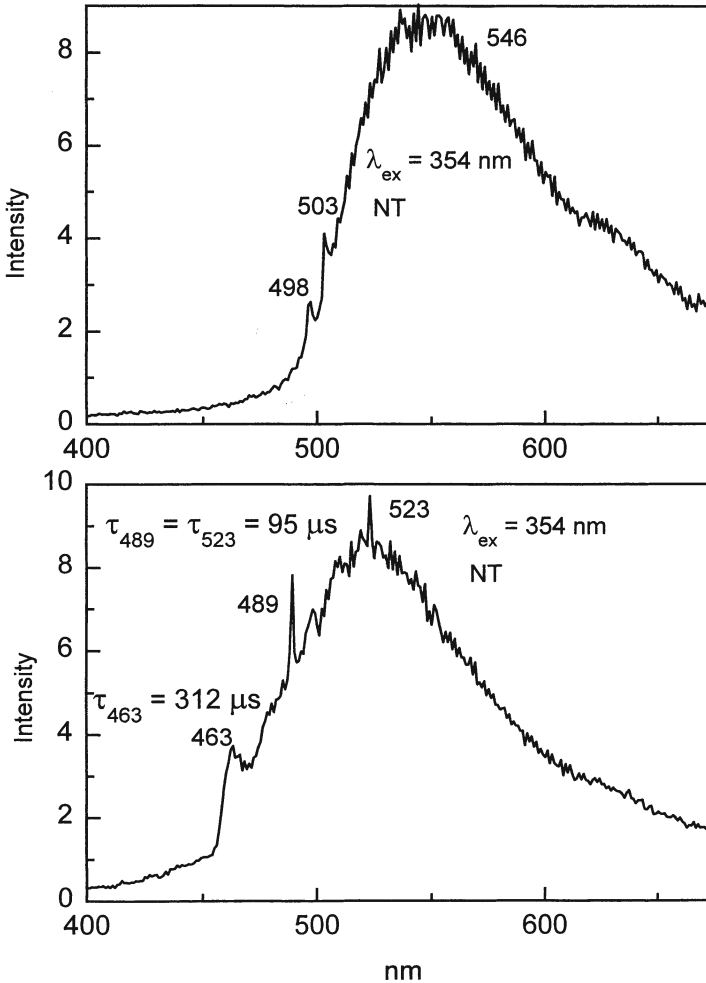


Fig. 3. Steady-state luminescence of H3, H4, S2 and S3 centers (NT, 77 K)

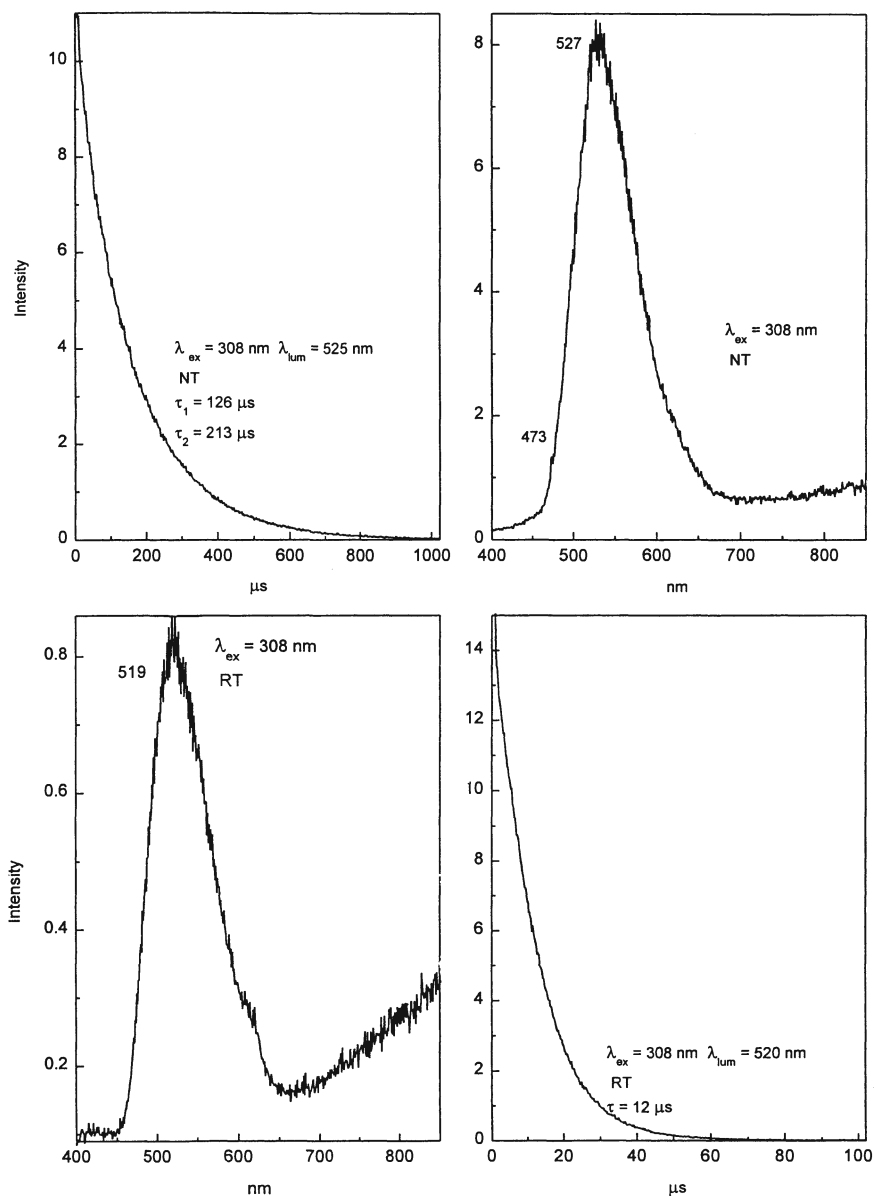


Fig. 4. Time-resolved luminescence and decay curves of H3 and S3 centers

These broad bands are sometimes accompanied by narrow lines (Fig. 5) of the GR1 center at 794 nm and at 700 and 788 nm (Bokii et al. 1986; Davies 1994). The relatively broad line at 463 nm which has a decay time of 312 s is not described in the literature (Fig. 3).

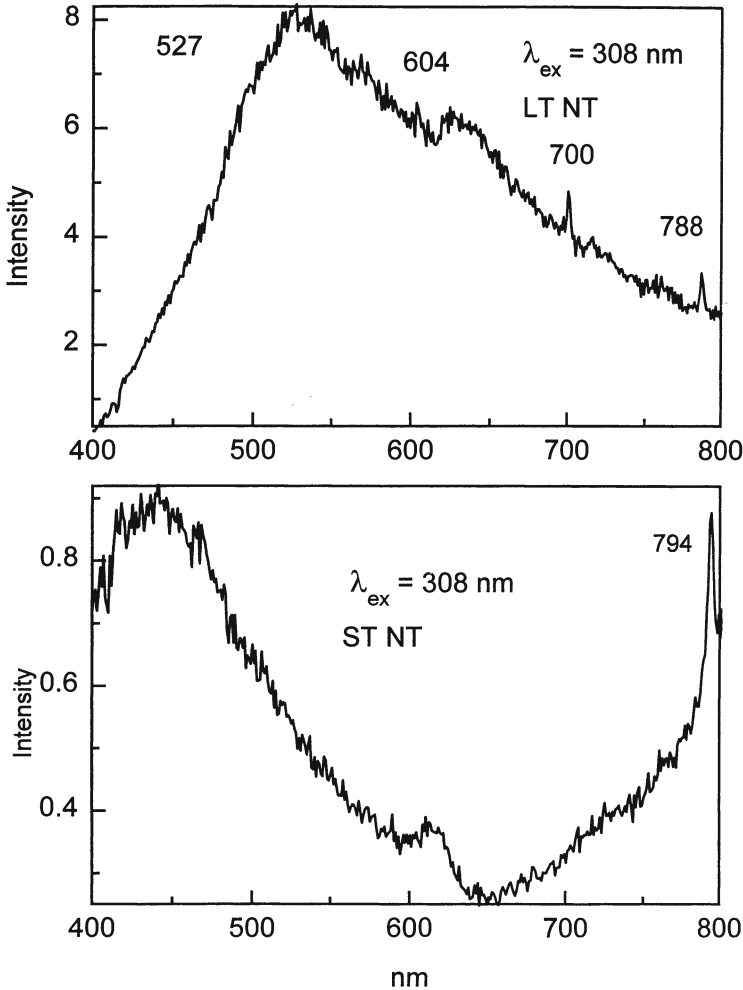


Fig. 5. Time-resolved luminescence spectra of GR1, 700 and 788 nm centers. *LT* Long decay spectra; *ST* short-decay spectra

3.1.3 S1 Center

Two broad bands exist in the yellow-red part of the spectrum (Fig. 6), characterized by a similar decay which has three main components and decay times of 4.8, 50 and 220 μs . The broad structureless band with a maximum at 570 nm may be identified as being due to an S1 center (Bokii et al. 1986; Davies 1994) although the band at 640 nm is not described in the literature.

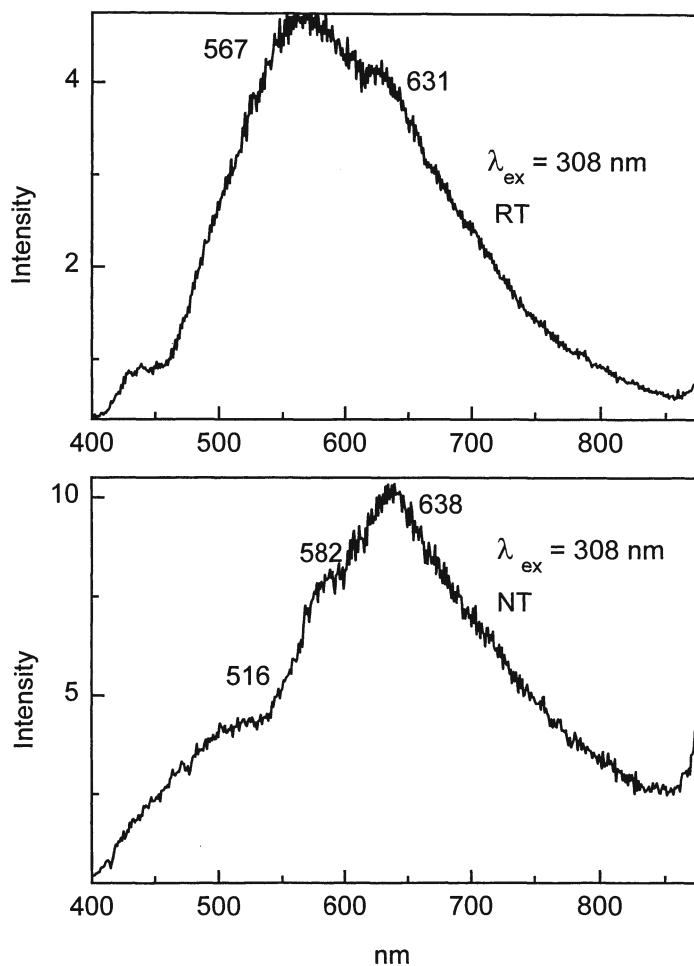


Fig. 6. Luminescence spectra of S1 center and 640 nm center (excitation: 308 nm)

3.1.4

Reabsorption Lines of Molecular Oxygen

The laser-induced time-delayed luminescence spectra of several diamonds contain a strong “negative” line at 760 nm (Fig. 7). The following results allow us to conclude that these lines are not due to noise or artefacts.

The spectral features are “negative”, thus they may not be related to second order lines or incidental sources of light.

The spectrum is presented without any smoothing or other mathematical treatment. It is clearly seen that negative lines are much stronger than the noise. Additionally, the negative lines always occur at the same energy. The invariability of the spectral positions provides evidence that they are not a result of fluctuations of the laser pulses and detection system.

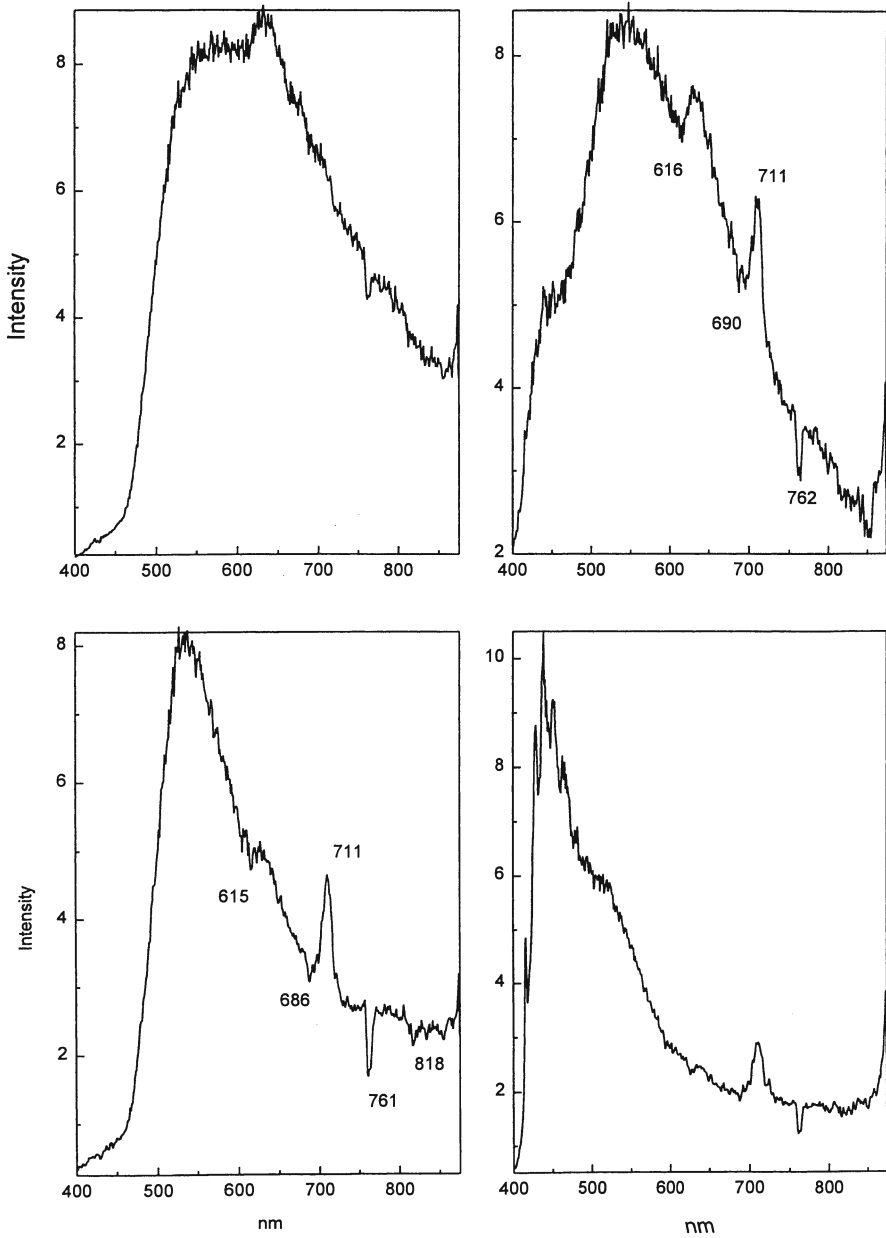


Fig. 7. Reabsorption spectra of molecular oxygen O_2 at 760 nm for four different diamonds

Such lines are well known in the atmosphere and recently have been found in magmatic and sedimentary apatites (Gaft et al. 1997). They are due to molecular oxygen absorption.

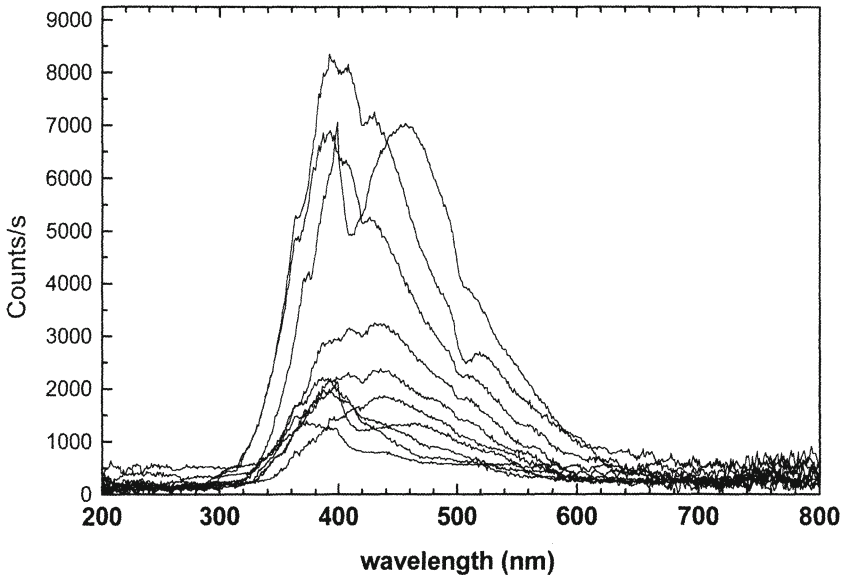


Fig. 8. Cathodoluminescence spectra of the Yakutian diamonds analysed by photoluminescence (Figs. 1-7)

3.2 Cathodoluminescence

All diamonds investigated are characterized by very similar CL with a maximum in the blue region of the spectrum (Fig. 8). This broad band is mainly a result of A centers.

4 Discussion

4.1 Fundamental Characteristics of Real Structures and Excited States

A fundamental investigation of the physical properties of diamonds is extremely important for applications in material science and technology, optoelectronics, semiconductors, radiation dosimetry, heat conductivity and lasers (Marfunin 1994).

Natural diamonds contain a series of coexisting interacting centers with energy transfer. Observed luminescence of one-two centers can be a consequence of interaction between several centers whether inducing radiative transitions or not. Taking into account established models of several centers and the existence of groups of centers, two classifications can be presented:

1. A classification based on the type of a center (N, B-Ni, vacancy, dislocation related, and aggregations of impurities and vacancies)
2. A classification based on the origin of a center (naturally or synthetically grown, caused by irradiation and/or heating, or plastic deformation)

4.2

Gemmology

Fluorescence characteristics are used in diamond quality gemmological certificates for distinguishing between natural and synthetic, irradiated and enhanced gem diamonds. In addition, in the jewelry industry there is a need to be able to quickly identify any particular diamond and to be able to distinguish it from others. For example, since the appearance of diamonds leaving the polishing factory bear no resemblance to the diamonds that entered it, the opportunity exists for the polished gems to be switched for less valuable ones (Yifrach and Neta 1992; Curtis 1989). The combination of luminescence properties (spectra of luminescence and excitation, decay time and intensity of luminescence) at 300 K, together with a suitable program for data treatment, enables reliable identification of specific diamonds and a means of distinguishing them from others. Time-resolved spectroscopy is especially effective because 50–70% of diamonds have a strong blue luminescence which hinders discrimination when distinguishing between N3 and N3-like centers. Also, with a 11 μ s delay the N3 emission is totally quenched and more individual bands with longer decay times appear.

4.3

Sorting

It has been maintained that sorting under X-ray excitation, which has similar properties to CL, is better than under UV lamp excitation. Moreover, new deposits have been discovered which contain diamonds that do not luminesce under X-ray excitation. Sometimes this portion, which is unrecoverable in X-ray luminescent sorters, is large enough to warrant the development of a new sorting method. For such diamonds UV excitation at 300 K proved to be very effective, not under UV lamps, but under powerful UV lasers (Gaft et al. 1989).

Luminescence is generated by two lasers operating at different wavelengths – an excimer laser operating at 222 nm which excites the A-band, and a nitrogen laser which excites mainly S3 and “578 nm” centers. The A-band is present in approximately 95% of investigated diamonds, but with large intensity variations. Practically all the diamonds with weak A-luminescence are characterized by strong luminescence under nitrogen laser excitation. Detection is carried out at two spectral and temporal selective windows – between 420 and 480 nm with a time delay of 3–9 ms and between 450 and 650 nm with a time delay of 1–20 ms.

Comparative investigation yielded the following results: in 12% of the samples laser excitation is much more effective and may be used even for recovering diamonds from the wastes of X-ray sorters. In 85% of samples laser excitation is bet-

ter and allows for higher feeding rates and recovery efficiency. In 3% of the samples the diamonds were non-luminescent under both kinds of excitation (Gaft 1993).

4.4 Genetic Features

Luminescence properties may be specific for diamonds of different genetic types (kimberlites, lamproites, high-pressure metamorphics, impact craters, interstellar dust) and different deposits with the same genesis.

5 Conclusions

Time-resolved laser-induced luminescence spectroscopy enables the detection of practically all types of luminescence centers existing in diamonds. The combinations of these centers are specific for each investigated diamond (Table 1). By contrast, conventional CL spectra for the same diamonds are very similar. (It may, of course, be possible to use time-resolved CL by pulsing the electron beam.) Thus time-resolved spectroscopy is somewhat more informative for both fundamental investigations and practical applications.

References

- Bokii G, Besrukov G et al (1986) Natural and synthetic diamonds, Nauka (In Russian)
- Davies G (1994) Properties and Growth of Diamonds. Gordon Davies, King's College, London
- Curtis A (1989) Sorting and/or confirming the identity of diamonds. UK Patent Application, N 8901759.4
- Gaft M (1993) Luminescent prints of minerals and their use in remote sensing. French-Israeli workshop on Apatites, Jerusalem, Abstracts, pp 70–71.
- Gaft M (1994) Diamonds photoluminescence at room temperature. International Mineralogical Association, 16th General Meeting, Abstracts, Pisa, Italy, pp 131–132
- Gaft M, Rassulov V et al. (1989) The using of laser induced luminescence of minerals for enrichment of ores. Sborn. Nauchno-Technich. Inform., Min Geol. SSSR, 11, pp 39–53 (In Russian)
- Gaft M, Reissfeld R. et al. (1997) Reabsorption lines of molecular oxygen and water in natural apatite. Optical 8, pp 143–148
- Marfunin A (1979) Spectroscopy, Luminescence and Radiation Centers in Minerals, Springer-Verlag
- Marfunin A (1994) Diamond: the mineral-absolute. Advanced Mineralogy, 1, pp 521–526
- Pereira E, Monteiro T J (1991) Delayed luminescence of the H3 center in diamond. J of Lumin. 48 & 49, pp 814–818
- Pereira E, Santos L (1993) Thez 2.96 eV centre in diamond. Physica B 185, pp 222–227
- Yifrach A, Neta U (1992) Method for identification gemstones, particularity diamonds. US Patent, 5, pp 118–181

Use of Cathodoluminescence for U-Pb Zircon Dating by Ion Microprobe: Some Examples from the Western Alps

DANIELA RUBATTO, DIETER GEBAUER

1

Introduction

The first report on cathodoluminescence (CL) of zircon goes back to the second half of the nineteenth century (Crookes 1879), however, only in the last 40 years has this phenomenon been addressed more frequently. The main CL emission bands have been related to different trace elements such as Mn and V (Leverenz 1968), Hf and Y (Ono 1976), Dy (e.g. Mariano 1978), Gd and Tb (e.g. Ohnenstetter et al. 1991). These elements would act as “activators” and enhance the “intrinsic” luminescence of pure zircon by non-stoichiometry, lattice damage or by structural defects (Marshall 1988). It has also been pointed out that elements such as Y can have a “quenching” effect on CL of zircon (Ohnenstetter et al. 1991) as they reduce the CL emission. A second approach to CL relates to the studies of CL zoning patterns to assist in the interpretation of U-Pb dating. This tool has proved to be indispensable when combined with U-Pb zircon dating by ion microprobe (e.g. SHRIMP). CL allows the identification of different types of zircon domains that then may be dated *in situ* by SHRIMP, with spatial resolutions between ca. 30 μm (e.g. Gebauer et al. 1988) and 15–20 μm (e.g. Gebauer 1996; Vavra et al. 1996).

This chapter deals in particular with CL related to dating, but some consideration is also given to the relation between emission and trace elements. Different zoning patterns within single crystals were recognised by CL and then dated by SHRIMP. The obtained ages were indispensable and support the hypotheses based on CL only. Moreover, the information on the concentrations of U and Th, obtained by SHRIMP and EMP, was integrated into the CL observations. The conclusions reached by the combination of these techniques were supported by geological and petrographic constraints and led to an understanding of the various geological processes that the zircons recorded during their multi-stage history (e.g. magmatism, deposition, metamorphism, hydrothermal alteration and metasomatic leaching of Th, U and Pb).

The aims of this chapter are: (1) to investigate the inverse correlation between CL emission and U-concentration in zircons, (2) to relate different types of zircon domains, distinguished on the base of their internal structure, to various geological processes. The cases studied are subdivided into sections on the basis of the different geological processes involved. In the discussion, our findings are

compared with other case studies and possible explanations for some of the characteristic zircon zoning patterns observed are suggested.

2 Geological Setting

The zircons investigated were separated from samples of two different tectonic units in the Western Alps: the Sesia-Lanzo Zone and the Zermatt-Saas-Fee ophiolites.

1. The Sesia-Lanzo Zone, studied in detail first by Dal Piaz et al. (1972), consists mainly of a Variscan metasedimentary basement intruded by abundant pre-Alpine granitoid and mafic bodies, which underwent Alpine subduction. All the samples were collected within the high-pressure (HP) unit of the “Eclogitic Micaschist Complex” (e.g. Compagnoni 1977). This zone is a slice of continental crust regarded by most of the authors as part of the Austroalpine domain (e.g. Dal Piaz 1993), representing part of the Adriatic margin involved into Alpine orogeny.
2. The Zermatt-Saas-Fee ophiolitic sequence consists mainly of metamorphosed ultramafic rocks, gabbros and basalts (Bearth 1967). The mafic complex is overlain by a discontinuous cover of Middle to Upper Jurassic deep-sea sediments (Bearth 1967). The Zermatt-Saas-Fee unit is considered to be a slice of oceanic crust, part of the Tethyan ocean, that was paleogeographically situated W-NW of the Sesia-Lanzo Zone. This ophiolitic sequence is Middle Jurassic in age (Rubatto et al. 1998).

During Alpine convergence both units underwent subduction which is recorded by HP or ultra-high-pressure (UHP) metamorphism. The Sesia-Lanzo Zone was subducted at around the Cretaceous-Tertiary boundary (Rubatto et al. 1999), a distinctly younger, Middle Eocene subduction affected the Zermatt-Saas-Fee ophiolites (Rubatto et al. 1998). In the Sesia-Lanzo Zone, peak metamorphic conditions of the eclogite-facies metamorphism are ca. 550–600 °C and 15–18 kbar (e.g. Pognante 1989). For the Zermatt-Saas-Fee ophiolites, the maximum estimated temperature is around 600 °C while the pressure reached up to ca. 28 kbar at Lago di Cignana, as documented by UHP parageneses containing coesite (Reinecke 1991). In the other area studied, the Täschental, a maximum pressure of more than 20 kbar was estimated (e.g. Fry and Barnicoat 1987).

Most of the samples analysed from both tectonic units preserve an eclogite-facies paragenesis and only in few cases a later greenschist-facies assemblage can be observed. Based on geological, petrographic and chemical constraints, it was possible to distinguish between meta-intrusives (granites and gabbros), meta-volcanics (basalts), metasediments and metamorphic veins (Table 1).

Table 1. List of samples analysed

Sample	Rock type	Zircon analysed	Number of spots
Sesia-Lanzo zone			
MUC2	HP-metagranite	17	47
MUC3	HP-metagranite	5	9
MUC4	HP-metagranite	4	7
MUC5	Eclogite	8	10
MUC6	Eclogite	7	13
MUC8	HP-vein	7	10
MUC10	HP-metagranite	5	8
QUI1	Leucogranitic dike	9	16
QUI2	Eclogite	7	11
MST1	HP-vein	12	20
MST2 A	Eclogitic micaschist	14	23
MSe10	Eclogite	10	15
CAv3	Low-grade vein	4	6
BZg1	Metagabbro	8	12
BZg2	Metagabbro	3	3
BZg13	Metagabbro	8	10
BZb14	Eclogite	5	5
BZf18	Leucogranitic dike	8	8
BZv5	HP-vein	17	18
Zermatt-Saas-Fee ophiolites			
MAT2	Metagabbro	8	14
MAT6	Metagabbro	4	5
TAS9	Leuco-metagabbro	3	4
TAS10	Leuco-metagabbro	6	15
TAS21	Leuco-metagabbro	5	7
TAS24	Leuco-metagabbro	4	8
TAS25	Metagabbro	4	4
TAS27	Oceanic metasediment	7	7
CIG1	Eclogite	3	5
CIG2	Eclogite	3	3
CIG3	Oceanic metasediment	9	18
CIG4	Oceanic metasediment	3	3
	Total	217	344

Metagabbro indicates a mafic rock in which a pre-Alpine gabbroic texture or paragenesis is still preserved. Eclogite indicates samples for which the mafic protolith (gabbro or basalt) is not clear based on petrography only. The number of spots refers to the spots analysed for each sample.

2.1

Sample Preparation and Analytical Techniques

The rock samples were crushed and sieved to less than 320 μm . The zircons were separated according to magmatic properties and density and finally selected by hand picking. The zircons from each sample were sorted into fractions according to shape, colour and dimension. They were embedded into epoxy and were polished down to a quasi-equatorial section. The same mount was used for CL analyses and SHRIMP dating. The selection of zircons for SHRIMP analyses was done on the basis of the CL images.

CL investigation was carried out on a CamScan 4 scanning electron microscope (SEM) at the Institut für Metallforschung und Metallurgie at the ETH in Zürich. The instrument is supplied with an ellipsoidal mirror for CL (e.g. Gebauer 1996). Panchromatic CL and secondary electron pictures of the zircons crystals were taken with 1 min scanning time on 125 ASA black and white films. Operating conditions for the SEM were of 13 kV at the cathode and an emission current of ca. 120 A.

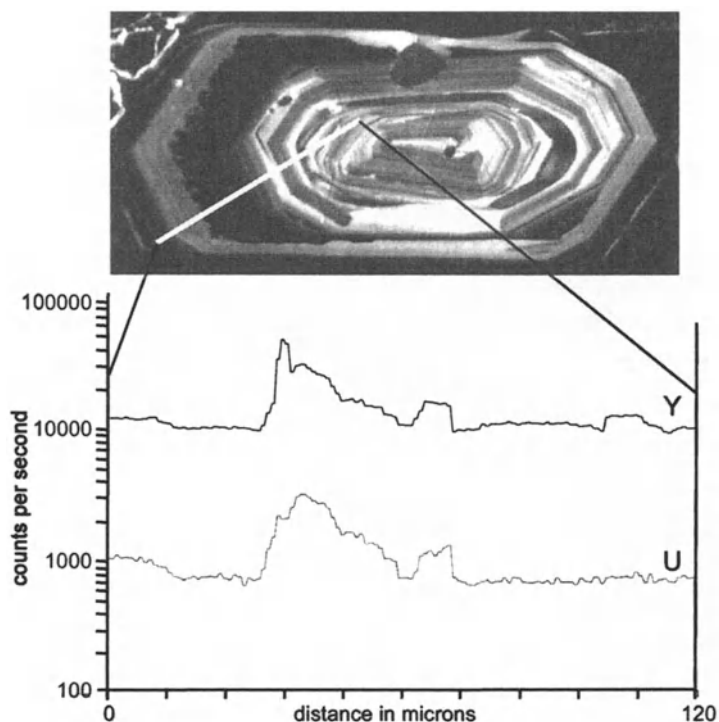


Fig. 1. Qualitative EMP profile across a zircon from a HP sheared-orthogneiss (MUC2) showing typical oscillatory, magmatic zoning. The change in trace element concentrations corresponds approximately to the change in CL emission. The zones dark in CL are relatively enriched in Y and U with respect to the brighter zones. The EMP analyses cannot resolve the very fine zonation bands in the centre of the zircon

The zircons were dated by the Sensitive High Resolution Ion Microprobes (SHRIMP II and I) at the Australian National University in Canberra. Instrumental conditions and data acquisition were generally as described by Compston et al. (1992). As reference, zircons from a pegmatite from Sri Lanka (SL13) were used in 1995 and 1996, while in 1997, zircons from a gabbro of the Duluth Complex in Minnesota (AS3) were used in addition.

Qualitative U and Y profiles were carried out by electron microprobe (EMP; Cameca SX-50) at ETH in Zürich (Institut für Mineralogie und Petrographie) equipped with five crystal spectrometers. Operating parameters include an acceleration potential of 15 kV, a beam current of 100 nA and a beam size of 1–2 μm . The qualitative analyses were collected in steps of ca. 1 μm with a measuring time of 20 s for each step. The small distance between the steps produced some overlapping, so that very fine zoning bands as in Fig. 1 could not be resolved.

3 Cathodoluminescence vs U Content

In CL, zircons are characterised by the alternation of relatively bright and dark zones, the distribution, shape and dimension of which give rise to different CL patterns. When zones with different intensities of CL are analysed by SHRIMP, mean U contents and Th contents (representative of a volume with a diameter of about 25 μm and a depth of ca. 2 μm) are obtained. Brighter fluorescing domains are relatively poorer in U than in the weaker fluorescing (dark) domains (Table 2 and Figs. 1–3, 5–9). This general observation is valid for the more than 200 zircons analysed, and is independent of rock type and conditions of zircon formation.

The U abundance detected by SHRIMP is supported by qualitative EMP profiles, which give information on the U and Y contents of the different zones with a more detailed spatial resolution. Figure 1 shows a profile through a zircon with alternating dark and bright fluorescing zones. Although the EMP analyses do not resolve the fine banding of the inner part of the zircon, where the element profiles are flat, for the broader bands the variations in U content correspond to the changes in CL emission. Y has a pattern similar to that of U, but with much higher counts. Bands richer in U and Y are darker in CL and brighter areas are relatively poor in these trace elements. It was also observed that two adjacent bands that look similar in CL do not necessarily have the same U and Y contents. This difference implies that the correlation between trace elements contents (U and Y) and CL emission is not linear, as already pointed out by Hanchar and Rudnick (1995).

Based on the combination of SHRIMP, EMP and CL data, it can be confirmed that the CL emission in zircons is inversely correlated to their contents of U and Y.

Table 2. SHRIMP data and CL observation for six of the studied samples

Spot name	U (ppm)	Th (ppm)	Th/U	CL intensity	CL pattern	Age
BZv5-17.1	13	8	0.60	Medium	Sector/oscillatory	Magmatic
BZv5-41.2	19	10	0.54	Medium	Sector/oscillatory	Magmatic
BZv5-4.1	5	1	0.21	High	Light rim	Mixing
BZv5-1.2	82	19	0.23	Medium	Cloudy rim	Mixing
BZv5-18.1	6	1	0.17	Medium	Cloudy rim	Mixing
BZv5-38.1	4	<1	0.03	Medium	Cloudy rim	Mixing
BZv5-24.1	37	33	0.91	High	Cloudy rim	Mixing
BZv5-6.1	10	6	0.58	Medium	Sector/oscillatory	Metamorphic
BZv5-28.1	2	<1	0.04	Medium	Cloudy rim	Metamorphic
BZv5-11.1	95	62	0.67	Low	(Oscillatory)	Metamorphic
BZv5-21.1	2	<1	0.02	Medium	Cloudy rim	Metamorphic
BZv5-23.1	2	<1	0.07	Medium	Cloudy rim	Metamorphic
BZv5-41.1	6	<1	0.03	Medium	Cloudy rim	Metamorphic
BZv5-12.1	2	<1	0.02	Medium	Cloudy rim	Metamorphic
BZv5-17.2	3	<1	0.03	Medium	Cloudy rim	Metamorphic
BZv5-42.1	3	<1	0.06	Medium	Cloudy rim	Metamorphic
BZv5-16.1	85	<1	<0.01	Medium	Cloudy rim	Metamorphic
BZg1-11.1	37	24	0.64	High	(Oscillatory)	Magmatic
BZg1-2.2	82	81	0.98	Medium	Oscillatory	Magmatic
BZg1-3.1	337	403	1.2	Low	Oscillatory	Magmatic
BZg1-4.1	429	434	1.0	Low	Oscillatory	Magmatic
BZg1-5.1	164	115	0.70	Medium	Oscillatory	Magmatic
BZg1-6.1	760	810	1.1	Low	Sector/oscillatory	Magmatic
BZg1-1.3	1	<1	0.01	Medium	Unzoned	Mixing
BZg1-20.1	4	3	0.81	High	Cloudy	Mixing
BZg1-2.1	5	1	0.18	High	Cloudy	Mixing
BZg1-1.1	7	<1	0.01	Medium	Cloudy	Metamorphic
BZg1-1.2	3	<1	0.01	Medium	Cloudy	Metamorphic
MUC5-15.1	429	125	0.29	Medium	Sector	Magmatic
MUC5-19.2	360	64	0.18	Medium	(Sector)	Magmatic
MUC5-13.1	211	66	0.31	Medium	Sector	Magmatic
MUC5-22.1	297	107	0.36	Medium	Sector	Magmatic
MUC5-3.1	263	45	0.17	Medium	Sector	Magmatic
MUC5-1.1	553	216	0.39	Medium	Sector	Magmatic
MUC5-19.1	145	1	<0.01	High	Cloudy	Metamorphic
MUC5-13.2	119	1	<0.01	High	Unzoned	Metamorphic
MUC5-25.1	69	<1	0.01	High	Unzoned	Metamorphic
MUC5-24.1	118	<1	<0.01	High	Unzoned	Metamorphic
TAS9-7.1	482	1188	2.5	Low	(Oscillatory)	Magmatic
TAS9-7.2	92	80	0.87	High	(Oscillatory)	Magmatic

Table 2. Continued

Spot name	U (ppm)	Th (ppm)	Th/U	CL intensity	CL pattern	Age
TAS9-1.1	335	643	1.9	Low	(Oscillatory)	Magmatic
TAS9-2.3	90	54	0.60	Medium	Cloudy	Magmatic
TAS9-2.4	187	302	1.6	Low	(Oscillatory)	Magmatic
TAS9-10.1	30	474	16	High	(Oscillatory)	Magmatic
TAS9-9.1	397	885	2.2	Medium	(Oscillatory)	Magmatic
TAS9-9.2	597	1760	3.0	Medium	(Oscillatory)	Magmatic
TAS9-10.4	70	504	7.2	High	(Oscillatory)	Mixing
TAS9-4.1	28	12	0.44	Medium	Oscillatory	Mixing
TAS9-10.5	45	151	3.4	Medium	Cloudy rim	Mixing
TAS9-10.2	28	<1	<0.01	Medium	Cloudy rim	Mixing
TAS9-10.3	55	4	0.07	Medium	Cloudy rim	Metamorphic
TAS9-2.1	5	<1	0.06	Medium	Cloudy rim	Metamorphic
TAS10-20.1	1299	3396	2.6	Low	Oscillatory	Magmatic
TAS10-19.1	1177	2528	2.2	Low	Oscillatory	Magmatic
TAS10-18.1	196	261	1.3	High	Oscillatory	Magmatic
TAS10-1.1	156	153	0.98	Medium	Unzoned	Magmatic
TAS10-1.2	968	2148	2.2	Low	Oscillatory	Magmatic
TAS10-12.1	200	192	0.96	High	Cloudy rim	Magmatic
TAS10-13.1	265	274	1.0	Medium	Cloudy rim	Mixing
MST2A-19.1	605	84	0.14	Low	Oscillatory	Inherited
MST2A-18.2	642	313	0.49	Low	Oscillatory	Inherited
MST2A-13.1	219	154	0.70	Medium	Oscillatory	Inherited
MST2A-13.2	213	8	0.04	Medium	Oscillatory	Inherited
MST2A-1.2	1346	687	0.51	Low	Oscillatory	Inherited
MST2A-17.1	504	51	0.10	Low	Oscillatory	Inherited
MST2A-12.2	271	141	0.52	Medium	Oscillatory	Inherited
MST2A-8.2	189	103	0.54	Low	Irregular	Inherited
MST2A-15.2	199	86	0.43	Medium	Oscillatory	Inherited
MST2A-9.1	184	82	0.45	Medium	Oscillatory	Inherited
MST2A-10.1	406	134	0.33	Medium	Oscillatory	Inherited
MST2A-4.1	274	17	0.06	Medium	Oscillatory	Inherited
MST2A-4.2	294	32	0.11	Medium	Oscillatory	Inherited
MST2A-4.3	1474	215	0.15	Low	Oscillatory	Inherited
MST2A-16.1	683	130	0.19	Medium	Oscillatory	Inherited
MST2A-18.1	148	1	0.01	Medium	Irregular	Metamorphic
MST2A-11.1	155	1	<0.01	Medium	Irregular	Metamorphic
MST2A-1.1	86	1	0.01	High	Irregular	Metamorphic
MST2A-15.1	140	3	0.02	Medium	Irregular	Metamorphic
MST2A-8.1	211	1	<0.01	Medium	Unzoned	Metamorphic
MST2A-12.1	101	1	0.01	Medium	Unzoned	Metamorphic

Table 2. *Continued*

Spot name	U (ppm)	Th (ppm)	Th/U	CL intensity	CL pattern	Age
MST2A-6.1	405	2	0.001	Medium	Irregular	Metamorphic
MST2A-4.4	210	1	0.01	Medium	Cloudy	Metamorphic

The first number after the sample name indicates the zircon crystal. The CL intensities are estimated according to the CL images and therefore are purely qualitative and significant only when spots from the same zircons or sample are compared. CL patterns not well defined are within brackets. The ages obtained by SHRIMP are classified as "Magmatic" if they date the intrusion of the protolith, "Metamorphic" if they date the metamorphism, "Mixing" if they represent a Mixing between these two ages, and "inherited" if they date Inherited cores of detrital origin. The Th/U data are the same as plotted in Fig. 4.

4 Magmatic Zircons

The zircons extracted from meta-igneous rocks display oscillatory zoning, with more or less narrow bands, parallel to the growing crystal faces (Figs. 2, 3). Alternatively to oscillatory zoning, sector zoning can be present. The different bands exhibit contrasting luminescence intensities and different U contents that range from a few thousands to a few ppm. A significant chemical characteristic of these domains are the Th/U ratios, which are generally higher than 0.1–0.2 and may be as high as 15.6 (Table 2, Fig. 4).

All the zircon domains that show these features and that were dated by SHRIMP yielded a geologically meaningful age for their magmatic protoliths. Few cases were observed in which, in spite of a magmatic age, the zircon domains did not show oscillatory or sector zoning (Table 2). In each of these cases the Th/U ratio was still higher than 0.1–0.2.

Therefore, it can be concluded that in the zircons studied the domains that show an oscillatory/sector zoning and that have Th/U ratios higher than 0.1–0.2 were formed during magmatic crystallisation.

4.1 Comparison Between Zircons from Granitic and Gabbroic Rocks

The zircons from granitic rocks (MUC2-4, MUC10, QUI1 and BZf18) are often elongated in shape (length/width ca 2:1, Fig. 2). Moreover, they have a particularly well-defined banding on a micron scale with relative strong contrasts in luminescence. The U contents are generally higher than 200–300 ppm and can reach several thousands of ppm.

In gabbroic rocks (MUC5-6, QUI2, MSe10, BZg1-2, BZg13, BZb14, CIG1-2, TAS9-25 and MAT2-6) zircons tend to be isometric (length/width close to 1:1, Fig. 3), even if elongated shapes are not uncommon. The contrast in luminescence between the different bands or zones is not as strong as in granitic zircons and growth banding

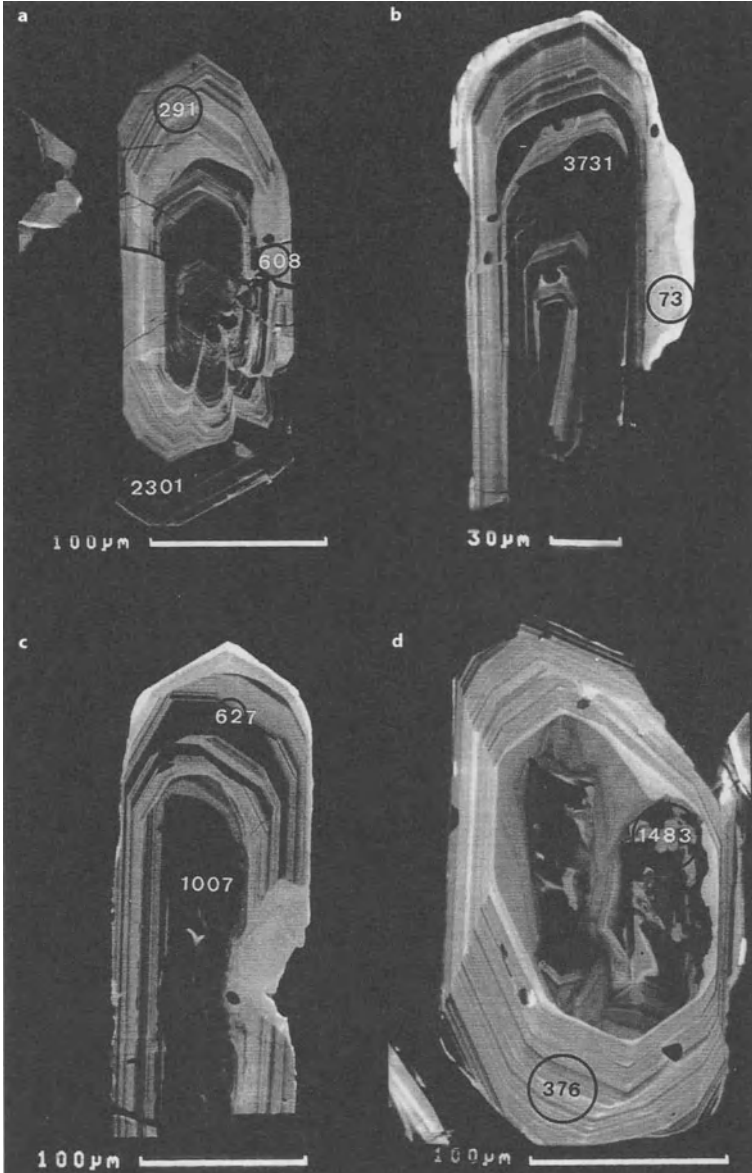


Fig. 2a–d. CL images of magmatically zoned zircons from metagranitic rocks. *Numbers* indicate U contents in ppm; *circles* show the location of the SHRIMP analyses. **a** Zircon from a HP sheared-orthogneiss (MUC2) that show a fine oscillatory zoning and a length/width ratio of 8/3. **b** Zircon from a HP metagranite (MUC10) with typical magmatic zoning. The bright unzoned rim yields a mixing age between the protolith and the metamorphic age. **c** Zircon from a metamorphic vein within a HP metagranite (MUC8) showing features similar to those of the zircons from the country rock (**a**). The bright rim is probably of metamorphic origin, but was not dated, as it is too narrow. **d** Zircon from an HP metagranite (MUC3). The oscillatory zoned domain surrounds a core with irregular zoning. Both domains yield the age of the magmatic crystallisation.

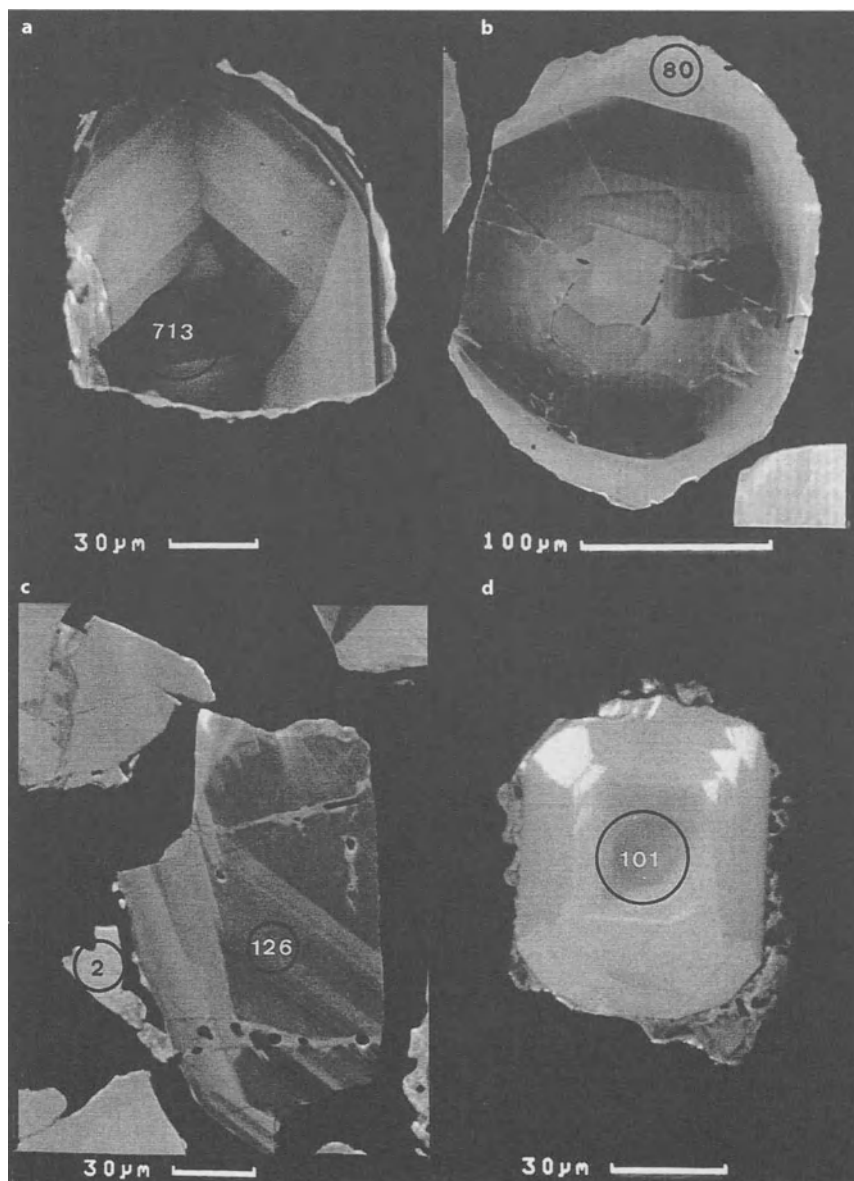


Fig. 3a–d. CL images of magmatic zoned zircons from metabasic rocks. *Numbers* indicate U contents in ppm; *circles* show the location of the SHRIMP analyses. **a** Zircon from the eclogite BZb14; it shows regular broad bands (10 μm scale) with gradational zoning and a low CL contrast when compared to the granitic zircons of Fig. 2. **b** Zircon from an eclogite (QUI2) with nearly isometric shape and sector zoning. **c** Zircon from the HP metagabbro TAS21; it displays a fine banded oscillatory zonation characterised by a lower contrast in U content between the zones. **d** Zircon from an Mn-rich metasediment from the Zermatt-Saas-Fee ophiolites (TAS27). It has a zonation pattern very similar to that of the zircons from the metagabbros collected within the same sequence. Note the sector zoning and the probably metamorphic rim

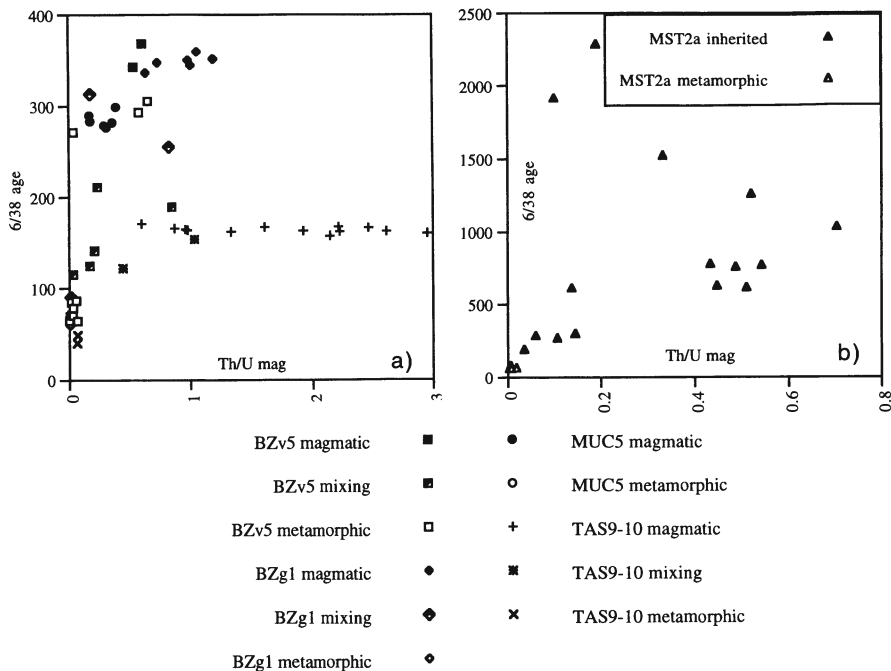


Fig. 4a,b. Ages in Ma vs Th/U ratios. The errors are not plotted because they are smaller than the symbol size. The distinction between magmatic, mixing, metamorphic and inherited domains is made on the basis of the SHRIMP age. a Data from meta-igneous rocks (BZv5, BZg1, MUC5 and TAS9 and 10). For graphical reasons in samples TAS9 and TAS10 the Th/U ratios higher than 3 are not represented. The “mixing” data from sample TAS9-10 refer to analyses that mixed zircon cores and rims. b Data from a metasedimentary rock (eclogitic micaschist MST2a)

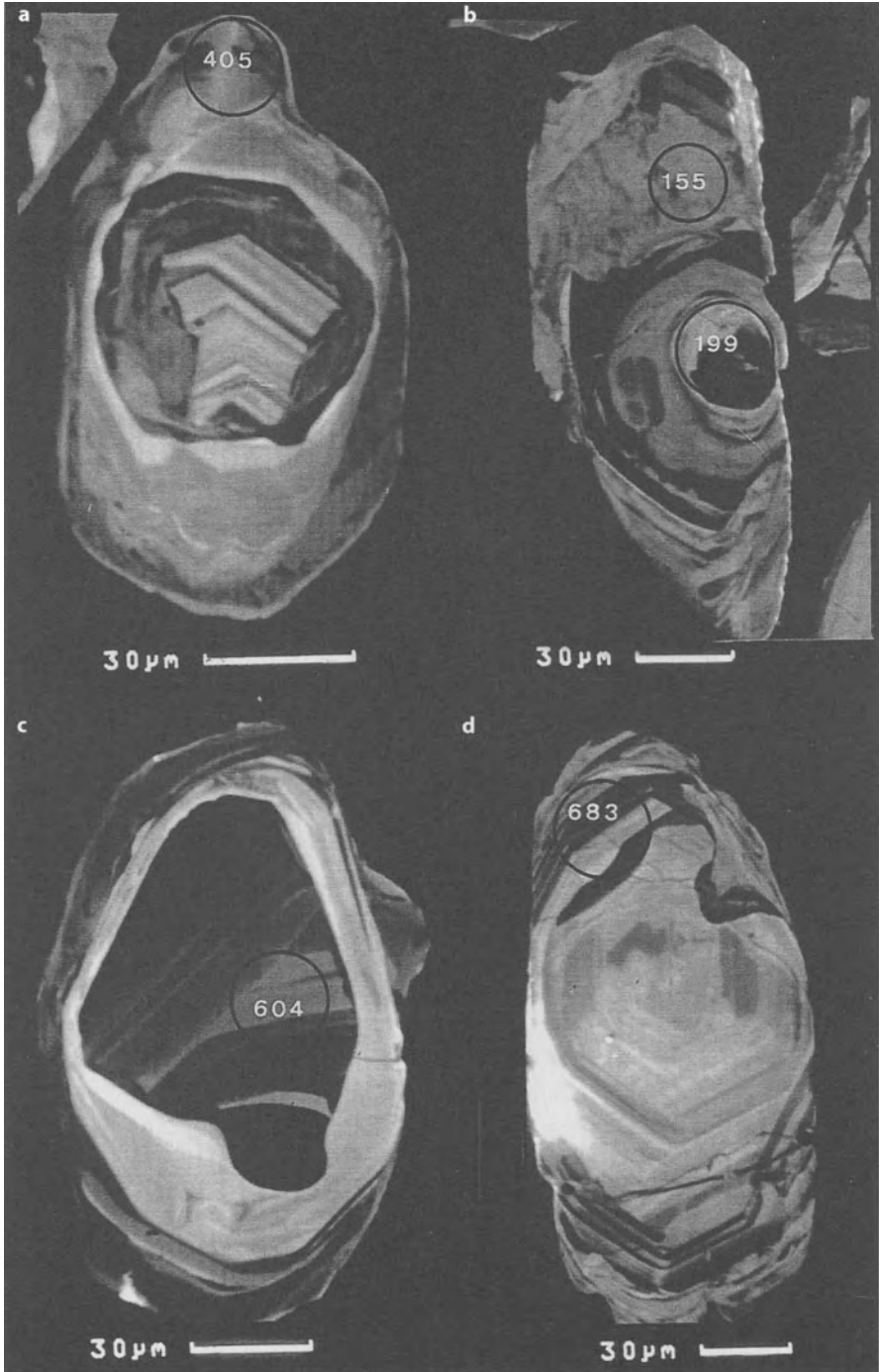
is, in several cases, broader (10 μm scale, Fig. 3a). In a few crystals a gradational zoning within the bands is observed. In ca. 30% of the zircons separated from mafic rocks sector zoning is superimposed on to the oscillatory zoning (Fig. 3b,d). The U content of magmatic zircons from the mafic rocks studied can be, in contrast to granitic zircons, even lower than 100 ppm. A few of the metagabbros sampled within the Zermatt-Saas-Fee ophiolitic sequence contain zircons with U contents even lower than 1 ppm, under or at the detection limit for SHRIMP analyses.

In summary, differences like type of growth banding, sector zoning and U content exist between magmatic zircons from granitic and gabbroic rocks.

5

Detrital Zircons

Four of the samples studied are metasediments: MST2a is a HP micaschist from the Sesia-Lanzo Zone; CIG3, CIG4 and TAS27 are deep-sea metasediments of the Zermatt-Saas-Fee ophiolitic sequence. CIG4 contains only metamorphic zircons;



in TAS27 the zircon population is homogeneous in CL zoning pattern, while the zircons separated from the CIG3 and MST2a show some common features. They always have cores with complicated zoning patterns characterised by different, more or less concentric domains that can display mutual cross cutting relations (Fig. 5). The rounded composite cores generally show embayments due to partial resorption and are surrounded by a later metamorphic rim (Fig. 5c,d). The transition from the detrital core to the younger rim is in some cases marked by a very dark CL zone (Fig. 5a,b), as described by Vavra et al. (1996) in zircons from the near Ivrea Zone.

The inherited cores are not always visible under the optical microscope. For instance, all the zircons from the sample MST2a show a core in the CL image. However, in transmitted light the same zircons only occasionally display cores, especially as most of the crystals are not transparent.

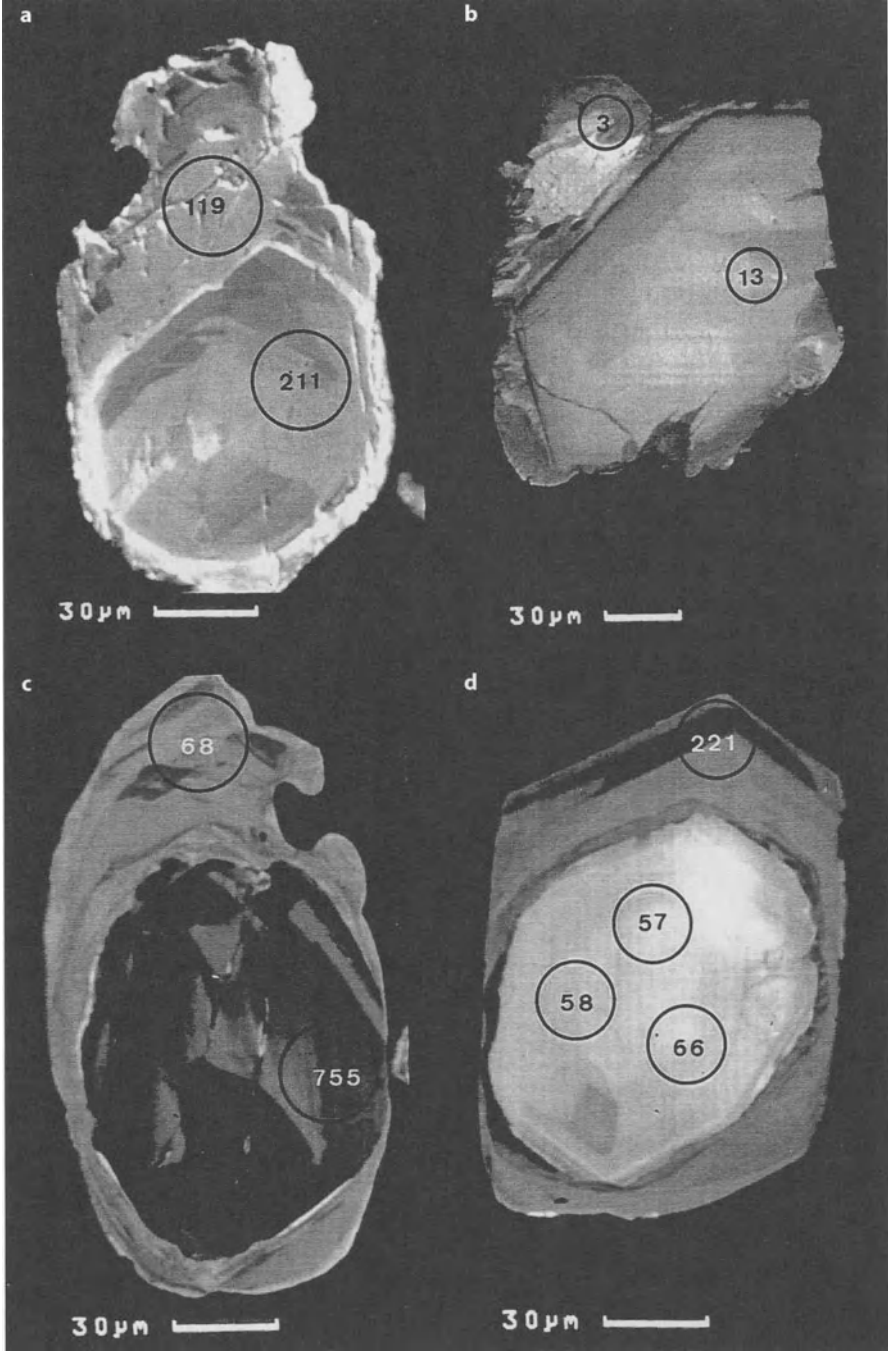
Different CL domains within the same detrital zircon core argue for a poly-phase evolution of the zircon's source, in contrast to detrital zircons with one single zoning pattern (e.g. TAS27, Fig. 3d). SHRIMP dating confirmed this hypothesis. In the samples MST2a and CIG1, even within the same core, different ages were obtained. Moreover, in both samples the different cores yielded different ages. Even if not all of these ages are necessarily geologically meaningful, as lead loss cannot be ruled out for all the data points, the data still argue for a provenance of the sediments from different sources.

6 Metamorphic Zircon Domains

All the sample analysed had a similar Alpine evolution and underwent HP or UHP metamorphism. As a consequence of this, most of the zircons have external zones, irregular in shape, which can form proper rims around older cores (Fig. 6). The most evident feature of these rims in CL is the absence of regular zoning, a rather homogeneous CL emission and thus an uniform U content, as shown also by the EMP profile of Fig. 7. Sometimes these domains display a weak cloudy or patchy zoning or even some relics of planar zoning (Fig. 6b-d).

The chemical composition of these domains is characterised by Th/U ratios systematically lower than 0.1, as shown in Table 2 and Fig. 4. Characteristic for the

←
Fig. 5a-d. CL images of zircons from a metasedimentary rock (eclogitic micaschist MST2a). Numbers indicate U contents in ppm; circles show the location of the SHRIMP analyses. Zircons (a), (b) and (c) have a core with complicated zoning patterns characterised by different, more or less concentric, domains that sometimes display mutual crosscutting relationships. The cores are surrounded by later metamorphic rims. a Zircon showing an inner core with magmatic zoning and an external core with metamorphic zoning. In zircons (a) and (b) an irregular zone very dark in CL marks the transition from the detrital core to the younger rim. c Zircon with a dark zoned magmatic core, which shows embayments due to partial resorption, surrounded by a bright rim. The more external rim is probably metamorphic. d Zircon showing a zoned magmatic core that shows embayments due to partial resorption and an irregular dark area separates it from a second magmatic zone



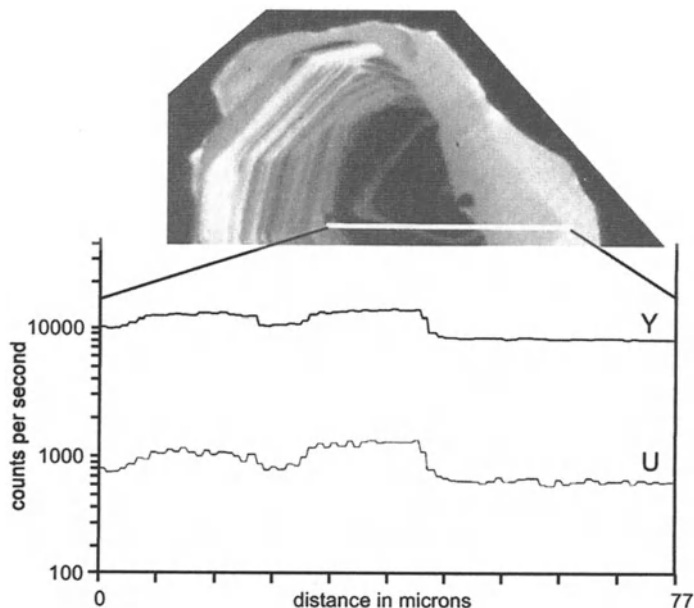


Fig. 7. Qualitative EMP profile across a zircon from a HP metagranite (MUC10) that shows a magmatic zoned core and an unzoned metamorphic rim. The change in trace element concentrations corresponds approximately to the changes in CL emission. The zones dark in CL are relatively enriched in Y and U with respect to the brighter zones. Note that the metamorphic rim shows a flat profile

metamorphic domains is also the low U content, generally less than 100–200 ppm, always lower than the cores. These features have been observed in samples derived from intrusive rocks, while the zircons from the metasediment MST2a have rims with U contents that are sometimes higher than in the detrital cores, but still with lower Th/U ratios.

Also in this case, SHRIMP analyses are of fundamental importance to check the CL interpretation. Most of the domains interpreted in CL as metamorphic yielded the age of the Alpine metamorphism, in agreement with data obtained by

←
 Fig. 6a–d. CL images of zircons with metamorphic rims. *Numbers* indicate U contents in ppm; *circles* show the location of the SHRIMP analyses. **a** Zircon from an eclogite (MUC5) where a metamorphic domain (U: 119 ppm) developed between two magmatically zoned areas. This is evidence for zircon recrystallisation during metamorphism. The metamorphic area is characterised by a high luminescence and the absence of any zonation. **b** Zircon from a HP metamorphic vein (BZv5) that shows a possible overgrown metamorphic rim. The rim probably grew externally to the crystal faces of an euhedral core, which does not show any resorption. **c, d** Zircons from metasedimentary rocks (MST2a and CIG3, respectively) that display rounded detrital cores surrounded by rims that yield metamorphic ages. In this case it is hard to recognise the processes by which the rims formed. Both rims (especially **d**) preserve some relics of regular zonation

other isotopic systems (e.g. Barnicoat et al. 1995; Inger et al. 1996; Duchêne et al. 1997). Others yielded a mixing age between the protolith and the metamorphic ages.

In summary, peripheral irregular zircon domains that show in CL no or weak irregular zoning, that are often bright in CL (U-poor) and are characterised, with respect to cores, by lower Th/U ratios, are interpreted to be of metamorphic origin.

7

Zircons from Metamorphic Veins

Seven of the 34 samples collected are from metamorphic veins (Table 1). All of them occur within HP terrains and were deformed prior to or during the eclogite-facies metamorphism. The only exception is CAv3, which is a late metamorphic vein formed during retrogression. The veins are a few cm up to 40 cm wide and can reach several meters in length. Most of the zircons separated from these veins are similar to the country rock zircons with respect to shape, CL patterns and ages (Fig. 2a). Only in one case (MST1) does the vein contain zircons different from the ones separated from the enclosing country rock (eclogitic micaschist MST2a) and these are the subjects of the next paragraph (Fig. 8).

The zircons from this vein are euhedral, elongated (length/width ca. 3:1) and are transparent under the optical microscope. In CL, they show an oscillatory zoning with unusually narrow growth bands that have a weak contrast in CL intensity (Fig. 8). Some of them also display irregular, interfingering, bright and dark domains, both displaying the same zoning bands (Fig. 8d). A few zircons show peripheral domains with cloudy zoning patterns in CL and are thus similar to metamorphic areas (Fig. 8c). Small rounded cores are sometimes preserved. In these cores it is very hard to distinguish any zoning because of the strong CL emission (Fig. 8a,b).

The U content of these zircons varies over a wide range (250–7400 ppm) and the Th/U ratios are, with the exception of the cores, less than 0.1, lower than in magmatic zircons, but comparable to zircon domains formed in metamorphic environments (Table 3).

The SHRIMP age determinations of the zircons from MST1 gave interesting results. With the exception of the cores, all the data points (within both cloudy and oscillatory zoned domains) yielded ages ca. 10 Ma older (76.1 ± 1.1 Ma, Rubatto et al. 1999) than the eclogite-facies metamorphism dated in the enclosing country rock (65.2 ± 4.6 Ma; Rubatto et al. 1999). As expected, the cores yield older ages similar to the zircon cores preserved in the country rock. An understanding of these zircon data requires geological and petrographic arguments. Therefore their discussion is postponed to Sect. 9.

Table 3. SHRIMP data and CL observations for the sample MST1 (hydrothermal zircons) and MUC6 (zircons affected by metasomatism)

Spot name	U (ppm)	Th (ppm)	Th/U	CL intensity	CL pattern	Age
MST1-15.1	518	3	0.01	Medium	Cloudy	Alpine
MST1-12.1	319	13	0.04	Very high		Alpine
MST1-10.1	259	11	0.04	Very high		Alpine
MST1-17.1	293	15	0.05	Very high	Oscillatory	Alpine
MST1-17.2	2105	160	0.08	Very low	Oscillatory	Alpine
MST1-11.1	2754	265	0.10	Very low	Oscillatory	Alpine
MST1-23.1	1814	5	<0.01	Low	Cloudy	Alpine
MST1-23.2	2618	204	0.08	Low	Oscillatory	Alpine
MST1-40.1	454	22	0.05	Medium	Cloudy	Alpine
MST1-34.3	8255	141	0.02	Very low	Oscillatory	Alpine
MST1-5.2	1859	130	0.07	Very low	Oscillatory	Alpine
MST1-9.2	2428	241	0.10	Very low	Oscillatory	Alpine
MST1-2.2	3819	316	0.08	Very low	Unzoned	Alpine
MST1-9.1	290	32	0.11	Very high		Inherited
MST1-5.1	340	57	0.17	Very high	Cloudy	Inherited
MST1-19.1	619	246	0.40	Medium	Oscillatory	Inherited
MST1-19.2	674	163	0.24	Low	Oscillatory	Inherited
MST1-34.1	595	199	0.33	Very high	Cloudy	Inherited
MST1-34.2	7408	102	0.01	Low	Cloudy	Inherited
MST1-2.1	1764	700	0.40	Medium	Cloudy	Inherited
MUC6.25.1	732	1273	1.7	Medium	Oscillatory	Magmatic
MUC6.25.2	183	100	0.55	Medium	Sector	Magmatic
MUC6-23.2	521	590	1.1	Low	Oscillatory	Magmatic
MUC6-7.2	262	208	0.79	High	Oscillatory	Magmatic
MUC6-12.2	348	163	0.47	Low	Oscillatory	Magmatic
MUC6-1.1	228	182	0.80	Medium	Oscillatory	Magmatic
MUC6-1.2	48	9	0.19	Medium	Unzoned	Magmatic
MUC6-29.1	1382	632	0.46	Low	Oscillatory	Magmatic
MUC6-25.3	30	3	0.10	High	Unzoned	Metasomatic
MUC6.23.1	30	5	0.16	Medium	Broad sector	Metasomatic
MUC6-4.1	17	2	0.09	High	Broad sector	Metasomatic
MUC6-12.1	42	5	0.11	High	Unzoned	Metasomatic
MUC6-7.1	18	3	0.14	High	Broad bands	Metasomatic

The first number after the sample name indicates the zircon crystal. Where no CL pattern is indicated the very high CL intensity does not permit any zoning to be seen. For information regarding "Age" and "CL intensity," refer to Table 2.

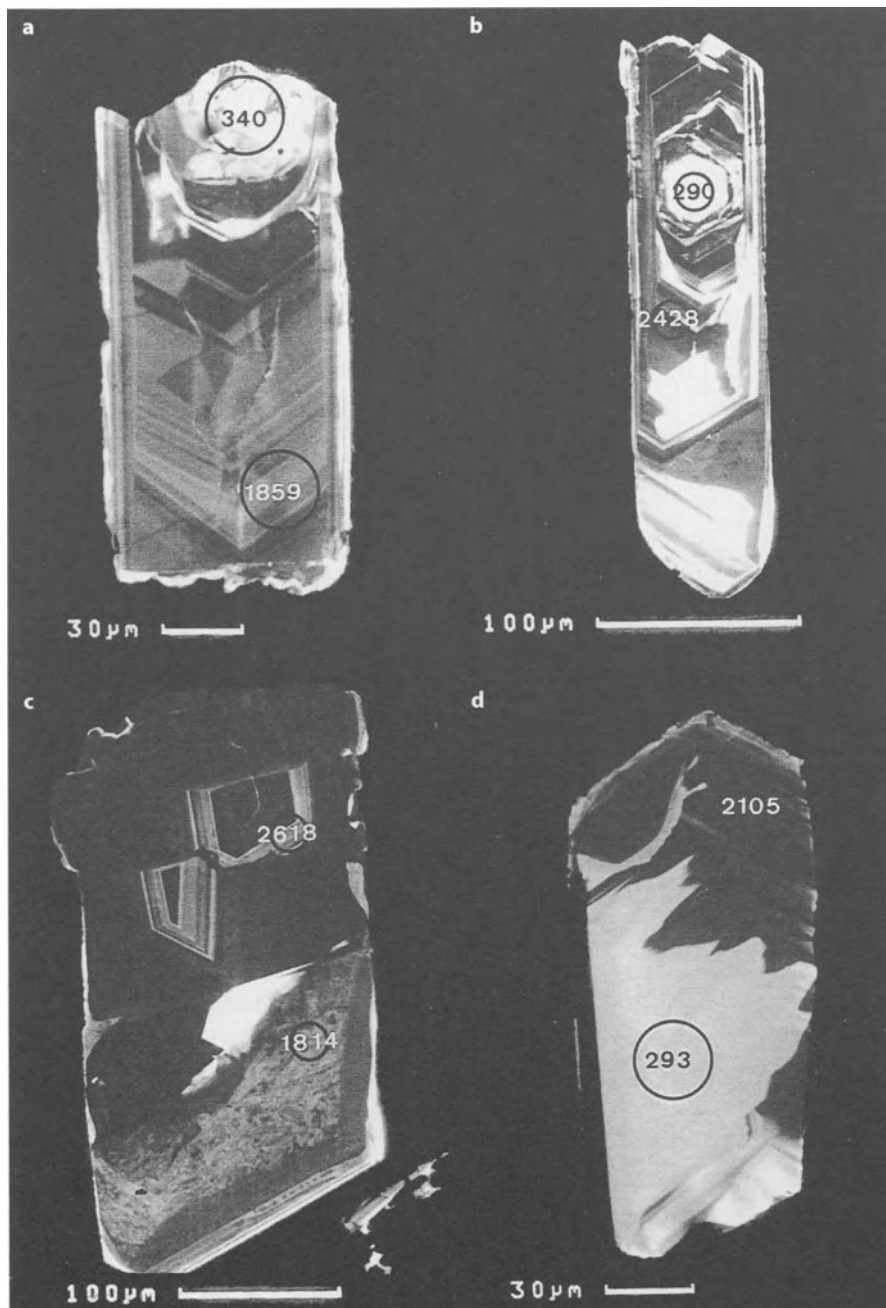


Fig. 8a–d. CL images of zircons from metamorphic vein MST1. Numbers indicate U contents in ppm; circles show the location of the SHRIMP analyses. The crystals are elongate in shape and show an oscillatory zoning with unusually narrow growth bands that display only a weak contrast in CL intensity. **a, b** Zircons that preserve a detrital core which has a very high CL emission.

8

Zircons Affected by Metasomatism

Zircons separated from an eclogite of the Sesia-Lanzo Zone, which preserves a fresh eclogite-facies paragenesis (MUC6, Fig. 9a,b), represent a very interesting and unusual case. They have magmatic cores that in CL display oscillatory and sector zoning. Domains brighter in CL, which display a weaker zoning, surround the cores. The oscillatory sector zoning of the cores gradually fades towards the rims. Sometimes it is crosscut by areas that show relatively broad, non-planar oscillating zones or sectors.

With only one exception, the peripheral portions are depleted in U (18–42 ppm) when compared to the cores (180–1380 ppm, Table 3). The chemical differences between the two types of domains are also marked by their Th/U ratios (Table 3).

The age of the cores corresponds to the age of the Permo-Carboniferous magmatic protolith (286 ± 6 Ma), in agreement with the age of the other eclogite (MUC5: 285 ± 7 Ma; Rubatto et al. 1999) and the metagranites (MUC 2, 3 and 4: 294 ± 3 Ma, and MUC10: 297 ± 18 Ma; Rubatto 1998) which were collected in the same area. The peripheral portions yield a significantly younger age (221 ± 14 Ma; Rubatto 1998). The five data points form a well defined cluster on the concordia diagram, which rules out the possibility of mixing ages and argues for a discrete geological event, discussed in the following section.

9

Discussion

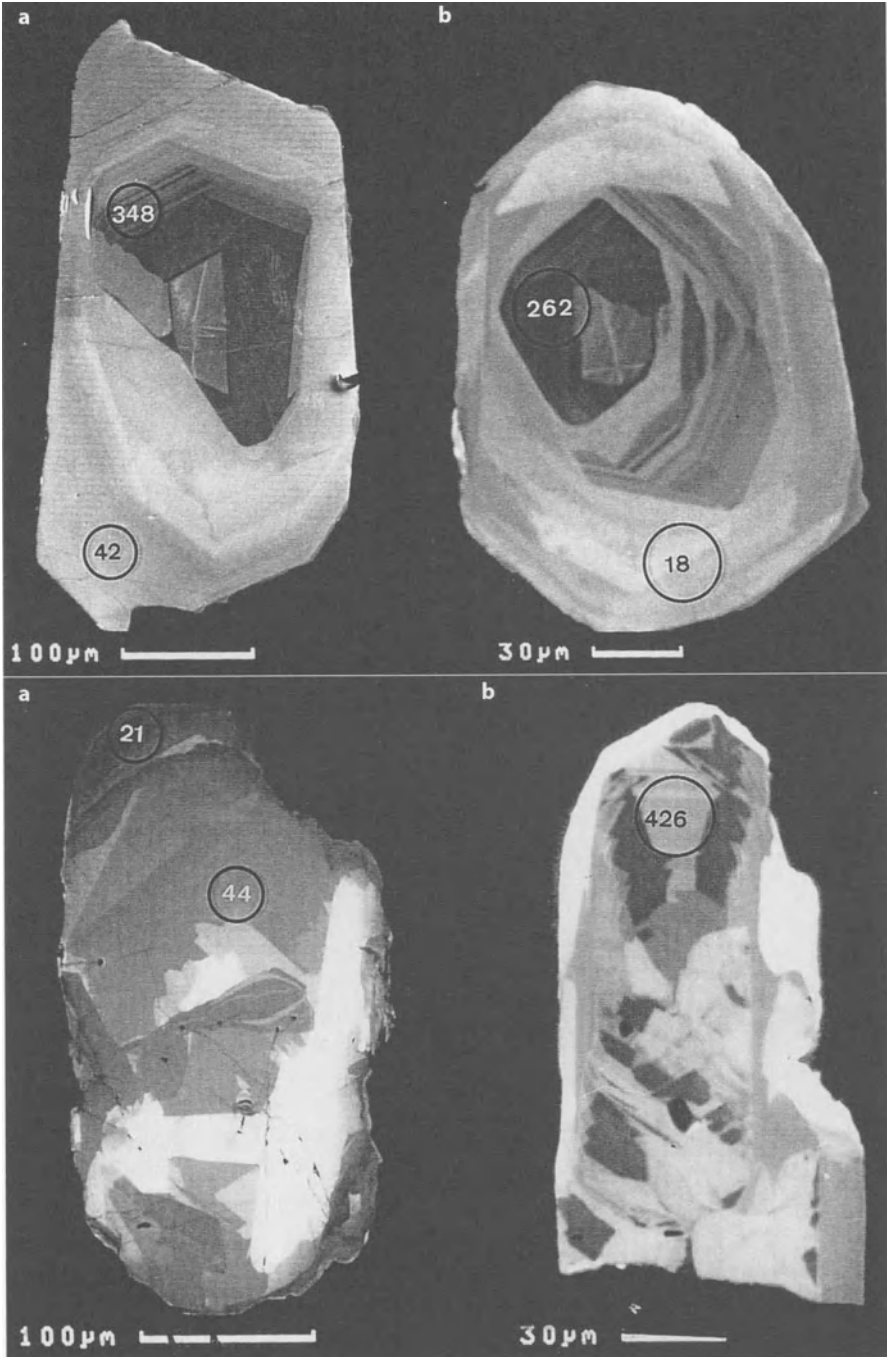
9.1

Cathodoluminescence and U Content

Our study confirms the earlier observation that CL emission of zircons shows a negative correlation to U and Y contents. This seems to indicate that these elements have a negative effect on CL. Unfortunately, SHRIMP analyses do not measure Y contents and therefore it is impossible at this stage to establish if this element is, as U, systematically negatively correlated to CL emission. However, the qualitative EMP profiles argue in favour of this (Figs. 1, 7). This observation implies that the CL emission is caused by elements other than U and, probably, Y.

It has been already observed that with increasing abundance of minor and trace elements (U, Th, Y, P, Ca, Hf, Fe, Al, Na and K) the relative intensity of CL in zircons decreases (Sommerauer 1974). However, studies of CL spectra using natural and doped zircons seem to suggest that Ti and U can induce, not reduce,

←
c Zircon showing a peripheral domain with a cloudy zoning pattern, similar to metamorphic domains. This domain yielded the same age as the oscillatory zoned areas. d Zircon that displays irregular interfingering bright and dark domains. Within the bright area traces of the same oscillation bands as in the dark area are visible



luminescence (Ohnenstetter et al. 1991). The negative correlation between CL and Y content observed in our profiles agrees with the hypothesis of Ohnenstetter et al. (1991). They suggested that, in zircons doped with Y, a particular emission band is due to lattice defects associated with the presence of this element, but that at high concentration levels the Y^{3+} has a quenching effect on luminescence. Therefore, it is likely that the abundance of trace elements, such as U and Y, decreases the CL emission by non-stoichiometry and/or structural defects. The time-dependent radioactive decay does not seem to play an important role in reducing luminescence, as old zircons (Precambrian) with relatively high U contents give CL images with a clear zoning and a variable CL intensity. Also, the possibility that U does not play any active role in reducing CL emission, but is systematically correlated to other trace elements more directly related to CL, has to be taken into consideration. Possible elements playing an important role as CL activators in zircons are, for instance, Dy and Tb (Hanchar and Rudnick 1995); however no information about the abundance of these elements was obtained during EMP or SHRIMP measurements.

At this stage it is not possible to understand whether in zircons the relatively low luminescence of domains enriched in U and Y is due to the presence of any of these two trace elements or to other elements associated with them. Nevertheless, the empirical observation that a negative correlation exists between U content and CL intensity is important. This correlation is a powerful qualitative tool to identify zircons and zircon domains relatively rich in U. The latter are generally more suitable for U-Pb dating by ion microprobe, when, as in our case, relatively young and U-poor zircons are studied. By contrast, in U-richer zircons the problems of lead-loss and discordance, occurring when very U-rich areas are dated, can be avoided.

9.2 Magmatic Zoning

Magmatic zoning has been widely described in the literature not only for zircons. Shimizu (1990) suggested possible mechanisms generating oscillatory zoning in augite, and Halden et al. (1993) discussed the case of zircons. All authors agree that zoning is due to oscillation in trace element chemistry. Our observation that the contrast in CL emission within the individual growth bands corresponds to depletion or enrichment of U and Y confirms that the classical oscillatory zoning of a magmatic zircon is caused by the oscillating depletion and enrichment of trace and minor elements at the crystal-melt interface.



Fig. 9a-d. CL images of zircons from eclogite MUC6 (a, b), UHP Mn-rich micaschist CIG3 (c) and eclogite CIG2 (d). Numbers indicate U contents in ppm; circles show the location of the SHRIMP analyses. The magmatic cores in (a) and (b) display an oscillatory/sector zoning that gradually fades in the direction of the rims. The rims show relatively broad, non-polygonal zoning. They are thought to have been affected by metasomatic leaching. Zircons (c) and (d) show irregular sector zoning with a nonsystematic alternation of bright and darker domains, which display a weak and very fine oscillatory zoning. These zircons yield the age of the metamorphism

In the present study, the comparison between zircons from granitic and gabbroic rocks led to some relevant observations. The U content of granitic zircons, generally higher than of mafic zircons, is a consequence of the enrichment in incompatible elements, such as U, in more differentiated melts. Nevertheless, this general observation cannot be taken as a rule as shown by U contents higher than 1000 ppm measured in one zircon from the eclogitic gabbro TAS10 (Table 2).

We described that granitic zircons have narrow bands with strong CL contrasts, while gabbroic zircons display reduced CL contrasts between bands which are sometimes broader. These observations are in tune with cases reported in the literature (Hanchar and Miller 1993; Pidgeon 1992; Pidgeon et al. 1990; Van Breemen et al. 1987; Vavra et al. 1996). One of the few examples of zircons from gabbros is described by Schärer et al. (1995), who shows CL images of crystals with a zoning pattern characterised by broad bands (>10 μm) crosscut by sector zoning similar to the one shown in Fig. 3b. The difference in magmatic zoning of zircons from rocks with different chemical compositions may be explained by the different temperatures at which the melts crystallized. Assuming saturation of ZrSiO_4 in a relatively cold granitic magma, the melt at the crystal surface will be frequently depleted in trace elements because of the relatively low diffusion rates of these elements. This causes a fine growth banding with strong CL contrasts due to a strong and frequent oscillation in U and other trace element concentrations at the crystal-melt interface. However, in a hotter mafic melt the faster diffusion rate of trace elements prevents strong enrichment and depletion at the interface so that the chemical zoning of the growing crystal is weaker, broader and sometimes gradual. In general, the diffusion coefficient of elements at a given temperature is a few orders of magnitude lower in rhyolitic melts than in basaltic melts (Brady 1995). This supports our hypothesis. Obviously, the above explanations are limited because additional work is needed to understand which other factors could control the U and trace element distribution within growing zircon crystals. For instance, little is known about the kinetics (e.g. growth rate), crystallisation sequence and chemical behaviour of zircons in different melts.

9.3

Detrital Zircons

The zoning pattern described in Sect. 5 revealed that CL is useful in the identification of detrital zircon cores. As the zircon population of a sediment results from the mixing of grains from different sources, detrital zircons will show different CL patterns. In poly-metamorphic terrains, detrital zircons with complex internal structures are expected. In an eclogitic micaschist of the Sesia-Lanzo Zone (MST2a) the presence of detrital zircon cores proves the sedimentary origin of the protolith. The complexity of the CL patterns as well as the different ages of the detrital cores argue for different sediment sources.

The identification of detrital zircon cores is of fundamental importance for conventional multigrain or single grain dating, in which inheritance causes discordant age patterns and mixing ages. Also, when laser ablation techniques are applied to zircons, the presence of inherited cores can be a cause of mixed ages if the laser penetrates too deeply into the crystal or if the spot size is relatively large

(40 μm). Using the SHRIMP technique, the cores can be dated precisely and relatively easily and thus a maximum depositional age can be derived via the youngest zircon core found. The deep-sea sediments overlying the Middle Jurassic ophiolites of the Zermatt-Saas-Fee (CIG3 and TAS27) are a good example of the application of CL study to metasediments. They contain zircons with cores as young as Middle Jurassic (Rubatto et al. 1998). In addition, most of the zircon cores show a zonation pattern quite typical for gabbroic rocks (Fig. 3d). This implies that the deposition occurred after the Middle Jurassic and that detrital components were coming mainly from the surrounding ophiolitic gabbros, the only known magmatic rocks that yield this age.

9.4

Metamorphic Zircons

Our study reports the first cases of metamorphic zircon domains formed at relatively low temperatures: metamorphic temperatures of both investigated units are well constrained at a maximum of 600 °C (Fry and Barnicoat 1987; Pognante 1989). In the more common case of granulite-facies metamorphism the formation of zircon domains is generally attributed to two different processes: (1) overgrowth, where partial melting induced zircon resorption and reprecipitation (Claesson 1987; Van Breemen et al. 1987; Vavra et al. 1996); (2) solid-state recrystallisation or replacement rather than new growth (Pidgeon 1992). In numerous zircons analysed during this study it is not always easy to establish whether a metamorphic domain represents an overgrowth or a re-orientation during solid state processes of a pre-existing crystal lattice (recrystallisation). If metamorphic domains cut across older magmatic zoning (Fig. 7) or if they clearly develop between two magmatically zoned areas (Fig. 6a) it is likely that they formed by sub-solidus recrystallisation of a previous magmatic crystal lattice. Relics of magmatic zoning within a metamorphic domain are further evidence for sub-solidus formation. Domains yielding intermediate ages ranging between the protolith age and the age of the metamorphism confirm the hypothesis of recrystallisation. However, metamorphic overgrowth could be an explanation for domains that occur externally to crystal faces of euhedral zircons, which do not show any resorption (Fig. 6b).

The chemical composition of most of the metamorphic zircon domains analysed (low Th/U ratio and often relative low U content) is in agreement with observations regarding zircon domains formed during granulite-facies metamorphism (Claesson 1987; Williams and Claesson 1987; Pidgeon 1992). Different processes can explain the low Th content in metamorphic zircons. (1) Th mobilised during metamorphism and thus available in the system at the time of zircon formation is trapped by other mineral phases. This process probably acts in rocks in which Th-rich phases such as monazite, titanite or allanite are forming or recrystallising during metamorphism. (2) Th is not mobilised from other mineral phases during metamorphic processes and therefore the new zircon overgrowth is relatively Th-poor. This explanation alone is plausible only in case of overgrowth, as it cannot explain the case of in situ recrystallised domains where Th would be retained. (3) At relatively low metamorphic temperatures (in our case ca. 600 °C) the amount

of trace and minor elements that can fit into the lattice is drastically reduced. Therefore, elements as U and Th, having atomic radii larger than that of Zr, are expelled in case of recrystallisation or they do not enter the crystal lattice in case of new overgrowth. Th might be even more incompatible than U because of its slightly bigger radius (e.g. Pidgeon 1992) or different charge distribution. This last process is preferred because it explains the fact that some of the domains partially reset in age show an intermediate Th/U ratio. When the sub-solidus re-orientation of the lattice is incomplete then both Pb and Th are only partially lost. However, it is likely that a combination of all these processes, either acting all together or one or another being prevalent cases, results in the very low Th/U ratios of metamorphic domains. The high pressures suffered by the investigated tectonic units cannot be considered to be a relevant factor in Th and U distribution as low Th/U ratios are typical also for metamorphic rims formed at lower pressures.

9.5

Zircon Behaviour in the Presence of Fluids

The case of zircons from the metamorphic vein MST1 can be interpreted when geological and petrographic constraints are integrated with the CL studies and SHRIMP dating. Mineral composition and field relations support a metamorphic origin of the vein. A magmatic protolith is ruled out because of the chemical composition of the vein (quartz and jadeite). In addition, no magmatic intrusions of that age are known. The presence of partial melting in this rock is excluded by the absence of quartz-feldspar pockets in the rock and by the too low temperature reached during metamorphism (600–550 °C). Therefore, the zircons within the vein did not crystallise from a melt. The euhedral, elongated crystal shape argues against a possible detrital origin of these zircons. Instead, crystal shape and zoning observed in CL suggest that the zircons have grown in equilibrium with a fluid phase, where euhedral crystal faces grew freely and the oscillations in U concentration at the crystal-fluid interface produced an oscillatory zoning. The relatively low Th/U ratios are in agreement with a metamorphic environment and the exceptionally high U content of some zircons indicates that the fluid was enriched in trace elements. This enrichment might be due to partial dissolution of zircons from the country rock. Therefore, it is suggested that the narrow growth zoning and the elongated euhedral shape of the zircons occurring in the metamorphic vein result from fast mineral growth in a hydrothermal environment. The age of these zircons, significantly older than the metamorphic peak dated in the country rocks, argues for a formation of the vein and the zircons during the prograde path. Quartz-rich veins within metapelites commonly form under low or very low-grade metamorphic conditions and the present mineral assemblage of the vein would then reflect the HP transformation of such a vein. The fact that the zircons from the vein did not record the eclogitic peak is not surprising: at time of high-pressure metamorphism they were only 10 Ma old, not yet metamict and therefore less subject to lead loss at such low temperatures.

The eclogite and the metasediments of Lago di Cignana (CIG2, 3 and 4) represent other cases of suspected zircon growth in the presence of metamorphic fluids. These low temperature (ultra-) high pressure rocks (600 °C and 28 kbar; Rei-

necke 1991) contain zircons with various type of domains yielding the age of metamorphism (Fig. 9c,d). Of particular interest are zircon crystals that in CL show irregular sector zoning with a non-systematic alternation of brighter and darker domains. The different sectors or areas have polygonal sharp boundaries and can display a weak and very fine oscillatory zoning (Fig. 9d). This zircon type is present in the eclogite and the two metasediments. It is suggested that these zircons, which have no traces of inherited components, grew during metamorphism in the presence of HP fluids close to peak metamorphic temperatures (600 °C). By contrast, zircons within the same samples that yield inherited ages and display typical magmatic CL zoning may have been protected as inclusions in stable minerals. Zr and trace elements (for instance U) were probably introduced into these rocks by the fluids, as the inherited zircons preserved are not resorbed. The metasedimentary sequence may have been the external source for those elements.

In eclogite MUC6, sharp boundaries between the core and weakly zoned U-Th-poor zircon rims may argue for the formation of these rims in a U- and Th-poor environment, after partial resorption of the pre-existing magmatic crystals. However, the age of the rims does not correspond to any regional event in this tectonic unit. The metamorphic evolution of the area is well known and no evidence of regional metamorphism, partial melting or magmatism at the time of formation of the zircon rims (221 ± 14 Ma) exists. It is suggested that the younger, peripheral portions probably reflect a metasomatic event during which fluid percolation, due to mafic underplating at lower crustal levels (Ivrea Zone), leached Pb, Th and U resetting the age of the zircon rims and preserving the cores. The problem of the sharp boundaries between the domains affected by metasomatic leaching and the magmatic zircon cores would be explained by sub-solidus lattice re-orientation of the rims due to fluids. By comparing the U-rich core with the U-poor rims a mobilisation during metasomatic leaching of circa 80–95% of the total U can be estimated. The removal of Th was even more dominant, up to 99%. During this process no complete annealing of the magmatic zoning was reached as evidenced by the preservation of ghost zoning. Fluid percolation, for instance along microfractures or grain boundaries, would not be detected by geological and/or petrographic evidence, especially because the unit was overprinted by later Alpine metamorphism. This would explain why this metasomatic event is only recorded by zircons. Similar ages were also found by Vavra et al. (1996) in zircons from the nearby Ivrea Zone and by Gebauer et al. (1997) in the Dora-Maira Massif (Western Alps). They interpreted these ages as the time of fluid infiltration during mafic underplating at the beginning of the continental breakup.

10

Conclusions

1. A negative correlation exists between CL emission and U content of different zircon bands or domains. This observation was made on a large number of zircons from different rock types having U contents between a few ppm and several thousands of ppm. Therefore, this correlation is independent of rock type and conditions of zircon formation.

2. The distinction of different zircon domains according to CL patterns and chemical composition (U content and Th/U ratio) is essential for accurate U-Pb dating of distinct geological processes.
3. Magmatic zircons show a planar, banded oscillatory zoning pattern. The contrast in CL emission between the oscillating zones reflects depletion or enrichment of trace elements (e.g. U and Y) at the crystal melt interface.
4. In the studied rocks, zircons from granitic and gabbroic rocks have been distinguished on the basis of the width of oscillatory growth bands, presence or absence of sector zoning and U content.
5. CL investigation is indispensable in the identification of detrital zircon cores. Moreover, the CL zoning pattern as well as SHRIMP dating of detrital cores help in understanding the maximum age of deposition and the source of sediments.
6. During low temperature-high pressure metamorphism (~550–600 °C and 15–28 kbar) neo-formation of zircon may occur. The metamorphic domains visible in CL are usually irregular in shape, unzoned or with a patchy, cloudy zoning. In rare cases they display some traces of regularly banded zoning. They are chemically characterised by lower U contents and lower Th/U ratios (<0.1) than magmatic zircons.
7. In one metamorphic vein zircons elongated and euhedral in shape are interpreted as having formed in the presence of hydrothermal fluids. They show CL patterns characterised by very narrow growth bands with relatively weak luminescence contrasts. These zircons can reach extraordinarily high U contents (up to 8255 ppm) and have Th/U ratios lower than 0.1.
8. The characteristic sector zoning observed in zircons from two UHP metamorphic rocks is attributed to zircon growth in the presence of metamorphic fluids.
9. In one sample zircon rims that show a weak, broadly spaced zoning and have U contents and Th/U ratios drastically reduced with respect to the magmatic cores are interpreted as affected by metasomatic leaching of Pb, U and Th related to fluid percolation.

Acknowledgements. We thank the SHRIMP group at the ANU in Canberra for the assistance given during ion microprobe analyses. A special acknowledgement goes to Mark Fanning for supervising the SHRIMP work during 1996 and 1997, and for making our visit at ANU very enjoyable. Jörg Hermann, Lourdes Sanchez Rodríguez and Urs Schaltegger are especially thanked for improving a first version of the manuscript. We are grateful to Diane Seward for correcting the English. This research was financially supported by the Swiss National Science Foundation (Project 20–32525.91).

References

- Barnicoat AC, Rex DC, Guise PG, Cliff RA (1995) The timing of and nature of greenschist facies deformation and metamorphism in the upper Pennine Alps. *Tectonics* 14(2):279–293
- Beaerth P (1967) Die Ophiolithe der Zone von Zermatt-Saas Fee. Stämpfli and Cie, Bern

- Brady JB (1995) Diffusion data for silicate minerals, glasses and liquids. In: TJ Ahrens (ed) *Mineral physics and crystallography. A handbook of physical constants 2*. AGU books board pp 269–290
- Claesson S (1987) Isotopic evidence for the Precambrian provenance and Caledonian metamorphism of high grade paragneisses from the Seve Nappes, Scandinavian Caledonides. I. Conventional U-Pb zircon and Sm-Nd whole rock data. *Contributions to Mineralogy and Petrology* 97:196–204
- Compagnoni R (1977) The Sesia-Lanzo Zone: high pressure-low temperature metamorphism in the Austroalpine continental margin. *Rendiconti della Societe Italiana di Mineralogia e Petrologia* 33: 335–374
- Compston W, Williams IS, Kirschvink JL, Zhang Z, Ma G (1992) Zircon U-Pb ages for the Early Cambrian time-scale. *Journal of the Geological Society, London* 149:171–184
- Crookes W (1879) Contributions to molecular physics in high vacua. *Philosophical Transactions of the Royal Society* 170:641–662
- Dal Piaz G. V (1993) Evolution of Austro-Alpine and Upper Penninic Basement in the Northwestern Alps from Variscan Convergence to Post-Variscan Extension. In: JF von Raumer, F Neubauer (eds) *Pre Mesozoic Geology in the Alps*. Springer Verlag, Berlin, Heidelberg, New York, pp 327–344
- Dal Piaz G. V, Hunziker J. C, and Martinotti G (1972) La Zona Sesia-Lanzo e l'evoluzione tettono-metamorfica delle Alpi Nord-Occidentali interne. *Memorie della Societa Geologica Italiana* 11:433–460
- Duchêne S, Blichert-Toft J, Luais B, Têlouk P, Lardeaux J.-M, and Albarède F (1997) The Lu-Hf dating of garnets and the ages of the Alpine high-pressure metamorphism. *Nature* 387:586–589
- Fry N, Barnicoat AC (1987) The tectonic implications of the high-pressure metamorphism in the western Alps. *Journal of the Geological Society, London* 144:653–359
- Gebauer D (1996) A P-T-t-Path for an (Ultra?) High-Pressure Ultramafic/Mafic Rock-Association and its Felsic Country-Rocks Based on SHRIMP-Dating of Magmatic and Metamorphic Zircon Domains. Example: Alpe Arami (Central Swiss Alps). In: *Earth Processes: Reading the Isotopic Code*. American Geophysical Union, pp 309–328
- Gebauer D, Quadt A, Compston W, Williams IS, Grünenfelder M (1988) Archean zircons in a retrograded, Caledonian eclogite of the Gotthard Massif (Central Alps, Switzerland). *Schweizerische Mineralogische und Petrographische Mitteilungen* 68:485–490
- Gebauer D, Rubatto D (1997) 35 Ma old UHP-metamorphism of the Dora Maira Massif and other Tertiary HP- and UHP- events in the Central and Western Alps: Geodynamic consequences. *Schweizerische Mineralogische und Petrographische Mitteilungen*
- Halden NM, Hawthorne FC, Campbell JL, Teesdale WJ, Maxwell JA, Higuchi D (1993) Chemical characterisation of oscillatory zoning and overgrowths in zircons using 3 MeV m-PIXE. *Canadian Mineralogist* 31: 637–647
- Hanchar J.M, Miller CF (1993) Zircon zonation patterns as revealed by cathodoluminescence and backscattered electron images: Implications for interpretation of complex crustal histories. *Chemical Geology* 110:1–13
- Hanchar JM, Rudnick RL (1995) Revealing hidden structures: The application of cathodoluminescence and back-scattered electron imaging to dating zircons from lower crust xenoliths. *Lithos* 36:289–303
- Inger S, Ramsbotham W, Cliff RA, Rex DC (1996) Metamorphic evolution of the Sesia-Lanzo Zone, Western Alps: time constraints from multi-system geochronology. *Contributions to Mineralogy and Petrology* 126:152–168
- Leverenz HW (1968) *An introduction to luminescence of solids*. Dover
- Mariano AN (1978) The application of cathodoluminescence for carbonatite exploration and characterisation. *Int. Symp. on Carbonatites, 1st*, 39–57
- Marshall DJ (1988) *Cathodoluminescence of geological materials*. Uuwin Hyman

- Ohnenstetter D, Cesbron F, Remond G, Caruba R, Claude JM (1991) Emission de cathodoluminescence de deux populations de zircons naturels: tentative d'interpretation. *Compt Rendu de l'Academie de Sciences, Paris* 113 (Ser. II), 641-647
- Ono A (1976) Chemistry and zoning of zircons from some Japanese granitic rocks. *J. Japan. Assoc. Min. Petr. Econ. Geol.* 71:-17
- Pidgeon RT (1992) Recrystallisation of oscillatory zoned zircon: some geochronological and petrological implications. *Contributions to Mineralogy and Petrology* 110:463-472
- Pidgeon RT, Wilde SA, Compston W, Shield MV (1990) Archaean evolution of the Wongan Hills Greenstone Belt, Yilgarn Craton, Western Australia. *Australian Journal of Earth Sciences* 37:279-292
- Pognante U (1989) Tectonic implications of lawsonite formation in the Sesia zone (Western Alps). *Tectonophysics* 162:219-227
- Reinecke T (1991) Very-high-pressure metamorphism and uplift of coesite-bearing metasediments from the Zermatt-Saas zone, Western Alps. *European Journal of Mineralogy* 3:7-17
- Rubatto D (1998) Dating of pre-Alpine magmatism, Jurassic ophiolites and Alpine subductions in the Western Alps. PhD Doctoral thesis, ETH, Swiss Federal Institute of Technology
- Rubatto D, Gebauer D, Compagnoni R (1999) Dating of eclogite-facies zircons: the age of Alpine metamorphism in the Sesia-Lanzo Zone (Western Alps). *Earth and Planetary Science Letters* 167:141-158
- Rubatto D, Gebauer D, Fanning M (1998) Jurassic formation and Eocene subduction of the Zermatt - Saas-Fee ophiolites: Implications for the geodynamic evolution of the Central and Western Alps. *Contributions to Mineralogy and Petrology* 132: 269-287
- Schärer U, Kornprobst J, Beslier M.-O, Boillot G, and Girardeau J (1995) Gabbro and related rock emplacement crust: U-Pb geochronological and geochemical constraints for the Galicia passive margin (Spain). *Earth and Planetary Science Letters* 130:187-200
- Shimizu N (1990) The oscillatory trace element zoning of augite phenocrysts. *Earth Sc. Rev.* 29, 27-37
- Sommerauer J (1974) Trace elements distribution patterns and mineralogical stability of zircons - An application for combined electron microprobe techniques. *Electron Microscopy Society of Southern Africa, Proceedings* 4:71-72
- Van Breemen O, Henderson JB, Loveridge WD, Thompson PH (1987) U-Pb zircon and monazite geochronology and zircon morphology of granulites and granite from the Thelon Tectonic Zone, Healey Lake and Artillery Lake map areas, N.W.T. *Current Research Geological Survey of Canada, Part A* 87-1A(2):783-801
- Vavra G, Gebauer D, Schmidt R, Compston W (1996) Multiple zircon growth and recrystallisation during polyphase Late Carboniferous to Triassic metamorphism in granulites of the Ivrea Zone (Southern Alps): an ion microprobe (SHRIMP) study. *Contributions to Mineralogy and Petrology* 122, 337-358
- Williams I.S, Claesson S (1987) Isotopic evidence for the Precambrian provenance and Caledonian metamorphism of high grade paragneisses from the Seve Nappes, Scandinavian Caledonides. II. Ion microprobe zircon U-Th-Pb. *Contributions to Mineralogy and Petrology* 97:205-217

A Combination of Single Zircon Dating by TIMS and Cathodoluminescence Investigations on the Same Grain: The CLC Method – U-Pb Geochronology for Metamorphic Rocks

ULRIKE POLLER

1

Introduction:

The Different U-Pb Dating Methods

An essential question in geoscience is the age of a rock. Geochronologists use different isotopic systems to obtain age information about geological events. The U-Th-Pb system is used in many cases to determine the time of crystallisation. Until now, there have been several U-Pb dating procedures: the conventional one (Krogh 1973; Oberli et al. 1981; Steiger et al. 1993), the Pb-Pb evaporation method (Kober 1986, 1987), the vapour digestion method (Wendt and Todt 1991) and SHRIMP (sensitive high resolution ion microprobe; Compston et al. 1986; Gebauer et al. 1989).

Dating of magmatic rocks by the conventional U-Pb method was successfully and widely applied for Archean to Tertiary rocks (Oberli et al. 1985; Barth et al. 1992). Even the Pb-Pb evaporation method yielded good results for single phase magmatic rocks (Kröner et al. 1991).

In contrast to the dating of such simple rocks, geochronological investigations of metamorphic rocks are much more difficult. Because zircons are very difficult to reset, different events are stored in the U-Pb isotopic signatures of zircons from metamorphic samples. The resulting measurements reflect a mixture of age information and are often difficult to interpret. There are several approaches to estimate the influence of metamorphism in the U-Pb systematics of zircons. All of these have demonstrated that metamorphic events cause overgrowth, resorption or new zircon crystallisation (Hart et al. 1968; Grauert 1974; Gebauer and Grünenfelder 1976; Mezger and Krogstad 1997). The combination of such effects results in discordant data points; if they belong to a two-phase system, they can be connected by a discordia line. Unfortunately, the upper and especially the lower intercepts of such discordia lines are difficult to interpret without any further information about the analysed zircons and rocks.

As a consequence, some geochronologists used scanning electron microscopes (SEM) with back-scattered detectors, cathodoluminescence (CL) detectors or even microprobes to find out more about the chemistry and the internal structures of zircons (Grauert 1974; Medenbach 1976; Wayne and Sihna 1988; Hanchar and Miller 1993). Such efforts provide much additional geochemical information. X-ray emission maps for elements such as Hf, U or Y showed, e.g., the enrichment

of U and Y in overgrowth areas of zircons from metamorphic rocks (Wayne and Sihna 1988). The use of such methods helps in understanding the mechanism of geochemical processes in zircon crystals during metamorphic overprints and results in a better interpretation of the data set.

The identification of core components and magmatic zonation as well as resorption zones under binocular is very difficult, sometimes even impossible. In some cases, cores can be recognised under oil with an optical microscope because of their high refringence, but the complex internal structures are best visible with CL on polished grains. As a consequence, the conventional U-Pb zircon method (based on the crystal selection under microscope) often results in discordant data, difficult to interpret in a geologically meaningful way.

The abrasion (Krogh 1982) of zircons from a metamorphic rock makes it possible to obtain more concordant points and to prove the age of the protolith formation. The ages around the lower intercept, indicating the last zircon growing event (crystallisation), cannot be improved by abrasion.

Another alternative, the Pb-Pb evaporation technique of Kober (1986 1987), has the advantage of providing different age information from one single zircon by stepwise heating. This method uses the whole grain and needs no additional chemical step when the analysis is carried out in a clean laboratory. The zircon is mounted directly into a filament without adding any spike. By stepwise heating, Pb of different stable areas from the individual zircon grain is evaporated, although no Pb, U or Th concentrations can be measured. Nevertheless, this method deals with the Pb isotopes only, and any controls by the mother/daughter ratio or the U and Th concentrations are lacking. As a consequence, the age information obtained makes it possible to identify the protolith age, but mixed ages cannot be resolved and interpreted in a geologically meaningful way.

Consequently, SHRIMP seems to be a more meaningful tool for U-Pb zircon dating of polymetamorphic rocks. This method enables optical, but not CL, control of the zircon (back-scattered imaging) before and during measurement. The analysed spots can be chosen with regard to the structures of the zircon, and thus it is possible to date different areas, such as the core and rim of the same grain (e.g. Compston et al. 1992; Maas et al. 1992; Schäfer et al. 1993).

Although SHRIMP seems to be the ultimate technique for zircon dating in polymetamorphic rocks, there are some disadvantages: the spot size of 20–30 μm using SHRIMP II might be too large for very finely zoned crystals. In addition, the precision for very young zircons is not as good as with conventional TIMS (thermal ionization mass spectrometer) measurements: since the radiogenic ^{207}Pb is of very low intensity, it must be measured very precisely. A 0.1% variation in $^{207}\text{Pb}/^{206}\text{Pb}$ ratio corresponds to a 2 Ma change in age. Finally, the availability of measurement time on currently running machines is limited. Thus, even SHRIMP is not a broad alternative for dating complicated rocks.

2 Cathodoluminescence as a Tool for Geochronology

The main problem in the successful zircon dating of polymetamorphic rocks is the selection of appropriate one-phase grains. Multi-grain and single-grain analyses have both shown that zircon selection under binocular and optical microscope, even under a high refraction liquid (to better detect inclusions), is not sufficient to find concordant crystals, because inherited cores are not always visible with this kind of equipment (Liebetrau et al. 1995; Poller et al. 1996).

The use of the zircon typology developed by Pupin (1976), based on the relationship between morphology and crystallisation conditions, is suitable for simple magmatic rocks. But even the combination of typological and geochemical studies, such as Hf/Zr ratios or absolute Hf, Y, Zr contents of crystals (Pupin 1988), does not allow any differentiation of complex polymetamorphosed zircons. Thus, the Pupin typology is a useful tool for magmatic rocks, but it is not sufficient for polyphase metamorphosed zircons with overgrowth.

The best tool to obtain information about the internal structures of zircons is CL connected to a SEM, which gives the necessary high resolution. With this method, internal structures like inherited cores, resorbed areas and magmatic zonations are clearly visible (Vavra 1990; Vavra et al. 1996).

For example, three grains from the same sample with the same shape, grain size and color, picked together as identical types using an optical microscope, may show three different internal structures when using CL (Fig.1). Figure 1a shows a homogeneously zoned crystal, ideal for dating the last magmatic event. Figure 1b is a zircon grain with resorbed areas possibly due to a metamorphic overprint. The third zircon (Fig. 1c) shows a large inherited component. This latter crystal should be abraded and might offer additional information about the protolith age of the rock.

Until now CL on zircons was used as a petrogenetic tool. For instance, Vavra (1990, 1994) has carried out extensive studies with CL on the kinematics of zircon growth. In some cases CL studies were combined with SHRIMP dating (Schäfer et al. 1993). As earlier investigations have shown, the parallel use of CL as a preliminary investigating method and TIMS U-Pb dating on similar grains is not satisfactory (Liebetrau et al. 1995; Poller et al. 1995, 1996): Grains with different internal structures seen by CL cannot be distinguished under the optical

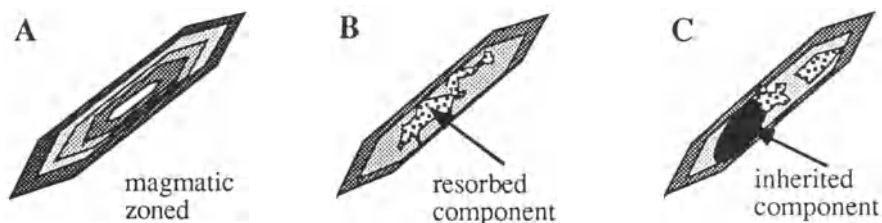


Fig. 1. Schematic drawing of internal structures in zircons, visible with CL

microscope and this results in discordant age data for zircons with a multistage history. These drawbacks may be overcome by performing CL and U-Pb dating by TIMS on the *same* grain (Poller et al. 1997a).

3 The CLC Method: Cathodoluminescence Controlled U-Pb Dating of Zircons

The zircons were separated using standard techniques. The most suitable zircons were hand picked and prepared in a standard microprobe mount using a low luminescent resin with low Pb content, controlled by blank measurements. Up to 70 grains were mounted together. In order to avoid the loss of crystals during the polishing process, only grains of the same size were mounted together.

The polishing of the mount has to be done without Pb-bearing materials, to avoid any contamination of the samples. The use of a Teflon wheel and diamond powder gave good results. Each mount was polished until the centre of the zircon was exposed and the internal structures could be observed by CL. After polishing, the mounts were coated with carbon for the CL imaging.

For CL documentation, a Hitachi S450, at the Max-Planck-Institut für Chemie, Mainz (Germany), was used. At the SEM different steps are possible, the most important one being CL imaging of each single grain. For better localization of the zircons, an overview picture can be taken in secondary electron (SE) mode. In addition to the CL photographs, back-scattered electron (BSE) images can give further information, especially in the case of inclusions. Such inclusions are frequently apparent in the zircons and might cause problems (such as a high common lead component) if they are, for instance, sulfides or apatites. For a fast qualitative identification of these inclusions, the energy dispersive system (EDX) of the SEM can be applied.

Using the CL images, suitable grains for the specific dating problem are selected for the U-Pb measurements.

The zircons are recovered from the resin mechanically in an ultra-clean lab using tungsten needles sharpened by electropolishing. Afterwards, a cold ultrasonic cleaning step with HNO₃ should follow for 5–10 min. Now each half zircon is transferred to a special Teflon bomb with small holes for each individual zircon (Wendt and Todt 1991). A ²⁰⁵Pb–²³³U or a ²⁰²Pb–²³³U mixed spike and 3 μl 28N HF were added into each hole and the “bomb” was placed in an oven at 200 °C for about 5 days. After complete dissolution, the samples were dried down and 3 μl 6N HCl were added, followed by 1 day in the oven at the same temperature. After this step the zircons were completely in solution, homogenized with the spike and ready to be measured.

To get a better signal on the mass spectrometer, U-Th-Pb can be separated and cleaned using microcolumns. For this purpose, 10 μl Teflon microcolumns with AG1-X8 (100–200 mesh) resin were used. Afterwards, the U and Pb fractions were dried down and loaded on Re single filaments with 3 μl of silica gel in 0.2N H₃PO₄. The isotopic measurements were done on a MAT 261 mass spectrometer using a secondary electron multiplier in peak-jumping mode.

The total Pb blank was about 3 pg. For blank Pb corrections the following ratios were used: $^{206}\text{Pb}/^{204}\text{Pb}=18.59$, $^{207}\text{Pb}/^{204}\text{Pb}=15.73$. For the common Pb correction, galena from the Tatra Mountains was measured. The resulting values for correction were: $^{206}\text{Pb}/^{204}\text{Pb}=18.493$, $^{207}\text{Pb}/^{204}\text{Pb}=15.665$. All ratios were corrected for fractionation using the NBS 982 standard as reference (Todt et al. 1996) and for U using an U nat. standard solution. The analyses were corrected with parallel determined fractionation values scattering for Pb between 2.9‰ and 3.1‰ per amu for the period of measurements (Loveridge 1986). The data are presented in Table 1.

4

The CLC Method Applied to Polymetamorphic Orthogneisses

The CLC method was applied to granitoids and polymetamorphic orthogneisses of the Western Tatra Mountains in Slovakia. The latter rocks were chosen because CL images show the complex internal structures of their zircons, and thus conventional U-Pb dating techniques without CL control seems to be very difficult. As a consequence the CLC method, which was specially developed for such multi-stage rocks, was used to date this rock group. The granitoids often show magmatic zonation without disturbing cores or resorbed areas. They were also dated under CL control to test the method on single-stage rocks.

The Tatra Mountains belong to the pre-Alpine basement of the Western Carpathians. Two tectonic units, separated by Variscan thrust faults, form an inverted metamorphic sequence where the upper unit is composed of granitoids and high-grade metamorphites (migmatitic ortho- and paragneisses, amphibolites). The lower unit is composed of micaschists. Orthogneisses exhibiting mylonitic texture occur at the base of the upper unit in the western part of the Tatra and are overlain by granitoid rocks. Weakly overprinted granites were sampled together with polymetamorphic orthogneisses for geochemical and geochronological investigations.

The CLC method was applied parallel to conventional single zircon dating to the Rohac granite (UP 1040) and to the Baranec granite (UP 1023) and the Baranec orthogneiss (UP 1025).

The Rohac granite belongs to the upper unit and is outcropped near the peak of Mount Rohac (Fig. 2). During Alpine overprint this granite has undergone low-grade metamorphism. Geochemical and isotopical analyses indicate the S-type character with a high alumina saturation index (1.22) and low epsilon Nd value, around -5, typical for continental crust.

In CL mode, the zircons of the Rohac granite exhibit typical, magmatic grown, single phase structures beside core-bearing crystals. Such complex zircons are very common in anatectical granitoids and are used to obtain information about the protolith.

For the CLC method, two grains of UP 1040 were chosen in combination with conventional measurements. The grain UP 1040-33 (Fig. 3a) shows regular magmatic zonation without inherited components. Its analyses resulted in a concor-

Table 1. U-Pb data of zircons from Tatra rocks

Zircon	Method	Utot: Pb ^c	Measured isotopic composition ^a				Isotopic ratios ^b				207Pb ^c : 206Pb ^c	2σ error		
			206Pb: 204Pb	2σ error	207Pb ^c : 206Pb ^c	2σ error	208Pb: 206Pb	2σ error	206Pb ^c : 238 U	2σ error			207Pb ^c : 235 U	2σ error
UP 1040-23	CLC	13.04	238.34	±1.86	0.13078	±32	0.24138	±73	0.06641	±43	0.6560	±136	0.07165	±35
UP 1040-29	CLC	16.43	331.76	±3.85	0.09584	±27	0.17645	±70	0.05474	±33	0.3955	±98	0.05240	±97
UP 1040-33	CLC	15.55	592.15	±8.90	0.07946	±41	0.10593	±92	0.05891	±55	0.4485	±118	0.05521	±98
UP 1040-4	VD	14.94	131.22	±1.87	0.16838	±52	0.36670	±141	0.05843	±61	0.4780	±280	0.05934	±38
UP 1040-5	VD	15.83	101.76	±0.51	0.19598	±38	0.45885	±112	0.05488	±41	0.4013	±148	0.05303	±48
UP 1023-1	CLC	16.13	554.63	±2.84	0.08316	±20	0.07939	±65	0.05836	±48	0.4623	±85	0.05745	±60
UP 1023-8	CLC	18.14	896.03	±26.77	0.06852	±55	0.03581	±75	0.05306	±120	0.3834	±192	0.05239	±177
UP 1023-2	VD	16.94	655.23	±7.07	0.07514	±16	0.06165	±23	0.05619	±32	0.4119	±63	0.05318	±49
UP 1023-4	VD	17.45	797.58	±11.81	0.07135	±24	0.05267	±24	0.05451	±48	0.4002	±80	0.05324	±65
UP 1023-5	VD	16.83	279.25	±3.60	0.10672	±27	0.14398	±52	0.05619	±46	0.4266	±127	0.05505	±130
UP 1025-14	CLC	13.98	236.50	±0.88	0.111365	±14	0.22906	±545	0.06382	±35	0.4617	±81	0.05247	±77
UP 1025-30	CLC	14.96	547.12	±5.32	0.07892	±21	0.16390	±43	0.05839	±77	0.4252	±109	0.05282	±57
UP 1025- A	VD	15.63	1306.41	±38.37	0.06533	±21	0.10324	±35	0.05705	±35	0.4268	±72	0.05427	±61
UP 1025- B	VD	13.30	602.29	±6.89	0.07811	±16	0.17927	±50	0.06452	±40	0.4807	±73	0.05397	±58
UP 1025- D	VD	16.51	700.24	±12.65	0.07460	±18	0.08931	±33	0.05596	±67	0.4159	±103	0.05390	±88
UP 1025- E	VD	13.58	886.47	±13.49	0.06986	±18	0.13093	±41	0.06484	±40	0.4780	±71	0.05347	±54

VD, vapour digestion; CLC, cathodoluminescence controlled; 2σ errors refer to the 2σ standard deviation of the mean of 2-6 blocks.

^aCorrected for fractionation.

^bCorrected for blank, spike and common Pb.

^cRadiogenic lead

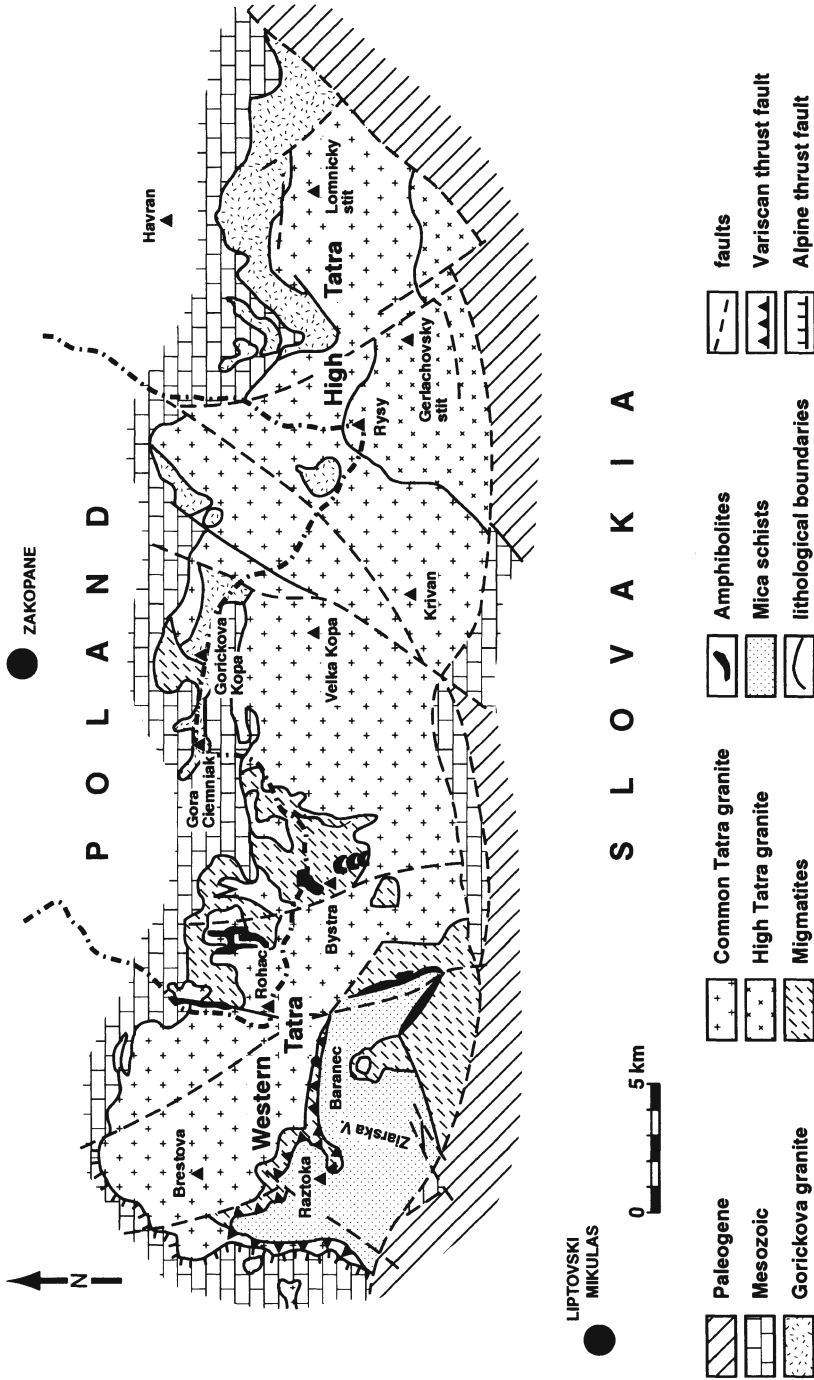


Fig. 2. Simplified geological map of the Tatra Mountains. (After Kohut and Janak 1994)

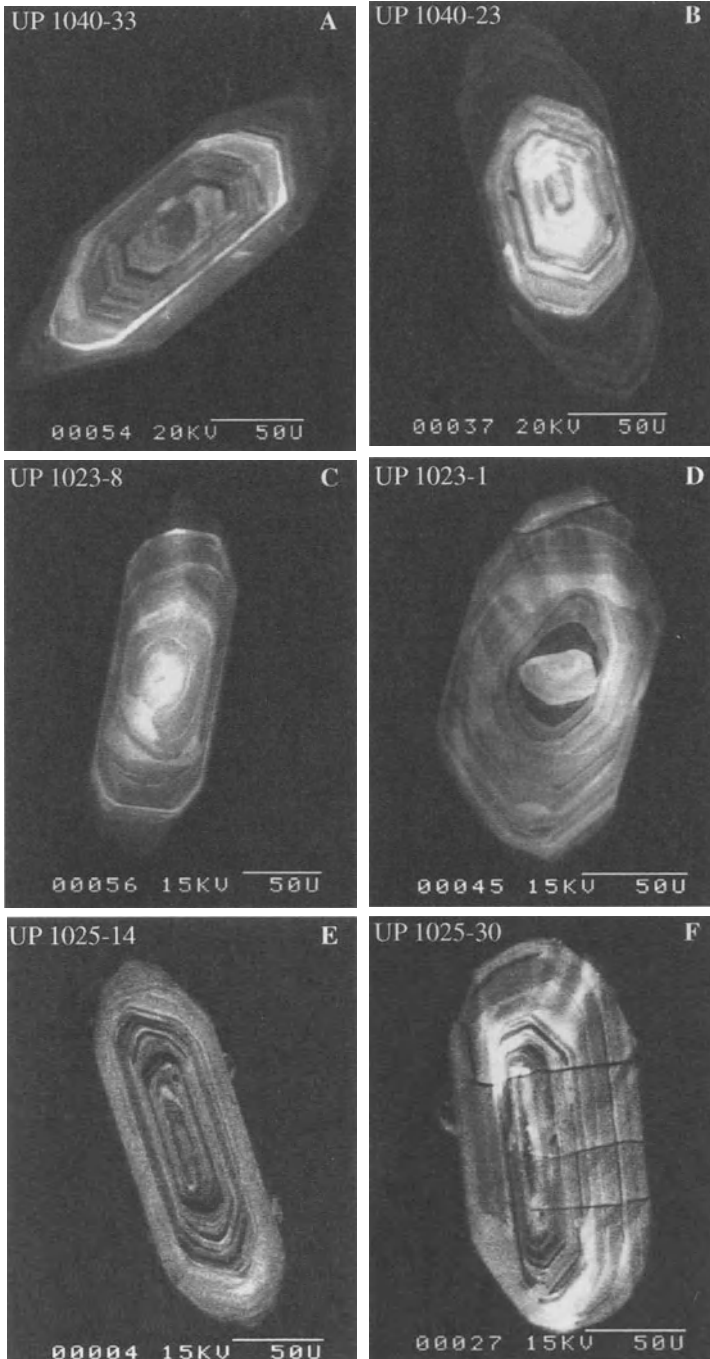


Fig. 3. Cathodoluminescence photographs of zircons from Rohac granite (A,B), Baranec granite (C,D) and Baranec gneiss (E,F). For explanations, see text

dant age at 368 ± 3 Ma. This age, interpreted as the crystallisation age of the Rohac granite, was supported by conventionally measured points (Fig. 4). The second zircon dated with CL control was grain UP 1040-23 (Fig. 3b). This crystal bears a large inherited component, with a bright CL signal but also regular zonation. The outer rim has a dark CL and the typical magmatic zones. This grain was expected to be discordant and indeed has a discordant position visible on the U-Pb concordia plot of Fig. 4. Together with conventional points it allows one to draw a discordia line, resulting in an upper intercept around 2600 Ma and a lower intercept around 365 Ma. Whereas the lower intercept is constrained by the concordant point UP 1040-33, the upper intercept agrees with a Nd model age of 2530 Ma for the whole rock sample.

The sample UP 1023, the Baranec granite, was also a granitoid rock, outcropping at the top of the Baranec mountain, 5 km southwest from the Rohac (Fig. 2). The Baranec granite belongs to the same upper unit as the Rohac granite. The geochemical characterisation shows a lower alumina saturation index (ASI, 1.0). Thus, this seems to be an I-type influenced rock, e.g. a Hs or a Hss hybridic granite, as described by Castro et al. (1991). In contrast to the very fresh Rohac sample, the Baranec granite has suffered high grade alteration. This should be responsible for the change in soluble element concentrations like Na_2O , K_2O or CaO . These elements are used for the calculation of the ASI, and the lower ASI value might be caused by the decrease due to alteration. As a consequence, characterisation of the Baranec granite by applying the ASI seems to be doubtful.

The complex zircon population gives evidence that the Baranec granite is not a simple I-type granitoid but a Hs- (hybridic granite with mostly S-type components) or S-type rock. Beside magmatic zoned zircons, core-bearing crystals are also present. For the dating, one magmatic zoned grain (UP 1023-8, Fig. 3c), one core-bearing zircon (UP 1023-1, Fig. 3d) and several grains (without CL) were analysed.

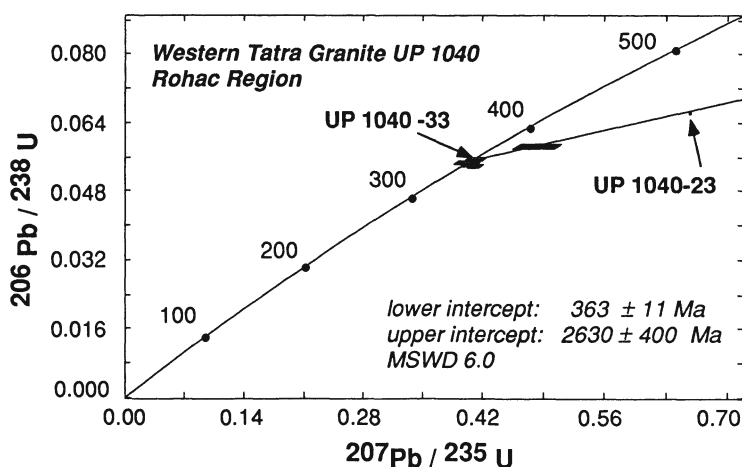


Fig. 4. U-Pb concordia plot of UP 1040, Rohac granite

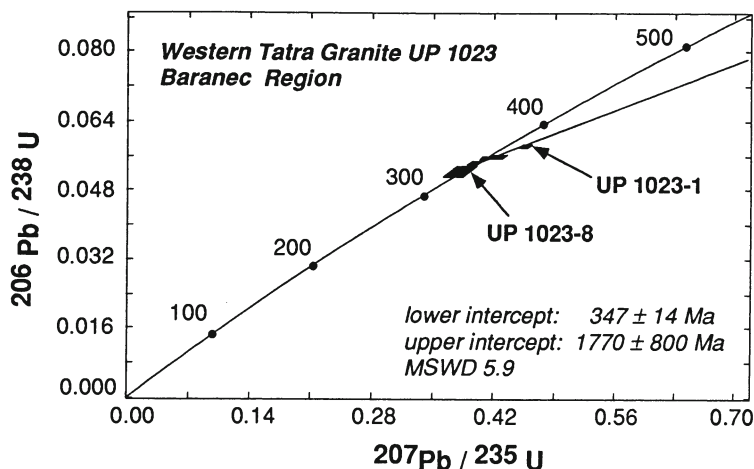


Fig. 5. U-Pb concordia plot of UP 1023, Baranec granite

As expected, the core-bearing crystal has a discordant position in the U-Pb concordia plot (Fig. 5), whereas the magmatic zoned zircon has a concordant age at $333 \pm 7 \text{ Ma}$. The other grains support this result and enable generation of a discordia line with $347 \pm 14 \text{ Ma}$ as lower and $1770 \pm 400 \text{ Ma}$ as upper intercepts. So the magmatic zoned grain UP 1023-8 gives the minimum age of the intrusion of the Baranec granite, whereas grain UP 1023-1 constrains the Proterozoic age of the protolith.

In contrast to the two described granites, the sample UP 1025 is a polymetamorphic orthogneiss. The rock also outcrops in the Baranec region and belongs to the upper unit. The metamorphic grade that the Baranec gneiss has suffered is higher, and thus the Baranec gneiss is assumed to be older than the Baranec granite and the other granitoids.

Consequently, the CLC method was also applied to this rock. Two purely magmatic zoned zircons, UP 1025-14 and UP 1025-30 (Fig. 3e,f) were dated and yielded concordant ages. The grain UP 1025-14 ($399 \pm 2 \text{ Ma}$), together with a second grain ($403 \pm 2 \text{ Ma}$), lies slightly above the concordia line. Analytical problems (e.g. less homogenisation of U) can be excluded because no chemistry was done. The geological significance of a Devonian event is constrained by the concordant zircon age, at $406 \pm 2 \text{ Ma}$ (Poller et al. 1997b), of a nearby upper unit orthogneiss (UP 1002, west of Baranec).

Whereas the grain UP 1025-14 marks an event in Devonian time around 400 Ma, the second zircon UP 1025-30 is 50 Ma younger and fits with the concordia around 360 Ma (Fig. 6).

Again, the predictions based on the CL images were confirmed: the single-phased zircons gave concordant ages. The two ages obtained by the CLC method were supported by conventional measurements. The young event in Carboniferous time is interpreted as a high temperature overprint during the intrusion of the Baranec granite, which allowed new zircon growth under magmatic condi-

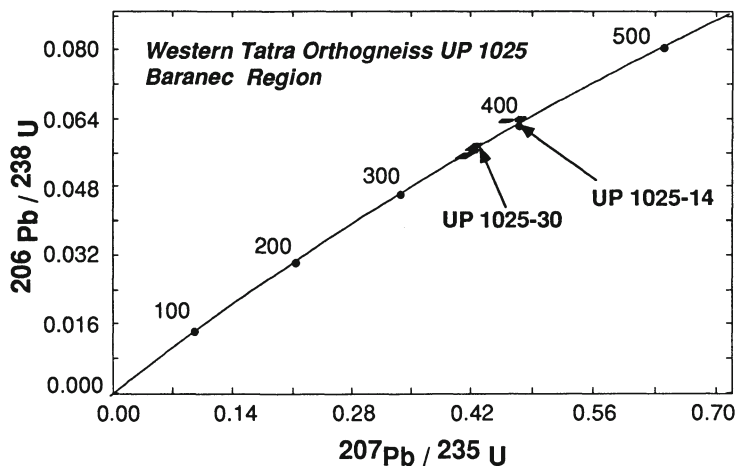


Fig. 6. U-Pb concordia plot of UP 1025, Baranec gneiss

tions and is responsible for the gneissification of the Baranec gneiss. The Devonian event is explained as crystallisation of the precursor of the orthogneisses. In correspondence to the internal zircon structures and geochemical analyses, this precursor was also an S-type granitoid.

5 Summary

The CLC method seems to be a useful tool for the dating of complex metamorphic rocks. The predictions of concordance of the investigated grains are precise and thus the dating of polymetamorphic rocks is easier, and the resulting ages are more convincing.

As the presented data have shown, the CLC method allows us to distinguish several geologic events for the Western Tatra granitoids:

1. The Rohac granite crystallised 368 ± 3 Ma ago.
2. The Protolith of the Rohac granite is Archean in age.
3. The Baranec granite crystallised 347 ± 14 Ma ago and the protolith is of Proterozoic age.
4. The precursor of the Baranec gneiss was overprinted parallel to the intrusion of the Baranec granite in Carboniferous time.
5. The precursor of the Baranec gneiss crystallised in the Devonian 400 ± 2 Ma ago.

All these results were obtained by successful measurement of zircons which had been pre-investigated with CL. With this method we can study the internal structures of zircons and interpret the results, obtained with a few grains, in a geologically meaningful way.

Nevertheless, this method is limited by the radiogenic Pb contents of each zircon. While preparing the CL investigations, half of each crystal is lost and the sample weights are extremely low (normally below 1 μg). The resulting contents of radiogenic Pb are very low and sometimes the signal is not high enough for good statistical measurements. This is, at least for young samples (300 Ma and younger), problematic. Nevertheless, the CLC method offers a good alternative to U-Pb zircon dating by TIMS for metamorphic rocks.

Acknowledgements. This research project of U. P. was funded by the DFG (Projects TO 67/3-1 and PO 608/1-1) and the Max-Planck-Society. I thank K. Mezger for discussions about zircons and metamorphism and a critical review of an earlier version of this manuscript. I also thank V. Liebetrau, who was involved with the first approaches of CLC dating. I gratefully acknowledge A. Hofmann for the opportunity to work at the MPI, W. Todt for his help in the field and the laboratory, J. Huth for his help with the cathodoluminescence and G. Feyerherd and I. Bambach for the drawings. I am grateful to M. Janak and M. Kohut for their support and their help in the field. I thank L. Feld for the corrections and R. Romer for the review of this paper.

References

- Barth, S, Oberli, , Meier, M (1992) U-Th-Pb systematics of morphologically characterized zircon and allanite: a high-resolution isotopic study of the Alpine Rensen pluton (northern Italy). *Earth Plan Sci Lett* 95:235–254
- Castro, A, Moreno-Ventas, I, de la Rosa, JD (1991) H-type (hybrid) granitoids: a proposed revision of the granite-type classification and nomenclature. *Earth Sciences Reviews*, 31:237–253
- Compston, W, Kinny, PD, Williams, IS, Foster, JJ (1986) The age and Pb loss behaviour of zircons from the Isua supracrustal belt as determined by ion microprobe. *Earth Plan Sci Lett* 80:71–81
- Compston, W, Williams, IS, Kirschvink, JL, Zichao, Z, Guogan, MA (1992) Zircon U-Pb ages for the Early Cambrian time-scale. *J Geol Soc*, 149:171–184
- Gebauer, D, Grünenfelder, M (1976) U-Pb zircon and Rb-Sr whole-rock dating of low-grade metasediments: Montagne Noire (Southern France). *Contrib Mineral Petrol* 59:13–23
- Gebauer, D, Williams, IS, Compston, W, Grünenfelder, M (1989) The development of Central European continental crust since the Early Archean based on conventional and ion-microprobe dating of up to 348 by old detrital zircons. *Tectonophysics*, 157:1–96
- Grauert, B (1974) U-Pb systematics in heterogeneous zircon populations from the Precambrian basement of the Maryland Piedmont. *Earth Plan Sci Lett* 23:238–248
- Hanchar, JM and Miller, CF (1993) Zircon zonation patterns as revealed by cathodoluminescence and backscattered electron images: Implications for interpretation of complex crustal histories. *Chem Geol* 110:1–13
- Hart, SR, Davis, GL, Steiger, RH, Tilton, GR (1968) A comparison of the isotopic mineral age variations and petrologic changes induced by contact metamorphism. In: Farquhar, RM and Hamilton, EI (eds) *Radiometric dating for geologists*. Interscience, pp 73–110
- Kober, B (1986) Whole-grain evaporation for $^{207}\text{Pb}/^{206}\text{Pb}$ -age-investigations on single zircons using a double filament thermal ion source. *Contrib Min Petrol* 93:482–490
- Kober, B (1987) Single grain evaporation combined with Pb emitter bedding for $^{207}\text{Pb}/^{206}\text{Pb}$ investigations using thermal ion mass spectrometry and implications for zirconology. *Contrib Min Petrol* 96:63–71

- Kohut, M, Janak, M (1994) Granitoids of the Tatra Mts, Western Carpathians: Field relations and petrogenetic implications. *Geologica Carpathica*, 45: 301–311
- Kröner, A, Byerly, GR, Lowe, DR (1991) Chronology of early Archean granite-greenstone evolution in the Barbarton Mountain Land, South Africa, based on precise dating by zircon evaporation. *Earth Plan Sci Lett* 103:41–54
- Krogh, TE (1973) A low-contamination method for hydrothermal decomposition of zircon and extraction of U and Pb for isotopic age determination. *Geochim Cosmochim Acta*, 37: 485–494
- Krogh, TE (1982) Improved accuracy of U-Pb zircon ages by the creation of more concordant systems using an air abrasion technique. *Geochim Cosmochim Acta*, 46:637–649
- Liebetrau, V, Poller, U, Nägler, TF, Frei, R, Sergeev, SA (1995) The problem of zircon-dating and geochemical discrimination of S-type granitoids in consideration of cathodoluminescence studies and Sm/Nd data: a case study from the Silvretta nappe/Central Alps. Supplement to *European Journal of Mineralogy*, 7:15
- Loveridge, WD (1986) Measurement of biases in the electron multiplier ion detection system of a Finnigan MAT Model 261 mass spectrometer. *Int J of Mass Spectr Ion Proc*, 74:197–206
- Maas, R, Kinny, PD, Williams, IS, Froude, DO, Compston, W (1992) The Earth's oldest known crust: A geochronological and geochemical study of 3900–4200 Ma old detrital zircons from Mt Narryer and Jack Hills, Western Australia. *Geochimand Cosmochim Acta*, 56:1281–1300
- Medenbach, O (1976) *Geochemie der Elemente in Zirkon und ihre räumliche Verteilung – Eine Untersuchung mit der Elektronenstrahlmikrosonde* PhD thesis, University Heidelberg, 58 pp
- Mezger, K, E J Krogstad (1997) Interpretation of discordant U-Pb zircon ages: an evaluation. *J Metamorph Geol* 15:127–140
- Oberli, F, Kagami, H, Meier, M, Steiger, RH (1985) Correlated Sm-Nd and U-Pb systematics of total-rock, zircon and other accessory minerals. *Terra Cognita* 5:324
- Oberli, F, Sommerauer, J, Steiger, RH (1981) U-(Th)-Pb systematics and mineralogy of single crystals and concentrates of accessory minerals from the Cacciola granite, central Gotthard massif, Switzerland. *Schweiz Min Petr Mitt* 61:323–348
- Poller, U, Liebetrau, V, Todt, W (1995) Cathodoluminescence studies combined with single zircon U-Pb dating: application to the geochronology of S-type granitoids. *Eur J Mineral (suppl)*, 7:190
- Poller, U, Liebetrau, V and Todt, W (1996) Cathodoluminescence and conventional U-Pb single zircon dating on the same grain applied to S-type granitoids. *J Conf Abstr* 1:478
- Poller, U, Liebetrau, V, Todt, W (1997a) U-Pb single-zircon dating under cathodoluminescence control (CLC-method): application to polymetamorphic orthogneisses. *Chem Geol* 139:287–297
- Poller, U, Todt, W, Janak, M, Kohut, M (1997b) Pre-variscan orthogneisses of the Western Tatra Mountains: U-Pb single zircon data by cathodoluminescence controlled dating (CLC-dating). *Terra Nova* 9:488
- Pupin, J-P (1976) *Signification des caractères morphologiques du zircon commun des roches en pétrologie Base de la methode typologique Applications* PhD thesis, University Nice
- Pupin, J-P (1988) Granites as indicators in paleogeodynamics. *Rend Soc Ital Mineral Petrol*, 43:237–262
- Schäfer, H-J, Gebauer, D, Nägler, TF, Eguluz, L (1993) Conventional and ion-microprobe U-Pb dating of detrital zircons of the Tentudia Group (Serie Negra, SW Spain): implications for zircon systematics, stratigraphy, tectonics and the Precambrian/Cambrian boundary. *Contrib Mineral Petrol* 113:289–299
- Steiger RH, Bickel, RA, Meier, M (1993) Conventional U-Pb dating of single fragments of zircon for petrogenetic studies of Phanerozoic granitoids. *Earth Plan Sci Lett* 115:197–209
- Todt, W, Cliff, RA, Hanser, A, Hofmann, AW (1996) Evaluation of a ^{202}Pb - ^{205}Pb double spike for high-precision lead isotope analysis. *Geophys Monogr*, 95:429–437
- Vavra, G (1990) On the kinematics of zircon growth and its petrogenetic significance: a cathodoluminescence study. *Contrib Min Petrol* 106:90–99

- Vavra, G (1994) Systematics of internal zircon morphology in major Variscan granitoid types. *Contrib Mineral Petrol* 117:331–344
- Vavra, G, Gebauer, D, Schmid, R, Compston, W (1996) Multiple zircon growth and recrystallisation during polyphase Late Carboniferous to Triassic metamorphism in granulites of the Ivrea Zone (Southern Alps): an ion microprobe (SHRIMP) study. *Contrib Min Petrol* 122:337–358
- Wayne, DM, Sihna, AK (1988) Physical and chemical response of zircons to deformation. *Contrib Mineral Petrol* 98:109–121
- Wendt, JI, Todt, W (1991) A vapour digestion method for dating single zircons by direct measurements of U and Pb without chemical separation. *Terra Abstr* 3:507–508

Relevance of Cathodoluminescence for the Interpretation of U-Pb Zircon Ages, with an Example of an Application to a Study of Zircons from the Saxonian Granulite Complex, Germany

ULF KEMPE, TORSTEN GRUNER, LUTZ NASDALA, DIETER WOLF

1

Introduction

In the last few years, an increasing number of papers dealing with applications of cathodoluminescence (CL) imaging – using both optical microscopes (OM-CL) and systems operating with secondary electron microscopes (SEM) or electron microprobes (SEM-CL) – to investigate the internal structures of zircon have been published. CL has been demonstrated to be a powerful tool for investigating zircons. This method yields high-resolution images of internal structures that often cannot be detected with other techniques (e.g., HF etching, Normarski interference). In most previous publications, CL images were interpreted assuming that CL is exclusively generated within the micro-areas that are irradiated with the electron beam (e.g., Hanchar and Miller 1993; Vavra et al. 1996). We want to demonstrate here that this assumption may in several cases lead to some misinterpretation of the internal structure of zircon.

CL investigations of zircon (ZrSiO_4), which commonly occurs as an accessory mineral in most magmatic, metamorphic and sedimentary rocks, is of special interest in understanding rock petrogeneses (Pupin 1980; Hoffman and Long 1984; Vavra 1990; Halden and Hawthorne 1993; Hanchar and Miller 1993; Vavra 1994; Hanchar and Rudnick 1995; Loth and Höll 1996). Furthermore, CL investigation is of importance for the geochronological interpretation of U-Pb and Pb-Pb data obtained by multi- and single-grain conventional investigations as well as ion microprobe analyses (Sommerauer 1976; Gebauer 1990; Lork and Koschek 1991; Koschek 1993; Kramm et al. 1993; Roger et al. 1995; Hanchar and Rudnick 1995; Gebauer 1996; Chemale et al. 1996; Poller et al. 1996; Rubatto and Gebauer 1996; Vavra et al. 1996; Zinger et al. 1996).

Zircon U-Pb data are usually interpreted in accordance with the concordia-discordia model, and an episodic loss of Pb is often assumed when the data points plot below the concordia curve (Faure 1986). Some apparent “paradoxes” were discovered when this model was applied to more complicated geological situations.

For example, Gebauer and Grünenfelder (1976), without the aid of CL or back scattered electron (BSE) imaging, found a single discordia age (lower intercept) for zircons from rocks of different degrees of metamorphism (staurolite gneisses, garnet and chlorite schists) belonging to a single nappe structure in Mon-

tagne Noire (France). These authors concluded that a "resetting" of the U-Pb system of zircon must occur under conditions of green-schist facies of metamorphism, possibly due to a low-temperature recrystallization of highly metamict zircons.

In another example, from the Southern Bohemian granulites, zircon ages of about 340–350 Ma, which are quite near to the 335–340 Ma age of the Moldanubian regional metamorphism, were interpreted as related to the high pressure and high temperature (granulitic) event which produced these granulites. Roberts and Finger (1996) argued that according to geological evidence this age interpretation must be wrong.

A contradictory result comes also from the Saxonian granulite complex (SGC), discussed in more detail here. Multi-grain, single-grain and SHRIMP (sensitive high resolution ion microprobe) zircon ages of granulites of about 330–340 Ma, assumed as the age of peak metamorphism (von Quadt 1993; Baumann et al. 1996), overlap with multi-grain, single-grain and SHRIMP zircon ages of both synkinematic (338 Ma; von Quadt 1993) and postkinematic (330 Ma; Baumann et al. 1996) granites. An extremely quick uplift of the complex was suggested to explain these data.

Application of CL and BSE imaging with other micro-methods such as the electron probe (Sommerauer 1976; Hoffman and Long 1984; Lork and Koschek 1991; Pupin 1991; Benisek and Finger 1993; Hanchar and Miller 1993; Hanchar and Rudnick 1995), TEM (transmission electron microscopy; Sommerauer 1976; Murakami et al. 1991; McLaren et al. 1994), Raman probe (Nasdala et al. 1995, 1996b) and SHRIMP (Compston et al. 1986; Black et al. 1986; Gebauer 1990; Pidgeon 1992; Hanchar and Miller 1993; McLaren et al. 1994; Hanchar and Rudnick 1995; Gebauer 1996; Rubatto and Gebauer 1996; Vavra et al. 1996) have newly provoked discussion on the stability of the U-Pb zircon system and its possible distortion under various conditions. In some studies, the U-Pb system in zircon is assumed to be very stable under some extreme geological conditions (e.g., Hanchar and Miller 1993; Kröner et al. 1994), whereas other authors discussed the U-Pb system as being quite sensitive even to small changes in the milieu (e.g., Black 1987). The discussion on stability of zircon is closely related to that of the phenomenon of metamictization (Lee 1993; Nasdala et al. 1997).

Furthermore, it is still controversial which internal zircon structures are formed during primary growth (Vavra 1990; Hanchar and Miller 1993; Vavra et al. 1996) and during recrystallization (Gebauer 1990; Pidgeon 1992). A question of particular interest is whether zircon growth is possible during regional metamorphism, metasomatism, and shearing of host rocks (e.g., Hanchar and Rudnick 1995; Pan 1997). Obviously, detailed knowledge about the internal structures and U-Pb systematics of zircons is necessary for more reliable interpretation of geochronological data.

The aim of this study is to discuss our interpretation of internal zircon structures revealed by CL imaging, especially their application to U-Pb and Pb-Pb dating in geochronology. An example of this interpretation, based on CL, SEM, electron microprobe, Raman microprobe and SHRIMP investigation, is given for zircons from the SGC in Germany.

2

Methods

Panchromatic and spectral CL investigations as well as BSE imaging and energy dispersive X-ray analysis (EDX) were carried out using a JEOL JSM 6400 SEM. This SEM is equipped with an Oxford MonoCL system, an additional panchromatic CL detector, two BSE detectors at different distances from the sample surface, and a Noran Series II EDX system with a light element Si(Li) detector. Operating conditions were selected to minimize damage to the sample and carbon coat due to the impact of the electron beam and for high spatial resolution. For panchromatic CL imaging, the accelerating voltage was 20 kV and the beam current was set in the range 0.6–1.6 nA. Higher beam currents were used on zircons with lower CL intensity. The beam current was generally above 1.3 nA and up to 1.9 nA for spectral CL investigations (i.e., monochromatic imaging and collection of emission spectra). Spectra were excited with a fully focused beam (0.8 μm diameter). The spectra were detected over the range 300–800 nm, with 0.5–2 nm steps and a dwell time of 2–4 s per step. The spectral resolution of the system was 0.5 nm, the blaze wavelength of the grating 500 nm. The detector was a photomultiplier tube with a detection range from 300 to 900 nm.

EDX measurements were done with an accelerating voltage of 20 kV and 0.6 nA beam current. In some cases, the accelerating voltage was increased up to 30 kV to improve the BSE contrast when acquiring images.

Elemental analyses were performed in the GeoForschungsZentrum, Potsdam, Germany, with a Cameca SX 50 electron probe operating at 20 kV and 50 nA with a spot size of 5 μm . Counting times for Si, Zr, Hf and Fe were 50 and 300 s for all other elements. Selected lines and standards were SiK α (wollastonite), PK α (erbium phosphate), CaK α (wollastonite), FeK α (hematite), YL α (yttrium phosphate), ZrL α (zircon), YbL α (ytterbium phosphate), HfL α (metallic Hf), UL β (metallic U) and ThL β (metallic Th). Other elements were in all cases below the detection limit of the electron microprobe.

Raman spectra were obtained with a Dilor XY Raman spectrometer with an Olympus petrographic microscope and confocal entrance optics. A detailed description of the experimental technique is given elsewhere (Nasdala et al. 1996b).

SHRIMP analyses of the isotopic composition of zircons were performed using the SHRIMP II at the Curtin University of Technology, Perth, Western Australia. SHRIMP was operated at a mass resolution of about 5000. The focused primary O²⁻ beam (10 kV and 3 nA) had a diameter of about 15 μm (Fig. 17). Unknowns were measured versus the Curtin CZ3 standard zircon (see Pidgeon et al. 1994). Isotopic ratios are corrected for common lead using the ²⁰⁴Pb method. A more detailed description of the experimental technique has been given, for example, by Compston et al. (1984).

3 Interpretation of Cathodoluminescence Imaging

As shown by Sommerauer (1976), Hoffman and Long (1984), Gebauer (1990, 1996), Vavra (1990, 1994), Hanchar and Miller (1993), and Hanchar and Rudnick (1995), CL provides excellent possibilities for revealing the internal structures of zircons. In most cases, the interpretation of observed structures is descriptive and based on visible relations. Previous authors assumed local emission of CL signal exclusively from a micro-area directly within the excitation volume of the electron beam. For correct interpretation of panchromatic images it is necessary to consider the spectral characteristics of the detected CL signal as well as the mechanisms of excitation and emission related to different emission centers.

3.1 Mechanism of Cathodoluminescence Emission and Escape Depth

Emission of CL is generated by activation of radiative transitions within a crystal during beam-lattice interaction. Band-band (intrinsic), non-phonon and phonon-assisted trap-band transitions or transitions within closed centers may occur. Traps in the band gap may be created by intrinsic defects of the lattice (e.g., intrinsic electron defects, excitons, and electron defects localized on vacancies) and impurities of trace elements (electron defects localized on impurities). Some of the impurities, particularly rare earth elements (REE), form closed centers with 4f or 5f electronic transitions within the centers that are only weakly influenced by the crystal field of the host mineral and not related to band transitions (Marfunin 1979; Remond et al. 1992). High concentrations of traps occur near the crystal surfaces as well as around dislocations, cleavage planes, grain boundaries and cracks. Therefore, an enhanced luminescence intensity was often observed during our work at such phase boundaries in cathodo- and UV-activated photoluminescence.

In the case of CL, activation of radiative transitions is non-specific for activation energy and mechanism of activation, since different types of radiation causing luminescence are present during beam-specimen interaction within the crystal (Goldstein et al. 1981). Electrons of the primary beam (typical with energies around 15–30 keV) as well as back-scattered, secondary, and Auger electrons form an energy continuum down to low energies in the range of optical transitions which leads to activation of different excitation levels of the electron structure in the mineral lattice (CL in the strict sense; Goldstein et al. 1981; Remond et al. 1992). X-ray radiation and phonon-induced temperature increases created by primary and scattered electrons cause additional X-ray luminescence and thermoluminescence (Remond et al. 1992). Local temperature increases due to the impact of the electron beam may be as high as some 100 °C in solids with low thermal conductivity (Kempe and Sorokin 1988).

A characteristic feature of luminescence is the relatively long relaxation time, allowing migration of energy through the crystal via different mechanisms of radiative and non-radiative interaction between different centers (Marfunin 1979; Barabanov et al. 1990). A crystal acts as a complex system during excitation of

band-related luminescence systems (Barabanov et al. 1990). Both mechanisms may lead to significant separation between excitation and emission centers in the crystal. This is particularly important if emission centers are absent or quenched in the area that is irradiated by the electron beam. As discussed by Remond et al. (1992), the CL signal may be additionally influenced by the crystal itself due to absorption and reflection on boundaries.

The sum of these factors leads to a complex CL signal in spectral composition generated from various escape depths and lateral areas, which is not directly comparable with other signals (SE, BSE, X-ray, etc.) in electron-beam analysis.

3.2

Comparison of Cathodoluminescence and Back-Scattered Electron Images

Internal structures of zircon crystals observed with CL appear to be quite similar to the structures that are sometimes revealed by means of other techniques. One of the most common features is growth ("oscillatory") zoning, which is frequently observed under the OM (Fielding 1970; Benisek and Finger 1993), after etching (Pidgeon 1992; Nasdala et al. 1997), by precise fission track mapping (Fielding 1970; Carpéna et al. 1987), in secondary electron (SE) and BSE images, and in element distribution patterns obtained by X-ray mapping. Heterogeneities were shown to be related to variations of the trace element concentrations of Y, Yb, P, U, Th, Hf, Ca, and Fe (Sommerauer 1976; Hoffman and Long 1984; Lork and Koschek 1991; Smith et al. 1991; Benisek and Finger 1993; Hanchar and Rudnick 1995; Chemale et al. 1996; Kosler et al. 1996; Nasdala et al. 1996b). According to these authors, zones enriched in trace elements are often colored in transmitted light, show decreased hardness (causing topographic contrast in polished sections visible in SE images; see Fig. 2b), and are less stable during etching as well as under the electron beam and during single-grain Pb evaporation (Ansdell and Kyser 1993). Sommerauer (1976) and Smith et al. (1991) suggested zoned metamictization in trace element-rich areas with high U and Th concentrations.

The interpretation of the CL and BSE contrast is, however, more complicated. It is well known that BSE contrast is closely related to the average atomic number of phases causing elastic scattering of electrons from the primary beam (Hall and Lloyd 1981). Correspondingly, high concentrations of Hf, Y, Yb, U, and Th (e.g., Sommerauer 1976; Hanchar and Miller 1993; Benisek and Finger 1993; Hanchar and Rudnick 1995) were shown or assumed (Kramm et al. 1993) to be related to high BSE intensity.

However, U, Th, Y and Hf-rich zones with low BSE signal were also observed in some cases (Peterman et al. 1986; Pointer et al. 1988; Smith et al. 1991; Kempe et al. 1997). The totals of electron probe analyses for such micro-areas are significantly lower than 100%. The deficit has been interpreted as due to an increased water content (Peterman et al. 1986; Smith et al. 1991). Nevertheless, as discussed by Pointer et al. (1988), low BSE contrast in those samples cannot be explained solely by the hypothetical water content. A more realistic explanation suggests a high concentration of vacancies (Pointer et al. 1988; Kempe et al. 1997), although water and other light elements may be also present in those regions (Smith et al. 1991).

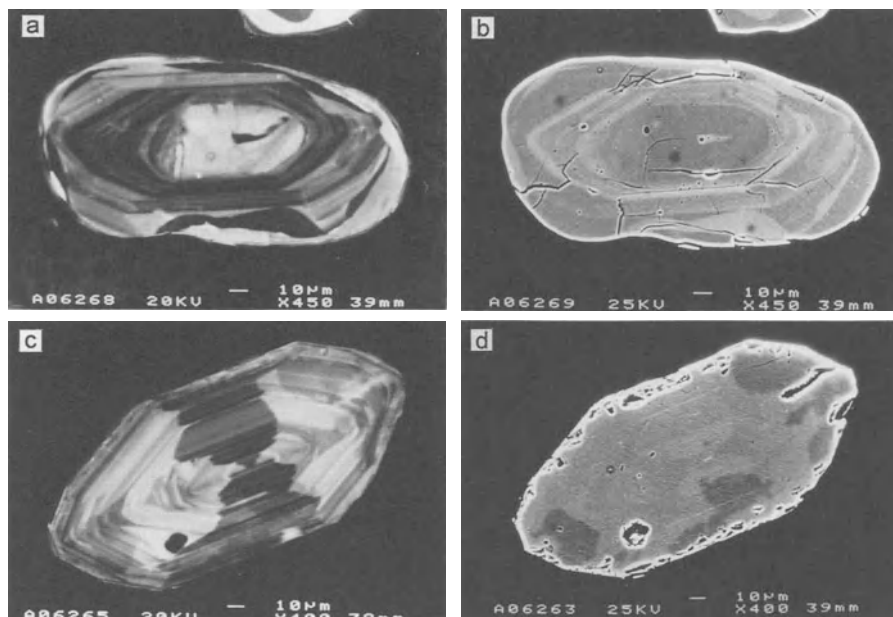


Fig. 1a–d. Internal structures of zircons revealed by CL and BSE imaging. Inverse behavior of CL (a) and BSE (b) for a zircon from the leucogranulite from Erlau, SGC, Germany (sample 84031). Inverse and concurring trends in CL (c) and BSE (d) intensity variations in one and the same zircon crystal from a porphyroid occurring near Neumühle, Greiz, Germany

High intensity BSE signals and correspondingly low intensity CL are mostly assigned to trace element-rich zones. This inverse behavior of CL and BSE signals was described in previous studies (Lork and Koschek 1991; Hanchar and Miller 1993; Koschek 1993; Roger et al. 1995; Hanchar and Rudnick 1995; Chemale et al. 1996; Vavra et al. 1996). It is our experience that the inverse behavior of CL and BSE intensities is most common. For example, inverse relations between BSE and CL were observed in nearly all zircon grains from the SGC investigated in this study (Fig. 1a,b).

However, inverse behavior is not always observed. The opposite case is represented by zircons showing concurring behaviors of BSE and CL intensities. For instance, BSE and CL images obtained on grains from samples W34 (Pidgeon 1992) and W61 from the Archaean granite from the Jack Hills, Western Australia, show remarkable similarities to each other not only in terms of structure patterns but also in terms of brightnesses (low BSE -low CL and vice versa; Fig. 2c,d). It is interesting to note that, using CL imaging, some internal structures were observed within recrystallized patches that appeared to be homogeneous under the OM and after etching.

We obtained similar results from zircons from postkinematic granites of the SGC, Hf-rich zircons from rare-metal bearing granites (Kempe et al. 1997), zircons from enclaves in gabbros from the MARK area, Mid-Atlantic Ridge (Pilot et al. 1997), and zircons from Archaean gneisses from the Belomor Complex, Kola

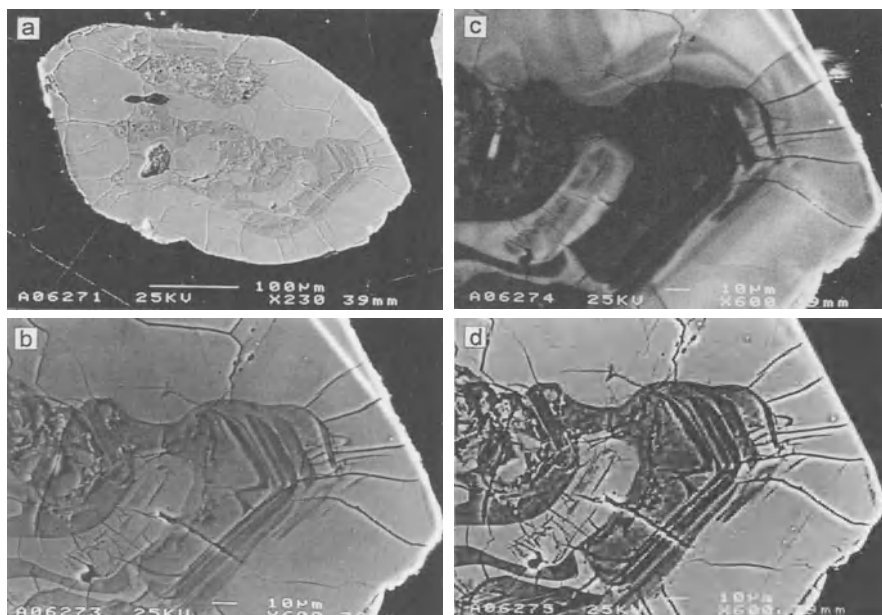


Fig. 2a–d. Internal structures of a granite zircon from the Jack Hills showing recrystallization (see Pidgeon 1992). Total view of the crystal in SE image (a). Concurring trends in the variations of the SE (b), CL (c), and BSE (d) signals. An additional structure revealed by CL (c) is visible within the recrystallized patches (sample W 61)

Peninsula (Savatenko et al. 1995). The intensity of the BSE signal of these zircons is one order of magnitude lower than that of zircons from the Saxonian granulites (i. e. the variations of the BSE contrast for the two types of zircons compared are at fundamentally different levels of absolute intensity).

In some rock types, both parallel and inverse behavior can be found in one and the same zircon. This is demonstrated using a specimen from the porphyroid from Neumühle near Greiz, Germany (Fig. 1c,d).

3.3 Spectral Cathodoluminescence Investigations

In accordance with observed luminescence colors, Ohnenstetter et al. (1991) and Remond et al. (1992) distinguished blue and yellow luminescent zircons. The samples from the SGC described in the present study belong mainly to the yellow type. Nevertheless, some zircons showing bluish luminescent cores and yellowish luminescent rims were found in the granulite from Erlau. Both types of luminescence color in the same crystal were also detected in a few zircons from other localities and origins. Typical CL spectra of zircons from the SGC are shown in Fig. 3a. The spectra are not corrected for instrumental response. They consist of a broad peak at 560 nm with two superimposed lines at 488 and 575 nm. The lack of the fine structure in the CL spectra may be related to the low resolution of the

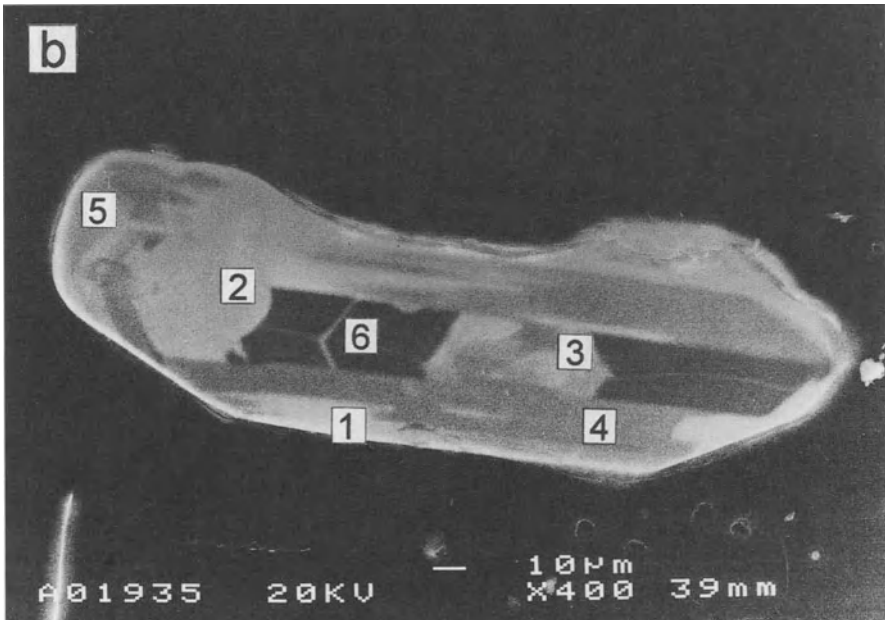
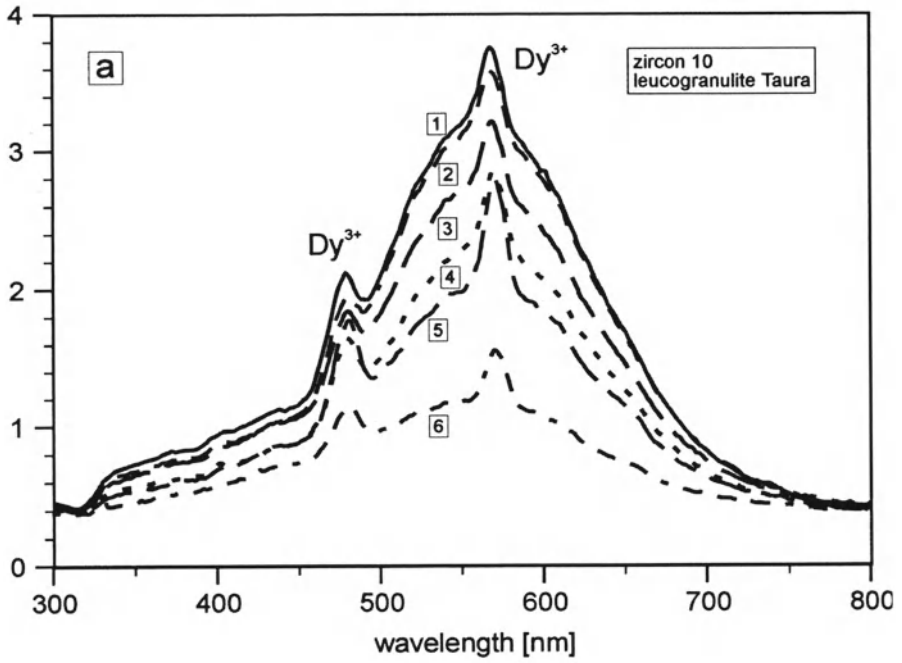


Fig. 3. CL spectra (a) obtained from six spots set within a single crystal from the leucogranulite from Taura (sample Pa III). Spectra are not corrected for instrument response. Spot location is shown in (b) in relation to panchromatic CL patterns

system used. However, since the optical resolution of the grating used was sufficient for line group detection, we assign this effect to temperature quenching caused by local heating under the focused electron beam.

The spectrum of the bluish luminescent cores in some zircons from the granulite from Erlau (Fig. 4; see Fig. 7d) suggests that there exists an additional CL peak at around 400 nm which is mainly suppressed due to detector sensitivity in the UV.

These results are in good agreement with the data of previous authors, especially if, as in our case, the spectra were obtained with detectors not sensitive in the UV (Mariano in Marshall 1988; Halden and Hawthorne 1993; Phillips et al. 1996; Chemale et al. 1996).

In all spectra observed in this study, integral intensities of the band luminescence predominate in the total CL intensities (Gruner et al. 1996). In our experience, luminescence of the superimposed narrow lines is mostly of minor importance for the total signal intensity, except for some zircons showing an extremely different CL behavior (Hanchar and Rudnick 1995; Götze et al. 1997). This conclusion agrees with the results reported by Remond et al. (1992).

Figure 3 also demonstrates another feature typical of granulite zircons from the SG: Areas with decreased yellow band CL (and, correspondingly, decreased total CL) show increased line CL and vice versa. However, the behavior of the band and line luminescence is not fully inverse but may be independent of each other. This fact suggests that these two signals are related to different luminescence centers.

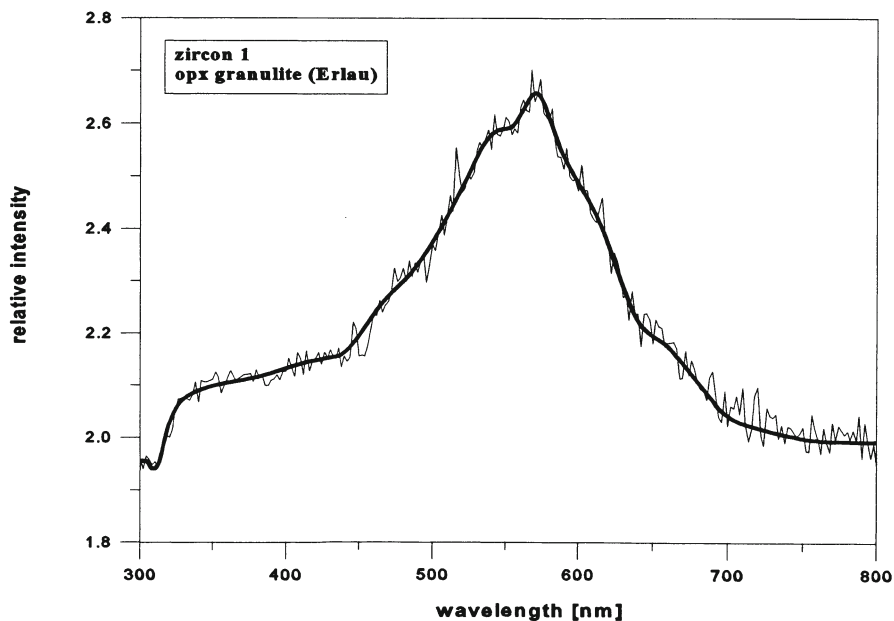


Fig. 4. CL spectra obtained from a bluish luminescent core of a zircon grain from the leucogranulite from Erlau (sample 84031). The panchromatic CL image of the grain is shown in Fig. 7d. The spectra is not corrected for instrument response

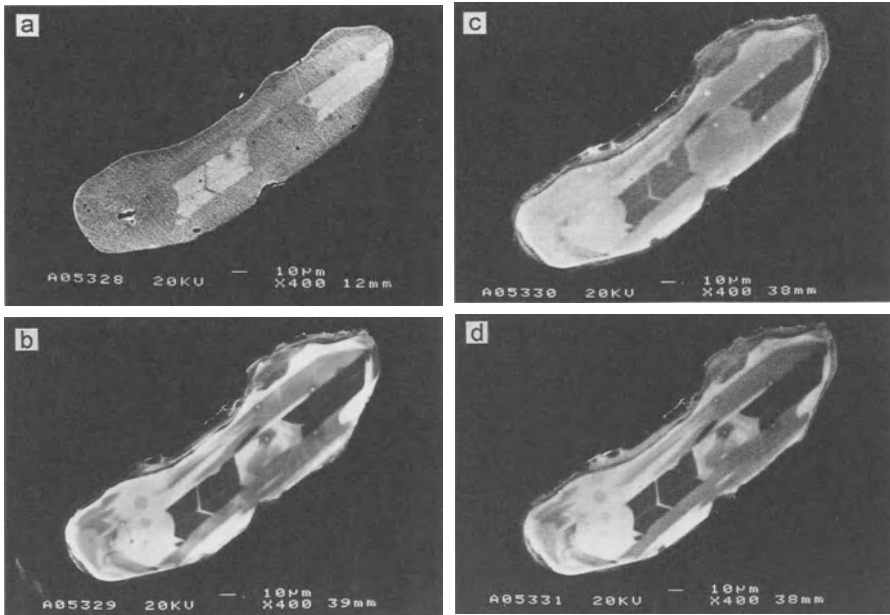


Fig. 5. Comparison of BSE (a), panchromatic (b), 482 nm (c), and 525 nm (d) CL images for the zircon crystal shown in Fig. 3 (sample Pa III, leucogranulite from Taura)

Monochromatic CL imaging (Fig. 5c,d) emphasizes the dominance of the band luminescence. Only small differences between the monochromatic 482 nm image (corresponding to the weakly band-influenced Dy luminescence) and the panchromatic image were registered. This is explained by the fact that the background from the “yellow band” yields still about 20–50% of the total signal intensity in the monochromatic 482 nm image.

3.4

Interpretation of the Cathodoluminescence Signal

A few publications dealing with the mechanisms of luminescence in zircon document contradictory results. In early publications, only relations between CL signal and total trace element content are discussed (Sommerauer 1976; Hoffman and Long 1984). Sommerauer (1976) reported a quenching of the CL signal for trace element totals above 1 wt%. More detailed examination of published data shows indeed variations in total CL intensity with changing trace element contents. However, changes of spectral characteristics of the CL were not detected. Different mechanisms of CL quenching have to be taken into account: (1) self-quenching at high concentration levels of luminescence centers, (2) quenching by non-radiative transitions provided by high contents of hole centers or “killer” elements, (3) annealing of luminescence centers by radioactive radiation related to U and Th contents, and (4) local distortion of the band structure in the crystal

caused by metamictization (α -recoils in the U and Th decay). In any case, the prevailing reasons are difficult to evaluate empirically since concentrations of most trace elements related to different quenching mechanisms are at least roughly correlated. Consequently, interpretations of zircon CL that consider only the total trace element content (Vavra 1990; Kramm et al. 1993) do not facilitate detailed discussions about internal structures and U-Pb isotopic data from CL imaging.

In several publications, Dy^{3+} is assumed to be the principal luminescence activator in zircon CL (Lork and Koschek 1991; Hanchar and Miller 1993; Phillips et al. 1996). The analysis of the CL spectra shows that in most cases line groups related to the emission of REE $^{3+}$ centers (with dominance of Dy^{3+}) are superimposed on broad bands of varying intensity. Consequently, integral zircon CL is a complex signal caused by the effect of different emission centers (e.g., Mariano in Marshall 1988; Ohnenstetter et al. 1991; Remond et al. 1992).

Luminescence of trivalent REE can be recognized in different hosts with relative ease because of the closed character of the centers (well defined energy levels only weakly influenced by the crystal lattice). Correspondingly, the emissions at 482 and 575 nm (which represent resolved or unresolved line groups) are assigned to the Dy^{3+} center in many investigations (Mariano in Marshall 1988; Ohnenstetter et al. 1991; Remond et al. 1992; Koschek 1993; Hanchar and Rudnick 1995; Phillips et al. 1996). Among other possible REE $^{3+}$ centers, only Er (Remond et al. 1992) and Tb (Hanchar and Rudnick 1995) are assumed to be activators in some cases. The other REE $^{3+}$ centers (Pr^{3+} , Sm^{3+} , Eu^{3+} , Gd^{3+} , Ho^{3+} and Tm^{3+}) are quite common in other host minerals and were detected in doped synthetic zircons (Cesbron et al. 1993; Hanchar, pers. comm. 1997) and by X-ray luminescence (Krasnobaev et al. 1988), but they were not reported for natural zircons. This phenomenon may be explained by specifics of the host lattice. REE contents, except heavy REE (HREE) in zircons are generally lower than in luminescent Ca minerals such as fluorite, apatite, and scheelite. Strong REE fractionation with depletion of light REE (LREE) and enrichment of HREE (especially Yb) and Y is caused by zircon lattice parameters. However, concentration of odd REE (Pr, Eu, Tb, Ho, Tm) is always lower than that of even REE, according to Oddo-Harkin's rule. In addition, the luminescence of Dy^{3+} centers in zircons is more efficient than that of Sm^{3+} and Er^{3+} centers at room temperature.

As discussed above, zircon CL in the visible range is often dominated by luminescence bands at 400 and 560 nm. This luminescence is not intrinsic in the narrow sense (Remond et al. 1992). The band gap for zircon is about 5.3–5.4 eV according to optical absorption investigations (Krasnobaev et al. 1988; Cesbron et al. 1993). Band-band transitions lie in the UV range around 255/265 nm (Krasnobaev et al. 1988) or 230 nm (Cesbron et al. 1993). Band-band transitions are quenched by defect-related centers and, therefore, they are found only in pure synthetic crystals (Remond et al. 1992; Cesbron et al. 1993). Additional bands in the UV range are reported around 280–295 nm (I), 315–320 nm (II; for synthetic zircons only) and 350–375 nm (III; Krasnobaev et al. 1988; Remond et al. 1992; Cesbron et al. 1993).

As already mentioned, main bands in the visible range are at 400 nm (IV; Remond et al. 1992; Koschek 1993; this study) and at 560–580 nm (VII; Krasnobaev et al. 1988; Mariano in Marshall 1988; Lork and Koschek 1991; Ohnenstet-

ter et al. 1991; Remond et al. 1992; Cesbron et al. 1993; Halden and Hawthorne 1993; Koschek 1993; Chemale et al. 1996; this study). These two bands are also observed in photoluminescence spectra (Krasnobaev et al. 1988; Aoki 1994). Further CL bands are detected at 425 nm (Lork and Koschek 1991), 450–466 nm (V; Ohnenstetter et al. 1991; Remond et al. 1992; Koschek 1993) and at 480–516 nm (VI; Remond et al. 1992; Koschek 1993; Chemale et al. 1996).

The nature of the band luminescence of zircon is still poorly understood. Different suppositions are made in previous studies. For example, band I is assumed to be related to OH^- defects (Remond et al. 1992), broken atomic bonds (Cesbron et al. 1993), or electron defects localized on Zr-O complexes or excitons (Krasnobaev et al. 1988).

Krasnobaev et al. (1988) found band III to be possibly caused by Ti impurities, through electron defects localized on O in Ti-O complexes, while Ohnenstetter et al. (1991) and Remond et al. (1992) discussed correlation with $\text{Y}^{3+} + \text{REE}^{3+}$ replacement not charge compensated by P. However, high Y contents not compensated by P rather lead to CL quenching (Hoffman and Long 1984; Remond et al. 1992; Cesbron et al. 1993). The latter authors refer to an intrinsic luminescence (from SiO_4 -groups) for bands IV and V. Koschek (1993) tried to interpret the zircon luminescence in analogy to quartz (bands IV, VI and VII as Si centers) and baddeleyite (band V as Zr-O center). Quite different assumptions exist for the “yellow center” (band VII). It is regarded as electron defects localized at SiO_4 groups (Krasnobaev et al. 1988; Koschek 1993), Ti^{4+} or U^{4+} centers (Ohnenstetter et al. 1991), radiogenic defects caused by U radiation damage (Remond et al. 1992), and Mn^{2+} or REE defects (Chemale et al. 1996).

Because of the non-specific activation of the centers, it is not possible to clarify the nature of the band luminescence by CL investigations only. Therefore, complex investigations including other spectroscopic methods are necessary. According to our knowledge, the only attempt in this manner was made by Krasnobaev et al. (1988). Non-intrinsic band luminescence is typical of semiconductors containing oxy-tetrahedra. In most cases, luminescence may be explained by electron defects or excitons localized on oxygens of the tetrahedron and sometimes stabilized by additional defects. In such cases, double bands corresponding to different O-O distances in the tetrahedron may be resolved. This thesis is supported by: (1) the Gaussian shape of the bands when plotted versus energy (Koschek 1993), (2) extremely large band half-widths (measured as full width at half height), and (3) indications from X-ray luminescence (Krasnobaev et al. 1988) and photoluminescence (Aoki 1994) for the existence of double bands at 255/265 nm; 280/295 nm (band I), 350/375 nm (band III), 400/450 nm (bands IV and V), and 540/580 nm (band VII).

Radiative transitions in zircon occur over quite a large energy range in the band gap. Luminescence, related to high-energy transitions, is quenched by emission of centers with lower energy. For instance, bands in the far UV (band-band transition and band I) are quenched by the band II emission (Krasnobaev et al. 1988) and REE^{3+} luminescence (Cesbron et al. 1993). If the intensity of the band III in the near UV is high, all bands in the far UV are quenched (Krasnobaev et al. 1988). The yellow center (band VII at 560 nm) quenches the blue luminescence (bands IV and V) and the emission of REE^{3+} centers.

We assume that emission in the far UV may be related to band-band and phonon-assisted band-band transitions. The intensive luminescence in the blue range is possibly exciton-assisted, as discussed above.

The trap of the yellow center lies relatively deep in the gap. There are some indications from our data for some fine structure of the 560 nm band, however, it seems not to be a typical double band. Therefore, the related center is possibly caused by an impurity and not by an intrinsic defect of the lattice. From spectral characteristics and crystal chemistry, the occurrence of Mn^{2+} , Ti^{4+} and U^{4+} centers seems to be unlikely. As discussed above, substitution of Zr by Y not charge compensated by P, as reported by Hoffman and Long (1984), Ohnenstetter et al. (1991), Remond et al. (1992) and Benisek and Finger (1993) for some natural samples, may cause CL quenching rather than emission. Radiative transitions for Y^{3+} have not been reported in the literature and are unlikely according to the electron structure. In our study, measured Y and P contents correlate well for all analyses in which concentrations exceed the detection limits of the electron probe (Fig. 6).

We propose another possible explanation for the yellow emission: a Yb^{2+} center created by "radioactive reduction" of Yb^{3+} due to U (and Th) radiation. There are some facts supporting this thesis:

1. The occurrence of REE^{2+} in minerals with ion lattices is well known (Marfunin 1979), and the reduction by ionizing radiation to the divalent stage (including the occurrence of Yb^{2+}) is well documented, for example, for natural fluorites (Chatagnon et al. 1982; Chatagnon and Meary 1982; Trinkler et al. 1993; Morozov et al. 1996).
2. The Yb content in natural zircon is always relatively high.
3. The Yb^{2+} emission in fluorite detected at 568–575 nm shows a comparable large band width (Feofilov 1956).

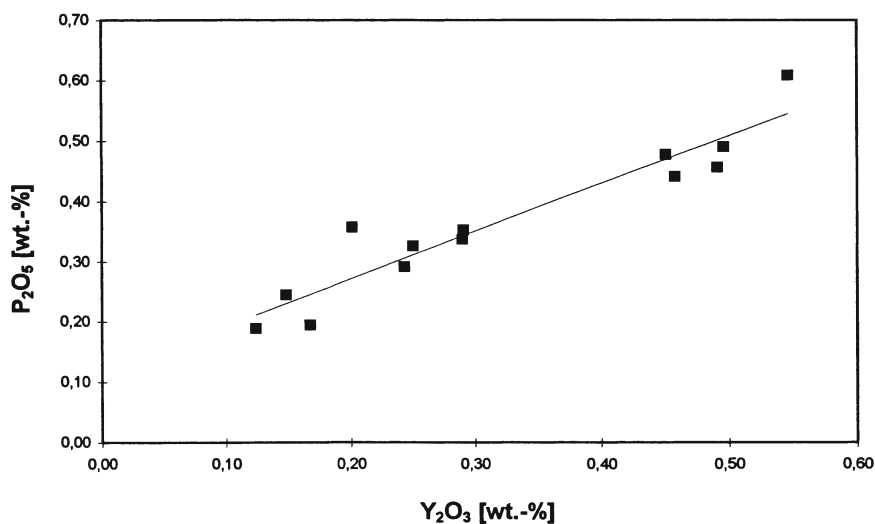


Fig. 6. Correlation between P_2O_5 and Y_2O_3 concentrations detected with electron probe (WDX) analysis from zircons from different granulites (samples Pa III, Pa X, and 84031) from the SGC

4. The yellow center is found only in natural zircons. Nevertheless, a very weak band at 565 nm was detected by Cesbron et al. (1993) in an Y-doped zircon.
5. Creation of yellow centers due to radioactive radiation was also discussed by Remond et al. (1992).
6. By X-ray luminescence and photoluminescence investigations, Krasnobaev et al. (1988) observed a quenching of the yellow center after annealing in air above 600 °C (with parallel increase in the REE³⁺ luminescence) and a corresponding increase of the yellow emission after annealing in a reducing atmosphere.
7. Another indication is the inverse behavior of CL and BSE intensities obtained on zircon samples from the SGC showing intensive yellow CL. As discussed above, BSE intensity variations may be related to various trace element (e.g., Hf, U, Th, Y, Yb, P) and vacancy concentrations. In agreement with results reported by other authors for granulite zircons, the trace element content in granulite zircons from the SGC is very low. In the majority of electron probe analyses performed in the present study, U, Th, Y, Yb, P, Fe, and Ca were found to be below the detection limits (about 500–100 ppm). Only the concentrations of U and Y reach up to 1000–2000 ppm. Variations of the Hf content within single crystals without cores are negligible for the SGC zircons. These results are in good agreement with PIXE (Gruner and Grambole 1996, unpubl.) and SHRIMP data. If the equation of Hall and Lloyd (1981; which was also employed by Pointer et al. 1988) was used for calculating the average atomic number, the variations of the average atomic number caused by trace variations would be found to be somewhat below the BSE detection limit. We used atomic% (instead of weight% as suggested by Hall and Lloyd 1981) for calculating the average atomic number, which has more physical significance. We found that differences in the BSE intensity that are caused by lateral trace element variations are clearly below the sensitivity of the BSE detector. Therefore, we assign the internal structures of granulite zircons from the SGC revealed by BSE mainly to variations in the vacancy concentration on the Zr sites. Moderate concentrations of vacancies (areas in SGC zircons with moderate BSE contrast) may stabilize and high concentration of Zr vacancies (low BSE signal) may quench the Yb²⁺ center if incorporation of trivalent elements is compensated by P. Additional work is necessary to clarify the nature of the yellow center in natural zircons.

3.5

Interpretation of Internal Structures in Zircons Visible in Panchromatic Cathodoluminescence Images

From the discussion above we conclude that contrast in panchromatic images may be caused by intensity variations of the blue and yellow luminescence bands (sometimes also by REE³⁺ CL variations) due to: (1) different degrees of CL quenching without changes in the spectral characteristics; or (2) changes in the relative efficiencies of various CL centers.

As shown by a large number of published data, growth zoning revealed by CL and/or BSE may be a principal characteristic of primary zircon growth. This the-

sis agrees with observations on growth phenomena in many other minerals (e.g., pyroxenes, feldspars, fluorite, topaz, cassiterite). As shown by Halden and Hawthorne (1993), by analysis of the fractal geometry of chaotic oscillatory zoned zircon from Silinjärvi carbonatite (Finland), the structure is caused by growth kinetics rather than temporal variations in the melt or fluid composition (see also discussion in Benisek and Finger 1993). Such zoning was also found as a primary growth phenomenon in zircons formed during metasomatic alteration in Thor Lake, Canada (Smith et al. 1991) and in Tsakhir, Mongolia (Kempe et al. 1996) and is not restricted to a magmatic environment, as assumed in most publications (Carpéna et al. 1987; Vavra 1990; Lork and Koschek 1991; Pidgeon 1992; Benisek and Finger 1993; Hanchar and Miller 1993; Rubatto and Gebauer 1996). Growth zoning is often accompanied by sector zoning (Hoffman and Long 1984; Carpena et al. 1987; Benisek and Finger 1993; Hanchar and Miller 1993) due to the anisotropic distribution of point defects (including trace elements and vacancies) during crystal growth.

Before discussing more complicated internal structures for zircons from metamorphic rocks, we would like to describe some artefacts often leading to misinterpretations of panchromatic CL images. As mentioned above, enhanced luminescence intensity on phase boundaries, cracks and holes in the sample surfaces may simulate internal crystal structures. CL may be created only at grain boundaries or certain local structures below the polished surface if it is quenched in the area directly irradiated by the beam. Interpretation of CL images obtained from transparent crystals as common in granulitic rocks is, therefore, sometimes quite difficult. In this case, a three-dimensional CL image (and not, as often assumed, a two-dimensional surface image) may be detected because of the high optical transparency of the crystal. An example is shown in Fig. 7c. Here, a phantom crystal, which can be recognized from the pronounced CL on its surface, is imaged whereas the central part and the outer rim of the crystal are transparent and almost free of luminescence (the polished grain surface is somewhat above the half-height of the crystal). In other cases, the three-dimensional luminescence structure is more complicated and more difficult to understand. The three-dimensional effect must be also taken into consideration in the case of images providing essentially two-dimensional information, as demonstrated in Fig. 1c.

If the CL contrast is very high, it is often difficult (or even impossible) to image variations in CL intensity both on the upper and lower limit of the gray levels. Such white or black imaged areas may be erroneously described as not showing any internal structure.

Another artefact is related to changes in spectral characteristics and to the detector sensitivity. An example is demonstrated in Fig. 7d, which shows the panchromatic CL image of a zircon with a highly luminescent core. It is interesting to note that yellow luminescence intensities for core and rim are roughly in the same range. The considerably increased total CL intensity in the core is caused by more intense blue luminescence and enhanced detector sensitivity in the blue wavelength range.

CL is often used for proving the existence of inherited cores in zircons from magmatic and metamorphic rocks (e.g., Gebauer 1990; 1996; Hanchar und Rudnick 1995; Vavra et al. 1996). As we have shown, interpretation of CL images must

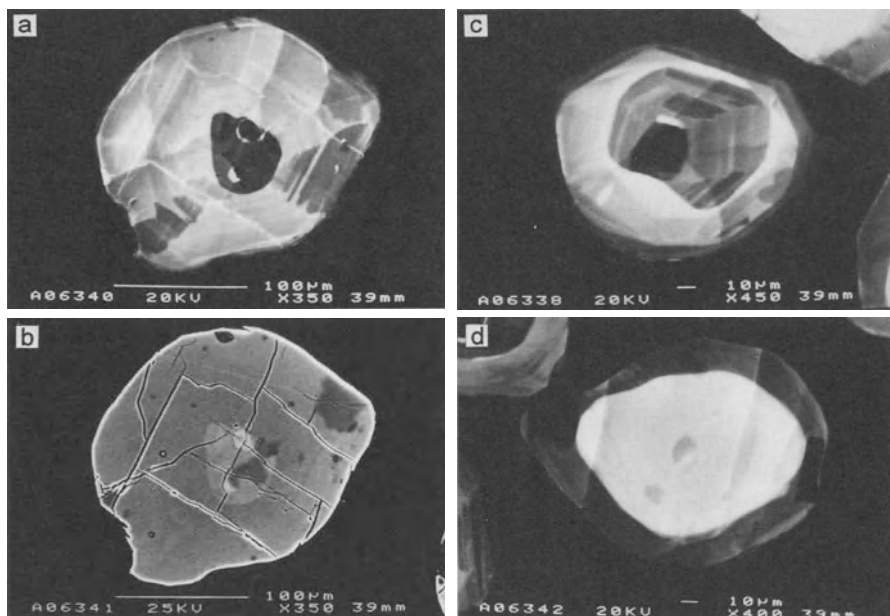


Fig. 7a–d. Illustration of possible “artefacts” sometimes influencing the interpretation of CL images. The zircon shown in the left contains a detrital core and shows thermal recrystallization deleting primary oscillatory zoning. The apparent sector zoning visible under CL (a) is related to radial cracks as proved by the BSE image (b). An luminescent phantom crystal within a weakly luminescent zircon is shown in c. The luminescence in the yellow range is in the same order of intensity for the core and the rim of the zircon imaged with CL in d. The bright luminescence of the core is caused by emission in the blue wavelength range. (All zircons from the leucogranulite from Erlau, sample 84031)

be done with appropriate care. For example, the dark area in the zircon shown in Fig. 7c cannot be assigned to a detrital core. Contrast in CL intensity alone is not a sufficient criterion for proving the existence of a core. More reliable indications pointing to the presence of a core are findings of clear discordances in the internal structure and often the observation of rounded surfaces of the assumed cores (e.g., see zircon in Fig. 7d or zircon with radial fractures containing a discordant detrital core in Fig. 7a,b as proved by CL and BSE images) as well as differences in trace element contents (Hanchar and Rudnick 1995; Hanchar, pers. comm. 1997).

The zircon shown in Fig. 7a demonstrates a further structure often detected in zircons from the SGC (see also Fig. 11) – deletion of growth zoning by development of bright luminescent areas, sometimes feeding in growth zoned areas along zone boundaries. This observation is interpreted as recrystallization during metamorphism. We emphasize that this recrystallization is different in nature compared with recrystallization phenomena that have been found, for example, in zircons from the Jack Hills (Pidgeon 1992; Fig. 2, this work): No phase boundary is detected between zoned and recrystallized sectors in the SGC zircons. In the Neumühle zircon (Fig. 1c,d), both types of recrystallization are observed.

The results of imaging the internal structures of about 600 zircons of different origin lead us to the conclusion that only very little or perhaps even no zircon growth takes place during regional metamorphism. Only in one case (zircons from amphibolites in the Erzgebirge region), we found clear indications for overgrowth and veinlets, cementing also broken crystals. The CL intensity of these newly formed areas was much higher than in recrystallized areas of other zircons from metamorphic rocks. The overgrowths have typically thicknesses of a few μm and show cloudy internal structures under CL. Therefore, more or less homogeneous “rims” or areas with bright luminescence often showing residues of primary growth zoning in SEM-CL within zircon grains from metamorphic rocks were interpreted as resulting from solid state recrystallization and not as metamorphic overgrowth. This inference agrees well with conclusions of Pidgeon (1992) and contradicts suggestions from Hanchar and Miller (1993), Hanchar and Rudnick (1995), and Vavra et al. (1996).

3.6

Relevance of Cathodoluminescence Imaging for Interpretation of U-Pb Data

Interpretation of internal structures revealed by CL combined with SE and BSE imaging provides additional constraints for discussing concordance/discordance of U-Pb isotope data obtained by different methods.

Discordance (in the sense of “normal”, i.e. non-reverse discordance) may be explained by: (1) analyses of composites (different isotope systems mixed in multi-grain samples, within a single zircon or in a spot); or (2) by Pb loss (and, less likely, U gain or diffusion of both of these elements). The various mechanisms of Pb diffusion in zircon (continuous or episodic) have been recently summarized by Lee (1993).

The possibility of discordance caused by composite analyses may be demonstrated by multi-grain analyses of zircons from gneisses with protracted history commonly containing detrital cores (e.g., Todt and Büsch 1981; Peterman et al. 1986; Tichomirowa et al. 1996). On a concordia diagram, such single data points often scatter over a wide range, erroneously suggesting quite different degrees of discordance. Similar results are obtained with the SHRIMP when the beam spot straddles a boundary between zircon phases with different isotope systems, as shown by Hanchar and Miller (1993). This possible falsification should be considered when discussing the isotopic data obtained on the zircon shown in Fig. 16c (see also Fig. 18). However, it seems to be unlikely that discordance measured in zircons showing growth zoning may be interpreted as such apparent discordance due to mix-analysis, as assumed by Hanchar and Miller (1993) and Chemale et al. (1996). Distinguishable differences between the initial isotope compositions of single growth zones resulting from one and the same event can hardly be expected.

Another possible explanation for discordance phenomena is the assumption of Pb loss (or less commonly U gain). Investigations on natural zircons showed that Pb loss at lower T is clearly enhanced by metamictization (Silver and Deutsch 1963; Nasdala et al. 1997).

Summarizing our data, two types of zircons showing metamictization or low degree of crystallinity are suggested. The first type of metamict or not well-crystallized zircon contains primary growth zones with enhanced trace element content (including Y, Yb, P, U, and Th) which are characterized by a relatively high intensity of the BSE signal and quenched CL, compared with the well crystallized zones. Low crystallinity may be assigned to the high level of trace element incorporation causing lattice destabilization with additional damage due to radioactive decay. This type is represented by magmatically grown zircons showing primary growth zoning, where enhanced trace element contents are restricted to certain zones (Benisek and Finger 1993). Uranium-lead data for such zircons or zircon micro-areas give concordant, or at most moderately discordant, data points which are plotted relatively close to the upper intercept of hypothetical discordia lines (see Black 1987; Nasdala et al. 1996a). In the case of low degrees of isotopic discordance, the model of episodic Pb losses cannot be distinguished from the model of continuous Pb losses (as reviewed by Faure 1986). The different degrees of discordance may be related to the presence of different pathways (cracks, dislocations, etc.) to the crystal surface providing Pb grain boundary diffusion out of the zircon lattice.

We suggest that such behavior of the U-Pb system may be a result of continuous Pb loss of varying intensity from trace element-rich and metamict zones. Our inference is supported by the correlation between degree of discordance and radioactive dosage that was observed by Gracheva et al. (1981) on granitic zircons, which in most cases show normal growth zoning (see Vavra 1994), whereas other zircons investigated by these authors were found to not follow this tendency.

The second type of metamict or low crystallized zircons is characterized by high U, Th, Y, and Yb and shows in particular enhanced Fe and Ca content. Metamictization is observed on entire zircons or zircon micro-areas which feed from the surface to the core of single crystals along cracks, growth zones or other heterogeneities probably by phase-boundary diffusion. These zircons show low CL and remarkably low BSE (see Sect. 3.2). Such characteristics were, for example, observed on zircons from the Jack Hills (see also microprobe analyses for Fe and Ca in Nasdala et al. 1996b), from granites belonging to the SGC (Baumann and Kempe, unpubl. data), and from gabbros from the MARK area (Haubrich and Kempe, unpubl. data). Since the same chemical features and BSE/CL behavior as named above were found on metasomatically grown, metamict zircons from Tsakhir and Thor Lake, we conclude that the occurrence of this type of low crystallinity and metamictization is related to metasomatic alteration.

This interpretation possibly explains the findings for the Jack Hills zircons. Both recrystallized (and well concordant) and growth zoned (discordant) areas lie on a single chord the lower intercept of which is still questionable (Pidgeon 1992). BSE and CL behavior suggests that the metasomatic alteration has affected both recrystallized and zoned areas. Therefore, we assume that the alteration process has fully reset the U-Pb system of the entire crystal both by recrystallization and defect-related diffusion because the pre-existing zoning was affected by the recrystallization only partly. The subsequent Pb loss is more extensive

in zoned than in recrystallized areas, due to increased Pb diffusion rates in zoned areas caused by more intense metamictization (Nasdala et al. 1997). According to the model discussed, only the age of metasomatic alteration may be dated by U-Pb measurements on zircons that underwent metasomatic recrystallization.

The classification of the two types of metamict or low crystallized zircons described is also in agreement with Raman microprobe data reported elsewhere (Nasdala et al. 1996b). Internal structures of metamict lattice domains far in the sub-micron range are below the resolution limits of methods used in this study. High-resolution-TEM and electron diffraction investigations are necessary to evaluate the metamict state in more detail. References in this field are limited, and reported investigations were carried out on some extreme samples (e.g., zircons from Sri Lanka carbonatites) because of difficulties in sample preparation (e.g., Murakami et al. 1991; McLaren et al. 1994).

Although distortion of the U-Pb isotope system is enhanced by metamictization, as discussed above, even well crystallized zircons may be affected by loss of radiogenic Pb. An example is Pb loss related to recrystallization at high T. As stated by Mezger (1996), zircon tends to recrystallize above 600 °C. According to Krasnobayev et al. (1988), partial recrystallization of metamict areas in granite zircons at about 600 °C causes increased X-ray and photoluminescence intensities. Above 600 °C, photoluminescence of granite zircons quenches. Only in this temperature range, the behavior of granite zircons is similar to that of zircons from kimberlites and pegmatites.

The process of thermal recrystallization leads to low trace element content and high CL intensities in more or less homogeneous areas (Fig. 7a,b and Fig. 11). The recrystallization happens in the solid state along lattice domains enriched in vacancies and impurities, since diffusion is more rapid here. Consequently, thermal recrystallization does not take place from the rim to the core (as metasomatic alteration does; see Fig. 1d) but from certain defect-rich domains in the crystal such as metamict detrital cores, defect-rich sectors in sector zoning, and boundaries between growth zones in oscillatory zoning (see Fig. 1 in Pidgeon 1992; Fig. 2 in Nasdala et al. 1997; see also Fig. 12a, this work). Resulting internal structures show extreme varieties. An example are fir tree structures described by Vavra et al. (1996; see also Fig. 11c, this work).

Thermal recrystallization, typical of regional metamorphism, causes episodic Pb loss leading to partial or complete reset of the U-Pb system. Data obtained from micro-areas that have been almost fully reset plot near the lower intercept of the discordia line. They may define the age of the metamorphic event causing Pb loss (e.g., Gebauer and Grünenfelder 1976; Todt and Büsch 1981; Kotov et al. 1990; Lork and Koschek 1991; Vavra et al. 1996). According to data reported by Pidgeon et al. (1966) and Kotov et al. (1990), thermal recrystallization may be stimulated by the presence of a fluid phase. This process is rather related to the whole complex of physico-chemical conditions (including the chemistry of the fluid involved) than exclusively to the temperature variations.

4

An Applied Cathodoluminescence, Scanning Electron Microscope, Microprobe, Raman and SHRIMP Study on Zircons from the Saxonian Granulite Complex, Germany

4.1

Introduction, Geological Setting, Sampling Sites

The SGC is an exotic crust fragment situated north of the Moldanubian, at the northern borderline of the Erzgebirge crystalline complex (Fig. 8; Kroner 1995). The complex consists of three types of granulitic rocks (leucogranulites, pyroxene-bearing granulites, and mafic granulites – so-called pyrciasites), which are overlaid by cordierite, garnet, and biotite gneisses. The outermost zone of the SGC is formed by a mantle of mica schists and phyllites. The rocks are intensively deformed and foliated, particularly in the southern part that lies parallel to the southeast boundary of the SGC (Kroner 1995). Magmatic rocks are represented by serpentinized gabbros set mainly at the southern and northern ends of the southeast border of the complex, as well as by concordant (foliated) and discordant granite intrusions of various scale. Significant granitoids are the large Mittweida granite, which is situated near the center of the SGC, and the foliated Berbersdorf granite, at the northeastern end of the SGC.

Notwithstanding the long history of investigation, the formation of the SGC is still controversial. According to Rötzler (1992), the main topics of discussion are: (1) determination of the protoliths of different granulites and gneisses (ortho- or para-nature of the rocks respectively); (2) dating of the granulite metamorphism; and (3) relation between the high-pressure/high-temperature metamorphism and the tectonic uplift of the complex.

Previously published data of isotopic age determinations were reviewed by von Quadt (1993) and discussed considering new Sm-Nd and U-Pb data. More recently, additional results were presented by Kröner et al. (1994) and Baumann et al. (1996).

Considering reliable isotopic data only, reported ages cluster mainly in two groups, around 340 and 450 Ma. Sm-Nd isotope systems of the whole rocks are clearly distorted (e.g., data in von Quadt 1993), whereas Sm-Nd mineral isochrons for leucogranulites from Erlau and Diethensdorf as well as for a mafic granulite from Diethensdorf and a pyroxene-bearing granulite from Hartmannsdorf yielded ages between 346 and 355 Ma (Chernyshev and Zhuravlev 1987; von Quadt 1993). Another mafic granulite from Diethensdorf with re-equilibrated apatite defines an age of 308 Ma, as discussed by von Quadt (1993). This author also reported an Sm-Nd mineral age of 380 Ma for a garnet pyroxenite from Klatschmühle, whereas Baumann et al. (1996) found 322 and 345 Ma (Sm-Nd mineral ages) for the same rock type, in agreement with U-Pb zircon age determinations. Using Rb-Sr analysis, Gorokhov et al. (1987) obtained similar Carboniferous ages (321 and 342 Ma) from thin slab profiles from leucogranulites. K-Ar dating of secondary biotites from leucogranulites gave ages of 336 and 350 Ma (Watznauer 1974).

Conventional multi-grain U-Pb dating, Pb-Pb single-grain evaporation data and SHRIMP analyses performed on zircons from different granulites confirm

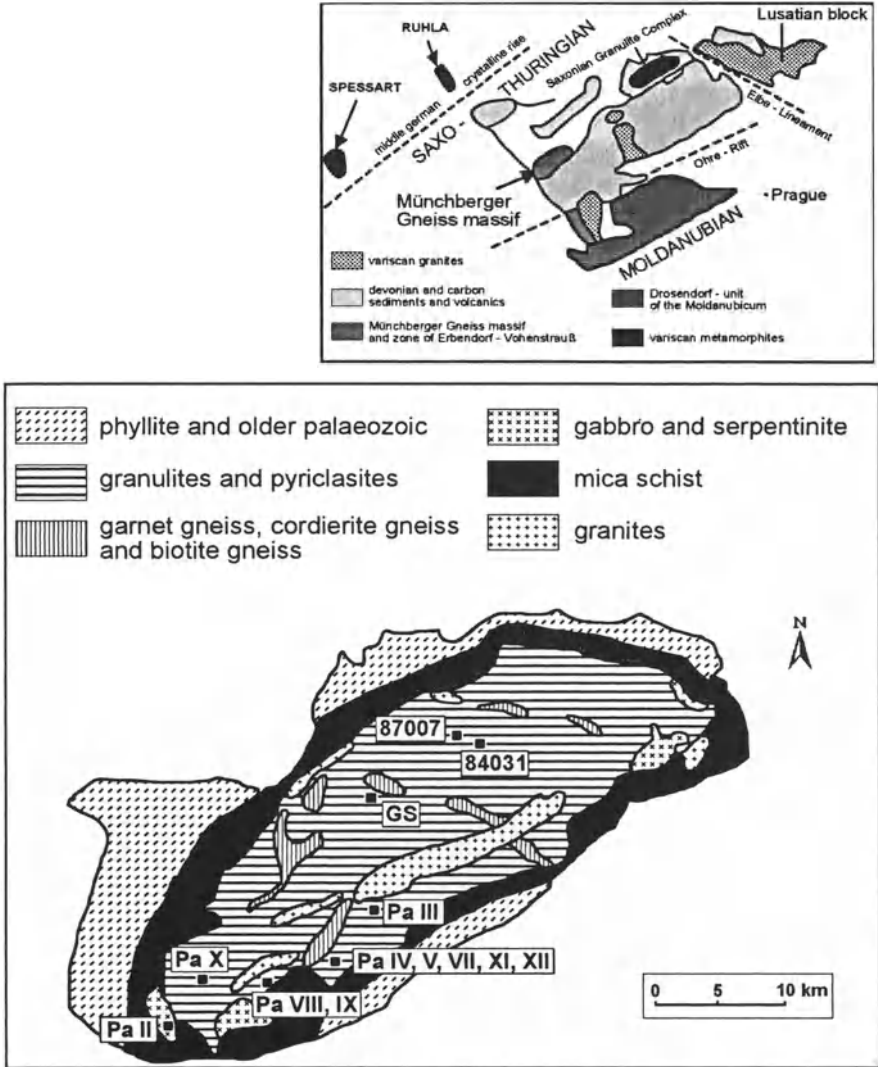


Fig. 8. Geological sketch of the Saxonian Granulite Complex (SGC) with regional geological setting and sample locations. (Modified after von Quadt 1993)

ages around 340 Ma (von Quadt 1993; Kröner et al. 1994; Baumann et al. 1996; Nasdala et al. 1996a), but an older inherited component (around 411–485 Ma) has also been identified (Gorokhov et al. 1987; Wenzel et al. 1990; von Quadt 1993; Kröner et al. 1994; Baumann et al. 1996; Nasdala et al. 1996a).

Other rock types of the SGC gave the same zircon age, around 340 Ma. Baumann et al. (1996) reported 320–365 Ma for cordierite gneisses (single-grain evaporation), and von Quadt (1993) found an age of 338 Ma for a garnet pyrox-

enite from Klatschmühle (U-Pb multi-grain analysis). Even the SGC granites show identical Carboniferous zircon ages: (1) 338 Ma for the foliated Berbersdorf granite was reported by von Quadt (1993; multi-grain analysis, data points plot near the upper intercept); (2) Kröner et al. (1994) found 333 Ma for the foliated granite from Wolkenburg by single-grain evaporation; and (3) 351 Ma for the Mittweida granite was calculated by Baumann et al. (1996) based on multi-grain analyses (data points plot near the upper intercept), whereas Nasdala et al. (1996a, 1997) measured 333 Ma (SHRIMP U-Pb dating). For the Mittweida granite, additional older ages (up to 470 Ma) were found by single-grain evaporation (Baumann et al. 1996).

Zircons from twelve samples of leucogranulites, pyroxene-bearing granulites and mafic granulites were investigated in the present study (locations are shown in Fig. 8). Leucogranulites from Knaumühle (Pa VIII), Kaufungen (Pa X) and Zschautz (87007) are foliated, white-grayish rocks consisting mostly of feldspar and quartz with visible red garnet and a very low content of mafic minerals. The leucogranulite from Taura (Pa III) is reddish due to the color of the K-feldspar. Pyroxene-bearing granulites from Hartmannsdorf (Pa IV, V, XI and XII) and Großstädten are grayish and contain high quantities of hypersthene and augite. The pyroxene granulite from Erlau (84031) is an orthopyroxene granulite (only with hypersthene). Mafic granulites from Hartmannsdorf (Pa VII) and Knaumühle (Pa IX) are dark colored rocks mainly consisting of pyroxene, garnet, and basic plagioclase.

The syenite granulite sample from Kiefernberg (Pa II) is from a xenolithic block within pyroxenite rocks. The specimen is yellowish-grayish and massive without visible foliation. Chemical analyses of the samples are presented in Table 1.

4.2 Zircon Morphology

Accessory zircons were separated from 10 kg of each rock sample. Some 30–40 zircon grains per sample were included in morphology investigations using an SEM.

The shapes and degrees of rounding of the zircon grains vary over a large range, from euhedral to anhedral (Figs. 9, 10). Idiomorphic grains, crystals with rounded edges, and spherically shaped zircons were found in every sample. Aggregates apparently consisting of several zircon grains are remarkably common (Fig. 10a; about 20–50% of the zircons from the samples described in the present study). Normally, the content of zircon aggregates in the zircon fractions from magmatic and metamorphic rocks is significantly lower. These aggregates may be interpreted as polycrystalline intergrowths or as a result of crushing of elongated zircon grains during shearing of the rocks.

It is difficult to quantify abundances of idiomorphic and rounded zircon crystals because all transitions between well-idiomorphic and spherical-shaped grains are observed. The shapes of idiomorphic zircons vary from short and prismatic to elongated (Fig. 9a,b). The more spherical zircon grains have more rounded edges (Fig. 9c,d). In addition, a conspicuous thinning of the central part of the

Table 1. Chemical composition of granulites from the SGC (compounds, wt%; elements, ppm)

Sample Rock type Location	Pa II Syenite Kieferberg	Pa III Leuco- granulite Taura	Pa IV Pyroxene granulite Hartmanns- dorf	Pa V Pyroxene granulite Hartmanns- dorf	Pa VII Pyriclasite Hartmanns- dorf	Pa VIII Leuco- granulite Knaumühle	Pa IX Pyriclasite Knaumühle	Pa X Leuco- granulite Kaufungen	Pa XI Pyroxene- granulite Hartmanns- dorf	Pa XII Pyroxene- granulite Hartmanns- dorf
SiO ₂	56.90	73.90	66.50	73.10	68.80	69.90	70.2	70.50	54.20	58.80
TiO ₂	1.97	0.23	1.23	0.30	1.12	0.62	1.05	1.25	3.00	2.57
Al ₂ O ₃	16.56	14.14	15.04	14.02	15.54	15.80	14.53	15.04	16.82	15.19
Fe ₂ O ₃ ^a	1.40	2.00	3.79	2.00	2.60	2.40	2.6	1.60	9.78	8.78
MgO	4.58	0.12	0.89	0.17	0.75	0.54	0.7	0.51	5.32	4.71
CaO	2.03	0.77	2.27	0.77	1.82	1.64	2.03	1.64	6.50	6.12
Na ₂ O	1.21	3.75	4.12	3.20	3.74	3.98	3.62	4.01	3.59	3.37
K ₂ O	9.97	4.95	3.56	5.12	3.60	3.89	4.02	4.11	0.70	0.84
P ₂ O ₅	0.31	0.02	0.19	0.07	0.07	0.03	0.1	0.03	0.08	0.05
H ₂ O ⁺	0.41	0.17	0.14	0.17	0.12	0.30	0.1	0.22	0.20	0.15
L.O.I.	2.11	0.02	0.47	0.05	0.25	0.21	0.16	0.09	n.d.	n.d.
Total	97.45	100.07	98.29	98.87	98.41	99.31	99.13	99.00	100.19	100.58
Ba	5811.0	210.0	532.0	193.0	559.0	504.0	380	518.0	<80	353.0
Rb	158.0	191.0	83.0	165.0	83.0	71.0	84	99.0	19.0	16.0
Sr	838.0	25.0	102.0	28.0	68.0	92.0	75	78.0	95.0	77.0
Pb	62.4	5.5	3.8	9.3	9.0	7.0	28.6	14.7	<2.4	6.8
Nb	54.4	6.9	5.3	8.0	9.4	5.4	7.1	8.7	22.6	17.6
Zr	728.0	84.0	90.8	106.0	62.9	17.9	30.1	28.2	93.8	89.6
V	22.8	<2.4	49.8	4.7	49.3	33.9	34.2	43.1	178.0	175.0
Cr	41.0	n.d.	26.5	78.7	33.2	23.3	75.9	30.3	184.0	198.0
Ni	40.9	4.2	25.0	4.8	17.4	12.8	14.4	9.5	177.0	157.0
Co	41.0	n.d.	9.3	<3.0	8.8	5.9	6.3	5.0	37.0	34.3
Cu	9.4	15.1	33.0	7.5	14.5	19.8	23	14.5	61.2	66.4
Mn	280.0	616.0	422.0	204.0	368.0	372.0	293	441.0	1175.0	1160.0

L.O.I., loss of ignition; n.d., not detectable; major compounds detected by chemical weight analysis; trace elements detected by optical emission spectroscopy (OES).

^aFe₂O₃: total content of iron oxides.

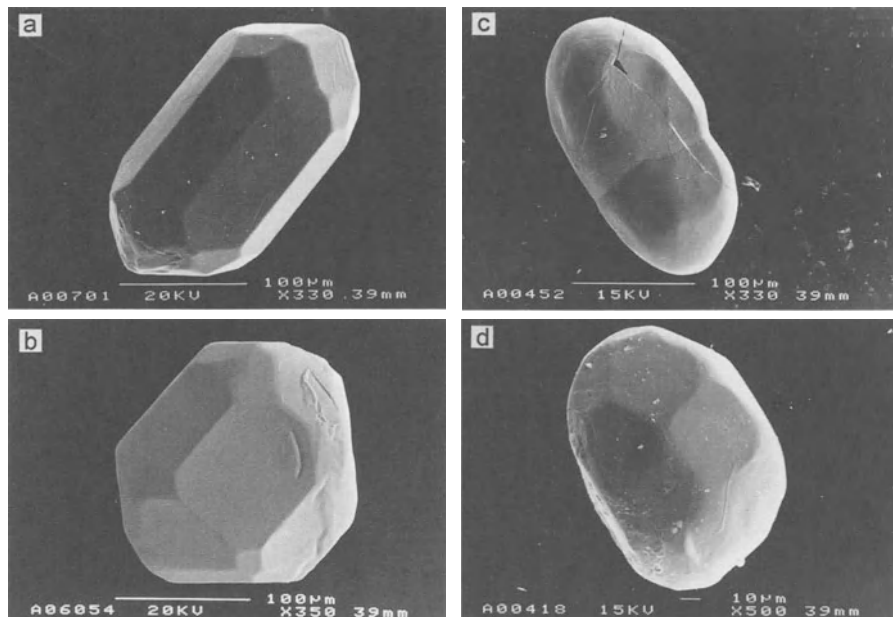


Fig. 9a–d. Morphology of zircons from the SGC. **a** Elongated idiomorphic crystal (pyroxene granulite from Großstädten, sample GS); **b** equant idiomorphic crystal (leucogranulite from Großstädten, sample GS); **c** rounded elongated crystal with thinning at the central part (leucogranulite from Kaufungen, sample Pa X); **d** rounded equant crystal (leucogranulite from Taura, sample Pa III). SE images

crystal (i.e. near the middle of the prism faces) is occasionally observed on elongated crystals (Fig. 9c). In the case of equant grains with spherical shape, it is difficult to recognize relics of crystal faces and edges (Fig. 10b).

Some general correlations between crystal shape and tectonics are recognized. As found by Kroner (1995), the shearing of the SGC is more intensive in the southeastern part. This trend correlates with the proportions between idiomorphic crystals and rounded grains plus aggregates in the granulite samples. About one third of the grains from the granulites from Kaufungen (Pa X), Zschauitz (87007), Erlau (84031), and Taura (Pa III) were found to be more or less idiomorphic in shape, whereas samples from Hartmannsdorf (Pa IV, V, VII and XI) and Knaumühle contain less than 25–20% idiomorphic zircons. Exceptions are the pyroxene granulite Pa XII from Hartmannsdorf, with about 50% equant and more or less idiomorphic crystals, and the syenite granulite Pa II from Kiefernberg where – in accordance with the massive texture of the rock – aggregates and rounded crystals as well as rounded edges were not found at all (Fig. 10c,d).

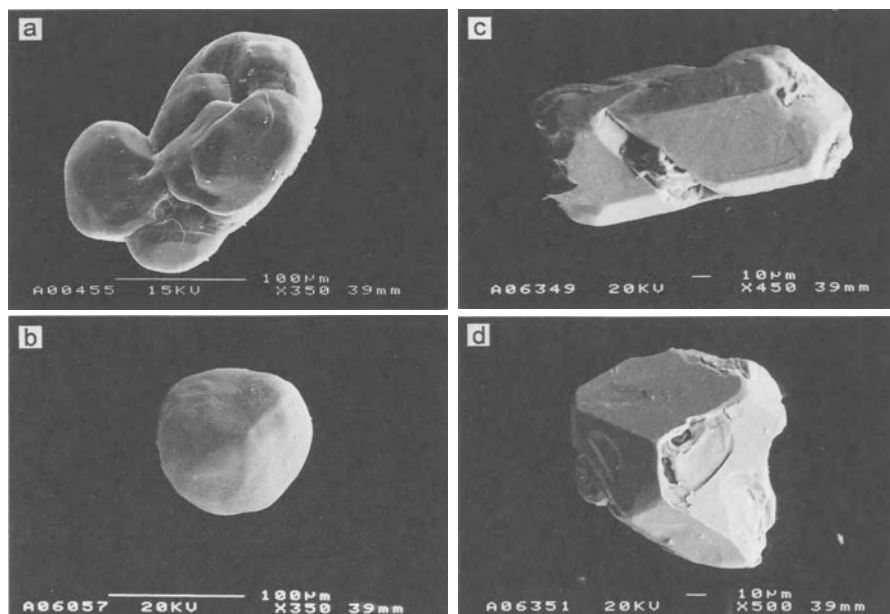


Fig. 10a–d. Morphology of zircons from the SGC. a Zircon aggregate (leucogranulite from Kaufungen, sample Pa X); b spherically shaped zircon (pyroxene granulite from Großstädten, sample GS); c idiomorphically elongated and d equant zircon crystals from the syenite granulite occurring at Kiefenberg (sample Pa II). SE images

4.3 Back Scattered Electron and Panchromatic Cathodoluminescence Imaging of the Internal Structure of Zircons

From the twelve rock samples investigated, 10–40 zircon grains each were separated. Polished microprobe mounts were prepared using epoxy epo-tek 301. The internal structures of the zircons were investigated by means of BSE and CL techniques (see Chap. 3).

As can be seen in Figs. 11 and 12, internal structures of zircons from the SGC vary considerably (see also Fig. 1a,; Fig. 4a,b as well as Figs. 7, 14, 16). Growth and sectoral zoning, highly luminescent cores in weakly luminescent rims (homogeneous or zoned), and vice versa, and three-dimensional effects were observed. No indications for metamorphic overgrowths were found. Thermal recrystallization developed in cores (Fig. 1a,b), rims (Figs. 7a,b, 16a,b,d), sectors, and along growth zones (Fig. 11a) is a principal feature of zircons from the SGC. Thermal recrystallization alters primary internal structures (as shown in Fig. 11), up to almost homogeneous patterns in spherically shaped crystals. However, there is no simple correlation between the morphology of the grains and their internal structures. BSE and CL imaging support the conclusion that rounding of elongated crystals and the occurrence of zircon aggregates are caused by crushing of long-prismat-

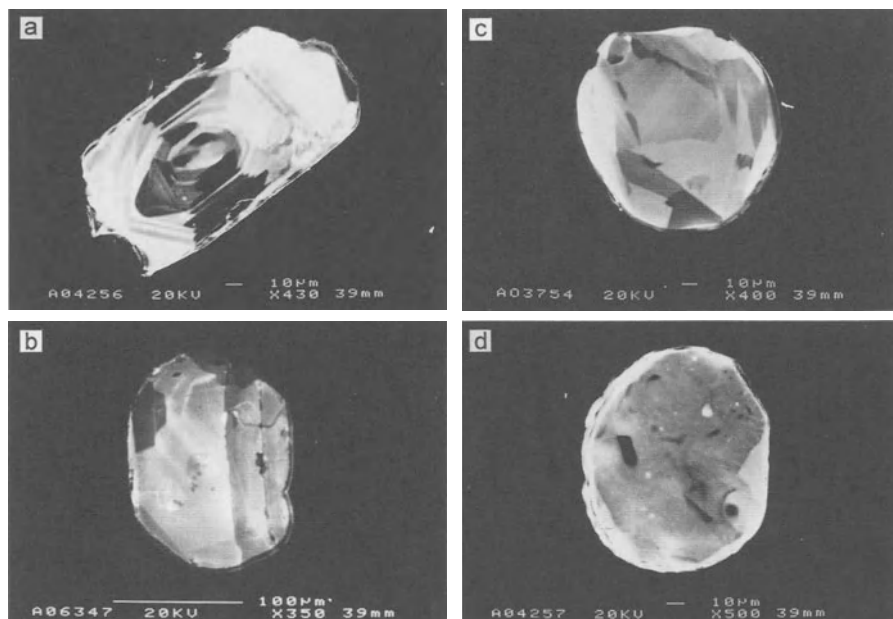


Fig. 11a–d. Internal structure of zircons from the SGC. Transition from oscillatory and sector zoned crystal fragments (a) to homogenized rounded grains (d). Thermal recrystallization starts from defect-rich sectors feeding into other parts along oscillatory zoning (a; mafic granulite from Hartmannsdorf, sample Pa VII). Thermal recrystallization leads to deletion of primary zoning (b; leucogranulite from Taura, sample Pa III). Recrystallization along primary zoning forms fir-tree structures (c; leucogranulite from Kaufungen, sample Pa X). In some cases, the internal structure is nearly homogeneous (d; mafic granulite from Hartmannsdorf, sample Pa VII). Note that the dark areas also consist of (very weakly luminescent) zircon. CL images

ic grains (Fig. 12). In Fig. 12c,d, an aggregate resulting from the deformation of the rim is shown. The internal structure of the core also documents strong deformations.

Although characteristics of zircons may vary appreciably, some features are generally found on zircons from a certain sample. For instance, equant and prismatic grains showing primary growth zoning without detrital cores prevail in the leucogranulite from Taura (Pa III). Rounded grains with varying degrees of thermal recrystallization appear to be fragments of larger crystals (e.g., Figs. 11b, 12b, 16d). Elongated grains are also characterized by recrystallized growth zoning (Figs. 4b, 12a).

Some typical internal structures were also found on zircons from the leucogranulite from Kaufungen (Pa X). Extremely weakly luminescent cores and highly luminescent rims (the latter occasionally being remarkably thin down to a few microns) are quite often present in equant grains (Figs. 14a, 16a,b). Another typical feature is sector zoning detected in the luminescent rims. Long and prismatic crystals are not common in the Kaufungen granulite.

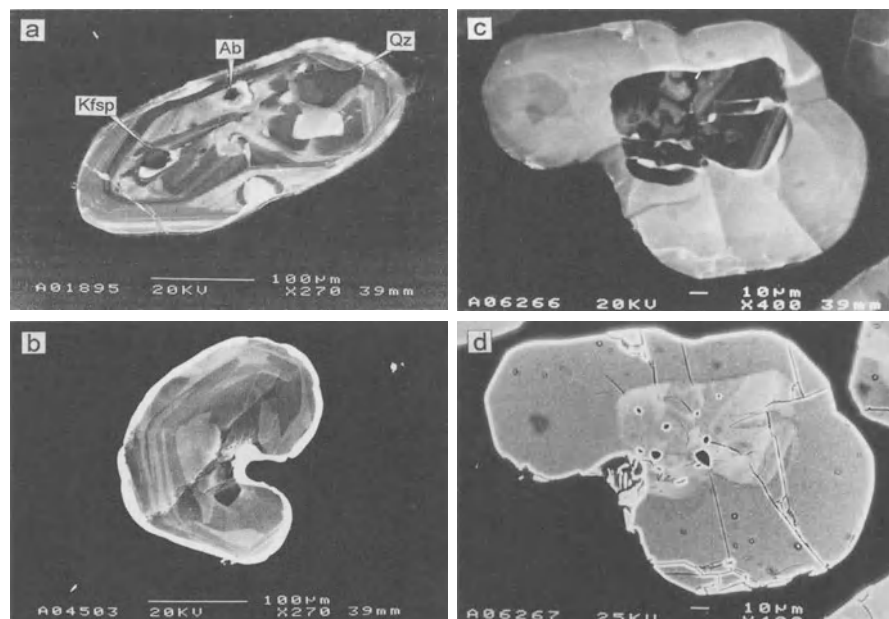


Fig. 12a–d. Internal structures of zircons from the SGC. **a** Primary oscillatory zoning in an elongated crystal is partly destroyed by recrystallization; **b** strongly deformed and partly recrystallized grain (both zircons from the leucogranulite from Taura, sample Pa III, CL images). Internal structure of a zircon aggregate revealed by CL (**c**) and BSE (**d**) images documents strong deformation of the rim and the core (leucogranulite from Erlau, sample 84031). *Kfsp* K-feldspar; *Ab* albite; *Qz* quartz

However, we would like to point out that the described general features do preferentially but not always occur. Zircons with differing characteristics are also found in each sample (see, e.g., Fig. 11c for the leucogranulite from Kaufungen).

4.4 Spectral Cathodoluminescence, Electron Probe and Raman Investigations

A few CL spectra were taken from one or two typical grains each from five samples of leucogranulites, pyroxene granulites and pyriclasites (locations Taura, Knaumühle, Kaufungen, Hartmannsdorf, and Erlau). We found some concurring spectral characteristics in each of the spectra: The total CL intensity is dominated by emission of the yellow center, and additional weak line groups assigned to Dy^{3+} were obtained (see Sect. 3.3). An exception is bluish luminescent cores, which were exclusively observed in some zircons from the orthopyroxene granulite from Erlau. An unusual phosphorescence was observed on a highly recrystallized zircon from the pyroxene granulite Pa IV (Hartmannsdorf) with an extremely low U content of about 10 ppm.

Electron probe analyses (142 spots on 33 zircons from five samples) revealed the overall low trace element content in the granulite zircons. As stated above, P and Y concentrations were only in a few cases found to be higher than the detection limits. In these cases, a positive correlation between these two elements (suggesting the xenotime-type substitution $Zr^{4+} + Si^{4+} \leftrightarrow Y^{3+}$, $REE^{3+} + P^{5+}$) is observed (Fig. 6).

Some indications concerning the precursors of the granulitic rocks may be derived from the Hf distribution. As can be seen in Fig. 13, the Hf content shows a normal distribution, with an average HfO_2 value of about 1.6 wt%. This result lies within the range typical of zircons from most magmatic (and metamorphic) rocks. The zircons from the leucogranulite from Taura (Pa III) are clearly more enriched in Hf, with an HfO_2 average of about 3.0 wt%. This is probably caused by Zr/Hf fractionation occurring in pegmatites and evolved granites (Kempe et al. 1997).

Raman microprobe analyses were done on a few zircon grains from selected samples (Pa III, Pa IV, Pa VIII, and Pa X). The results support the assumption that the total luminescence intensity (i.e., emission from the yellow center) correlates well with the degree of crystallinity (Fig. 14). For example, very weakly luminescent cores in zircons from the leucogranulite Kaufungen (Pa X) were found to be metamict whereas highly luminescent patches in the elongated zircon from Taura (Pa III, Fig. 14b) correspond to very well-crystallized areas (see Nasdala et al. 1996b).

4.5 SHRIMP Ion Probe Measurements

SHRIMP analyses were carried out on selected grains (one to five point analyses per grain) from the samples Pa III (Taura) and Pa X (Kaufungen). Spot positions were chosen in accordance with the internal structures revealed by BSE/CL imag-

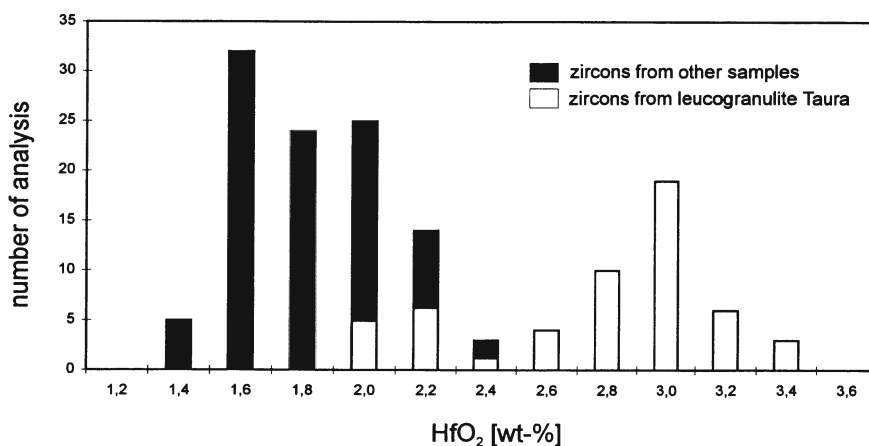


Fig. 13. Distribution diagram for the HfO_2 content in zircons from SGC granulites (WDX analyses). Note the distinct distribution for the data obtained from sample Pa III, (leucogranulite from Taura)

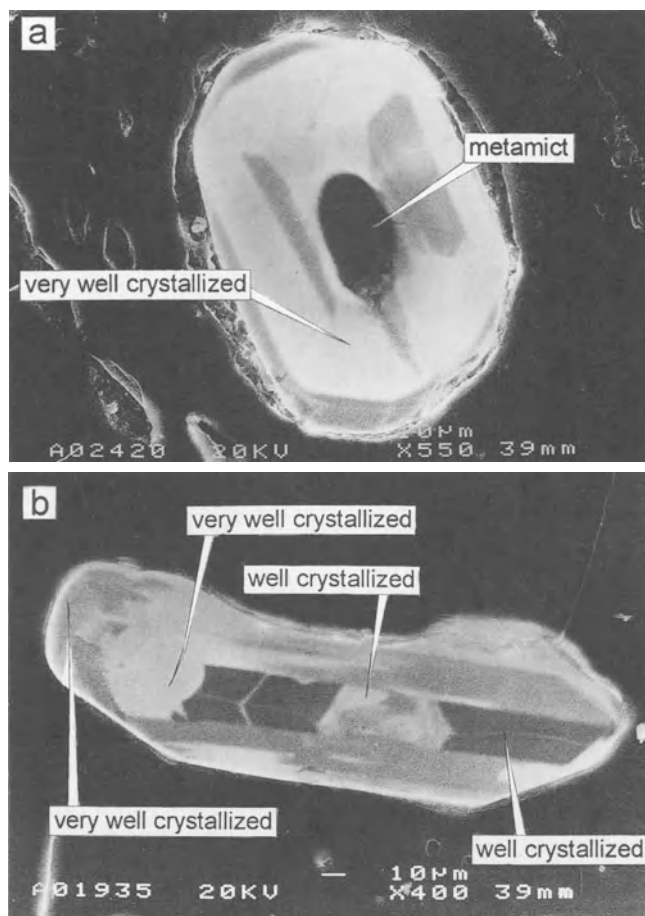


Fig. 14a,b. Examples for possible relationships between the degree of crystallinity obtained by Raman microprobe measurements and structures imaged by CL. **a** Zircon from leucogranulite from Kaufungen, sample Pa X; **b** zircon from leucogranulite from Taura, sample Pa III, also shown in Figs. 3 and 4

ing, performed in order to check the identified detrital cores of different types in comparison with the “common” zircons. Another aim of the ion probe investigations was to examine possible relations between the internal structures of the zircons and the degree of disturbance of their U-Pb isotope systems. Results are shown in Table 2 and in Figs. 15 and 16.

As demonstrated in Fig. 15 (comparison of “apparent SHRIMP ages” with data obtained by Baumann et al. 1996 using the single-grain evaporation technique), our data confirm results reported by other authors. Most of the calculated ages cluster around 340 Ma, and some older ages around 450 Ma are also detected. As reported elsewhere, there is evidence for inherited zircons with ages greater than 1200 Ma (Nasdala et al. 1996a).

Table 2. SHRIMP data from selected SGC zircons

Sample	U [ppm]	Th [ppm]	U/Th	$^{206}\text{Pb}/^{238}\text{U}$	$^{207}\text{Pb}/^{235}\text{U}$	$^{207}\text{Pb}/^{206}\text{Pb}$	$^{206}\text{Pb}/^{238}\text{U}$ age	
Leucogranulite Taura	Pa III Z1a	365	65	5.6	0.05197±0.00059	0.43916±0.02330	0.06128±0.00309	326±4
	Pa III Z1b	313	52	6.0	0.05311±0.00062	0.41795±0.03074	0.05707±0.00406	333±4
	Pa III Z1c	480	76	6.3	0.04917±0.00056	0.40891±0.02260	0.06031±0.00317	309±4
	Pa III Z1d	478	74	6.5	0.05254±0.00059	0.38518±0.02229	0.05316±0.00294	330±4
	Pa III Z1e	477	76	6.3	0.05147±0.00057	0.40374±0.01943	0.05688±0.00258	323±4
	Pa III Z2a	71	10	7.1	0.05426±0.00101	0.56053±0.11326	0.07492±0.01489	343±6
	Pa III Z2b	130	28	4.6	0.05397±0.00074	0.46459±0.06324	0.06343±0.00834	339±5
	Pa III Z2c	76	10	7.6	0.05473±0.00101	0.47928±0.11252	0.06350±0.01471	344±6
	Pa III Z2d	82	16	5.1	0.05348±0.00098	0.43221±0.10830	0.05861±0.01451	335±6
	Pa III Z2e	69	10	6.9	0.05206±0.00112	0.29799±0.13115	0.04151±0.01813	327±7
	Pa X Z1a	109	61	1.8	0.05384±0.00118	0.42708±0.12882	0.05750±0.01718	338±7
	Pa X Z1b	81	69	1.2	0.05325±0.00159	0.37670±0.19864	0.05129±0.02680	335±10
	Pa X Z1c	1219	61	20.0	0.07357±0.00099	0.56774±0.01048	0.05596±0.00061	458±6
	Pa X Z1d	1184	58	20.4	0.07202±0.00097	0.56316±0.01036	0.05671±0.00061	448±6
Leucogranulite Kaufungen	Pa X Z1f	1099	55	20.0	0.06893±0.00093	0.53048±0.00969	0.05585±0.00056	430±6
	Pa X Z1e	1267	65	19.5	0.07218±0.00097	0.56019±0.01063	0.05628±0.00066	449±6
	Pa X Z2a	374	36	10.4	0.05009±0.00068	0.37643±0.01597	0.05455±0.00208	315±4
	Pa X Z2b	429	55.0	7.8	0.05817±0.00079	0.43939±0.02045	0.05481±0.00235	364±6
	Pa X Z2c	198	105	1.9	0.07374±0.00101	0.57450±0.02950	0.05673±0.00256	457±6
	Pa X Z3a	423	33	12.8	0.04997±0.00069	0.35549±0.02002	0.05159±0.00273	314±4
	Pa X 1/1a	112	104	1.1	0.05251±0.00244	0.38994±0.06641	0.05384±0.00851	330±15
	Pa X 1/1b	108	100	1.1	0.05176±0.00243	0.33530±0.08246	0.04698±0.01106	325±15
	Pa X 1/1c	116	109	1.1	0.05268±0.00247	0.37616±0.08072	0.05178±0.01054	331±15
	Pa X 1/1d	1342	177	7.6	0.05039±0.00230	0.37200±0.02165	0.05353±0.00164	317±14
	Pa X 1/1e	1619	217	7.5	0.05707±0.00260	0.43586±0.02163	0.05538±0.00080	357±16

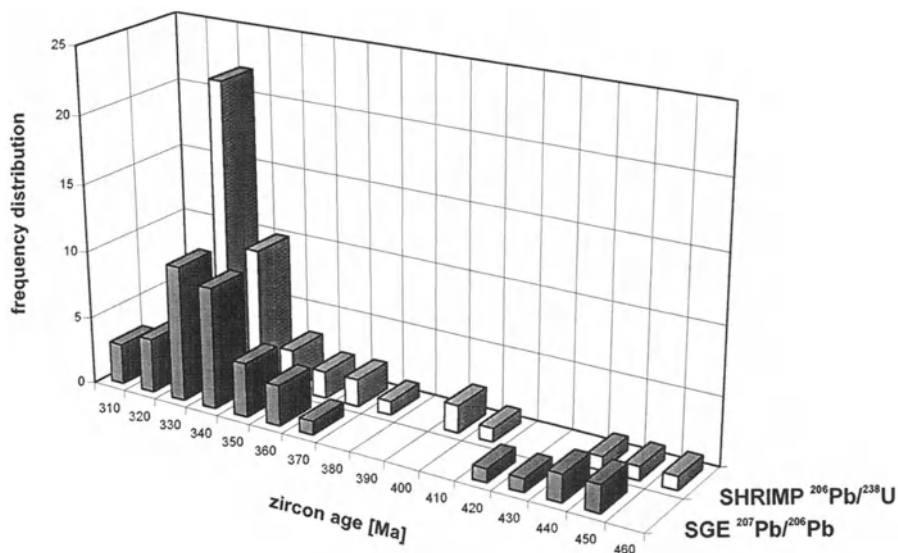


Fig. 15. Comparison of $^{206}\text{Pb}/^{238}\text{U}$ ages calculated from single SHRIMP analyses (this study) with $^{207}\text{Pb}/^{206}\text{Pb}$ ages from single grain evaporation reported by Baumann et al. (1996)

Ages of about 340 Ma were obtained from crystals without inherited cores or in rims independently of the internal structures (including degree of recrystallization revealed by CL) of the analyzed areas (see Fig. 16 and results for the zircon from Taura shown in Fig. 11b). The latter was analyzed in five spots placed in the zoned and recrystallized areas).

The ages around 450 Ma were found in detrital cores that do not show radial cracks (as in the case of the zircon from Kaufungen, Pa X, shown in Fig. 16a). Again, the age does not depend on the internal structure of the analyzed cores. (Note that the central part of the zircon in Fig. 16d is not a detrital core and the bright luminescent rim is formed by thermal recrystallization).

The extent of the spot analyzed by the ion probe may be checked by SEM investigation (Fig. 17). Analysis pits from measurements set in brightly luminescent, well-crystallized areas with low trace element contents show smooth walls and bottoms (Fig. 17b). In contrast, tiny holes were found at the bottom of pits in areas that are rich in trace elements (Fig. 17a). As an additional feature, patterns of parallel cracks within and around such pits were found in some cases (Fig. 17a). These surface features are similar to structures detected in evaporated zircon grains and may be assigned to the local heating of the zircon lattice under the ion beam during analysis. Holes and cracks provide diffusion of material from deeper and unstable domains into the area of sputtering. The structures visible after irradiation by the ion probe may perhaps indicate zonal metamictization of the zircon investigated.

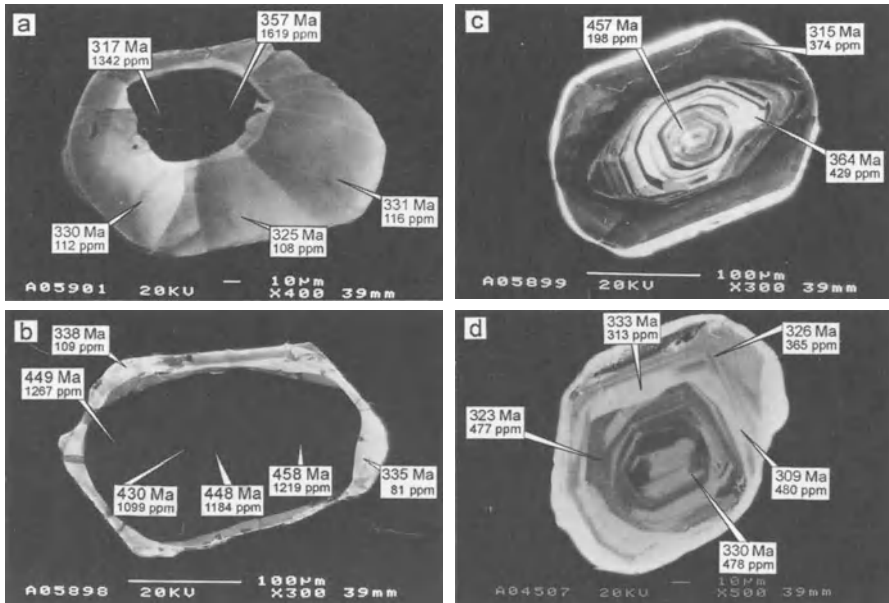


Fig. 16a–d. Relation between $^{206}\text{Pb}/^{238}\text{U}$ ages (*top*), U content (*bottom*) from SHRIMP analyses and internal zircon structures revealed by CL for some zircons with metamict (a,b), primary zoned (c) and apparent (d) cores. The cores from the first three zircons from sample Pa X (leucogranulite from Kaufungen) may yield an age around 450 Ma (b,c) independent of their internal structures, provided that they are “closed” systems (which is not the case for a). The apparent “core” for the zircon (d) from the leucogranulite Taura (sample Pa III) is formed by inhomogeneous recrystallization (only the rim was recrystallized). The 364 Ma age in (c) is a mixed age: Zircon from both the core and the rim were analyzed here. CL from the oscillatory zoned core in this part is generated from areas not exposed at the polished surface

4.6 Interpretation of Morphology, Internal Structures and Isotope Data

We interpret variations of the zircon morphology as a result of foliation of the rocks caused by intensive shearing during uplift of the SGC, but not as a result of “granulitic” (i.e. metamorphic) growth. Equant crystals were rounded whereas elongated crystals were deformed and crushed with formation of aggregates or subsequent rounding of the fragments. Thus, it is possible to explain the high content of zircon aggregates and the occurrence of both idiomorphic and rounded grains in one and the same rock sample. Our inference is in accordance with the interpretation of zircon morphology for rocks from the Belomor complex by Zinger et al. (1996) and is supported by the observation of widely idiomorphic crystals in weakly deformed granulites from southwestern Norway (Bingen et al. 1996). In other words, spherically shaped zircons are not typical of “granulitic growth” but represent intensive foliation of metamorphic rocks caused by deformation processes. If this hypothesis is true, we may conclude from our results that

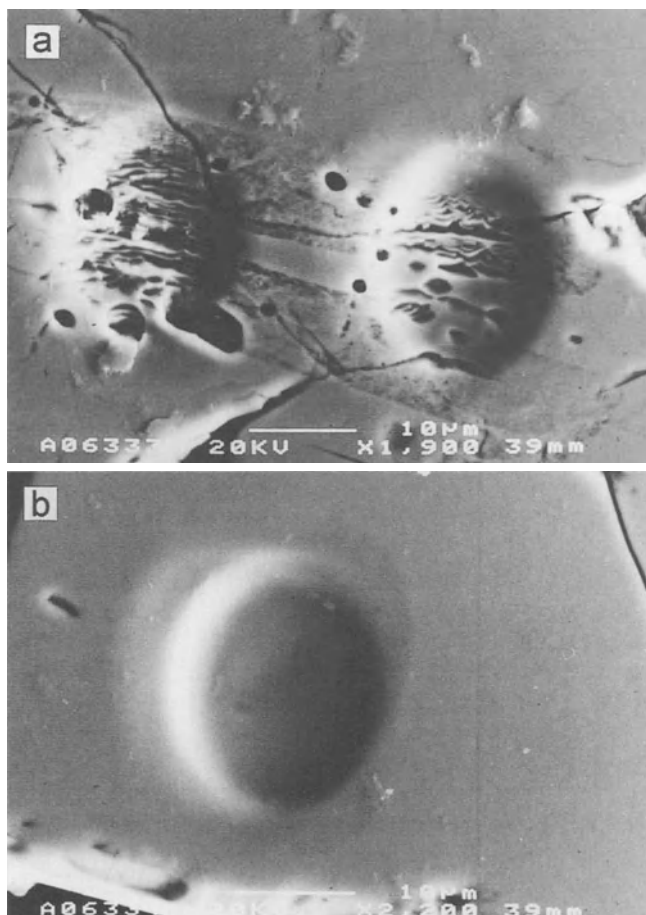


Fig. 17a,b. SE images of SHRIMP analysis pits in zircon grains from the SGC (sample Pa X). The spots in **a** were set in an area with more than 1000 ppm U whereas the area around the spot in **b** contains less than 150 ppm U

mafic granulite protoliths must have contained mainly short-prismatic zircons whereas elongated and prismatic crystals prevailed in the precursor rocks of the leuco- and pyroxene granulites.

Our conclusions are supported by results obtained using CL and BSE imaging of the internal zircon structures along with chemical and structural data. The assumed rounding and crushing of the crystals is accompanied by thermal recrystallization in defect-rich areas. The resulting more homogeneous cores, rims, and patches can be recognized as brightly luminescent domains. They generally contain low trace element concentrations. The occurrence of rounded and homogeneous rims is, therefore, interpreted as a result of recrystallization. Consequently, these rims are not metamorphic overgrowths, as was assumed by Hoppe (1966), Hanchar and Miller (1993), and Vavra et al. (1996). If zircon growth

during regional metamorphism occurred, newly formed rims would be a general feature for the majority of zircon grains from metamorphic rocks, as reported by Hanchar and Rudnick (1995) for lower crustal granulite xenoliths.

Relationships between U-Pb ages, internal structures, total CL intensity, and U content are compiled in Fig. 18. Detailed interpretation of the internal structures of the granulite zircons allows us to discuss critically the meaningfulness of U-Pb and other isotopic data.

According to Kroner (1995), two distinct events have taken place in the tectonic development of the SGC: (1) granulite facies regional metamorphism, and (2) uplift of the complex with intensive shearing of the rocks and metasomatic alteration. We assume that the latter event corresponds to age determinations around 340 Ma. The presence of a fluid phase (stimulating distortion and/or resetting of K-Ar, Rb-Sr, Sm-Nd and U-Pb isotope systems) may be indicated by the local occurrence of synkinematic polymetallic and scheelite-bearing mineralization and by alteration (biotitization and serpentinization) of the respective rocks. Clear indications for the synkinematic age are concurring K-Ar ages for secondary biotite and U-Pb data for the syn- and postkinematic granites of the SGC. According to the reported P-T paths with temperatures greater than 600°C (Rötzler 1992), recrystallization processes in defect-rich zircon grains could possibly have occurred.

Our conclusions are in good agreement with interpretations based on regional and local geological data (Rötzler 1992, Franke 1993) and contradict the age

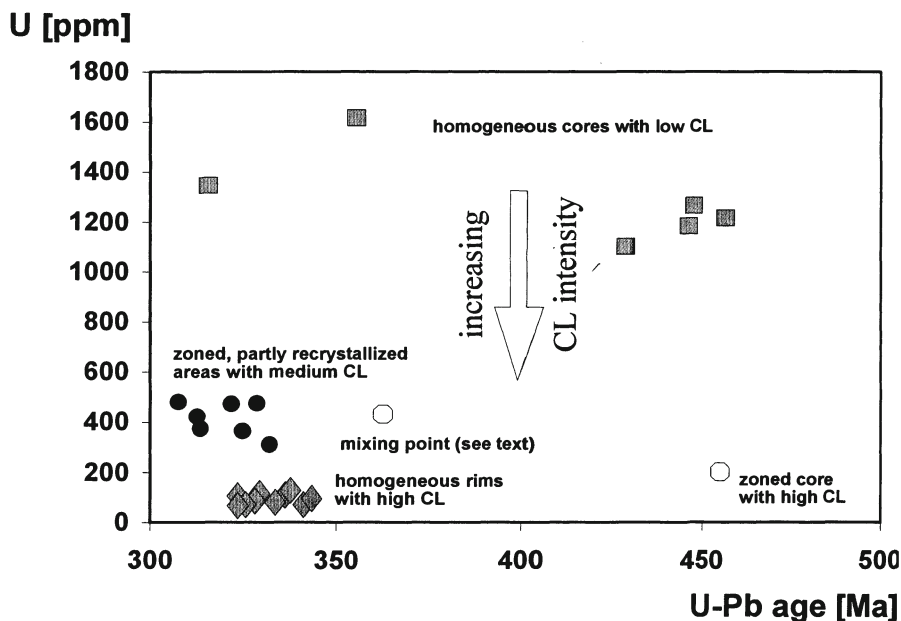


Fig. 18. Compilation of relationships between calculated $^{206}\text{Pb}/^{238}\text{U}$ ages and U concentrations from SHRIMP analyses, internal structures and CL intensities for zircons from the SGC (samples Pa III and X)

interpretation presented by von Quadt (1993). It is interesting to note that thermal recrystallization influences the U-Pb system of the zircons more sensitively than the internal structures. Whereas the U-Pb system mostly experienced complete reset, the internal structures are only partly smudged (Figs. 16, 18).

The interpretation of U-Pb and Pb-Pb zircon ages around 450 Ma is more complicated. The fact that these ages are measured in detrital cores independently of their zoned or unzoned internal structures (Figs. 16, 18) suggests a metamorphic event because in this case it appears to be more probable that cores of different history may yield the same age information. We interpret these ages as perhaps representing the granulite facies metamorphism (leading role of static pressure and temperature) which have reset all zircons and most detrital cores (excluding the old core with an age >1000 Ma, probably related to a protholite age). During the following uplift, the cores were not affected to the same extent as the rims by stress and external fluids.

Due to extreme conditions during granulite metamorphism and uplift, it is very difficult to determine the age of the precursor rocks unambiguously. Nevertheless, some information may be derived by systematic checks of U-Pb systems of detrital zircon cores. As stated before, a highly discordant data point measured on a granulitic zircon core pointed to a Precambrian age (Nasdala et al. 1996a).

Interpretation of internal structures of granulite zircons provides some additional information about the nature of the precursor rocks. More uniform characteristics of relics of the primary structures (i.e. growth zoning throughout without detrital cores), observed on zircons from mafic granulites from Hartmannsdorf and from the leucogranulite from Taura, suggest magmatic protoliths of these rocks. For the leucogranulite from Taura, this inference is supported by the distribution of the Hf content in the zircon, yielding relatively high values, around 3 wt% HfO₂.

5 Concluding Remarks

1. Visible CL signals generated in zircon grains under the electron beam are in most cases dominated by band luminescence. Additional spectroscopic investigations are necessary for clearing up the nature of the band luminescence in natural zircons. Separate detection of the Dy³⁺ luminescence superimposed on the band luminescence may provide additional information, since the related centers show a distinct distribution in the lattice.
2. To avoid misinterpretations of internal structures revealed by panchromatic CL imaging, careful checks for possible artefacts (phase boundaries, small holes, etc.) must be done using SE and BSE imaging. In the case of transparent crystals, possible three-dimensional images have to be taken into consideration. Lateral variations of the CL intensity may be caused by local quenching of the luminescent centers as well as by changes of the spectral characteristics of the luminescence.
3. Primary zircon growth with growth and sectoral zoning may occur not only during magmatic but also during metasomatic processes. Strong growth zon-

- ing corresponding to large variations of trace element (Hf, U, Th, Y, Yb, and P) content is in some cases related to the behavior of the U-Pb isotope system.
4. Defect-rich areas may provide thermal recrystallization leading to the generation of brightly luminescent cores, rims, and patches with well-crystallized lattices and low trace element content. Therefore, homogeneous and brightly luminescent rims are in most cases not regarded as metamorphic overgrowths.
 5. Another phenomenon obtained on some zircon grains is metasomatic recrystallization spreading from the rim to the core of the grains. Metasomatically altered zircons are characterized by low CL and BSE contrast and enhanced Fe and Ca concentrations.
 6. The U-Pb isotope system may be more sensitive to secondary processes than often assumed. A more or less continuous Pb loss from metamict, trace element-rich zones formed during primary growth may occur. Metasomatic recrystallization (Pb loss or U gain), thermally induced recrystallization (episodic Pb loss during regional metamorphism or shearing of the rocks with synkinematic rock alteration), and other geological events may also influence the U-Pb system.
 7. The interpretation of zircon morphology and internal structures of zircons from granulitic rocks from the SGC leads us to the following conclusion: Spherical shapes of zircon grains and the occurrence of zircon aggregates together with idiomorphic crystals in one and the same sample are a result of rounding and crushing of the zircons caused by intensive shearing of the rocks during uplift, and not, as often assumed, of zircon growth during granulitization.
 8. Based on the inferences above, and considering the results of SHRIMP analyses, an age of around 340 Ma (which has been measured by many authors using different methods of isotope dating on different rock types from the SGC) are assigned to the uplift of the complex. This interpretation is in good agreement with local and regional geological evidence.
 9. An age of about 450 Ma, found on some zircons by single-grain evaporation and SHRIMP analysis, is believed to represent the granulitic event.
 10. The assumption of a complete reset of the U-Pb system during intensive metamorphic deformation solves apparent contradictions observed by dating of metamorphic rocks.
 11. Reliable interpretation of U-Pb zircon ages requires not only consideration of geological and petrologic data but has to be accompanied by detailed mineralogical investigations, especially of morphology and internal structures of the dated zircons.
 12. The precision and accuracy of U-Pb zircon ages are not only limited by analytical precision. Calculated "ages" may scatter around the real age of the event by a considerably larger extent than analytical errors and, therefore, must be checked by additional studies.

Acknowledgements. It is a pleasure to thank R.T. Pidgeon, A.K. Kennedy, and A.A. Nemchin for their constructive help with SHRIMP analyses. Furthermore, R.T. Pidgeon kindly made zircon samples from the Jack Hills available for investiga-

tion. We would like to thank D. Rhede, R. Oberhänsli and A. Appelt for supporting electron probe analyses. H. Pache separated zircons and made chemical analyses of the rock samples used in this study. I. Nasdala and A. Obst are thanked for taking SE pictures. M. Gehmlich and L.K. Levsy provided zircon crystals from the porphyroid from Neumühle and from the Belomor complex, respectively. We are grateful to N. Baumann, C.D. Werner, and H.-J. Pilot for fruitful discussions and putting zircon grains from sample GS at our disposal. M. Pagel kindly supported our publication. The text benefited from reviews by J. M. Hanchar and J.M. Bertrand, whose help is gratefully acknowledged. This study was supported by grants of the German Research Council (DFG) and the German Academic Exchange Service (DAAD).

References

- Andsdell KM, Kyser TK (1993) Textural and chemical changes undergone by zircon during the Pb-evaporation technique. *American Mineralogist* 78: 36–41
- Aoki K (1994) Fluorescence spectra of zircons from Italian alpine plutonic rocks. *Bulletin of the Yamagata University (Natural Science)* 13(3): 199–204
- Barabanov VF, Goncharov GN, Zorina ML, Sakharov AN, Sorokin ND, Sukharzhevskij SM (1990) Modern physical methods in geochemistry. Leningrad State University, Leningrad (in Russian)
- Baumann N, Pilot J, Werner CD, Todt W (1996) Datings on minerals as contributions to clearing up the geological history from the Saxonian Granulite Complex. *Journal of Conference Abstracts* 1(1): 50 (abs.)
- Benisek A, Finger F (1993) Factors controlling the development of prism faces in granite zircons: a microprobe study. *Contributions to Mineralogy and Petrology* 114: 441–451
- Bingen B, Demaiffe D, Hertogen J (1996) Redistribution of rare earth elements, thorium, and uranium over accessory minerals in the course of amphibolite to granulite facies metamorphism: The role of apatite and monazite in orthogneisses from southwestern Norway. *Geochimica et Cosmochimica Acta* 60(8): 1341–1354
- Black LP (1987) Recent Pb loss in zircon: a natural or laboratory induced phenomenon? *Chemical Geology (Isotope Geoscience Section)* 65: 25–33
- Black LP, Williams IS, Compston W (1986) Four zircon ages from one rock: the history of a 3930 Ma-old granulite from Mount Sones, Enderby Land, Antarctica. *Contributions to Mineralogy and Petrology* 94: 427–437
- Carpéna J, Gagnol I, Mailhé D, Pupin JP (1987) L'uranium marqueur de la croissance cristalline: mise en évidence par les traces de fission dans les zircons gemmes d'Espaly (Haute-Loire, France) *Bull. Minéral* 110: 459–463
- Cesbron F, Ohnenstetter D, Blanc Ph, Rouer O, Sichere MC (1993) Incorporation de terres rares dans des zircons de synthèse: étude par cathodoluminescence. *C.R. Acad. Sci. Paris* 316 (II): 1231–1238
- Chatagnon B, Galland D, Gloux P, Méary A (1982) L'ion paramagnétique Tm^{2+} dans la fluorite. *Mineralium Deposita* 17: 411–422
- Chatagnon B, Méary A (1982) Nouvelle méthode d'étude des terres rares dans les gisements fluorés basée sur des corrélations RPE – analyse par activation neutronique. *Bulletin du BRGM*, (2), sec. II, No 4, 359–364
- Chemale LT, Steele IM, Vasconcellos MAZ (1996) Zircon zonation: an experimental study using electron probe microanalysis, cathodoluminescence spectroscopy and synchrotron X-ray fluorescence. In: Pagel, M. (ed.) *International conference on cathodoluminescence and related techniques in geosciences and geomaterials*. Nancy, 39–40 (abs.)

- Chernyshev IV, Zhuravlev DZ (1987) Sr-Nd isotope systematics and the age of granulites in the Saxonian massif (exemplified in the Hartmannsdorf region). In: Gerstenberger H (ed.) Contributions to the geology of the Saxonian Granulite Massif (Sächsisches Granulitgebirge). ZFL-Mitteilungen 133: 63-72
- Compston W, Kinny PD, Williams IS, Foster JJ (1986) The age and Pb-loss behavior of zircons from the Isua supracrustal belt as determined by ion microprobe. Earth and Planetary Science Letters 80: 71-81
- Compston W, Williams IS, Meyer C (1984) U-Pb geochronology of zircons from lunar breccia 73217 using a Sensitive High Mass-Resolution Ion Microprobe. Journal of Geophysical Research 89 (suppl.): B525-B534
- Faure G (1986) Principles of isotope geology. Wiley & Sons, New York
- Feofilov PP (1956) Absorption and luminescence of divalent REE in synthetic and natural fluorite. Optika i spektroskopiya 1(8): 992-1001 (in Russian)
- Fielding PE (1970) The distribution of uranium, rare earth, and color centers in a crystal of natural zircon. American Mineralogist 55: 428-440
- Franke W (1993) The Saxonian Granulites: a metamorphic core complex? Geologische Rundschau 82: 505-515
- Gebauer D (1990) Isotopic systems - geochronology of eclogites. In: Carswell DA (ed.) Eclogite facies rocks. Blackie, Glasgow and London: 141-159
- Gebauer D (1996) A P-T-t path for an (ultra?-) high-pressure ultramafic/mafic rock-association and its felsic country-rocks based on SHRIMP-dating of magmatic and metamorphic zircon domains. Example: Alpe Arami (Central Swiss Alps). In: Bsau A, Hart S (eds.) Earth processes: reading the isotopic code. Geophysical Monograph 95. American Geophysical Union, Washington, 307-329
- Gebauer D, Grünenfelder M (1976) U-Pb zircon and Rb-Sr whole-rock dating of low-grade metasediments. Example: Montagne Noire (Southern France). Contributions to Mineralogy and Petrology 59: 13-32
- Goldstein JI, Newbury P, Echlin P, Joy DC, Fiori C, Lifshin E (1981) Scanning electron microscopy and X-ray microanalysis. Plenum Press, New York
- Gorokhov IM, Anderson EB, Melnikov NN, Mitrofanov FP, Kut'yavin EP, Bizunok MB, Rocheva ON (1987) Geochronology of metamorphic rocks of the Sächsische Granulitgebirge (GDR). In: Gerstenberger H (ed.) Contributions to the geology of the Saxonian Granulite Massif (Sächsisches Granulitgebirge). ZFL-Mitteilungen 133: 43-62
- Götze J, Habermann D, Kempe U, Nasdala L, Richter DK (1997) High resolution cathodoluminescence combined with U-Pb geochronology (SHRIMP) of detrital zircons: A case study of the Cretaceous Weferlingen quartz sand (Germany). Gaea heidelbergensis 3, 18th IAS Regional European Meeting of Sedimentology, Heidelberg: 145-146 (abs.)
- Gracheva TV, Bibikova EV, Akhmanova MV (1981) Ascertaining of geochronologic role of metamictization degree of zircon using IR spectroscopy. Geochimiya (2): 274-291 (in Russian)
- Gruner T, Kempe U, Wolf D (1996) Interpretation von integralen SEM-CL Abbildungen granulitischer Zirkone. Berichte der DMG. European Journal of Mineralogy 8(Beiheft1): 83 (abs.)
- Halden NM, Hawthorne FC (1993) The fractal geometry of oscillatory zoning in crystals: Application to zircon. American Mineralogist 78: 1113-1116
- Hall MG, Lloyd GE (1981) The SEM examination of geological samples with a semiconductor back-scattered electron detector. American Mineralogist 66: 362-368
- Hanchar JM, Miller CF (1993) Zircon zonation patterns as revealed by cathodoluminescence and back-scattered electron images: Implications for interpretation of complex crustal histories. Chemical Geology 110: 1-13
- Hanchar JM, Rudnick RL (1995) Revealing hidden structures: The application of cathodoluminescence and back-scattered electron imaging to dating zircons from lower crustal xenoliths. Lithos 36: 289-303
- Hoffman JE, Long JVP (1984) Unusual sector zoning in Lewisian zircons. Mineralogical Magazine 48: 513-517

- Hoppe G (1966) Zirkone aus Granuliten. *Ber. deutsch. Ges. geol. Wiss.* B 11(1): 47–81
- Kempe U, Dandar S, Lehmann J, Goldstein S, Wolf D (1996) Mineralogische Untersuchungen an Nb-Zr-REE-Mineralisationen von Khaldzan Buregte (Mongolischer Altai): Mehrphasige Vererzungen im Dach hybrider Karbonatit-Granit-Intrusionen. *Berichte der DMG, European Journal of Mineralogy* 8 (Beiheft 1): 136 (abs.)
- Kempe U, Gruner T, Renno AD, Wolf D (1997) Hf-rich zircons in rare-metal bearing granites: magmatic or metasomatic origin? In: Papunen H (ed) *Research and exploration – where do they meet?* Balkema, Rotterdam, 643–646
- Kempe U, Sorokin ND (1988) Replacement processes in wolframite. *Doklady Akademii nauk SSSR* 303(1): 203–206 (in Russian)
- Koschek G (1993) Origin and significance of the SEM cathodoluminescence from zircon. *Journal of Microscopy* 171(3): 223–232
- Kosler J, Svojtka M, Jelínek E (1996) U-Pb geochronology of granulite facies rocks: implications from BSE study of zircons. *Journal of Conference Abstracts* 1(1): 326 (abs.)
- Kotov, NV, Maslennikov AV, Levchenkov OA, Bogomolov ES, Yakovleva SZ (1990) Behavior of metamict zircons under high temperature and high pressure: significance for geochronology. *Geochimiya* (4): 619–622
- Kramm U, Chernyshev IV, Grauert B, Kononova VA, Bröcker W (1993) Zircon typology and U-Pb systematics: a case study of zircons from nepheline syenite of the Il'meny Mountains, Ural. *Petrology* 1(5): 536–549
- Krasnobaev AA, Votyakov SL, Krokhalev VYa (1988) Spectroscopy of zircons (properties and geological application). Nauka, Moscow (in Russian)
- Kroner U (1995) Postkollisionale Extension am Nordrand der Böhmisches Masse – Die Exhumierung des Sächsischen Granulitgebirges. *Freiberger Forschungshefte C457*, 1–114
- Kröner A, Jaeckel P, Reischmann T, Kroner U (1994) Further evidence for an early Carboniferous (approx. 340 Ma) age of high-grade metamorphism in the Saxonian Granulite Complex (in prep.)
- McLaren AC, Fitz Gerald JD, Williams IS (1994) The microstructure of zircon and its influence on the age determination from Pb/U isotopic ratios measured by ion microprobe. *Geochimica et Cosmochimica Acta* 58(2): 993–1005
- Lee JKW (1993) Problems and progress in the elucidation of U and Pb transport mechanisms in zircon. In: Boland JN, Fitz Gerald JD (eds) *Defects and processes in the solid state geoscience applications*. Elsevier, Amsterdam, Oxford, New York, 423–446
- Lork A, Koschek G (1991) Einsatz der KL-Technik bei der Beurteilung isotopengeochemisch bestimmter Alter von Zirkonen. *Beiträge zur Elektronenmikroskopischen Direktabbildung von Oberflächen* 24(1): 147–166
- Loth G, Höll R (1996) Cathodoluminescence investigation of the evolution of zircon crystal shapes applied to supplement geochemical studies. *Journal of Conference Abstracts* 1(1): 379 (abs.)
- Marfunin AS (1979) *Spectroscopy, luminescence and radiation centers in minerals*. Springer-Verlag, Berlin, Heidelberg, New York
- Marshall DJ (1988) *Cathodoluminescence of geological materials*. Unwin Hyman, Boston
- Mezger K (1996) Metamorphism and geochronology. *Berichte der DMG, European Journal of Mineralogy* 8(Beiheft 1): 189 (abs.)
- Morozov M, Trinkler M, Plötze M, Kempe U (1996) Spectroscopic studies on fluorites from Li-F and alkaline granitic systems in Central Kazakhstan. In: Shatov V et al. (eds) *Granite-related ore deposits of Central Kazakhstan and adjacent areas*. Glagol, St. Petersburg, 359–369
- Murakami T, Chakoumakos BC, Ewing RC, Lumpkin GR, Weber WJ (1991) Alpha-decay event damage in zircon. *American Mineralogist* 76: 1510–1532
- Nasdala L, Gruner T, Nemchin AA, Pidgeon RT, Tichomirowa M (1996a) New SHRIMP measurements on zircons from Saxonian magmatic and metamorphic rocks. – In: *Freiberger Isotopenkolloquium 1996. Proceedings*. TU Bergakademie Freiberg, Freiberg, 205–214
- Nasdala L, Irmer G, Wolf D (1995) The degree of metamictization in zircon: a Raman spectroscopic study. *European Journal of Mineralogy* 7: 471–478

- Nasdala L., Pidgeon RT, Wolf D. (1996b) Heterogeneous metamictization of zircon on a microscale. *Geochimica et Cosmochimica Acta* 60(6): 1091–1097
- Nasdala L., Pidgeon RT, Wolf D, Irmer G (1997) Metamictization and U-Pb isotopic discordance in single zircons: a combined Raman microprobe and SHRIMP ion probe study. *Mineralogy and Petrology* (in press)
- Ohnenstetter D, Cesbron F, Remond G, Caruba R, Claude JM (1991) Émissions de cathodoluminescence de deux populations de zircons naturels: tentative d'interprétation. *C.R. Acad. Sci. Paris* 313 (II), 641–647
- Pan Y (1997) Zircon- and monazite-forming metamorphic reactions at Manitouwadge, Ontario. *Canadian Mineralogist* 35: 105–118
- Peterman ZE, Zartman RE, PK Sims (1986) A protracted Archean history in the Watersmeet gneiss dome, Northern Michigan. *US Geological Survey Bulletin* 1622: 51–64
- Phillips MR, Kalceff MAS, Moon AR (1996) Cathodoluminescence spectroscopy of natural zircon. In: Pagel, M. (ed.) *International conference on cathodoluminescence and related techniques in geosciences and geomaterials*. Nancy, 115–116 (abs.)
- Pidgeon RT (1992) Recrystallisation of oscillatory zircon: some geochronological and petrological implications. *Contributions to Mineralogy and Petrology* 110: 463–472
- Pidgeon RT, O'Neil JR, Silver LT (1966) Uranium and lead isotopic stability in a metamict zircon under experimental hydrothermal conditions. *Science* 154: 1538–1540
- Pidgeon RT, Furfaro D, Kennedy AK, Nemchin AA, van Bronswijk W (1994) Calibration of zircon standards for the Curtin SHRIMP II. 8th Int Conf Geochronol Cosmochronol Isotope Geol, Berkeley (US Geol Surv Circ 1107): 251 (abs.)
- Pilot J, Werner CD, Haubrich F (1997) 330 and 1600 Ma old zircons in drilled gabbros from MARK area, Mid-Atlantic Ridge (in prep.)
- Pointer CM, Ashworth JR, Ixer RA (1988) The zircon-thorite mineral group in metasomatized granite, Ririwai, Nigeria. 2. Zoning, alteration and exsolution in zircon. *Mineralogy and Petrology* 39: 21–37
- Poller U, Liebetrau V, Todt W (1996) Cathodoluminescence and conventional U-Pb single zircon dating on the same grain applied to S-type granitoids. *Journal of Conference Abstracts* 1(1): 478 (abs.)
- Pupin JP (1980) Zircon and granite Petrology. *Contributions to Mineralogy and Petrology* 73: 207–220
- Pupin JP (1992) Les zircons des granites oceaniques et continentaux: couplage typologie-geochimie des elements en traces. *Bull. Soc. geol. France* 163(4): 495–507
- von Quadt A (1993) The Saxonian Granulite Massif: new aspects from geochronological studies. *Geologische Rundschau* 82: 516–530
- Remond G, Cesbron F, Chapoulie R, Ohnenstetter D, Roques-Carmes C, Schwoerer M (1992) Cathodoluminescence applied to the microcharacterization of mineral materials: a present status in experimentation and interpretation. *Scanning Microscopy International* 6(1): 23–68
- Roberts MP, Finger F (1996) Significance of zircon ages for Southern Bohemian Granulites; evidence for late zircon growth as a consequence of long-term melt residence during retrograde metamorphic evolution. *Journal of Conference Abstracts* 1(1): 513 (abs.)
- Roger F, Calassou S, Lancelot J, Malavielle J, Mattauer M, Zhinquin X, Ziwen H, Liwei H (1995) Miocene emplacement and deformation of the Konga Shan granite (Xianshui He fault zone, west Sichuan, China): Geodynamic implications. *Earth and Planetary Science Letters* 130: 201–216
- Rötzler J (1992) Zur Petrogenese im Sächsischen Granulitgebirge (Die pyroxenfreien Granulite und Metapelite). *Geotektonische Forschung* 77: 1–100
- Rubatto D, Gebauer D (1996) Use of cathodoluminescence for U-Pb zircon dating by ion microprobe (SHRIMP): some examples from high-pressure rocks of the Western Alps. In: Pagel, M. (ed.) *International conference on cathodoluminescence and related techniques in geosciences and geomaterials*. Nancy, 131–132 (abs.)
- Savatenkov VM, Morozova IM, Kutjavin EP (1995) Study of Rb-Sr geochemical behavior in the contact zone of Ozeraya Varaka intrusion. *Geochimica* (5): 687–696 (in Russian)

- Silver LT, Deutsch S (1963) Uranium–lead isotopic variations in zircons: A case study. *Journal of Geology* 71: 721–758
- Smith DGW, St. Jorre Ld, Reed SJB, Long JVP (1991) Zonally metamictized and other zircons from Thor Lake, Northwest Territories. *Canadian Mineralogist* 29: 301–309
- Sommerauer J (1976) Die chemisch–physikalische Stabilität natürlicher Zirkone und ihr U–(Th)–Pb System. PhD Thesis, Zürich 151 p
- Tichomirowa M, Belyatsky B, Nasdala L, Berger HJ, Koch E, Bombach K (1996) Zircon dating of gray gneisses from the Eastern Erzgebirge. Comparison of different dating methods (Pb/Pb evaporation, conventional U/Pb, SHRIMP) and geological meaning. In: *Freiberger Isotopenkolloquium 1996. Proceedings. TU Bergakademie Freiberg, Freiberg*, 241–249
- Todt AW, Büsch W (1981) U-Pb investigations on zircons from pre–Variscan gneisses – I. A study from the Schwarzwald, West Germany. *Geochimica et Cosmochimica acta* 45: 1789–1801
- Trinkler M, Kempe U, Plötze M, Rieser U (1993) Über rosa und braunen Fluorit aus Sn-W-Lagerstätten. *Chemie der Erde* 53: 165–181
- Vavra G (1990) On the kinematics of zircon growth and its petrogenetic significance: a cathodoluminescence study. *Contributions to Mineralogy and Petrology* 106: 90–99
- Vavra G (1994) Systematics of internal zircon morphology in major Variscan granitoid types. *Contributions to Mineralogy and Petrology* 117: 331–344
- Vavra G, Gebauer D, Schmid R, Compston W (1996) Multiple zircon growth and recrystallization during polyphase Late Carboniferous to Triassic metamorphism in granulites of the Ivrea Zone (Southern Alps): an ion microprobe (SHRIMP) study. *Contribution to Mineralogy and Petrology* 122: 337–358
- Watznauer A (1974) Beitrag zur Frage des zeitlichen Ablaufes der Granulitgenese (Sächsisches Granulitgebirge). *Krystalinikum* 10: 181–192
- Wenzel Th, Pilot J, Hengst M, Hofmann J (1990) First single zircon ^{207}Pb – ^{206}Pb ages from the Saxonian granulite massif. *Proceedings of the 5th Meeting Isotopes in Nature*. ZFI, Leipzig: 193–202
- Zinger TF, Götze J, Levchenkov OA, Shuleshko IK, Yakovleva SZ, Makeyev AF (1996) Zircon in polydeformed and metamorphosed Precambrian granitoids from the Wite Sea Tectonic Zone, Russia: morphology, cathodoluminescence, and U-Pb chronology. *International Geology Review* 38: 57–73

Cathodoluminescence in Applied Geosciences

JENS GÖTZE

1

Introduction

Cathodoluminescence has developed into a standard technique for mineralogical and petrological investigations in geosciences. This is especially due to several advantages which have made cathodoluminescence (CL) a powerful tool in the analysis of solid matter. Generally, CL has been applied to investigations of crystallographic and typomorphic properties of minerals (real structure, zonation, etc.), the identification of mineral constituents, and the reconstruction of mineral- and rock-forming processes (Walker 1985; Marshall 1988; Remond et al. 1992). Investigations of gemstones by CL have especially focused on the evaluation of typomorphic properties to distinguish natural from synthetic gemstones (e.g. Gaal 1976, 1977; Ponahlo and Koroschetz 1985; Ponahlo and Brandstätter 1996).

In several fields of applied geosciences, CL is an effective addition to conventional analytical methods such as polarizing microscopy, X-ray diffraction (XRD), scanning electron microscopy (SEM) or microprobe analysis (McCauley 1975; Götze 1995). Using modern CL equipment it is possible to reveal textures and variations in the chemical composition of solids regardless of their crystallinity. Thus, CL results are of special interest in materials in which a high content of amorphous components, low concentrations of mineral phases and/or extremely heterogeneous materials limit other analytical methods. CL analysis plays a significant part in specific investigations of geomaterials, industrial minerals, and technical products such as:

1. Natural and synthetic minerals, gemstones
2. Industrial raw materials
3. Products of coal and waste combustion (fly ashes, slags)
4. Metallurgical slags and dust
5. Structural materials (natural stones, bricks, mortar, concrete)
6. Ceramics, glasses, refractory materials
7. Archaeological materials

Several luminescence spectroscopic methods have been applied to prospecting and exploration purposes or for mineral processing (Gorobets et al. 1989; Hagni 1984; Kogut and Hagni 1995; Gorobets and Rogozhin 1996; Gorobets et al. 1996). Minerals which were successively sorted by X-ray luminescence or photoluminescence

are represented by technical and building materials (e.g. fluorite, feldspar, calcite, wollastonite), chemical raw materials (e.g. apatite, datolite, danburite, barite, sylvinite), and gemstones such as diamond, ruby, spinel or beryl (Gorobets et al. 1996).

Although CL has been fully accepted in geological investigations, its important role in the study of the mineralogy involved in a wide variety of problems of environmental significance has not been fully recognized. For instance, dark-field ore microscopy and CL microscopy were found to provide excellent methods to determine the mineralogy, porosity, and permeability of roast products of gold metallurgy in sulfide ores or cyclone dust, sludge, and accretions from iron-making plants (Hagni and Hagni 1996; Hagni et al. 1996). Furthermore, the identification of phases in fly ashes and slags of lignite combustion is more effective using CL microscopy (e.g. Münch and Götze 1994; Walther et al. 1995; Götze 1996a).

Many of the phases occurring in ceramics, glasses, and refractory materials show distinct CL properties allowing a rapid identification of phase distribution and phase transformations (Götze et al. 1993; Alvarez et al. 1996; Karakus and Moore 1996; Phillips et al. 1996). Luminescence techniques are also widely used in the characterization and dating of archaeomaterials and archaeological objects (Schvoerer 1996). Different materials have been investigated including ceramics, glasses, terra cotta, mortars or painted coatings.

In the field of structural materials, such as natural stones, bricks, concrete and mortars, CL helps to identify the phase composition and to reveal reaction processes during firing of natural and synthetic raw materials or phase transformations due to weathering (Götze and Klemm 1994; Mumenthaler et al. 1995; Fratini et al. 1996; Motzet et al. 1997).

Three case studies are presented here which illustrate the advantages of CL microscopy, optical CL combined with high resolution spectral CL and a combination of CL microscopy and image analysis for investigations of geological samples and technical products.

2

Application of Cathodoluminescence Microscopy to Fly Ashes and Slags of Lignite Combustion

The growing interest in the study of mineral matter in coals and products of coal combustion is especially due to environmental aspects and problems of waste disposal. Accordingly, information about the behavior of chemical elements, minerals and their phase transformation during coal combustion are important (Raask 1985; Smith 1987; Querol et al. 1994, 1995). Furthermore, during the last few years research has focused on the characterization of combustion products of large power stations in order to use this material in industry (e.g. building material).

Waste materials often show a heterogeneous chemical and phase composition which complicates their deposition and/or utilization in industry. Although there is a basic knowledge concerning the phase composition of lignite fly ashes and combustion slags, there is a lack of data especially regarding the glass particles which are important in the hydraulic reactions of these products (Keyn and Schreiter 1985; Werner et al. 1988, Enders 1995). Chemical analysis alone gives

only partial information about the behavior of some elements during coal conversion processes because of the heterogeneity of the natural raw materials. Other conventional analytical methods such as polarizing microscopy, SEM, transmission electron microscopy (TEM) and XRD cannot completely determine the phase composition because of the very complex composition of the particles.

In the present study, the phase composition (mineral phases and glassy spheres) of lignite fly ashes of some of the most important German power stations (Lower Lusatia lignite area, Rhenic area, central German area, and Upper Lusatia area) and synthetic combustion slags was analyzed using a combination of hot-cathode luminescence microscopy and chemical microanalysis. The ashes and slags were investigated in detail using chemical analysis (i.e. inductively coupled plasma, atomic absorption spectroscopy) as well as XRD, SEM, microprobe, and CL microscopy. The study was focused on the characterization of particles modified, transformed and newly formed during combustion processes.

The major mineral phases in lignites used for coal combustion are kaolinite, illite, quartz, gypsum, pyrite/marcasite, and feldspar. The phase transformations during the combustion of the coals result in the formation of the crystalline phases anhydrite, free lime, calcium ferrites (e.g. brownmillerite $2\text{CaO} \cdot (\text{Al}, \text{Fe})_2\text{O}_3$), and iron oxides in the lignite fly ashes, as confirmed by XRD analysis (for details of the transformation processes, see Querol et al. 1994). The mineral phases resulting from the high-temperature processes also include quartz and feldspar as residuals and considerable amounts of glassy spheres and devitrification products such as anorthite and gehlenite (Fig. 1). The chemical composition of

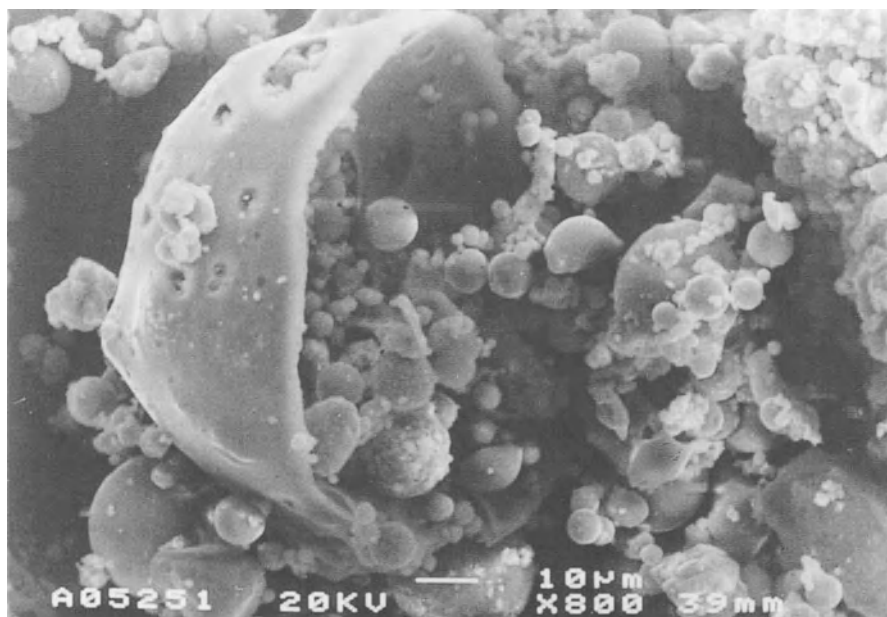


Fig. 1. SEM micrograph showing several ash particles in a lignite fly ash from Jänschwalde (Lusatia area, Germany) including glassy spheres

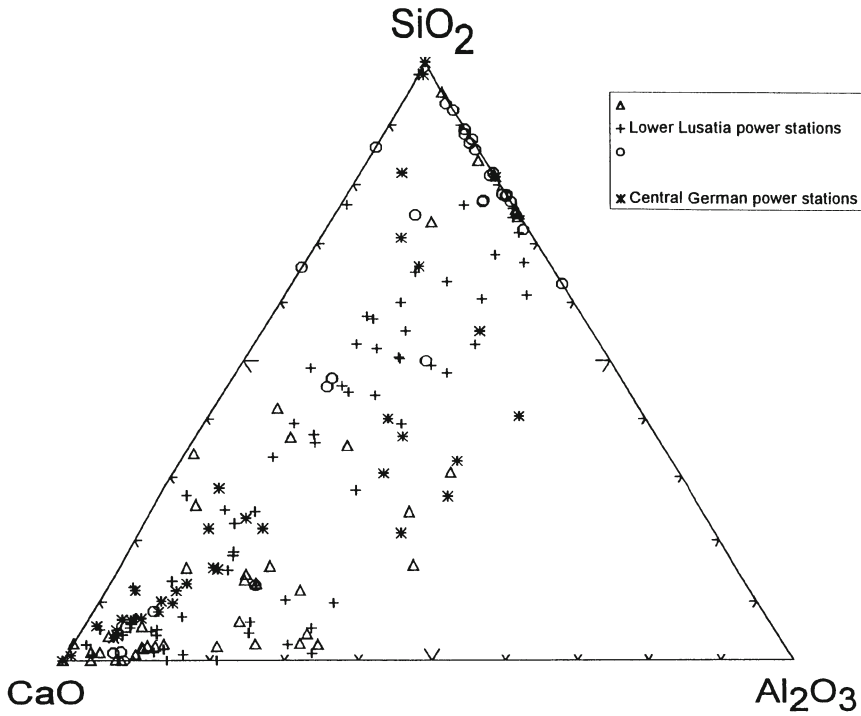


Fig. 2. Chemical composition of glassy spheres in lignite fly ashes of various origin. (After Münch and Götze 1994)

these particles is very complex, as shown in Fig. 2. Comparison of Al/Si ratios of initial phases (clay minerals: kaolinite, illite) with those of glassy spheres produced during combustion revealed that the starting material underwent processes of amorphization and dehydration but also chemical reactions between the components.

Investigations of different ash samples by CL microscopy show that a clear differentiation of mineral particles is possible regardless of their crystallinity (Fig. 3A,B). This is especially important for the characterization of constituents which are not discernible by conventional polarizing microscopy and non-crystalline phases which cannot be identified by XRD.

Clastic particles (e.g. quartz, feldspar, zircon) are clearly identifiable in the ashes, indicating that their characteristic luminescence properties were not changed during thermal treatment (Fig. 3B). The different primary origin of quartz grains (e.g. blue/blue-violet luminescing igneous quartz or brown luminescing metamorphic quartz, see Fig. 3B) can still be detected in the samples. Additionally, certain components were revealed in agglomerates (Fig. 3B).

Yellowish luminescing and non-luminescing glassy spheres were mainly observed by CL (Fig. 3A,B). Particles with green, reddish or violet CL colors are

minor. The CL spectrum in Fig. 4 shows a strong emission around 550–600 nm for a yellowish luminescing glassy sphere. It is uncertain whether this broad band emission is caused by an activator element (e.g., Mn^{2+} as in feldspar) or is due to another luminescence center (e.g. electron defects localized on SiO_4 groups). This aspect needs further investigation.

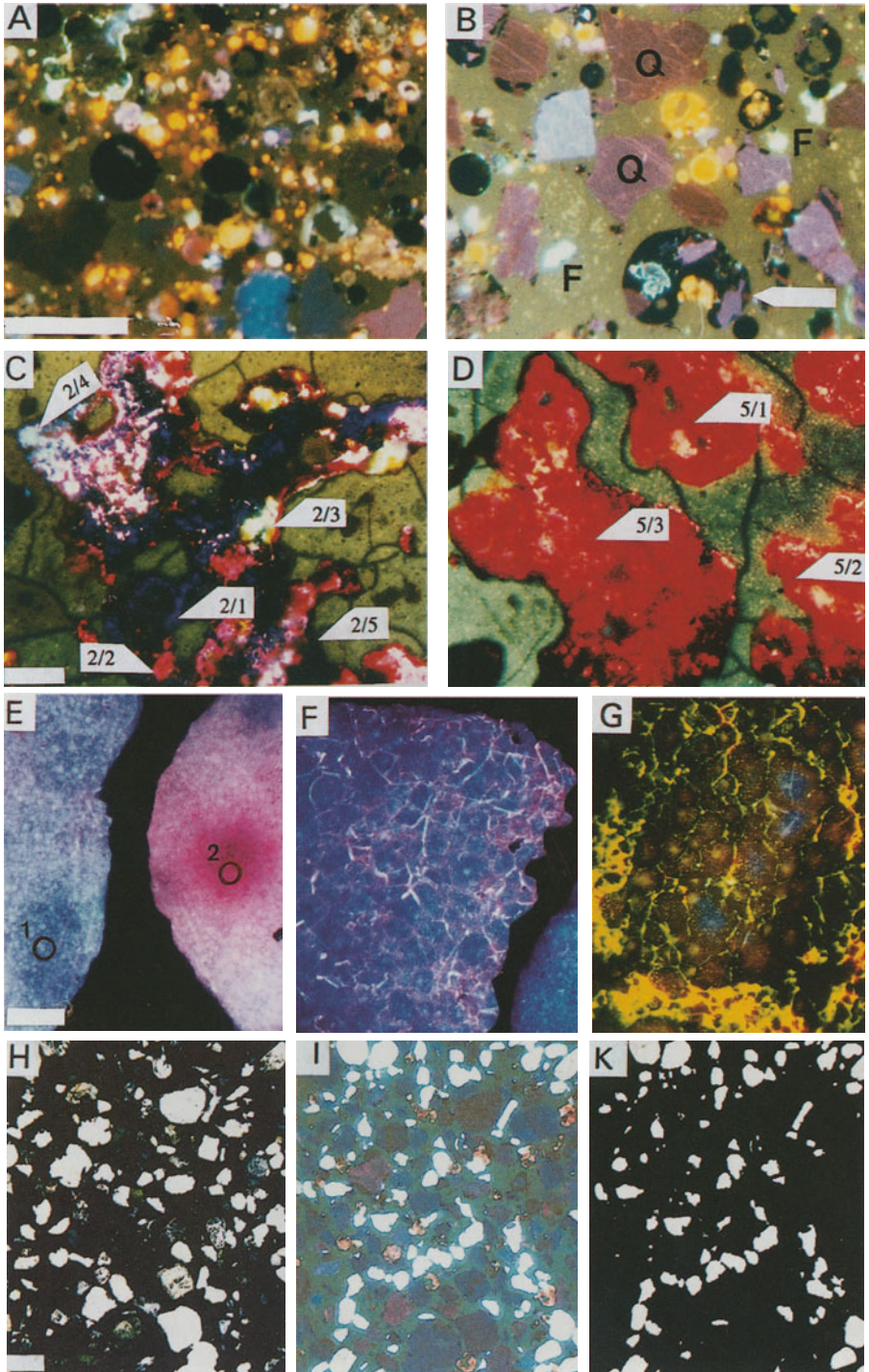
In general, the samples of the Lower Lusatia area and the Central German area show all luminescence types, samples of Rhenish power stations are dominated by yellow CL colors, and the content of luminescing particles is low in the Upper Lusatia ashes. A comparison of CL colors and microchemical analyses shows a correlation between chemical composition and luminescence properties of the glassy spheres. A plot of the most common luminescence colors (yellow CL and non-luminescent) in the $CaO/(SiO_2+Al_2O_3)/Fe_2O_3$ triangle (Fig. 5) indicates that variations in the chemical composition of the ash particles influence their luminescence. The CL color is dominantly caused by the Ca:Fe ratio. Other elements such as Mg, Na, K and S have no influence on CL properties.

Based on these results, glassy spheres were classified based on their luminescence and chemical composition. Particles with high CaO contents (>35 wt-%) and low concentrations of $(SiO_2+Al_2O_3+Fe_2O_3)$ show a typical yellow luminescence color, whereas phases with low CaO content and high concentrations of $(SiO_2+Al_2O_3+Fe_2O_3)$ generally do not luminesce (Fig. 6).

Assuming that the chemical composition of ash particles causes differences in luminescence, the recognition of particles with varying elemental composition is possible. Furthermore, changes during chemical reactions of various components should be detectable by CL. Therefore, samples of raw ashes and hydrated ashes of the same locality were analyzed to obtain information about phase transformation processes in these samples. Hydrated ashes show a significant decrease in yellowish luminescing particles. This indicates that especially the high CaO-containing particles underwent alteration processes, resulting in changes in luminescence behavior. This would confirm results of Enders (1995), who proposed a boundary in the chemical composition of glassy spheres in lignite fly ashes at 25 wt% CaO, which separates highly reactive glassy spheres from less reactive spheres.

The promising results concerning the phase composition of lignite fly ashes encouraged us to study the luminescence behavior of slags from lignite combustion. We investigated model slags formed during gasification of brown coal from the Lower Lusatia area and a mixture of this coal with 35% sewage sludge at 600, 800, and 1200 °C under oxidizing and reducing conditions. Furthermore, combustion products of coal and 1% added potassium dichromate were analyzed to obtain more information about the chemical bonding of potential toxic elements in such combustion slags.

In general, the amount of amorphous phases in the slags is high, sometimes very high (estimated up to 90%). The most common crystalline constituents detected by XRD are quartz and iron oxides (hematite, maghemite, magnetite), the former deriving from clastic input into the samples (Table 1). High concentrations of anhydrite were detected in all samples gasified at 600 °C, which was confirmed by high contents of SO_3 (12.4–19.5%). At 1200 °C, Ca and Mg preferentially formed silicate phases (melilite) and ferrites. The addition of sewage sludge caused the formation of Ca- and Ca-Mg-phosphates during gasification at 600 °C



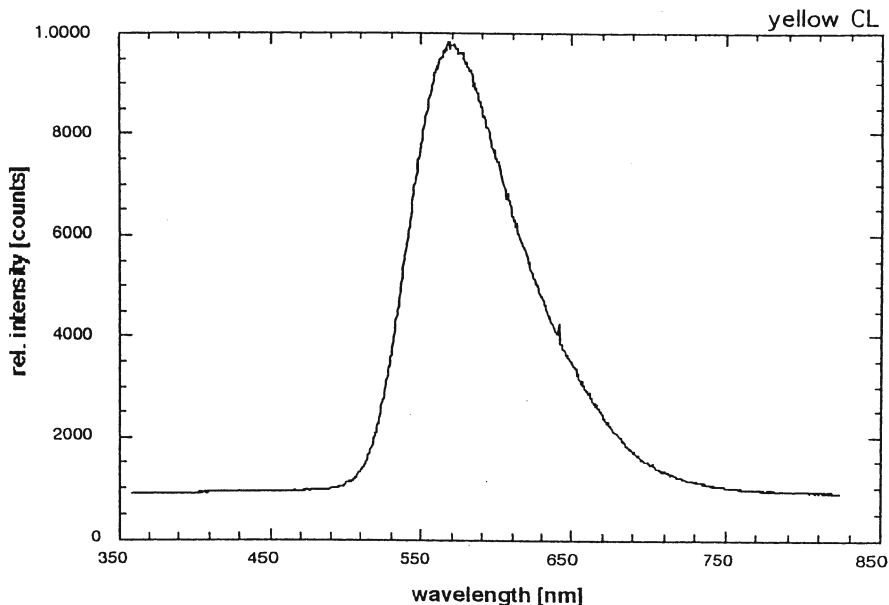


Fig. 4. CL emission spectrum of a yellowish luminescing glassy sphere in a lignite fly ash from Jänschwalde, Germany

←

Fig. 3A–K. Cathodoluminescence micrographs of investigated geological samples and technical products. Scale bar is 200 μm . A Lignite fly ash from the central Germany area. The amount of glassy spheres is very high, dominated by yellow luminescent and non-luminescent particles; glassy spheres with greenish and red-violet CL are minor. The different particles are only discernible by CL. B Lignite fly ash from the Lower Lusatia area with high contents of detrital quartz (Q) and feldspar (F). Glassy spheres are characterized by yellow CL (Ca-rich) or lacking CL (Fe-, Al-, Si-rich). In agglomerates (arrow) different crystalline and glassy components are distinguishable by CL. C Synthetic combustion slag (coal, 1200 °C). The sample shows extreme differences in luminescence color and intensity contrasting several phases (compare with Table 2) which are not discernible by optical microscopy. Differences in CL color reveal phase formation in small areas including glasses of varying chemical composition. D Synthetic combustion slag (coal+sewage sludge, 1200 °C). The addition of sewage sludge at 1200 °C results in red-pink luminescence colors of Ca phosphate and Ca silicate phases; high Fe contents can inhibit the CL. E CL micrograph of MgO, periclase, at room temperature (20 °C). CL reveals blue and red luminescing MgO grains due to lattice defects (blue CL) and trace element impurities (Mn^{2+} , Cr^{3+} : red CL). 1, 2, analytical points for spectral CL measurements (see Fig. 7). F The MgO grain after thermal treatment at 950 °C exhibits heterogeneous CL distribution due to partial recrystallization (blue luminescing grain cores) and diffusion of impurities to grain boundaries (red CL) (see Fig. 8). G MgO brick in the direct contact to the iron melt. The MgO grains show features of cracking and alteration visible by different CL colors. Yellow-greenish luminescing slag material (spinel) is distributed in micro-cracks and in the pore space. H–K Images of a feldspathic sandstone representing the processing algorithm for quantitative phase determination by combined CL and image analysis: H crossed polars, I CL mode showing dark blue-violet luminescing quartz grains, yellow-orange carbonate and bright luminescing (overexposed) feldspar, K contrasting and quantification of feldspar in the binary mode

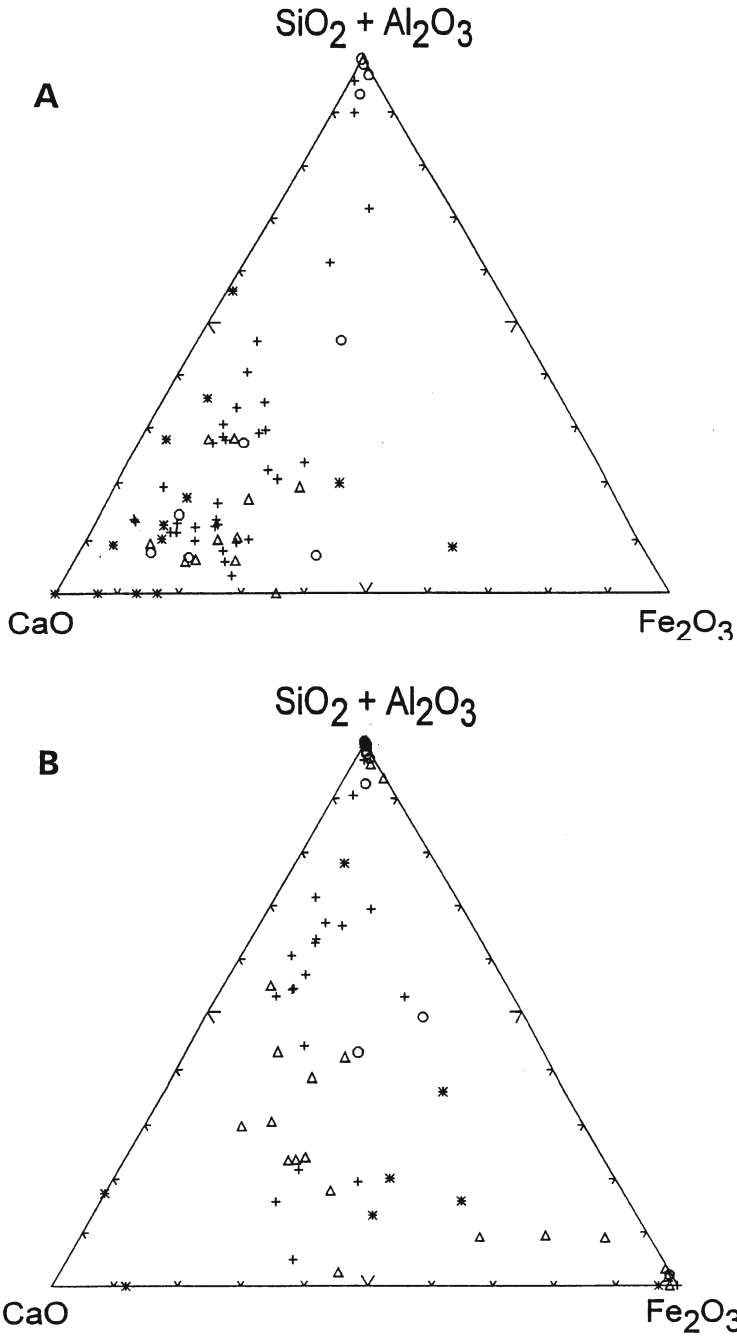


Fig. 5. Chemical composition of yellowish luminescing (A) and non-luminescing (B) glass particles of investigated lignite fly ashes (symbols as in Fig. 2) (After Münch and Götze 1994)

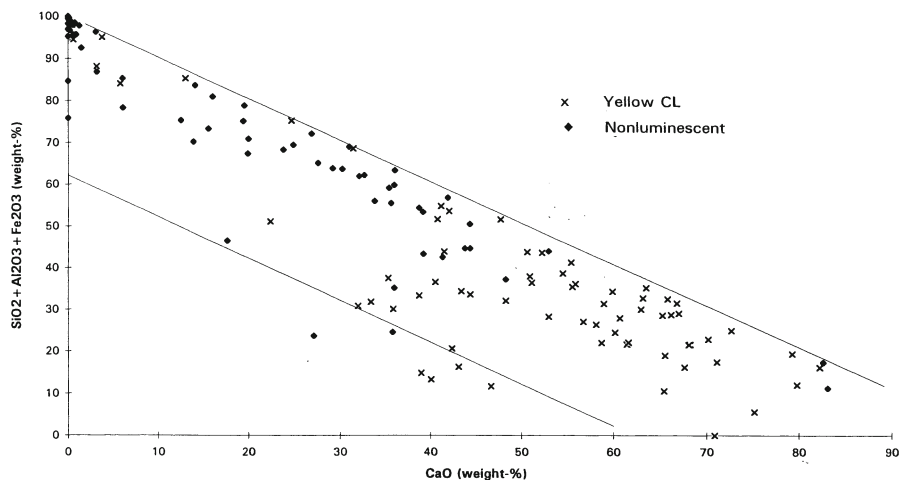


Fig. 6. Discriminating plot of luminescence behavior vs chemical composition of glass particles in investigated lignite fly ashes. (Modified after Münch and Götze 1994)

Table 1. Crystalline phases detected in model slags by X-ray diffraction analysis. (Walther et al. 1995)

Sample	1	2	3	4	5	6	7	8	9	10	11	12
T (°C)	600	1200	600	1200	1200	800	1200	800	1200	800	1200	1200
Composition	C	C	C+S	S	C+S	C	C	C+S	C+S	C+P	C+P	C+P
Oxi-dizing								Reducing		Oxidizing		Red.
Anhydrite	X		X			X		X	x	X	x	
Hematite/maghemite	x	X	x	x	X	x	X	x	x	x	x	x
Mg-Al-Fe spinel		x									x	x
Ca/Ca-Mg ferrite		x				x	x					
Apatite					X				X			
Ca/Ca-Mg phosphate			x	x	x			x				
Ca/K feldspar				X							x	
Melilite		X			x		X		X			
Forsterite					x							
Mg-chromite/chromite										X	X	X
Periclase											x	x
Quartz	X		X	X		X	x	x		x		

C, coal; S, sewage sludge; C+S, coal+35% sewage sludge; C+P, coal+1% potassium dichromate; X, main constituent; x, minor constituent.

and apatite at 1200 °C, respectively. Further minerals detected were feldspar, forsterite, periclase and minerals of the spinel group. The addition of potassium dichromate caused the formation of minerals of the chromite type.

CL revealed some extreme differences in luminescence color and intensity within single aggregates, indicating formation of different phases in small areas (Fig. 3C,D). Furthermore, the differentiation of several glass phases was possible. Although a general correlation of phase composition and luminescence color is not possible yet, some preliminary conclusions could be drawn from this study. The following particles can be distinguished based on their luminescence color (Table 2): Ca-Fe sulfate (green CL), CaO (red), Ca-Mg silicate (blue-violet) and particles with feldspathic composition (yellow). High Fe-, Ti- and Cr-bearing samples are mostly non-luminescent. The samples containing sewage sludge show dominantly red-pink luminescence resulting from a mixture of phosphate and silicate phases (Fig. 3D). Accordingly, CL microscopy reveals phase distribution in samples in which a high content of amorphous components, low crystallinity, low concentration of mineral phases and/or extremely heterogeneous material limit other analytical methods. This gives CL microscopy promising perspectives in specific investigations of minerals and technical products such as glasses, ceramics or waste materials.

3 Investigation of MgO Refractories by Optical and Spectral Cathodoluminescence

Refractory materials are commonly used due to their high-temperature mechanical behavior in several fields of industrial high-temperature processes. MgO bricks, for instance, are used in LD converters, molten-iron ladles and electric arc furnaces because of their thermochemical and thermomechanical properties. MgO, periclase, is not only an important refractory material in industry but also a very interesting mineral phase of the earth's interior. Therefore, understanding the thermal behavior of MgO is important for many problems ranging from thermal expansion and alteration processes in refractory materials (Vu et al. 1997) to modeling relations of the earth's interior (Reeber et al. 1995).

To enhance the service time of refractory materials in the industry, their microstructure should be well understood. Both the technological parameters during production processes and the varying properties of the raw materials (e.g. crystallinity, incorporation of impurities) can considerably influence the properties of the manufactured refractory material. Furthermore, these parameters can change during thermal treatment due to thermal expansion, recrystallization or diffusion of trace impurities. To detect variations of structural parameters in synthetically treated MgO materials and periclase bricks used as refractory materials both optical and spectral CL were used.

At room temperature (20 °C) periclase exhibits blue and/or red CL. Figure 3E illustrates that the MgO grains are partially heterogeneous under CL, reflecting differences in structure and chemical composition. These differences are not discernible using conventional reflected light or polarizing microscopy.

Table 2. Results of microchemical analysis and CL microscopy of selected slag particles

	No.	Na ₂ O	K ₂ O	CaO	MgO	MnO	Al ₂ O ₃	Fe ₂ O ₃	Cr ₂ O ₃	TiO ₂	SiO ₂	P ₂ O ₅	SO ₃	Cl	CL color
Coal (1200 °C)	2/1	-	-	41.79	7.18	-	16.89	0.86	-	0.57	32.70	-	-	-	Blue
	2/2	-	-	52.43	12.25	-	-	-	-	-	35.32	-	-	-	Violet
	2/3	7.96	0.75	5.13	-	-	26.70	-	-	-	59.45	-	-	-	Yellow
	2/4	-	-	65.38	-	-	-	0.59	-	0.38	33.64	-	-	-	Bright blue
	2/5	-	-	1.99	18.48	0.68	11.98	65.67	-	0.49	0.71	-	-	-	No CL
Coal+sewage sludge (600 °C)	3/1	-	0.65	20.59	3.32	-	-	35.26	-	-	-	-	34.67	5.51	Green
	3/2	-	-	20.06	1.51	-	-	34.16	-	-	1.13	-	37.31	5.84	Green
	3/3	-	-	22.96	5.52	-	4.51	24.31	-	-	-	-	41.97	0.73	Green
Coal+sewage sludge (1200 °C)	5/1	-	-	41.39	2.24	-	5.14	4.74	-	1.40	5.66	37.93	1.51	-	Pink
	5/2	-	-	46.85	1.93	0.54	1.14	0.64	-	-	-	46.33	2.56	-	Pink
	5/3	-	-	38.99	2.58	-	9.38	5.34	-	2.95	13.90	26.08	0.78	-	Pink
Coal+potassium dichromate (1200 °C)	11/1	-	-	2.92	20.97	2.32	7.55	23.79	42.45	-	-	-	-	-	No CL
	11/2	-	-	2.59	22.14	0.50	11.99	22.56	40.22	-	-	-	-	-	No CL

The CL spectra (Fig. 7) reveal that the CL emission of MgO consists of three broad bands: in the blue region between 400 and 500 nm, at about 615 nm, and in the red region around 750 nm. According to Fiske et al. (1994) the blue emission is due to intrinsic lattice defects. Sathyamoorthy and Luthra (1978) concluded from doped MgO samples that Ni^{2+} gives a blue-green emission near 490 nm although they found no correlation between the intensity of this emission and the Ni content. The 615 nm band can be related to Mn^{2+} , and the incorporation of Cr^{3+} causes the emission band in the red region around 750 nm and shows some vibrational structures (Sathyamoorthy and Luthra 1978). The role of Fe^{3+} as an activator of red CL, as in many other minerals, is still uncertain because Sathyamoorthy and Luthra (1978) considered Fe^{3+} as a quencher under thermoluminescence.

The comparison of the CL spectra of blue and red luminescing MgO grains shows that the blue luminescing grain has a stronger emission in the 400–500 nm region whereas the red luminescing grain exhibits stronger CL emission at 615 nm and in the red region. This indicates that MgO grains with blue CL have more intrinsic lattice defects and lower concentrations of Mn^{2+} and Cr^{3+} than red luminescing MgO. Similar results were reported by Alvarez et al. (1996), who published microprobe analyses of blue luminescing magnesia with low Cr and Mn (0–310 and 0–230 ppm, respectively) and red magnesia containing high contents of these elements (340–890 ppm Cr and 460–930 ppm Mn). Accordingly, CL spectroscopy is very sensitive to both lattice defects and trace element impurities in MgO.

This is emphasized by results of thermally treated periclase samples. During the thermal treatment at 550 °C changes of the CL of MgO are detectable. Micro-

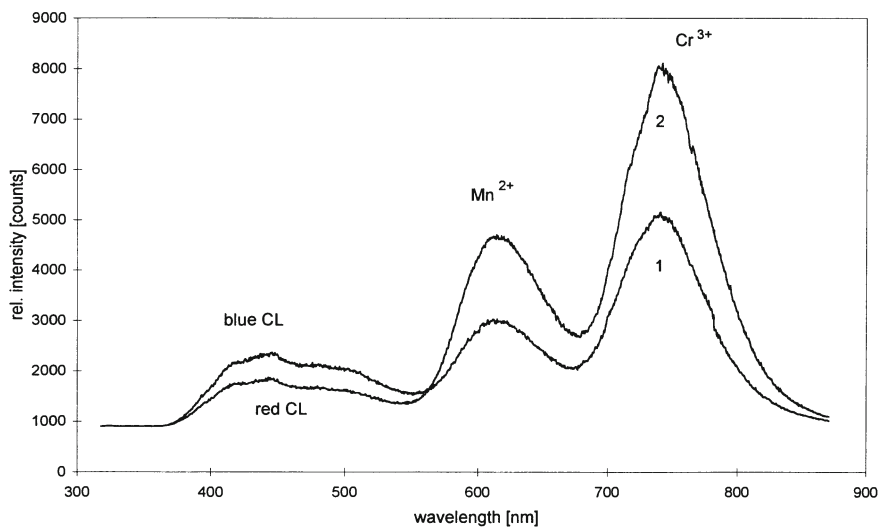


Fig. 7. CL spectra of blue (1) and red (2) luminescing MgO grains (see Fig. 3E). The red grain shows two strong emission bands, at 615 nm and around 750 nm, which are caused by Mn^{2+} and Cr^{3+} , respectively

cracks, which result from the thermal expansion of the material, are visible in the MgO grains due to bright CL. An increase in the CL emission in the blue region can be interpreted as an increase in lattice defects. High densities of lattice defects are especially detectable in the area of micro-cracks where the thermal expansion has probably caused non-bridging atoms and vacancies.

Further thermal treatment up to 950 °C promotes this effect. Figure 3F illustrates high densities of micro-cracks in the treated samples. Moreover, diffusion of impurities resulted in very heterogeneous MgO grains visible under CL as blue and red grain areas. The impurities (especially Mn^{2+} and Cr^{3+}) are concentrated in the red luminescing grain boundaries and cracks which are clearly detectable in the CL spectra (Fig. 8). Compared to the blue luminescing sub-grain areas the red areas show strong emission bands at 615 and 750 nm.

To continue the study of the thermal and chemical behavior of periclase bricks, samples from the contact zone between the MgO refractory material and an iron melt were investigated. CL is a powerful tool in order to detect changes in the microstructure of the MgO bricks and to distinguish several phases formed due to the reaction of MgO with the melt. Figure 3G characterizes the reaction zone in the outer rim of the bricks. The primary MgO grains are partially dissolved and almost completely altered, only small blue luminescing cores have been left. Most of the grains show dull brown CL and the marginal zones are nonluminescent. This significant change of the CL properties of MgO can be explained by the very reduced redox conditions (low oxygen partial pressure) in the contact with the iron melt which caused a reduction of the transition ele-

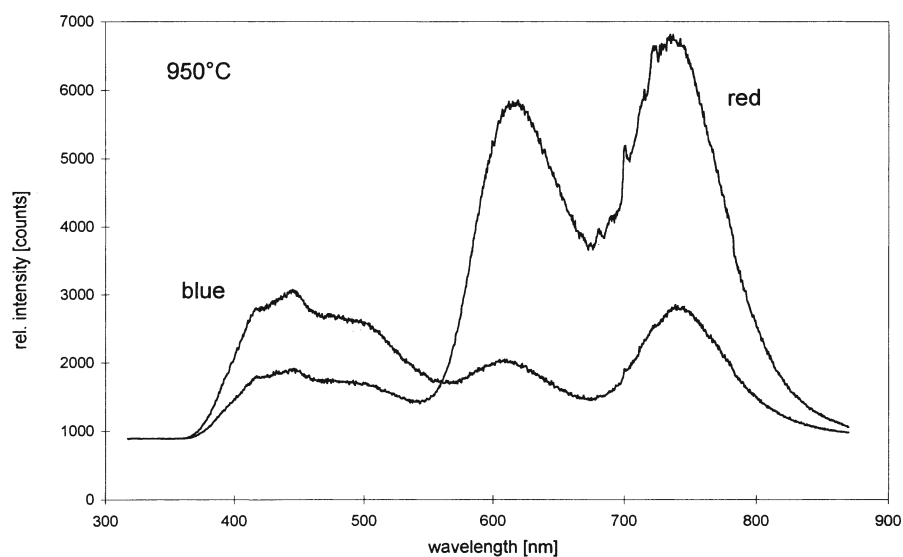


Fig. 8. CL spectrum of MgO grain after thermal treatment at 950 °C (see Fig. 3F). The blue sub-grains show a strong CL emission between 400 and 500 nm (intrinsic lattice defects), whereas the red luminescing areas are dominated by emissions due to Mn^{2+} and Cr^{3+} which probably diffused to the subgrain boundaries

ments. Furthermore, iron which diffused into the MgO grains can strongly quench the CL intensity.

The internal grain structure of the MgO grains is marked by small cracks filled with yellowish-green material, which is also present in the pore space between the grains. Microprobe analysis showed that spinel was formed, which is clearly detectable by CL due to the bright luminescence.

With increasing distance from the contact (in the order of some mm) the influence of the melt on the refractory material decreases. Only the outer rims of the MgO grains show effects of thermal treatment. The intergranular pore space is partially filled with bright bluish-green luminescing spinel which has formed due to reactions between the melt and the refractory material. Where no spinel is detectable, a porous magnesia zone is formed showing bright red CL. This zone exhibits a strong emission in the 750 nm range.

In conclusion, investigations of MgO refractories by optical and spectral CL revealed differences in the trace element content and microstructure of the initial material, crystal chemical changes during thermal treatment, and formation of new phases in the contact zone between the refractory bricks and the melt.

4

Quantification of Mineral Phase Proportions Using Combined Cathodoluminescence Microscopy and Image Analysis

Mineral identification and quantification are important problems for mineralogists and petrologists in the geosciences. Generally, conventional analytical techniques are used such as XRD, polarizing microscopy, SEM or chemical analysis. However, identification and quantification of minerals are often unreliable because of certain short-comings in analytical techniques.

For instance, low concentrations of mineral phases or the nearly identical structure of two minerals may limit the amount of information obtainable from XRD analysis. Some of these problems may be solved using Rietveld analysis (Hill et al. 1993). However, no information can be obtained concerning rock fabric, mineral intergrowth or porosity. In some cases, even, conventional polarizing microscopy can be problematic if the crystal structure is very heterogeneous or the mineral very fine-grained. The quantification of the mineralogical composition by point-counting is time-consuming and not always accurate, especially when fine-grained material is present.

Using CL it is possible to distinguish certain mineral constituents by color contrast, even in fine-grained material. These high-contrast color patterns can be effectively quantified by computer-aided image analysis, and additional information can be obtained at the same time on texture, grain-size distribution, or grain shape. The results of Evans et al. (1994) illustrated the advantages of combined SEM-CL and image analysis in quantifying quartz cements in sandstones. In the present study combined hot cathode luminescence microscopy and image analysis were used to quantify the abundance of mineral phases in Turonian sandstone samples of the Elbe zone (Germany). Previous investigations have shown that the

sandstone material consists mainly of quartz, feldspar, carbonate minerals, and clay minerals (predominantly kaolinite). Because of the high abundance of these minerals in clastic sediments, their recognition and quantification are common problems in sedimentary petrography. Furthermore, a reliable differentiation of these constituents in fine-grained material by CL is possible using the characteristic CL properties of the minerals (Marshall 1988; Ramseyer et al. 1988; Machel and Burton 1991; Habermann et al. 1996; Götze 1996b; Götze et al. 1996). Therefore, CL in combination with image analysis should be tested to see whether or not a reliable mineral composition is produced.

Artificial standard sample sets were first investigated to test the suitability of the analytical and processing algorithm. To simulate possible variations in the properties of the natural samples, varying grain-size distribution and variations in the mineralogical composition of the samples were considered (Table 3). When preparing thin sections of the standard samples, the resin was colored by Epodye. In this way pore space could be quantified and total mineral contents could be calculated in the loose material by eliminating the artificial pore space.

Carbon-coated polished thin sections of both standard samples and natural sandstone samples were analyzed using a CL microscope (Neuser et al. 1995) with a hot cathode electron gun (acceleration voltage 14 kV, beam current 0.5 mA). Luminescence images were captured "on-line" during CL operations by means of an adapted digital video camera (KAPPA 961-1138 CF 20 DXC) coupled with computer-aided image equipment (KS-300, distributed by Kontron Electronics). Installed on a personal computer, this configuration allows the acquisition of digital signals from the video camera and the processing of high-contrast color patterns produced by CL as real color images (Fig. 3H-K). The image processing algorithm comprises the following steps:

1. Shadow correction by means of low-pass filtering
2. Basic image processing (focus, contrast, brightness, etc.)
3. Definition of the CL colors of the different mineral phases by combination of the values of color and brightness

Table 3. Comparison of the theoretical composition (wt%) and the analyzed contents of quartz (Q), feldspar (F), calcite (C) and opaque minerals (O) in synthetic standard samples. (Götze and Magnus 1997)

Sample no.	Grain size fraction (mm)	Theoretical composition (wt%)	Composition determined by combined CL and image analysis											
							(vol%)				(wt%; calculated)			
			Q	F	C	O	Q	F	C	O	Q	F	C	O
1	0.1-0.5	45	5	49	1	45.7	5.3	48.4	0.6	46.3	4.5	48.5	0.7	
2	0.1-0.5	35	25	39	1	35.2	26.1	38.1	0.6	36.0	25.2	37.8	1.0	
3	0.1-0.5	79	10	10	1	79.3	10.4	9.8	0.5	84.7	8.2	6.4	0.7	
4	0.063-0.1	5	44	50	1	5.0	45.7	48.7	0.6	4.8	45.3	48.5	1.4	
5	0.063-0.1	35	35	29	1	35.0	36.3	28.2	0.5	36.9	34.2	27.8	1.1	
6	0.063-0.1	79	10	10	1	79.3	10.4	9.8	0.5	82.7	8.7	8.0	0.6	

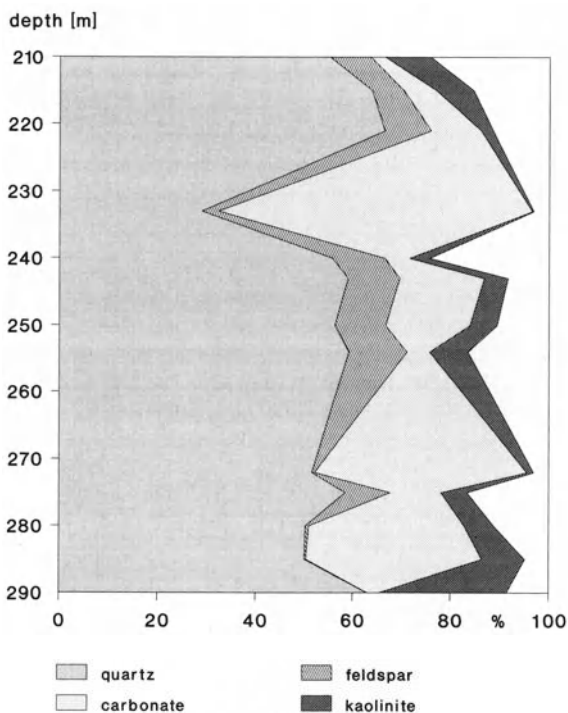
4. False color imaging of the different minerals (thresholding) and conversion to binary mode
5. Processing of phases in the binary mode
6. Definition of options and measuring
7. Extraction of data and interpretation

The strategy for image processing can vary in detail, depending on specific sample characteristics. Because of heterogeneities existing in natural samples, several fields of view must be analyzed to obtain reliable phase abundances. Several factors influence the analytical procedure including the heterogeneity of the sample investigated, magnification used, and contents of mineral phases analyzed. Accordingly, in coarse-grained sandstones more sample points must be analyzed than in fine-grained samples. It was found that 10–20 fields of view were suitable to give a statistically meaningful result (Götze and Magnus 1997).

In the investigated samples mineral phases are clearly distinguishable due to their luminescence colors. The feldspar fraction is only composed of bright blue luminescing alkali feldspar, which is different from the deep blue CL color of kaolinite. The intensity of quartz CL is significantly weaker. The carbonate minerals show typical yellowish-orange luminescence colors. In some cases different integration times were used to improve the color contrast between the mineral phases.

The mineral contents of the investigated sandstone samples analyzed are summarized in Fig. 9. Changes in the mineralogical composition are clearly

Fig. 9. Mineral composition of a section through the Lower Turonian sandstone from Graupa (Elbe zone, Germany) determined by combined CL and image analysis. (Data from Magnus and Götze 1996)



detectable. The standard deviation of the various mineral contents is strongly influenced by the scattering of single analytical results, depending especially on the homogeneity or heterogeneity of the sample investigated. Because of pore space and the occurrence of non-luminescent minerals the sum of mineral abundances detected is lower than 100%.

The contents of selected oxides and their associated minerals are correlated in Fig. 10. The theoretical mineral composition was calculated from the chemical analysis and is indicated by a correlation line. Assuming that the samples consist of the detected minerals, only the proportions of oxides were calculated from the mineral formula. The mineral contents plot somewhat below the theoretical line indicating that small amounts of additional Ca-, Mg-, Al-, and Si-bearing minerals are present. In particular, the deviating samples in Fig. 10 may be caused by relatively large amounts of illite, which was confirmed by XRD analysis.

The results of the study illustrate that quartz, feldspar, calcite, and kaolinite are successfully distinguishable in sandstone samples. The advantages of the method presented are:

1. CL and optical microscopy images can be compared directly.
2. The method can be readily automated.
3. Additional information (grain-size distribution, roundness, pore space) can be obtained simultaneously using computer-aided image analysis.

Furthermore, all investigations can be carried out on a polished thin section of the sample. This enables information derived from CL and polarizing microscopy to be combined and the same material to be used for further investigations (e.g. microprobe). Accordingly, combined CL and image analysis is not only relevant for sedimentary petrology but also in many other fields of geosciences. However, the image processing can lead to unreliable results if the luminescent properties of the minerals do not permit a clear distinction between different phases. If a mineral phase completely loses the characteristic properties (e.g. due to alteration) or if the phases have no luminescence, the application of CL to determine phase proportions is useless.

5 Conclusions

Cathodoluminescence is an excellent method which can supplement petrographic observations and geological considerations made by polarizing microscopy and other conventional analytical methods. Additionally, this method can also provide a specific contribution to the phase characterization of technical products and waste materials, especially in combination with XRD, SEM and microprobe analysis. CL microscopy alone provides at least a clear differentiation of several phases even in samples with a high content of non-crystalline components or extremely heterogeneous material. In combination with spectral measurements of the CL emission, conclusions concerning structural states of solids and trace element incorporation are possible. This enables detection of differences in the crystal structure and monitoring of diffusion processes or can reveal process-

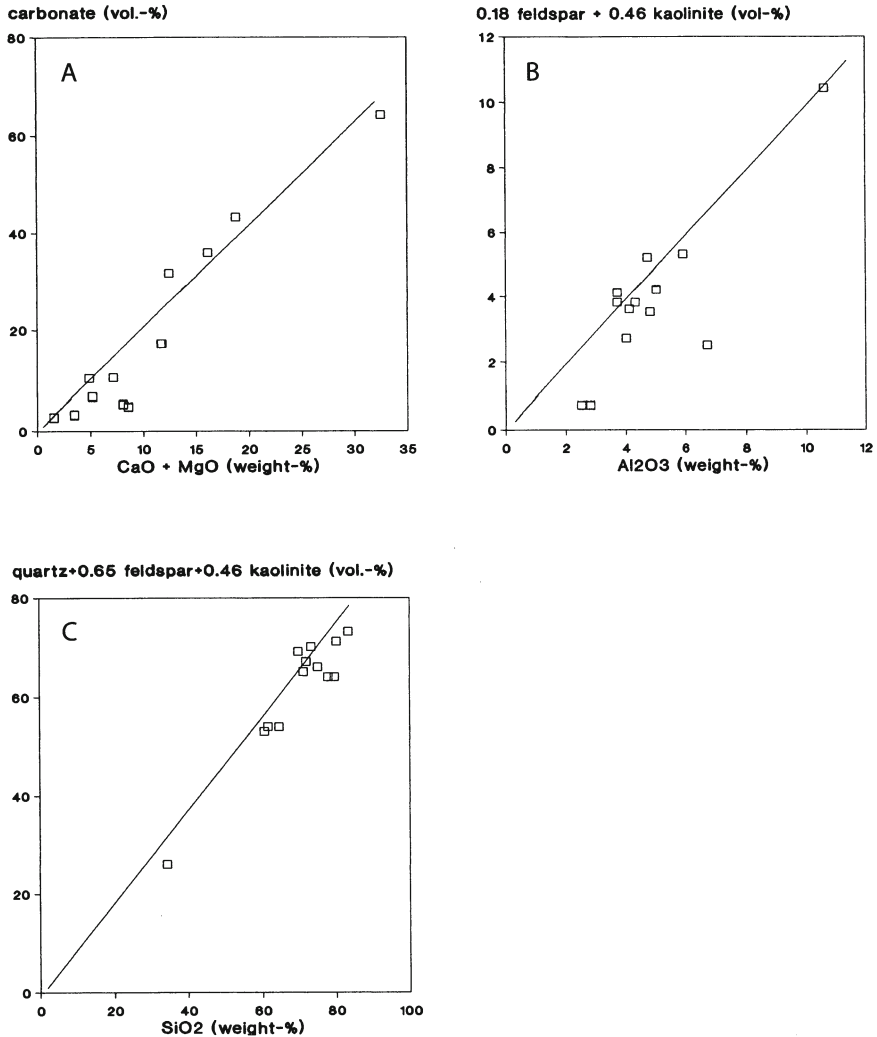


Fig. 10. Correlation of contents of selected oxides obtained from chemical analysis and their associated mineral contents detected by combined CL and image analysis. The proportions of oxides were calculated from the mineral formulae

es of alteration and formation of new phases. A combination of CL microscopy and image analysis allows quantification of different mineral phases. Only when the phases in rocks or technical products with a complex mineralogy have no luminescence, the use of CL to determine phase proportions is limited. All these advantages of CL offer promising perspectives in the specific investigations of minerals and technical products in research and industrial application.

Acknowledgements. I thank Vu Anh, M. Magnus, U. Münch, H. Walther, and D. Wolf (Freiberg) for their support during the investigations, for providing samples

and their helpful discussions. Dirk Habermann (Bochum) kindly provided spectral CL measurements. The help of R. Kleeberg (Freiberg) and U. Kempe (Freiberg) during XRD and microprobe analysis is gratefully acknowledged. Prof. Born and his colleagues from the Institute of Energy Process Engineering and Chemical Engineering (Freiberg) are thanked for the preparation of the model slags. I am very grateful to Guy Libourel for critical reading of the manuscript.

References

- Alvarez C, Benito MI, Baudin C, Mas R (1996) Cathodoluminescence as a tool to characterize MgO-C based refractories. In: International conference on cathodoluminescence and related techniques in geosciences and geomaterials, Nancy, Abstracts, pp 13–14
- Enders M (1995) Microanalytical characterization (AEM) of glassy spheres and anhydrite from a high-calcium lignite fly ash from Germany. *Cement Concrete Res.* 25:1369–1377
- Evans J, Hogg AJC, Hopkins MS, Howarth RJ (1994) Quantification of quartz cements using combined SEM, CL, and image analysis. *J. Sed. Petrol.* A64:334–338
- Fiske PS, Stebbins JF, Farnan I (1994) Bonding and dynamical phenomena in MgO: A high temperature $\{17\}O$ and $\{25\}Mg$ nmR study. *Phys. Chem. Miner.* 20:587–593
- Fratini F, Manganelli C, Pecchioni E (1996) The application of cathodoluminescence to characterize medieval mortars. In: International conference on cathodoluminescence and related techniques in geosciences and geomaterials, Nancy, Abstracts, pp 13–14
- Gaal RAP (1976–77) Cathodoluminescence of gem materials. *Gems and Gemology* 15:238–244
- Gorobets BS and Rogozhin AA (1996) Luminescence spectroscopy of mineral materials. In: 5-th International Congress on Applied Mineralogy, Warsaw, Programme and Abstracts, p 57
- Gorobets BS, Gaft ML, Podolski AM (1989) Luminescence of minerals and ores (in Russ). Ministry of Geology of the USSR, Moscow
- Gorobets BS, Litvintsev EG, Rogozhin AA (1996) Luminescence sorting of nonmetallic raw materials. In: 5-th International Congress on Applied Mineralogy, Warsaw, Programme and Abstracts, p 93
- Götze J (1995) Perspectives of hot-cathode luminescence microscopy in applied mineralogy. *Europ. J. Miner.* 7, Bh. 1: 91
- Götze J (1996a) Application of cathodoluminescence in environmental mineralogy. In: 5-th International Congress on Applied Mineralogy, Warsaw, Programme and Abstracts, p 61
- Götze J (1996b) Kathodolumineszenz von Quarz – Grundlagen und Anwendung in den Geowissenschaften. *Aufschluß* 47:215–223
- Götze J and Klemm W (1994) Comeback für die Dresdner Frauenkirche – Selektiver Rückbau weltberühmter Trümmer (Untersuchungen an Natursteinen und Mörteln historischer Gebäude). *Baustoff Recycling + Deponietechnik* 6:48–52
- Götze J and Magnus M (1997) Quantitative determination of mineral abundance in geological samples using combined cathodoluminescence microscopy and image analysis. *Europ J Miner* 9:1207–1215
- Götze J, Höhne D, Do TQ (1993) Genesis and melting behaviour of quartz raw materials. *Sprechsaal International Ceramics & Glass Magazine* 126:473–478
- Götze J, Krbetschek M, Habermann D, Rieser U., Wolf D (1996) Investigation of feldspars by spectral TL, CL, and (IR)OSL. In: 3rd European Meeting “Spectroscopic Methods in Mineralogy”, Kiev, Programme & Abstracts, p 21
- Habermann D, Neuser RD, Richter DK (1996) REE-activated cathodoluminescence of calcite and dolomite: high-resolution spectrometric analysis of CL emission (HRS-CL). *Sed Geol* 101:1–7
- Hagni RD (1984) Cathodoluminescence microscopy applied to mineral exploration and beneficiation. In: Park WC, Hausen DM, Hagni RD (eds) *Applied Mineralogy (Proc. 2nd Int. Congr. Appl. Miner.)*, AIME, New York, pp 41–66

- Hagni RD and Hagni AM (1996) The importance of ore microscopy and cathodoluminescence microscopy in the study of selected environmental problems. In: 5-th International Congress on Applied Mineralogy, Warsaw, Programme and Abstracts, p 33
- Hagni RD, Cash JW, Stewart KL (1996) Mineralogy and textures of cyclone dust, sludge, and accretions from a direct ironmaking plant at Universal, Pennsylvania. In: 5-th International Congress on Applied Mineralogy, Warsaw, Programme and Abstracts, p 91
- Hill RJ, Tsambourakis G, Madsen IC (1993) Improved petrological modal analyses from X-ray powder diffraction data by use of the Rietveld method I. Selected igneous, volcanic, and metamorphic rocks. *J Petrol* 34:867–900
- Karakus M and Moore RE (1996) Cathodoluminescence microscopy applications in ceramics. In: International conference on cathodoluminescence and related techniques in geosciences and geomaterials, Nancy, Abstracts, pp 73–74
- Keyn J and Schreiter P (1985) Zum Phasen- und Gefügebau von Braunkohlenfilter-aschen im Feinstkornbereich. *Silikattechnik* 36:341–343
- Kogut AI and Hagni RD (1995) Mineralogical characterization of phosphorus in fluorite ores and concentrates from Southern Africa. In: Hagni RD (ed) *Process Mineralogy XIII*, The Minerals, Metals & Materials Society, pp 15–27
- Machel HG and Burton EA (1991) Factors governing cathodoluminescence in calcite and dolomite, and their implications for studies of carbonate diagenesis. In: Barker CE and Kopp OC (eds) *Luminescence Microscopy: Quantitative and qualitative aspects*, SEPM, Dallas, pp 37–58
- Magnus M and Götze J (1996) Mineral composition of Lower Turonian sandstones of the Elbe zone: evidence from combined CL and image analysis. *Zbl Geol Paläont Teil I, H.1/2*: 287–306
- Marshall DJ (1988) *Cathodoluminescence of geological material*. Allen & Unwin, London
- McCauley JW (1975) Structural and chemical characterization of processed crystalline ceramic materials. In: Burke J (ed) *Proceedings of the 20th Sagamore Army Materials Research Conference*, Syracuse, Syracuse University Press, pp 175–209
- Motzet H, Göske J, Pankau H-G, Pöllmann H (1997) Kathodolumineszenz zur Untersuchung von Zementklinkern. *Europ J Miner* 9, Bh 1:258
- Mumenthaler T, Schmitt W, Peters T, Ramseyer K, Zweili F (1995) Tracing the reaction processes during firing of carbonate containing brick mixes with the help of cathodoluminescence. *Ziegeleiindustrie International* 5:307–319
- Münch U and Götze J (1994) Phasencharakterisierung von Braunkohlenflugaschen. *Abfallwirtschafts J* 6:772–781
- Neuser RD, Bruhn F, Götze J, Habermann D, Richter DK (1995) Cathodoluminescence: method and application. *Zbl Geol Paläont Teil I, H.1/2*:287–306
- Phillips MR, Moon AR, Stevens Kalceff MA (1996): The origin of cathodoluminescence from aluminium oxide. In: International conference on cathodoluminescence and related techniques in geosciences and geomaterials, Nancy, Abstracts, pp 113–114
- Ponahlo J and Brandstätter F (1996) The significance of cathodoluminescence on gemstone recognition. In: International conference on cathodoluminescence and related techniques in geosciences and geomaterials, Nancy, Abstracts, pp 123–124
- Ponahlo J and Koroschetz T (1985) Quantitative Kathodolumineszenz – ein neues Verfahren zur Unterscheidung echter von synthetischen Smaragden und Rubinen. *Z dt Gemmol Ges* 34:132–142
- Querol X, Fernandez-Turiel JL, Lopez-Soler A (1994) The behaviour of mineral matter during combustion of Spanish subbituminous and brown coals. *Miner Mag* 58:119–133
- Querol X, Fernandez-Turiel JL, Lopez-Soler A (1995) Trace elements in coal and their behaviour during combustion in a large power station. *Fuel* 74:331–343
- Raask E (1985) Mineral impurities in coal combustion. Behaviour, problems and remedial measures. Springer-Verlag, Berlin
- Ramseyer K, Baumann J, Matter A, Mullis J (1988) Cathodoluminescence colours of α -quartz. *Min Mag* 52:669–677

- Reeber RR, Goessel K, Wang K (1995) Thermal expansion and molar volume of MgO, periclase, from 5 to 2900 K. *Europ J Mineral* 7:1039–1047
- Remond G, Cesbron F, Chapoulie R, Ohnenstetter D, Roques-Carmes C, Schvoerer M (1992) Cathodoluminescence applied to the microcharacterization of mineral materials: a present status in experimentation and interpretation. *Scanning Microscopy* 6:23–68
- Sathyamoorthy A and Luthra JM (1978) Mechanism of thermoluminescence in magnesium oxide. *J Mat Sci* 13:2637–2644
- Schvoerer M (1996) Cathodoluminescence applications to archaeomaterials. In: International conference on cathodoluminescence and related techniques in geosciences and geomaterials, Nancy, Abstracts, pp 139–140
- Smith I (1987) Trace elements from coal combustions: emissions. IEA Coal Research, London
- Vu TA, Götze J, Burkhardt K, Ulbricht J, Habermann D (1997) Application of optical and spectral cathodoluminescence in the study of MgO refractories. *Interam* 47:164–167
- Walker G (1985) Mineralogical applications of luminescence techniques. In: Berry FJ and Vaughan DJ (eds) *Chemical bonding and spectroscopy in mineral chemistry*. University of Birmingham, pp 103–140
- Walther HB, Götze J, Wolf D (1995) Phase characterization of model slags. *Europ J Miner* 7, Bh. 1:260
- Werner M, Adam K, Schreiter P (1988) Die chemische Zusammensetzung der Glasphase und quantitative Phasenbestände von Flugaschen braunkohlenbefuerter Großkessel. *Silikattechnik* 39:263–266

Cathodoluminescence as a Tool in Gemstone Identification

JOHANN PONAHLLO

1

Introduction

The introduction of a method such as cathodoluminescence (CL) in gemmology calls for two prerequisites. First, the new method must be applied non-destructively, furnishing unambiguous results. Second, it has to enable a trained gemmologist to differentiate quickly and accurately between a natural gemstone, a synthetic or an artificial stone.

The first publication on CL was by Crookes (1879). Afterwards, it was Michel (1914, 1926) who systematically studied the CL phenomena of gemstones; and Pochettino (1913) who, at the same time, was investigating CL of minerals by means of a special spectrophotometer. Twenty years later spectral CL analyses of gemstones were carried out by Deutschbein (1932). In the following decades the interest in CL studies seems to have slackened. The renaissance began first among sedimentologists, with Sippel (1965) and many others, as soon as an easy-to-handle, cold cathode apparatus was developed by Herzog et al. (1970; see also Nickel 1978). Using this method, CL investigations of gemstones were started again by Gaal (1977) and later by Ponahlo (1988). In the 1970s, when petrologists became more and more interested in CL microscopy of thin sections and the use of CL spectroscopy, these techniques were practically unknown among gemmologists and restricted to research centres investigating diamonds. In this chapter, some recent developments of CL of diamonds will be discussed. Broader consideration will be given to the application of CL in testing coloured stones, since good results can be obtained with alexandrites, cordierites, emeralds, kyanites, some sapphires, spinels, topazes, and other gemstones. Special attention will be paid to the CL of green ornamental stones which are commonly known as jades and to some jade simulants. Important diagnostic CL features of some major synthetic counterparts will also be discussed.

2

Methods

When accelerated electrons hit the surface of a solid mineral or a semiconductor material CL may visually be observed. To work with energised electrons one

needs an evacuated compartment. For the study of CL effects in minerals and gemstones electron guns of the cold cathode type are frequently used. These are commercially available, whereas hot cathode apparatuses are still tailor-made for the application of the thin slide technique. The results described in this chapter were obtained with a cold cathode Luminoscope (Nuclide Corp., USA) making use of a large compartment that can house bigger stones or even a group of crystals. The Luminoscope was fixed to the table stand of a microscope. For visual observations, a Nikon F3 was mounted on the trinocular. The large compartment can be loaded, for example, with more than a dozen 1 ct cut diamonds, which can be inspected visually and the results documented in a very short time.

For taking CL spectra the trinocular of the microscope was combined with a motor-driven monochromator (380–1000 nm), a photomultiplier and an amplifier. This assemblage, manufactured by Zeiss, Germany, was connected to a Hewlett-Packard computer system. The microspectrophotometric computer-assisted assemblage was automated to run CL spectra within 20–25 s between 400 and 900 nm. The stepper motor could be adjusted to intervals of 0.5 nm or larger. CL spectra of one variety of gemstones were always taken under the same conditions of excitation with a reference stone. The distance between the surface of each sample and the front lens of the microscope was kept constant. The spectra were not corrected for spectral response. The experiments were carried out at room temperature.

3 Results

3.1 Diamonds

Cut and polished natural and synthetic diamonds were used for CL studies with their table facets as the target for the impinging electron beam. To compare CL results of natural with synthetic diamonds, only yellowish to brown natural diamonds were tested. Most of these diamonds show blue CL colours and straw-yellow geometric patterns. Figure 1a presents a microphoto of the CL colours of a luminescing brownish cut natural diamond. Some of these natural diamonds show also reddish, brown, green uniform CL and/or blue irregularly distributed blotches and, rarely, so-called Pueblo structures (Ponahlo 1992).

Synthetic diamonds are grown as cubo-octahedra. The samples that could be investigated were large experimental specimens made available by De Beers. They displayed yellow, green or blue CL colours within distinct growth sectors. The {001} faces of such cubo-octahedral synthetic diamonds luminesce in a yellowish green to greenish yellow CL colour, each sector exhibiting delicate parallel growth lines. Higher indexed faces show blue CL colours. The {111} faces remain dark at high temperatures. Some synthetic large diamonds contain small bundles of needles luminescing in a bright orange CL colour (Fig. 1b). The same kind of needles has been found in a synthetic diamond synthesised in Russia. Recently, four Siberian cognac-brown, cubo-octahedral synthetic diamonds were tested. One

specimen had its table facet polished. The other three stones contained artificially roughened table facets. They display a mixture of brown, green, violet and white CL colours. Fig. 1d documents the yellowish-tinted green CL of one of these synthetic diamonds with the polished table facet containing distinct sectoral growth zones. The {111} faces show up in black. In the roughened table facets of each of the three other synthetic stones a seed crystal was detected.

A CL microphoto of a natural rough diamond with cuboid growth – such stones are found commonly in the Jwaneng mine in Botswana, Africa – is reproduced in Fig. 1c, exhibiting growth features different from all the other natural and synthetic diamonds investigated so far.

In a recent study by Ponahlo et al. (1994) plasma-enhanced chemical vapor deposition (CVD) diamond films were investigated by means of cold cathode CL and CL microspectrophotometry. The films were grown by the same plasma-enhanced CVD method on various substrates such as SiAlON, Nb, Ta, W, cast iron, Ni, and Co. Cubic, octahedral and ballas-type diamonds could be differentiated by their respective CL colours and CL spectra. Two optical CL effects obtained with plasma-enhanced CVD diamond layers on SiAlON substrates are shown in Fig. 1e. The octahedral habit CVD diamond layers exhibit a mauve to violet CL colour; the cubic CVD diamond samples all luminesce in a yellow-orange CL colour.

3.2 Emerald

Over the last decade many natural and synthetic emeralds from all over the world have been observed by cold cathode CL. Up to now, nearly all specimens (for exceptions, see below) show a red CL. The CL intensities vary. Striking differences in CL intensities can be observed between natural and synthetic stones, both visually and by comparing the CL spectra, when taken under standardised conditions (Ponahlo and Koroschetz 1985; Ponahlo 1988). Typical examples of CL spectra of natural and synthetic emeralds are presented in Fig. 2.

3.3 Alexandrite

Alexandrite is a rare variety of chrysoberyl whose colour changes from green in daylight to red in incandescent light. Alexandrite is also synthesized by various enterprises because of its properties as a tunable laser material and has entered the gem market. Similar results to those described with emeralds may be obtained when studying the CL phenomena of alexandrites of gem quality from the major mining localities of the world. More than 170 specimens have been tested so far. Natural alexandrites are characterised by distinctly low CL intensities, synthetic alexandrites by higher ones. Older synthetic stones show additional effects, as reported by Gaal (1977) and Ponahlo (1989). The lowest CL intensities were found in alexandrites from the Takowaya mine in Russia. In Fig. 3, various CL spectra are presented which illustrate the differences in the intensities between natural alexandrites and man-made stones.

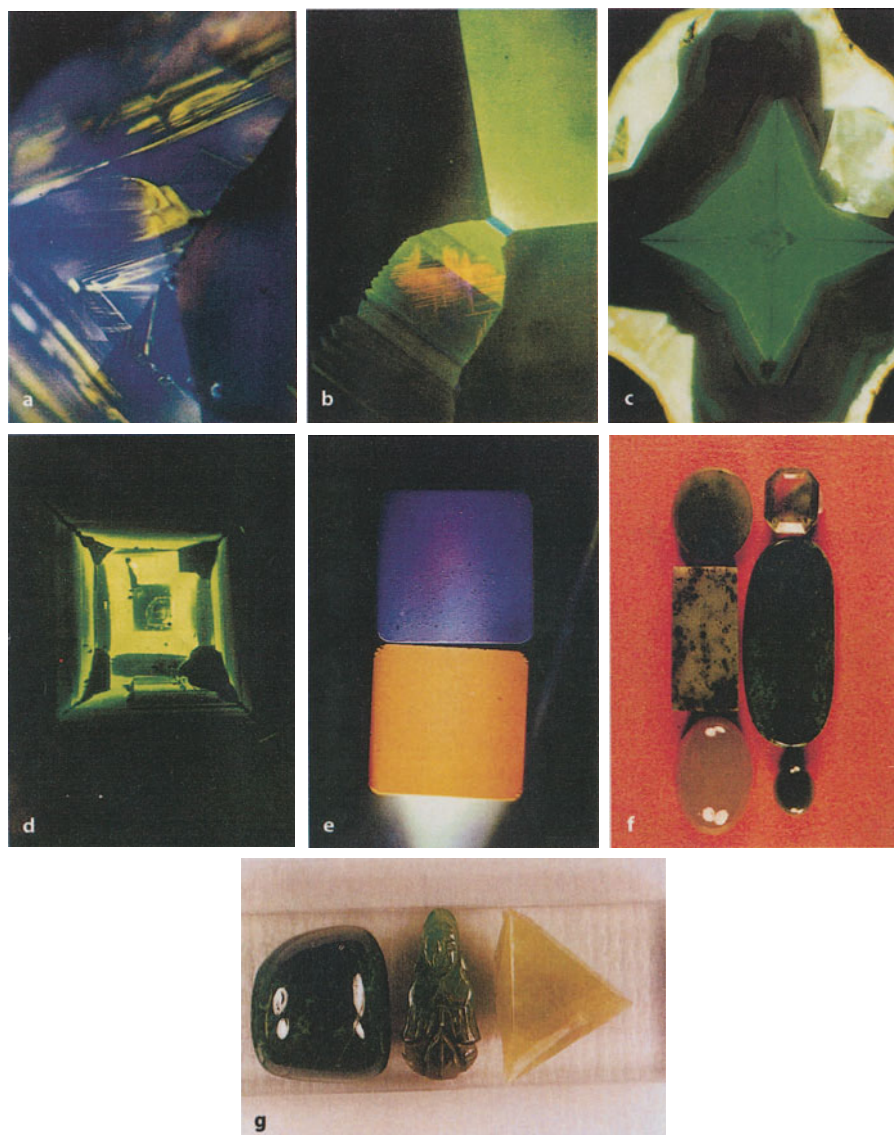


Fig. 1. **a** Brownish yellow, brilliant cut diamond (0.644 ct). CL blue and yellow. Conditions of excitation: 7.7 kV; 0.92 mA; magnification: 50 \times (24 \times 36 mm), Nikon F3, Kodacolor 400 ASA. **b** De Beers' experimental large synthetic diamond DMY 3 (4.104 ct) luminescing greenish yellow. It shows strong zoning of {100} faces and an intercalated blue CL of a higher indexed face. Also visible are orange needles of unknown origin. Conditions of excitation: 15 kV; 0.9 mA. 20 \times (24 \times 36 mm). **c** Small platelet of a cuboid natural diamond from the Jwaneng mine, Botswana, exhibiting a saturated green CL colour. Mixed habit growth made visible by means of CL is a characteristic feature of cuboid diamonds. Conditions of excitation: 15 kV; 0.9 mA. 40 \times (24 \times 36 mm). **d** Polished table facet of a cognac-brown synthetic diamond (0.852 ct) from Russia luminescing yellowish green showing sectoral growth. {111} faces are non-luminescent. Conditions of excitation: 10.0 kV; 0.85 mA. 28 \times (24 \times 36 mm). **e** CVD diamonds on SiAlON-substrates showing a yellowish green CL.

low orange CL colour for cubic habit, and a violet CL colour for octahedral habit. Conditions of excitation: 10.0 kV; 0.95 mA; macrophoto: $\beta=0.93$ (24x36 mm). f Vertical row, *left: top*, nephrite, Switzerland; *centre*, hydrogrossular, Transvaal; *below*, chalcedony, unknown locality. *vertical row, right: top*, glass; *center*, "maw-sit-sit", Myanmar (Burma); *below*, williamsite, USA. Largest diameter of the "Maw-sit-sit" cabochon=21.3 mm. g *Left*, a large hydrogrossular cabochon, misnamed "Transvaal Jade"; *centre*, a carved jadeite figurine; *right*, a polished triangle of californite. The jadeite is said to come from Myanmar (Burma). The californite is from a locality in the Austrian Alps. *Macrophoto*, incandescent light. The total length of the carved figurine=25 mm

CL SPECTRA OF NATURAL AND SYNTHETIC EMERALDS

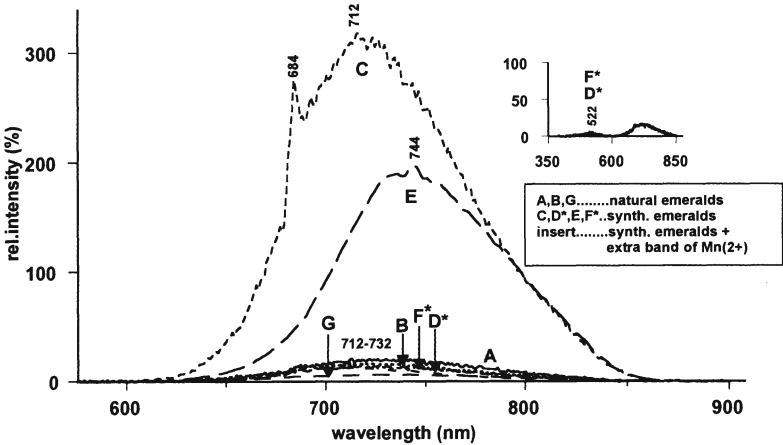


Fig. 2. CL spectra of natural and synthetic emeralds using a natural emerald as a reference stone. Standard conditions of excitation: 7.5 kV; 0.5 mA

CL SPECTRA OF A SYNTHETIC ALEXANDRITE REFERENCE STONE AND OF SOME NATURAL ALEXANDRITES FROM VARIOUS LOCALITIES

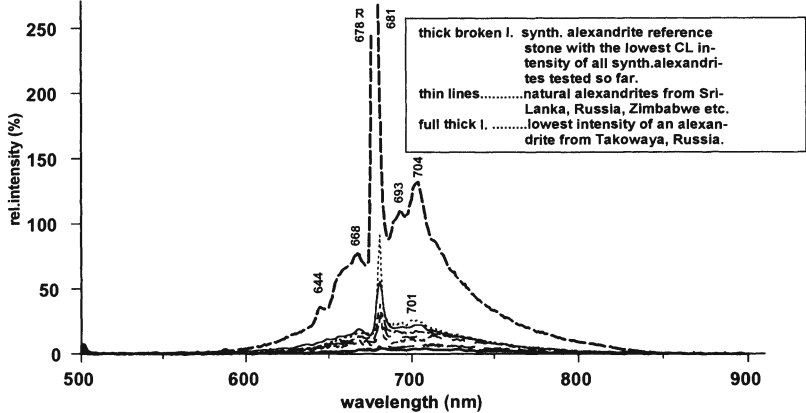


Fig. 3. CL spectra of natural alexandrites from various localities and a synthetic reference stone from Japan (1985). Standard conditions of excitation 9.0 kV; 0.9 mA

Since 1993 some natural alexandrites which were said to come from the new Malisheva mine in the same Ural region as the Takowaya mine exhibited such high CL intensities that at first they were considered to represent a new type of synthetic. On the table facet of an emerald-cut stone the CL intensity was 200 times that of a Takowaya alexandrite. Careful investigations of rough material from Malisheva put the natural origin of these alexandrites beyond doubt. Moreover, it was possible to excite the Cr^{3+} doublet at 683 nm by means of low energised incident wavelengths between 440 and 580 nm. This feature gave rise to the hypothesis that an unknown co-activator might be present, sensitising the CL of Cr^{3+} ions. But trace element analyses by means of EDPXRF (energy dispersive polarised X-ray fluorescence) to less than 5 ppm has failed to indicate the presence of a co-activator up to now. The form of the broad-band emission and the wavelength of the laser doublet is consistent with those discussed in detail by Henderson and Imbusch (1989, p.428; Figs. 9, 10). Some CL spectra of Malishevan alexandrites exhibit an additional broad CL band in the green and yellow spectral range never found in the CL spectrum of other natural alexandrites or synthetic stones. Figure 4 illustrates this fact. Further tests are underway to clarify these discrepancies.

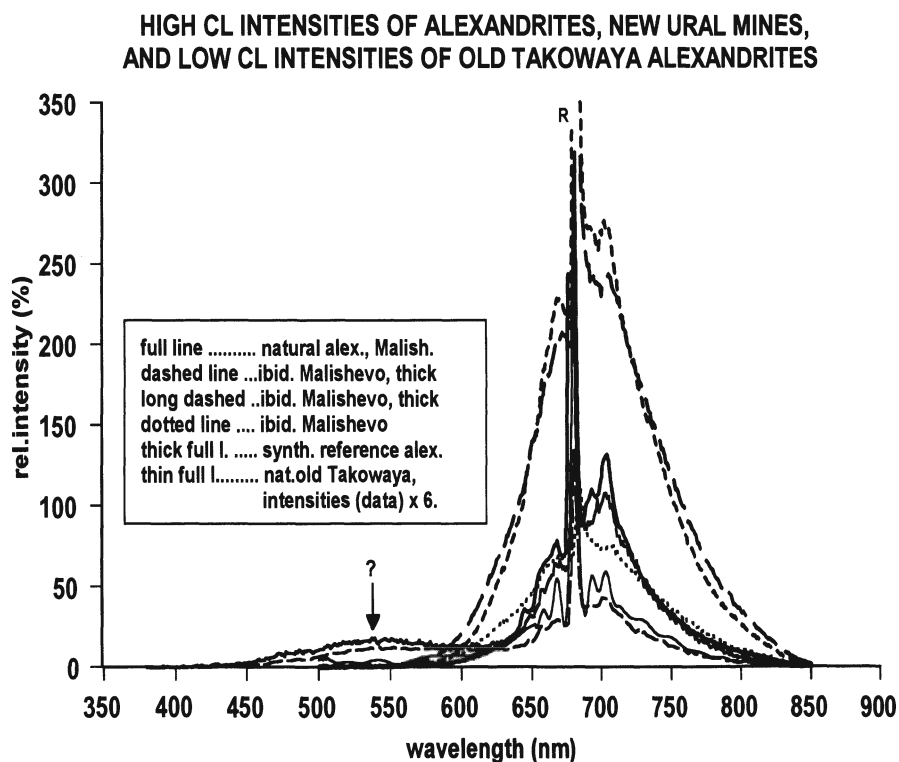


Fig. 4. CL spectra of rough and cut alexandrites from the new mine "Malisheva" in the Ural compared to CL spectra of old alexandrites from the Takowaya mine in the same region. Standard conditions of excitation: 9.0 kV; 0.9 mA

3.4 Ruby

Cathodoluminescence tests of rubies did not give such unequivocal results as found for emeralds and alexandrites. It is well known that modern heat-treated Verneuil rubies do not show optically curved striae. In a CL test the curved striae of such Verneuil synthetics nevertheless become visible and/or irregular colour patches or wavy growth lines may disclose their man-made origin. CL spectra can sometimes be useful when they contain side bands not observed in natural stones.

3.5 Sapphire

The blue sapphires from Sri Lanka and Burma both contain enough chromium to luminesce in a violet-red CL colour and display a distinct CL spectrum. Sapphires rich in iron do not luminesce at all. They can be recognised by both their primary and secondary inclusions and/or by colour zoning. If patchy rose-red or violet-red CL effects are observed, the sapphires have most probably been subjected to heat treatment. Diffusion-treated off-coloured stones from Burma, Sri Lanka or Thailand do not show any luminescence. Sometimes the nature of a blue sapphire can be elucidated by means of its CL spectrum. CL spectra of natural and synthetic blue sapphires have been published (Ponahlo 1990, 1993a,b).

CL spectra are helpful to differentiate quickly and non-destructively between a blue sapphire, a kyanite and other blue stones like lazurite. If such stones are cut "en cabochon" or mounted or carved, CL microspectrophotometry offers a fast and reliable method rendering unequivocal results (see also Ponahlo 1989; Figs. 24, 27; 1993a, Fig. 3).

3.6 The Cathodoluminescence of Colourless Gemstones

Colourless gemstones are interesting objects for CL research. Colourless topaz, fluorite, spinel, enstatite, and spodumene exhibit different CL colours and spectra. Occasionally, colourless sapphire crystals are found which show a blue and a red luminescing zone. The corresponding CL spectra are presented in Fig. 5. The dashed line represents the blue luminescing part and the full line the red one. The element concentrations of both zones determined by EDPXRF are listed in Table 1.

Table 1. Trace analyses of a colourless sapphire crystal

Element	Red area	Blue area I	Blue area II
Titanium	340	450	470
Chromium	13	7	5*
Iron	640	540	340
Gallium	130	140	150
Zinc	21	16	9

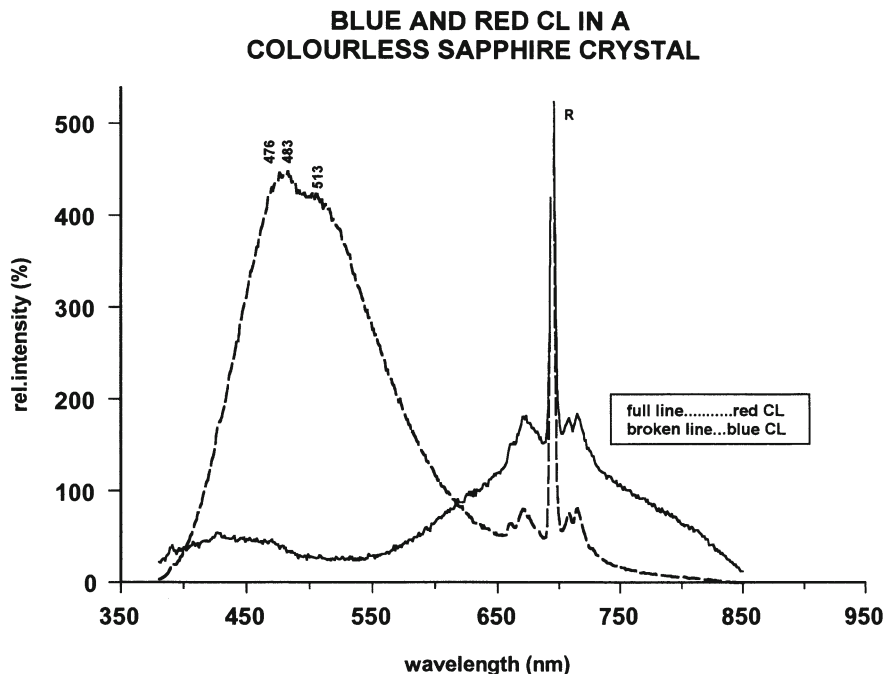


Fig. 5. CL spectra of a colourless corundum crystal exhibiting blue and red CL colours. Conditions of excitation: 8.5 kV; 0.6 mA

Surprisingly, 6 ppm chromium are capable of exciting a weak Cr^{3+} doublet, and 13 ppm chromium give rise to a full ruby spectrum with prominent side bands, even in the presence of more than 500 ppm iron. The blue CL of the crystal results from a broad short-wave CL band characterised by two peaks, at 472 and 483 nm, respectively, the nature of which is obscure.

3.7

Jade and Its Simulants

3.7.1

Jadeite

Jade in its proper sense comprises two minerals: jadeite, which is luminescent, and inert nephrite. Gemmologists have added the mineral chloromelanite (Keverne 1991; Deer et al. 1978). Also “maw-sit-sit” should be included here as a bright-green ornamental stone which originates from the same locality in northern Burma where most of the jadeite rough material of today comes from. “Maw-sit-sit” is a rock consisting of chrome-rich jadeite, kosmochlor and small black patches of chromite. Other green ornamental stones which are frequently confused with jadeitic jades do not luminesce and can be sorted out: chalcedony, glass, serpentine, smaragdite, steatite, verde-antique and verdite. Important luminescent sim-

ulants are amazonite, anorthoclase, hydrogrossular and californite. A green hydrogrossular variety of gem quality is mined in South Africa. It is sometimes misnamed "Transvaal Jade". Californite is a massive green variety of vesuvianite (Webster 1983).

In the macrophoto of Fig. 1f, taken in incandescent light, a series of commercial "jades" are presented. Vertical row, right: top, glass; center, maw-sit-sit, Burma; below, "williamsite", a chrysotile from the USA; vertical row, left: top, nephrite, Switzerland; center, hydrogrossular, Transvaal; below, green chalcedony, unknown locality. Of these six "jades" only two are luminescing, i.e. maw-sit-sit and the mineral hydrogrossular. Figure 1g shows a large hydrogrossular cabochon simulant on the left, a carved jadeite figurine in the center, and a polished yellow triangle of a "californite" on the right. Figure 6g illustrates the CL colours of two of these. The parrot-green to canary-yellow CL colour of the figurine contrasts with the characteristic reddish egg-yolk to reddish brown CL of the hydrogrossular. The latter shows some dark spots of non-luminescent chromite inclusions. CL spectra, dealt with later, facilitate the visual discrimination.

3.7.2

Visual Cathodoluminescence of Jadeite

The most important phase of luminescent natural jadeitic specimens is the mineral jadeite $\text{NaAl}(\text{Si}_2\text{O}_6)$. Other luminescent pyroxenes found in such samples are diopside $\text{CaMg}(\text{Si}_2\text{O}_6)$, chloromelanite $(\text{Ca},\text{Na})(\text{Mg},\text{Fe}^{2+},\text{Fe}^{3+})(\text{Si}_2\text{O}_6)$ and kosmochlor $\text{NaCr}(\text{Si}_2\text{O}_6)$, the chromium analogue of jadeite. Non-luminescing phases are amphiboles and chlorites, as described by Chhibber (1934), Harlow (1994), Morkovkina (1960), Takayama (1986) and others.

When studying the CL of jadeite samples under the microscope, two indicators for natural untreated jadeite were found: parrot-green to canary-yellow CL colours, and an interlocking granular texture (Fig. 6c). Less frequently, rhythmic zoning was observed (Fig. 6e). If the jadeite grades into chloromelanite, the bright green of jadeites turns into a much darker green, and the textural changes and CL colours become manifold, like those documented in Fig. 6d. Comparing Fig. 6d with Fig. 6a and 6g the CL phenomena may help to discriminate a green chloromelanite from a similarly coloured hydrogrossular. Maw-sit-sit may show a similar flame-like texture to chloromelanite, but is luminescing predominantly red. Moreover, their CL spectra differ. Figure 6f reveals that maw-sit-sit consists of relicts of chromite grains embedded in a ground mass of kosmochlor.

3.7.3

Cathodoluminescence Spectra of Jadeites

The CL spectra of jadeites are presented in Fig. 7. Parrot-green and/or canary-yellow luminescing samples exhibit three distinct bands. The most prominent one is in the green, with a maximum at 554 ± 4 nm. The smallest and weakest band can be found in the blue violet, peaking between 410 and 418 nm. A third broad band of varying intensity lies in the red spectral range extending into the NIR. Many green samples have the maximum of this red band between 686 and 693 nm. Rose-red luminescing green or greyish jadeites have this band shifted into the NIR, exhibiting a broad peak between 745 and 760 nm. If green or greyish green

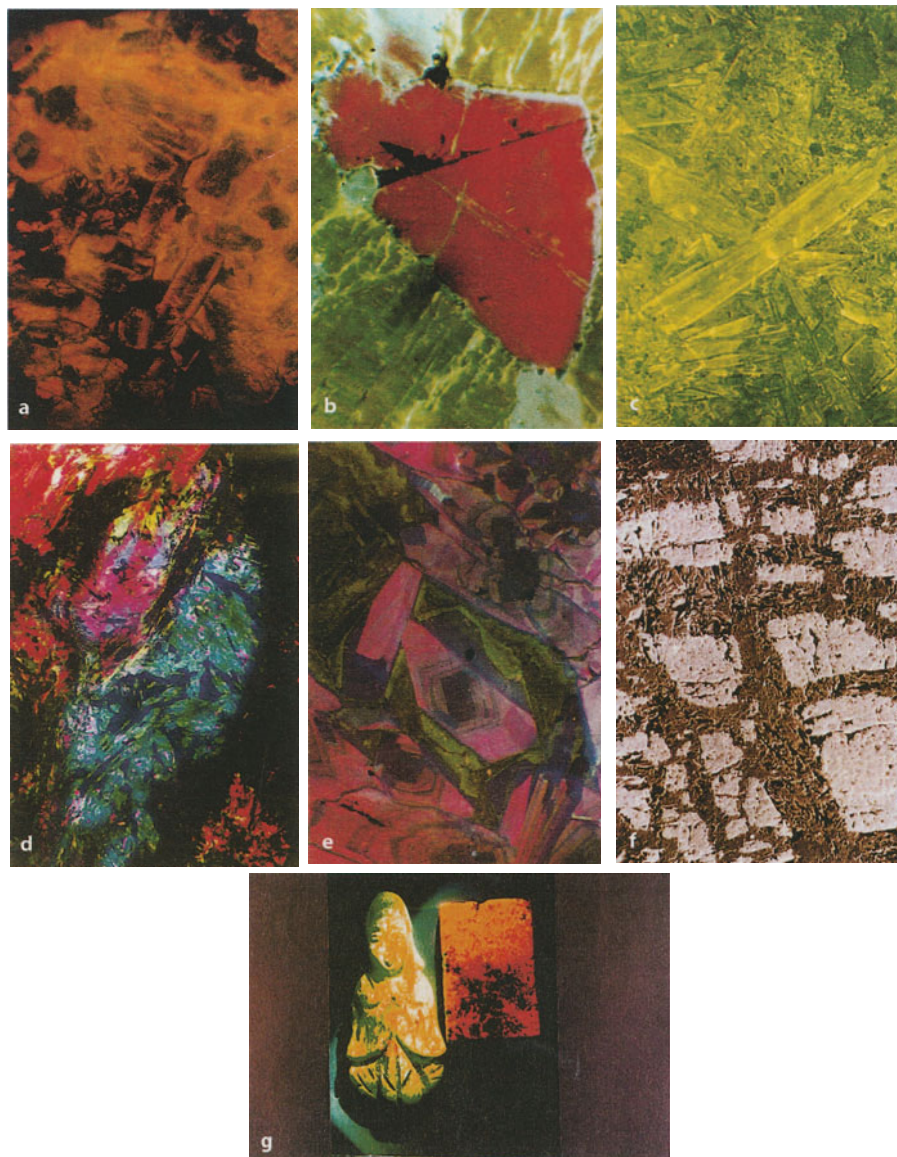


Fig. 6. **a** Hydrogrossular of Fig. 1f, *centre left*. All hydrogrossulars investigated so far exhibit a distinct yellow and/or brown to reddish brown CL of varying intensity. Under the impact of electrons relicts of choked and zoned feldspar grains become noticeable. Conditions of excitation: 7.0 kV; 0.80 mA; 40× (24×36 mm). **b** CL of an anorthoclase from Tanzania. Exsolved albite I shows sky-blue CL embedded in masses of fine tapering cross-hatched lamellae of anorthoclase. They appear brown or brownish purple to the eye, but as a brownish-tinted green on the photo. The large blocky crystal inclusion is albite II of different chemistry luminescing in a rubiginous CL colour. Length of the albite II inclusion=1.3 mm. Conditions of excitation: 15 kV; 0.9 mA; 40× (24×36 mm). **c** Natural green jadeite from Myanmar with a distinct columnar to fibrous texture. Parrot-green to canary-yellow CL. Conditions of excitation: 15.0 kV; 0.9 mA.

125× (24×36 mm). d Dark green chloromelanite from Myanmar showing red, blue and green mottled and patchy CL colours at higher beam energies. Conditions of excitation: 17 kV; 0.9 mA. 125× (24×36 mm). e Natural untreated green jadeite from Myanmar exhibits rhythmic zoning of predominantly red, green, blue CL colours. Conditions of excitation: 17 kV; 0.9 mA. 125× (24×36 mm). f “Maw-sit-sit” of Fig. 1f, *centre right*, with predominantly violet-red CL colour. The electron microscope reveals blocky relicts of non-luminescing chromite (bright) embedded in luminescing kosmochlor (dark brown). Length of the largest chromite grain (*lower right*)=27 μm. g CL elucidates the presence of two different minerals which show very similar daylight colours. Jadeite luminesces parrot-green to canary-yellow; hydrogrossular exhibits a brownish yellow to brownish-red CL colour. The californite of Fig. 1g is not shown. Conditions of excitation: 7.0 kV; 0.85 mA

jadeites luminesce blue-violet, the blue CL band remains unaltered, but the otherwise prominent band at 554 nm is reduced to medium or weak intensity. The band in the red becomes broader, its tail reaching into the NIR. The CL spectra of natural white or violet-tinted jadeites consist of a single strong to very strong small band in the blue-violet, like the CL spectra of some green samples, but without any feature in the red or NIR, and with a greatly diminished signal in the yellow-to-green spectral range.

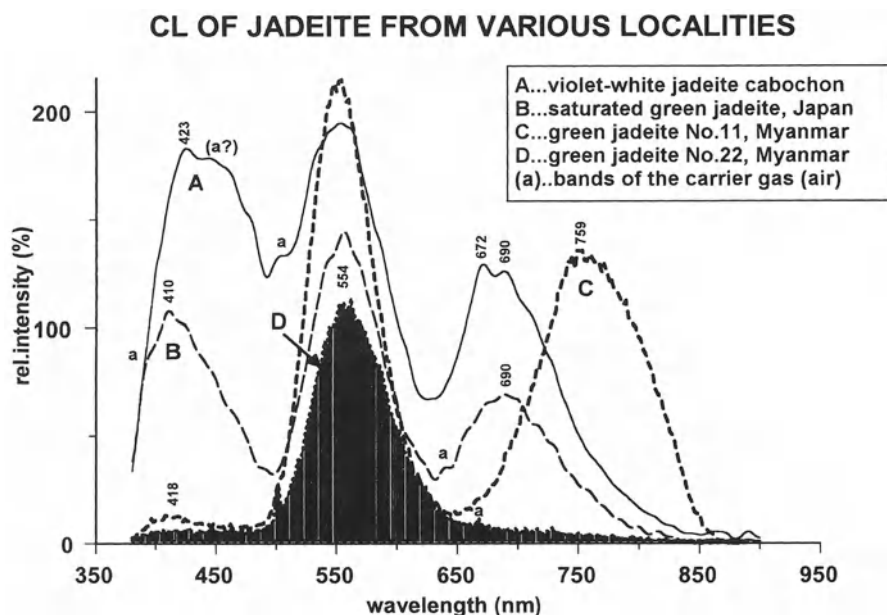


Fig. 7. CL spectra of green jadeites from Myanmar (Burma) and Japan. The filled spectral band has been found in all spectra of jadeites investigated so far. Most probably, it is caused by Mn^{2+} ions which would be responsible for the parrot-green to canary-yellow CL colours. Conditions of excitation: 12.5 kV; 0.9 mA

3.7.4

Cathodoluminescence and Cathodoluminescence Spectra of Maw-Sit-Sit and Chloromelanite

Comparing the CL spectra of maw-sit-sit in Fig. 8 with those of jadeite in Fig. 7, the strong and characteristic band of jadeite at 554 nm seems to have lost its strength in the former, becoming barely visible in maw-sit-sit. Moreover, maw-sit-sit does not show any CL feature in the blue spectral range. If the amount of kosmochlor in maw-sit-sit increases, the red CL band moves further into the NIR with a broad peak between 760 and 800 nm. In the microscope this red/NIR band becomes noticeable as a subdued violet-tinted red CL colour. Occasionally, small bright red luminescing inclusions in maw-sit-sit may exhibit thermoluminescence at higher beam energies.

3.7.5

Cathodoluminescence of Amazonite and Anorthoclase

Green amazonite is not frequently used in jewelry, but fine material can be obtained from various localities in Canada, Mozambique, Norway, USA, etc. Amazonite can be distinguished visually from jadeitic jade or nephrite by its content of exsolved white albite. A new jade simulant is anorthoclase of gem quality, which supposedly originates from Tanzania. It is characterised by a fine gridiron of microperthitic exsolution lamellae, not so well resolved as in amazonite. CL

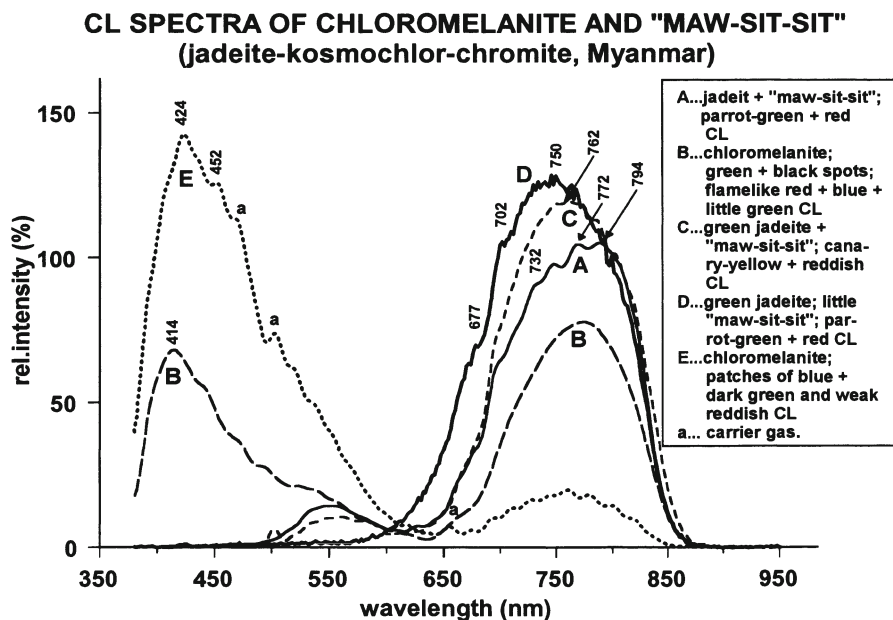


Fig. 8. CL spectra of "maw-sit-sit" and chloromelanite from Myanmar. "Maw-sit-sit" lacks spectral features below 500 nm. Chloromelanite does not show a significant CL band in the green and yellow spectral range. Conditions of excitation: 15 kV; 0.9 mA

tests of anorthoclase reveal the sky-blue CL colour characteristic of albite (Fig. 6b). This exsolved feldspar (albite I) is embedded in the main constituent of anorthoclase, which exhibits a brownish-red CL colour. It contains cross-hatched, fine tapering lamellae. The large crystal inclusion in the centre of the anorthoclase sample is an albite of different chemical composition (albite II). It displays a ruby-like CL colour unlike anything observed in jadeitic jades.

3.7.6 Cathodoluminescence Spectra of Amazonites and Anorthoclase

Amazonites exhibit three types of CL spectra. They are presented in Fig. 9. Type 1 is characterised by a single strong band in the violet (E). Amazonites from Pike's Peak, USA (C), from Norway and the Pack, Austria (A), belong to the spectral type 2 with a single broad band extending from 380 to 750 nm and showing two maxima, one at ~475 and the other at ~518 nm. South African amazonites show the same type (D) of CL spectrum, but with a weak band in the NIR that extends between 816 and 834 nm. The anorthoclase furnishes the third type of CL spectrum (F). It consists of a smaller type 2 band in the blue spectral range plus a new strong band in the red, peaking between 706 and 720 nm. Monapo amazonites from Mozambique show a similar CL spectrum (B). The same holds for the CL spectrum of the albite II inclusion of Fig. 6b shown as (G), except for the CL band in the red which has tripled intensity.

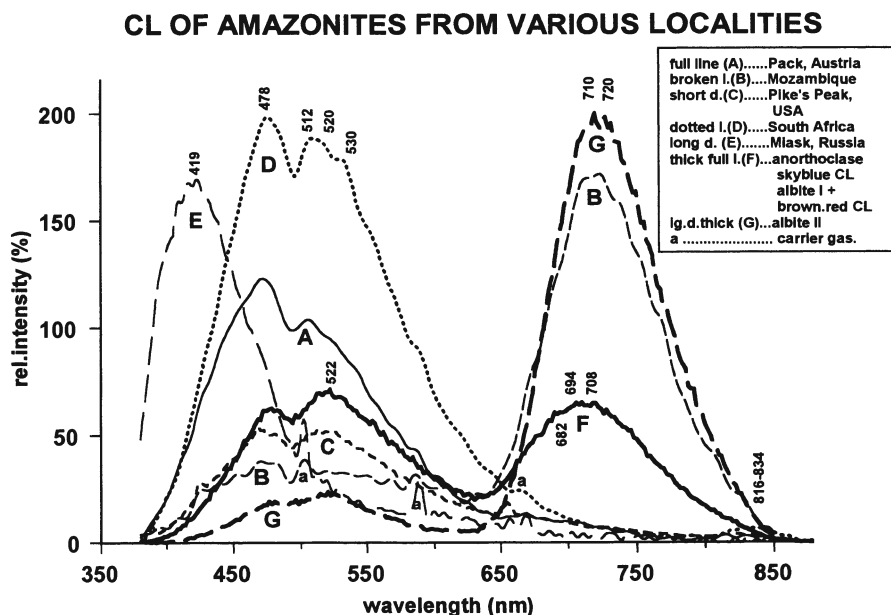


Fig. 9. CL spectra of rough and polished amazonites from various localities. Condition of excitation: 15.0 kV;0.9 mA. For details, see text

3.7.7 Cathodoluminescence of Hydrogrossular and Californite

Hydrogrossular of gem quality was first described by Hall (1925). It is found at Buffelsfontein in the Rustenburg district, South Africa, as a red and a green variety. Only the green one is of interest as a simulant of jadeitic jades. The yellow and/or brown CL of green hydrogrossulars is reproduced in the microphoto of Fig. 6a. The relicts of feldspar grains can clearly be recognised without making use of a destructive thin section technique. The non-luminescing phases in this plate are serpentinised clinopyroxenes. Similar results are obtained with cabochons or carved pieces of hydrogrossular (Fig. 1f,g and Fig. 6g). Polished californites tested so far luminesce in a uniform brownish copper-red colour without a significant texture, which helps to distinguish them from jadeitic jades and the other simulants mentioned. The CL spectra of hydrogrossular and californite are dealt with in the Discussion (Sect. 4.4.3.).

4 Discussion

4.1 Diamonds

Within the last two decades a number of industrial enterprises have started production of synthetic diamonds for technical purposes. Today synthetic diamonds can be produced of near-colourless quality (Pal'yanov et al. 1990). Analytical methods of their detection have also been refined, which should help gemmologists to distinguish between natural diamonds and their synthetic counterparts: UV, VIS, IR spectral analyses and X-ray topography (Field 1992; Shigley et al. 1995; Welbourn et al. 1996). By bombarding diamonds with electrons, Woods and Lang (1975), Vishnevsky (1975), and later Hanley et al. (1977), showed that most natural yellow or brown cut stones are characterised by peculiar CL patterns forming straw-yellow triangles or polygons within an overall blue luminescing sample. Macrophotos of CL tests with large experimental synthetic diamonds have been published by Burns et al. (1990) and by Pohnahlo (1992). Recently, a chart was issued by the GIA (Gemological Institute of America; Shigley et al. 1995) proposing suggestions for the visual CL method as a future standard technique for testing diamonds. Figure 1a,b gives evidence for the fine details of growth conditions made visible by means of CL. Even the latest near-colourless synthetic diamonds investigated can be differentiated by uneven luminescence patterns of blue CL and sectoral growth zones (Shigley et al. 1997) together with a prolonged phosphorescence.

The nature of the orange needles in synthetic diamonds shown in Fig. 1b could not be discerned. When Shigley et al. (1993) reported on the use of cold cathode CL to reveal sectoral growth phenomena in yellow diamonds grown in Russia, they did not mention orange needles in the synthetic diamonds they investigated. Quite recently Shida (1997) has reported on the advantage of testing a broad

range of natural yellow cut diamonds by means of CL microscopy, used as a routine method in Japan.

As to the CL features of cuboid natural diamonds (Fig. 1c), such a mixed habit growth has not been detected with any synthetic diamond grown during high temperature and high pressure synthesis. They are grown as nearly perfect cubo-octahedra. Therefore the CL image of Fig. 1d reveals octahedral growth features along the four arms, which luminesce bright green, and cubic growth features in between, leading to re-entrant outer surfaces of these type of diamonds which have already been described by Suzuki and Lang (1976) and Welbourn et al. (1989).

The use of CL in the study of CVD diamond films has been documented by Collins et al. (1989a,b) and Robins et al. (1989) among others, but they used SEM techniques, not cold cathode CL microscopy or CL microspectrophotometry. Robins et al. (1989) mentioned violet CL colours of octahedral CVD diamond layers on silicon substrates.

Our own recent cold cathode CL studies showed that a yellow orange CL colour is excited in cubic CVD diamonds on SiAlON substrates and a violet CL colour in octahedral CVD diamonds on the same substrates as shown in Fig. 1e. Using CL microspectrophotometry defect centres in the CVD diamond layers became visible. The CL result obtained with 30 CVD samples make it feasible to characterise CVD diamond layers on different metal and ceramic substrates. It was proposed to use the cold cathode CL method for control of the morphology in a possible industrial production of CVD diamond films.

4.2 Emeralds

As early as 1879, Crookes reported the crimson-red CL of emeralds. However, Gaal (1977) tested emeralds visually by means of cold cathode CL microscopy and found no luminescence. From the CL spectra of Fig. 2 it is evident that emeralds emit CL that can be measured and quantified. The area under the spectral curve is integrated and the result compared with those of other emeralds whose CL spectra have been taken under the same conditions of excitation. The integrated area is proportional to the CL intensity. From Fig. 2 follows that natural emeralds are characterised by a low CL intensity, whereas synthetic stones show a high CL intensity, several times that of natural ones. The effect is based on the activation of CL by Cr^{3+} ions and on the quenching effect by Fe^{3+} ions. All synthetic emeralds contain very little or no iron. Thus the CL of a synthetic emerald must be higher than that of a natural one. Synthetic emeralds deliberately grown with high iron contents to quench CL do not match the pleasing emerald-green daylight colour. Their absorption spectra disclose strong iron lines that can even be detected with a hand spectroscope. Yet, among the emeralds tested so far, some exceptions to this rule exist:

1. Some Russian hydrothermally grown synthetic emeralds. They may show no CL at all apart from a short-lived green flash at the beginning of the bombardment.
2. Australian synthetic "Byron" emeralds. They are coloured by vanadium instead of chromium. Such specimens betray themselves by careful inspection in the

direction of the optical axis under crossed polarisers by strong undulous extinction phenomena.

3. Some hydrothermal synthetic emeralds produced in Austria. Their CL spectrum (Fig. 2, insert) contains an additional distinct emission band at 522 nm, probably caused by traces of Mn^{2+} ions. A similar band between 518 and 528 nm has been found in many spinels. Lanver and Lehman (1978) have ascribed it to Mn^{2+} ions in tetrahedral configuration. The same holds for the green CL spectrum of willemite at 525 nm.

4.3

Rubies and Sapphires

Cathodoluminescence macro- and microphotos as well as CL spectra of rubies from various localities have been published (Ponahlo 1988, 1989, 1993a,b), but no routine method could be defined that would clearly differentiate between the majority of natural and synthetic rubies on the market today. The examples given indicate the possibilities offered by cold cathode CL.

Studies of the CL effects in sapphires would comprise investigations of a great variety of coloured specimens from different localities including heat-treated and diffusion-treated stones, besides the many blue synthetics of countless producers. Some preliminary information has already been provided by Ponahlo (1993a). Only a few diffusion-treated blue sapphires have been studied at the present time. These stones show strong quenching effects of CL. This results from the increase of Fe^{2+} , Fe^{3+} and Ti^{4+} ion concentrations in the outermost thin diffusion-treated layers of the cut stone which the electron beam cannot penetrate. Thus, for surface-treated gemstones and ornamental stones, further tests will show whether CL offers an advantage as a non-destructive, discriminatory analytical method.

Sometimes the nature of a blue sapphire can be elucidated by means of its CL spectrum (Ponahlo 1993). CL spectra may help to distinguish between different blue minerals like sapphire, kyanite and lazurite, especially if stones are cut "en cabochon", carved or mounted (see also Ponahlo 1989, Figs. 24 and 27; 1993a, Fig. 3).

4.4

The Jade Group and Its Simulants

4.4.1

Jadeite, Chloromelanite and Maw-Sit-Sit

Very few publications exist on CL phenomena of jadeite and jadeitic jades; none on maw-sit-sit. Görz et al. (1970) mentions a wine-red CL of jadeite with a rapidly decaying intensity (cited in Marshall 1988, p. 52).

The visual microscopic distinctions of jadeites and simulants by means of the CL colours and textures given above are self-explanatory. Despite the many shades of CL colours observed with jadeite, the CL spectra show only a few diagnostic features (Fig. 7). The blue band peaking between 410 and 418 nm cannot be assigned to any activator ion at present. In the opinion of many researchers any blue CL in silicates is excited by one or two hitherto unknown defect centres

(Walker 1983). By analogy with CL spectra of diopsides the broad strong band at 554 nm is assigned to Mn^{2+} ions. It is well known that diopside emits two CL bands that have been assigned to Mn^{2+} ions in M1 sites at 588 nm and to Mn^{2+} ions in M2 sites at 690 nm (Walker 1985). Manganese has a preference for the latter, but diopsides also show the 588 nm emission band. In spectra of jadeites the band is shifted to 554 nm and signals the presence of Mn^{2+} in M1 sites where it replaces Na^+ . There it is responsible for the parrot-green to canary-yellow CL colour of many jadeites and jadeitic jades. It is missing in most chloromelanites and maw-sit-sits (see Fig. 8). The third strong band of jadeite in the red and/or NIR may be excited either by Cr^{3+} or Fe^{3+} ions. Gorobets and Walker (in Marfunin 1995, p. 142) prefer to ascribe this band to low-field Cr^{3+} ions. This explanation seems plausible because in white or violet jadeites which do not contain Cr^{3+} ions, no CL band could be observed between 684 and 696 nm. The frequently observed shift of this band towards longer wavelengths up to 760 nm cannot be explained at present. Low temperature CL and excitation spectra might bring more insight.

A recent CL investigation of chemically treated and impregnated jadeites (Ponahlo 1996) furnished diagnostic evidence for how to distinguish quickly between untreated and chemically treated and/or dyed jadeites.

4.4.2

Amazonite and Anorthoclase

Marfunin (1979) and Tarashchan et al. (1973) describe defect centres in amazonite feldspars. They propose Pb^+/Pb^{2+} ions being responsible for a CL band in the UV range at 294 nm. This spectral range could not be investigated. Tarashchan (1978, p. 191) mentions albite with a broad band at 470 nm which he assigns to an AlO_4^{4-} centre and another one at 570 nm excited by Mn^{2+} ions. In this work the band maxima are found at 478 nm and between 512 and 530 nm. The first one causes the sky-blue CL colour which is observed in albites from many localities, as documented by Marshall (1988). No explanation for the second band can be given at the present time. The strong band in the NIR of albite II of anorthoclase, of amazonites from Monapo and from other localities is most probably evoked by Fe^{3+} ions in tetrahedral configuration (Telfer and Walker 1978; Tarashchan 1978). SEM analyses support such an assignment, with albite I containing 0.08 wt% and albite II 0.23 wt% Fe_2O_3 . Many adularia feldspars show similar CL bands in the same spectral ranges (Ponahlo 1993a).

4.4.3

Hydrogrossular and Californite

The brownish CL colour of hydrogrossulars is reflected in the spectrum documented in Fig. 10. However, the texture (Fig. 6a) is also a diagnostic aid to differentiate it from jadeite, chloromelanite and maw-sit-sit. The green hydrogrossular is characterised by two strong bands, one in the yellow, the other of equal intensity in the red. The latter extends into the NIR and has narrow peaks at 689, 701 and 717 nm. Californite emits a single band with a maximum at 593 nm that nearly coincides with the 590 nm band of the green hydrogrossular variety. The red hydrogrossular variety lacks the long wave band.

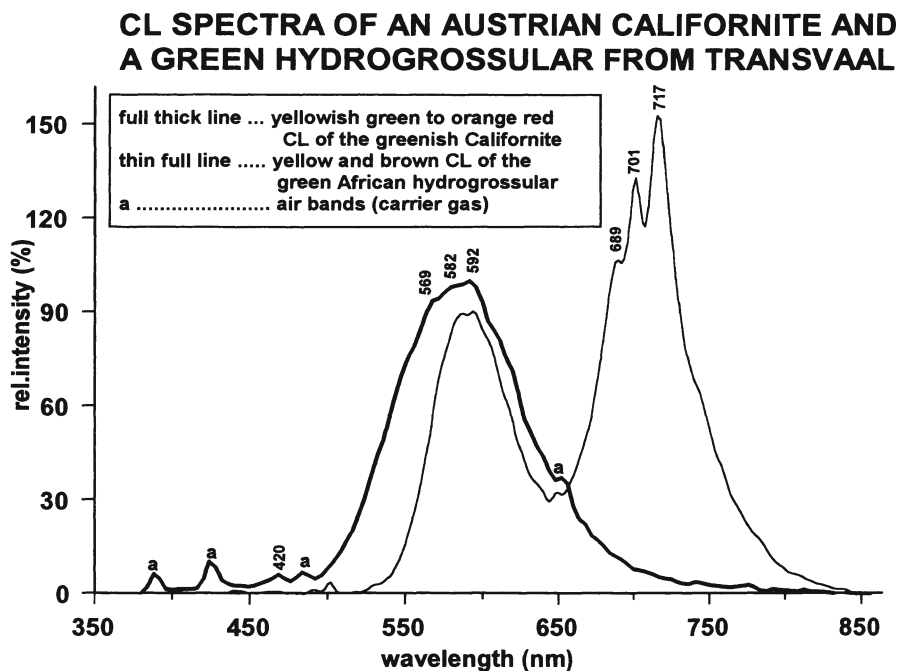


Fig. 10. CL spectra of a green hydrogrossular from Transvaal and a brownish yellow californite from Austria. Conditions of excitation: 7.0 kV; 0.85 mA

Arguing that the lattice of the hydrogrossular contains eightfold coordinated Ca^{2+} ions which can be replaced by Mn^{2+} ions, Green (1981) assigns the 590 nm band to activated Mn^{2+} ions. Octahedrally coordinated Al^{3+} can be replaced by Cr^{3+} ions. For the CL band in the red both Mn^{2+} and Cr^{3+} ions are possible candidates. Green (1981) finds a Cr^{3+} activated band in the NIR at 752 nm, but his findings are based on (OH)-free grossulars. The mean ratios of Cr/Fe calculated for the hydrogrossulars of this investigation were 0.33 and ≤ 0.06 for the green and the red samples, respectively. The iron content of red and green hydrogrossulars varied between 0.4 and 7 wt% FeO. The mean manganese content of five green hydrogrossular samples was 1.6 wt%, that of the red specimens as high as 5.3 wt%. If the CL band in the red is excited by chromium ions, then, most probably, the red CL band in the red variety is quenched by its high iron content. In green hydrogrossulars this CL band could always be excited but not the 590 nm band.

5

Conclusions

These investigations have made obvious the great diagnostic potential of CL in disclosing subtle chemical and physical changes of surface structures and textures in many gemstones, ornamental stones and artefacts. Evidently, one main field of

application is the discrimination of natural and synthetic diamonds. Figure 1a–d reveals striking CL differences between natural diamonds and their synthetic counterparts. The visual CL microscopy at low beam energies can easily be used by trained gemmologists and will render unequivocal results. Photographs of luminescing diamonds of any kind should be taken at less than 7 kV and 0.4 mA and a beam density of $\leq 15 \text{ Wcm}^{-2}$. The excitation parameters can easily be modified as soon as new types of synthetic diamonds may appear on the market.

CVD diamonds can also be tested by the same methods especially for studies of the morphology of diamond layers. But further tests would need to be applied as a quality control method in the production of low pressure synthesised diamond layers.

The examples given with emeralds and alexandrites show that cold cathode CL and microspectrophotometry are reliable and fast. Because of the ease of preparation and the number of specimens that can be tested in one run, it seems feasible to introduce CL as a routine method in gemmological laboratories, especially for differentiating between natural and synthetic alexandrites, should they lack significant inclusions. The same holds for emeralds, but with the reservations already mentioned, and by considering the worldwide efforts made to enhance low quality emeralds and to improve synthetic products.

Given the increasing number of simulants and treated jades on the market in Asia, the most promising results are obtained when studying ornamental stones of the jade group. For these materials, cold-cathode CL methods should become much more significant. Green jadeite and jadeditic jades are differentiated by their CL colour, rhythmic zonation, texture and CL spectra from simulants like green hydrogrossular, saussurite (Ponahlo and Brandstätter 1997), californite, dyed jades, chloromelanite and maw-sit-sit. Necklaces, carved figurines and cabochons can also be tested non-destructively. The size of a sample is limited only by the construction of the CL compartment that rests on the table stand of the microscope (Luminoscope, maximum sample size: $7 \times 4 \times 3.5 \text{ cm}$).

Acknowledgements. The author, who works as an independent research associate at the Museum for Natural History in Vienna, is much indebted to Prof. Dr. Gero Kurat, Director of the Department for Mineralogy and Petrography in the Museum for Natural History, and to the reviewers for very valuable advice and most helpful criticism. He gratefully acknowledges the support of this work by HR Dr. Gerhard Niedermayr of the same department, supplying on loan various samples of alexandrites, jades and simulants from the collection of the Museum for Natural History in Vienna. His thanks also go to Dr. Franz Brandstätter at the same department for carrying out the SEM analyses of gemstones and for the excellent cooperation.

References

- Burns RC, Cvetkovic V, Dodge CN, Evans DJF, Rooney M-LT, Spear PM, Welbourn CM (1990) Growth-sector dependence of optical features in large synthetic diamonds. *J. Cryst. Growth*, 104, 257–279

- Chhibber HL (1934) The mineral resources of Burma. Macmillan, London
- Collins AT, Spear PM (1983) The 1.40 eV and 2.56 eV centres in synthetic diamond. *J. Phys. C: Solid State Phys.*, 16, 963–973
- Collins A T, Kamo M, Sato Y (1989a) Optical centres related to nitrogen, vacancies and interstitials in polycrystalline diamond films grown by plasma-assisted chemical vapour deposition. *J. Phys. D: Appl. Phys.* 22, 1402–1405
- Collins AT, Kamo M, Sato Y (1989b) Intrinsic and extrinsic cathodoluminescence from single-crystal diamonds grown by chemical vapour deposition. *J. Phys.: Condens. Matter* 1, 4029–4033
- Crookes, W (1879) Contributions to molecular physics in high vacua. *Phil. Trans.* 170, 641–662
- Deer WA, Howie RA, Zussman J (1978) *Rock-Forming Minerals*, 2 A, Single Chain Silicates, 2nd ed., Longman
- Deutschbein O (1932) Die linienhafte Emission und Absorption der Chromphosphore. *Ann. Phys.* 14, Teil I: 712–728, Teil II: 729–754
- Field JE (1992) The properties of natural and synthetic diamond. Academic Press Ltd., London
- Gaal RAP (1977) Cathodoluminescence of gem materials. *Gems & Gemology* 15, 237–244
- Görz HN, Bhalla RJR, White E (1970) Detailed cathodoluminescence characterization of common silicates. *Penn State Univ Spec Pub* 70–101, 62–70
- Green CR (1981) Spectroscopic studies of transition metal luminescence centres in silicates. PhD Thesis, University Manchester
- Hall AL (1925) Jade (massive garnet) from the Bushveld in the Western Transvaal. *Trans. Geol. Soc. South Africa* 27, 39–55
- Hanley PL, Kiflawi I, Lang AR (1977) On topographically identifiable sources of cathodoluminescence in natural diamonds. *Phil. Trans. Roy. Soc. London, A* 284, No. 1324, 329–368
- Harlow GE (1994) Jadeitites, albitites and related rocks from the Montagua Fault Zone, Guatemala. *J. metamorphic Geol.* 12, 49–68
- Henderson B and Imbusch GF (1989) *Optical spectroscopy of inorganic solids*. Oxford Science Publications, Clarendon Press
- Herzog LF, Marshall DJ, Babione RF (1970) The luminoscope – a new instrument for studying the electron-stimulated luminescence of terrestrial, extra-terrestrial and synthetic materials under the microscope. In: *Space Science Applications of Solid State Luminescence Phenomena*. J.N. Weber & E. White (eds.) MRL Publ.70–101. Pennsylvania State University, Univ. Park, PA, USA, 79–98
- Keverne R (1991) *Jade*. Van Nostrand Reinhold, New York
- Lang AF, Meaden GM (1991) Complementary orientation-dependent distribution of 1.40 and 2.56 eV cathodoluminescence on vicinals on {111} in synthetic diamonds. *J. Crystal Growth* 108, 53–62
- Lanver U, Lehman G (1978) Luminescence spectra of Mn (II) in different symmetries. *J. Luminescence* 17, 225–235
- Marfunin AS (1979) *Spectroscopy, Luminescence and Radiation Centres in Minerals*. Springer Verlag New York
- Gorobets BS, Walker G (1995) in Marfunin AS (ed): *Advanced Mineralogy, Vol.2, Methods and Instrumentation*. Springer-Verlag, Berlin
- Marshall DJ (1988) *Cathodoluminescence of Geological Materials*. Unwyn Hyman, Boston
- Michel H (1914) *Die künstlichen Edelsteine*. 1st ed. Wilhelm Diebener G.m.b.H., Leipzig
- Michel H (1926) *Die künstlichen Edelsteine*. 2nd ed. Wilhelm Diebener G.m.b.H., Leipzig
- Morkovkina VF (1960) Jadeitites in the hyperbasites of the Polar Urals. *Izvestia Akademia Nauk. SSSR, series geologia*, 4
- Nickel E (1978) The present status of cathode luminescence as a tool in sedimentology. *Minerals Sci. Engng.* 10, (2), 73–100
- Pal'yanov Yu N, Malinovskyf IYu, Borzdov YuM, Khokhryakov AF, Chepurov AI, Godovikov AA, Sobolev NV (1990) Use of the “split sphere” apparatus for growing large diamond crystals without the use of a hydrolic press. *Doklady Akademii Nauk SSR, Earth Science Section*, 315, No. 5, 1221–1224

- Pochettino A (1913) Über die Lumineszenzerscheinungen in Kristallen. *Z. Kryst.* 51, 113–131
- Ponahlo J (1988) Quantitative cathodoluminescence – a modern approach to gemstone recognition. *J. Gemm.* 21, 3, 182–193
- Ponahlo J (1989) Mikrospektralphotometrie der Edelstein-Kathodolumineszenz. *Z. Dt. Gemmol. Ges.* 38, Nr.2/3, 63–84
- Ponahlo J (1990) Kathodolumineszenz- und Absorptionsspektren gelber Saphire. *Z. Dt. Gemmol. Ges.* 39, Nr.4, 225–228
- Ponahlo J (1992) Cathodoluminescence (CL) and CL spectra of De Beers' experimental synthetic diamonds. *J. Gemm.*, 23, No.1, 3–17
- Ponahlo J (1993a) Kathodolumineszenz (KL) und KL-Spektren von Edelsteinen (Ausgewählte Beispiele), Teil I. *Z. Dt. Gemmol. Ges.* 42, Nr.2/3, 101–113
- Ponahlo J (1993b) Kathodolumineszenz (KL) und KL-Spektren von Edelsteinen (Ausgewählte Beispiele), Teil II. *Z. Dt. Gemmol. Ges.* 42, Nr.4, 149–162
- Ponahlo J (1996) Cathodoluminescence: A fast, non-destructive method to distinguish between natural jadeite, dyed jadeite and dyed quartz simulants. *JewelSiam* April-May, 60–65
- Ponahlo J, Brandstätter F (1997) The cathodoluminescence (CL) of jade and its simulants. Poster session at the 26th International Gemmological Conference, Oberhambach, Germany
- Ponahlo J, Haubner R, Lux B (1994) Cathodoluminescence (CL) and CL spectra of microwave plasma-enhanced CVD Diamond. *Microchimica Acta*, 116, 143–156
- Ponahlo J, Koroschetz T (1985) Quantitative Kathodolumineszenz – ein neues Verfahren zur Unterscheidung echter von synthetischen Smaragden und Rubinen. *Z. Dt. Gemmol. Ges.* 34, Nr.3/4, 132–142
- Robins LH, Cook LP, Farabaugh EN, Feldmann A (1989) Cathodoluminescence of defects in diamond films and particles grown by hot-filament chemical-vapour deposition. *Phys. Rev. B* 39, 18, 13367–13377
- Shida J (1997) Characteristics of cathodoluminescence for yellow diamonds of various types. 26th International Gemmological Conference, Oberhambach, Germany
- Shigley JE, Fritsch E, Koivula JI, Sobolev NV, Malinovsky IY, Pal'yanov YA (1993) The gemological properties of Russian gem-quality synthetic yellow diamonds. *Gems & Gemology*, 29, No. 4, 228–247
- Shigley JE, Fritsch E, Reinitz I, Moses TM (1995) A chart for the separation of natural and synthetic diamonds. *Gems & Gemology*, 31, No. 4, 256–264
- Shigley JE, Moses TE, Reinitz I, Elen S, McClure SF, Fritsch E (1997) Gemological properties of near-colorless synthetic diamonds. *Gems & Gemology*, 33, No.1, 42–53
- Sippel RF (1965) Simple device for luminescence petrography. *Rev. scient. Instrum.* 36, II, 1556–1558
- Suzuki S, Lang AR (1976) Internal structures of natural diamonds revealing mixed-habit growth. *Diamond Research* 1976, 39–47. Daniel P (ed.), Industrial Diamond Information Bureau, Ascot, England
- Takayama M (1986) Mode of occurrence and significance of jadeite in the Kamuikotan metamorphic rocks, Hokkaido, Japan. *J. metamorphic Geol.* 4, 445–454
- Tarashchan AN, Serebrennikov A, Platonov AN (1973) Features of lead ions luminescence in amazonite, in: *Constitution and Properties of Minerals* 7, 106–111
- Tarashchan AN (1978) Luminescence of minerals, *naukova dumka*, Kiev
- Telfer DJ, Walker G (1975) Optical detection of Fe³⁺ in lunar plagioclase. *Nature*, 258, 694–695
- Telfer DJ, Walker G (1978) Ligand field bands Mn²⁺ and Fe³⁺ luminescence centres and their site occupancy in plagioclase feldspars. *Modern Geology*, 6, 199–210
- Vishnevsky AS (1975) Sectorial structure and laminar growth of synthetic diamond crystals. *J. Cryst. Growth* 29, 296–300
- Walker G (1983) Luminescence centres in minerals. *Chemistry in Britain*, 19, 824–831
- Walker G (1985) Ch.4 in « *Chemical Bonding and Spectroscopy in Mineral Chemistry* » (ed. Berry FL and Vaughan DJ), Chapman Hall, London, 103–140
- Webster R (1983) *Gems*. Butterworth, London, 4th rev. ed

- Welbourn CM, Rooney M-LT, Evans DJF (1989) A study of diamonds of cube and cube-related shape from the Jwaneng mine. *J. Cryst. Growth*, 94, 229–252
- Welbourn CM, Cooper M, Spear PM (1996) De Beers natural versus synthetic diamond verification instruments. *Gems & Gemology*, 32, No. 3, 156–169
- Woods GS, Lang AR (1975) Cathodoluminescence, optical absorption and X-ray topographic studies of synthetic diamonds. *J. Cryst. Growth* 28, 215–226
- Wojtowicz AJ, Lempicki A (1990) Cr³⁺ in kyanite – a new mechanism of thermally enhanced E decay. *J. Lumin.*, 46, 271–276

Subject Index

A

- A centers 369
- absorption of CL
 - factor 121
 - correction 68
- acceptors 64
- activators
- activity ratios 275
 - carbonate 272, 290
 - Fe³⁺ as CL activator 256
 - feldspar 250
 - nature of 5
 - quantitative analysis of activator elements 331
 - self-activating (*see* self activated) 131, 133, 143
 - self-quenching at high activator concentration 345
- adularia 264
- Al³⁺, substitution of Al³⁺ for Si⁴⁺ 251
- alexandrite 481
 - CL spectra 484
- albite 262
- algae 319
- alkali feldspar, paramagnetic centers 248
- alkali-compensated aluminium centres 31
- amazonites 264, 490, 491, 495
 - polished 491
 - rough 491
- amorphous
 - silica 51
 - silicon dioxide 197, 208
 - - CL emissions from ultrapure amorphous and crystalline silicon dioxide 208
 - - extrinsic and intrinsic CL from crystalline and amorphous silicon dioxide polymorphs 197
 - SiO₂ 194, 195, 207
- analysis / analytical
 - analytical electron microscopy 62
 - high resolution spectral analysis of Mn²⁺ in sedimentary calcite 331–356
 - image analysis 470
 - microanalysis (*see there*) 115, 194
 - quantitative
 - - CL analysis 104, 331–356
 - - REE analysis 351
 - PIXE (proton-induced X-ray emission) analyses 274, 308, 317, 320, 333, 352
 - SHRIMP analyses 417, 434, 442, 446
- anhydrite 129–132, 135, 136
- annealing of luminescence 424
- anorthite 257
- anorthoclase 258, 490, 495
- apatite 3, 130
 - Fluorapatite 154
 - chlorapatite 129
 - Hydroxylapatite 132
- applications 12
 - paleoenvironmental 303
 - paleontological 303
- applied geosciences, CL in 457–477
- aragonite 2, 46, 47, 305, 312
 - CL of aragonite samples 47
 - lock-in amplifier recorded CL spectra from Mn and Fe doped aragonite 48
 - luminescence of 305
 - Mn²⁺ activation in yellow-green luminescing biogenic aragonite 317
- archaeological materials 457
- artefacts, interpretation of CL images 430
- ash, lignite fly ashes 458
- atomic force micrograph 217
- authigenic
 - feldspars 249
 - phases 234
 - quartz 226

B

- back-calculation of fluid compositions 278, 291
- back-scattered electron and CL imaging 439
- baddeleyite 426
- Ba-feldspar, Cl emission of 254
- band(s)
 - band gap, E_g 63
 - component bands 44
 - conduction band electrons 63
 - deformation bands 235
 - distortion of band structure 424
 - Fe^{3+} emission band in feldspars 26
 - feldspars, CL emission bands 265
 - valence band electrons 63
 - wavelength dependence of the Mn emission bands in carbonates 46
- beam
 - currents 172
 - electrons 61
 - sample heating, beam-induced 199
 - spectra irradiated by an electron beam and proton beam 348
 - voltages 172
- biogenic carbonates 303–329
- blue-violet luminescing albite, Cl emission spectrum of 262
- brachiopod shells 318
- brecciation 13
- brittle deformation 225–243
- broad
 - emission 131
 - peaks 71
- BSE emission / imaging 62, 416, 419, 420, 447
 - internal structures 420
- bulk solution disequilibrium 281, 292
 - partitioning 281
- C**
- Ca / calcium
 - activity of calcium and salinity gradients 295
 - calcic plagioclases 256
 - Mn^{2+} ion in Ca and Mg position 337
 - calcite 2, 25, 44, 129, 130, 132, 135, 136, 305, 331–356
 - carbonate diagenesis 273, 322
 - CL emission spectrum of Mn^{2+} in calcite 25, 315
 - CL micrographs 355
 - CL spectroscopy 342
 - of calcitic oysters 315
 - fields of CL in calcite and dolomite 276
 - high resolution spectral analysis of Mn^{2+} in sedimentary calcite 331–356
 - - Dy^{3+} -activated 350
 - - REE 349
 - - Sm^{3+} -activated 350
 - - Mg-calcite 335, 336
 - - Mn^{2+} and Cr^{3+} in spodumene 37
 - - Mn^{2+} activation
 - - in calcite and dolomite 334
 - - in orange luminescing biogenic calcite 315
 - - regenerative 312
 - - saturation states 287
- calibration 90, 167
 - transmission function calibration 9, 167
 - wavelength 9, 90, 168
- californites 492, 495, 496
- camera, CCD 85
- capture
 - electrons 10
 - large capture cross section for emission 48
- carbonate 46, 271–301, 303–329
 - diagenesis 271–301, 322
 - - activators 272, 290
 - - CL in carbonate, scale dependent 296
 - - CL zonation 278
 - - closed system diagenesis 284
 - - growth rates 291, 292
 - - quenchers 272, 290
 - - REE 272, 291
 - - saturation states 287
 - - sensitizers 272, 275, 290
 - sedimentary calcite 334
 - shells 303–329
 - - biochemical vs diagenetic process 303
 - - biogenic 303, 305
 - - CL of micrograph of carbonates 304, 314
 - - Fe^{2+} carbonate 305
 - - fossil shells 313
 - - Mn^{2+} carbonate 305
 - - mollusk shells 313
 - wavelength dependence of the Mn emission bands, different carbonates 46
- cassiterite 2
- cation
 - charge compensating cations 196
 - of luminescence centers in silicates 79
- causes of CL in minerals 23
- CCD camera 85
- Ce^{3+} 140, 143, 249, 260, 275, 347
- cement / cementation
 - quantification of quartz cement volumes 226

- stratigraphy 289, 292
 - - stratigraphic correlations 297
 - syn- and postkinematic cements 237
 - textural detailed cementation and recrystallization 290
 - transverse fractures 233
 - centers
 - A centers 369
 - alkali feldspar, paramagnetic centers 248
 - cation of luminescence centers
 - - in diamonds 362
 - - in silicates 79
 - classification
 - - based on the origin of a center 370
 - - based on type of a center 370
 - Dy³⁺ center 425
 - E₂' center 196
 - non-bridging / non-holding oxygen hole centers 181, 187
 - precursor hydroxyl defect centers 187
 - REE centers 180, 425
 - - luminescence centers in silicates 180
 - cephalopods 316
 - ceramics 457
 - charge trapping mechanisms 120
 - chemiluminescence 1
 - chemistry / chemical
 - chemical species in solution 281
 - of feldspar minerals 247
 - periclase bricks 466
 - physico-chemical conditions of crystal formation 182
 - chlorapatite 129, 131, 132
 - emission spectra of Dy doped-chlorapatite 152
 - chloromelanite 487, 490
 - CL spectra of maw-sit-sit 490
 - chromium-rich spodumene (*see also* spodumene) 25
 - clastic diagenesis 183
 - clay mineral diagenesis 285
 - CLC method - U-Pb geochronology 401-414
 - closed system diagenesis 284
 - Co²⁺ 2
 - quenching effect 187, 345
 - coal combustion 457, 458
 - products 458
 - coating 7
 - cold cathode microscopic equipment / system 5, 174
 - collector 76
 - color prints 171
 - combustion
 - coal 457
 - slags (*see also there*) 457, 458, 461
 - waste 457
 - component bands 44
 - computer-aided image analysis 473
 - concordant ages 410
 - conduction band electrons 63
 - continuous pulsed electron excitation 24
 - copper 181
 - corals 318
 - correction curve for total CL 8
 - corundum, CL spectra 486
 - Cr³⁺ 24, 28, 35, 52, 181, 264
 - CL in applied geosciences 468
 - gemstone identification 484, 495, 496
 - crack-seal microstructure 233
 - cross-cutting relations 239
 - crushing 13
 - crustaceans 319
 - crystals / crystalline
 - crystalline SiO₂ 194
 - feldspar, crystal structure 247, 261
 - growth / growth rate 185, 280
 - hydrothermal alteration 183
 - internal structures of zircon crystals 419
 - physico-chemical conditions of crystal formation 182
 - recrystallization (*see there*) 13, 431, 433
 - silicon dioxide 197, 208
 - - CL emissions from ultrapure amorphous and crystalline silicon dioxide 208
 - - extrinsic and intrinsic CL from crystalline and amorphous silicon dioxide polymorphs 197
 - textural detailed cementation and recrystallization 290
 - U-Pb zircon ages 418
 - zonation of (*see* zoning) 13
 - Cu²⁺ 251
 - current density 43
- D**
- decay
 - radiative and non-radioactive 28
 - short-decay spectra 362
 - times 363
 - deconvolution 44
 - decreases, CL intensity 10
 - defects 194
 - distribution of defects 193
 - halogen vacancy type 52
 - hydrogen 217
 - impurity 63, 211
 - intrinsic 210, 418

- irradiation-induced 195
- mobile defect species, thermal and electro-migration 214
- O⁻ defects 249
- OH⁻ defects 426
- oxygen deficient defects 207
- point defects (*see also there*) 72, 203
- preexisting-induced 195
- radiation-induced 179
- structural 63, 131, 249
- deformation
 - bands 235
 - brittle 225–243
 - sediment compaction, deformation associated 228
- density, current 43
- depth distribution of CL emission 118
- detection
 - limit of quantitative CL 344
 - variations 166
- detrital
 - quartz grain 11, 183–185, 226
 - zircon core 383, 385, 394, 395
- diagenesis / diagenetic processes 8
 - carbonate (*see there*) 271–301
 - clastic 183
 - sandstone 225–243
 - shells, diagenetic evolution of 322
- diamonds 2
 - CL spectra of *Yakutian* diamonds 369
 - gemmology 370
 - gemstone identification 492
 - luminescence centers 362
 - natural 359–371, 480
 - - discrimination of 497
 - pure-type 361
 - synthetic 480
 - - discrimination of 497
- diffraction gratings 43
- diopside 487, 495
- disequilibrium, bulk solution 281, 292
 - partitioning 281
- distribution
 - coefficients 275
 - of defects 193
 - spatial distribution of CL 62
- dolomites 30, 45
 - carbonate diagenesis 273
 - fields of CL in calcite and dolomite 276
 - Mn²⁺ activation in calcite and dolomite 334
- donors 64
 - donor-acceptor pairs (DAP) 70
- dust 457
- Dy
 - Dy-doped zircon spectrum 165
 - emission spectra doped-chlorapatite of Dy 152
 - Sm and Dy in zircon 169
- Dy³⁺ 9, 24, 96, 98, 261, 441
 - calcite 350
 - carbonate diagenesis 274
 - center 425
 - luminescence 449
 - photo-emission 113
 - related CL emission 134
 - spectra of zircon doped with Dy³⁺ 9, 98, 136
- E
- E₂' center 196
- echinoderm tests 318
- eclogite 382
 - CL images of zircons 393
- ecological parameters 312
- eggshells 319
- Eh, pH / Eh changes 289, 295
- elastic scattering 61
- electro and thermal-migration, mobile defect species 214
- electroluminescence 1
- electron(s)
 - analytical electron microscopy 62
 - back scattered electron and CL imaging 439
 - beam 61
 - - spectra irradiation 348
 - capture 10
 - conduction band electrons 63
 - continuous pulsed electron excitation 24
 - electron beam / electron beam energy 43
 - electron-hole
 - - pairs 64
 - - recombination 53
 - electron-solid interactions 61–64
 - energy transitions of inner electrons 274
 - EPMA (electron probe micro-analyser) 59
 - pulsed excitation 24
 - valence band electrons 63
- emeralds 2, 36
 - gemstone identification 493
 - natural 481, 483
 - synthetic 481, 483
- emission / CL emission spectra 8, 41–57, 97
 - beam, spectra irradiated by an electron beam and proton beam 348
 - broad emission 131

- CL and X-ray data / X-ray emission 63, 110, 114, 116
- - blue-violet luminescing albite 262
- - from α -SiO₂ 202, 206
- - labradorite 258, 260
- - in natural zircon 102
- - from Nd:YAG 50
- - from silicon dioxide polymorphs 204
- - red luminescing albite 256
- - ZnS 80
- CL spectra 50, 80, 102, 132
- of Cr³⁺ in spodumene 37
- depth distribution of CL emission 118
- Dy doped-chlorapatite 152
- emission spectra (*see there*) 41-57, 97, 152
- excitation spectra of Mn²⁺ 34
- extrinsic and intrinsic CL from crystalline and amorphous silicon dioxide polymorphs 197
- Fe³⁺ emission band in feldspars 26
- fluorapatite, natural, emission spectra of 154
- high resolution spectral analysis of Mn²⁺ in sedimentary calcite 331-356
- intrinsic emission 347
- irradiation response spectra 215
- of jadeite 30
- kinetics 212
- large capture cross section for emission 48
- laser-induced luminescence spectra 150
- lock-in amplifier recorded CL spectra from Mn and Fe doped aragonite 48
- luminescence excitation spectra 33, 37
- of Mn²⁺
- - emission 26
- - in spodumene 37
- of NaCl 52, 53
- natural zircon 97
- - problems associated with collection of signals 42
- parallel spectral measurement 84, 93
- peak fitting / peak shape, spectral 69, 105
- phase-tuned spectra 29, 32
- polarised
- - CL emission spectra 31, 249
- - excitation spectra 33
- qualitative interpretation of CL emission 150
- quantitative interpretation of CL emission 151
- raman spectra 417
- rare earth ion emission sites 48
- REE 132
- - shape and position of REE luminescence spectra 261
- resolution 92
- sapphire sample 51, 52
- self-activated emission 133
- shape of CL emission lines 151
- short-decay spectra 362
- spectral acquisition
- - capability 161
- - time 167
- spodumene, luminescence emission spectrum 24
- from ultrapure amorphous and crystalline silicon dioxide 208
- time-resolved spectra 24, 27, 360
- UV, emission in the far UV 427
- Yb²⁺ emission 427
- of zircon doped with Dy³⁺ 9
- energy
- inner electrons, energy transitions 274
- scale 43
- shifts in the transition energies 45
- enstatite 485
- environment / environmental
- conditions 320
- of ion 33
- paleoenvironmental applications 303
- Er³⁺ 96
- Er impurities, natural zircon specimen 98
- erratic luminescence behavior 352
- Eu²⁺ 143, 249, 260, 274
- Eu³⁺ 24, 274
- exciton / excited
- emissions / exciton-like emission spectra 53, 70
- lifetimes, excited state 52
- self-trapped exciton (STE) 32, 71, 181
- experimental factors of CL 59-126
- exposure times in CL photography 172
- extrinsic effects 63
- F
- f-d* transitions 4, 140, 143
- Fe, lock-in amplifier recorded CL spectra from Mn and Fe doped aragonite 48
- Fe²⁺ 2
- carbonate diagenesis 273
- quenching effect 312, 345
- sedimentary calcite 331
- Fe³⁺ 181, 249
- as CL activator 256
- CL in applied geosciences 468
- carbonate shells 305
- emission band in feldspars 26, 254

- gemstone identification 495
- impurities 249
- in plagioclases 257
- feldspar minerals / feldspar(s) 26, 181, 245–270, 472
 - activators 250
 - alkali feldspar 248, 258
 - - paramagnetic centers 248
 - applied geosciences 472
 - authigenic 249
 - Ba-feldspar, Cl emission of 254
 - chemistry 247
 - CL emission bands 265
 - CL micrographs of feldspar samples 266
 - crystal structure 247, 261
 - Fe³⁺ emission band 26, 254
 - group 181
 - lunar 182, 246
 - structural
 - - defects 249
 - - state 257
- f-f* transitions 4, 140
- FI term 68
- fluid
 - back-calculation of fluid compositions 278, 291
 - planes of fluid inclusions 227, 239
 - zircon behaviour in presence of fluids 396
- fluorapatite, natural, emission spectra of 154
- fluorescence spectroscopy 1
 - quantitative X-ray 332
- fluorite 3, 129–136, 485
- flux-growth method 128
- foraminifera tests 318
- forsterite, CL emission spectrum 25–27
 - of Mn²⁺ 25
 - of Ni²⁺ 27
 - synthetic 26
- fossil
 - ghosts 323
 - shells 313
- fracture(s)
 - inherited 230
 - intragranular 227
 - microfracturing 13
 - reservoirs, fractured 225–243
 - - studies 237
 - transcement 233
 - transgranular 233
- G**
 - gabbroic rocks 380, 434
 - gallium 252
 - gas, guide to oil- and gas-field 239
 - gastropods 316
 - Gaussian*
 - components 203, 205
 - de-convolution techniques 31, 44
 - shape 426
 - gemmology 370
 - gemstone 457
 - CL photomicrographs 482, 488
 - identification 479–500
 - geological slices, preparation 43
 - geosciences, CL in applied 457–477
 - glasses 457, 458
 - glass particles 458
 - luminescence properties of glassy spheres 461
 - götzenite 13
 - grain / grain boundaries
 - detrital quartz grain 11, 183–185, 226
 - internal grain structure 470
 - interpenetrating 231
 - MgO grains, CL spectra 468
 - recrystallization grain-boundary 13
 - single-grain 416
 - sutured 230
 - zircon grain 95
 - granite intrusions 434
 - granitoid / granitic / granulitic rocks 374, 380, 405, 434
 - granular, intragranular fractures 227
 - grossular garnets 35, 36
 - groundwater 286
 - growth
 - carbonate diagenesis, growth rates 291, 292
 - crystal growth 185
 - flux-growth method 128
 - - REE 128
 - - zircon 128
 - oscillatory zoning 419
 - quartz overgrowth 11
 - zoning 13, 186, 429
 - guide to oil- and gas-field 239
- H**
 - halogen vacancy type defects 52
 - healed plane, microfractured 13
 - heating effects 55
 - beam-induced sample heating 199
 - into quartz 55
 - high resolution spectral analysis of Mn²⁺ in sedimentary calcite 331–356
 - Ho³⁺ 274
 - hole, electron / hole
 - pairs 64

- recombination 53
- hot cathode CL 6
 - instrument 183
 - microscope 246
- Huang-Rhys* factor 25
- hydrated fused silicon dioxide 200
- hydrocarbon traps 286
- hydrogen defects 217
- hydrogrossular 492, 495, 496
- hydrothermal
 - alteration of crystalline rocks 183
 - method 129
- hydroxylapatite 132
- I
- image / imaging
 - analyses 470
 - artefacts, interpretation of CL images 430
 - CL and BSE imaging 447
 - computer-aided image analysis 473
 - monochromatic 7, 216, 424
 - panchromatic 7, 74, 95, 424, 428, 439
 - scanning CL images from natural zircon 9
 - radiation (*see there*) 14, 54
 - X-ray emission 63
- impurities
 - defects 63, 211
 - Er impurities, natural zircon specimen 98
 - hole on oxygen adjacent to divalent impurity 251
 - manganese 44
 - silicon dioxide polymorphs, substitution of impurity ions 196
 - substitution of impurity ions for silicon 196
 - trace elements 418
 - zircon Dy impurities 98, 136
- industrial raw materials 457
- inelastic scattering 61
- inherited
 - cores 403, 429
 - fractures 230
- instrument response 198
 - total 202
- interpenetrating grain boundaries 231
- intragranular fractures 227
- intramolecular vibrations 71
- intrasectoral zoning 13, 185
- intrinsic
 - defects 210
 - - of lattice 418
 - effects 51, 63
 - emission 347
 - oxygen vacancy centres 51
 - ion
 - environment of ion 33
 - microprobe, U-Pb zircon dating 13, 373-400
 - Mn²⁺ ion 337, 495
 - - in Ca and Mg position 337
 - oxygen ions 50
 - rare earth ion 48, 105, 181
 - - emission sites 48
 - substitution of impurity ions for silicon 196
 - Ti³⁺ ions 52
 - transition-metal ion centres 32
 - trivalent rare-earth ions 28
- ionoluminescence 1, 170, 349
- IR domain 8
- irradiation / irradiation-induced
 - defects 195
 - response spectra 215
 - time 205
 - zone of past α -irradiation 14
- J
- jadeite, CL emission spectra 30, 486, 494
- K
- K⁺-Na⁺ substitution 258
- kaolinite 472
- kosmochlor 487
- K-ratio determination 108
- kyanite 494
- L
- labradorite, CL emission spectra 258, 260
- laser
 - CL spectra from Nd:YAG 50
 - excitation 24
 - luminescence spectra, laser-induced 150
 - microluminescence laser-induced (LIL) 3
 - UV laser luminescence spectra 360
- lattice
 - coordination 274
 - intrinsic defects of 418
- lazurite 494
- lead 2, 181
- lifetime
 - excited state lifetimes 52
 - luminescence 27
- lignite
 - fly ashes 458
 - slags from lignite combustion 461
- limestone standard 170
- location of trace elements 14

- lock-in amplifier
 - detector 47
 - recorded CL spectra from Mn and Fe doped aragonite 48
- luminescence
 - annealing 424
 - of aragonite 305
 - blue-violet luminescing albite, Cl emission spectrum of 262
 - bright blue luminescing orthoclase, Cl emission of 252
 - of calcite 305
 - cation of luminescence centers
 - - in diamonds 362
 - - in silicates centers 305
 - chemiluminescence 1
 - centres in minerals 23-40
 - electroluminescence 1
 - erratic luminescence behavior 352
 - excitation spectra 33, 37
 - extrinsic CL emissions from crystalline and amorphous silicon dioxide polymorphs 197
 - glassy spheres, luminescence properties of 461
 - green luminescing lunar plagioclases, CL emission of 255
 - intrinsic 197, 273
 - - CL emissions from crystalline and amorphous silicon dioxide polymorphs 197
 - ionoluminescence 1, 170, 349
 - laser-induced luminescence spectra 150
 - lifetime 27, 52
 - mechanisms of luminescence in zircon 424
 - Mn²⁺ activation
 - - in orange luminescing biogenic calcite 315
 - - yellow-green luminescing biogenic aragonite 317
 - microluminescence (*see there*) 3
 - microscopy and spectroscopy 161-175
 - photoluminescence 1, 49, 273, 359
 - quenching 45
 - radioluminescence 1, 45
 - REE, shape and position of REE luminescence spectra 261
 - red luminescing albite, Cl emission spectrum of 256
 - self-activated luminescence 131
 - spodumene (*see there*) 24-26, 37
 - thermoluminescence 1, 45
 - triboluminescence 1
- lunar feldspars 182
 - plagioclases 246, 255
- M
- manganese impurities 44
- magmatic
 - zircons 380-383
 - - CL images of magmatically zoned zircons 381, 382
 - zoning 393
- magnesite 335, 336
- matrix effects 67, 113
- maw-sit-sit, CL spectra 490
- metamictization 425, 432
- metamorphic
 - fluids 396
 - veins 388, 390
 - zircon domains 385, 387, 395, 396
- metasedimentary basement 374
- metasomatism, zircons affected by 391
- meteorite impacts 186
- Mg-calcite 335, 336
- MgO grains, CL spectra 468
- microanalysis, quantitative 115, 194
 - X-ray microanalysis 115
- microcline 258
- microfracturing 13
 - healed plane, microfractured 13
- micrograph
 - atomic force micrograph 217
 - CL micrographs
 - - applied geosciences 462
 - - of calcite 355
 - - of carbonates 304, 314
 - - of feldspar samples 266
 - - of quartz samples 184
 - - of zircon 95, 381-446
 - - of gemstones 482, 488
- microluminescence, laser induced (LIL) 3
- microscope / CL microscopy 74-76, 161-175
 - analytical electron microscopy 62
 - cold cathode microscopic equipment / system 5, 174
 - collectors 76
 - hot cathode CL microscope 246
 - microscopy and spectroscopy 161-175, 332-334
 - optical 85
 - scanned 74, 86, 88, 89
- migration, thermal and electro-migration of mobile defect species 214
- mineral(s)
 - generations 12
 - luminescence centres in minerals 23-40

- quantification of mineral phases 7, 182, 470
 - species, quantitative separation 12
 - synthetic
 - - doped minerals 127
 - - REE-bearing minerals 128
 - textural relationship between minerals 13
 - Mn concentrations 337
 - Mn²⁺ 2, 181, 249, 252, 331
 - activation in
 - - calcite and dolomite 334
 - - orange luminescing biogenic calcite 315
 - - yellow-green luminescing biogenic aragonite 317
 - carbonate
 - - diagenesis 273
 - - shells 305
 - centres 28
 - CL in applied geosciences 468
 - CL emission spectrum of Mn²⁺ 25, 26
 - in aragonite 317
 - - in calcite 25, 315, 342-343
 - - in synthetic forsterite 26
 - excitation spectra of Mn²⁺ 34
 - - lock-in amplifier recorded CL spectra from Mn and Fe doped aragonite 48
 - gemstone identification 496
 - high resolution spectral analysis of Mn²⁺ in sedimentary calcite 331-356
 - Mg-calcite 335, 336
 - Mn²⁺ ion in Ca and Mg position 337
 - quenchers 275
 - sedimentary calcite 334
 - sensitizers of 275
 - transition-metal ion Mn²⁺ 179
 - wavelength dependence of the Mn emission bands, different carbonates 46
 - modulation frequency 47
 - molecular species 71
 - intramolecular vibrations 71
 - mollusk shells 313
 - monochromatic image 7, 216, 424
 - multiplet 136, 162, 169
- N**
- NaCl 52, 53
 - CL spectra of 53
 - nature of activators 5
 - Nd:YAG (*see also* laser) 50
 - CL spectra from Nd:YAG 50
 - Nd³⁺ 261
 - neomorphism 322
 - Ni²⁺ 2
 - CL in applied geosciences 468
 - CL emission spectrum of Ni²⁺ 27
 - quenching effect 345
 - noise levels 167
 - non-radiative decay 28
- O**
- O⁻ defects 249
 - OH⁻ defects 426
 - oil, guide to oil- and gas-field 239
 - opal 210
 - operating conditions 130
 - ophiolitic sequence 374
 - optical
 - CL microscopy 5, 85
 - reflection 77
 - organic matter and clay mineral diagenesis 285
 - organisms, CL observations on recent organisms 312
 - orthoclase 252, 258, 264
 - anorthoclase 258, 490, 495
 - bright blue luminescing orthoclase, CL emission of 252
 - orthogneisses, polymetamorphic 405
 - oscillatory zoning 13, 185, 282, 380, 419
 - oxygen 10, 50
 - deficient defects 207
 - diffusion coefficient 215
 - enrichment of surface regions 216
 - hole on oxygen adjacent to divalent impurity 251
 - intrinsic oxygen vacancy centres 51
 - ions 50
 - non-bridging / non-holding oxygen hole centers 181, 187
 - reabsorption lines of molecular oxygen 367
 - vacancy 10, 179
- P**
- paleoenvironmental applications 303
 - paleontological applications 303
 - panchromatic CL image 7, 74, 95, 424, 428, 439
 - scanning CL image of natural zircon 95
 - past α -irradiation, zone of 14
 - Pb²⁺ 2, 261, 275, 347
 - peak
 - CL peak profile 106
 - spectral peak fitting 105
 - relative peak heights 168
 - shape of CL emission 69
 - precursor hydroxyl defect centers 187
 - periclase bricks 466

- thermal and chemical behavior 469
 - petrology
 - metamorphic 183
 - sandstone 226
 - pH / Eh 289, 295
 - changes 289
 - phase-tuned spectra 29, 32
 - phosphorescence 1
 - phosphorus 110
 - photoemission, Dy³⁺ 113
 - photographic recording 161, 170
 - photoluminescence 1, 49, 273, 359
 - photomicrographs
 - of gemstones 482, 488
 - of quartz samples 184
 - photomultiplier 43, 130
 - CL detectors 225
 - physico-chemical conditions of crystal formation 182
 - PIXE (proton-induced X-ray emission)
 - analyses 274, 308, 317, 320, 333, 352
 - Mn 317
 - sedimentary calcite 333, 352
 - plagioclases 181, 255, 256
 - calcic 256
 - Fe³⁺ 257
 - green luminescing lunar plagioclases, CL emission of 255
 - planes of fluid inclusions 227, 239
 - point defects 72
 - intrinsic 193
 - polishing damage 49
 - polarization 77, 111
 - CL emission 10, 249
 - degree of 209
 - effect 96, 136
 - polishing, mechanical 121
 - polymetamorphic rocks, zircon dating of 403, 411
 - powellite 129, 132
 - precipitation method 129
 - preparation of CL geological slices 43
 - pressure solution 232
 - problems associated with collection of signals 42
 - program, standard 161
 - proton-beam, spectra irradiation 348
 - proton-induced X-ray emission (*see* PIXE) 274, 308, 317, 320, 333, 352
 - provenance indicators 226
 - pulsed electron excitation 24
- Q**
- qualitative interpretation of CL emission 150
 - quantification of mineral phases 7, 182, 470
 - quartz 2, 11, 31, 32
 - authigenic 226
 - CL zoning in quartz 226
 - detrital quartz grain 11, 226
 - heating effects 55
 - phase-tuned spectra CL, spectra of quartz 32
 - quantification of quartz cement volumes 226
 - quartz overgrowth 11
 - synthetic, high purity quartz 200
 - quenchers / quenching 3, 15, 256, 272, 275, 312, 345, 424
 - carbonate diagenesis 272, 290
 - centers 28
 - Fe²⁺ 312, 345
 - Mn²⁺ 275
 - self-quenching (*see there*) 345, 424
 - thermal quenching 345
- R**
- radiation
 - damage 14, 54, 186
 - defects, radiation-induced 179
 - irradiation (*see there*) 14, 195, 215
 - radiative
 - decay 28
 - recombination
 - - centres 104
 - - mechanism 64
 - - of STE 207
 - transitions in zircon 426
 - radioluminescence 1, 45
 - radiolysis 72
 - raman
 - microprobe 442
 - spectra 417
 - ramsayite 13
 - rare-earth
 - element (*see* REE)
 - ion exhibits 105
 - trivalent rare-earth ions 28
 - reciprocity correction 174
 - recombination
 - centre (RC) 65
 - electron-hole recombination 53
 - radiative recombination mechanism 64
 - recrystallization 290
 - grain-boundary 13
 - solid-state recrystallization 431

- thermal 433, 449
- red luminescing albite, CL emission spectrum of 256
- redox-potential, changes in 284
- REE (rare-earth element) 69, 96, 97, 127, 143, 260, 261, 272, 305, 349, 350, 418
 - calcite 351
 - carbonate diagenesis 272, 291
 - CL spectra / CL emission 132, 137
 - feldspar 260
 - flux-growth method 128
 - quantitative REE analysis 350
 - sedimentary calcite 349
 - self-activated 143
 - shape and position of REE luminescence spectra 261
 - silicates, REE luminescence centers 180
 - synthetic REE-bearing minerals 128
 - U-Pb zircon ages 418
- refractory materials 457, 466
- reliable CL intensities 115
- resolution / resolution of CL 166
 - spatial 87, 88
 - spectra 92
- R-lines 36
- ruby/rubies 2, 52, 485, 494

- S
- salinity gradients 295
- sandstone diagenesis 225–243
 - petrology, sandstone 226
- sanidine 258
- sapphires 2, 52, 485, 494
 - CL spectra, sapphire sample 51, 52
- scale dependent, CL in carbonate 296
- scan / scanned / scanning CL images 225–243
 - microscopy, scanned CL 74, 86, 88, 89
 - natural zircon 99
 - panchromatic scanning, of natural zircon 95
- scattering 61
 - elastic 61
 - inelastic 61
- scheelite 129–135
- sectoral zoning 13, 185, 283, 294, 380, 429, 440
- sediment
 - compaction, deformation associated 228
 - metasedimentary basement 374
- self-activated
 - emission 133
 - luminescence 131
 - REE 143
 - self-quenching 345, 424
 - at high activator concentration 345
- self-trapped exciton (STE) 32, 71, 181
- sensitizers / sensitizer elements 2, 347
 - carbonate diagenesis 272, 275, 290
 - of Mn²⁺ 275
- separation, quantitative of mineral species 12
- sharp lines 24, 69
- shells
 - brachiopod 318
 - carbonate (*see there*) 303–329
 - diagenetic evolution of 322
 - eggshells 319
 - fossil 313
 - mollusk 313
 - repair of 319
- SHRIMP (sensitive high resolution ion microprobes) 377, 416
 - age determinations 388
 - analyses 417, 434, 442, 446
- Si⁴⁺, substitution of Al³⁺ for Si⁴⁺ 251
- signals
 - absolute signal intensities 169
 - problems associated with collection of signals 42
- silica / silicates 177–191
 - amorphous 51
 - cation of luminescence centers in silicates 179
 - cause of CL in silicates 179
 - heating effects 55
 - REE luminescence centers in silicates 180
- silicon dioxide polymorphs 193–224
 - CL spectra 204
 - - CL emissions from ultrapure amorphous and crystalline silicon dioxide 208
 - - extrinsic and intrinsic CL from crystalline and amorphous silicon dioxide polymorphs 197
 - dioxide bridging Si-O bond precursor 213
 - hydrated fused silicon dioxide 200
 - nonbridging hydroxyl Si-OH precursor 213
 - silicon structure 194
 - substitution of impurity ions 196
- SIMS, sedimentary calcite 333
- single zircon dating 401–414
- Si-O bonds 179
 - dioxide bridging Si-O bond precursor 213
- SiO₂
 - amorphous 194, 195, 207
 - CL spectra from α -SiO₂ 202, 206, 216
 - crystalline 194

- stoichiometry of SiO₂ polymorphs 201
- Si-OH precursor, nonbridging hydroxyl 213
- slags combustion 457, 458
- lignite combustion 461
- slit width 93
- Sm in zircon 169
- Sm²⁺ 140, 143
- Sm³⁺ 24, 260, 261, 274
- calcite 350
- Sn²⁺ dopants 54
- solid
 - concentration of trace elements in solids 278
 - electron-solid interactions 61-64
 - solid-state recrystallization 431
- sorting, diamonds 370
- spatial
 - distribution of CL 62
 - resolution of CL 87, 88
- specimen
 - charging 199
- spectra / spectral field of CL (*see* emission / CL emission spectra)
- spectrometer / CL spectrometer 82-84, 130
- parallel CL spectrometer / parallel spectral measurement 84, 93
- sequential CL spectrometer 82
- spectroscopy (*see also* emission spectra)
 - ionoluminescence (IL) spectroscopy 349
 - luminescence 161-175
 - microscopy and spectroscopy 161-175, 332-334
 - quantitative X-ray fluorescence spectroscopy 332
 - spectroscopic features 107
 - sedimentary calcite 333
- spinel 485
- spodumene, luminescence emission spectrum 24-26, 36, 485
- chromium-rich spodumene 25
- Mn²⁺ and Cr³⁺ in spodumene 37
- STE (self-trapped exciton) 32, 71, 181
- radiative recombination STE 207
- stoichiometry of SiO₂ polymorphs 201
- Stokes shift 33
- structural
 - defects 63, 131
 - materials 457
- surface
 - charging effects 73
 - thermal conductivity of the surface 54
- sutured grain boundaries 230
- symmetry of site and valence of trace element 5
- synthetic
 - doped minerals 127
 - forsterite 26
 - REE-bearing minerals 128
 - synthetic, high purity quartz 200
- system
 - response / response curve 8, 90-92
 - wavelength dispersive system 43
- T
- Tb³⁺ 132, 261, 274
- technical products 463
- temperature
 - low temperatures of transitions 25
 - sample temperature 43
- textural relationship between minerals 13
- thallium 2, 181
- thermal
 - conductivity of the surface 54
 - mobile defect species, thermal and electro-migration 214
 - periclase bricks 466
 - recrystallization 433, 449
- thermoluminescence 1, 45
- Ti³⁺ 52, 181, 251
- impurities 249, 426
- Ti⁴⁺ 181
- time-resolved spectra 24, 27, 360
- TIMS, single zircon dating 401-414
- tin 181
- Tl 249, 261
- Tm³⁺ 135
- topaz 485
- trace elements
 - concentration of trace elements in solids 278
 - impurities 418
 - location of 14
- transgranular and transcement fractures 233
- transient defect effects 53
- transitions 4
 - energy transitions of inner electrons 274
 - *f-d* transitions 4, 140, 143
 - *f-f* transitions 4, 140
 - low temperatures of 25
 - shifts in the transition energies 45
 - transition-metal(s) 69, 71
 - - ion centres 32
 - - ion Mn²⁺ 179, 181
 - - ion Ti²⁺ 181
 - - ion Ti³⁺ 181
 - - UO₂²⁺-complex 181

- transmission
– calibration, transmission function 167
– and detection variations 166
triboluminescence 1
trivalent rare-earth ions 28
- U**
U-abundance 377
U-contents 377, 391–393
UO₂²⁺-complex 181
U-Pb zircon dating
– dating 415–455
– CLC method – U-Pb geochronology 401–414
– by ion microprobe 13, 373–400
– – sample preparation 376
– isotopic signatures of zircons 401, 431
UV
– domain 8
– emission in the far UV 427
– laser luminescence spectra 360
- V**
Valence
– band electrons 63
– changing 10
– of trace elements 5
visible domain 8
vitrification 186
volume
– loss 232
– quantification of quartz cement volumes 226
- W**
waste combustion 457
wavelength 7, 43, 46
– accuracy 166
– calibration 90, 168
– dependence of the Mn emission bands, different carbonates 46
– dispersive systems 43
– conversion to energy scale 43
– shift 46
wöhlerite 3
wollastonite 181
Wood's anomalies 81
- X**
X-ray
– CL and X-ray data / X-ray emission 63, 110, 114, 116
– proton-induced X-ray emission (*see also* PIXE) 274, 317, 320, 333, 352
– quantitative X-ray
– – fluorescence spectroscopy 332
– – microanalysis 115
- Y**
Y contents 377
Yb²⁺ 140
– emission 427
Yb³⁺ 140
- Z**
zero-phonon line (ZPL) 25, 69, 361
zircon / natural zircon 2, 128, 130, 132, 136, 162, 373, 385
– metasomatism 391
– CL emission spectra 97, 102, 421–423, 440
– CL photographs 408
– detrital zircon core 383, 385, 394, 395
– Dy impurities 98, 136
– Dy-doped zircon spectrum 165
– eclogite 393
– Er impurities 98
– fluids, zircon behaviour in presence of 396
– flux-growth method 128
– grain 95
– inherited cores in zircons 429
– internal structures 403, 418, 419, 429, 439
– magmatic 380
– mechanisms of luminescence in zircon 424
– metamorphic zircon domains 385, 387, 395, 396
– metasedimentary rock, CL images of 385
– monochromatic CL imaging 424
– morphology 436–439, 446
– panchromatic scanning CL image 95, 424
– polymetamorphic rocks, zircon dating of 403, 411
– radiative transitions in zircon 426
– scanning CL images 99
– single zircon dating 401–414
– spectra of doped with Dy³⁺ 9, 98
– U-Pb zircon
– – dating 415–455
– – dating by ion microprobe 13, 373–400, 415–455
– – isotopic signatures of zircons 401
ZnS
– CL spectra from 80
– natural ZnS crystals 120
zonation of crystals / zone / zoning 13
– CL zoning in quartz 226
– CL zonation in diagenetic carbonate 278
– concentric zoning 282, 292

-
- and correlation element stratigraphy 292
 - crystals, zonation of (*see there*) 13
 - cyclic zoning 292
 - growth zoning 13, 86, 429
 - intrasectorial zoning 13, 283
 - magmatic zoning 393
 - oscillatory zoning 13, 282, 380
 - past α -irradiation, zone of 14
 - sectorial zoning 13, 185, 280, 283, 294, 380, 429, 440